STUDIA UNIVERSITATIS
BABEŞ-BOLYAI

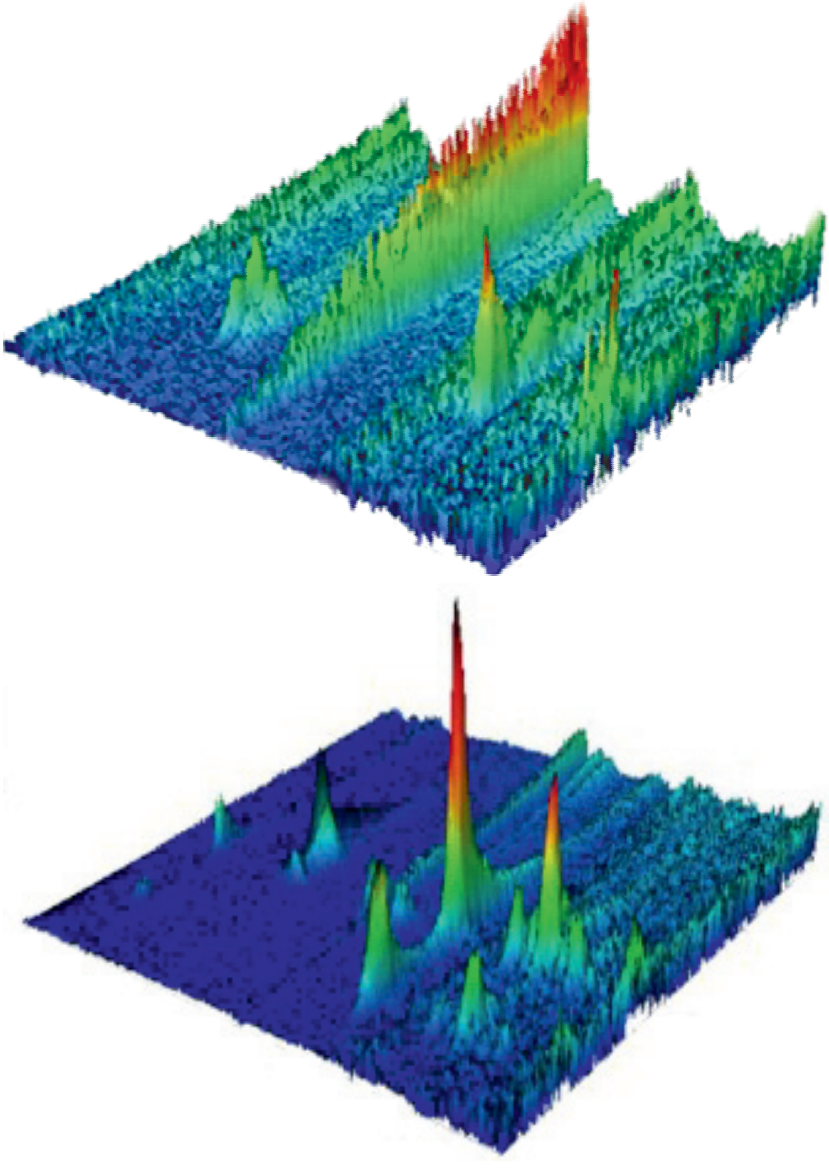

CHEMIA

2/2015
Tom I

STUDIA
UNIVERSITATIS BABEŞ-BOLYAI

CHEMIA

2/2015
Tom I

EDITORIAL BOARD OF
STUDIA UNIVERSITATIS BABEŞ-BOLYAI CHEMIA

http://chem.ubbcluj.ro/~studiachemia/; studiachemia@chem.ubbcluj.ro
http://www.studia.ubbcluj.ro/serii/chemia/index_en.html

YEAR **Volume 60 (LX) 2015**
MONTH **JUNE**
ISSUE **2, Tom I**

S T U D I A
UNIVERSITATIS BABEŞ-BOLYAI CHEMIA

2,
Tom I

STUDIA UBB EDITORIAL OFFICE: B.P. Hasdeu no. 51, 400371 Cluj-Napoca, Romania, Phone + 40 264 405352

CUPRINS – CONTENT – SOMMAIRE – INHALT

Studia Universitatis Babes-Bolyai Chemia has been selected for coverage in Thomson Reuters products and custom information services. Beginning with V. 53 (1) 2008, this publication is indexed and abstracted in the following:

- Science Citation Index Expanded (also known as SciSearch®)
- Chemistry Citation Index®
- Journal Citation Reports/Science Edition

STUDIA UBB CHEMIA, LX, 2, Tom I, 2015 (p. 7-14)
(RECOMMENDED CITATION)

CONCISE SYNTHESIS OF SOME (4-AMINOPHENOXY)ALKANOIC ACIDS BASED ON PARACETAMOL

CRISTINA MORAR[a], LAVINIA COST[a], MIRCEA DARABANTU[a,*]

ABSTRACT. Starting from *N*-(4-hydroxyphenyl)acetamide (*Paracetamol*), a three steps synthesis of (4-aminophenoxy)acetic acid and 4-(4-aminophenoxy) butyric acid is comparatively discussed.

Keywords: *(4-aminophenoxy)acetic acid, 4-(4-aminophenoxy)butyric acid, Williamson etherification, acidolysis*

INTRODUCTION

(4-Aminophenoxy)acetic acid **1a** and 4-(4-aminophenoxy)butyric acid **1b** (Scheme 1) are known compounds as early as for the end of XIX-century and the starting of XX-century [1-4].

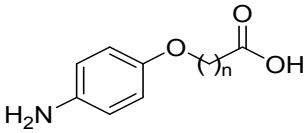

1a (n=1), **1b** (n=3)

Scheme 1

The first reported synthesis of (4-aminophenoxy)acetic acid consisted of reduction of its corresponding nitro precursor, the last one being available from Williamson etherification of 4-nitrophenol with monochloroacetic acid in alkaline conditions [1-3]. Closer to our days, the same etherification strategy still was actual by using, in the key step, *N*-(4-hydroxyphenyl)acetamide (*Paracetamol*) in reaction with monochloroacetic acid [5, 6] with yields around 60%. However, the expected soft nucleophilicity of the conjugated *p*-substituted phenoxides[1] prompted other authors to explore the use of

[a] *Babeş-Bolyai University, Faculty of Chemistry and Chemical Engineering, Department of Chemistry, 11 Arany Janos St., RO-400028, Cluj-Napoca, Romania.*
[*] *Corresponding author: darab@chem.ubbcluj.ro*
[1] p*K*a (*Paracetamol*): 9.38; p*K*a (4-nitrophenol): 7.16

bromoacetic acid [7] or of its low alkyl esters against deprotonated forms of *Paracetamol* [8a] or even *p*-nitrophenol [8b]. Overall, the nowadays increased interest in (*N*,*O*-masked) forms of (4-aminophenoxy)acetic acid arises from their bioimpact, i.e. when targeting new analgesic, antipyretic and anti-inflammatory agents [6], new potential antisickling agents [7], bioabsorbable as biocompatible polyurethanes and polyamides for medical [8] devices.

In contrast, there are very few reports concerning the synthesis of 4-(4-aminophenoxy)butyric acid **1b** (Scheme 1) in spite of its first mentioning in the literature in 1917 [4]. Similar to its lower homologue **1a**, **1b** can be obtained by reduction of 4-(4-nitrophenoxy)butyric acid resulted, from the regioselective ring cleavage of γ-butyrolactone upon treatment with sodium 4-nitrophenoxide (Scheme 2) [9a, 9b] or by Williamson etherification of the latter, as reported very recently [9c, 9d].

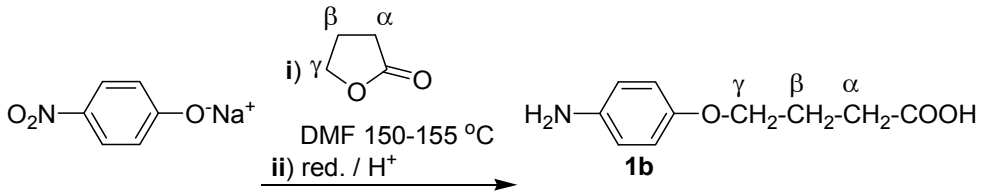

Scheme 2

Lately, the use of **1b** as polyconjugate for delivery of RNA triggers to tumor cells *in vivo* [9c], as intermediate in the synthesis of new anti-*Helicobacter pylori* agents [10] and side-chain component of some cancer inhibitors of the cellular checkpoint kinase Wee1 [11] was reported.

Therefore, the aim of the present preliminary communication is to present a common and concise synthetic pathway towards (4-aminophenoxy)alkanoic acids **1a** and **1b** (Scheme 1) based on a Williamson approach.

RESULTS AND DISCUSSION

The chemistry we performed is resumed in Scheme 3.

(4-Aminophenoxy)acetic acid hydrochloride **3a** was prepared in two steps, **I** and **II**, both inspired from Bezwada's recent Patent [8a]. They consisted of Williamson etherification of *Paracetamol* (**I**, 90% yield against lit. 80% [8a]) followed by acidolysis of the amidoester **2a** (**II**, 92% yield against lit. 77.6% [8a]), hence, an overall yield of 83% (lit. 62%, [8a]). In step **III**, we isolated the free amine **1a** by manipulating its solubility in water in such a way that we avoided contamination with potassium chloride.

In order to access 4-(4-aminophenoxy)butyric acid **1b**, we first planned the ring opening of γ-butyrolactone with the use of sodium phenoxide of *Paracetamol* in similar conditions with those already reported in the case of sodium 4-nitrophenoxide (Scheme 2) [9a]. In our hands no reaction occurred, the starting *N*-(4-hydroxyphenyl)acetamide being recovered. That is, once more we moved our interest towards Williamson

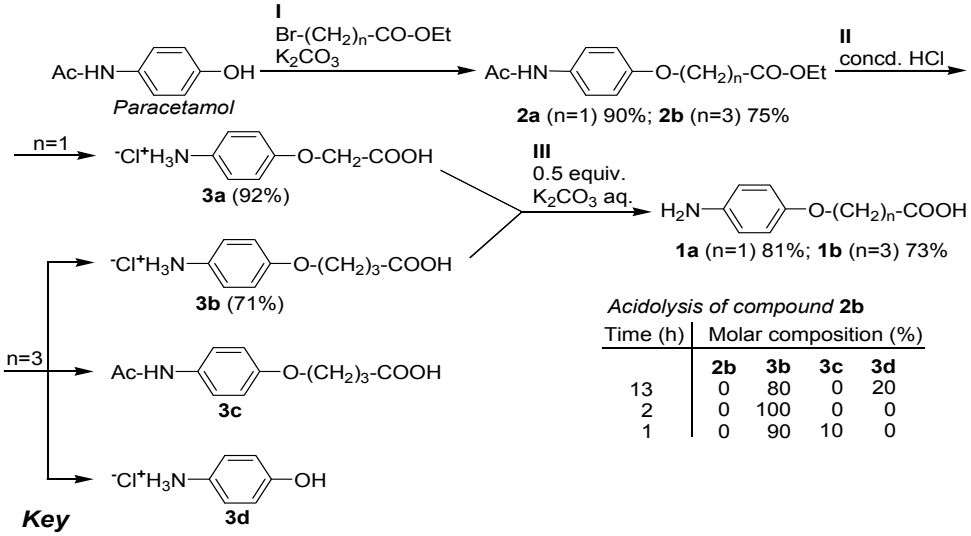

Acidolysis of compound **2b**

Time (h)	Molar composition (%)			
	2b	**3b**	**3c**	**3d**
13	0	80	0	20
2	0	100	0	0
1	0	90	10	0

I (n=1) **2a**: 3.93 equiv. anh. K_2CO_3, 1.36 equiv. ethyl bromoacetate / acetone, 52 ^oC,15 h
I (n=3) **2b**: 3.93 equiv. anh. K_2CO_3, 1.10 equiv. ethyl 4-bromobutyrate / DMF / 70 ^oC, 16 h / r.t., 72 h
II (n=1, 3): 69.0 equiv HCl as aq. soln. 37% / reflux, 13 h (**3a**), 2 h (**3b**)
III (n=1, 3) **1a**, **1b**: 0.50 equiv. K_2CO_3 / H_2O / r.t., 1 h

Scheme 3

methodology. Thus, inspired from the similar reactivity of *N*-(4-hydroxybenzyl)acetamide [10], we obtained (**I**) the amidoester **2b** with good yield[2]. However, acidolysis (**II**) of **2b** carried out in identical conditions as for **2a**, resulted in a crude reaction mixture whose ^1H NMR spectrum revealed, besides formation of the desired **3b**, the existence of the hydrochloride of 4-aminophenol **3d** issued from the acidolysis of the etheric connection (Figure 1). ^1H NMR monitoring of the process showed the reaction reaching completion within 2 h, i.e. in a much shorter time in comparison with **3a** (Scheme 3). As for **1a**, the free amine **1b** was isolate simply (**III**) by modulating its solubility in water against that of potassium chloride. To conclude, the overall yield in the synthesis of **1b** was 39%.

[2] Compound **2b** was previously mentioned by Katsura and co-workers in 2000 (Ref. [10]) with no experimental assignment (synthesis and / or analytical data)

CONCLUSIONS

Starting from *N*-(4-hydroxyphenyl)acetamide, we described a three steps expeditious synthetic pathway in the direction of two (4-aminophenoxy)alkanoic acids. The common key step, a Williamson etherification yielding amidoesters of the target aminoacids, appears to be a good option if ethyl bromoalkanoates are used. In contrast, the key step,

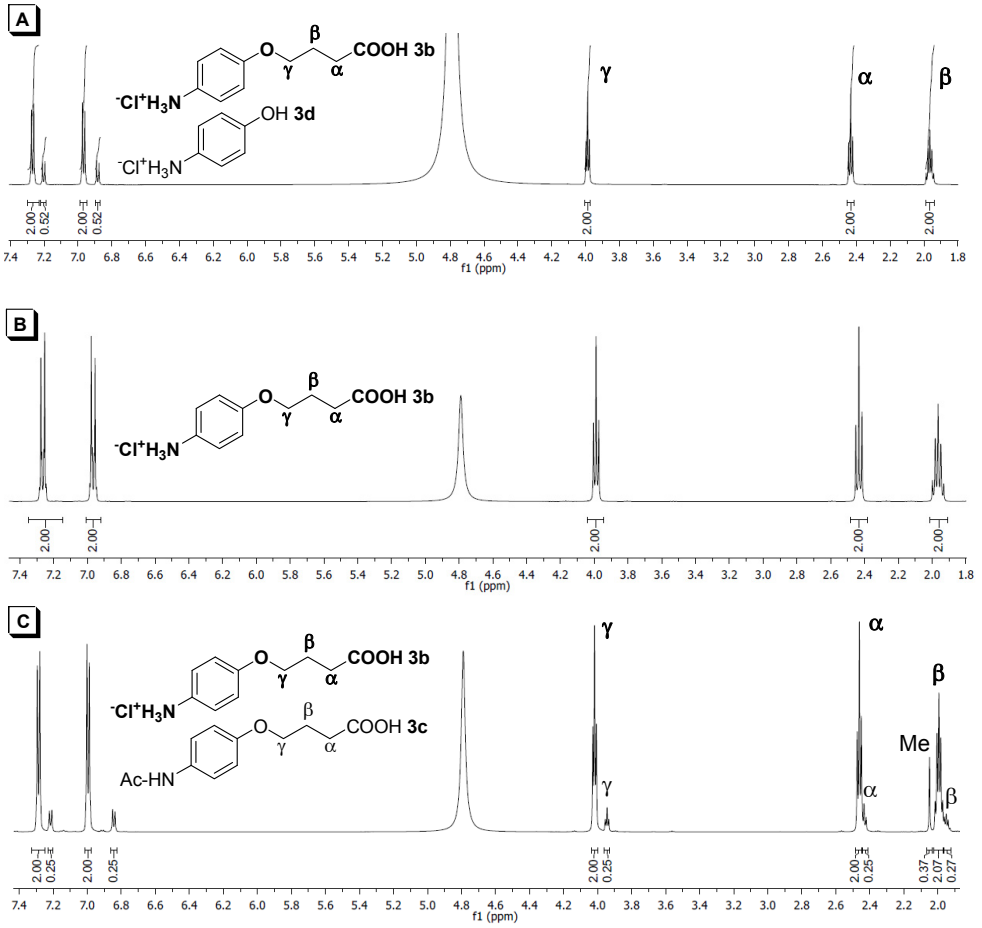

Figure 1. ^{1}H NMR monitoring of acidolysis of amidoester **2b** (600 MHz, D_2O, 298 K): crude reaction mixture after 13 h (**A**), 2 h (**B**), 1 h (**C**).

N,*O*-deprotection of the resulting amidoesters by acidolysis, strongly depends on the size of the (poly)methylenic chain (n=1 vs. n=3).

EXPERIMENTAL SECTION

***General*.** Melting points were measured on an Electrothermal® instrument and are not corrected. NMR spectra were recorded on Bruker® AV 400, or AV 600 instruments operating at 400 or 600 MHz for ^{1}H and at 100 or 150 MHz for ^{13}C nuclei respectively. All chemical shifts (δ values) are given in parts per million (ppm); all homocoupling patterns ($^{n}J_{H,H}$ values) are given in Hertz. TLC was performed by using aluminium sheets with silica gel 60 F_{254} (Merck®). IR spectra were recorded on a Bruker® FT-IR Vector 22 Spectrometer. Microanalyses were performed on a Carlo Erba® CHNOS 1160 apparatus. Mass spectra were carried out on a Schimadzu® GC-MS QP-2010 PLUS instrument equipped with a Column HP-5MS under EI (70 eV) ionisation. All solvents and reagents were of analytical grade and required no purification prior to use.

***Typical procedure for Williamson etherification. Preparation of compound* 2b**. Into a DMF (30 mL) solution containing *N*-(4-hydroxyphenyl) acetamide (3.00 g, 19.85 mmol) and ethyl 4-bromobutyrate (3.14 mL, 4.26 g, 21.83 mmol), anhyd. K_2CO_3 (10.81 g, 78.2 mmol) was added with vigorous stirring. The resulted suspension was heated at 70 °C for 16 h then let to stir at room temperature for additional 72 h. Water (50 mL) and ethyl acetate (100 mL) were added to the reaction mixture with stirring, then the resulted two layers were separated. The organic layer was washed with water to complete removal of DMF (5 × 50 mL), dried over anhyd. Na_2SO_4 and evaporated under reduced pressure. The crude solid product was crystallised from min. amount of ethyl acetate to afford 3.95 g pure compound **2b** [75% yield with respect to *N*-(4-hydroxyphenyl)acetamide] as a white solid.

Ethyl (4-N-acetylamino)phenoxyacetate (**2a**); yield 90% [1.41 g **2a** starting from 1.00 g *N*-(4-hydroxyphenyl)acetamide], white powder, mp 102.3-103.5 °C (toluene/hexane 1:5 v/v) (Lit. [8a]: 104.2-106.2 °C); [Found: C, 61.05; H, 6.57; N, 6.24%. $C_{12}H_{15}NO_4$ (237.10) requires: C, 60.75; H, 6.37; N, 5.90 %]; R_f (ligroin/acetone 2:1 v/v) 0.51. $\nu_{max.}$ (KBr) 3382 (m), 2994 (w), 1741(s), 1678 (m), 1532 (m), 1510 (s), 1428 (w), 1408 (w), 1322 (w), 1251 (m), 1215 (s), 1175 (w), 1089 (m), 1015 (w), 833 (m), 810 (m), 678 (w), 595 (w) cm^{-1}. ^{1}H NMR (400 MHz, DMSO-d_6, 298 K) δ_H 1.20 (3 H, t, $^{3}J_{H,H}$=7.0 Hz, CH_2CH_3), 2.00 (3 H, s, CH_3), 4.15 (2 H, q, $^{3}J_{H,H}$=7.0 Hz, CH_2CH_3), 4.71 (2 H, s, CH_2), 6.86 (2 H, d, $^{3}J_{H,H}$=9.2 Hz, H-3, -5, Ar), 7.47 (2 H, d, $^{3}J_{H,H}$=9.2 Hz, H-2, -6, Ar), 9.83 (1 H, s, NH) ppm. ^{13}C NMR in J_{mod} (100 MHz, DMSO-d_6, 298 K) δ_C 14.1 (CH_2CH_3), 23.8 (CH_3), 60.6 (CH_2CH_3), 64.9 (CH_2), 114.6 (C-3, -5, Ar), 120.5 (C-2, -6, Ar), 133.2 (C-4, Ar), 153.4 (C-1, Ar), 167.9 (NH-CO), 168.9 (COO) ppm. GC-MS (MeOH) *m*/*z* (rel. int. %) 223 [M, - CH_3] (23); [APCI(+), MeCN] *m*/*z* (rel. int. %) 238.11 [M+1].

Ethyl 4-(4-N-acetylamino)phenoxybutyrate (**2b**); yield 75% [3.95 g **2b** starting from 3.00 g *N*-(4-hydroxyphenyl)acetamide], white crystals, mp 88-90 °C (ethyl acetate); [Found: C, 63.56; H, 7.10; N, 5.34%. $C_{14}H_{19}NO_4$ (265.13) requires: C, 63.38; H, 7.22; N, 5.28%]; R_f ($CHCl_3$/MeOH 5:0.5 v/v) 0.51. $\nu_{max.}$ (KBr) 3325 (m), 2992 (w), 2944 (w), 2914 (w), 2874 (w), 1730 (s), 1659 (s), 1533 (s), 1513 (m), 1409 (m), 1377 (m), 1319 (m), 1266 (m), 1249 (m), 1179 (s), 1101 (w), 1055 (m), 1032 (w), 965 (m), 943 (w), 828 (m), 603 (w) cm^{-1}. ^1H NMR (400 MHz, DMSO-d_6, 298 K) δ_H 1.16 (3 H, t, $^3J_{H,H}$=7.2 Hz, CH_2CH_3), 1.93 (2 H, tt app. qv., $^3J_{H,H}$=6.8 Hz, β-CH_2), 1.99 (3 H, s, CH_3), 2.43 (2 H, t, $^3J_{H,H}$=6.0 Hz, α-CH_2), 3.92 (2 H, t, $^3J_{H,H}$=6.2 Hz, γ-CH_2), 4.05 (2 H, q, $^3J_{H,H}$=7.2 Hz, CH_2CH_3), 6.83 (2 H, d, $^3J_{H,H}$=9.2 Hz, H-3, -5, Ar), 7.45 (2 H, d, $^3J_{H,H}$=8.8 Hz, H-2, -6, Ar), 9.79 (1 H, s, NH) ppm. ^{13}C NMR in J_{mod} (100 MHz, DMSO-d_6, 298 K) δ_C 14.2 (CH_2CH_3), 23.9 (CH_3), 24.4 (β-CH_2), 30.3 (α-CH_2), 60.0 (γ-CH_2), 66.7 (CH_2CH_3), 114.5 (C-3, -5, Ar), 120.6 (C-2, -6, Ar), 132.6 (C-4, Ar), 154.3 (C-1, Ar), 167.9 (NH-CO), 172.7 (COO) ppm. GC-MS (MeOH) *m*/*z* (rel. int. %) 265.1 [M^+] (5).

Typical procedure for acidolysis. Preparation of compound **3b**. Ethyl 4-(4-*N*-acetylamino)phenoxybutyrate **2b** (3.95 g, 14.90 mmol) was added to aq. concd. 37% HCl soln. (86 mL solution, 1028.10 mmol HCl) and the reaction mixture was refluxed for 2 h. The resulted white suspension was cooled at 0 °C for 24 h, filtered off and washed with anh. THF to afford 2.45 g pure compound **3b** (71% yield with respect to **2b**) as white crystals.

(4-Aminophenoxy)acetic acid hydrochloride (**3a**); yield 92% (5.31 g **3a** starting from 6.70 g **2a**), beige powder, mp 219.6-220.9 °C (aq. HCl) (Lit. [8a]: 224-226 °C); [Found: C, 47.51; H, 4.64; N, 6.94%. $C_8H_{10}ClNO_3$ (203.03) requires: C, 47.19; H, 4.95; N, 6.88%]; R_f (EtOH 100%) 0.43. $\nu_{max.}$ (KBr) 3101 (s), 3016 (s), 2968 (s), 2850 (s), 2585 (m), 1761 (m), 1736 (s), 1614 (w), 1574 (w), 1500 (s), 1435 (w), 1407 (w), 1309 (w), 1277 (w), 1242 (w), 1178 (s), 1073 (m), 1053 (m), 812 (m), 771 (m), 732 (m), 672 (w), 629 (w) cm^{-1}. ^1H NMR (400 MHz, D_2O, 298 K) δ_H 4.68 (2 H, s, CH_2), 7.00 (2 H, ddd app. dt, $^3J_{H,H}$=9.6 Hz, $^4J_{H,H}$=$^5J_{H,H}$= 2.8 Hz, H-3, -5, Ar), 7.29 (2 H, ddd app. dt, $^3J_{H,H}$=9.7 Hz, $^4J_{H,H}$=$^5J_{H,H}$= 2.8 Hz, H-2, -6, Ar) ppm. ^{13}C-RMN in J_{mod} (100 MHz, D_2O, 298 K) δ_C 65.0 (CH_2), 115.8 (C-3, -5, Ar), 123.4 (C-4, Ar) 124.4 (C-2, -6, Ar), 157.3 (C-1, Ar), 173.1 (C=O) ppm. GC-MS (MeOH) *m*/*z* (rel. int. %) 169 [M, - HCl, + CH_3] (24).

4-(4-Aminophenoxy)butyric acid hydrochloride (**3b**); yield 71% (2.45 g **3b** starting from 3.95 g **2b**), white crystals, mp 191-193 °C (aq. HCl); [Found: C, 52.06; H, 6.15; N, 5.96%. $C_{10}H_{14}ClNO_3$ (231.07) requires: C, 51.84;

H, 6.09; N, 6.05%]; R_f (ligroin/acetone 1:1 v/v) 0.5. $\nu_{max.}$ (KBr) 3119 (m), 3026 (s), 2918 (s), 2868 (s), 2604 (w), 2559 (w), 1734 (s), 1616 (m), 1565 (m), 1503 (s), 1465 (m), 1440 (w), 1406 (m), 1378 (w), 1345 (w), 1261 (s), 1172 (s), 1118 (w), 1050 (m), 943 (m), 840 (m), 814 (m), 768 (w), 645 (w) cm^{-1}. ^1H NMR (400 MHz, D_2O, 298 K) δ_H 1.96 (2 H, tt app. qv., $^3J_{H,H}$=6.7 Hz, β-CH_2), 2.43 (2 H, t, $^3J_{H,H}$=7.0 Hz, α-CH_2), 3.99 (2 H, t, $^3J_{H,H}$=6.0 Hz, γ-CH_2), 6.97 (2 H, ddd app. dt, $^3J_{H,H}$=9.6 Hz, $^4J_{H,H}$=$^5J_{H,H}$= 3.1 Hz, H-3, -5, Ar), 7.26 (2 H, ddd app. dt, $^3J_{H,H}$=9.6 Hz, $^4J_{H,H}$=$^5J_{H,H}$=3.1 Hz, H-2, -6, Ar) ppm. ^{13}C NMR in J_{mod} (100 MHz, D_2O, 298 K) δ_C 23.8 (β-CH_2), 30.5 (α-CH_2), 67.6 (γ-CH_2), 115.8 (C-3, -5, Ar), 122.6 (C-4, Ar), 124.2 (C-2, -6, Ar), 158.3 (C-1, Ar), 178.1 (C=O) ppm. GC-MS (MeOH) *m*/*z* (rel. int. %) 209 [M -HCl, + CH_3] (20).

Typical procedure for isolation of (4-aminophenoxy)alkanoic acids as free amine. Isolation of compound **1b**. 4-(4-aminophenoxy)butyric acid hydrochloride **3b** (2.45 g, 10.60 mmol) was dissolved in distilled water (20 mL). To this solution, anhyd. K_2CO_3 (0.73 g, 5.30 mmol) was added portionwise. The resulted suspension was stirred for 1 h at r.t. then filtered off to give 1.51 g pure compound **1b** (73% yield with respect to **3b**) as a white powder.

(4-Aminophenoxy)acetic acid (**1a**); yield 81% (0.20 g **1a** starting from 0.30 g **3a**), white powder, mp 214 °C (dec.) (Lit. 312 °C [2], 220 °C [3], 215-220 °C [7]); [Found: C, 57.58; H, 5.88; N, 8.25%. $C_8H_9NO_3$ (167.06) requires: C, 57.48; H, 5.43; N, 8.38%]; R_f (EtOH 100%) 0.54. $\nu_{max.}$ (KBr) 2931 (m), 2870 (m), 2630 (m), 2100 (w), 1619 (m), 1592 (m), 1544 (m), 1511 (s), 1411 (m), 1338 (w), 1301 (w), 1258 (m), 1227 (m), 1182 (w), 1057 (m), 916 (w), 822 (m), 729 (m), 596 (w), 578 (w) cm^{-1}. ^1H NMR (600 MHz, DMSO-d_6, 298 K) δ_H 4.47 (2 H, s, CH_2), 5.51 (3 H, br s, NH_2 ⇆ COOH exchangeable), 6.52 (2 H, d, $^3J_{H,H}$=9.0 Hz, H-3, -5, Ar), 6.64 (2 H, d, $^3J_{H,H}$=9.0 Hz, H-2, -6, Ar) ppm. ^{13}C-RMN in J_{mod} (150 MHz, DMSO-d_6, 298 K) δ_C 65.5 (CH_2), 115.2 (C-3, -5, Ar), 115.5 (C-2, -6, Ar), 142.5 (C-4, Ar), 149.5 (C-1, Ar), 170.9 (C=O) ppm. GC-MS (MeOH) *m*/*z* (rel. int. %) 109 [M+1, - CO_2, - CH_3] (100).

4-(4-Aminophenoxy)butyric acid (**1b**); yield 73% (1.51 g **1b** starting from 2.45 g **3b**), white powder, mp 143-145 °C (H_2O) (Lit. 145.5-146 °C [4]).; [Found: C, 61.75; H, 6.48; N, 6.95%. $C_{10}H_{13}NO_3$ (195.09) requires: C, 61.53; H, 6.71; N, 7.18;%]; R_f (ligroin/acetone 1:1 v/v) 0.5. $\nu_{max.}$ (KBr) 2959 (m), 2872 (m), 2590 (m), 2148 (w), 1623 (m), 1601 (m), 1519 (s), 1507 (s), 1405 (m), 1387 (w), 1302 (m), 1216 (w), 1174 (w), 1077 (w), 1050 (w), 1024 (w), 832 (m), 810 (w), 766 (w), 663 (w) cm^{-1}. ^1H NMR (600 MHz, DMSO-d_6, 298 K) δ_H 1.86 (2 H, tt app. qv., $^3J_{H,H}$=6.9 Hz, β-CH_2), 2.35 (2 H, t, $^3J_{H,H}$=7.2 Hz, α-CH_2), 3.81 (2 H, t, $^3J_{H,H}$=6.3 Hz, γ-CH_2), 6.51 (2 H, d, $^3J_{H,H}$=9.0 Hz, H-3, -5, Ar),

6.64 (2 H, d, $^3J_{H,H}$=8.4 Hz, H-2, -6, Ar) ppm. ^{13}C NMR in J_{mod} (100 MHz, DMSO-d_6, 298 K) δ_C 24.6 (β-CH_2), 30.3 (α-CH_2), 67.1 (γ-CH_2), 115.1 (C-3, -5, Ar), 115.5 (C-2, -6, Ar), 142.3 (C-4, Ar), 150.0 (C-1, Ar), 174.4 (C=O) ppm. GC-MS (MeOH) *m*/*z* (rel. int. %) 195 [M^+] (10).

ACKNOWLEDGMENT

The financial support from a Grant provided by the Research Council Romania (project PN-II-ID-PCE-2011-3-0128) is gratefully acknowledged.

REFERENCES

1. J. Fritzsche, *J. Prakt. Chem*. (Leipzig), **1879**, *2*, 283
2. J. Kym, *J. Prakt. Chem*. (Leipzig), **1897**, *2*, 122
3. W.A. Jacobs, M. Heidelberger, *J. Am. Chem. Soc.*, **1917**, *39*, 1435
4. W.A. Jacobs, M. Heidelberger, *J. Am. Chem. Soc.*, **1917**, *39*, 2188
5. P.M. Mistry, R. Bradbury, US Pat. 6 559 292/06.05.**2003**
6. R. Kumar, S. Jain, N. Jain, *Der Pharma Chem*., **2013**, *5*, 73
7. D.J. Abraham, P.E. Kennedy, A.S. Mehanna, D.C. Patwa, F.L. Williams, *J. Med. Chem.*, **1984**, *27*, 967
8. a) R.S. Bezwada, US Pat. 8 143 325 B2/03.27.**2012**; b) K. Hidaka, T. Kimura, A.J. Ruben, T. Uemura, M. Kamiya, A. Kiso, T. Okamoto, Y. Tsuchiya, Y. Hayashi, E. Freire, Y. Kiso, *Bioorg. Med. Chem.*, **2008**, *16*, 10049–10060
9. a) V.A. Barashkin, *J. Org. Chem. USSR* (English Translation), **1970**, *6*, 2274; *Zh. Org. Khim.*, **1970**, *6*, 2266; b) M. Nutiu, R. Bacaloglu, M. Darabantu, Z. Pap *Scientific and Technical Bulletin of Polytechnic Institute "Traian Vuia" Timisoara, Chemistry Series,* **1981**, *26*, 79; c) W. Cheng, S. Wong, A.M. Almeida, D.B. Rozema, A.V. Blokhin, J.C. Carlson, US Pat. 2015/45573 A1/02.12. **2015**; d) X. Zhang, B. Bao, X. Yu, L. Tong, Y. Luo, Q, Huang, M. Su, L. Sheng, J. Li, H. Zhu, B. Yang, X. Zhang, Y. Chen, W. Lu, *Bioorg. Med. Chem.*, **2013**, *21*, 6981
10. Y. Katsura, T. Tomishi, Y. Inoue, K. Sakane, Y. Matsumoto, C. Morinaga, H. Ishikawa, H. Takasugi, *J. Med. Chem.*, **2000**, *43,* 3315
11. B.D. Palmer, J.B. Smaill, G.W. Rewcastle, E.M. Dobrusin, A. Kraker, C.W. Moore, R.W. Steinkampf, W. Denny, *Bioorg. Med. Chem. Lett.*, **2005**, *15*, 1931

STUDIA UBB CHEMIA, LX, 2, Tom I, 2015 (p. 15-26)
(RECOMMENDED CITATION)

SILICA GEL MODIFIED WITH FUNCTIONALIZED CALIXARENES. PREPARATION AND CHARACTERIZATION

RAUL RANETE[a], PETRONELA M. PETRAR[a], RALUCA ŞEPTELEAN[a], IOANA PERHAIŢĂ[b], GABRIELA NEMEŞ[a*]

ABSTRACT. This work presents the synthesis and characterization of novel products obtained by the chemical bonding of lower rim substituted calix[4]- and calix[8]arene macrocycles to silica gel surfaces modified with aminopropyl chains. The products were investigated by thermogravimetric analysis (DTG, EGA), surface area analysis (BET), as well as by electron microscopy (TEM, SEM).

Keywords: *functionalized silica gel, calixarenes, thermal analyses, electronic microscopy.*

INTRODUCTION

Calix[n]arenes (n = 4 – 20) are phenolic metacyclophanes obtained by the condensation of para- substituted phenol with formaldehyde or para-formaldehyde [1] and they can be functionalized with organic groups by esterification, etherification, sulphonation, nitration or alkylation reactions [2, 3, 4, 5] at the lower rim (the OH phenol groups) or the upper rim (the para position of the phenyl rings). The cavity formed by the phenolic rings and the possibility of functionalizing the calixarenic framework with various organic groups, make these organic macrocycles very interesting for a wide range of applications including biomedical research [6], chromatography [7, 8], selective metal extraction [9, 10], electrochemical and luminescent sensors [11], catalysis [12], and selective gas adsorption [13]. In recent years, more emphasis was put on the immobilization of calixarenes on silica gel substrates, thus improving their possible application in separation sciences [14,15]. One of the most accessible ways to bond calixarene macrocycles to the SiO_2 layer is through alcoxy-silanes of the type $X\text{-}(CH_2)_n\text{-}Si(OR')_3$ [16,17], where X is a functional group that allows coupling reactions with the calixarenic system, usually at the lower rim.

[a] *Facultatea de Chimie şi Inginerie Chimică, Universitatea Babeş-Bolyai Cluj-Napoca, Str. Arany Janos, nr 11, RO-400028.*
[b] *Institutul de Cercetări în Chimie Raluca Ripan, Str. Fântânele, nr. 30, Cluj-Napoca RO-400294*
[*] *Corresponding author: sgabi@chem.ubbcluj.ro*

Following this trend, we have studied the preparation of modified silica gel, using 3-aminopropyl-tri-methoxy-silane (APTMS) as a spacer, in order to obtain new products with possible applications in ion metal separation. The reactions were performed in anhydrous conditions by the nucleophilic attack of hydroxyl groups from the silica gel surface at the APTMS spacer, with the elimination of methanol [18].

RESULTS AND DISCUSSION

New modified silica gel with 3-aminopropyl-tri-methoxy-silane (APTMS) and the compound obtained by attaching of this system to the acetylated p-tertbutyl calix[n]arene (n = 4, 8) were synthesized and investigated by specific physico-chemical methods.

A first stage in the synthesis of functionalized calixarenes linked to the silica gel substrate through an aminopropyl spacer requires the preparation of lower rim substituted calixarenes. The starting p-tertbutyl calix[n]arenes (n = 4, 8) and their acetyl derivatives were synthesized according to the methods described in the literature [1,[19],[20]] (Scheme 1, compounds **1**, **2**).

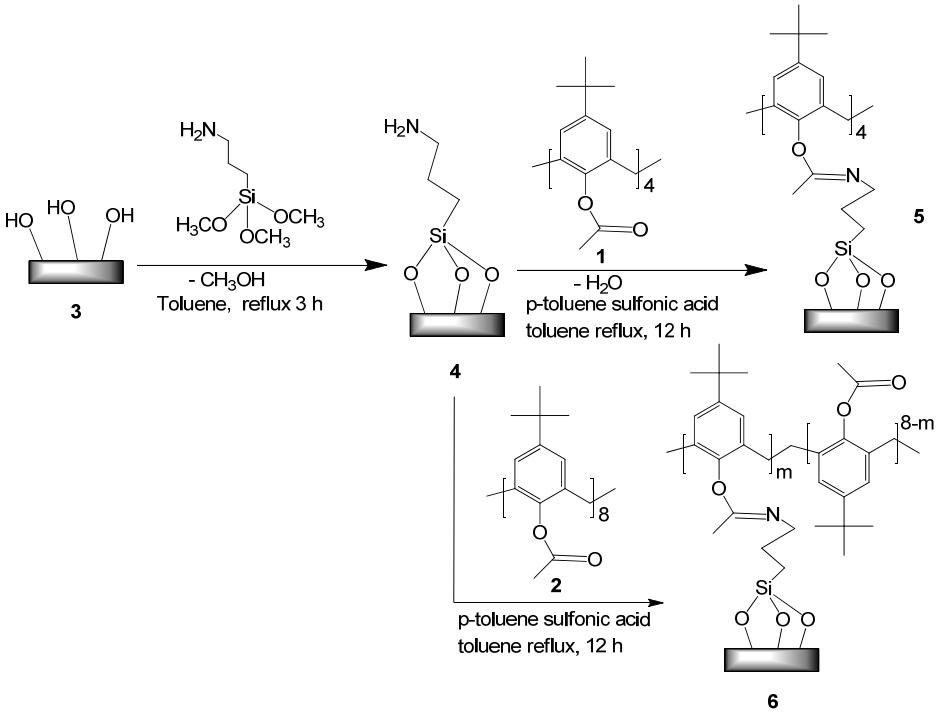

Scheme 1

The APTMS-chemosorbed silica gel **4** was prepared starting from pre-activated silica gel by heating it at 600 °C under reduced pressure (10^{-6} bar) for an hour and products 5 and 6 was performed by a modified literature method [21].

The acetyl functionalized calixarene precursors **1** and **2** were characterized by ^{1}H-NMR and IR spectroscopy, all the obtained data being in agreement with published results [1,19,20]. The new products **5** and **6** were characterized by thermogravimetric methods, surface electron microscopy (SEM), transmission electron microscopy (TEM) and Brunauer-Emmett-Teller surface analysis (BET).

The binding of the functionalized calixarenes to the silica surface, with the formation of products **5** and **6** (Scheme 1), was investigated using thermal analysis and electron microscopy (SEM and TEM). The results suggest that the functionalized calixarenic systems **1** and **2** are chemically bonded to the ATPMS modified silica, most likely by means of a C=N bond.

Thermal analysis

Thermal analysis for the new products has been carried out. The thermograms were also recorded for the heat-activated silica gel **3** and the APTMS-modified silica **4**, for comparison. After the treatment of the modified silica **4** with p-tertbutyl calix[4]arene tetra-acetate and the calix[8]arene analogue, the derivative thermogravimetric plots (DTG) differ sharply from those of the calixarene-free materials, as shown in Figure 1 and Table 1.

Table 1. Thermogravimetric analysis data for products 1, 2, 4, 5, and 6.

Product	Quantity (mg)	Thermogravimetric (TG) and (DTG) analysis			
		Total mass loss (Δm_T)	Temperature range	Partial mass loss (Δm_p)	T_{max} (°C)
1	36.5506	86.00 %	25 -260 °C	6.23 %	177
			260 -480 °C	63.48 %	413
			480 -1100 °C	16.30 %	506
2	7.9157	87.26 %	25 -230 °C	4.37%	90
			230 -480 °C	60.12 %	402
			480 -1100 °C	22.81 %	482
4	40.0067	17.15 %	25 -140 °C	3.94 %	70
			140 -800 °C	11.01 %	464
			800 -1100 °C	2.21 %	1008

Product	Quantity (mg)	Thermogravimetric (TG) and (DTG) analysis			
		Total mass loss (Δm_T)	Temperature range	Partial mass loss (Δm_p)	T_{max} (°C)
5	50.8478	36.97 %	25 -160 °C	3.24 %	64
			160 -430 °C	24.51 %	368
			430 -790 °C	7.05 %	458
			790-1100 °C	2.32 %	796
6	26.9450	37.02 %	25 -140 °C	3.39 %	68
			140 -350 °C	17.83 %	279
			350-450 °C	8.83 %	377
			450 – 794 °C	5.18 %	449
			794-1100 °C	1.96 %	815

The thermal analysis data for product **5** indicates that the acetylated p-tertbutyl calix[4]arene is bonded to the silica surface through the APTMS spacer (Figure 1c). The mass loss interval at 160 – 430 °C (24.5 %) is correlated with the elimination of the macrocycle from the system. Another significant mass loss (7 %), between 430 and 600 °C, can be attributed to the decomposition of the aminopropylic chain tethered to the surface.

For derivative **6**, the significantly higher total mass loss (Table 1) indicates the bonding of the organic macrocycles within the new material.

The recorded DTG curve for APTMS-modified silica gel shows a mass loss in the 360-450 °C range, attributed to the decomposition of the APTMS (Figure 1b). The full thermogravimetric data recorded for products **1** – **6** are presented in Table 1.

The comparison of the two DTG recorded for **5** and **6** suggests a stronger bonding of the acetylated calix[4]arene (Figure 1c) on the inorganic surface than in the case of the calix[8]arene analogue (Figure 1d), as the first significant mass loss occurs at higher temperature values for product **5** (Table 1). This can be explained by the preference of calix[4]arenes for a basket geometry, which means that all the acetyl groups in derivative **1** are on the same side of the macrocycle cone [22]. However, larger calixarenes (n = 5, 6, 8), are conformationally mobile, and the cone conformation is almost never preferred. Therefore, it can be assumed that the acetylated calix[8]arene would adopt a conformation allowing fewer connectivity points to the APTMS-modified silica gel via chemical bonding, while physical interactions between the calixarenic unit and the modified substrates are still possible. The coupling of the calix[4]arene to the APTMS-modified silica gel surface through all its connective points can be correlated to the higher decomposition temperature.

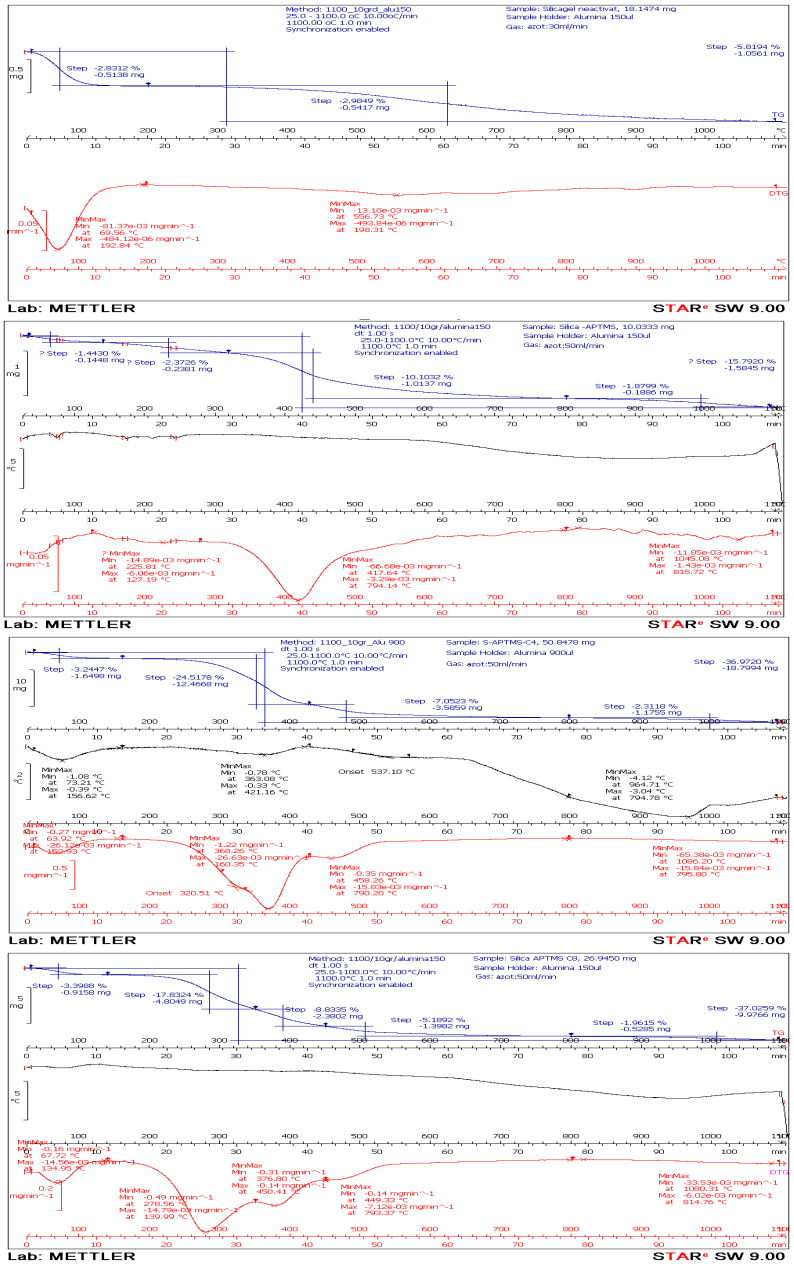

Figure 1. TG and DTG plots for (a) silica gel, (b) APTMS-modified silica gel **4**, (c) silica gel-APTMS-acetyl-p-tertbutyl calix[4]arene **5**, (d) silica gel-APTMS-acetyl-p-tertbutyl calix[8]arene **6**.

Complementary analysis of the new products **5** and **6** by EGA correlates the decomposition of the organic layer to the TG-DTG data. Figure 2 details the recorded EGA data for product **5** (silica gel-APTMS-acetylated calix[4]arene) compared to the starting acetylated calix[4]arene and the APTMS-modified silica gel.

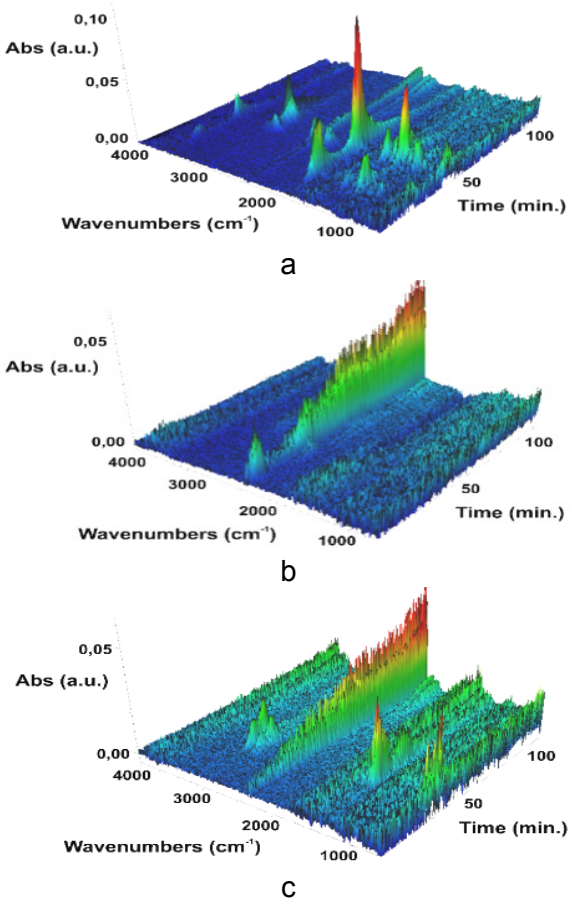

Figure 2. EGA 3D plots for (a) tetra-acetyl derivative of p-tertbutyl calix[4]arene **1**, (b) functionalized silica gel with APTMS **4**, (c) product **5**.

The pattern in the EGA - 3D plot recorded for the decomposition of compound **5** (Figure 2c) indicates the presence of both a calixarene moiety and APTMS fragments, which suggests that the calixarene system is bonded to the inorganic substrate. Similar results were obtained for the calix[8]arene-containing material.

Brunauer–Emmett–Teller surface area analysis

The new products and the starting materials were also investigated through BET surface analysis. As expected, the pore volume of the APTMS functionalized silica gel is much lower than that of the unfunctionalized silica gel due to the covering of the pores with the organic phase (the pore volume decreases from 0.83 cm^3/g to 0.48 cm^3/g). Furthermore, the pore volume in the case of material **5** differs significantly from that obtained for **6**. The larger pore volume of silica gel-APTMS-acetyl-calix[8]arene (0.15 cm^3/g) by comparison with the silica gel-APTMS-acetyl-calix[4]arene system (0.03 cm^3/g) can be explained by a larger cavity of the calix[8] derivative together with a better covering of the silica surfacein the case of **5** (Figure 3).

The pore sizes are relatively small and with a narrow distribution in the meso-porous range (20 - 500 Å). A reduction in pore size was noticed, from an interval of about 50-100 Å determined for the unmodified silica gel to about 35-70 Å for the final product silica gel-APTMS- acetyl calix[8]arene (**6**), (Figure 3). The same pore size interval was determined for the product obtained with the calix[4]arene tetra-acetate (**5**).

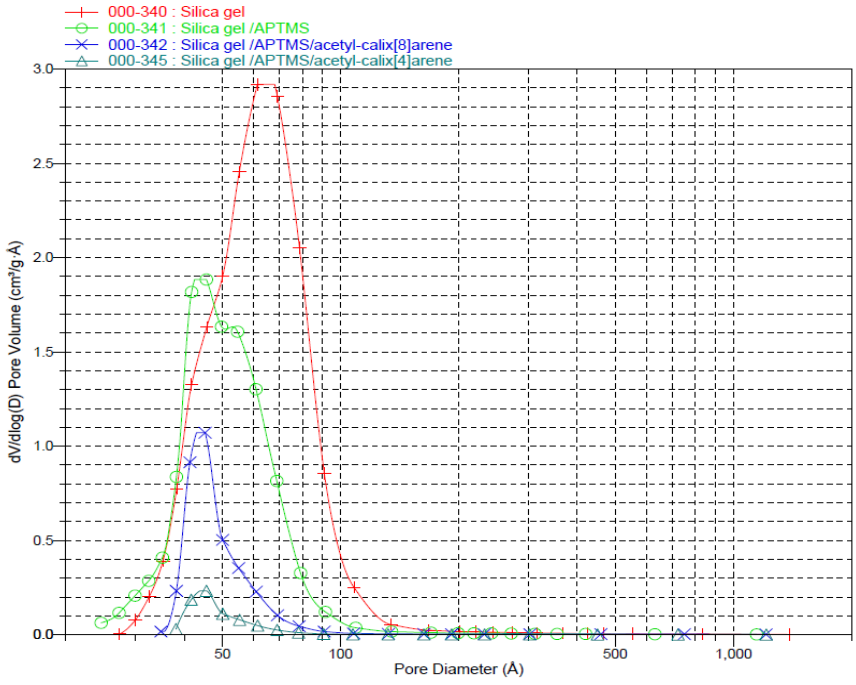

Figure 3. BJH desorbtion pore volume distribution curve according to pore diameter for silica gel (red), silica gel-APTMS **4** (green), silica gel-APTMS-acetyl-calix[4]arene **5** (dark green) and silica gel-APTMS-acetyl-calix[8]arene **6** (blue).

The BET analysis clearly shows that a decrease in pore volume is noticeable after the treatment of the inorganic substrate with APTMS and the calixarene macrocycles, proving that the organic layer covers the silica surface. The BET surface area decreases from 462.20 m^2/g for the silica gel to 301.47 m^2/g for the APTMS modified silica gel and 63.99 m^2/g for product **6** and 11.75 m^2/g for product **5** respectively.

Scanning electron and transmission electron microscopy investigations

SEM images suggest that in both cases the lower rim functionalized calix[n]arenes have been deposited on the APTMS-modified silica gel surface (Figure 4). The images show a relative smooth surface for the unmodified silica gel (Figure 4a), when compared with the products containing either APTMS or the calix[4]arene macrocycle. The APTMS covering of the silica surface does not seem to be uniform (Figure 4b). The same can be told about product **5**, for which the covering of the inorganic substrate is discontinuous. It can be hypothesized that the covering occurred only at the regions on the surfaces already modified with the amino-propyl spacer. By contrast, a smoother surface is observed in the case of product **6**. This, together with the thermal analysis data indicate that the surface is covered uniformly with an organic layer of calix[8]arene.

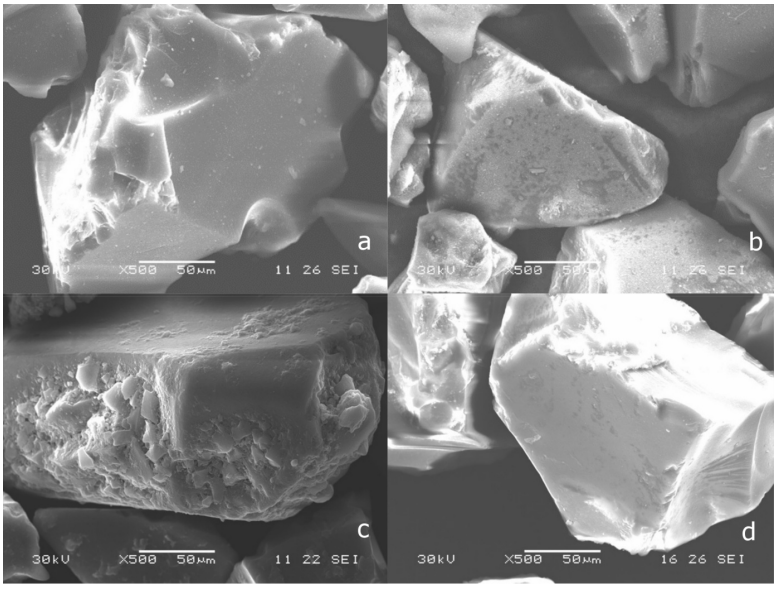

Figure 4. SEM images of (a) silicagel, (b) silica gel-APTMS **4**, (c) silica gel-APTMS-acetyl-calix[4]arene **5** and (d) silica gel-APTMS-acetyl-calix[8]arene **6**.

The new obtained products were also investigated by TEM. Images of the starting activated, unmodified silica gel as well as of the APTMS-modified silica gel are presented for comparison (Figure 5a and b).

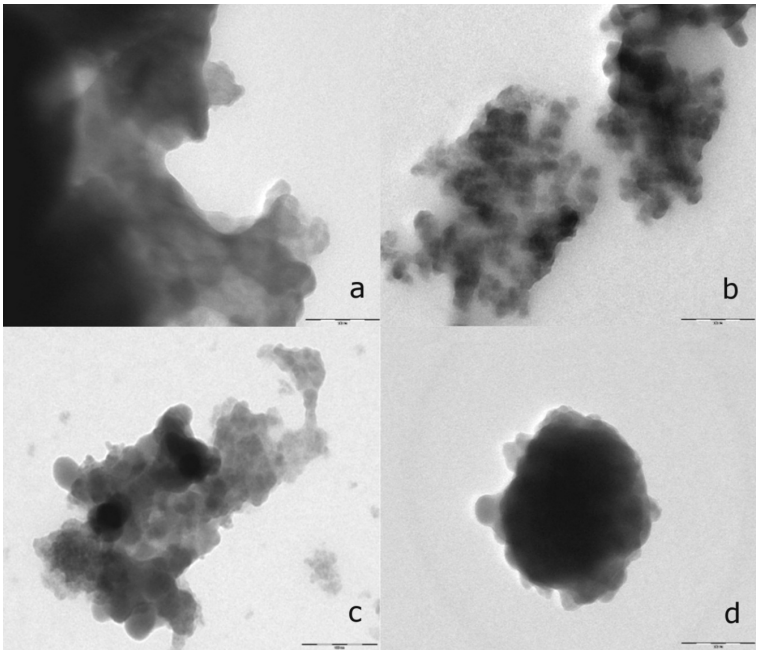

Figure 5. TEM images (Scale: 100 nm) of (a) silica gel, (b) silica gel-APTMS **4**, silica gel-APTMS-acetyl-calix[4]arene **5** and (d) silica gel-APTMS-acetyl-calix[8]arene **6**.

The TEM images of silica gel-APTMS-acetyl-calix[4] arene **5** (Figure 5c) and silica gel-APTMS- acetyl- calix[8]arene **6** (Figure 5d) show that in the case of product **6**, the silica particles aggregate in a higher degree by comparison to the analogue product **5**. This is consistent with the thermogravimetry data suggesting the possibility of calix[8]arene - based material to contain multi-directional bonds of the organic layer to the silica particles while a macrocycle of acetylated calix[4]arene would bond to only one particle.

CONCLUSIONS

This work presents the successful binding of functionalized calix[n]arene (n = 4, 8) derivatives to silica gel by means of 3-aminopropyl trimethoxysilane. The silica substrate was thermally and chemically activated with 3-aminopropyl

trimethoxysilane according to literature procedures. The new silica gel-APTMS-acetyl-calix[n]arene systems were characterized by specific methods including DTG, EGA, SEM and TEM, which prove the chemical bonding of the calixarenic macrocycles to the inorganic substrate.

EXPERIMENTAL

All the chemicals were used as purchased from chemical suppliers (Merck, Sigma Aldrich), without any further purification. All reactions have been carried out under argon.

The ^{1}H NMR spectra were recorded on a Bruker Avance 400 MHz spectrometer in $CDCl_3$, with TMS as reference at a frequency of 400.13 MHz.

Thermogravimetric analysis (TGA) was performed using a Mettler Toledo TGA/SDTA851e Thermal Analysis System. All the experiments were done in an alumina crucible (900 µl), with a heating speed of 10°C/min in an interval ranging from 25 to 1100 °C. The measurements were carried out in a nitrogen atmosphere with a flow of 50 ml/min.

The evolved gas analysis (EGA) was performed on a Thermo Scientific Nicolet 6700 FT-IR spectrometer equipped with a TG module, operating at 280 °C. Surface area measurements were done on a Tristar II 3020 – Micromeritics (nitrogen adsorption at 77 K, sample decontamination at 150 °C for 24 h, under nitrogen flow).The scanning electron microscopy experiments were performed on a Jeol JSM5510LV (Jeol, Japan) –3.5 nm rezolution, accelerating voltage 0.5-30 kV system. The transmission electron microscopy images were obtained with a Hitachi Automatic TEM H7650 system (accelerating voltage 40-120 kV, zoom 200x-600000x).

Preparation of APTMS-modified silica gel 4. The silica gel was pre-activated by heating it at 600 °C under reduced pressure (10^{-6} bar) for an hour [23]. After the system returned to room temperature, 3-aminopropyl-trimethoxysilane (1.8 mmoles, 0.33 ml) in 20 ml of toluene was added under inert gas and the system was heated to reflux for 3 h. The obtained solid **4** was washed with toluene for 12 h in a Soxhlet extractor.

Synthesis of products 5 and 6. Product **5** was obtained from 2 g of **4**, 0.33 g of **1** and 0.017 g anhydrous p-toluene sulphonic acid in 100 ml of toluene. The mixture was refluxed for 12 h and the resulting solid was then washed with toluene for 12 h in a Soxhlet extractor. Product **6** was obtained in similar conditions from 0.33 g of p-tertbutyl-calix[8]arene octa-acetate **2**.

ACKNOWLEDGMENTS

R.R. thanks Babes-Bolyai University for financial support through a research scholarship. Dr. Gabriel Katona is gratefully thanked for the recording the TEM images and, together with Dr. Eng. Andrada Maicaneanu, for the helpful discussions.

REFERENCES

[1]. C.D. Gutsche, J.F. Stoddart, Calixarenes Revisited, The Royal Society of Chemistry, Cambridge, **1998**.
[2]. B. Dhawan, S.-I. Chen, C.D. Gutsche, *Macromolecular Chemistry and Physics*, **1997**, *188* (5), 921.
[3]. A. Saponar, E.-J.Popovici, N. Popovici, E. Bica, G. Nemes, P. Petrar, I. Silaghi-Dumitrescu, *Revista de Chimie*, **2009**, *60* (3), 278.
[4]. A. Saponar, E-J. Popovici, R. Grecu, I. Silaghi-Dumitrescu, N. Popovici, *Studia UBB Chemia*, **2009**, *44* (4), 203.
[5]. S. Saying, M. Yilmaz, M. Tavasli, *Tetrahedron*, **2011**, *67*, 3743.
[6]. R.V. Rodik, V.I. Boyko, V.I. Kalcheno, *Current Medicinal Chemistry*, **2009**, *16* (13), 1630.
[7]. B. Mokhtari, K. Pourabdollah, N. Dalali, *Chromatographia*, **2011**, *73* (9-10), 829.
[8]. M. Sliwka-Kaszynka, *Critical Reviews in Analytical Chemistr*y, **2007**, *37* (3), 211.
[9]. A. Saponar, E.-J. Popovici, R. Septelean, E. Bica, I. Perhaita, G. Nemes, *Revista de Chimie*, **2013**, *64* (1), 55.
[10]. A. Saponar, E.-J. Popovici, G. Nemes, N. Popovici, I. Perhaita, E. Bica, I. Silaghi-Dumitrescu, *Revista de Chimie,* **2012**, *63* (3), 249.
[11]. J.S. Kim, D.T. Quang, *Chemical Reviews*, **2007**, *107* (9), 3780.
[12]. Y. Kurusu, D.C. Neckers, *Journal of Organic Chemistry*, **1991**, *56* (6), 1981.
[13]. E. Soto-Cantu, R. Cueto, J. Koch, P.S. Russo, *Langmuir*, **2012**, *28* (13), 5562.
[14]. S. Sayin, F. Ozcan, M. Yilmaz, *Journal of Hazardous Materials*, **2010**, *178* (1 - 3), 312.
[15]. C. Ding, K. Qu, Y. Li, K. Hu, H. Liu, B. Ye, Y. Wu, S. Zhang, J*ournal of Chromatography A*, **2007**, *1170* (1 - 2), 73.
[16]. K. Miyatake, O. Ohama, Y. Kawahara, A. Urano, A. Kimura, *SEI Technical Review,* **2007**, 65.
[17]. K.C. Vrancken, L. De Coster, P.V. Der Voort, P.J. Grobet, E.F. Vansant, *Journal of Colloid and Interface Science*, **1995**, *170* (1), 71.
[18]. B. Arkles, *CHEMTECH 7,* **1977**, 766.
[19]. G.D. Andreetti, V. Böhmer, J.G. Jordon, M. Tabatabai, F. Ugozzoli, W. Vogt, A. Wolff, *Journal of Organic Chemistry,* **1993**, *58*, 4023.
[20]. C.D. Gutsche, L.G. Lin, *Tetrahedron*, **1986**, *42* (6), 1633.

[21]. V. Ivanovskia, M. Bukleskia, M. Madalska, E. Hey-Hawkins, Vibrational Spectroscopy, **2013**, *69*, 57.
[22]. C.D. Gutsche, B. Dhawan, J.A. Levine, K.H. No, L.J. Bauer, **1983**, *39* (3), 409.
[23]. V. Ivanovskia, M. Bukleskia, M. Madalska, E. Hey-Hawkins, *Vibrational Spectroscopy*, **2013**, *69*, 57.

STUDIA UBB CHEMIA, LX, 2, Tom I, 2015 (p. 27-44)
(RECOMMENDED CITATION)

INFLUENCE OF GRAIN AND CRYSTALLITE SIZE ON THE GIBBSITE TO BOEHMITE THERMAL TRANSFORMATION

VIKTOR ZSOLT BARANYAI[a,b], FERENC KRISTÁLY[c,*], ISTVÁN SZŰCS[a]

ABSTRACT. Thermal decomposition processes of three different samples of hydrated alumina: Bayer precipitated size fractioned, Bayer precipitated ground and fine precipitated, were studied. These were investigated with special regard to evolution of boehmite. The original samples contained 75-85 wt% of gibbsite, while remaining material with gibbsite-like Al_2O_3-H_2O ratio did not show long range order crystallinity. Decomposition reactions were observed by thermal analysis and reaction products were investigated by powder X-ray diffraction. Grain sizes were determined by laser diffraction and morphological changes of grains were observed by scanning electron microscopy. Boehmite formation is influenced mainly by grain and crystallite sizes of starting materials, while degree of crystallinity is of less importance. Transformation of gibbsite to boehmite was most pronounced in the case of coarse grains, nevertheless in fine particles boehmite evolution seemed retarded.

Keywords: *gibbsite decomposition, boehmite evolution, nanocrystalline boehmite, Rietveld-refinement*

INTRODUCTION

Gibbsite (γ–$Al(OH)_3$), end-product of the Bayer cycle is essential raw material of calcined alumina (Al_2O_3). Utilization of aluminum oxide in ceramic technologies has long history [1], however beyond the prevalent technologies, application of gibbsite or boehmite in ceramic green bodies, green fibers has appeared for increasing the final porosity of sintered material [2-4] or stabilizing of alumina foams [5, 6]. In this case the chemically bound water content of raw material is removed during sintering.

[a] *University of Miskolc, Department of Combustion Technology and Thermal Energy, H-3515 Miskolc-Egyetemváros, Hungary*
[b] *Bay Zoltán Nonprofit Ltd. for Applied Research, Department of Advanced Materials, H-3519 Miskolc, Iglói út 2.*
[c] *University of Miskolc, Institute of Mineralogy and Geology, H-3515 Miskolc-Egyetemváros, Hungary*
[*] *Corresponding author: kristalyf@gmail.com*

The Bayer precipitated particles are agglomerates of single pseudohexagonal plate-like crystallites. The structure and properties of the particles are influenced by the processes during formation: nucleation, agglomeration, crystal growth and attrition [7, 8]. During calcination the wet gibbsite loses its adhesive moisture first, further the bound water (~34 % referring to the dry hydrated material) exits. All of decomposition pathways are closed by the formation of the only thermodynamically stable oxide phase, corundum (α-Al_2O_3) [1]. The decomposition pathway is influenced by the factors of calcination. The major factors are the physicochemical properties of the initial raw (untreated) material (e.g. particle size, shape, substituting elements) and the circumstances of the heat treatment (temperature, heating rate, composition of the atmosphere, pressure) [9, 10].

The thermal decomposition reactions of aluminum-hydroxides has been reported since the middle of 20th century in a row of papers. Figure 1. summarizes the reaction pathways depending on the conditions of thermal treatment and the physical properties of particles. The following decomposition reactions are given for normal atmospheric air pressure. Dehydroxylation of gibbsite begins above the temperature of 200-300 °C. At higher temperatures different amorphous and crystalline alumina phases appear. The last step of all decomposition pathways is the formation of corundum (α-Al_2O_3). Over 200 °C a part of gibbsite loses two moles of H_2O and changes into oxi-hydroxide, as boehmite. Above 300 °C gibbsite decomposes directly into aluminum-oxide. Boehmite loses the remaining one mole of H_2O at 450-550 °C [1]. Decomposition temperatures are influenced by heating rate: the faster the temperature increase, the higher the starting temperature of decomposition is [11, 12].

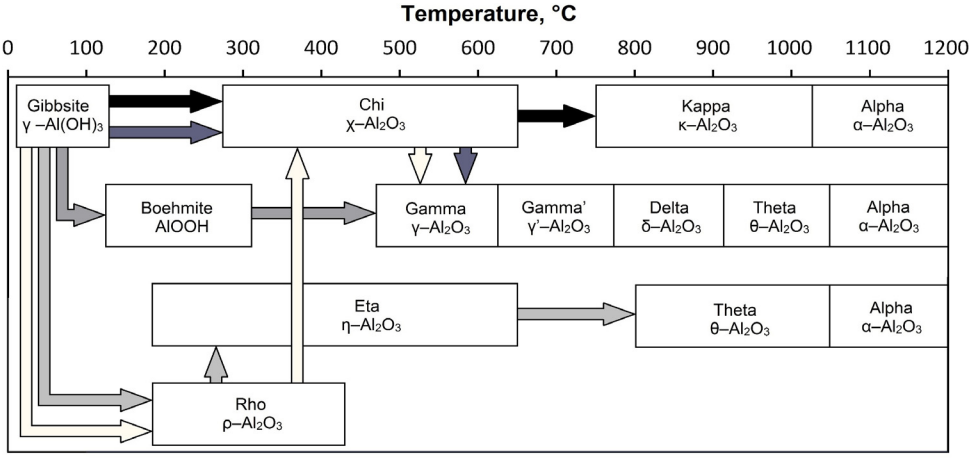

Figure 1. Thermal decomposition pathways of gibbsite, adapted from Perander [10].

Phenomenon of boehmite formation is explained by several authors, in different ways. Conditions causing higher internal steam pressure within the particle (coarse particles, high heating rate, and high concentration of water steam) favor the decomposition via boehmite. With slow heating, fine particles retard the formation of boehmite, favoring the direct decomposition into oxides [13, 14]. These predicates are prevalent in case of heat treatment at normal atmospheric pressure. If the pressure is lower (vacuum) or higher (overpressure) as normal atmospheric pressure, the decomposition processes are different [15-17]. Opposed to the above arguing, Mercury et al. [9] states that gibbsite decomposes to boehmite irrespective of particle size distribution. In case of amorphous material, the decomposition yields oxides, without boehmite formation [9, 18].

Effect of long term grinding of gibbsite is the amorphisation and appearing of gel-like hydroxide phases. The original water content of gibbsite remains invariable or slightly decreases. The product of thermal decomposition of gel-like hydroxides is amorphous oxide which transforms to crystalline form at elevated temperature [19, 20].

Several authors investigated the thermal decomposition processes of long term ground materials, like gibbsite, bayerite and boehmite [21-24].

Physical properties of alumina products applied as adsorbents, catalysts or catalyst carriers are highly influenced by decomposition processes of gibbsite [23, 25, 26]. The accompanying phenomena of dehydroxilation are in number of cases undesired. Ceramics industry utilizes boehmite when large shrinkage and porosity formation must be avoided [27, 28]. Plastics and electronics industries use increasingly boehmite as fire retardant filler, because boehmite is more stable at higher temperatures compared to gibbsite [29]. The above examples prove the necessity of knowledge expansion over gibbsite thermal decomposition processes.

Present study compares thermal decomposition of three aluminum hydroxide materials: Bayer precipitated, fine precipitated, and short term ground. All of the three samples consisted prevailingly of gibbsite. We attempted to find out, how grain and crystallite size influences the thermal decomposition processes, considering the formation of boehmite as intermediate product.

RESULTS AND DISCUSSION

1. Chemical composition and particle size of starting materials

Chemical composition of C and FP samples is shown in Table 1. As expected, only trace amounts of contaminant elements were detected. Loss on ignition values confirm the $Al(OH)_3$ composition of samples. The measured

Na_2O content is normal for these materials, as residual component from the Bayer-process. Altogether, no chemical compounds were observed that would influence the results of thermal behavior.

Particle size distribution of “original Bayer precipitated” material, CU, GU and FPU can be seen in Figure 2. The “original Bayer precipitated” sample has wide distribution of particle diameter, the size of the finest 10 % of particles is below 30 μm, while the coarsest 10 % of particles exceed 120 μm of size. Size fractionation made the mean particle size overrepresented: limits of finest and coarsest 10 % were 52 and 99 μm, respectively. Grinding reduced the median size of original material to 13 μm. Above figures of ground particle diameter are in accordance with the results of Tsuchida et al. [19]. Further milling causes only moderate decrease in particle size, but degrades the crystal structure. FPU sample has shown the finest particle distribution with median diameter at 1.9 μm.

Table 1. Chemical composition of samples

wt%	SiO_2	Al_2O_3	CaO	Na_2O	K_2O	Fe_2O_3	MnO	TiO_2	P_2O_5	L.O.I
C	0.01	65.4	0.01	0.10	0.05	0.03	0.001	n.d.	0.001	34.398
FP	0.02	65.4	0.01	0.13	0.05	0.02	0.001	n.d.	0.001	34.368
ppm	S	Cu	Zn	Pb	As	Ga	Zr	In	Ge	Sr
C	653	30	275	22	n.d	93	n.d.	n.d	n.d.	n.d
FP	468	12	178	24	n.d	91	n.d.	n.d.	n.d.	n.d

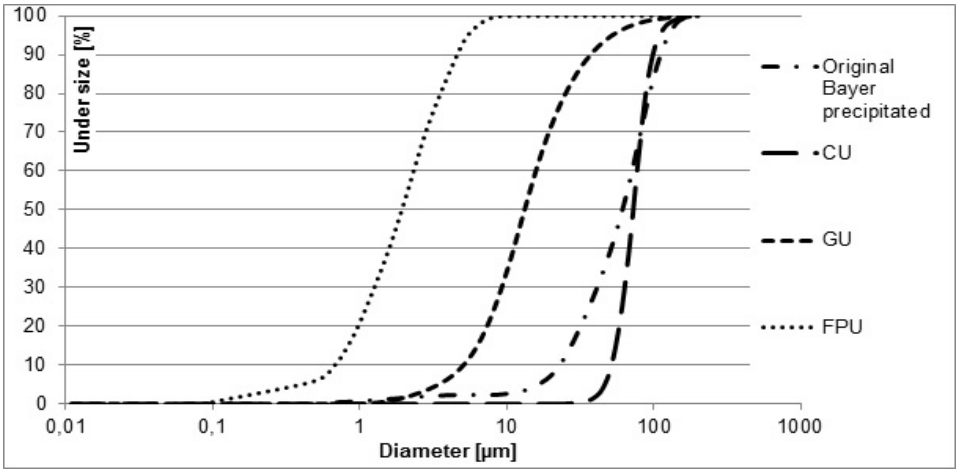

Figure 2. Cumulative particle size distribution of original Bayer precipitated, classified, ground and fine precipitated samples

2. Evaluation of experimental results

2.1. Weight loss during thermal treatment at 260 °C

Boehmite during thermal decomposition of gibbsite evolves between 200-300 °C and remains stable until 400-450 °C [9, 19, 30]. The course of boehmite evolution is followed by direct transformation of gibbsite to oxide. The intersection of the two partially overlapped processes appears between 250-270 °C depending on the conditions of heating. The temperature of heat treatment was chosen as 260 °C, according to our previous survey [31]. We have heated 10 grams of each sample in programmable furnace (Nabertherm, with ±5 °C thermal inertia) at 260 °C for 30 minutes.

Table 2 summarizes the codes of heat treated and unheated samples.

Table 2. Sample codes

Sample	Classified	Ground	Fine precipitated
unheated	CU	GU	FPU
heated	C260	G260	FP260

The weight losses of samples are 18.24 % for C, 22.57 % for G and 9.00 % for FP. The remarkable differences may be caused by different properties of sample materials. At the chosen temperature of heat treatment the coexistence of gibbsite-boehmite and gibbsite-oxide transition reactions is observable. Taken into consideration that at the above temperature the reactions are not finished, it is ascertainable that the extent of mass loss is highly influenced by residence time, properties of material (packing density, heat conductivity) and experimental conditions like water vapor pressure. Diminished mass loss during thermal treatment of FP sample can be referred to the fine sized particles and small packing density [32, 33]. Beyond the experimental and material conditions, the effect of mechanical treatment is assumable too. Largest mass loss was detectable on ground sample, suggesting that the evolved grain structure (higher porosity, flat shape) benefits the escape of water [22, 23, 34].

2.2. X-ray powder diffraction

Boehmite was not detected in the starting materials, and variable material contents without long range order were determined (Table 3). Due to a large deviation of crystallite size values, a complex peak broadening occurred. This was not readily modelled by available options in software, neither did strain refinement and modelling give a solution. As an empirical approach, two similar crystal structures were applied to fit the gibbsite peaks: one for nanocrystalline (<300 nm) and one for microcrystalline (>300 nm) fractions. Crystallite shape effects produced strong preferred

orientation for (*00l*) peaks, modelled by March-Dollase model. Minor preferred orientation was also observed and corrected for (*hk0*) peaks. The C samples gave a similar content for the <100 nm and >500 nm mean crystallite size fractions. The grinded material had mainly microcrystalline fraction, which is realistic for original Bayer process Al-hydroxide [35]. Thus, comparing C and G samples, sieving helped in uniformization of macro- to nanocrystalline fraction ratio. In a contrasting way, FP sample is dominantly nanocrystalline, according to mean crystallite sizes (Table 3A), also indicated by BET results.

Table 3. Mineralogical composition of aluminum hydroxide samples (CS_m=mean crystallite sizes in nanometer)

A						
	CU		GU		FPU	
Phase Name	wt%	CS_m [nm]	wt%	CS_m [nm]	wt%	CS_m [nm]
Gibbsite-n	44.3	78	8.6	220	7.4	270
Gibbsite	40.7	4800	75.4	2000	67.6	350
Crystallinity undetectable	14.0		16.0		25.0	
B						
Phase Name	C260		G260		FP260	
Gibbsite-n	7.2	95	10.0	55		
Gibbsite	42.9	600			62.3	350
Boehmite	27.9	55	14.0	53	8.7	60
Crystallinity undetectable	22.0		76.0		29.0	

Phases with undetectable crystallinity were observed as two separate humps (Figure 3.), attributed to the differences in chemical composition. However, the hump centered between 10 Å and 8 Å marks an angular ranger, where the main peaks of scarbroite group minerals have their main XRD peaks. Scarbroite [$Al_5(CO_3)(OH)_{13}$•$5(H_2O)$, $d_{(003)}$=8.660 Å – $I_{\%}$=100, $d_{(-102)}$=8.340 Å – $I_{\%}$=40] and hydroscarbroite [$Al_{14}(CO_3)_3(OH)_{36}$•(H_2O), $d_{(100)}$=9.000 Å – $I_{\%}$=100] are hydrated Al-hydroxide-carbonates. Our presumption is that similar compounds may appear during precipitation, in low amounts and rather low crystallite sizes, thus their presence may not be detected. In our unheated samples these broad peaks gave crystallite sizes of a few nanometers only, therefore we chose to fit them as amorphous humps. The second hump at ~4.3 Å is considered to be an amorphous phase of gibbsite composition, as not crystallized residuum of precipitation. The

amorphous content slightly increased with grinding, due to minor amorphisation. The elevated amorphous content of FP sample is derived from its technological process and is supposed to be of Al-hydroxide composition.

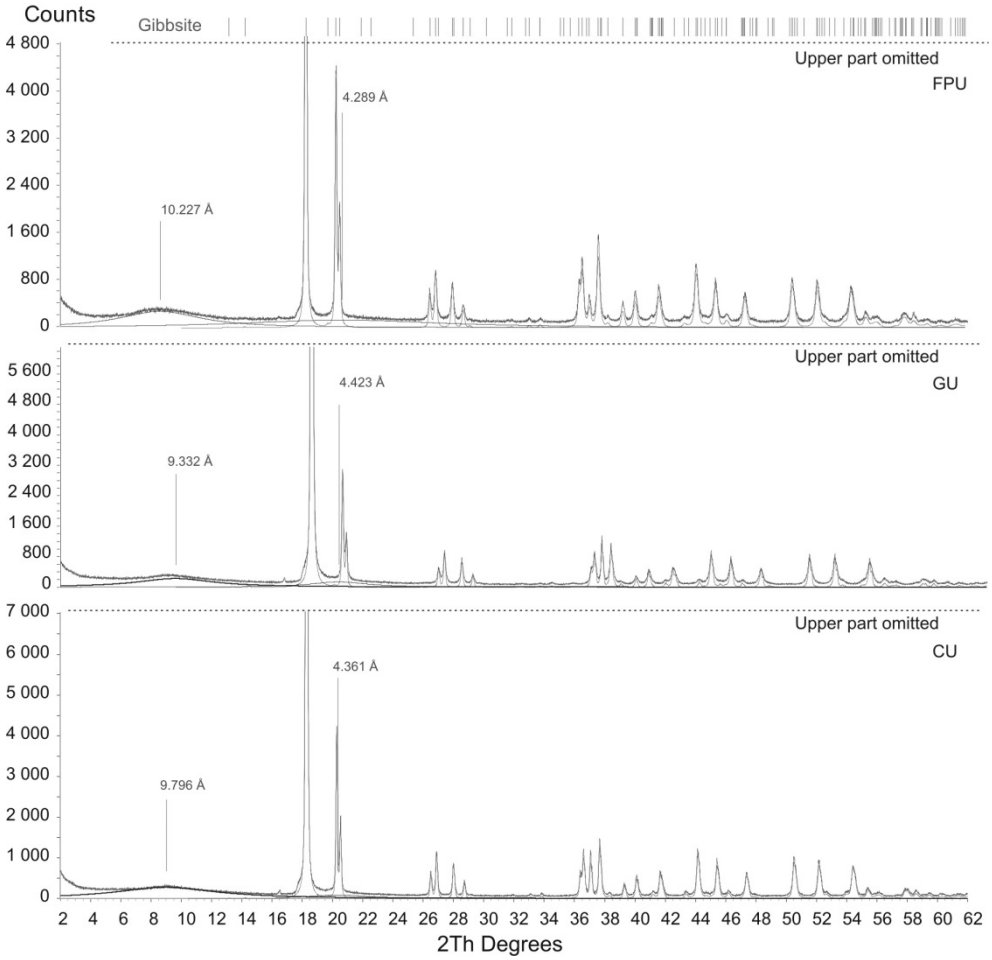

Figure 3. Rietveld-refinement results on XRD patterns for unheated samples

After heat treatment, the microcrystalline fractions were reduced or eliminated, transformed into nanocrystalline fraction (Table 3B). The amorphous content was highly raised in G sample, while only a moderate and minor increase was observed for C and FP samples, respectively. The amorphous hump at ~10Å was shifted to higher d(Å) values in G and FP, and was reduced in C sample (Figure 4). The persistence of ~10Å hump is assumed

to the presence of larger grains in unground material. The new broad peaks are due to the formation of partly dehydroxylated $Al(OH)_{3-x}$ or oxide phases. However, we did not found any similar results among available published data. Boehmite also was formed in different amounts for each material type. In C sample its amount is the highest, which is partly due to the higher nanocrystalline gibbsite content, which is readily transformed into boehmite in this stage. The boehmite to gibbsite ratio is higher in G material, but the boehmite amount is low, most of the microcrystalline and nanocrystalline gibbsite was decomposed. The lowest boehmite formation was observed in FP material, with almost all of the gibbsite being retained. To explain this behavior we have to take into account several influencing factors.

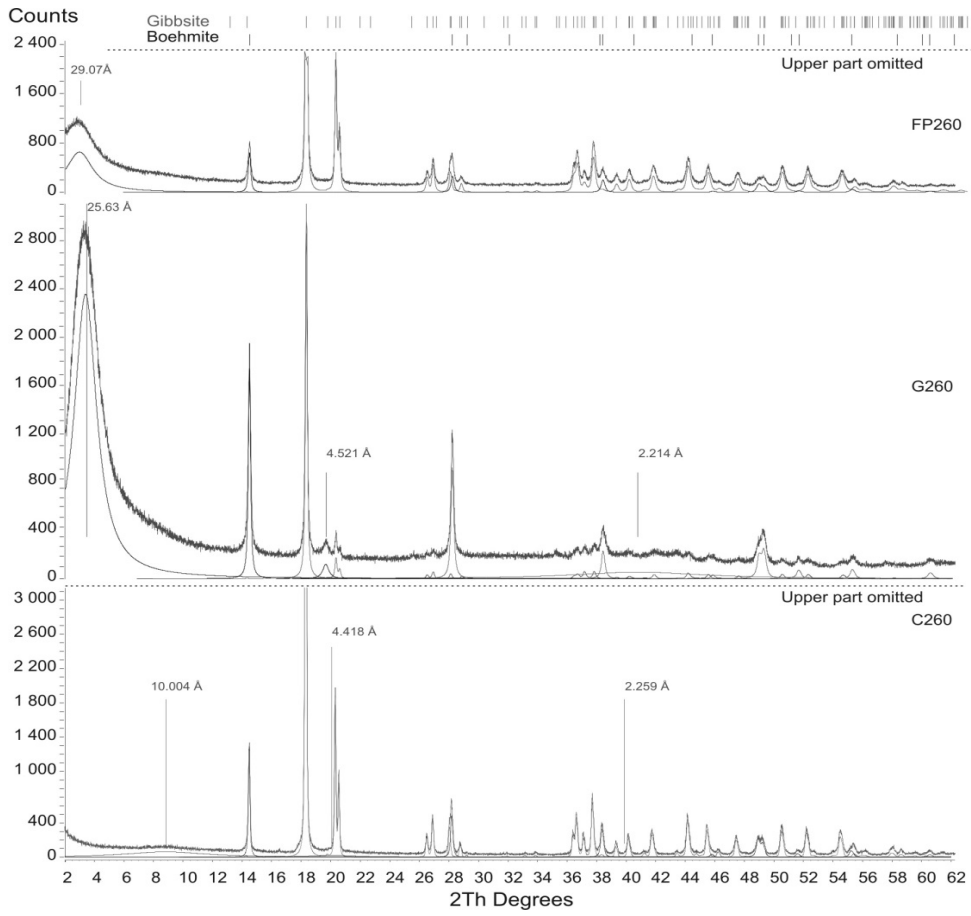

Figure 4. Rietveld-refinement results on XRD patterns for heat treated samples

The small particle diameters do not promote the hydrothermal conditions necessary for boehmite formation within the core of crystals [14, 15, 23, 36, 37]. Considerable affecting factors can be the retarded heat transfer mechanism in the volume of material and consequently the decelerated warming rate and the shorter soaking time. The finer grained the material, the more closed pores can be formed in the intergranular space, by agglomeration, reducing thermal conductivity. In the meantime, due to the increases in grain boundary ratio with decreasing grain size, and small packing densities, diffusion of heat is also slowed down [32, 33]. We must also take into account the higher amorphous content of FP sample. If the amorphous material is present as a layer on Al-hydroxide grains, by dehydration may form a coating layer, which is also inhibiting the rising of boehmite. These factors together may result in the low boehmite formation and gibbsite retaining in FP260 sample.

According to our XRD evaluations, the crystallite size also suffered variations during thermal treatment. In both C and G samples the mean crystallite size of retained gibbsite is <100 nm and the resulted boehmite gave results of ~50 nm. In FP sample, most of the microcrystalline gibbsite was retained, with high crystallite size (unaffected by heating) but the resulted boehmite also gave values of ~60 nm (Table 3B).

2.3. Thermal analysis

Individual sub-processes of thermal decomposition of gibbsite are more or less distinguishable on TG-DTA curves, depending on the conditions of analysis. Experimental curves were divided into the following four steps: I. loosing of adsorbed water (up to 200 °C); II. transformation of gibbsite to boehmite (beginning: 200-220 °C, end: 260-285 °C); III. transformation of gibbsite to oxide (beginning: 260-280 °C, end: 385-440 °C); IV. dissociation of boehmite to oxide (beginning: 435-480 °C, end: 560-595 °C). Some of the above processes are partly overlapped (step II. and step III.), making impossible the exact evaluation of data. Step I. was negligible in case of unheated samples. During step IV. not only the boehmite contained by the sample, but boehmite evolved during step II. is decomposed. Evaluated data are shown in Table 4 and Figure 5.

Step I. is only detectable on heat treated samples. Water which escapes during step I. is derived not from original sample, but adsorbed during the time passed between heat treatment and analysis. Summing the mass decrements of thermal analysis (on basis of unheated material) and mass decrement of heat treatment results in higher total loss, in case of

C260 and G260 samples, than the stoichiometric calculated (34.6 %) loss. Subtracting mass decrement during step I. from total loss yields a result approximating eligibly the theoretic mass loss.

Table 4. TG changes and DTA peak areas during thermal analysis

		Unheated			Heat treated		
		C	G	FP	C	G	FP
Step I.	TG decrement [%]	n.d.	n.d.	n.d.	2.5	3.3	1.8
	TG decrement calculated for U sample [%]				2.0	2.5	1.6
	DTA peak area [uV s/mg]				17.4	17.8	8.6
Step II.	TG decrement [%]	5.5	2.2	n.d.	n.d.	n.d.	n.d.
	TG decrement calculated for U sample [%]	-	-				
	DTA peak area [uV s/mg]	43.2	13.3				
Step III.	TG decrement [%]	21.6	25.6	30.5	14.5	9.0	21.9
	TG decrement calculated for U sample [%]	-	-	-	11.8	6.9	19.9
	DTA peak area [uV s/mg]	237.4	244.3	274.2	130.8	37.3	180.1
Step IV.	TG decrement [%]	3.9	2.9	1.5	5.3	3.7	2.7
	TG decrement calculated for U sample [%]	-	-	-	4.4	2.9	2.4
	DTA peak area [uV s/mg]	36.2	15.5	5.4	41.6	12.2	5.0
Total mass loss [%]		34.1	33.6	34.5	23.3	17.4	27.7
Total mass loss calculated for U sample [%]		-	-	-	19.1	13.5	25.2

The unheated samples contain phases considered as amorphous. Those phases exhibit crystalline hydroxide-like behavior during thermal analysis. Presence of above phases has not caused observable deviance between stoichiometric and measured weight loss, nor resulted in surplus peaks. Thermal decomposition under 200 °C can be attributed to mechanically amorphised hydroxides, and is characteristic in case of prolonged/intensive grinding [19, 22, 23]. Neither GU nor G260 samples have shown signs of grinding caused amorphisation.

Step II. is detectable only in case of untreated samples, what suggests that remaining gibbsite content of heat treated samples will not transform to boehmite. Difference between TG decrements and DTA peaks (C>G>FP) of unheated samples during Step II. indicates different amounts of boehmite evolved due to the dissimilar particle and crystalline sizes of powders.

All of samples had shown TG decrease during step III. The total mass losses of untreated samples are comparatively correspondent. Consequently the extent of step III. is influenced by boehmite evolution and decomposition (boehmite evolves at expense of gibbsite). Remaining hydroxide content, therefore mass loss during step III., of heat treated samples is affected by losses during previous decomposition processes.

Step IV. indicates the decomposition of boehmite formed during Step II. or previous heat treatment. Similarly to Step II., extent of TG decrement and DTA area during Step IV. correlates to the inclination of boehmite formation of original samples, what is influenced by particle and crystalline sizes. Largest TG decrease and DTA area belongs to C samples (heat treated and untreated too) while G samples show considerably smaller, and FP samples indicate the smallest values. This suggests that during calcination of Bayer precipitated coarse aluminum-hydroxide particles the decomposition pathway via boehmite is more significant compared to ground or fine precipitated materials. Considerable differences were not experienced between heat treated and unheated samples in extent of Step IV.

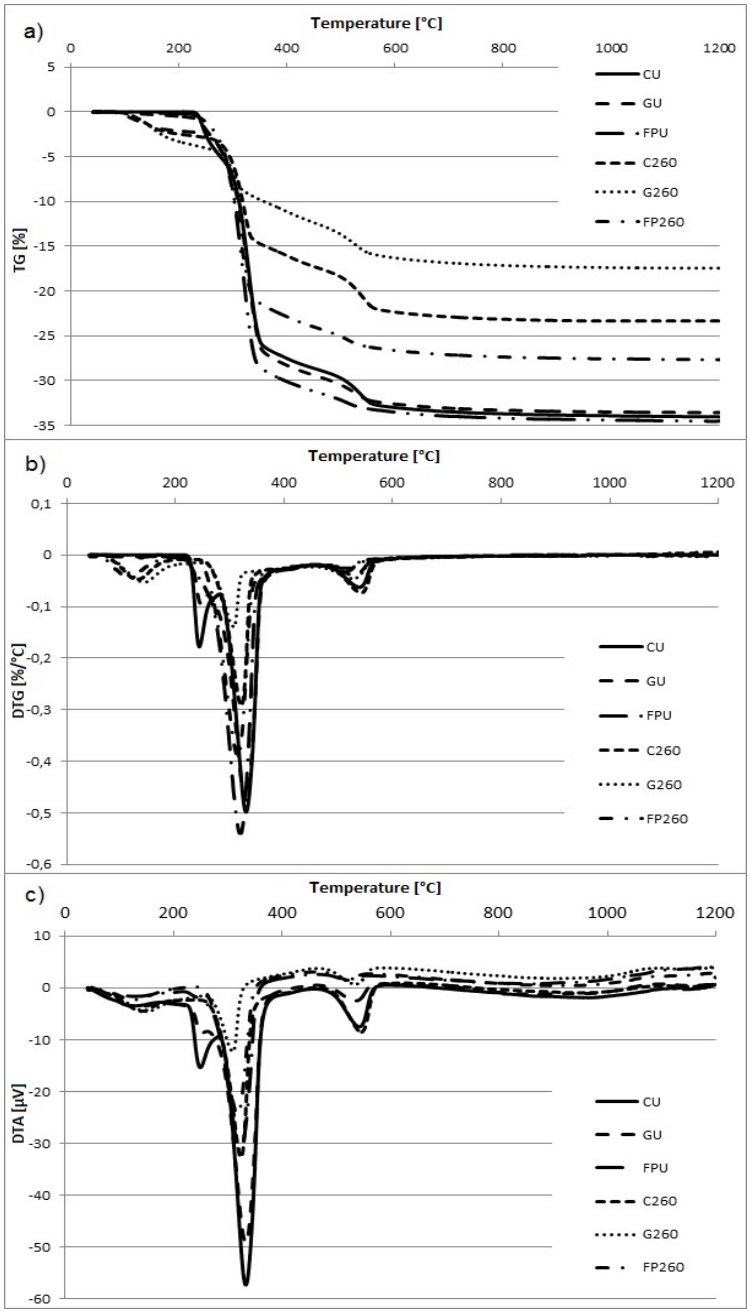

Figure 5. Thermoanalytical curves of samples: a) TG, b) DTG, c) DTA

2.4. Specific surface area

BET specific surface areas of the samples are visible on Figure 6. CU sample has the smallest value (0.12 m^2/g), while grinding increased that to 4.33 m^2/g. FPU is the finest sample (difference in particle size between FP and G is approximately one order of magnitude), the BET specific surface are of FPU is 2.96 m^2/g. It suggests that bigger surface area caused by grinding evolves not only because of attrition and emerging new surfaces, but contribution of porosity can be considerable too. Initial stage of calcination causes rapid growing of porosity and specific surface area. This is attributable to evolved water molecules escaping to the particle surface, forming slit shaped pores parallel to the 001 plane [10, 36]. As it is noticed, BET specific surface areas of C260 and FP260 samples are approximately equivalent (97.29 m^2/g and 101.24 m^2/g, respectively), while in case of G260 sample it is larger (234.34 m^2/g). It must be taken into account that heat treatment of different samples resulted in different degree of decomposition.

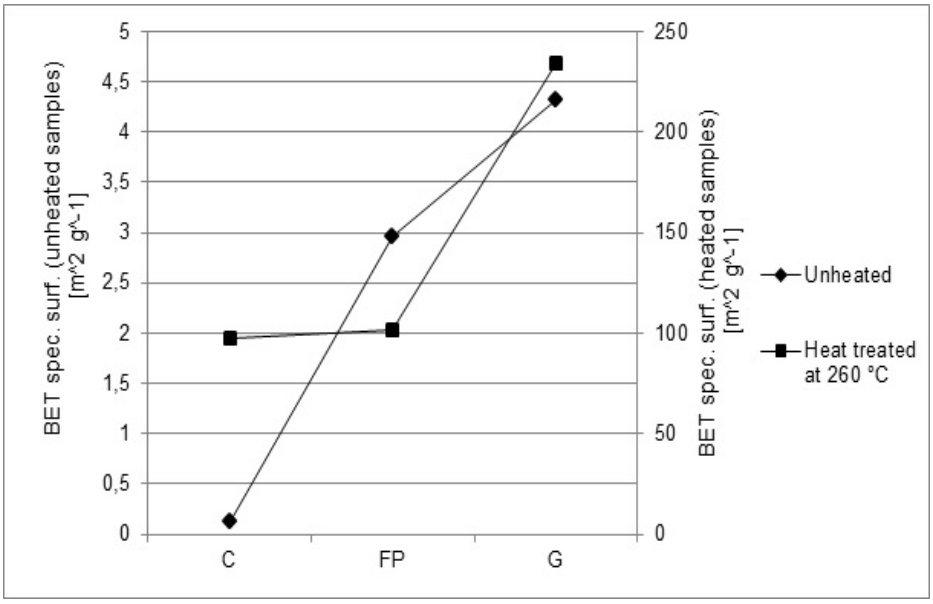

Figure 6. BET specific surface area of unheated (left axis) and heated (right axis) samples

2.5. Scanning electron microscopy

CU sample particles are agglomerates of single pseudohexagonal platy crystallites (Figure 7a). Heat treatment at 260 °C has not caused change on morphological appearance, while the long-shaped pores parallel to 001 plane are distinguishable (Figure 7b). Grinding caused considerable decrease of particle size, however particle fragments above size of 30 μm are observable too. Those relatively big particle fragments are plate like shaped, cracked along the 001 plane (Figure 7c). Craks are perceptible on the sides parallel to 001 plane of the lumps within heat treated sample (Figure 7d). Difference between particle size of GU and FPU samples is approximately one order of magnitude. Occurrence of particles with diameter above 1 μm is extremely rare in FPU. Morphological differences between FPU and FP260 samples with available method was not detectable (Figure 7e-f).

CONCLUSIONS

Both the L.O.I. values at XRF measurements and TG weight loss proved that all the samples have a $Al(OH)_3$ ($\pm$ H_2O) chemical composition, regardless of their crystalline or amorphous state. The possible presence of hydrated (and carbonated?) Al-hydroxide was indicated by XRD, considered as amorphous.

The phases with undetectable crystallinity calculated from XRD are not influencing the weight losses by heating, but in the case of FP sample it might have a role in inhibiting boehmite formation. According to TG results, the higher weight loss was recorded in FPU sample, with the lowest crystallite sizes for gibbsite. Accordingly, the lowest weight loss was observed for GU samples, with the highest microcrystalline gibbsite content.

Specific surface area is increased by grinding, due to the opening of closed nanopores by disaggregation. The highest degree of amorphous formation happened in the material with highest specific surface area, proving the importance of free grain surfaces in gibbsite decomposition.

Boehmite formation is mainly promoted by aggregate grain size and internal morphology (relevant for steam pressure generation) but also the microcrystalline nature of gibbsite, as a secondary factor.

As we could observe, thermal treatment affected the grain integrity of samples, cracking appeared on crystallographic directions, mainly in the (*001*) plane. From XRD results also a decrease in crystallite size for gibbsite is observed. This indicates, that the cracking observed by SEM is affecting the integrity of crystallites.

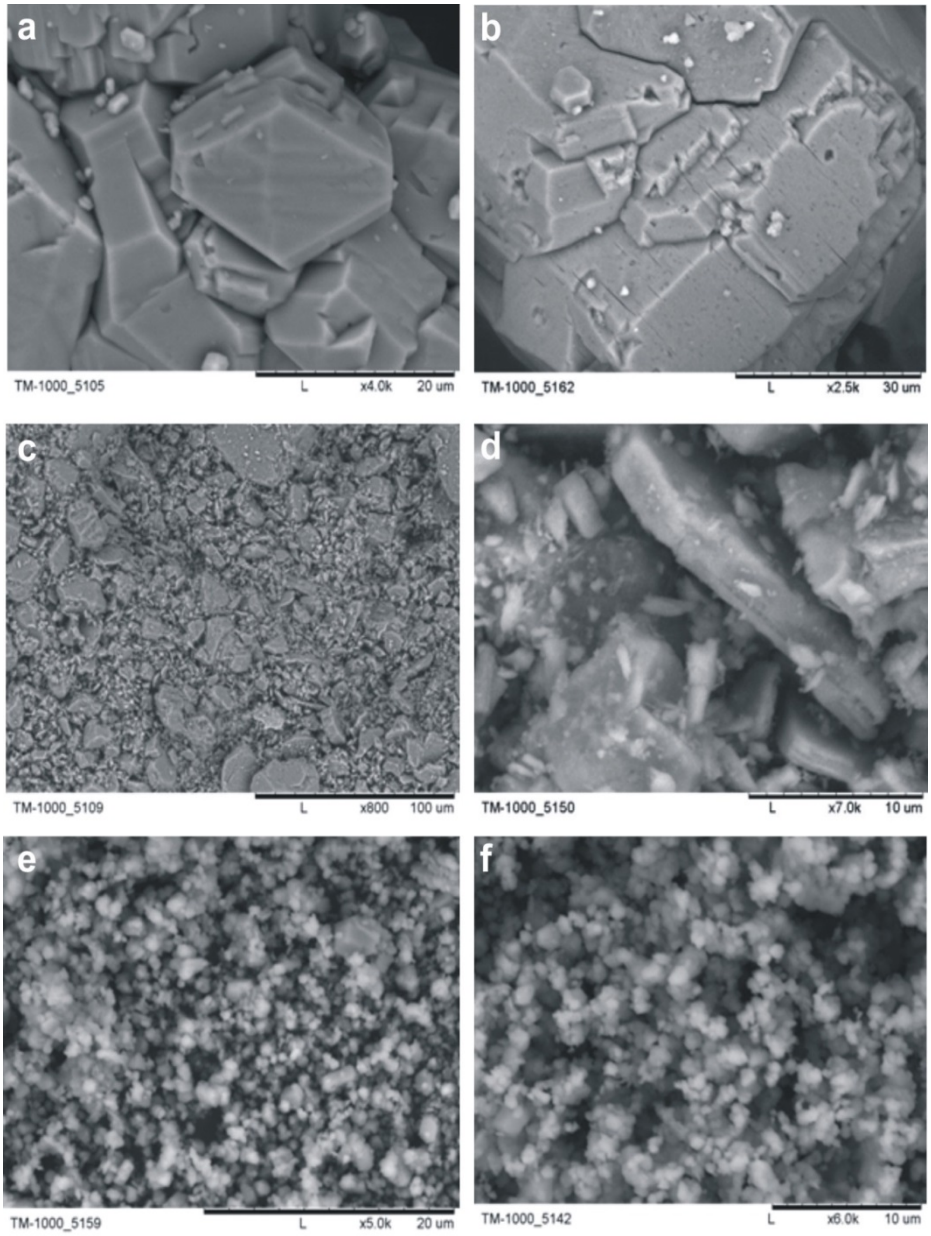

Figure 7. SEM images of samples; a) CU, b) C260, c) GU, d) G260, e) FPU, f) FP260

EXPERIMENTAL SECTION

1. Instrumentation

Particle size determinations were done on a Horiba LA-950 laser scattering particle size distribution analyzer in presence of sodium pyrophosphate solution. Samples were dispersed in ultrasonic bath for one minute before the measurement.

The chemical composition of C and FP samples was measured by X-ray Fluorescence Spectrometry (XRF, Rigaku Supermini200, WD-system, Pd source, 50kV-4nA).

X-ray powder diffraction (XRD) was performed for each material (Bruker D8 Advance, Cu-Kα source, 33 kV and 50 mA, Bragg-Brentano with Våntec-1 position sensitive detector). Measurement time of 5 minutes was allowed, to avoid rehydration of heated samples. Quantitative results were obtained by Rietveld-refinement, in Bruker TOPAS4 software, using ICSD database, unit cell parameters were refined and mean crystallite sizes determined.

Thermal analysis by simultaneous differential thermal analysis (DTA), thermogravimetry (TG) and derivative thermogravimetry (DTG) was made on a Setaram Setsys 24 instrument (heating rate 10 K min^{-1} up to 1200 °C, 55-60 mg sample, dispensed into ceramic crucible, in synthetic high flow air atmosphere). The base-line correction of DTA curves was done with measured correction data (α-Al_2O_3), smoothing of TG and DTA data was unnecessary.

Scanning electron microscopy (SEM) for morphological examinations were performed on a Hitachi TM 1000 instrument at 15 kV acceleration voltage and 10nA probe current. The powder samples were deposited on self-adhering carbon plates, without surface coating, in low vacuum chamber, to avoid morphology and aggregate structure deterioration. Back-scattered electron (BSE) images were recorded.

Specific surface area was measured on TriStar 3000 analyzer by multipoint BET method (77.35 K temperature, N_2 adsorptive, 0.3-0.5 g sample).

2. Materials

Examined materials were obtained from original Bayer precipitated, by sieving – size fractioned Bayer precipitated (C), and grinding – ground Bayer precipitated (G) aluminum hydroxide. Sieving was done in dry state between sieves with mesh size of 63 and 100 μm, shaken for 5 minutes. Size fractionation allows to avoid the disturbing effects in analytical results, caused by extremely fine and coarse particles. Ground sample was prepared in planetary mill by dry grinding (Fritsch Pulverisette 6). Six grams of C Al-hydroxide was

charged into an agate jar of 250 ml together with six agate balls (18 mm diameter). Duration of grinding was 15 minutes at a rotational speed of 500 rpm, stopped in every five minutes, to remove the adhered material from the inner wall of jar. Conditions of milling corresponded to our former experiment [31].

Also a fine precipitated (FP) aluminum hydroxide, with a finer grains size, was used in experiments, to compare its behavior with C and G. Original Bayer precipitated and fine precipitated materials were purchased from MAL Co. Ltd. Ajka Plant (Hungary). Purity of fine precipitated aluminum hydroxide (type of ALOLT 60DLS) is above 99.5 %, analyzed contaminations are SiO_2: 0.004 mass % and Fe_2O_3: 0.006 mass % (results given by MAL Co. Ltd.).

ACKNOWLEDGMENTS

The work described was carried out as part of the TÁMOP-4.2.1.B-10/2/KONV-2010-0001 project in the framework of the New Hungarian Development Plan. The authors are grateful for the help of Dr. Gábor Mucsi (grain size analysis) and Tibor Ferenczi (BET specific surface area analysis). Dr. Prof. László A. Gömze is aknowledged for his help in obtaining the SEM images.

REFERENCES

1. W.H. Gitzen, „Alumina as a Ceramic Material”, American Ceramic Society, Westerville, **1970**.
2. R. Salomão, J. Brandi, *Ceram. Int.,* **2013**, *39*, 8227.
3. R. Salomão, M.O.C. Villas Bôas, V.C. Pandolfelli, *Ceram. Int.*, **2011**, *37*, 1393.
4. L. Peng, X. Xu, Z. Lv, J. Song, M. He, Q. Wang, L. Yan, Y. Li, Z. Li, *J. Therm. Anal. Calorim.*, **2012**, *110*, 749.
5. W.J. Tseng, P. Wu, *Ceram. Int.*, **2012**, *38*, 4461.
6. W.J. Tseng, P. Wu, *Ceram. Int.*, **2012**, *38*, 2711.
7. F. Habashi, “Extractive Metallurgy of Aluminum”, in G.E. Totten, D.S. MacKenzie, “Handbook of Aluminum: Volume 2: Alloy Production and Materials Manufacturing”, Taylor & Francis, New York, Basel, **2003**.
8. A.R. Hind, K.S. Bhargava, C.S. Grocott, *Colloid. Surface*, **1999**, *146*, 359.
9. J.M.R. Mercury, P. Pena, A.H.D. Aza, D. Sheptyakov, X. Turrillas, *J. Am. Ceram. Soc.*, **2006**, *89*, 3728.
10. L.M. Perander, “Evolution of Nano- and Microstructure During the Calcination of Bayer Gibbsite to Produce Alumina”, PhD thesis, The University of Auckland, Auckland, **2010.**
11. B. Zhu, B. Fang, X. Li, *Ceram. Int.*, **2010**, *36*, 2493.

12. B. Xu, P. Smith, *Thermochim. Acta*, **2012**, *531*, 46.
13. B.K. Gan, I.C. Madsenb, J.G. Hockridge, *J. Appl. Crystallogr.*, **2009**, *42*, 697.
14. J. Rouquerol, F. Rouquerol, M. Ganteaume, *J. Catal.*, **1975**, *36*, 99.
15. J. Rouquerol, M. Ganteaume, *J. Therm. Anal.*, **1977**, *11*, 201.
16. N. Koga, S. Yamada, *Solid State Ionics*, **2004**, *172*, 253.
17. C. Novák, G. Pokol, V. Izvekov, T. Gál, *J. Therm. Anal.*, **1990**, *36*, 1895.
18. I.N. Bhattacharya, S.C. Das, P.S. Mukherjee, S. Paul, P.K. Mitra, *Scand. J. Metall.*, **2004**, *33*, 211.
19. T. Tsuchida, N. Ichikawa, *React. Solid.*, **1989**, *7*, 207.
20. J. Temuujin, K.J.D. MacKenzie, M. Schmücker, H. Schneider, J. McManus, S. Wimperis, *J. Eur. Ceram. Soc.*, **2000**, *20*, 413.
21. T.C. Alex, *J. Therm. Anal. Calorim.*, **2014**, *117*, 163.
22. K.J.D. MacKenzie, J. Temuujin, K. Okada, *Thermocim. Acta*, **1999**, *327*, 103.
23. N. Koga, *J. Therm. Anal. Calorim.*, **2005**, *81*, 595.
24. N. Koga, T. Fukagawa, H. Tanaka, *J. Therm. Anal. Calorim.*, **2001**, *64*, 965.
25. E.E. Kiss, G.C. Boskovic, *Rev. Roum. Chim.*, **2013**, *58*, 3
26. C. Dan, E.-J. Popovici, F. Imre, E. Indrea, P. Mărginean, I. Silaghi-Dumitrescu, *Studia UBB Chemia*, **2007**, *LII*, 91.
27. S. Cassiano-Gaspar, D. Bazer-Bachi, J. Chevalier, E. Lécolier, Y. Jorand, L. Rouleau, *Powder Technol.*, **2014**, *255*, 74.
28. K. Okada, T. Nagashima, Y. Kameshima, A. Yasumori, *Ceram. Int.*, **2003**, *29*, 533.
29. C.J. Oh, Y.K. Yi, S.J. Kim, T. Tran, M.J. Kim, *Powder Technol.*, **2013**, *235*, 556.
30. M. Földvári, "Handbook of thermogravimetric system of minerals and its use in geological practice", Magyar Állami Földtani Intézet, Budapest, **2011**.
31. V.Z. Baranyai, F. Kristály, I. Szűcs, *Materials Science and Engineering: A Publication of the University of Miskolc*, **2013**, *38*, 15.
32. H.W. Zhang, Q. Zhou, H.L. Xing, H. Muhlhaus, *Powder Technol.*, **2011**, *205*, 172.
33. K.C. Smith, T.S. Fisher, *Int. J. Hydrogen Energy*, **2012**, *37*, 13417.
34. K.J.D. MacKenzie, J. Temuujin, M.E. Smith, P. Angerer, Y. Kameshima, *Thermochim. Acta*, **2000**, *359*, 87.
35. D.A. Ksenofontov, Y.K. Kabalov, *Inorg. Mater.*, **2012**, *48*, 142.
36. B. Whittington, D. Ilievski, *Chem. Eng. J.*, **2004**, *98*, 89.
37. V. Balek, J. Šubrt, J. Rouquerol, P. Llewellyn, V. Zeleòák, I. M. Bountsewa, I.N. Beckman, K. Györyová, *J. Therm. Anal. Calorim.*, **2003**, *71*, 773.

STUDIA UBB CHEMIA, LX, 2, Tom I, 2015 (p. 45-58)
(RECOMMENDED CITATION)

POROUS TITANIUM - AN ENHANCED SUPPORT FOR HUMAN OSTEOBLASTS AFTER ANODIZATION AND c-RGD IMMOBILIZATION

ANA-MARIA SALANTIU[a,*], OLGA SORITAU[b], NOEMI DIRZU[b], FLORIN POPA[a], LIANA MURESAN[c], VIOLETA POPESCU[a], PETRU PASCUTA[a], CATALIN POPA[a]

ABSTRACT. Porous titanium is the material of choice for hard tissue implants but an enhanced osseointegration can be achieved only through subsequent surface conditioning. In this work, we aimed to study the effect of both surface conditioning and immobilization of cyclic Arg-Gly-Asp (RGD) peptide onto two types of porous titanium samples designed for endosseous applications and obtained by Powder Metallurgy (PM) in view of osteoblast cells attachment and proliferation. Cyclic RGD peptide was chosen as bioactive target and was covalently immobilized on anodized PM porous titanium. The samples, formerly pressed with 200 or 400 MPa and sintered at 1100°C in vacuum, were first anodized using a constant voltage of 2V for 1 hour with 0.25 M sulphuric acid to enhance the thickness of titanium oxide layer. An intermediary aminoalkylsilane molecule (APTES) was then covalently linked to the oxide layer, followed by the covalent binding of cyclic RGD peptide to the free terminal NH_2 groups using polyethylenglycol diglycidyl ether (PEGDE) as coupling agent. The samples were characterized by micro CT, X-ray diffraction (XRD), scanning electron microscopy (SEM) and Fourier transform infrared spectroscopy (FT-IR). Anodized titanium samples display anatase and rutile on the surface and, after functionalization, two important amide characteristic regions, confirming the presence of cyclic RGD peptide. Cells seeded on samples pressed with 400 MPa, anodized and c-RGD immobilized, displayed a more flattened shape and a more obvious tendency of spreading into pores.

Keywords: *porous titanium, cyclic RGD, anodic oxidation, human osteoblasts*

[a] *Technical University of Cluj-Napoca, Faculty of Materials and Environmental Engineering, 103-105 Muncii Avenue, RO-400641, Cluj-Napoca, Romania,*

[b] *" Prof. I.Chiricuta" Oncological Institute, 34-36 Republic str., RO- 400015, Cluj-Napoca, Romania,*

[c] *Babeş-Bolyai University, Faculty of Chemistry and Chemical Engineering, 11 Arany Janos str., RO-400028, Cluj-Napoca, Romania.*

[*] *Corresponding author: bolfa_anamaria@yahoo.com*

INTRODUCTION

Ti and Ti alloys are intensively studied for most dental and orthopedic applications [1,2]. Porous structures gained an increased interest for medical applications due to their low elastic modulus, matching that of bones [3,4]. A porous surface enhances the implant/ bone bonding by growth of tissue into the pores [5]. To this aim, it was reported that the optimal pore size for bone ingrowth should be between 100 μm and 600 μm [6]. Besides the use of porous surfaces, osseointegration of titanium implants is influenced also by surface properties which are often the basis of successful endosseous implantology [7,8]. Various techniques have been studied and applied to improve the osseointegration of titanium implants [9], such as acid etching, plasma spraying, anodizing [10,11] and also by the use of bioactive coatings [12]. Titanium surface conditioning *via* anodizing has been reported to increase the surface area and the activity of the contacting cells [13]. On the other hand, bioactive coatings have the role to create a strong interface between bone tissues and implant [14]. It is fundamental that the method used to attach a biomolecule to the implant surface is stable enough to keep the biomolecule in place until the desired response is triggered [15].

A method commonly employed to covalently attach biomolecules onto hydroxylated surfaces is functionalization using an aminosilane reaction and subsequent chemical attachment using crosslinkers [15,16]. 3-Aminopropyltriethoxysilane (APTES) is a silane molecule commonly used in the biomedical literature to bond an assortment of materials [16]. The presence of NH_2 end groups on the silanized surface has a major importance in biological applications as it allows proteins or other biomolecules to be attached in a simple way [17]. Bioactive peptides have been used to promote cell adhesion, in particular extensive scientific investigations have been described using RGD peptide, a short amino acid sequence present in several adhesive extracellular matrix proteins, for improving cell adhesion *via* cell membrane integrins reactions [18-20]. It was reported that RGD-related peptides influence also osteoblast mineralization, cytoskeleton reorganization and migration *in vitro* [21].

The purpose of this study was to evaluate the influence of both surface conditioning and c-RGD peptide immobilization on porous titanium with respect to osteoblast adhesion and proliferation.

RESULTS AND DISCUSSION

Microstructural analysis of porous titanium samples

The linear analysis performed on optical images of surfaces revealed an average porosity of 33% for samples pressed with 200 MPa

and 28% for 400 MPa pressed ones, while the average pore size was of 31 μm and 26 μm respectively. Nevertheless, large pores with the conventional diameter of more than 100 μm can be observed for both types of samples (Figure 1a and b). The shape of pores is irregular, with sharp edges; interconnected pores are representing the majority, as it can be observed also by micro CT images of the cross section of samples (Figure 1b'). This aspect of structure is well suited for osseointegration, while providing a low Young's modulus.

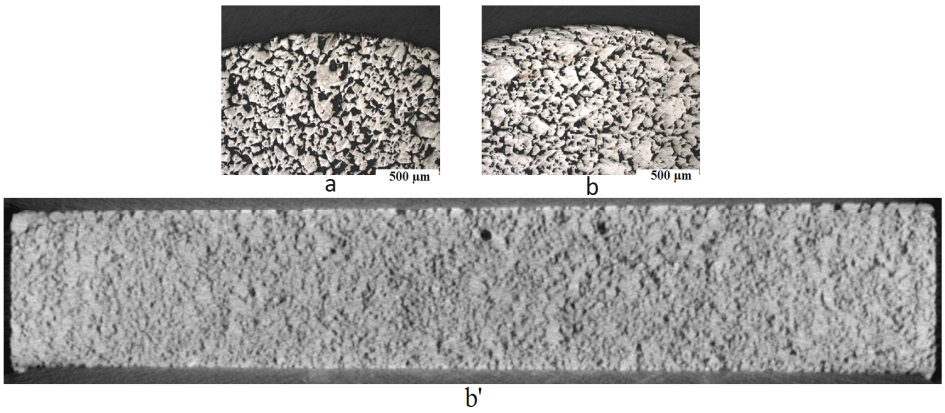

Figure 1. Optical images for titanium pressed samples with 200 MPa (a) and 400 MPa (b) and microCT image for the titanium sample pressed with 400 MPa (b').

Electrochemical behaviour of anodized PM porous titanium

To inspect the influence of manufacturing conditions for the titanium samples pressed with 200 or 400 MPa, chronoamperometric tests were devoted to analyse the influences upon the titanium oxide formation. The curves are shown in Figure 2. The current density / time measurements showed that overall process can be described in two stages. The first stage represents the nucleation of a titanium oxide layer on the porous surface, which lowers the current density in the circuit. In the last stage, the current density remained stable, increasing the thickness of the titanium oxide layer.

When comparing the chronoamperograms results for the different types of titanium samples, Figure 2, it was found that samples pressed with 200 MPa presented the highest intensity of oxidation / dissolution reactions. Such behaviour is explained by the increased active surface of the electrode. In contrast, the curve for the sample pressed with 400 MPa, after the first stage, present an increasing tendency of current density, a certain

instability, which could be related with the sharp edges pores that are more pronounced on this sample (see Figure 1).

Lattice structure of anodized Ti oxide

Figure 3 shows the XRD patterns for untreated porous titanium and anodically oxidized porous titanium in 0.25 M H_2SO_4 for 1hour at 2V and then heat treated at 700°C. For any temperature of the heat treatment below 700°C, no peak corresponding to any of the oxides occurred. Only the peaks of titanium could be observed for the untreated porous Ti sample (Figure 3a). The peaks of rutile and anatase occurred for titanium samples pressed with 200 MPa and then oxidized at 2V (Figure 3b). From Figure 3c it can be seen that a higher compaction pressure of 400 MPa resulted in a decrease of the peak intensity of the rutile phase while no peaks for anatase phase appeared. The trends in anatase and rutile formation should be attributed to the higher thermodynamic stability of the rutile phase with respect to the anatase phase, which makes rutile more likely to form. The differences in the oxide nucleation and growth for the two types of samples, as seen in Figures 2 and 3, are supposed to be generated by the effects at the bottom of pores, as both porosity and pores size display small differences.

Chemical functionalization of anodized porous titanium surfaces and cyclic RGD immobilization

FTIR spectra in the range from 4000 cm^{-1} to 500 cm^{-1} for APTES and PEGDE/c-RGD films grafted on the porous titanium surfaces are shown in Figures 4 and 5. APTES films prepared from toluene solution show similar features in the range presented before, on the anodized titanium samples pressed with 200 and 400 MPa (Figures 4b and 5b). Around 3400 cm^{-1}, the symmetric and asymmetric –NH stretch modes from amino group in APTES were very weak in the spectra. In Figure 4b and also in Figure 5b, between 2800 and 3000 cm^{-1} are found several CH stretch modes corresponding to APTES backbone and ethoxy groups [14]. The most important structural information regarding APTES films is found between 1800-900 cm^{-1}. A vibrational mode around 1655 cm^{-1} is due to the presence of an imine group formed by the oxidation of an amine bicarbonate salt. Two dominating vibrational modes are found around 1575 and 1485 cm^{-1}. Such vibrational modes arise when surface amino groups form bicarbonate salts in a reaction with atmospheric CO_2, as was reported previously [22]. The mode near 1195 cm^{-1} arise from unhydrolyzed ethoxy moieties in APTES ($-OCH_2CH_3$). The peak located around 1110 cm^{-1} is attributed to Si-O-Si from polymerized APTES indicating that the silane agent had been grafted onto the surface of anodized titanium surfaces [23].

Curing of silanes at elevated temperature, 110°C, seemed to enhance the siloxane layer formation on the TiO_2 surface of titanium substrate.

FTIR spectra corresponding to PEGDE/c-RGD peptide films grafted on silanized titanium samples pressed with 200 and 400 MPa are presented in Figures 4c and 5c. The intense band at approximately 2870 cm^{-1} was attributed to the symmetric stretch of the methylene group. Bands in the region 1500-1100 cm^{-1} were generally due to the bending, wagging and twisting modes of the CH_3 and CH_2 groups and the methylenes of the $O\text{-}CH_2\text{-}CH_2\text{-}O$ group. The most intense band at 1093 cm^{-1} was assigned to the asymmetric C-O-C stretch [24].

The ATR-FTIR spectrum of c-RGD-PEGDE for both of the two types of samples show all the characteristic peaks presented before, which demonstrates that c-RGD/PEGDE films have the similar base structure as PEGDE films. However, cRGD/PEGDE films show two more important characteristic regions at 1650 cm^{-1} and at 1559 cm^{-1}, which correspond to the vibrations of amide (-CO-NH) I and II, respectively [25].

These amide groups are from the c-RGD peptide, indicating that c-RGD peptide is present on the films surface anchored on porous titanium samples.

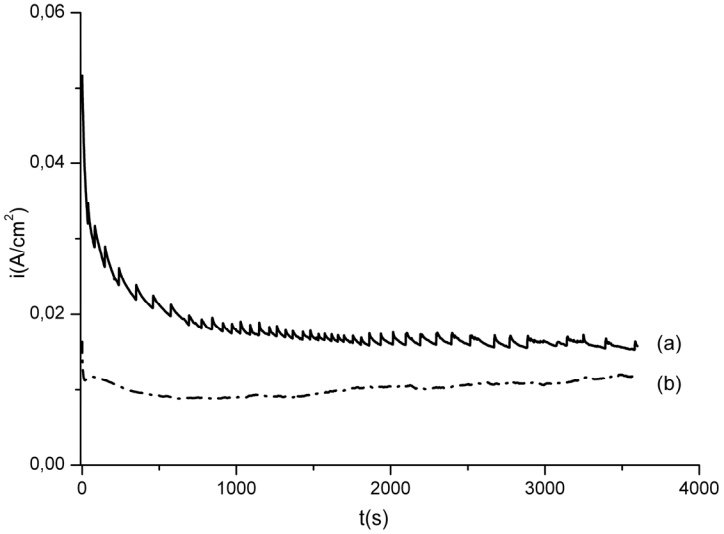

Figure 2. Chronoamperograms for anodic oxidation of titanium samples pressed with 200 MPa (a) and 400 MPa (b).

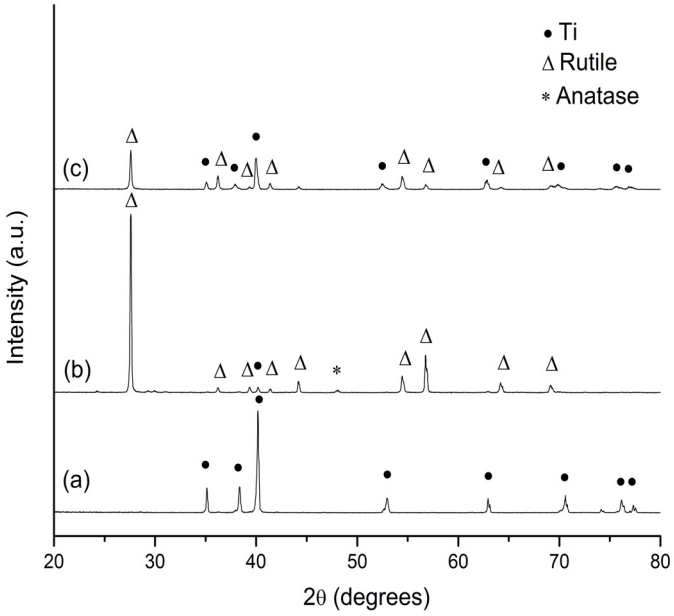

Figure 3. XRD patterns of untreated porous titanium (a) and anodized titanium samples pressed with 200 MPa (b) and 400 MPa (c) at 2V for 1h and then heat treated at 700°C.

Adhesion and proliferation of human osteoblasts

Adhesion and proliferation were evaluated on untreated and on modified (TiO_2, c-RGD) porous titanium samples. To assess cell attachment and morphology, PKH26 marked osteoblast cells were analysed by fluorescence microscopy after 1 hour, 4 days and 14 days of cultivation on the samples mentioned before. The presence of c-RGD peptide increased cell attachment one hour after seeding on both 200 and 400 MPa titanium pressed samples (Figure 6a). After 4 days of osteoblasts cultivation, 200 and 400 MPa titanium pressed samples coated with c-RGD peptide (Figure 6b), sustained a higher number of cells. Cell spreading was observed especially on anodized titanium samples. The best cell proliferation rate after 14 days was observed for c-RGD coated samples pressed with both 200 and 400 MPa, Figure 6c, as well as for untreated and anodized titanium samples pressed with 400MPa.

Cells counting of PKH26 stained cells was performed after the capture of images in three different microscopic fields randomly selected and the obtained results are shown in Figure 7 as cells number/mm^2. After one hour, 400 MPa-RGD samples displayed by far the highest number of attached cells, while the 400 MPa-anodizing samples displayed the lowest. The latter one might be due to the oxidation instability proven in Figure 2b. The same trend could be observed after 4 hours, but all differences were smaller. After 14 days, the highest number of cells corresponds to 400 MPa-anodizing samples and RGD samples come after. The increased fluorescence intensity observed in the optical images for c-RGD coated samples (Figure 6), could be explained by the presence of cells on the RGD samples surface due to cell capture by the peptide sequences, capture which does not allowed their migration into the pores of the samples, as in the case of only anodized samples. For these ones, it seems that along the 14 days, the oxide layer became stable enough.

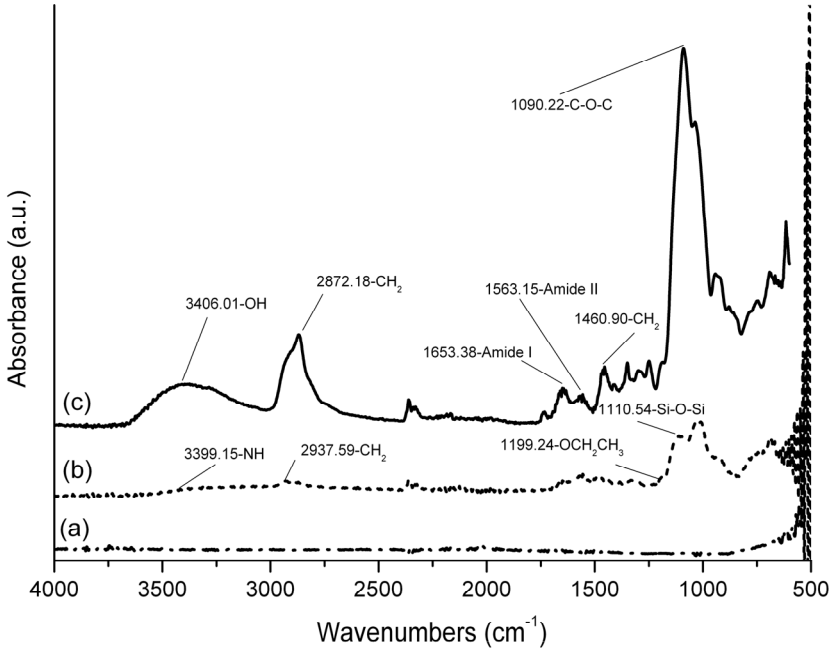

Figure 4. FTIR spectra of (a) anodized, (b) silanized and (c) c-RGD peptide grafting on titanium sample pressed with 200 MPa.

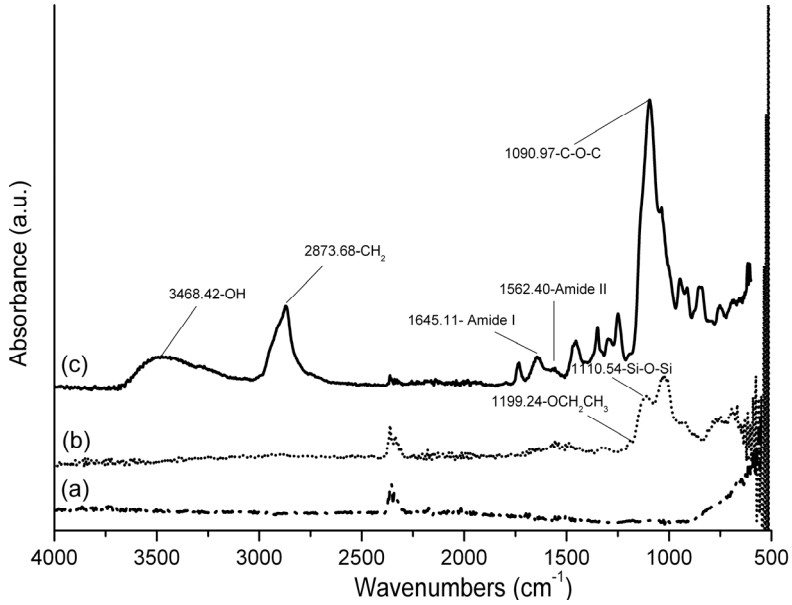

Figure 5. FTIR spectra of (a) anodized, (b) silanized and (c) c-RGD peptide grafting on titanium sample pressed with 400 MPa.

SEM morphological analysis

Figure 8 illustrates the surface SEM micrographs of untreated and modified titanium samples pressed with 200 and 400 MPa without and with osteoblast cells. After 29 days of culture, cells on untreated titanium samples pressed with 400 MPa, Figure 8a, appeared in higher number, more spread and with traces of mineralization in comparison with the sample pressed with 200 MPa. On the anodized titanium sample pressed with 200 MPa without osteoblast cells seeded, Figure 8b, an advanced coverage of the pores with a titanium dioxide layer occurred. For the other type of samples, the difference between untreated and anodized state is not so visible because the coverage with a titanium dioxide layer was reduced. In Figure 8b it can be seen that the osteoblast cells migrated and adhered into the pores of anodized titanium samples, which is consistent to the conclusions for Figure 7.

The presence of c-RGD peptide attachment on the surface of TiO_2 after coating with an intermediate layer of APTES without osteoblast cells seeded was observed as irregular deposits. For the titanium sample pressed with 400 MPa and coated with c-RGD, (Figure 8c), we can observe

the presence of c-RGD attachment at the surface but also in the pores. The presence of the c-RGD peptide on titanium samples pressed with 400 MPa induced a more flattened cell shape with tendency of cell spreading into pores in contrast with the round shape of cells cultivated on c-RGD surface coated titanium samples pressed with 200 MPa, also consistent with the conclusions referring to Figures 6 and 7.

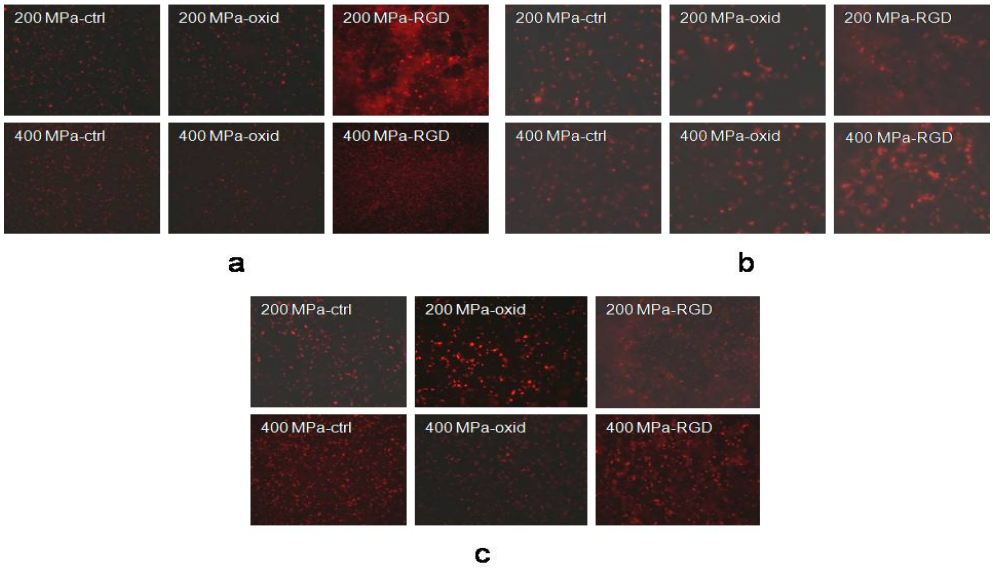

Figure 6. Fluorescence microscopy images (10x) of osteoblast cells stained with PKH26 dye and cultivated on different surface treatment of porous Ti substrate after 1 hour (magnification X100) (a), 4 days (magnification X200) (b) and 14 days (magnification X100) (c).

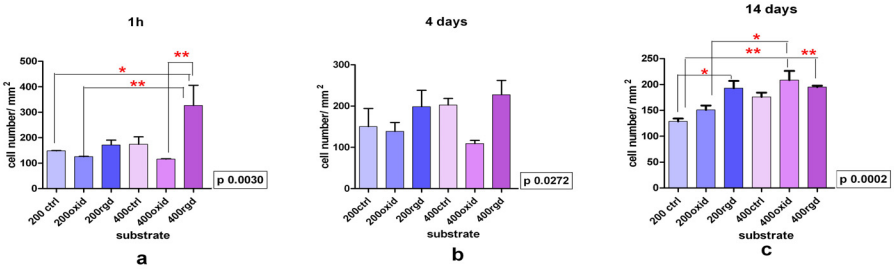

Figure 7. Cell counting graphs for evaluating the cell adhesion one hour after osteoblasts seeding (a) and proliferation rates of osteoblasts on different uncoated and coated titanium surfaces after 4 days (b) and 14 days (c) of cultivation. * indicates a significant statistical difference ($p<0.05$).

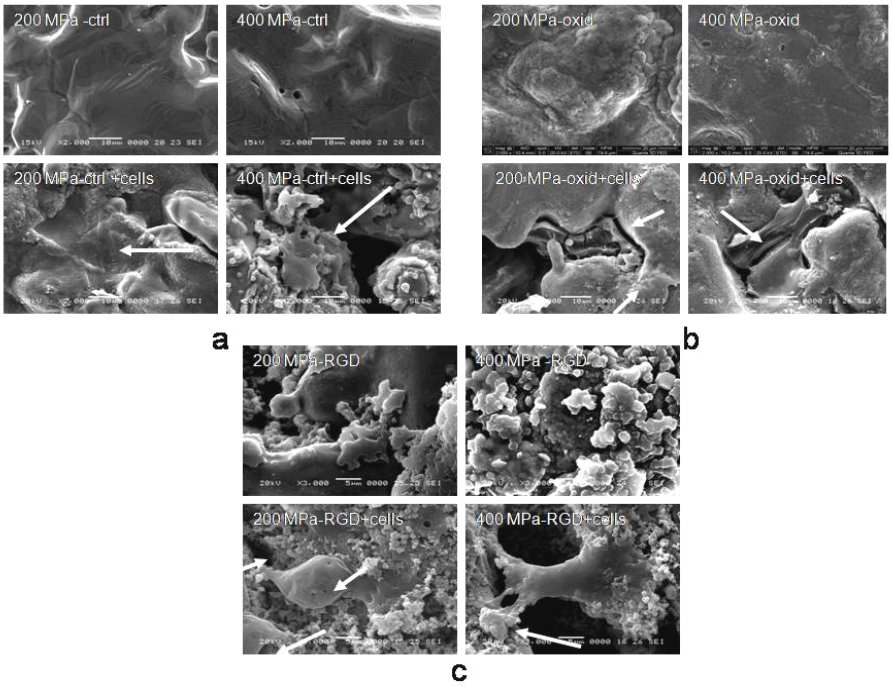

Figure 8. SEM micrographs of untreated titanium samples pressed with 200 MPa and 400 MPa (a), following anodizing (b) and c-RGD immobilization (c) without and with osteoblast cells after 29 days of culture. Arrows indicate adhered cells on samples surface.

CONCLUSIONS

In this study, c-RGD peptide was successfully covalently grafted onto the surface of anodized TiO_2 after coating with an intermediary layer of APTES. Furthermore, the c-RGD peptide promoted the adhesion and proliferation of osteoblast cells. The results of *in* vitro tests showed that c-RGD peptide accelerated the initial attachment of osteoblast cells, phenomenon which is not consistent for a longer time. Therefore, we believe that applying an RGD coating onto TiO_2 anodically grown on porous Ti implants may contribute to the improvement of osseointegration for a design of the implant that provides also other surfaces (i.e. surfaces that were only anodized) to take over the process after the first stages after implantation (weeks time). The porosity resulted after PM processing with various compacting pressures plays also a role in the enhancement of the

biocompatibility for porous titanium. In the conditions of this work, we found that the best behaviour is unexpectedly obtained for pressing with 400 MPa before sintering, leading to a smaller porosity compared to 200 MPa pressing.

EXPERIMENTAL SECTION

Samples preparation

The CP Ti powder (with a purity higher than 99.5%) obtained by hydration-milling-dehydration process with powder particles size lower than 150 μm was used to manufacture porous samples with 11.5 mm diameter. Closed die pressing was performed with 200 and 400 MPa and sintering of the specimens was carried out at 1100˚C for 1h in a high vacuum furnace using a heating and cooling rate of 10˚C/min and a minimum vacuum level of 10^{-5} Torr was guaranted.

Microstructural characterization of the porous titanium samples was performed on the surface by optical/ electron microscopy (Olympus GX51) and in volume by microCT (Bruker microCT analyzer).

Anodizing

Anodic oxidation was performed using a conventional three electrode cell with a porous titanium disk (samples pressed with 200 and 400 MPa) as the working electrode, a platinum electrode as the counter electrode and a saturated calomel electrode (SCE) as the reference electrode. Electrochemical measurements (chronoamperometric investigations) were conducted using a commercial potentiostat PAR 2273 at room temperature. The anodic oxidation was performed at 2V during 1hour in 0.25 M H_2SO_4 solution. All solutions were prepared from reagent grade chemicals and deionized water. After the anodizing, the samples were rinsed with deionized water, dried at 60°C, and then heat treated at 700°C for 1h to crystallize the as-formed amorphous titanium oxide. The film lattice structure was examined by X-ray diffraction (Shimadzu XRD 6000).

Silanization and c-RGD immobilization on porous titanium surfaces

Silanization of porous titanium oxidised samples was performed in 3% Aminopropyl-triethoxysilane (APTES; Sigma Aldrich) in toluene at room temperature overnight. After cleaning in toluene and ethanol, samples were cured at 110°C for 1h. Subsequently, aminosilanised Ti samples were spin coated with 3% solution of polyethyleneglycol diglycidylether (PEGDE; Sigma Aldrich) in 50 mM carbonate-buffer (pH 9), using the following parameters: 1000 rpm, 30s. The excess solution was removed by repeated rinsing with

water. After the deposition of the polyethyleneglycol diglycidylether films, the substrate was heat treated at 80°C for 2h in an oven with a heating and cooling rate of 2°C/min. RGD immobilisation was then immediately performed by spin coating with 0.5 mg/mL RGD peptide (c-RGDFV peptide, Cyclic Calbiochem) in carbonate-buffer with the same parameters presented before (see Scheme 1).

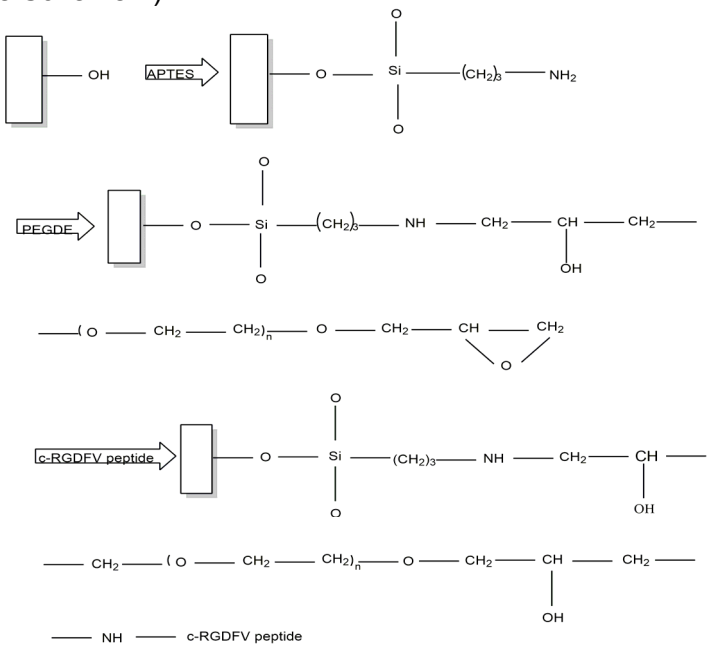

Scheme 1. Reaction schematic diagram for the functionalization and c-RGD peptide grafting onto anodized porous titanium: (I) APTES treatment; (II) bifunctional cross-linker (PEGDE) connection; (III) c-RGD peptide grafting.

FTIR-ATR was used to investigate the structure of APTES, PEGDE, and c-RGD films and the modification of porous titanium surface by a Perkin-Elmer FTIR model equipped with ATR accessory (PIKE MIRacle^{TM}) with diamond crystal plate.

Cell culture

Human osteoblasts at passage eight, isolated and characterized as described by Tomuleasa et al. [26] were cultured in Dulbecco's modified Eagle's medium (DMEM) / F-12HAM (Sigma) containing 10% foetal calf serum (FCS), 2mM L-Glutamine, 1% antibiotics, 1% non-essential aminoacids (NEA) (all reagents from Sigma). Test samples were placed in 12 well plates (Nunc); $1.2x10^5$ cells were seeded in each well.

Cell membrane fluorescent labelling

Fluorescent marking of osteoblasts was performed using PKH26 Red Fluorescent Cell Linker Kits (Sigma-Aldrich). This staining ensures maintenance of fluorescence of live cells for a longer period of time. After trypsinization, $1x10^6$ cells were washed twice with PBS by centrifugation at 1000 rpm, 5 min and the cell pellet was resuspended in 1ml Diluent C and 1ml of Dye Solution (4µl of PKH26/ml) was added, followed by gentle pipetting. The staining was stopped after 5 min by adding 2 ml of complete medium containing 10% foetal calf serum and cells were centrifuged for 10 min at 1000 rpm. Another two washing steps were performed with 10 ml of complete medium and then cells were counted, resuspended in complete medium and seeded in 12 well plates on the surface of titanium samples.
The samples were formerly sterilized by immersion in 70° alcohol and exposing 3 hours to UV radiation.

Cell adhesion

After 1 hour, adherent cells were visualized by fluorescence microscopy (Zeiss Axiovert D1), using filters of 546 nm and the fluorescence intensity was measured using a BioTek Synergy 2 plate reader (excitation 540 nm, emission 620 nm). We used the option of area scan in BioTek measurements that offers multiple values (13 readings) of fluorescence obtained by scanning the whole specimen surface. This is the procedure by which we obtained the final graphical representation.

Cell proliferation

Cell proliferation was quantified using two methods: counting PKH26 stained cells on captured images in 3 different microscopic fields, randomly selected, and by fluorescence intensity measurements with BioTek Synergy 2 plate reader. Readings were performed at 4 days and 14 days.

Statistical analysis

Statistical analysis of cell counts was performed using a GraphPad Prism 5 software, Bonferroni Multiple Comparison post-test. Statistical significance was set at $p < 0.05$.

SEM morphological analysis

The cells were studied after 29 days of culture. Specimens were sputter coated with a gold layer using a Desk V coating device. The surface morphology of the samples with or without seeded cells was studied by scanning electron microscopy (JEOL 5600 LV).

ACKNOWLEDGMENTS

This work was supported partially by the project STEMREG PN-II-PT-PCCA-2011-3.1-0700 and partially by the strategic grant POSDRU/159/1.5/S/137070 (2014) of the Ministry of National Education, Romania, co-financed by the European Social Fund - Investor in People, within the Sectorial Operational Programme Human Resources Development 2007-2013.

REFERENCES

1. S. Nayak, T. Dey, D. Naskar, et al., *Biomaterials*, **2013**, 34, 2855.
2. N.A. Al-Mobarak and A.A. Al-Swayih, *Int. J. Electrochem. Sci*., **2014**, 9, 32.
3. T. Marcu, A.M. Salantiu, I. Gligor, et al., *J. Optoelectron. Adv. Mater*, **2013**, 15**,** 847.
4. I. Gligor, T. Marcu, M. Todea, et al., *J. Optoelectron. Adv. Mater,* **2011**, 13, 879.
5. B. Dabrowski, W. Swieszkowski, D. Godlinski, et al., *J Biomed Mater Res B Appl Biomater* **2010**, 95, 53.
6. L.M. Reis de Vasconcellos, D. Oliveira Leite, F. Nascimento de Oliveira, et al., *Braz Oral Res,* **2010**, 24, 399.
7. D. Arya, S. Tripathi and R Bharti, *J Dent Implant,* **2012**, 2, 93.
8. A.B. Novaes Jr, S.L. Scombatti de Souza, R.R. Martins de Barros, et al., *Braz. Dent. J* , **2010**, 21, 471.
9. H.S. Kim, Y. Yang, J.T. Koh, et al., *J Biomed Mater Res Part B: Appl Biomater*, **2009**, 88B**,** 427–435.
10. S.Oh,K.S. Moon, S.H. Lee, *J. Nanomater,* **2013***,* doi.org/10.1155/2013/965864.
11. S.Y. Park, H.S. Kim, J.H. Kim et al., *J.Tissue Eng Regener. Med*., **2012**, 9, 194.
12. M.L. Schwarz, M. Kowarsch, S. Rose, et al., *J.Biomed Mater Res A.,* **2009**, 89, 667.
13. E.S. Gawalt, M.J. Avaltroni, M. Danahy, et al., *Langmuir,* **2003**, 19, 200.
14. G. Tan, L. Zhang, C. Ning, et al., *Thin Solid Films,* **2011**, 519, 4997.
15. E.C. Pegg, G.S. Walker, C.A. Scotchford, et al., *J. Biomed Mater Res A,* **2009**, 90, 947.
16. P. Renoud, B. Toury, S. Benayoun, et al., *PLoS ONE* 7(7): e39367.2012, **2012**, doi: 10.1371/journal.pone.0039367.
17. N. Aissaoui, L. Bergaoui, J. Landoulsi, et al., *Langmuir,* **2012**, 28, 656.
18. G. Forget, L. Latxague, V. Héroguez, et al. In: *Conf. Proc. IEEE Eng Med Biol Soc.* **2007**, 5107.
19. P.W. Kämmerer, M. Heller, J. Brieger, et al., *Eur Cell Mater* **2011**, 21, 364-372.
20. M. Dettin, T. Herath, R. Gambaretto, et al., *J.Biomed Mater Res A*., **2009**, 1, 463.
21. H. Huang, Y. Zhao, Z. Liu, et al., *J Oral Implantol.* **200**3, 29, 73.
22. J. Kim, P. Seidler, L.S. Wan, et al., *J. Colloid Interface Sci.,* **2009**, 329, 114-119.
23. J.P. Matinlinna, S. Areva, L.V.J. Lassila, et al., *Surf. Interface Anal.*, **2004**, 36, 1314-1322.
24. T.T. Nguyen, M. Raupach and L.J. Janik, *Clays Clay Miner,* **1987**, 35, 60-67.
25. J. Zhu, C. Tang, K. Kottke-Marchant, et al., *Bioconjug Chem*., **2009**, 20, 333-339.
26. C.I. Tomuleasa, V. Foris, O. Soritau, et al., *Rom. J. Morphol. Embryol.,* **2009**, 50, 349-355.

STUDIA UBB CHEMIA, LX, 2, Tom I, 2015 (p. 59-70)
(RECOMMENDED CITATION)

COMPARATIVE EVALUATION OF THE APICAL SEALING ABILITY OF FOUR DENTAL MATERIALS USED IN ENDODONTIC SURGERY – AN *IN VITRO* STUDY

ANDREEA IULIANA GULIE (căs. KUI)[a,*], GHEORGHE ZSOLT NICULA[b], CODRUTA POPESCU[c], EUGEN MIRONESCU[d], MANDRA BADEA[e]

ABSTRACT. The aim of this in vitro study was to assess dye microleakage and sealing ability of four dental materials: a polycarboxilate cement (Adhesor Carbofine® - Spofa Dental), a glass ionomer cement (Kavitan Plus®- Spofa Dental), a composite resin (Core-It®- SpiDent) and a MTA based cement (MTA Fillapex®- Angelus). Forty, extracted, human teeth with single root canals were selected for this study. The teeth were randomly divided into four study groups and one control group. The root canals were instrumented and filled with gutta-percha and sealer. Root-ends were resected and 3 mm deep cavities were prepared. Root-end cavities were filled, each with a type of material. Methylene blue dye was used for determination of dye leakage. Afterwards, Scanning Electron Microscopy was used to evaluate the sealing ability of each material. Kolgorow-smirnow z test was used to determine the type of data distribution. One-way analysis of variance (ANOVA) followed by a Tukey test were used to determine the statistical difference between groups, with $P < 0.05$ set as significant. All the four sealers produced apical leakage to a certain extent and there was no statistically significant difference between the five experimental groups. For SEM evaluation, the results showed that there is a statistically significant difference between the control group and the Adhesor Carbofine group. MTA based cement provides leakage results comparable to other commonly used root-end filling materials.

Keywords: *Electronic microscopy, Composite cements, Cement paste, MTA*

[a] *University of Medicine and Pharmacy "Iuliu Hatieganu", Faculty of Dentistry, Department of Prosthodontics, Cluj-Napoca, Romania*
[b] *University of Medicine and Pharmacy "Iuliu Hatieganu", Faculty of Medicine, Dept. of Cell and Molecular Biology, Pasteur St. No. 6, Cluj-Napoca, Romania*
[c] *University of Medicine and Pharmacy "Iuliu Hatieganu", Faculty of Medicine, Department of Socio-Humanistic Sciences – History of Medicine, Cluj-Napoca, Romania*
[d] *University of Medicine and Pharmacy "Iuliu Hatieganu", Faculty of Medicine, Dept. of Cell and Molecular Biology, Pasteur St. No. 6, Cluj-Napoca, Romania*
[e] *University of Medicine and Pharmacy "Iuliu Hatieganu", Faculty of Dentistry, Department of Dental Prevention, Cluj-Napoca, Romania*
* *Corresponding author: guile.andreea@umfcluj.ro*

INTRODUCTION

In endodontic therapy, non-surgical treatments and re-treatments are indicated and are considered a first option in the presence of persistent apical periodontitis. When optimal results cannot be achieved by a non-surgical orthograde re-treatment, then endodontic surgery is indicated. [1]

Apicoectomy (apicectomy/root-end resection) with retrograde obturation is a widely applied procedure in endodontics, when all efforts for the successful completion of orthograde endodontic therapy have failed. The main purpose of endodontic treatment is to eliminate micro-organisms from the root canal systems and prevent its re-infection. [2] In vitro studies suggest that a root-end filling is essential to prevent leakage from root canal space and dentinal tubes.

Placing a root-end filing material during periapical surgery should guarantee the complete sealing of the root canal. A correct apical sealing avoids recontamination and leads to a reduction of microorganisms, therefore to a successful treatment. [3]

Several materials have been indicated as root-end filling materials, though each of these materials has its own limitations. Different materials have been used in this direction, such as amalgams, ZOE cements, glass ionomer cements, composites. [5]

Zinc polycarboxylate cement consists of a powder which contains zinc-oxide, magnesium oxide, bismuth, aluminium oxides and stannous fluoride. The bond strength to enamel is greater than to dentin. The sealing ability of policarboxylate cement, using dye penetration methods is inferior to amalgam. [6]

Glass ionomer cement was introduced in the early 1970's as a new restorative material. The sealing ability of light-curing glass ionomer cements was significantly better than amalgam and also slightly better than conventional glass ionomer cements. [6]

The use of composite resin in addition to bonding agents is likely to produce a leak-resistant seal. There are studies showing an excellent long term success of composites along with dentin bonding agent, but presence of a dry field during placement is important. In addition, some components found in conventional composite resins, like inorganic fillers and silane coupling agent may be the reason why the materials presents anti-bacterial effects against bacteries like *P. gingivalis, P. intermedia, E. foecalis and P. endodontalis*. [6]

Mineral Trioxide Aggregate (MTA) has shown excellent seal and hard tissue repair compared with other root-end filling materials. Its main advantages are osteogenic and regenerative potential, biocompatibility and also anti-bacterial properties against *E. foecalis, S.aureus, P. aeruginosa,* especially when used after mixing with 0, 12% clorhexidine. [6]

It is a real challenge to design and test in laboratory a reliable experimental procedure that can be easily repeated and be clearly in explaining the results. Therefore, as an attempt to solve this problem, different methods, such as dye bacterial leakage or microscopy analysis, were suggested in order to assess the sealing ability of different root-end filling materials. [3] Our study aims a comparative evaluation of dye leakage and apical sealing ability for a polycarboxilate cement (Adhesor Carbofine® - Spofa Dental), a glass ionomer cement (Kavitan Plus® - Spofa Dental), a composite resin (Core-It® - SpiDent) and a MTA based cement (MTA Fillapex® - Angelus).

RESULTS AND DISCUSSION

For the dye-leakage evaluation, linear dye penetration was measured independently by two observers at two different times under same conditions; the mean value of the recorded measurements was chosen as the extent of dye penetration into each specimen. For each image, two measures were made, annotated with “Dim L” and “Dim R”; the annotation reveals the side of the root-canal where the measures were made, respectively left and right. All the four sealers produced apical leakage to a certain extent. The teeth in the control group showed maximum penetration. There was no statistically significant difference between groups (Dim.R) regarding apical leakage as determined by one-way ANOVA ($F(4, 40) = 2.009$, $p = .115$). Also, there was no statistically significant difference between groups (Dim.L) regarding apical leakage as determined by one-way ANOVA ($F(4, 40) = 1.58$, $p = .201$). (Table 1)

For the SEM evaluation the measures were made on the calibrated images obtained. The measures were made by two observers at two different times under same conditions; the mean value of the recorded measurements was chosen as the extent of the gap size for each specimen. There were chosen four points to measurement for each root, two different points for each side (left and right) of the root-canal filling (first point at the bottom and the second point at the top of the root-end filling). (Figure 1)

Table 1. Results of micro-leakage assessment of the five experimental groups

	Group	Dye penetration length Mean (µm) ±SD	Nr. Teeth	F	p	p1	p2	p3	p4	p5
Dim.R	CG	1.58±0.77	8			-	.579	.885	.983	.921
	PC	1.07±0.96	8			.579	-	.136	.877	.166
	GI	1.37±0.46	8	2.009	.115	.885	.136	-	.591	1.00
	MTA	1,32±0.46	8			.983	.877	.591	-	.653
	CR	1.94±0.82	8			.921	.166	1.00	.653	-

	Group	Dye penetration length Mean (μm) ±SD	Nr. teeth	F	p	p1	p2	p3	p4	p5
Dim.L	CG	1.52±0.77	8			-	.730	.993	.980	.771
	PC	1.07±0.96	8			.730	-	.924	.960	.138
	GI	1.37±0.46	8	1.58	.201	.993	.924	-	1.00	.516
	MTA	1.32±0.46	8			.980	.960	1.00	-	.431
	CR	1.94±0.82	8			.771	.138	.516	.431	-

Dim.R and Dim.L – the places where the measures were made for the apical leakage test, SD – standard deviation; CG – control group, PC – polycarboxylate cement, GI – glass ionomer cement, MTA – MTA based cement, CR – composite resin; F and P – values by one-way ANOVA; p1 – compared with CG; p2 – compared with PC; p3 – compared with GI; p4 – compared with MTA; p5 – compared with CR

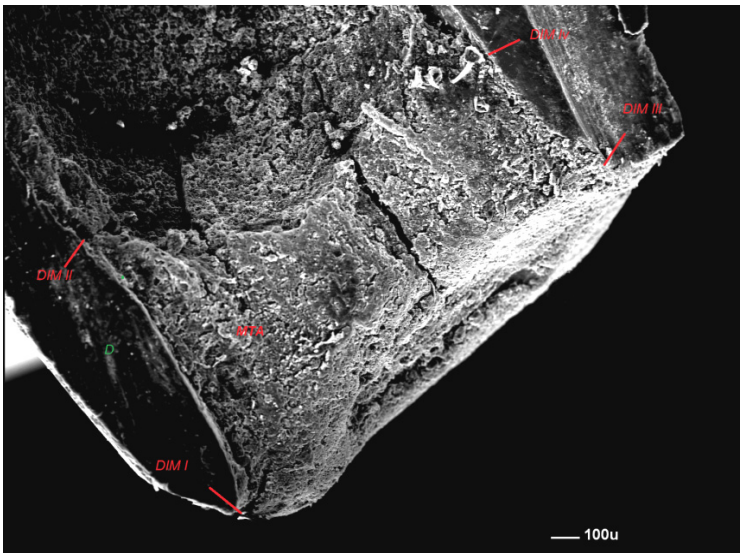

Figure 1. - SEM image in sagittal view, showing retrofilling material/dentin interface. D - dentin, MTA – MTA based cement; DIM. I to IV – the points where the measures were made for each sample SEM – Scanning Electron Microscopy (magnification 45x)

There was a statistically significant difference between groups as determined by one-way ANOVA (F (4, 40) = 3.28, p = .015). A Tukey post-hoc test revealed that dim.I was statistically significantly lower in CG (13.45±5.99μm, p= .006) comparing to PC group (51.90±25.41μm), as well as the dim.II was statistically significantly lower in CG (9.75±4.27μm, p= .020) comparing to PC group (41.86±24.53μm). A Tukey post-hoc test revealed that dim.III was

statistically significantly lower in CG (9.99±3.98μm, p= .041) comparing to PC group (39.02±29.23μm). Also dim. IV was statistically significantly lower in CG (7.33±5.31μm, p= .019) comparing to PC group (47.98±41.11μm).

There was also a statistically significant difference in CR group (9.23±6.61μm, p=.028) comparing to PC group (47.98±41.11μm) regarding just dim.IV. There were no statistically significant differences between GI and MTA groups (p = .538) and between PC and MTA groups (p=.466). (Table 2)

Table 2. Results of SEM evaluation of sealing ability for the five experimental groups

	Group	The gap size Mean(μm)±SD	Nr. teeth	F	P	p1	p2	p3	p4	p5
	CG	13.45±5.99	8	4.61	.004	-	.006	.096	.653	.979
	PC	51.90±25.41	8			.006	-	.773	.146	.024
Dim.I	GI	39.97±31.73	8			.096	.773	-	.742	.279
	MTA	27.45±18.94	8			.653	.146	.742	-	.928
	CR	19.21±8.25	8			.979	.024	.279	.928	-
		The gap size Mean(μm)±SD	**Nr. teeth**	**F**	**P**	**p1**	**p2**	**p3**	**p4**	**p5**
	CG	9.75±4.27	8	4.76	.004	-	.020	.057	.603	1.00
	PC	41.86±24.53	8			.020	-	.993	.388	.017
Dim.II	GI	37.63±23.86	8			.057	.993	-	.647	.048
	MTA	24.04±26.97	8			.603	.388	.647	-	.559
	CR	9.06±5.90	8			1.00	.017	.048	.559	-
		The gap size Mean(μm)±SD	**Nr. teeth**	**F**	**P**	**p1**	**p2**	**p3**	**p4**	**p5**
	CG	9.99±3.98	8	3.36	.020	-	.041	.052	.858	.859
Dim.III	PC	39.02±29.23	8			.041	-	1.00	.302	.302
	GI	38.08±28.72	8			.052	1.00	-	.350	.350
	MTA	19.70±12.52	8			.858	.302	.350	-	1.00
	CR	19.70±8.58	8			.859	.302	.350	1.00	-
		The gap size Mean(μm)±SD	**Nr. teeth**	**F**	**P**	**p1**	**p2**	**p3**	**p4**	**p5**
	CG	7.33±5.31	8	3.28	.015	-	.019	.433	.503	1.00
	PC	47.98±41.11	8			.019	-	.538	.466	.028
Dim.IV	GI	28.73±17.02	8			.433	.538	-	1.00	.525
	MTA	27.28±32.09	8			.503	.466	1.00	-	.598
	CR	9.23±6.61	8			1.00	.028	.525	.598	-

Dim. I to IV – the points where the measures were made for each sample; SD – standard deviation; CG – control group, PC – polycarboxylate cement, GI – glass ionomer cement, MTA – MTA based cement, CR – composite resin; F and P – values by one-way ANOVA; p1 – compared with CG; p2 – compared with PC; p3 – compared with GI; p4 – compared with MTA; p5 – compared with CR

The present study compared the sealing ability of four root-end filling materials (Adhesor Carbofine®, Kavitan Plus®, MTA Fillapex® and Core-It®). This research compared these four different materials under the same conditions, which represents a novelty for the experimental studies regarding root-end fillings. Also, the materials were compared using two methods of evaluation in order to determine more accurate results.

For the evaluation of apical leakage, the results failed to demonstrate any significant difference between the four root-end fillings materials used. This method, using dye penetration, has been chosen in order to assess microleakage. We used methylene blue because it is not expensive, has a high degree of staining and has a lower molecular weight than bacterial toxins. The limitation of dye leakage studies is that they measure the degree of leakage in only one dimension, which makes it impossible to evaluate the total amount of leakage. [14, 15, 16, 17]

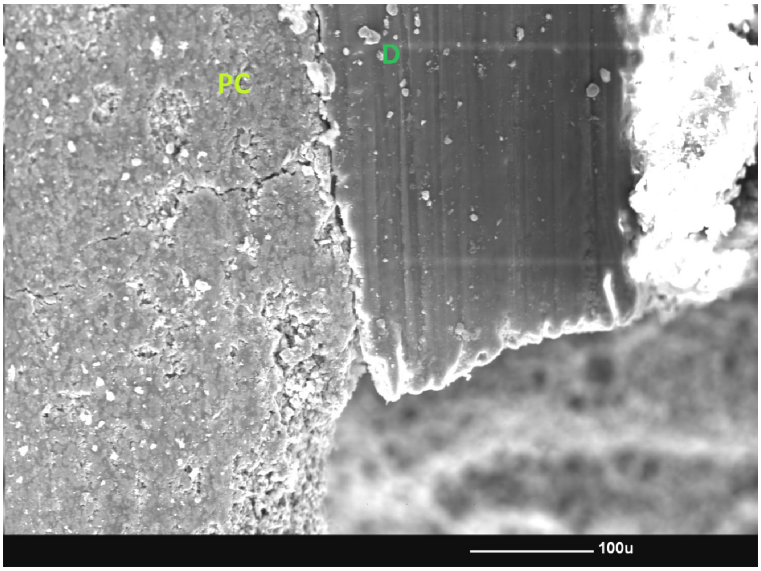

Figure 2. - SEM image in sagittal view, showing retrofilling material/dentin interface. D- dentin, PC – polycarboxylate cement; SEM – Scanning Electron Microscopy (magnification 200x)

For Scanning Electron Microscopy (SEM) evaluation the results demonstrate a significant difference in sealing abilities between the control group and the first group (Adhesor Carbofine®). Polycarboxylate cement has not a specific indication when used as a root-end filling material, studies showing that it leaks at level significantly greater than amalgam or gutta-percha.

Significant differences were found between the control group and poycarboxylate cement, meaning that policarboxilate cement showed a lower sealing ability than the sealer used in control group. (Image 2) [18]

In our study, MTA Fillapex® was used as a MTA based cement. This material was developed as a paste/paste sealer in a formulation that allows its appropriate insertion into the root canal. [22] MTA contains tricalcium silicate, tricalcium aluminate, tricalcium oxide, silicate oxide and other mineral oxides forming a hydrophilic powder which sets in presence of water. Several studies have indicated that MTA exhibits significantly lesser leakage than other materials. [5, 18, 20, 21] The results found in this research showed a good sealing ability for MTA Fillapex, but not significantly different when compared with the other materials studied. (Image 3)

Figure 3. - SEM image in sagittal view, showing retrofilling material/dentin interface. D- dentin, MTA – MTA based cement; SEM – Scanning Electron Microscopy (magnification 45x)

Glass ionomer cements can be used for repairing perforated root canals or as retrograde root fillings. [19] Sealing ability of glass ionomer cements was adversely affected when the root end cavities were contaminated with moisture at the time of placement of cement. [18] Although in our study the root end cavities were completely dry before applying the glass ionomer cement, the sealing ability of Kavitan Plus® was poor. (Image 4) In our study, there was no statistically significant difference between the sealing ability of glass ionomer cement and the other three materials used.

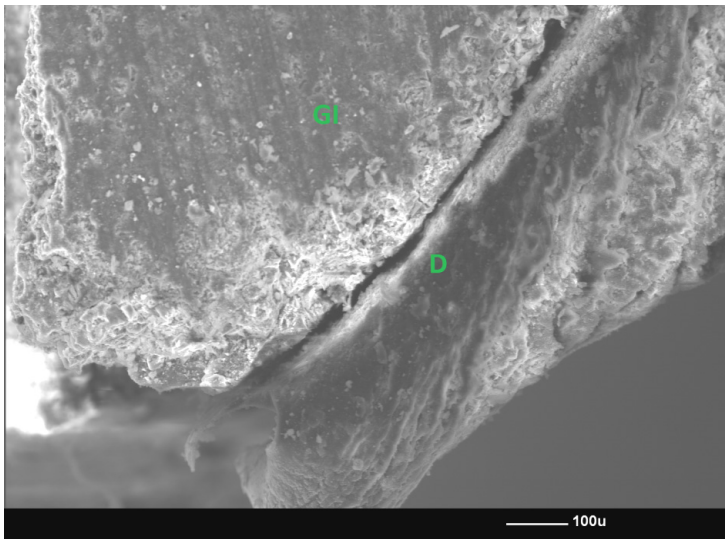

Figure 4. - SEM image in sagittal view, showing retro-filling material/dentin interface. D- dentin, GI– glass ionomer cement; SEM – Scanning Electron Microscopy (magnification 100X)

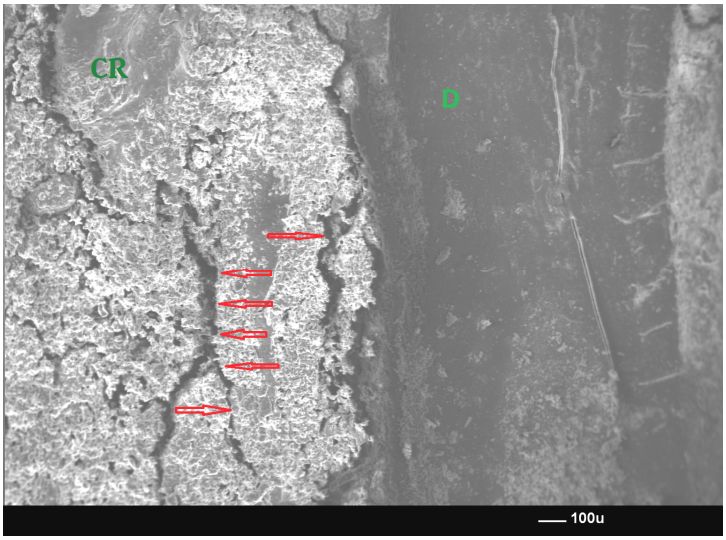

Figure 5. - SEM image in sagittal view, showing retrofilling material/dentin interface. D- dentin, CR – composite resin; red arrows showing the cracks in the material; SEM – Scanning Electron Microscopy (magnification 45X)

The composite resin has a good sealing ability, which was proven also in this study. In clinics, the composite resin presents difficulties in endodontic surgery, because the presence of a dry field during placement is mandatory. [6,18] In our study, composite resin (Core-It®) showed a good sealing ability, in association with a bonding agent, but the SEM images revealed cracks in the material. (Image 5)

CONCLUSIONS

Within the limitations of this study the results in the present study revealed no difference in microleakage between all four materials used as root-end fillers.

Scanning Electron Microscopy (SEM) evaluation showed a significant difference between the sealing ability of polycarboxylate cement versus the control group. No statistically significant difference was observed between the four materials used in this experimental study. However, further *in vitro* and *in vivo* investigations should be conducted to assess the sealing ability of each material used in this study.

EXPERIMENTAL SECTION

Forty, extracted, human teeth with single, straight root canals were selected for this *in vitro* experimental study. The teeth were extracted for different periodontal problems and stored in distilled water and thymol (0, 2%) until use. The study was approved by the Ethics Committee of the University of Medicine and Pharmacy “Iuliu Haţieganu”, Cluj Napoca (Protocol No. 805/ 25.06.2013).

Teeth surfaces were scaled in order to remove calculus and were immersed in NaOCl 5,25% in order to remove organic tissue. After 1 h of immersion in NaOCl, an orifice was created inside each tooth’s crown, as an access for the root canal, using a high speed hand piece under continuous water spray.

A #15 K-file (Dentsply®) was used to establish the working length for each root canal. Crown-down root canal preparation was performed using a 0.06 ProTaper (Dentsply®) rotary instruments to the size of #40. During mechanical preparation, 5ml of 5,25% NaOCl was used for irrigation and at the end of the chemo-mechanical preparation, as the final flush, 5 ml of sterile saline were used. Root canals were dried with paper points (Gapadent®) and obturated with gutta-percha (Gapadent®) and sealer AH26 sealer (Dentsply, DeTrey, Konstanz, Germany) by the lateral condensation method. IRM cement was used to fill the coronal cavities. Afterwards, the sealer set completely for 24h.

From each root, a 3mm apical region was removed perpendicular to the long axis of root, under continuous water irrigation. The teeth were then divided into five groups, first group being the control group. In the control group we included 8 teeth with the apicoectomy made and for the other 4 groups of teeth, using a 008 diamond root bur; the root-end cavities were prepared, to a depth of 3 mm. For the second group the root-end cavity was filled with Adhesor Carbofine®, for the third group the cavities were filled with Kavitan Plus®, for the teeth in the forth group it was used MTA Fillapex® and for the fifth group a composite resin, Core-It® it was used, after applying etching gel and a bonding. For the last group, the material was immediately light cured for 40 seconds. All materials were prepared according to the manufacturer's directions. After the set of the materials, all specimens were stored in distilled water at 37^0C at 100% humidity for 72h.

Study A: Evaluation of apical leakage

All the external surfaces were coated with two layers of nail polish except the sectioned apical region. [8] All the teeth were afterwards immersed in methylene blue 1% for 24h. The samples were then taken out of the methylene blue and sectioned longitudinally by grooving the roots with a diamond disk in the bucco-lingual direction and splitting them with a chisel. All sections were photographed under a light microscope at 10X magnification using a digital camera and the images were analyzed using Cell D (Olympus) program. Afterwards, for each sample it was measured the length of dye penetration. Linear dye penetration was measured independently by two observers at two different times under same conditions; the mean value of the recorded measurements was chosen as the extent of dye penetration into each specimen. [9]

Study B: SEM evaluation

The sections obtained from the teeth were immersed in 6 mol LHCl for 30s, for acid dissolution (inorganic part), and 1% NaOCl for 30 min (organic part) and dried for 24h. Afterwards, the samples were mounted on aluminium stubs, gold sputtered in a Polaron E-5100 plasma-magnetron sputter coater (Polaron Equipment Ltd., Watford, Hertfordshire, UK) in argon atmosphere [10] of about 20 nm and then examined under Scanning Electron Microscopy (SEM) (*Jeol JSM 25S - Jeol, Japan*) at different magnifications (45X, 70x, 100x, 200x, 300x and 700x) for adaptation of each root-end material into the canal walls and the findings were measured, for each sample choosing 4 points to measure. All the images were captured using image processor Deben Pixie–3000 (Deben UK Ltd., Debenham, Suffolk, UK) [11] and then calibrated for measuring using a Cell^*D* software (Olympus Imaging Software Solutions, Germany) [12] Sagital

examination was performed, as the roots were sectioned longitudinaly. The Image tool programe includes functions as dimensional (distance, angle, perimeter, area) and gray scale measurement. The gap size was measured at four points in the longitudinal section. [13]

Statistical analysis was performed by SPSS software package, Version 21.0 for Windows (SPSS Inc. Chicago, IL, USA). Quantitative values are presented as mean ± standard deviation (SD). Kolgorow-smirnow z test was used to determine the type of data distribution. One-way analysis of variance (ANOVA) followed by a Tukey test were used to determine the statistical difference between groups, with $P < 0.05$ set as significant.

ACKNOWLEDGMENTS

This research was funded by POSDRU grant no.159/1.5/S/138776 grant with title: “Model colaborativ institutional pentru translatarea cercetarii stiintifice biomedicale in practica clinica– TRANSCENT”.

REFERENCES

1. Ashraf H., Faramarzi F., Paymanpour P., *Iranian Endodontic Journal*, **2013**, *8*, 177.
2. Moradi S., Ghoddusi J., Forghani M., *Journal of Endodontics*, **2009**, *31*, 1563.
3. Kazem M., Mahjour F., Dianat O., Fallahi S., Jahankhah M., Root-end filling with cement-based materials: *Dental Research Journal* (*Isfahan*), **2013**, *10*, 46.
4. Friedman S., *Journal of Endodontics*, **2011**, *37*, 577.
5. Torabinejad M., Ford P., Rooi T.R., *Endodontics and Dental Traumatology*, **1996**, *12*, 161.
6. Priyanka S.R., *Journal of Medical and Dental Sciences*, **2013**, *9*, 20.
7. Castelucci A., Endodontics, Second edition. Il Tridente, **2003**, 548.
8. Kumar N.S., Palanivelu A., Narayanan L.L., *Journal of Conservative Dentistry*, **2013**, *16*, 449.
9. Shahi S., Yavari H.R., Rahimi S., Eskandarinezhad M., Shakouei S., Unchi M., *Journal of Oral Sciences*, **2011**, *53,* 517.
10. G. Nicula, St. Balici, A. Florea, E. Mironescu, R. Munteanu, P. Murea, Gh. Benga, *Annals of the Romanian Society for Cell Biology*, **2010**, *15,* 22.
11. Flegler S.L., Heckman J.W., Komparens K.L., Scanning and transmission electron microscopy: an introduction, W.H. Freeman and Comp., New York, **1993**, 151.
12. Dudea D., Florea A., Mihu C., Câmpeanu R., Nicola C., Benga Gh., *Romanian Journal of Morphology and Embryology,* **2009**, *50*, 435.
13. Khalid, Al-Garawi Z., Al-Hezaimi K., Javed F., Al-Shalan T., Rotstein I., *International Journal of Oral Sciences*, **2012**, 202.

14. Ahlberg K.M., Assavanop P., Tay W.M., *International Endodontic Journal*, **1995**, *28*, 30.
15. Tamse A., Katz A., Kablan F., *International Endodontic Journal*, **1998**, *31*, 333.
16. Wu M.K., Wesselink P.R., *International Endodontic Journal*, **1993**, *26*, 37.
17. Ozata F., Erdilek N., Tezel H., *International Endodontic Journal*, **1993**, *26*, 241.
18. Vasudev S.K., Goel B.R. TS, ABSTRACT. *Endodontology*. **2003**, *15,* 12.
19. Kamel F.M., *Saudi Dental Journal*, **1994**, *6*, 107.
20. Torabinejad M., Higa R.K., McKendry D.J., Pitt Ford T.R., *Journal of Endodontics*, **1994**, *20*, 159.
21. Tang H.M., Torabinejad M., Kettering J.D., *Journal of Endodontics*, **2002**, *28*, 5.
22. Yoshino P., Nishiyama C.K., Modena K.C.D.S., Santos C.F., Sipert C.R., *Brazilian Dental Journal*, **2013**, *24,* 111.

STUDIA UBB CHEMIA, LX, 2, Tom I, 2015 (p. 71-80)
(RECOMMENDED CITATION)

THE STUDY OF NEW COMPOSITES WITH GRAPHENE USED IN DENTISTRY

SORINA SAVA[a,*], CODRUTA SAROSI[b], BOBOIA STANCA[b], ANDRADA TONEA[a], CAMELIA ALB[a], DIANA DUDEA[a]

ABSTRACT. The development of graphene nanopowder in a polymer matrix has opened, in recent years, a new and exciting area in the science of dental materials. Physico-chemical and mechanical properties of these materials are improved at a very low filler loading in the polymer matrix. The novelty of this study is the utilization of graphene-silver nanopowder as filler in new dental composites to improve the physico-mechanical properties. Three experimental composites, two with different percent in graphene-silver nanopowder and one commercial nanohybrid composite Herculite XRV Ultra (Kerr) were investigated by water absorption and solubility in distilled water and artificial saliva (1, 7, 14 and 21 days), respectively flexural strength and Young's modulus properties. One-way analysis of variance (ANOVA) test, for multiple comparisons between means to determine significant differences was used at a significance level set at $p \leq 0.05$. The experimental results show that composite with a greater amount of graphene (G2) present better results of water absorbtion and flexural strength.

Keywords: *graphene, dental composites, water sorbtion, flexural strength*

INTRODUCTION

The development of graphene nanopowder in a polymer matrix has opened, in recent years, a new and exciting area in the science of dental materials. These nanohybrid materials show a significant improvement in physico-chemical and mechanical properties that cannot normally be achieved using conventional composites, especially for dental composites. The extent of the improvement is related directly to the degree of nanofillers dispersion

[a] *Univestity of Medicine and Pharmacy Iuliu Hatieganu, Faculty of Dental Medicine, 32 Clinicilor Str., RO-400006, Cluj-Napoca, Romania.*
[b] *Babeş-Bolyai University, Raluca Ripan Chemistry Research Institute, 30 Fantanele Str., RO-400294, Cluj-Napoca, Romania.*
** Corresponding author: savasorina@yahoo.com*

in the polymer matrix. The most important aspect of composites with graphene-silver nanopowder is that all these improvements are obtained at very low filler loading in the polymer matrix [1-4]. There have been studied most graphene composites according to the type of the processing method, the polymer matrix and fillers, but none is being used in dentistry. The interaction mechanism in (polymer/graphene/nanofiller of glasses) composites used in dentistry depends on: polarity, molecular weight, hydrophobicity, particles size and shape, reactive groups, etc., present in the polymer, graphene and nanofiller [5-7]. Composites used in dentistry are available as hybrid types, containing milled glass fillers and discrete nanoparticles (40–50 nm) and as nanofill types [8,9]. They containing both nano-sized filler particles, called nanomers, and agglomerations of these particles described as “nanoclusters”. Polymer composites absorb water and release unreacted monomers in an aqueous oral environment. The water ingress into dental composites in the oral cavity can, over time, lead to deterioration of the physical/mechanical properties. There are studies on water absorption [10-13] or ethanol/water solution [11] or ethanol [12] for experimental and commercial light-cured dental composites.

The novelty of this study is the utilization of graphene-silver nanopowder as filler in new dental composites to improve the physico-mechanical properties.

In this study we have three experimental composites, two with different percent of graphene-silver nanopowder, comparing with commercial nanohybrid composite Herculite XRV Ultra (Kerr), in determination of water absorption and solubility in distilled water and artificial saliva (1, 7, 14 and 21 days), respectively flexural strength and Young’s modulus properties. The values reported in tables and figures represent mean values and standard deviation of replicates. One-way analysis of variance (ANOVA) test, for multiple comparisons between means to determine significant differences was used at a significance level set at $p \leq 0.05$.

RESULTS AND DISCUSSION

Studies determining the water sorption and solubility of composite materials used in dentistry are especially important for their relative values, while numerical comparisons are not always possible.

The preparation, characterization and properties of graphene as filler in different composites for a large number of polymers are discussed in most papers [14,15,16]. Most of the properties of polymer/graphene composites were superior to the base polymer matrix as well as other carbon filler (carbon nanotubes, carbon nanofiber, and graphite) based composites. These improved properties of the composites are obtained at very low graphene contents (≤2 wt%).

Water sorption is different in many studies [17] and there are several factors influencing water uptake values. Water sorption is a diffusion-controlled process that occurs in the organic matrices, but the kinetics of water sorption is slower for some resins and may not have reached equilibrium even after several days [18]. In these study composites with greater amount of grapheme presented low solubility in saliva and higher solubility in water. The composite experimental without graphene is maintained at constant value in both water and saliva, in solubility and absorption.

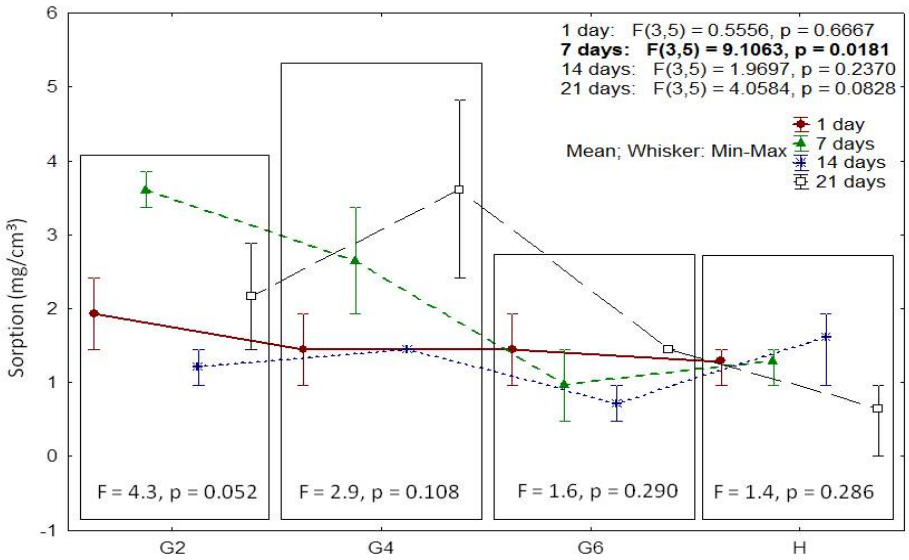

Figure 1. The statistical parameters from testing ANOVA at water sorption in distilled water when the comparison has been done for the same day (1, 7, 14, 21) so that it can be seen if is a statistically significant difference between the type the sample for the same day. The statistical parameters obtained through ANOVA test, when comparisons has been done for the same group (G2, G4, G6, H) such that it can be seen that there is no a statistically significant difference between days at same sample type.

Considering only the same day (Figure 1) as a factor, we can say that the studied composite materials G2, G4, G6 and H have a different evolution of water absorption over time, depending on the immersion solution used in the study (Figure 1, 2). In the case of samples immersed in water statistically significant differences were found between measurements made on 7 and 21 days, not identifying significant pairs. For samples in artificial saliva significant differences could not be identified (Figure 2). Water absorption material was identified as having significant values in the case of samples immersion in

water. Immersion in artificial saliva does not seem to determine significant differences in absorption between materials. Comparing the studied composites can be seen (Figure 1) that G2 and G4 had statistically significant differences compared to the Herculite, for water immersion. There were no significant pairs on the artificial saliva immersion studies.

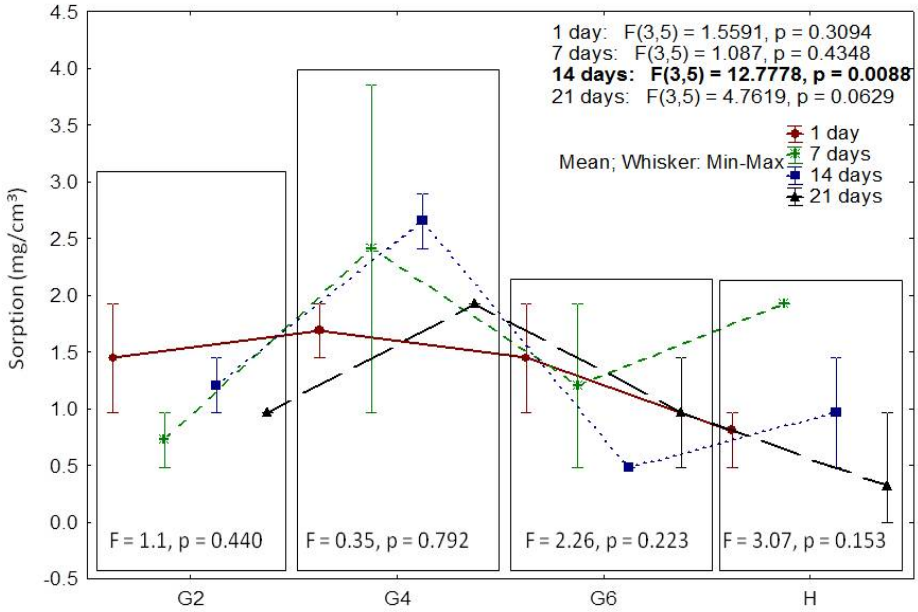

Figure 2. The statistical parameters at water sorption in artificial saliva, when the comparison has been done for the same day (1, 7, 14, 21) so that it can be seen if is a statistically significant difference between the type the sample for the same day. The statistical parameters at water sorption in artificial saliva, when comparisons has been done for the same group (G2, G4, G6, H) such that it can be seen that there is no a statistically significant difference between days at same sample type.

It shows a trend of water absorption increasing for G4 material; a final value at the end of the study relatively equal with the beginning value of the study for the G2 and G6 experimental materials and a slight decline for Herculite. Even if the differences of absorption values can be seen during the experiment, the final value is close to the initial measured value.

Taking into account only the time as a factor, we can say that the studied materials have different solubility evolution (figure 3, 4) in time, regardless of the immersion solution used in the study. A pair wise comparisons material has highlighted that G4 material presented statistically significant differences compared to other materials in both immersion solutions.

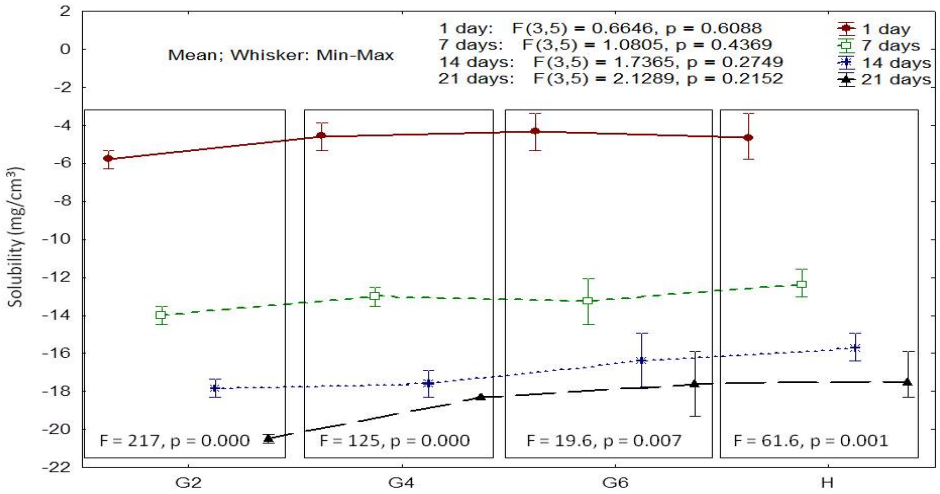

Figure 3. The statistical parameters from testing ANOVA at solubility in distilled water when the comparison has been done for the same day (1, 7, 14, 21) so that it can be seen if is a statistically significant difference between the type the sample for the same day. The statistical parameters obtained through ANOVA test, when comparisons has been done for the same group (G2, G4, G6, H) such that it can be seen that there is no a statistically significant difference between days at same sample type.

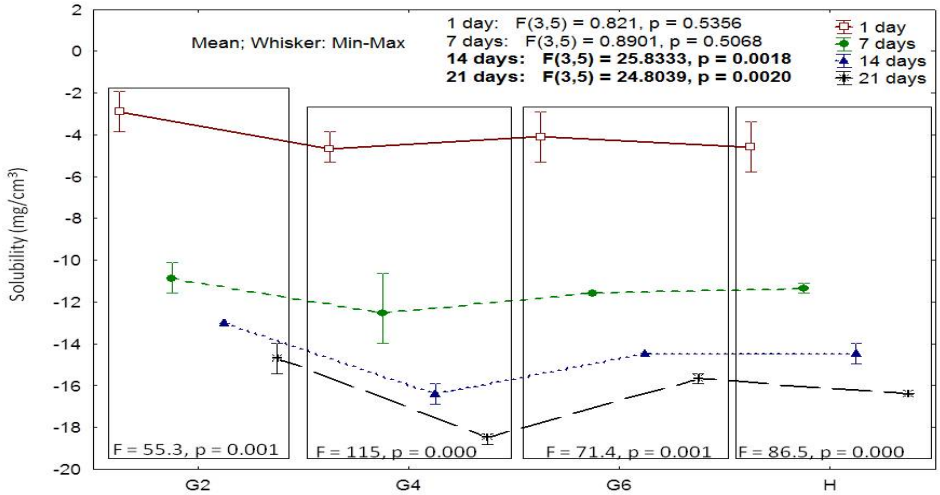

Figure 4. The statistical parameters from testing ANOVA at solubility in artificial saliva, when the comparison has been done for the same day (1, 7, 14, 21) so that it can be seen if is a statistically significant difference between the type the sample for the same day. The statistical parameters obtained through ANOVA test, when comparisons has been done for the same group (G2, G4, G6, H) such that it can be seen that there is no a statistically significant difference between days at same sample type.

Evolution water solubility (figure 3) of the four materials studied it is considered significantly different only between G2 and G4 composites respectively G4 and Herculite. For solubility in artificial saliva (figure 4) it is considered significantly different only between G2 and H composites, respectively G4 and G2. Comparing these two charts remark that the solubility in artificial saliva (figure 4) is lower than solubility in water (figure 3) of experimental materials, while for Herculite composite the values is similar in both medium.

Differences in the chemical composition of the composites considerably influence the degradation behavior of the resins [19]. This is attributed to the different chemistry of their organic matrix. The organic matrix of experimental and commercial composites consists of Bis-GMA and TEGDMA, aromatic and aliphatic dimethacrylate monomers, and show that the aromatic content is higher than that of the aliphatic [20]. Artificial saliva or water uptake in the organic matrix of polymer composites causes generally two opposing processes. The solvent will extract unreacted components, mainly the residual monomer, loss of weight and reduction in mechanical properties [21, 22].

The results obtained for the flexural strength and flexural modulus of the studied composites after immersion in water 37±1^{0}C for 24 hours are shown in figure 5.

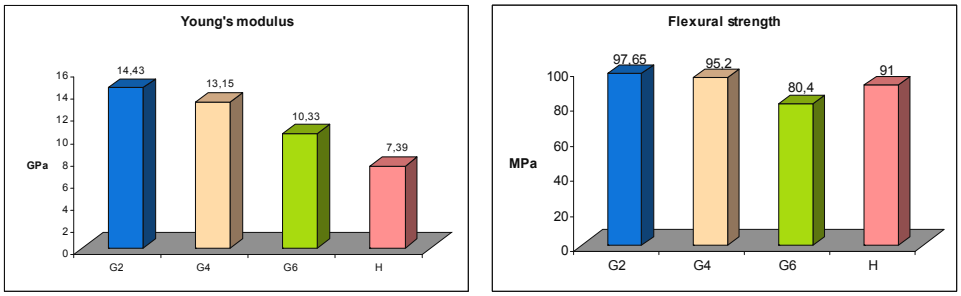

Figure 5. The average values for: a) Young's modulus and b) Flexural strength recorded after 24 hours in distilled water at 37^{0}C for two composite G2 and G4 with the graphene, two composite, without the graphene, G6 and H

After immersion in distilled water for 24 hours at 37ºC of the four materials studied (G2, G4, G6 and Herculite), G2 showed the greatest flexural strength, and followed by Herculite. This result shows that the flexural strength depends not only on the filler content but also on the filler chemistry. The composite G2 have in composition 10 wt % nanopowder with graphene (HA-Ag graphene). The flexural modulus of composites after immersion for 24 hours day follows the order H < G6 < G4 < G2. Comparison of flexural strength after immersion for 24 hours in water showed the values obtained are comparable and no significant difference was observed for the other

composites. Comparison of flexural modulus after immersion in water did not show any significant difference ($p< 0.05$) for 24 hours at 37^0C. Several researchers [23] have determined the intrinsic mechanical properties of the single, bi- and multiple layers of graphene. After polymerization the composites were immersed in water and artificial saliva. Water or artificial saliva uptake in the polymeric phase of dental composites causes generally two opposing processes. The solvent will extract unreacted components, mainly the residual monomer which leads to loss of weight and reduction in mechanical properties.

CONCLUSIONS

Correlating the results for sorption in water and artificial saliva with mechanical properties (flexural strength and Young's modulus) we can conclude that the experimental composites with a greater amount of graphene (G2) shows better results. After carbon nanotubes, graphene has been reported to have the highest elastic modulus and strength.

EXPERIMENTAL SECTION

Materials

One commercial and three experimental restorative materials were selected for evaluation from physico-mechanical point of view (Table 1).

Table 1. Description of materials used in this study

Material	*Organic Phase*	*Inorganic phase*	*Company*
Experimental nanocomposite G2	*Bis-GMA TEGDMA*	*HA-Ag graphene 10% (%wt) Sr-Zr glass Quartz*	*ICCRR Cluj-Napoca*
Experimental nanocomposite G4		*HA-Ag graphene 5% (%wt) Sr-Zr glass Quartz*	*ICCRR Cluj-Napoca*
Experimental nanocomposite G6		*Sr-Zr glass Quartz HA*	*ICCRR Cluj-Napoca*
Herculite XRV Ultra (H)	*Bis-GMA TEGDMA*	*Barium glass filler Colloidal silica Prepolymerized filler*	*Kerr*

Bis-GMA - 2,2-bis(4-(2'-hydroxy-3'methacryloyloxy-propoxy)phenyl)propane; **HA** - hydroxylapatite (synthetized in *ICCRR Cluj-Napoca* laboratory); **TEGDMA**- triethyleneglycol- dimethacrylate (Aldrich); **DMAEM**-2-dimethyl(aminoethyl)methacrylate (Aldrich); **Cq-** camphorquinone (Aldrich).

The inorganic filler consists of silanizated powders based on mixture of colloidal silica - SiO_2 (Degussa), hydroxyapatite (HA) with 15% graphene-silver nanoparticles and Sr-Zr bioglass (35-SiO_2, 20-SrO, 10-ZrO_2 10-Al_2O_3, 13-B_2O_3, 6-NaF, 6-CaF_2, wt.%), obtained as a mass through the conventional melting method in ICCRR laboratory. Surface treatment of the fillers was made by γ-methacriloyloxypropyl-trymethoxysilane (A174) (Aldrich).

Graphene-silver nanoparticles (Gr-Ag) composite were synthesized by the Radio-Frequency catalytic Chemical Vapor Deposition (RF-CCVD) method [12] using silver nanoparticles distributed over magnesium oxide (Ag_x/MgO, where x = 3 wt.%). The synthesis was performed using a methane flow rate of 80 mL/min and a reaction time of 60 minutes [24].

The *HA- graphene-silver* nanoparticles (Gr-Ag) were synthesized by precipitation of HA in presence of graphene-silver. The starting materials were CaO, H_3PO_4 (Aldrich) for synthesis of HAP. The mixed sols were subjected to heat treatment at 120ºC and 400ºC for 2 h.

*The organic matrix***-** monomers mixture consists of: Bis-GMA/TEGDMA in 65/35 ratio. Bis-GMA was synthesised in ICCRR laboratory.

The experimental composites **G2**, **G4**, **G6** were prepared as monopaste, by dispersing in the organic matrix the silanizated bioactive inorganic fillers, in ratio 20/80 wt.%. The comercial composite Herculite XRV Ultra (**H**), in ratio 21/79 wt.%, was used as a reference material. In order to initiate the photochemical curing, there have been introduced in the monomer mixture an initiator system consisting of: *photosensitizer* - camphorquinone (Aldrich) 0.5% relative to the liquid mixture and a *polymerization accelerator* 2-dimethyl (aminoethyl)methacrylate (Aldrich) 1%.

Methods

A total of four groups were formed. For the water sorption and solubility measurements, ten disc specimens were prepared for each material. A mold for the preparation of a disc specimen 15+1 mm in diameter and 1 mm thickness was used. Sorption and solubility tests were determined according to the method described in ADA Specification No. 27-1993/ISO 4049/2000 regarding filling materials.

The specimens were light-cured, under a glass microscope slide, with an activated light source (Woodpecker®Dental Curing Light LED.B lamp) polymerization unit. The samples were irradiated in different positions for 40 s until the entire area was exposed. The discs removed from the mould were dried in the desiccator in the presence of calcium chloride at 37 ± 1° C for 24 hours. Before being weighed, the specimens are kept in the desiccator at 23° C. Weighed discs are divided into 2 groups, prior to be immersed in

distilled water and artificial saliva respectively, at 37 ± 1°C and maintained for 1:7:14:21 days (during which theirs weight was measured daily). After this time, discs were removed from water or artificial saliva with tweezers, wiped with paper, air-dried for 15 seconds and 1 minute after removal samples are weighed. The extent of absorption in water and artificial saliva for each disc was calculated using the formula:

$$Wsp = (m_2 - m_3) / V$$

where: m_2 - mass of the sample after immersion in water for 24 h (μg)
m_3 - mass of the sample kept in desiccator until constant mass (μg)
V - volume of the sample (mm^3)

Solubility tests were performed on the same composites (G2, G4, G6, H). Solubility tests were completed using the same samples as for absorption test, by maintaining the discs in water and artificial saliva at 37°C and values were recorded at 1, 7, 14 and 21 days Experimental values for solubility are expressed in μg/ mm^3 using the formula:

$$SL = (m_1 – m_3)/V$$

Where: m_1 – constant weight of the sample before water immersion (μg)
m_3 – constant weight of the sample maintain in the desiccator (μg)
V – Sample volume (mm^3)

The specimens for the mechanical tests, flexural strength (FS), were performed at 23°C, according to ISO 4049/2000. The samples were prepared using teflon molds with 2x2x25mm which did not offer resistance to the displacement of the specimen, minimizing the formation of cracks and flaws within the bulk material and surface during their preparation. After 24 ± 1 h , the specimens were loaded at a crosshead speed of 0.5 mm/min until fracture with a Lloyd Instruments-LR5k Plus mechanical testing machine controlled, using the Nexygen Software on a Windows PC.

ACKNOWLEDGMENTS

This paper was published under the frame of European Social Found, Human Resources Development Operational Programme 2007-2013, project no. POSDRU/159/1.5/S/138776.

REFERENCES

1. V. Singh, D. Joung, L. Zhai, S. Das, S. I. Khondaker, S. Seal, *Progress in Materials Science*, **2011**, *56*, 1178
2. Z.-S. Wu, W. Ren, L. Gao, B. Liu, C. Jiang, H. M. Cheng, *Carbon,* **2009**, *47*, 493
3. C. Lee, X. Wei J. W. Kysar, J. Hone, *Science*, **2008**, *321*, 385
4. S. Stankovich,D.A. Dikin, G.H.B. Dommett, K.M. Kohlhaas, E. J. Zimney, E. A. Stach, *Nature*, **2006**, *442*, 282
5. Z. Fan, J. Wang, Z. Wang, H. Ran, Y. Li, L. Niu, P. Gong, B. Liu, S. Yang, *Carbon*, **2014**, *66*, 407
6. A. Cândido dos Reis, D. Tornavoi de Castro, M. A. Schiavon, L. Jardel da Silva, J.A. Marcondes Agnelli, *Brazilian Dental Journal*, **2013**, *24*, 599
7. S. Thomaidis, A. Kakaboura, W. D. Mueller, S. Zinelis, Dental Materials, **2013**, *29*, 132
8. M. O. Daltoé, C. P. Lepri, J. G. Wiezel, D. C. Tornavoi, J. A. M. Agnelli, A. C. Reis, *Minerva Stomatol*, **2013**, *62*, 63
9. C. P. Turssi, J. L. Ferracane, K. Vogel K, *Biomaterials*, **2005**, *26*, 4932
10. N. Martin, N. Jedynakiewicz, *Biomaterials*, **1998**, *19*, 77
11. E. Mortier, D. A. Gerdolle, A. Dahoun, M. M. Panighi, American Journal Dentistry, **2005**, *18*, 177
12. D. L. Leonard, D. G. Charlton, H. W. Roberts, M. E. Cohen, *Journal of Esthetic Restoration Dentistry,* **2002**, *14*, 286
13. J. A. von Fraunhofer, P. Jr. Curtis, *Dental Materials*, **1989**, *5*, 365
14. S. Stankovich, D. A. Dikin, R. D. Piner, K. A. Kohlhaas, A. Kleinhammes, Y. Jia, *Carbon,* **2007**, *45*, 1558.
15. J. I. Paredes, S. Villar-Rodil, A. Martinez-Alonso, J. M. D. Tascon, *Langmuir,* **2008**, *24*, 10560.
16. Y. Xu, Z. Liu, X. Zhang, Y. Wang, J. Tian, Y. Huang, *Adv Mater,* **2009**, *21*, 1275
17. I. Sideridou, S.A. Dimitris, C. Spyroudi, M. Karabela, *Biomaterials*, **2004**, *25*, 367
18. D. Dudea, M. Moldovan, L. Silaghi-Dumitrescu, H. Colosi, A. Botos, A. Irimie, C. Alb, *Studia UBB Chemia*, **2010**, *LV 1*, 66
19. S.B. Berger, A.R. Muniz Palialol, V. Cavalli, M. Giannini, *Brazilian Dental Journal*, **2009**, *20*(4), 314
20. C. Sarosi, A. Antoniac, C. Prejmerean, O. Pastrav, D. Patroi, G. Popescu, M. Moldovan, *Key Engineering Materials,* **2014**, *614*, 113
21. C. Lee, X.D. Wei, Q.Y. Li, R. Carpick, J.W. Kysar, J. Hone, *Physica Status Solidi*, **2009**, *246*, 2562
22. I.D. Sideridou, M.M. Karabela, E. Ch. Vouvoudi, *Dental Materials*, **2011**, *27*, 598
23. H. Porwal, S. Grasso, M.J. Reece*, Advances in Applied Ceramics*, **2013**, *12*(8), 443
24. A.R. Biris, S. Ardelean, M.D. Lazar, E. Dervishi, F. Watanabe, A. Ghosh, A. Biswas, A.S. Biris, *Carbon*, **2012**, *50*, 2252

STUDIA UBB CHEMIA, LX, 2, Tom I, 2015 (p. 81-92)
(RECOMMENDED CITATION)

THE USE OF BIODENTINE™ AS A ROOT-END FILLING MATERIAL

ANDREEA IULIANA GULIE (căs. KUI)[a,*], MÎNDRA BADEA[b]

ABSTRACT. Biodentine™ is a calcium silicate based cement and it was released in January 2011 by Septodont (France). The purpose of this study was to evaluate the literature regarding the use of Biodentine™ in order to emphasize the performances and effectiveness of this product in comparison with other dental materials used as retrograde filling materials and also to help clinicians make an informed choice about which dental material should use in periapical surgery. According to the published literature, BiodentineTM could be an efficient alternative to mineral trioxide aggregate or other dental cements to be used as a root-end filling material because of its physical, biological and handling properties. Although it seems it has a good behaviour in clinical practice, more clinical studies are required in order to support the indication as a root-end filling material.

Key words: *Biodentine™, root-end filling, tricalcium silicate cement*

INTRODUCTION

Apicoectomy, followed by a retrograde obturation, is a surgical technique applied in endodontics, when all the efforts for a successful orthograde endodontic therapy have failed. The purpose of the retrograde filling is to seal the root canal and prevent passage of bacteria or their toxins from the canal space into periradicular tissues. A root-end filling material is placed in direct contact with periapical tissues and it should have several qualities as it influences the tissue response and the outcome of surgical endodontic treatment. [1]

An ideal root-end filling material should adhere to the root canal walls and seal the root-end three-dimensionally. It should not promote (preferably it should inhibit) the growth of pathogenic microorganism, be well tolerated

[a] *Department of Prosthodontics, Faculty of Dentistry, Iuliu Hatieganu University of Medicine and Pharmacy, Cluj-Napoca, Romania*
[b] *Department of Dental Prevention, Faculty of Dentistry, Iuliu Hatieganu University of Medicine and Pharmacy, Cluj-Napoca, Romania*
* *Corresponding author: guile.andreea@umfcluj.ro*

by periradicular tissues with no inflammatory reactions and stimulate the regeneration of normal periodontium. A root-end filling material should also be dimensionally stable and unaffected by moisture in either the set or unset state; it should be easily distinguished on radiographs and be easy to handle. [2]

Biodentine™ is a calcium silicate based cement and it was released in January 2011 by Septodont (France). According to the manufacturer it can be used for crown and root dentin repair treatment, repair of perforations or resorbtions, apexification and root-end fillings. [3]

The purpose of this study was to evaluate the literature regarding the use of Biodentine™ in order to emphasize the performances and effectiveness of this tricalcium silicate in comparison with other dental materials used as retrograde filling. This will help clinicians make an informed choice about which dental material should use in periapical surgery.

RESULTS AND DISCUSSION

According to the manufacturer, Biodentine™ has large range of applications including endodontic repair (root perforations, apexification, resorptive lesions), as a retrograde filling material in endodontic surgery and as a pulp capping. This calcium silicate cement is performed using the MTA-based cement technology but with some improved properties, such as physical qualities and handling. This material has been frequently studied in recent literature and serves as an important representative of tricalcium silicate based cements; we believe that a review of these researches regarding the properties of Biodentine™ as a root-end filling material is contributory in generating a clearer picture about the general characteristics.

Two independent reviewers (A.G. and M.B.) conducted a literature search for publications from 2004 to November the 1st 2014 in Medline (PubMed) Embase, Web of Science, CENTRAL (Cochrane), Scopus, SciELO and clinicaltrials.gov. The search terms used were “biodentine”, “tricalcium silicate”, “root-end filling” and “endodontic surgery” (Image 1). The electronic search resulted 1766 articles.

For this review we considered clinical trials, case reports, in vitro studies, in vivo studies and other reviews, all written in English language. We excluded articles written in other languages, short communications and non-topic related articles or articles with no abstract available; from the total of 1766 articles, 52 formed the basis of the present review. Most of the articles were in vitro studies and written between 2012 and 2014. (Image 1)

We organized the present paper in several categories as fallows. In section 1 the mechanical and chemical properties, in section 2 dimensional stability, solubility and push-out bond strength, sealing ability in section 3, section 4 biocompatibility and antibacterial effect and in section 5 radioopacity.

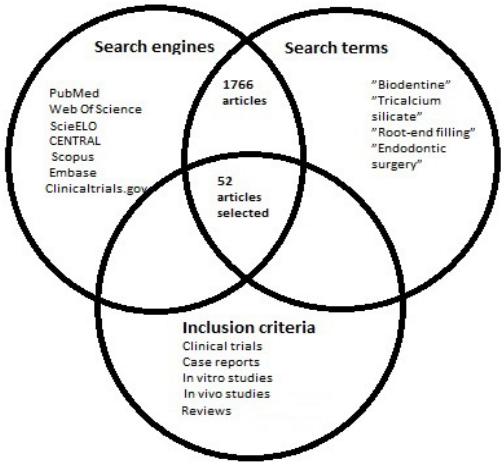

Figure 1. – Overview of the search methodology and selection criteria used in this literature review

1. Composition, mechanical and chemical properties

Biodentine™ is dispensed in a fixed powder: liquid proportion, providing a shorter setting time of 12 min (manufacturer's data sheet). The powder contains a main component (tricalcium silicate), a filler material (calcium carbonate), a radioopacifier (zirconium oxide) and traces of dicalcium silicate, calcium oxide and iron oxide. The liquid is an aqueous solution of a hydrosoluble polymer (water reducing agent) combined with calcium chloride which decreases the setting time. [4,5] Septodont is using a new technological platform named „Active Biosilicate Technology"™ in order to control the purity of the raw materials. This fact is proved also by Camilieri et al. in their study, when they could not found minor elements in the composition of Biodentine™, which can be beneficial for producing dental cements.

The calcium carbonate is used in the powder of Biodentine™ for its biocompatibility and its calcium content. The hydrosoluble polymer in the liquid is based on polycarboxilate and maintains a balance between low water content and consistency of the mixture. [6]

Although setting reaction is not fully investigated it is believed that Biodentine™ sets through a hydration reaction. In addition, researchers found a type of interfacial interaction called “the mineral infiltration zone” for calcium-silicate-based cements, including Biodentine™. [7]

When compared to other root-end filling materials (Bioaggregate™ or IRM™) Biodentine™ proved to have a shorter setting time, a higher compressive strength and micro-hardness and low fluid uptake. The addition of a water-soluble polymer in the liquid allows a higher strength, micro-hardness and very low water-cement ratios. [5]

J. Camilleri evaluated in several studies the properties of Biodentine™, especially its porosity. Porosity of tricalcium silicate-based cements occurs as a result of the spaces between the un-hydrated cement grains. [8] After the hydration, these spaces will be filled with water. When used as a root-end filling material, the porosity of Biodentine™ is affected by ambient conditions and material additives. Biodentine™ is less porous than other tricalcium silicate-base materials. In their study, Camilleri et al. concluded that Biodentine™ demonstrated cracks at the interface between root-dentine and the material interface, but also within the bulk of the material.

Biodentine™ also demonstrated leakage when used in a sandwich restoration overlaid with composite, both when the material was left unprepared and when it was etched. [9] Apparently, the etching created surface changes for Biodentine™ that might have the potential to enhance bonding of resinous materials. [10]

2. Push-out bond strength, solubility and dimensional stability

In case of a periapical surgery, a dental material should provide a strong bond with the canal walls, but also resist to the dislodgement during function. This is why the push-out bond strength is an important quality for a root-end filling. In our search, we found several articles about the push-out bond strength of Biodentine™ and other calcium silicate cements.

Aggarwal et al. studied the push-out bond strength of three cements (Biodentine™, MTA™ and MTA Plus™) when used as a furcation repair material. They used 120 extracted molar, which were divided in groups according to the type of material used, blood contamination and setting time (24 hours and 7 days). The results showed that Biodentine™ has a better push-out bond strength than MTA after 24 hours and blood contamination has no effect in the perforations repaired with Biodentine™. [11]

Alhodiry et al. also studied the effect of saliva and blood contamination on bi-axial flexural strength and setting time of Biodentine™ and Portland cement™. They confirmed a shorter setting time for Biodentine™, than Portland

cement™. The setting time of Biodentine™ was less affected by contaminants when compared to Portland cement™. The authors found no significant difference in bi-axial flexural strength between Biodentine™ and Portland cement™. [12]

Guneser et al. evaluated the effect of various endodontic irrigants on the push-out bond strength of Biodentine™ compared to MTA™, amalgam and Dyract AP™. But after being exposed to various endodontic irrigants, Biodentine™ showed considerable performance as a perforation repair material compared to the other dental materials. [13] Elnaghy obtained similar results when exposed Biodentine™ under the effect of QMix™ and other conventional endodontic irrigants. QMix™ did not affect the bond strength of Biodentine™ and MTA™; Biodentine™ showed higher resistance than MTA™ to dislodgement forces from root dentin. [14]

The push-out bond strength of Biodentine™ and other silicate cements is apparently affected by the presence of smear layer on the canal walls and is also influenced by acidic environment. [15,16]

Few studies were found regarding other mechanical properties: dimensional stability and solubility. Caronna et al. studied the micro-hardness of three dental materials (MTA™, EndoSequence™ and Biodentine™) after setting in moist or dry conditions. They concluded that Biodentine™ setting was unaffected by the artificial periodontal conditions, but ProRoot wMTA™ showed greater hardness than Biodentine™ and EndoSequence™ in either environment tested. [17]

When used as a posterior restoration material Biodentine™ can be used for up to six months, at this time it suffers abrasion but without any marginal discoloration. In a case report published by Sihha et al. Biodentine™ was used as an apical barrier for the apexification of a maxillary right central incisor. After 12 month follow up, the tooth presented no clinical symptoms and on the XRay they observed a progressive involution of periodontal radiolucency and healing with a calcified barrier at the apex. The authors concluded that more clinical studies are needed in order to validate Biodentine™ as a suitable material in apexification, but they suggested that it can be a good alternative to MTA™, as Biodentine™ is simpler to be placed in the root-canal. [18] We also found that another two case reports studies confirm the successful use of Biodentine™ in apexification. [19,20]

3. Sealing ability

The sealing ability is, in fact, the capacity of adherence of a dental material to the canal dentine walls. It is imperative for a root-end filling material to have a good sealing ability, in order to prevent leakage between the root canal and periodontal space. We found only two in vitro studies regarding the sealing ability of Biodentine™ used as a root-end filling. (Table 1) We decided to include in our review another 3 studies where Biodentine™ is used

as a furcation repair material, as the clinical conditions are not very different. Another three clinical studies were found regarding the use of Biodentine™ as a root-end filling material.

Ravichandra et al. investigated the marginal adaptation of glass-ionomer cement, MTA™ and Biodentine™ as a root-end filling material. [21] In another study, Soundappan et al. investigated IRM™, MTA™ and Biodentine™ for their apical seal ability. [22] Both studies used for evaluation transversal sections of the resected roots which were examined by Scanning Electron Microscopy (SEM). In the first study, the authors concluded that Biodentine™ had a better marginal adaptation than the other two materials used in the study (MTA™ and a glass-ionomer cement). In the second study, Soundappan et al. concluded that Biodentine™ had a lower sealing ability at 2 mm depth of the root-end obturation, while MTA™ had the best results. Similar results were obtained, within the limits of their study, by Ozbay et al., were Biodentine™ exhibited a lower sealing ability than MTA™, on a dye penetration test. [23]

When used as a furcation repair material, Biodentine™ demonstrated lower sealing capacity than Micro-Mega MTA™, Pro-root MTA™ or MTA Angelus™. [24,25,26]

Three case reports studies were found, in which Biodentine™ was used as a root-end filling material in apicoectomy. In the first study, Caron et al. presented two case reports, both in which they used Biodentine™ as a root-end filling material. [27] The follow up was made until 24 months and the authors concluded that although Biodentine™ has a low radioopacity, because of its biological properties and its clinical setting time it may be suitable for surgical endodontics. Pawar et al. obtained similar results when using Biodentine™ as a root-end filling material, after a periodontal surgery for two teeth that were previously traumatized and with a large periapical lesion. [28]

In the other clinical study, Biodentine™ was used successfully as a root-end filling material in the management of a palatogingival groove, because of its good mechanical properties and biocompatibility. [29]

Table 1. – Overview of sealing ability of Biodentine™ compared with other materials

Type of study	Evaluation Technique	Folllow up	Clinical Aplications	No. of teeth	Materials Tested	Reference
1	2	3	4	5	6	7
In vitro study	Dye penetration	X	Interradicular Furcation	40	MICRO-MEGA MTA™; Endosequence™; Biodentine™	Jeevani et al. (2014) [25]
In vitro study	Dye penetration	X	Interradicular Furcation	84	MTA Angelus™; Biodentine™ GC Fuji lining LC™; Aquafix Portland cement™	Nikoloudaki et al. (2014) [26]
In vitro study	SEM evaluation	X	Root-end filling	30	MTA™; Biodentine™ IRM™	Soundappan et al. (2014) [22]

Type of study	Evaluation Technique	Folllow up	Clinical Aplications	No. of teeth	Materials Tested	Reference
1	2	3	4	5	6	7
In vitro study	Dye penetration	X	Interradicular Furcation	30	Biodentine™; Pro-root MTA™; Calcium Phospfate cement™	Sanghavi et al. (2013) [24]
In vitro study	Dye penetration	X	Root-end filling	21	MTA Angelus™; Biodentine™	Ozbay et al. (2014)[23]
Case report	Xray	24 months	Root-end filling	2	Biodentine™	Caron et al. (2014) [24]
Case report	Xray	24 months	Root-end filling	1	Biodentine™	Johns et al. (2014) [29]
Case report	Xray	18 Months	Root-end filling	2	Biodentine™	Pawar et al. (2013) [28]

4.a. Biocompatibility

Biocompatibility refers to the ability of a material to perform with an appropriate host response in a specific situation. [30] This allows to a biomaterial to perform its desired function with respect to a medical therapy, without eliciting any undesirable local or systemic effects in the recipient or beneficiary of that therapy, but generating the most appropriate beneficial cellular or tissue response in that specific situation, and optimising the clinically relevant performance of that therapy. [31]

We found numerous studies regarding the biocompatibility of Biodentine™. In vitro studies evaluated cytotoxicity on different types of human cells, like osteoblasts, dental pulp cells, fibroblasts, mesenchymal stem cells and monicytes or even murinae odontoblastic cells. (Table 2)

In several studies, the authors mention a good biocompatibility of Biodentine™, which is comparable with MTA–based products (Ortho-MTA™, ProRoot MTA™, MTA Angelus™). However, in their study, Samyuktha et al. concludes that MTA™ had a lower cytotoxicity on human periodontal ligament fibroblasts than Endosequence™ and Biodentine™. [32] Similar results obtained Jung et al. who compared cytotocicity of Biodentine™, MTA™ and Bioaggregate™ on human dental pulp cells. They concluded that both, Biodentine™ and Bioaggregate™ are biocompatible, but Biodentine™ had a relative higher cytotoxicity than MTA™. [33]

We found 2 in vivo studies on animals who evaluated biocompatibility of Biodentine™. The first study, evaluated the effect of Biodentine™ on dog pulp cells. [34] The authors applied Biodentine™ and MTA™ for pulp capping and pulpotomy. There was no statistically significant difference between the two materials. In another in vivo study, the researchers evaluated the subcutaneous tissue reaction of rats in the presence of Biodentine™, MTA™ and zinc oxide eugenol cement. [35] After 14 days, the histological analyses showed good results for Biodentine™ as well as for MTA™.

Nowicka et al evaluated Biodentine™ and MTA™ as pulp capping materials on teeth scheduled for extraction (orthodontic reasons). After 6 weeks the extractions were made and histological analyses showed a good biocompatibility both for MTA and Biodentine™. [36]

Lee et al. investigated in their study the effect of 3 endodontic bioactive cements (MTA™, Biodentine™, Bioaggregate™) on the differentiation of mesenchymal cells. Within the limitations of their study, the authors concluded that all three cements induced the differentiation of mesenchymal cells into osteoblasts. [37]

Table 2. - Overview on biocompatibility studies over Biodentine™

Type of study	Type of cells/tissues	Evaluation technique	Materials	Reference
1	2	3	4	5
In vitro study	MG63 osteoblast-like cells	Cytotoxicity using MTT assay; Protein quantification analysis; SEM analysis.	Biodentine™; MTA™	Attik et al. 2014 [42]
In vitro study	Immortalized human dental pulp cell line	Cytotoxicity using3-(4,5-dimethylthiazolyl-2-yl)-2,5-diphenyltetrazolium Bromide Assay; Effect of Materials on Odonto-blastic Differentiation; Signal Pathways of Materials	Biodentine™; MTA Angelus™; Ortho-MTA™;IRM™	Chang et al. 2014 [43]
In vitro study	Fibroblast 3T3 cells	Cell Viability Assay; SEM analysis; Measurement of Citokine Expression at the mRNA Level	Biodentine™;MTA™; GC Fuji IX™	Corral Nunez et al. 2014 [44]
In vitro study	Human gingival fibroblasts	Flow Cytometry; Cell Adhesion Assay	Biodentine™;Pro-root MTA™; GC Fuji IX™	Zhou et al. 2013 [45]
In vitro study	Human periodontal ligament fibroblasts	Cytotoxicity evaluation with trypan blue	Biodentine™; MTA™; Endosequence™	Samyuktha et al. 2014 [32]
In vitro Study	Rat odontoblast cells	Cytotoxicity using MTT assay; Antibacterial effect	Dycal™;Calcicur™; Calcimol LC™; TheraCal LC™;MTA Angelus™;Biodentine™	Poggio et al. 2014 [38]
In vitro study	Murinae odonto-blast cell line	Cytotoxicity evaluation; Confocal Laser Scanning Microscope	Dycal™;ProRoot MTA™;MTA Angelus™; Biodentine™	Poggio et al. 2014 [47]
In vitro study	MDPC-23 and Od-21 cell lines	Spheroid (3D) formation Real time PCR; Scanning electron microscopy	Biodentine™;MTA™	Perard et al. 2013 [48]
In vitro study	Human dental pulp cells	Alkaline Phosphatase Staining and Activity Analysis; Alizarin Red Staining and Quantifi-cation; Quantitative Real-time Reverse-transcrip-tase Polymerase Chain Reaction	Biodentine™	Luo et al. 2014 [49]

Type of study	Type of cells/tissues	Evaluation technique	Materials	Reference
1	2	3	4	5
In vitro study	Mesenchymal stem cells	Cell Viability Assay; Reverse-transcription Polymerase Chain Reaction and Quantitative Real-time Polymerase Chain Reaction; ALP Staining	Biodentine™ MTA™; Bioaggregate™	Lee et al. 2014 [37]
In vitro study	Human dental pulp cells	Direct pulp capping with Biodentine; TGF-b1 secretion by pulp cells	Biodentine™	Laurent et al. 2012 [50]
In vitro study	Human monocytes	Cytotoxicity assay	ProRoot MTA™; Biodentine™; CEM cement™; Tech Biosealer™	Khedmat et al. 2014 [51]
In vitro study	Human dental pulp cells	Cell viability assay; Reverse transcription-polymerase chain reaction; Alizarin red S staining; Western blot analysis	Biodentine™;MTA™; Bioaggregate™	Jung et al. 2014[33]
In vitro study	Human dental pulp cells	Cell proliferation assay; Migration assay; Adhesion assay; Quantitative real-time reverse-transcriptase polymerase chain (qRT-PCR)	Biodentine™	Luo et al. 2014 [53]
In vitro study	Human dentin	Hydroxyproline Assay; Transmission Electron Microscopy	Biodentine™; MTA Plus™	Leiendecker et al. 2012 [54]
In vivo study	Dogs pulp cells	Qualitative and quanti-tative histopathologic analyses	ProRoot MTA™; Biodentine™	Rossi et al. 2014 [34]
In vivo study	Rats subcutaneous tissue	Histopathologic analyses	Zinc oxide eugenol™;MTA Angelus™; Biodentine™	Mori et al. 2014 [35]
In vivo study	Human dental pulp	Clinical examination; Histopathologic analyses	Biodentine™; MTA™	Nowicka et al. 2013 [36]

4.b. Antibacterial effect

A biocompatible dental material should not only promote tissue repair reaction, but it should have antibacterial and healing induction properties. [38] This is why Poggio et al. found necessarily to test the antibacterial effect of several cements used in endodontics (Dycal™; Calcicur™; Calcimol LC™; TheraCal LC™; MTA Angelus™ and Biodentine™). The results showed that Biodentine™ had antibacterial effect on *Streptococcus sanguis* and on *Streptococcus salivarius*. When testing antibacterial effect on *Streptococcus sanguis* and *Streptococcues mutans,* Biodentine™ had a lower value than other cements, like Dycal™. The authors concluded that tricalcium silicate cements showed a better antibacterial activity and a lower cytotoxicity, unlike other cements investigated.

Nikhil et al. also investigated the antibacterial effect of Biodentine™ on *Staphylococcus aureus, Enterococcus faecalis, Candida albicans* and *Streptococcus mutans.* [39] Another aim of the present study was to explore the effect of adding one of these substances, chlorhexidine and doxycycline, to Biodentine™ as root-end filling material. The authors found a clear antibacterial effect of Biodentine™ alone on all the tested bacteria and fungi. Adding 2% clorhexidine enhanced the antibacterial activity of Biodentine™ alone, but 10% of doxycycline added decreased the antibacterial activity of Biodentine™ alone.

5. Radioopacity

An ideal repair material should be sufficient radio-opaque in order to be easily discerned from the other structures. [40] For retrograde fillings this property is very important so that the radiograph taken post-operatively confirm that the material is within the cavity, well placed and it is easy discerned from the other tissues (dentine and bone trabeculae). [41]

Biodentine™ exhibits a radioopacity value higher than 3 mm according to ISO 6786(2001). In the study presented by Grech et al. Biodentine™, as well as other materials tested (MTA™, Bioaggregate™ and IRM™), lost its radioopacity over time, but with no statistically significant difference. [5] Camilleri et al. concluded in their study that Biodentine™ contains only 5% zirconium oxide and this is why it has lower radioopacity than MTA Angelus™. [4]

CONCLUSIONS

According to the published literature Biodentine™ could be an efficient alternative to mineral trioxide aggregate or other dental cements to be used as a root-end filling material because of its physical, biological and handling properties.

However, in order to draw definitive conclusions about the use of Biodentine™ in periodontal surgery are necessary more prospective clinical studies and randomised control trials with a long term follow up.

ACKNOWLEDGEMENTS

This research was funded by POSDRU grant no.159/1.5/S/138776 grant with title: “Model colaborativ institutional pentru translatarea cercetarii stiintifice biomedicale in practica clinica– TRANSCENT

REFERENCES

1. Saxena P., Gupta S.K., Newaskar V., *Restorative Dentistry & Endodontics,* ***2013****, 38, 119.*
2. Chong B.S., Pitt Ford T.R., *Endodontic Topics,* **2005**, *11*, 114.
3. Septodont - France. Biodentine™ (Brochure), **2011**.
4. Camilleri J., Sorrentino F., Damidot D.*, Dental Materials*, **2013**, *29, 580*.
5. Grech L., Mallia B., Camilleri J., *Dental Materials,* **2013**, *29, 20*.
6. Camilleri J., Kralj P., Veber M., Sinagra E., *International Endodontic Journal,* **2012**, *45*, 737.
7. Festy F., Watson T.F., *Biomaterials and Bioengineering*, **2012**, *91*, 454.
8. Camilleri J., *Dental Materials*, **2014**, *30, 709*.
9. Camilleri J., *Journal of Denstistry,* **2013**, *41, 600*.
10. Kayahan M.B., Nekoofar M.H., Kazandağ M., Canpolat C., Malkondu O., Kaptan F. et al., *International Endodontic Journal*, **2009**, *42,* 1004.
11. Aggarwal V., Singla M., Miglani S., Kohli S., *Journal of Conservative Dentistry*, **2013**, *16*, 462.
12. Alhodiry W., Lyons M..F, Chadwick R.G., *European Journal of Prosthodontics and Restorative Dentistry*, **2014**, *22,* 1.
13. Guneser M.B., Akbulut M.B., Eldeniz A.U., *Journal of Endodontics*, **2013**, *39,* 380.
14. Elnaghy A.M.*, Journal of Adhesive Dentistry*, **2014**, *16,* 277.
15. El-Ma'aita A.M., Qualtrough A.J.E., Watts D.C., *Dental Materials*, **2013**, *29*, 797.
16. Elnaghy A.M., *Journal of Endodontics*, **2014**, *40, 953*.
17. Caronna V., Himel V., Yu Q., Zhang J.-F., Sabey K., *Journal of Endodontics*, **2014**, *40*, 986.
18. Sinha N., Singh B., Patil S.*, Journal of Conservative Dentistry*, **2014**, *17*, 285.
19. Khetarpal A., Chaudhary S., Talwar S., Verma M., *Indian Journal of Dental Research*, **2014**, *25,* 513.
20. Nayak G., Hasan M.F., *Restorative Dentistry and Endodontics*, **2014**, *39*, 120.
21. Ravichandra P.V., Vemisetty H., Deepthi K., Reddy S.J., Ramkiran D., Krishna M. JN et al., *Journal of Clinical and Diagnostic Research*, **2014**, *8*, 243.
22. Soundappan S., Sundaramurthy J.L., Raghu S., Natanasabapathy V., *Journal of Dentistry of Tehran University of Medical Sciences,* **2014**, *11*, 143.
23. Ozbay G., Kitiki B., Peker S., Kargul B., *ACTA Stomatologica Croatica,* **2014**, 132.
24. Sanghavi T., Shah N., Shah R.R., *National Journal of Medical Research,* **2014**, *4*, 56.
25. Jeevani E., Jayaprakash T., Bolla N., Vemuri S., Sunil C.R, Kalluru R.S., *Journal of Conservative Dentistry*, **2014**, *17*, 340.
26. Nikoloudaki G.E., Kontogiannis T., Meliou H.A., Kerezoudis N.P., *Open Journal Stomatology*, **2014**, *4*, 402.
27. Caron G., Azérad J., Faure M.-O., Machtou P., Boucher Y., *International Journal of Oral Sciences,* **2014**, *2, 1*.
28. Pawar A.M., Kokate S.R., Shah R., *Journal of Conservative Dentistry*, **2013**, *16, 573*.

29. Johns D.A., Shivashankar V.Y., Shobha K., Johns M., *Journal of Conservative Dentistry*, **2014**, *17, 75*.
30. Black J., Biological Performance of Materials: Fundamentals of Biocompatibility, Fourth Edn CRC Press, **2006**.
31. Williams D.O., *Biomaterial*, **2008**, *2,* 2,941.
32. Samyuktha V., Ravikumar P., Nagesh B., Ranganathan K., Jayaprakash T., Sayesh V., *Journal of Conservative Dentistry*, **2014**, *17,* 467.
33. Jung J.-Y., Woo S.-M., Lee B.-N., Koh J.-T., Nör J.E., Hwang Y.-C., *International Endodontic Journal*, **2015**, *48,* 178.
34. Rossi A. De, Assed L., Silva B., Nelson-Filho P., Assed R., Queiroz A.M. De, *Journal of Endodontics*, **2014**, *40,* 1362.
35. Mori G.G., Teixeira L.M., Oliveira D.L. De, Jacomini L.M., *Journal of Endodontics***, 2014**, *40,* 1485.
36. Nowicka A., Lipski M., Parafiniuk M., Sporniak-Tutak K., Lichota D., Kosierkiewicz A. et al., *Journal of Endodontics*, **2013**, *39,* 743.
37. Lee B.-N., Lee K.-N., Koh J.-T., Min K.-S., Chang H.-S., Hwang I.-N. et al., *Journal of Endodontics*, **2014**, *40,* 1217.
38. Poggio C., Ceci M., Beltrami R., Dagna A., Colombo M., Chiesa M*., Annals of Stomatology (Roma),* **2014**, *4,* 69.
39. Nikhil V., Madan M., Agarwal C., Suri N., *Journal of Conservative Dentistry*, **2014**, *17,* 271.
40. Tagger M., Katz A., *International Endodontic Journal,* **2004**, *37,* 260.
41. Tanalp J., Karapınar-Kazandağ M., Dölekoğlu S., Kayahan M.B., *Scientific World Journal,* **2013**; DOI.org/10.1155/2013/594950.
42. Attik G.N., Villat C., Hallay F., Pradelle-Plasse N., Bonnet H., Moreau K. et al., *International Endodontic Journal,* **2014**, *12*, 1.
43. Chang S.-W., Lee S.-Y., Ann H.-J., Kum K.-Y., Kim E.-C*., Journal of Endodontics,* **2014**, *40*, 1194.
44. Corral Nuñez C.M., Bosomworth H.J., Field C., Whitworth J.M., Valentine R., *Journal of Endodontics,* **2014**, *40,* 406.
45. Zhou H., Shen Y., Wang Z., Li L., Zheng Y., Häkkinen L. et al., *Journal of Endodontics,* **2013**, *39,* 478.
46. Zanini M., Sautier J.M., Berdal A., Simon S., *Journal of Endodontics*, **2012**, *38,* 1220.
47. Poggio C., Arciola C.R., Beltrami R., Monaco A., Dagna A., Lombardini M. et al., *Scientific World Journal,* **2014**, *2,* 1819.
48. Pérard M., Le Clerc J., Meary F., Pérez F., Tricot-Doleux S., Pellen-Mussi P., *Journal of Materials Sciences*, **2013**, *2,* 1527.
49. Luo Z., Kohli M.R., Yu Q., Kim S., Qu T., He W., *Journal of Endodontics*, **2014**, *40,* 937.
50. Laurent P., Camps J., About I., *International Endodontic Journal,* **2012**, *45,* 439.
51. Khedmat S., Dehghan S., Hadjati J., Masoumi F., *Restorative Dentistry and Endodontics,* **2014**, *7658*, 149.
52. Jang Y.-E., Lee B.-N., Koh J.-T., Park Y.-J., Joo N.-E., Chang H.-S. et al., *Restorative Dentistry and Endodontics,* **2014**, *39,* 89.
53. Luo Z., Li D., Kohli M.R., Yu Q., Kim S., He W.-X., *Journal of Dentistry*, **2014**, *42,* 490.
54. Leiendecker A.P., Qi Y.-P., Sawyer A.N., Niu L.-N., Agee K.A., Loushine R.J. et al., *Journal of Endodontics,* **2012**, *38,* 829.

STUDIA UBB CHEMIA, LX, 2, Tom I, 2015 (p. 93-100)
(RECOMMENDED CITATION)

IMMUNOMODULATORY POTENTIAL OF PALLADIUM(II) COMPLEXES WITH (1E,6E)-1,7-BIS (3,4-DIMETHOXYPHENYL) HEPTA-1,6-DIENE-3,5-DIONE

EVA FISCHER-FODOR[a,c,*], ROMAN MIKLÁŠ[b], LUDOVIC TIBOR KRAUSZ[c,d], PIROSKA VIRAG[a], DANIELA CRISTINA MOLDOVAN[e], MARIA PERDE SCHREPLER[a], IOANA BERINDAN-NEAGOE[c], FERDINAND DEVÍNSKY[b], NATALIA MIKLÁŠOVÁ[b*]

ABSTRACT. In the cancer chemotherapy the metal-based cytotoxic drugs are invariable components of therapeutic protocols, despite the biologic drugs expansion. A current tendency is to design metal-based drugs with highest efficacy and limited toxicity on normal human cells implicated in immune response. Therefore we synthesized and characterized two palladium(II) complexes with (1*E*,6*E*)-1,7-bis(3,4-dimethoxypenyl)hepta-1,6-diene-3,5-dione, a curcuminoid like ligand; their cytotoxicity towards tumor cells was tested, and their expected impact on T and B lymphocytes was measured *in vitro*. The lymphocytes treatment with the free ligand, and with the two complexes **1** and **2**, increased significantly the proportion of the T helper CD4 positive cell population, concomitant with the decrease of T effector CD8 positive cells. The B cells were not affected by **1**, but **2** has a minor inhibitory effect on CD19+ and CD45RA+ cells. The cells function was tested through the compounds modulator effect on membrane markers CD25 and GITR, both being slightly down regulated by **2**, compensating of CD4+ overexpression and CD8+ down regulation. Moreover, complex **1** displayed minimal interferences with the cellular antitumor immunity, acting as a selective inhibitor of cancer cells growth.

Keywords: *(1E,6E)-1,7-bis(3,4-dimethoxyphenyl)hepta-1,6-diene-3,5-dione, palladium complex, cancer therapy, immune response*

[a] *Research Department, Institute of Oncology "Prof. Dr. I. Chiricuta", 34-36 Republicii Str., RO-400015, Cluj-Napoca, Romania*
[b] *Department of Chemical Theory of Drugs, Faculty of Pharmacy, Comenius University in Bratislava,8 Kalinčiakova Str., 83232 Bratislava, Slovakia*
[c] *Faculty of Medicine, Iuliu Hatieganu University of Medicine and Pharmacy Cluj Napoca, 8, Babes Str, RO-400012, Cluj-Napoca, Romania*
[d] *Public Health Center, 1 Miko Str., RO-530174, Miercurea Ciuc, Romania*
[e] *Regional Blood Transfusion Center, 19 Nicolae Balcescu Str, RO-40000, Cluj-Napoca, Romania*
** Corresponding authors: Eva Fischer-Fodor: fischer.eva@iocn.ro;*
Natalia Miklasova: miklasova@fpharm.uniba.sk.

INTRODUCTION

Several metal-based drugs were introduced in the clinical practice; among them the platinum complexes having cytotoxic properties are drugs of choice for systemic therapy of cancer [1]. When using cytotoxic drugs against different cancer localizations, besides the beneficial effect of tumor cell destruction, the normal cells are damaged as well, but more hazardous is the human immune systems damaging, because it cuts the human body self-defense mechanism.

A new tendency in the drug discovery encourages the development of drugs which exhibit cytotoxicity and stimulate the antitumor immunity; in the case of metal compounds, a possible approach is the employment of appropriate ligands. The natural compound curcumin displayed anticancer properties [2] selectively against tumor cells [3] and it is immunostimulatory [4]. The metal complexes of curcumin exhibit as well antitumor properties [5, 6], palladium being one of the central metals which form biological active compounds with curcumin analogues [7,8].

In the present study the curcuminoid (1*E*,6*E*)-1,7-bis(3,4-dimethoxyphenyl)hepta-1,6-diene-3,5-dione, and its palladium(II) complexes were synthesized and characterized. T and B lymphocytes are implicated in the adaptive immunity, being the basis of cell-mediated antitumor immunity in humans [9, 10], responsible for the quality of the cellular immune response. We estimated *in vitro* the Pd(II) complexes capacity to influence the lymphocytes activation processes, in order to establish weather they will hinder the immune response of the host organism.

RESULTS AND DISCUSSION

The curcuminoid (1*E*,6*E*)-1,7-bis(3,4-dimethoxypenyl)hepta-1,6-diene-3,5-dione was synthesized following a former procedure [11]. Complexes **1** and **2** (Scheme 1) as well as the precursor palladium complexes were synthesized based on a procedure reported in our previous studies [8,9].

The curcuminoid and the complexes **1** and **2** were tested *in vitro* on two human tumor cell lines: A2780 ovary and the HT-29 colon carcinoma, and on a primary culture of normal lymphocytes. Cytotoxicity was expressed as the half inhibitory concentration (IC50), the concentration which reduce with 50% the amount of living cells. IC50 values were obtained using the sigmoidal dose-response relation, and they reflect the compounds cytotoxicity against tumor and normal cells (Table 1). The curcuminoid, **1** and **2** exhibit *in vitro* cytotoxicity against the tumor cells and they have a milder effect on normal human lymphocytes.

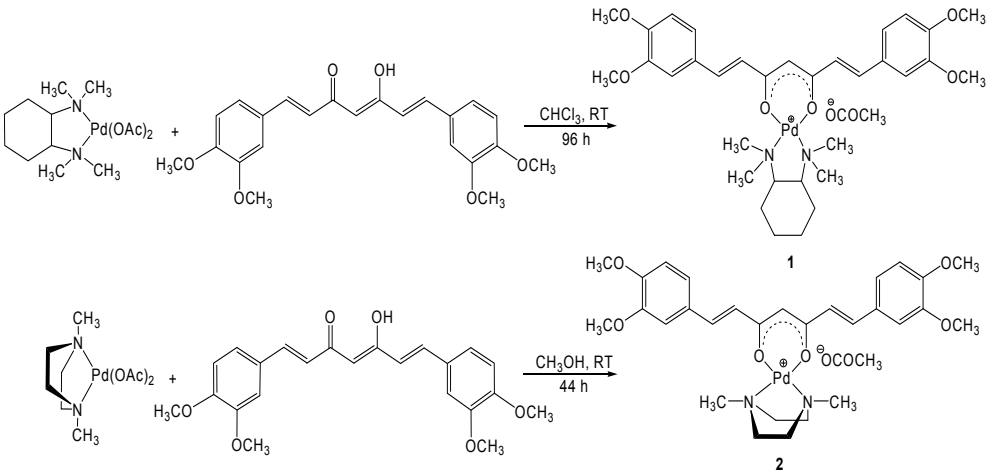

Scheme 1. Synthesis of palladium(II) complexes **1** and **2.**

Table 1. Half inhibitory concentrations IC50 of curcuminoid and palladium(II) complexes (SD standard deviations).

Cell type	A2780 ovary cancer cells		HT-29 colon cancer cells		Normal lymphocytes	
IC50 values (mM)	Median values	SD	Median values	SD	Median values	SD
Curcumin	2.082	0.240	4.325	0.248	6.375	0.419
Complex **1**	1.522	0.141	0.767	0.099	3.857	0.307
Complex **2**	0.944	0.091	0.577	0.027	5.512	0.071

The treatment with curcuminoid, **1** and **2** increases significantly the number of CD4 positive cells in the population (Figure 1), but the standard drug oxaliplatin raise even more the CD4+ cells percent. In CD8 positive population a significant decrease occurred in the cell number after the treatment with all compounds ($p < 0.01$), related to untreated cells. Complex **2** diminish at a lower extent the CD8+ population, and its effect is milder as of oxaliplatin.

No significant difference was observed in CD19 cells expression between the untreated cells and curcumin ($p > 0.5$) and **1**, and **2** cause a decrease with limited importance, as depicted in Figure 2 (not significant in 95% confidence interval). GITR-positive lymphocytes proportion decreases when treated with **2**, which has a weak effect (p 0.0498, significant decrease in 95% confidence interval), while curcumin (p 0.0844) and complex **1** (p 0.0823) show no significant effect on these population. The same tendency was observed in CD25 positive population.

CD45R transmembrane signaling molecule [13] is characteristic for mature B cells and also for some T cell populations. CD25 is a transmembrane protein present on activated T and B cells; CD4+CD25+ suppressor cells and CD8+CD25+ T regulatory cells are critical in clearance of tumor cells. GITR is the glucocorticoid-induced tumor necrosis factor related protein; its expression increase upon T-cell activation and is implicated in programmed cell death and stimulates the antitumoral responses [14].

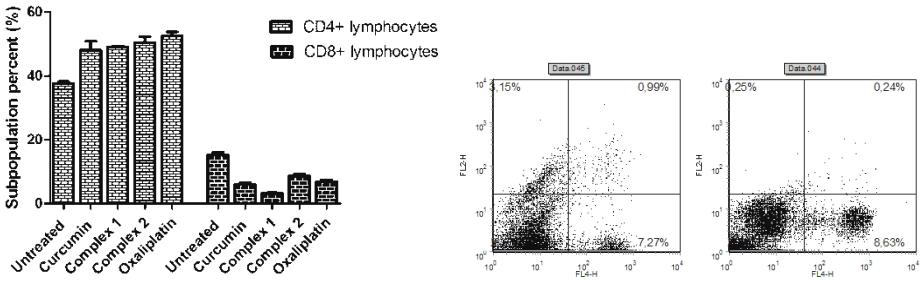

Figure 1. The effect of the complexes effect on CD4+ and CD8+ lymphocytes (left image) and histograms corresponding to flow cytometry measurements for complexes **1** (center) and **2** (right).

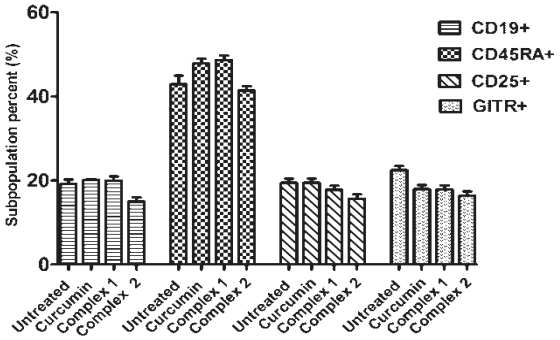

Figure 2. Modulation of CD19, CD45R, CD25 and GITR lymphocyte populations by the treatment with palladium (II) complexes.

The compounds stimulate the survival of the T helper CD4-positive cells in the whole population, and the 24-hours treatment of lymphocytes with the curcumin or his palladium complexes: **1** and **2** give rise to CD4+ enriched cell population.

Cytotoxic CD8-positive T cells are depleted as a consequence of the same treatment, but it is compensated by the enrichment in CD4+ (proportion of CD8 depletion and CD4 enrichment are interrelated). Therefore if non-self

cells destruction mechanism could be affected by novel compounds, the antibody recognition and antigen-presenting mechanisms will work better. The inhibitory effect against CD8+ lymphocyte have highest degree in complex **1** treatment, while the best proliferation in CD4+ lymphocytes is provided by **2**.

Only **2** decreases the survival of CD19 lymphocytes, curcumin and **1** does not interfere with B cells survival, therefore they will not influence the production of antibodies. **2** slightly inhibit B cells survival, but, the proportion of mature CD45R-expressing cells remains unaltered, therefore it couldn't significantly affect the immunoglobulin-secretor function of the B cells.

The activated lymphocytes proportion remains unchanged following the treatment with all compounds, CD25+ and GITR-expressing cells will be not affected, but **2** inhibit somewhat the GITR expression. The novel compounds will not influence lymphocyte activation, an important step in antitumor immune response of the host. Moreover, CD25+ proportion being unchanged and CD4+ increasing, it is obvious that among CD4 population the CD4+CD25+ suppressor cells involvement decreased which could enforce the antitumor response, and will lead to the amplification of effector function. Only in complex **2** effect it is observed a simultaneous increase in CD4+expression concomitant with CD25+ steadiness.

The patterns of CD19+ and CD45R+ cells modulation through curcumin compounds are similar; none of the compounds exert a significant effect on CD19, or CD45RA markers. CD8+CD45R+ cells are suppressor effectors cells [15]; it is very likely that their activity is amplified, because even if CD8+ population drop off, CD45RA+ cells are not affected, thus the proportion of CD8+CD45R+ suppressor effector cells ponder does not modify significantly, and despite the overall CD8 positive population depletion, the cytotoxic effect will be preserved a certain extent. GITR activate the CD4+ and CD8+ T cells [16], and induces tumor rejection [17]. Since curcumin and **1** does not affect GITR expression, and GITR+ cell survival exhibit a moderate decrease due to **2** action, the antitumor immune mechanisms involving CD4+ T cells and B cells will enhance, and the effect of CD8+ drop will be compensate once again by the reliability of GITR expression on the different cell populations, including CD8+ T-cells.

CONCLUSIONS

The curcuminoid and complexes **1** and **2** exhibit a very moderate toxicity against normal human lymphocytes; they do not inhibit the main cell subsets implicated in the signaling pathways of the antitumor response. The curcuminoid inhibits only the CD8+ cells, helps the CD4+ cells survival and it causes no impairment in the other epitopes expression in lymphocytes.

The immune response pathways are not affected by the treatment with the free ligand. Complex **1** action overall on the studied lymphocytes subsets indicates that he has many compensatory effect on the effector cells of the immune system, despite his inhibitory effect on CD8+ cluster, and we anticipate a positive modulation on immunity following *in vivo* administration. Complex **2** inhibitory effects on CD8+ cells and the slight decrease in CD19+ cell expression and GITR, can be a source of moderate immunodepression of the host organism *in vivo*. Overall, the curcuminoid and its palladium(II) complexes will be no source of severe side effects in a potential application as anticancer drugs.

EXPERIMENTAL SECTION

All chemicals for syntheses were of reagent grade and were used as they received; $Pd(OAc)_2$ was purchased from Sigma Aldrich.

All NMR spectra were measured on a Varian Gemini 2000 spectrometers at working frequencies 300 MHz (for ^{1}H-NMR) and 75 MHz (for ^{13}C-NMR). Spectra were measured in CD3OD, using as internal standard TMS. Infrared spectra were recorded on a FT-IR Impact 400 D spectrophotometer on KBr disks. Column chromatography was performed on silica gel (silica 0.035-0.070 mm 60 Å, Acros).

The measurements for biologic effect were made using FACSCalibur flowcytometer (Becton Dickinson, USA) and Synergy2 multiplate reader (BioTek, USA). A2780 and HT-29 tumor cell lines were from ECACC; lymphocytes were isolated on Histopaque separation media from the whole blood of a 42-years old female healthy donor following her informed written consent. We used RPMI-1604 and McCoy's5 cell culture media supplemented with 2mM glutamine, 10% fetal bovine serum, and penicillin-streptomycin solution for cell cultures, all media and supplements were provided by Sigma Aldrich Chemicals. Oxaliplatin was acquired from Actavis Pharma.

Syntheses: Complex **1**: 0.126 mmoles (0.05 g) of (1*E*,6*E*)-1,7-bis(3,4-dimethoxyphenyl)hepta-1,6-diene-3,5-dione were dissolved in 5 mL of dry chloroform. To this solution was added dropwise 0.126 mmoles (0.05 g) of Pd(II) complex containing (*R,R*)-*N,N,N',N'*-tetramethylcyclohexane-1,2-diamine dissolved in 5 mL of $CHCl_3$. Then, 30 µL of NaOH (1M) were added to the reaction mixture. After 96 hours of stirring at room temperature, the reaction mixture was checked by TLC and no unreacted starting curcuminoid was observed. Complex **1** was isolated as a yellow powder (0.06 g; 55%).

^{1}H-NMR (CD_3OD, 300 MHz) δ (ppm) 1.29-1.39 (m, 2H) 1.48-1.59 (m, 2H) 1.81 (m, 2H) 1.89 (s, 3H) 2.20 (m, 2H) 2.85 (s, 6H) 2.87 (s, 6H) 3.25 (m, 2H) 3.87 (s, 6H) 3.89 (s, 6H) 5.89 (s, 1H) 6.75(d, 2H) 6.98 (d, 2H) 7.21 (d, 2H) 7.25 (s, 2H) 7.47 (d, 2H). ^{13}C-NMR (CD_3OD, 75 MHz) δ (ppm) 25.89 (1C) 26.77 (2C) 27.36 (2C) 45.49 (4C) 58.25 (2C) 58.35 (2C) 70.90 (2C) 75.05 (2C) 113.28 (2C) 114.51 (2C) 125.83 (2C) 125.95 (2C) 131.49 (2C) 131.70 (2C) 143.49 (2 C) 152.67 (2C) 181.88 (2C). IR (KBr) ν_{max} (cm^{-1}) 3436, 2931, 2860, 1728, 1620, 1597, 1508, 1465, 1400, 1268, 1139, 1025, 997, 845, 697, 585.

Complex **2**: 0.20 mmoles (0.08 g) of (1*E*,6*E*)-1,7-bis(3,4-dimethoxyphenyl)hepta-1,6-diene-3,5-dione were dissolved in 10 mL of dry methanol. To this solution was added 0.20 mmoles of Pd(II) complex containing 1, 4-dimethylpiperazine dissolved in 5 mL of MeOH. The final product was isolated as a yellowish powder (0.05 g; 62.5%).

^{1}H-NMR (CD_3OD, 300 MHz) δ (ppm) 1.90 (s, 3H) 2.64 (s, 6H) 2.75 (d, 4H) 3.86 (s, 6H) 3.88 (s, 6H) 3.90 (d, 4H) 5.89 (s, 1H) 6.72 (d, 2H) 6.96 (d, 2H) 7.16 (dd, 2H) 7.21 (s, 2H) 7.49 (d, 2H). ^{13}C-NMR (CD_3OD, 75 MHz) δ (ppm) 24.98 (1C) 46.72 (2C) 56.45 (2C) 56.56 (2C) 59.62 (4C) 106.11 (1C) 111.40 (2C) 112.71 (2C) 123.92 (2C) 124.00 (2C) 129.77 (2C) 141.93 (2C) 150.87 (2C) 152.69 (2C) 179.94 (2C). IR (KBr) ν_{max} (cm^{-1}) 2929, 1618, 1597, 1580, 1503, 1451, 1393, 1257, 1136, 1021, 997, 996, 834, 797, 697.

Biologic activity: The cytotoxicity was assessed with the MTT (3-(4,5-dimethylthiazol-2-yl)-2,5-diphenyltetrazolium bromide, from Sigma Aldrich) colorimetric method, as described earlier [18]. The treated lymphocyte subpopulations were analyzed using flow cytometry, before and after 24 hours incubation with 0.5 mM curcumin, **1** or **2**. We analyzed the proportion of different cell types among the whole lymphocyte population as described before [19] using antibodies conjugated with fluorochromes: CD4 FITC, CD8 APC, CD25 FITC, CD19PE, CD45R FITC and GITR FITC. The biostatistical analysis was performed with the Graph Pad Prism5 software (GraphPad, USA).

ACKNOWLEDGMENTS

This work was supported by the Slovak Research and Development Agency under the contract No. APVV-0516-12, and by Romanian UEFISCDI Grant for Exploratory Research Project PN-II-ID-PCE-2011-3-1057. This publication is the result of the project implementation: Comenius University in Bratislava Science Park supported by the Research and Development Operational Programme funded by the ERDF Grant number: ITMS 26240220086. Dr. Eva Fischer-Fodor acknowledges financial support from a POSDRU grant, no 159/1.5/138776 grant with title "Model colaborativ institutional pentru translatarea cercetarii stiintifice biomedicale in practica clinica-TRANSCENT".

REFERENCES

1. S. Dasari, P.B. Tchounwou, *European Journal of Pharmacology*, **2014**, *740*, 364.
2. N. Hashima, B.B. Aggarwal, *International Journal of Biochemistry and Molecular Biology*, **2012**, *3*, 328.
3. S.C. Gupta, S. Prasad, J.H. Kim, S. Patchva, L.J. Webb, I.K. Priyadarsini, B.B. Aggarwal, *Natural Products Report*, **2011**, *28*,1937-55.
4. Z.C. Ding, G. Zhou, *Clinical and Developmental Immunology*, **2012**, *2012*, 890178.
5. A. Valentini, F. Conforti, A. Crispini, A. De Martino, R. Condello, C. Stellitano, G. Rotilio, M. Ghedini, G. Federici, S. Bernardini, D. Pucci, *Journal of Medicinal Chemistry*, **2009**, *52*, 484.
6. L. Baum, A. Ng, *Journal of Alzheimer's Disease*, **2004**, *6*, 367.
7. N. Miklášová, R. Mikláš, F. Devínsky, *Palladium complexes of curcumin and its analogues and methods of preparation of the same*, Patent WO 2014/175841 A1, **2014**.
8. N. Miklášová, E. Fischer-Fodor, R. Mikláš, L. Kucková, J. Kožíšek, T. Liptaj, O. Soritau, J. Valentová, F. Devínsky, *Inorganic Chemistry Communications*, **2014**, *46*, 229.
9. G. Karp. *Cell and Molecular Biology- Concepts and Experiments*, John Wiley & Sons, Hoboken, USA, ISBN-13 978-0-470-48337-4, 6th Ed, **2010**, Chapter 17.
10. V.C. Liu, L.Y. Wong, T. Jang, A.H. Shah, I. Park, X. Yang, Q. Zhang, S. Lonning, B.A. Teicher, C. Lee, *Journal of Immunology*, **2007**, *178*, 2883.
11. P.J. Roughley, D.A. Whiting, *Journal of the Chemical. Society Perkin Transactions 1*, **1973**, *2379*.
12. A. Kessel, T. Haj, R. Peri, A. Snir, D. Melamed, E. Sabo, E. Toubi, *Autoimmunity Reviews*, **2012**, *11*, 670.
13. J.A. Ledbetter, N.K. Tonks, E.H. Fischer, E.A. Clark, *Proceedings of the National Academy of Sciences of the USA*, **1988**, *85*, 8628.
14. G. Nocentini, C. Riccardi, *European Journal of Immunology*, **2005**, *35*, 1016.
15. C. Morimoto, T. Takeuchi, S.F. Schlossman, *Clinical and Experimental Rheumatolology*, **1989**, *7*, S3.
16. T. Ramirez-Montagut, A. Chow, D. Hirschhorn-Cymerman, T.H. Terwey, A.A. Kochman, S. Lu, R.C. Miles, S. Sakaguchi, A.N. Houghton, M.R. van den Brink, *Journal of Immunology*, **2006**, *76*, 6434.
17. A.L. Côté, P. Zhang, J.A. O'Sullivan, V.L. Jacobs, C.R. Clemis, S. Sakaguchi, J.A. Guevara-Patiño, M.J. Turk, *Journal of Immunology*, **2011**, *186*, 275.
18. E. Fischer-Fodor, A.M. Vălean, P. Virag, P. Ilea, C. Tatomir, F. Imre-Lucaci, M. Perde Schrepler, L.T. Krausz, L.B. Tudoran, C.G. Precup, I. Lupan, E. Hey-Hawkins, L. Silaghi-Dumitrescu, *Metallomics*, **2014**, *6*, 833.
19. J. Ceballos-Torres, P. Virag, M. Cenariu, S. Prashar, M. Fajardo, E. Fischer-Fodor, S. Gómez-Ruiz. *Chemistry - A European Journal*, **2014**, *18*, 10811.

STUDIA UBB CHEMIA, LX, 2, Tom I, 2015 (p. 101-108)
(RECOMMENDED CITATION)

PROGNOSTIC FACTORS IN LIVER FAILURE IN CHILDREN BY DISCRIMINANT ANALYSIS OF CLINICAL DATA. A CHEMOMETRIC APPROACH

HORIA F. POP[a], COSTEL SÂRBU[b,*], ANA ŞTEFANESCU[c], AUREL BIZO[c], TUDOR LUCIAN POP[c]

ABSTRACT. Discriminant analysis was applied as an efficient method to identify an objective score concerning liver failure in children using clinical data. Discriminant analysis was not only used for classifying the patients according to the survival status, but also for detecting the most important factors that discriminate between surviving and deceased patients. Based on the considered factors, we were able to compute a complete separation between surviving and deceased patients. The factors responsible for the separation were age, K and total bilirubin (3rd sampling day). The smallest contribution was obtained for aspartate aminotransferase (3rd sampling day), hemoglobin, thrombocytes, albumin. The obtained results confirm that clinical analysis combined with the multidimensional analysis of data gives an interesting and very useful way for correlations, interpretations, problem solving and cost effectiveness.

Keywords: *Chemometrics, clinical data, discriminant analysis, liver failure prognosis*

INTRODUCTION

Liver failure in children could have acute or chronic evolution. Acute Liver Failure (ALF) is a relatively rare but often fatal event in children [1]. Definition of ALF is hepatic necrosis resulting in loss of liver function within few months of the onset of clinical liver disease. Acute liver failure accounts

[a] *Babeş-Bolyai University, Faculty of Mathematics and Computer Science, 1 M. Kogălniceanu St., Cluj-Napoca, RO-400084, Romania*
[b] *Babeş-Bolyai University, Faculty of Chemistry and Chemical Engineering, 11 Arany Janos St., Cluj-Napoca, RO-400028, Romania*
[c] *Iuliu Haţieganu University of Medicine and Pharmacy, 8 Victor Babeş St., Cluj-Napoca, RO-400012, Romania*
** Corresponding author: csarbu@chem.ubbcluj.ro*

for 10-15% of liver transplantation in USA [2]. The mortality without treatment, including liver transplantation, in ALF patients is over 70%. There are few patients with spontaneous regeneration of the liver with excellent long-term evolution [1].

It is very important to have an accurate evaluation of the prognosis of the patients with ALF in order to select the patients that will need liver transplantation in order to survive.

There are few reliable criteria for determination of the prognosis in ALF in children. Many attempts have been made to correlate clinical and laboratory data in order to establish the prognosis. Pediatric Acute Liver Failure (PALF) Study Group is a multicenter and multinational consortium created for this kind of studies with the most important results in children with ALF. Overall prognosis in children with ALF is variable with the etiology of the disease, between 68% survival in acute hepatitis A and 12% in drug toxicities [1]. Other parameters analyzed were age, degree of hepatic encephalopathy, severity of coagulopathy, bilirubin level [3]. In a British study of ALF due to acetaminophen intoxication prothrombin time, hypoglycemia, serum creatinine, acidosis and grade III encephalopathy were factors with poor prognosis [4].

Liver transplantation is the ultimate solution for patients with liver failure, acute or acute on chronic liver disease. King's College Criteria (using biochemical and clinical parameters available on admission: age, etiology, pH, prothrombin time, serum bilirubin, serum creatinine, encephalopathy) are widely used for selection of the patient with ALF for liver transplantation but they have not been validated in a large pediatric cohort [5].

The current prognostic score in use for organ allocation and the stratification of the need for liver transplantation is the MELD score (Model for End-Stage Disease), with its pediatric variant, the PELD score. The scores were developed in the early years of this century to improve organ allocation, discarding the “waiting time” on the transplant list as not being a good indicator of medical urgency [6-8]. The MELD score included creatinine, bilirubin and International Normalized Ratio measuring blood coagulability (INR) as parameters in the calculation formula, while the team designing PELD chose albumin, INR, total bilirubin, age (with more points attributed to children under the age of one) and evidence of failure to thrive. It proved to be a more efficient system, with fewer deaths while on the waiting list, despite the still high rate of mortality in the under two years of age group [9]; in this particular study, the change in PELD score proved to be an important predictor of outcome for children on the list. However, after the tempered enthusiasm of the first success, with higher rates of survival [10], criticisms ensued: the scoring system underestimated the near-term risk of death and subjected

children to several serious complications while “waiting”, which forced health-care professionals and patients to resort to the “exception” mechanism that enabled the access to graft in spite of lower score. Further studies raised suspicions on the objectivity of the system, claiming inter-laboratory variability in the determination of INR [11], and in 2010 a modified PELD was proposed as a means of correcting and improving its efficacy [12].

Although the access to liver transplantation in children is rather limited in our country, the importance of a better risk stratification for children with liver failure remains unquestionable. Our goal is to analyze the PELD parameters as well as other factors of possible influence on morbidity and survival (sodium, ammonia, creatinine, and lactate) of patients with acute or acute-on-chronic liver failure and propose an alternate scoring system, based on their survival rates. In this order, the discriminant analysis (DA) has successfully been applied.

RESULTS AND DISCUSSION

The computed data set included 49 patients and the following 31 factors (variables or characteristics): age, leucocytes, hemoglobin, thrombocytes, C reactive protein, Aspartate aminotransferase (1st sampling day, AST_1), Alanine aminotransferase (1st sampling day, ALT_1), Aspartate aminotransferase (2nd sampling day, AST_2), Alanine aminotransferase (2nd sampling day, ALT_2), Aspartate aminotransferase (3rd sampling day, AST_3), Alanine aminotransferase (3rd sampling day, ALT_3), total bilirubin (1st sampling day, TB_1), Direct bilirubin (1st sampling day, DB_1), Total bilirubin (2nd sampling day, TB_2), Total bilirubin (3rd sampling day, TB_3), protein, albumin, pediatric end-stage liver disease (PELD), International Normalized Ratio measuring blood coagulability, value on the first day (INR_1), Na, K, glycaemia, urea, creatinine, worst creatinine level (V52_A), QT level on hospitalization day 1 (TQ_1), QT level on hospitalization day 2 (TQ_2), QT level on hospitalization day 3 (TQ_3), International Normalized Ratio measuring blood coagulability (INR), worst prothrombin index level (IP). We have to mention that the majority of measured variables (age, leucocytes, hemoglobin, thrombocytes, protein, albumin, Na, K) have a normal distribution according to the Kolmogorov-Smirnov statistical test. The chemometric analysis has been performed by using Statistica 7.1 software (StatSoft, Inc., Tulsa, USA).

After application of the stepwise DA to the matrix data (49 x 31) the factors (variables) presented in Table 1 were retained in the model. The statistics from this table illustrates the contribution to the patients discrimination of the considered factors (clinical data) according to different parameters.

Knowing that Wilks' lambda (λ^*) describes the unique contribution of each variable to the discriminatory power of the model (the smaller the value of λ^*, the more the model is discriminating and the larger the lambda λ^*, the more likely it is significant) and large values for F and close to 0 for λ^* shows that the variable has a significant contribution, the following statements may be retained.

It is easy to observe that the greatest contribution is given by age (λ^* = 0.831; F = 6.524). The next highest are K (λ^* = 0.834; F = 6.352) and BT_3 (λ^* = 0.0843; F = 5.958). The smallest contribution was obtained for AST_3 (λ^* = 1.000; F = 0.002), hemoglobin (λ^* = 0.993; F = 0.223), thrombocytes (λ^* = 0.984; F = 0.509), albumin (λ^* = 0.981; F = 6.33). Also a small contribution brings the protein (λ^* = 0.958; F = 1.387).

We performed also a canonical correlation analysis that determined the successive functions and canonical roots (the term root refers to the eigenvalues that are associated with the respective canonical function). The maximum number of functions will be equal to the number of groups minus one, or the number of variables in the analysis, whichever is smaller.

The corresponding standardized canonical discriminant function coefficients (c) corresponding to the single eigenvalue (4.126) are also showed in Table 1.

Table 1. Statistic results concerning discriminant analysis of clinical data

Factor in the model	Wilks' λ	λ*	F	p-level	c	r
INR	0.208	0.936	2.195	0.148	0.366	0.294
Albumin	0.199	0.981	0.633	0.432	-0.227	-0.257
AST_3	0.195	1.000	0.002	0.963	0.018	0.271
K	0.234	0.834	6.352	0.017	0.561	0.285
Hemoglobin	0.196	0.993	0.223	0.640	-0.183	-0.132
Age	0.235	0.831	6.524	0.016	-0.697	-0.174
Thrombocytes	0.198	0.984	0.509	0.481	-0.207	-0.107
V52_A	0.222	0.878	4.453	0.043	0.612	0.141
BT_3	0.231	0.843	5.958	0.020	0.903	0.160
Leukocytes	0.221	0.882	4.298	0.046	-0.737	0.004
ALT_3	0.205	0.950	1.682	0.204	0.539	0.205
TQ_3	0.208	0.937	2.145	0.153	0.328	0.224
Urea	0.215	0.908	3.224	0.082	-0.585	0.084
AST_1	0.222	0.878	4.457	0.043	-0.685	0.096
AST_2	0.214	0.911	3.127	0.087	0.569	0.251
Protein	0.204	0.958	1.387	0.248	-0.289	-0.216

As we know the higher the discriminant coefficient (absolute value) and the closer the correlation coefficient (r) is to 1 respectively, the more the variable importance for the separation of patients in defined groups.

The highest standardized discriminant coefficients correspond to BT_3 (0.903), leukocyte (0.737), age (0.697), AST_1 (0.685), K (0.561).

A common result that one looks at in order to determine how well the current classification functions predict group membership of cases is the classification matrix.

The classification matrix shows the number of cases that were correctly classified (on the diagonal of the matrix) and those that were misclassified.

The classification matrix presented in Table 2 indicates a complete separation of patients in a good agreement to their behavior.

Table 2. Matrix classification of patients

Group	Percent Correct	Yes p=.5102	No p=.4898
Yes	100.00	25	0
No	100.00	0	24
Total	100.00	25	24

We can also visualize how the functions discriminate between groups by plotting the individual scores for the discriminant function. The Figure 1 supports the excellent separation of the patients and their (dis)similarities according to scores obtained as linear combinations of the variables (factors) retained in the model.

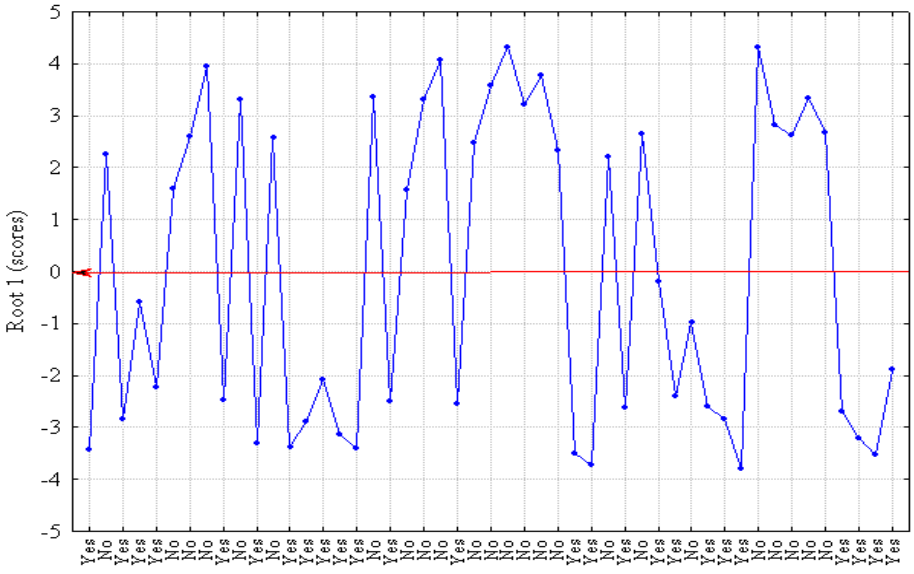

Figure 1. Graphic representation of scores corresponding to the 49 analyzed patients

CONCLUSIONS

Generally, Discriminant Analysis is a very useful tool for (1) detecting the variables that allow the researcher to discriminate between different (naturally occurring) groups, and (2) classifying cases into different groups with a better than chance accuracy**.**

Discriminant analysis was used not only for classifying the patients according to their disease but also for detecting the most important factors (variables) that discriminate between the groups.

This study illustrates two features of DA: the ability to determine the factor making the most important contribution to the difference between the two groups, and the ability to make an important contribution in the clinical setting. When support for a positive or negative diagnosis is required, DA may be able to provide such a binary decision, based on the multiple factors already available.

Clinical analysis combined with the multidimensional interpretation of data gives an interesting and very useful way of disease correlations, interpretations, problem solving and cost effectiveness.

DISCRIMINANT ANALYSIS

Discriminant Analysis (DA) was introduced and discussed in 1936 by R.A. Fisher [13], as a supervised classification method with large applications even today.

The method's main purpose is to predict class membership from a set of predictor variables by creating a function to produce the maximum between-group variance and the minimum intra-group variance. The predictor variables are related to these classes and the constructed memberships are then compared to the groups memberships indicated *a priori* by the user. This enables the user to test the grouping validity based on actual data, to test the created groups, or to assign groups membership to objects.

DA assumes the calculation of linear discriminant functions of independent variables starting from a qualitative dependent variable and two or more quantitative independent variables [14-17]. This is a parametric method, which means that it is based on certain statistical assumptions. The equality between the variance-covariance matrices of the groups to be separated and normal distribution of data are two of requirements for optimal application of DA. However, the difficulties due to the unfavourable statistical characteristics only influence the boundaries and therefore the classification by DA, but not the determination of the discriminant functions [18].

The contribution of the independent variables to the discrimination of groups can be appreciated either by the assay of the classes homogeneity using statistics F, like in the case of analysis of variance method, or by using Wilks' lambda for each variable. Wilks' lambda is the standard statistics used to express the significance of the overall discriminatory power of the variables in the model, where the value 1.0 indicates no discrimination power, while the value 0 indicates a perfect discrimination power. The partial Wilks' lambda describes the unique contribution of each variable to the model's discrimination power. The closer the partial lambda is to 0, the better the discrimination force of the variable is. In addition, the tolerance value illustrates the redundancy of the variable in the model. It is defined as the proportion of the variance contributed by respective variable, and is computed as 1 minus R-square of the respective variable, with all other variables included in the model. If the variable is completely redundant, the squared tolerance value approaches zero.

This information can also be obtained from the discriminant coefficients associated to the descriptive variables, and from the correlation coefficients between the descriptive variables and the scores. The higher the discriminant coefficient is in absolute value, and the closer the correlation coefficient is to one, the higher the variable importance for the cases separation into groups is. As well, the standardized discriminant coefficients, like, for example, the beta weights in regression methods, are used to asses the relative classification importance of the independent variables.

Multivariate analysis methods, including DA, have successfully been applied for the prognosis of liver failure and liver diseases using different clinical data [19, 20].

ACKNOWLEDGMENTS

This work was supported by a grant of the Romanian National Authority for Scientific Research, CNDIUEFISCDI, project number PN-II-PT-PCCA-2011-3.2-0917.

REFERENCES

1. P.F. Whitington, E.M. Alonso, R.H. Squires, *Acute liver failure.* In: Kelly D. (editor). *Diseases of the liver and biliary system in children*, Third Ed., Wiley-Blackwell, Oxford, **2008**, pp.169-188.
2. E.M. Alonso, R.H. Squires, P.F. Whitington, *Acute liver failure in children*. In: F.J. Suchy, R.J. Sokol, W.F. Balistreri WF (editors). *Liver disease in children*. Trd. Ed., Cambridge University Press, New York, **2007**, pp. 71-96.
3. R.H. Jr. Squires, B.L. Shneider, J. Bucuvalas, *J. Pediatr.*, **2006**, *148*, 652.

4. S.B.K. Mahadevan, P.J. McKiernan, P. Davies, D.A. Kelly, *Arch. Dis. Child*., **2006**, *91*, 598.
5. J.G. O'Grady, G.J.M. Alexander, K.M. Hayllar, *Gastroenterol*., **1989**, *97*, 439.
6. R.H. Wiesner, S.V. McDiarmid, P.S. Kamath, *Liver Transpl*., **2001**, *7*, 567.
7. R.B. Jr. Freeman, R.H. Wiesner, A.M. Harper, *Liver Transpl*., **2002**, *8*, 851.
8. R.B. Jr. Freeman, *Transplantation Proceedings*, **2003**, *35*, 2425.
9. R.B. Jr. Freeman, R.H. Wiesner, J.P. Roberts, *Am. J. Transplant*., **2004**, *9,* 114.
10. S.V. McDiarmid, R.M. Merion, D.M. Dykstra, A.M. Harper, *Liver Transpl*., **2004**, *10*, S23.
11. R. Arjal, J.F. Trotter, *Clin. Liver Dis*., **2009**, *13*, 67.
12. J. Seda Neto, E. Carone, *Liver Transpl*., **2010**, *16*, 426.
13. R.A. Fisher, *Ann. Eugenic*., **1936**, *7*, 179.
14. W.R. Klecka, *Discriminant Analysis*, Sage Publications, Iowa, **1980**.
15. G.H. McLachlan, *Discriminant Analysis and Statistical Pattern Recognition*, Wiley, New York, **2004**.
16. C. Sârbu, H.F. Pop, R.S. Elekes, G. Covaci, *Rev. Chim*.(Bucharest), **2008**, *59*, 1237.
17. H.F. Pop, C. Sârbu, *MATCH*, **2013**, *69*, 391.
18. D.L. Massart, B.G.M. Vandeginste, S.N. Deming, Y. Michotte, L. Kaufman, *Chemometrics, a Textbook,* Elsevier Science Publishers, Amsterdam, **1988**.
19. M. Hamilton, *J. Clin. Path*., **1977**, *30*, 454.
20. R.T. Russell, I.D. Feurer, P. Wisawatapnimit, E.S. Lillie, E.T. Castaldo, C. Wright Pinson, *HPB*, **2008**, *10*, 30.

STUDIA UBB CHEMIA, LX, 2, Tom I, 2015 (p. 109-116)
(RECOMMENDED CITATION)

FATTY ACIDS DETERMINATION IN TROUT PLASMA AND MEAT BY GC-MS

SONIA SUVAR[a], ELENA HORJ[a], PAULA PODEA[b], ANDREEA IORDACHE[c], DANIEL COCAN[d], MONICA CULEA[a*]

ABSTRACT. The aim of this study was to develop a simple and reliable GC-MS method to compare the fatty acids in trout plasma and meat. The lipids were extracted from 0.5 mL of plasma and 1 g of meat using chloroform: methanol 1:2 (v:v) and then derivatized into fatty acids methyl esters (FAMEs) by esterification with methanol: acetyl chloride 4:1 (v:v). For FAMEs quantitation, undecaenoic acid (C11:1) was used as internal standard. High proportions of unsaturated fatty acids (UFAs) were found both in plasma and in meat samples. The highest proportion of UFAs in meat samples (53%) was represented by the ω-3 fatty acids.

Keywords: *DHA, EPA, essential fatty acids, FAME, GC-MS, SFA, UFA.*

INTRODUCTION

Gas chromatography coupled to mass spectrometry (GC-MS) is the method of choice for fatty acids identification and quantitation [1-3]. Fatty acids methyl esters (FAMEs) are the most widely used derivatives for GC analysis due to their easy derivatization procedure, volatility and good chromatographic separation [4].

In the vast family of fatty acids, only the polyunsaturated fatty acids (PUFAs) are essential nutrients. They were named *essential fatty acids* (EFA) and divided in two main categories: ω-6 fatty acids and their homologous and ω-3 fatty acids. Unlike the linear and rigid chemical structure of the saturated fatty acids (SFA), the structure of PUFAs is bended, twisted and flexible [5].

[a] *Babeş-Bolyai University, Faculty of Physics, 1 Kogălniceanu str., 400084 Cluj-Napoca, Romania.*
[b] *Babeş-Bolyai University, Faculty of Chemistry and Chemical Engineering, 1 Kogălniceanu str., 400084 Cluj-Napoca, Romania.*
[c] *National R&D Institute for Cryogenics and Isotopic Technologies, 4 Uzinei str., 240050 Râmnicu Vâlcea, Romania.*
[d] *University of Agricultural Sciences and Veterinary Medicine, 3-5 Mănăştur str., 400372 Cluj-Napoca, Romania.*
[*] *Corresponding author: culea.monica@phys.ubbcluj.ro*

The ω-3 fatty acids get into our diet through a food chain that starts from the algae – the richest ω-3 fatty acids sources – which are consumed by small aquatic animals, and ends with the fish, which eat them. Other sources of dietary ω-3 fatty acids, but with a shorter carbon chain, are the flaxseeds and the walnuts. The sources of ω-6 fatty acids in our diet are mostly the vegetable and seed oils [6].

Once consumed and absorbed into the body, the ω-3 and ω-6 fatty acids are incorporated into the cell membranes. Then, they are converted into intermediate molecules and finally, into hormone-like substances named *eicosanoids*. Among the *eicosanoids*, the most important are the *prostaglandins* – cellular signaling molecules that mediate the inflammatory process, fighting against infections and performing multiple roles within the immune and cardiovascular systems, and even within the brain [5, 6]. Recent studies have confirmed that mankind has evolved due to a balanced diet in ω-3 and ω-6 fatty acids. The ideal ω-3/ω-6 ratio, established by nature, is 1:1, while, in the modern world, in the typical American diet, this ratio has reached 1:20 [6].

Docosahexaenoic acid (4,7,10,13,16,19-DHA; $C_{22}H_{32}O_2$) is an ω-3 PUFA. Highest body concentrations of DHA are found in retinal membranes [5].

Eicosapentaenoic acid (5, 8, 11, 14, 17 -EPA; $C_{20}H_{30}O_2$) is the other major dietary ω-3 PUFA. EPA is present in blood components [5] and when working in tandem with DHA, the EPA eicosanoids derivatives maintain control over DHA eicosanoids derivatives [6].

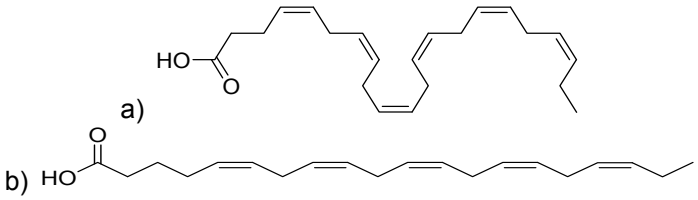

Figure 1. The ω-3 fatty acids chemical structures: a) DHA (C22:6 ω-3); b) EPA (C20:5 ω-3).

The nutritional quality of fish species can be evaluated from the fatty acids profile and by determining the EPA and DHA proportions [7].

The purpose of this research was to develop and validate a GC-MS method in order to investigate the essential fatty acids composition of rainbow trout (*Oncorhynchus mykiss*) plasma and meat.

RESULTS AND DISCUSSION

The fatty acids profile of freshwater fish is unique in variety and degree of unsaturation [8-16]. Their nutritional role is recognized. The two main omega-

3 fatty acids eicosapentaenoic acid and docosahexaenoic acid appear to decrease the risk of cancer [17-18]. Seasonal variation of these nutrients study is also very much studied [19-21].

Therefore, it is essential to have a simple and rapid method for qualitative and quantitative characterization of less common fatty acids (e.g. long-chain polyunsaturated fatty acids). The sensitivity and selectivity of GC-MS make it a powerful tool for the analysis of FAMEs [3].

Figure 2 presents the total ion current chromatogram of a mixture of trout plasma fatty acids. The FAMEs were identified using the NIST Mass Spectral Library.

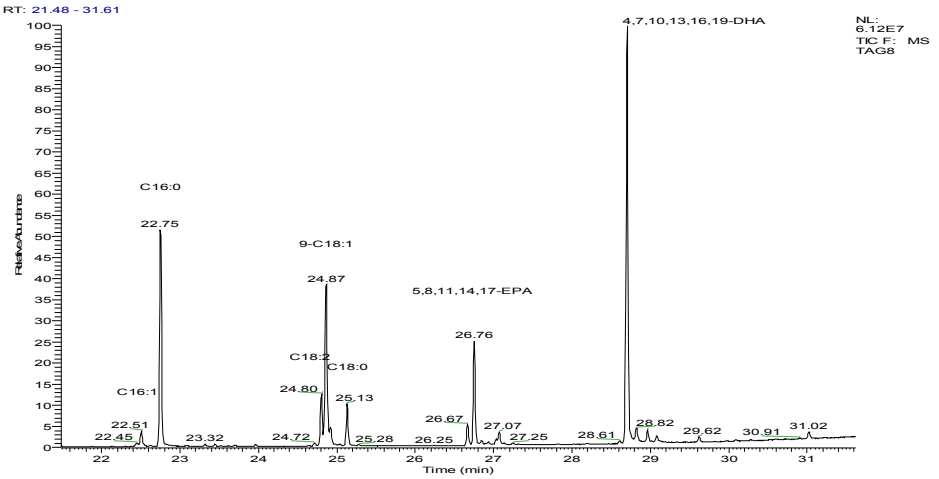

Figure 2. TIC chromatogram of trout plasma FAMEs obtained from GC-MS analysis.

The method was validated using fatty acids standards of 20 µg/ml. The limit of detection (LOD) was 1ng and precision and accuracy gave values lower than 20%.

Table 1 shows the fatty acids composition (weight% of total fatty acids) of trout plasma and meat. Saturated fatty acids represent only 25.61% (in plasma) and 31.04% (in meat) of the total fatty acids, palmitic acid (C16:0) having the highest concentration. Stearic acid (C18:0) is present in relatively smaller proportions (5.42% and 6.27%).

The unsaturated fatty acids (UFAs) constitute more than half of the total fatty acids found in plasma and meat samples (74.39% and 68.95%, respectively). The major monounsaturated fatty acids (MUFAs) were: C16:1, C18:1n-7, C18:1n-9, oleic acid (C18:1n-9) being the most abundant. Linoleic acid (C18:2 ω-6) represents 19% (in plasma) and 11.3% (in meat) of the total UFAs. The ω-3 PUFAs (the sum of EPA and DHA) represent approx. 26% and 36.6% respectively, of the total FAs found in trout plasma and meat.

Table 1. Fatty acid concentrations (%) in trout plasma and meat n = 5 (R_t – retention time; SFA – saturated fatty acids, UFA – unsaturated fatty acids; SFA = C16:0 + C18:0; UFA = C16:1 + C18:2 + 9-C18:1 + C18:1 + EPA + DHA)

		Fatty acids (%)	
	R_t (min)	Plasma	Meat
hexadecenoic acid (C16:1)	22.51	2.86	2.19
hexadecanoic acid (C16:0)	22.75	20.18	24.78
9,12 octadecadienoic acid (C18:2)	24.80	14.13	7.81
9-octadecenoic acid (C18:1)	24.87	27.79	18.91
octadecenoic acid (C18:1)	24.93	3.62	3.43
octadecanoic acid (C18:0)	25.13	5.42	6.27
5,8,11,14,17 eicosapentaenoic acid (C20:5)(EPA)	26.76	5.41	8.51
4,7,10,13,16,19 docosahexaenoic acid(C22:6)(DHA)	28.71	20.59	28.11
SFA		25.61	31.04
UFA		74.39	68.95
EPA		5.41	8.51
DHA		20.59	28.11

The representatives mass spectra of DHA and hexadecanoic acid (palmitic acid) as FAMEs are shown in figures 3 and 5.

In the mass spectrum of DHA methyl ester the molecular ion is missing but it presents the specific ions M-15 (m/z 313), M-101 (m/z 227) of small intensity, indicating the molecular mass (M=328) and also high intensity ions, specific for alkyl group with double bonds, as m/z 55, 67, 79, 91 etc.

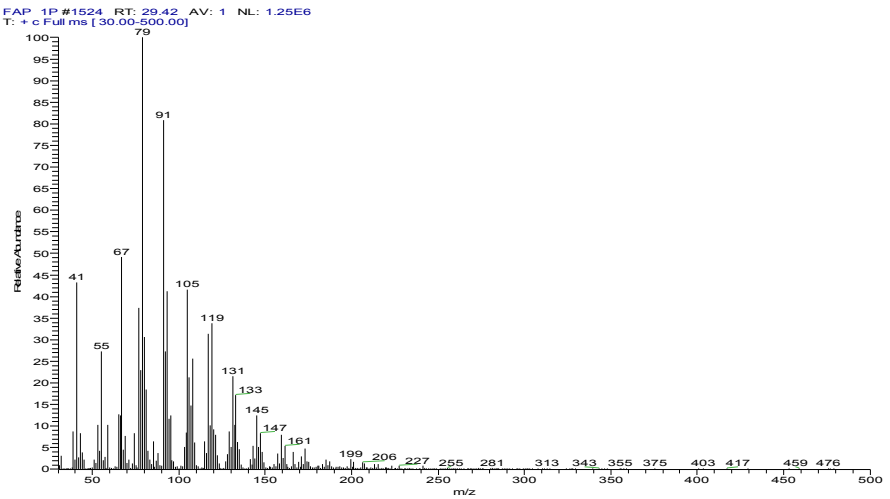

Figure 3. Representative mass spectrum of 4,7,10,13,16,19 DHA methyl ester (M=328) in trout meat.

In figure 5, the ion m/z 270 represents the molecular ion peak of palmitic acid methyl ester. The ion m/z 239 $[M-31]^+$ representing loss of a methoxy group confirming a methyl ester compound. *m/z* = 227 $[M-43]^+$ represents loss of a C_3 unit (carbons 2 to 4), via a complex rearrangement, and *m/z* = 74 is the McLafferty rearrangement ion, also a specific ion confirming that the spectrum is that of a methyl ester. The series of ions *m/z* = 87, 101, 115,129, 143, 157, 199, etc., of general formula $[CH_3OCO(CH_2)_n]^+$, is a series of related ions formed by losses of neutral aliphatic radicals14 amu, of which that at *m/z* = 87 is most abundant.

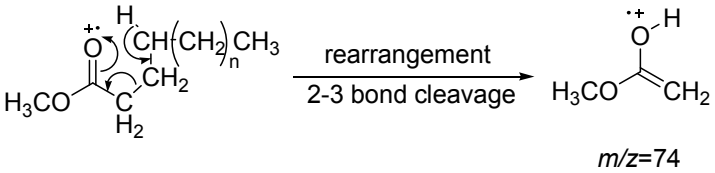

Figure 4. McLafferty rearrangement ion m/z 74 [9]

In the rearrangement ion m/z 74, a hydrogen atom from position 4 of the aliphatic chain migrates to the carbo-methoxy group, through a six-membered transition state, which is sterically favoured. If one of the hydrogen atoms on carbon 4 is substituted, the McLafferty ion will be lower in intensity, as appears in the mass spectra of derivatives of unsaturated fatty acids with increasing numbers of double bonds. The ion *m/z* = 227 $[M-43]^+$ is formed by a loss of a propyl radical. The ion at $[M-29]^+$ results by a cleavage between carbons 3 and 4 [9].

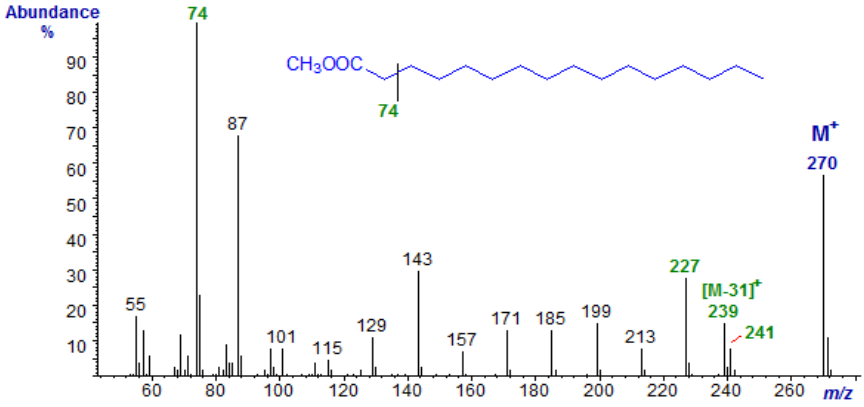

Figure 5. The mass spectrum of hexadecanoic acid methyl ester (palmitic acid, M=270) [9]

Fig. 6 shows the considerable proportion of UFAs in comparison with SFAs, both in plasma and in meat. It should be noted that in meat samples, the ω-3 PUFAs represent 53% of the total UFAs.

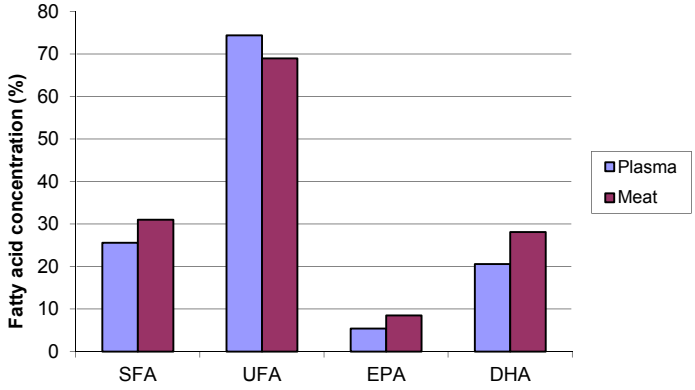

Figure 6. Fatty acids content of plasma and meat trout samples.

In plasma, the ω-3/ω-6 ratio was 1.84, while in meat, 4.68. The DHA/ EPA ratio was 3.8 in plasma and 3.3 in meat. This result can be explained by the fact that EPA is not found in great amounts in tissues as it is quickly used in DHA and eicosanoids biosynthesis [5].

CONCLUSIONS

The GC-MS method developed here for determining the fatty acid profile of trout plasma and meat samples is simple and reliable. Good validation parameters were obtained.

The PUFAs concentration found in trout plasma and meat was higher than that of the other FAs, in the following order: PUFA>MUFA>SFA. Our results proved that trout meat is a valuable source of essential fatty acids.

EXPERIMENTAL SECTION

Materials and methods

Acetyl chloride was purchased from Fluka (Germany) while all the other chemicals were from Merck (Darmstadt, Germany).

To quantify the FA concentrations by GC-MS, undecaenoic acid (C11:1) was used as internal standard.

The fatty acids (FA) were determined from trout plasma and meat samples. The FA were extracted from 0.5 mL of plasma by adding 0.5 mL chloroform: methanol 2:1 (v:v). The solution was shaken vigorously for 30 s, at room temperature.

1 g of trout meat was crushed with 1 g of quartz sand in a ceramic dish and homogenized with 5 mL distilled water. After a 5 min centrifugation, the supernatant was collected and the FAs were extracted by using the same solvent extraction conditions as for plasma. The samples were centrifuged for 5 min (5800 rot/min) and the upper methanol - water phase was removed. The lower chloroform phase containing the extracted fatty acids was then dried in a nitrogen flow, at 60°C.

The lipids were converted to corresponding FAMEs (fatty acids methyl esters) by esterification of the carboxylic functions with 200 µL methanol: acetyl chloride 4:1 (v:v), 20 min, 80°). The derivatives were evaporated to dryness by a nitrogen stream, at 60°C, and then dissolved in 500 µL dichloromethane. 10 µg of C11:1 was added to each sample for GC-MS quantitation.

GC – MS apparatus

The fatty acids were separated and identified using a Gas chromatograph Trace GC equipped with an Rtx-5MS capillary column (30m x 0.25mm I.D., 0.25 µm film thickness) and coupled to a quadrupole mass spectrometer Trace DSQ (Thermo Finnigan). The temperature program for FAMEs separation was: 50°C for 2 min rising with a rate of 8°C/min at 310°C (8 minutes). Helium was used as carrier gas at a flow rate of 1 mL/min. 1µL of each sample was injected into the GC-MS using the split mode (10:1) and a TriPlus autosampler. The mass spectrometer operated in electron impact (EI) mode at 70 eV. The following conditions were ensured: the transfer line temperature was set at 250°C, the injector temperature, at 200°C and the ion source temperature, at 250°C. The emission current was 100µA. The qualitative analysis was carried out in the 50-500 a.m.u. mass range.

GC – MS quantitation

The quantitative analysis was performed with respect to the internal standard (C11:1), by using the following formulas:

$$F_i = \frac{\frac{A_i}{A_j}}{\frac{m_i}{m_j}} \quad (1)$$

$$m_i(\mu g) = m_j(\mu g)\frac{A_i}{F_i \cdot A_j} \quad (2)$$

where F_i is the response factor of the compound *i*, m_i is the quantity of compound i, m_j is the internal standard quantity; A_i and A_j are the peak areas of the compounds (*i* and *j*).

ACKNOWLEDGMENTS

This paper is a result of a doctoral research made possible by the financial support of the Sectoral Operational Programme for Human Resources Development 2007-2013, co-financed by the European Social Fund, under the project POSDRU/159/1.5/S/132400 - "Young successful researchers – professional development in an international and interdisciplinary environment".

REFERENCES

1. E.D. Dodds, M.R. McCoy, L.D. Rea, J.M. Kennish, *Lipids*, **2005**, *40*, 419.
2. R.C. Murphy, S.J. Gaskell, *J. Biol. Chem.*, **2011**, *286*, 25427.
3. E.O. Abu, I. Oluwatowoju, *Prostaglandins, Leukotrienes and Essential Fatty Acids,* **2009**, *80*, 189.
4. N. Dubois, G. Barnathan, J.-P. Gouygou, J.-P. Bergé, *Eur. J. Lipid Sci. Technol.,* **2009**, *111*, 688.
5. J.P. SanGiovanni, E.Y. Chew, *Progr. in Retinal and Eye Research*, **2005**, *24*, 87.
6. S.L. Andrew, *"The omega-3 connection: the groundbreaking omega-3 antidepression diet and brain program*", Elena Francisc Publishing, Bucharest, **2005**, chapter 2.
7. M.D. Huynh, D.D. Kitts, *Food Chem.,* **2009**, *114*, 912.
8. U. Chukwuemeka, G.I. Ndukwe, T.O. Audu*, Internet J. Food Safety*, **2008**, *10*, 9.
9. http://lipidlibrary.aocs.org/ms/ms03/index.htm
10. N.M. Arat, I.H. Haliloğlu, Ö. Ayik, *Turkish J. Vet. Animal Sci.*, **2003**, *27*, 311.
11. R.K. Booth, R.S. McKinley, J.S. Ballantyne, *J. Fish Biol.,* **1999**, *55*, 260.
12. C. Cahu, J.Z. Infante, T. Takeuchi, *Aquaculture J.,* **2003**, *227*, 254.
13. I.H. Haliloğlu, N.M. Aras, *Turkish J. Vet. Animal Sci.*, **2002**, *26*,1097.
14. R.J. Henderson, *Arch. Anim. Nutr.*, **1996**, *49*, 5.
15. C. Ugoala, G.I. Ndukwe, T.O. Andu, *Internet J. Food Safety*, **2008**, *10*, 9.
16. A.P. Simopoulos, *Eur. Heart J.Suppl.,* **2001**, *3*, 8.
17. A. Hjartåker, *Scandinavian Journal of Nutrition*, **2003**, *47*(3), 111-122.
18. N. Kaba, Y. Sennan, B. Birol, *Journal of Animal and Veterinary Advances*, **2009**, *8*(3), 541-544.
19. T. Kandemir, N. Polat, *Journal of Fisheries and Aquatic Sciences*, **2007**, *7*, 27-31.
20. C. Stripp, K. Overvad, J. Christensen, L.B. Thomsen, A. Olsen, S. Møller, A. Tjønneland, *The Journal of Nutrition*, **2003**, *133*, 3664-3669.
21. D.R. Tocher, *Journal of Fisheries Science*, **2003**, *11*(2), 107-184.

STUDIA UBB CHEMIA, LX, 2, Tom I, 2015 (p. 117-124)
(RECOMMENDED CITATION)

ASSESSEMENT OF TRIAZINE HERBICIDES CONTENT IN HONEY SAMPLES BY SOLID-PHASE EXTRACTION AND HPLC ANALYSIS

ANDREEA DRĂGUŞ[a], MIHAIL SIMION BELDEAN-GALEA[a*]

ABSTRACT. Triazines are a group of compounds used as selective pre-emergence herbicides in different types of crops, such as corn, soybean, as well as orchards and vineyards. Due to their large use in the agricultural sector triazines have been detected in different types of food matrices. In the present study, the triazines content in different honey samples collected directly from private producers in various countryside areas from Romania is evaluated. The clean-up and extraction procedure was carried out by solid phase extraction and further analysis and quantification undertaken with high performance liquid chromatography. In the analyzed samples, the presence of triazine herbicides was detected. Their concentrations ranged between 4.97 and 997.5 µg/kg honey, exceeding in almost all analyzed samples the EU MRLs requirements for triazines in honey.

Keywords*: triazine herbicides, honey, solid phase extraction, high-performance liquid chromatography*

INTRODUCTION

The agricultural sector is the most significant user of pesticides. In the long term, these chemicals can cause deleterious effects upon the environment [1]. Contamination of different matrices allows pesticides to spread through the food chain, thus impacting human health [2, 3]. Therefore, the European Union has established Maximum Residue Levels (MRLs) in order to meet food safety requirements, the maximum residual levels of pesticides being established in Regulation (EC) No. 396/2005, the lowest limit being 0.01 mg/kg and the highest 1 mg/kg.

Triazines represent a class of compounds used as selective pre-emergence herbicides in different types of crops, such as corn, soybean, as well as orchards and vineyards Their persistence in soil has been shown to

[a] *Babeş-Bolyai University, Faculty of Environmental Science and Engineering, 30 Fântânele Street, RO-400294, Cluj-Napoca, Romania.*
[*] *Corresponding author: simion.beldean@yahoo.com*

have a DT_{50} (half-life) of 40 days and can reach up to 166 weeks, depending on the soil type [4, 5].

Different studies showed the presence of triazine herbicides in various matrices such as water [6-10], soil [4, 5] agricultural products [11], seaweeds [12] food samples [13-15] etc. which suggest that these chemicals are mobile in the environment.

Taking into account that triazine compounds can act as endocrine disruptors, mimicking hormonal activity [16], in the last period different methods for the analysis of these compounds in various matrices have been developed.

The most employed techniques involved in the quantification of triazine herbicides are gas and liquid chromatography [6-18].

For the extraction, different methods, such as liquid phase extraction (LPE) [8, 9, 11, 13, 14], solid phase extraction (SPE) [10, 12, 17] or supercritical fluid extraction (SFE) [18, 19] have been used.

Since LPE requires the use of significant volumes of toxic organic solvent and SFE involves an expensive instrumentation, SPE remains the most suitable method for the analysis of triazine herbicides in liquid samples.

Honey is a staple product consumed by a large percentage of society due to its beneficial properties on human health. One of the most important checked parameter from honey samples is the pesticides residue.

Pesticides residue can get into honey via spraying the crops during the collection of pollen and nectar [20]. Due to this reason the assessment of pesticides pertaining to this matrix presents importance for quantifying their risk to human health.

In this paper, the assessment of triazine herbicides content in honey samples collected directly from private producers in various countryside areas from Romania located in Transylvania, Moldova and Dobrogea is reported. The analysis of triazines was performed by solid-phase extraction followed by high performance liquid chromatography analysis. The results of the analyzed samples showed the presence of triazine herbicides in concentrations ranging from tens to hundreds μg/kg honey.

The novelty of this work consists in the assessment of triazine content in matrices that is not subjected to routine monitoring. Thus, the risk associated with their consumption is difficult to predict.

RESULTS AND DISCUSSION

1. Analytical performance of the analysis method

The performance of the HPLC method used for the analysis of triazine herbicides in honey samples was expressed by precision, linearity, limit of detection (LOD) and limit of quantification (LOQ) (Table 1).

Precision was expressed as intra-day precision (repeatability) by means of five replicates (n = 5) of a triazine standard mixture in concentration of 1.25 µg/mL. The obtained results were situated under 3% which prove a good repeatability of the method.

Table 1. Analytical performances of HPLC method

Compound	Linear curve equation (linear range 0.62-10 ng)	R^2	Slope	SD	LOD (µg/L)	LOQ (µg/L)	RSD %
Simazine	y = 49916x - 3596.3	0.996	49916	379	0.023	0.076	1.24
Prometon	y = 46067x - 782.58	0.992	46067	542	0.035	0.118	1.75
Atrazine	y = 42868x - 3430.5	0.999	42868	797.9	0.056	0.186	2.98
Ametryn	y = 43269x + 1969.7	0.998	43269	452	0.031	0.104	1.55
Propazine	y = 43269x + 1969.7	0.999	43269	586.1	0.041	0.135	1.98
Prometryn	y = 37949x + 2154.8	0.996	37949	441.9	0.035	0.116	1.67
Terbutryn	y = 37711x + 3049.9	0.999	37711	673.0	0.054	0.179	2.64

R^2 - coefficient of determination; SD - standard deviation; LOD - limit of detection, LOQ - limit of quantification, RSD - relative standard deviation for (n = 5);

The quantification of the target compounds in real samples was made using the calibration curve method. The data from Table 1 shows a good linearity for all target triazines and the R2 values ranging from 0.992 to 0.999. LOD and LOQ of studied triazines were determined using the standard deviation and the slope of each calibration curve. LODs were situated in the range of 0.076 - 0.056 µg/L and LOQs in the range of 0.076 – 0.18 µg/L, respectively.

2. Accuracy of SPE procedure

Because for the extraction of the triazines from honey samples a slightly modified Albero et al. [21] method was used, the accuracy of the extraction procedure was tested.

The accuracy was expressed by extraction recovery (ER) and was calculated using the follow equation:

$$ER\,(\%) = \frac{(amount\ found - initial\ amount)}{spiked\ amount}\ x\,100$$

The results presented in Table 2 show good recoveries of the studied compounds, the values being situated over 80%. Thus the SPE protocol has been used for the extraction of the triazine herbicides from collected honey samples.

Table 2. Recoveries of the triazine herbicides in honey samples

Compound	Initial Amount (ng)	Spiked amount (ng)	Amount found(*) (ng)	ER ± SD (%)
Simazine	-	500	446	89.2 ± 0.70
Prometon	-	500	446	89.2 ± 1.50
Atrazine	-	500	483	96.6 ± 1.53
Ametryn	-	500	480	96 ± 2.08
Propazine	-	500	437	87.4 ± 2.52
Prometryn	-	500	439	87.8 ± 3.51
Terbutryn	-	500	460	92 ± 3.56

(*) - mean value of three replicates

3. Analysis of honey samples

The analyses employed in the present study demonstrate the presence of triazines in the honey samples. In Figure 1 it is shown a juxtaposed chromatogram of a honey sample and a standard mixture where the presence of the triazines can be observed.

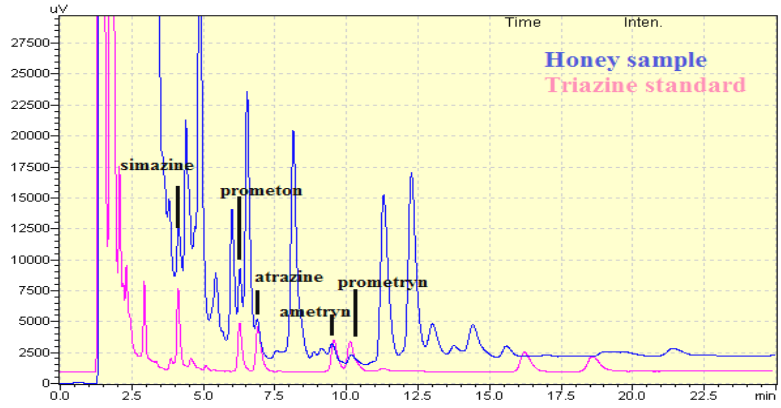

Figure 1. Chromatogram of tested triazines in honey sample (honey sample – upper chromatogram; triazine standard mixture (1.25 µg mL^{-1}) – lower chromatogram)

The results of the analyzed samples showed that the concentrations of triazine herbicides from the honey samples are dependent on the sampling area (Table 3).

Thus, the highest amounts of triazine herbicides were found in the samples collected from Dobrogea and Moldova areas, where modern agriculture is practiced which involves the use of pesticides for plant treatments. The found concentrations ranged between 50.2 and 102.11 µg/kg in Tulcea County (sample 4T, 5T) and 80.67 and 997.54 µg/kg in Vaslui County (samples 7V, 8V, 9V, 10V, 11V, 12V, 13 V).

Table 3. The occurence of triazine herbicides in analyzed honey samples

Sample code	Concentration (µg/kg)							
	Simazine	Prometon	Atrazine	Ametryn	Propazine	Prometryn	Terbutryn	Total
2 C	nd	nd	1.19	nd	5.65	nd	nd	6.84
3 C	nd	nd	4.97	nd	nd	nd	nd	4.97
4 T	50.20	nd	nd	nd	nd	nd	nd	50.20
5 T	34.59	26.08	11.18	16.34	13.92	nd	nd	102.11
7 V	80.49	nd	nd	nd	nd	nd	34.58	115.07
8 V	58.56	54.96	nd	nd	nd	nd	nd	113.52
9 V	3.80	7.80	75.97	60.29	88.74	nd	15.00	251.6
10 V	116.05	31.66	nd	nd	20.04	nd	nd	167.75
11 V	82.05	17.15	nd	nd	4.78	nd	nd	103.98
12 V	32.73	nd	nd	nd	nd	nd	47.94	80.67
13 V	490.0	507.5	nd	nd	nd	nd	nd	997.5
14 B	nd	nd	nd	nd	nd	nd	nd	-

nd- not detected

The lowest concentrations ranged between 4.97 and 6.84 µg/kg were found in samples collected from Cluj County (sample 2 C and 3 C), while in the sample collected from Bistrita-Năsăud County (sample 14 B) triazines did not occur. In these two regions usually traditional agriculture is practiced and the amount of pesticides use for plant treatments is low or entirely missing.

The high concentrations of triazine herbicides found in acacia honey samples (sample 8V, 9V, 11V,) could be explained by the fact that the flowering of acacia tree corresponds to the period in which these herbicides have been applied on the corn crop.

It is also observed that the most prevalent herbicides are simazine and prometon while prometryn was not found in any samples.

If it is taken into consideration that atrazine, simazine and terbutryn have been recently introduced on the list of priority substances regarding the Water Framework Directive (WFD) (2000/60/EC) their use in agriculture should be limited.

Moreover, analyzing the obtained results and taking into consideration that the MRLs for simazine in honey established by the EU is 0.01 mg/kg it can be observed that in the analyzed samples the total content of triazine exceeds the regulatory framework for those samples collected from Moldova and Dobrogea areas.

CONCLUSIONS

This study showed the presence of triazine herbicides in honey samples in concentrations which are dependent on the sampling zone.

The highest content of triazines which exceeds the EU regulatory framework was found in the samples collected from Moldova and Dobrogea, areas where modern agriculture is practiced.

In Transylvania area where usually traditional agriculture is practiced the content of triazines does not exceed EU requirements.

The presence of triazine herbicides in honey sample obtained from tree flowers and poly-flora proves the mobility of these chemicals in environmental compartments.

EXPERIMENTAL SECTION

1. Reagents and solutions

A standard mixture of seven triazine herbicides (simazine, prometon, atrazine, ametryn, propazine, prometryn and terbutryn) with a concentration of 100 µg/mL each herbicide, dissolved in methanol was purchased from Sigma-Aldrich (USA). The working solution with a concentration of 10 µg/mL for each herbicide was obtained by dilution of the standard mixture in methanol. Acetonitrile and methanol (HPLC grade) were obtained from Merck (Germany). Milli-Q water was prepared using a Milli-Q Plus water system from Millipore (USA). Potassium dihydrogen phosphate (KH_2PO_4) with a purity of 99% was purchased from Sigma-Aldrich.

2. Instrumentation and chromatographic conditions

Chromatographic separation and determination of the triazine herbicides were carried out on a Shimadzu high performance liquid chromatograph, equipped with a 10 LC pump, 10 LSD UV-Vis detector and a manual injection valve with a loop of 5 µL. A NovaPak-C18 column (30 cm × 3.9 mm, 4 µm, Waters, USA) was used for the separation of the compounds.

Separation of the analytes was performed by isocratic elution with a mixture of acetonitrile:phosphate buffer (25 mM) (40:60, *v/v*) at a flow rate of 1.2 mL/min. The detection wavelength was set at 220 nm.

The quantification of the target compounds in real samples was made by means of the calibration curve. For this purpose five standard solutions in concentration of 0.625; 1.25; 2.5; 5 şi 10 µg/mL were prepared by dilution of the standard mixture with methanol. The calibration curves were built using the chromatographic peak area and the concentration of each triazine herbicide.

3. SPE procedure

Isolation and preconcentration of the target compounds from the honey samples were carried out on a SPE device (Supelco) using C18 EC (end capping) cartridges purchased from Phenomenex, USA. Before extraction

the SPE cartridges were conditioned in three steps using 5 mL Milli-Q water, followed by 5 mL MeOH and again by 5 mL Milli-Q water.

For the extraction of the triazine herbicides from the honey samples it was employed a slightly modified version of Albero et al. [21] as follows: 10 g of honey were dissolved in 40 mL mixture of Milli-Q water:methanol (70:30 *v/v*) and subjected to sonication for 15 minutes. The obtained solution was passed through the extraction cartridge at a flow rate of 2 mL/min for the retention of the herbicides. After that, the cartridge was washed by passing 5 mL of Milli-Q water through the cartridge in order to remove the interferences. Finally, the target compounds were eluted with 3 mL of methanol and evaporated to dryness under nitrogen. The residue was diluted in 0.5 mL methanol and then injected into the chromatographic system for the analysis of target compounds.

To study the accuracy of the SPE procedure 10 g of honey dissolved in 40 mL mixture of Milli-Q water:methanol (70:30 *v/v*) were spiked with 500 ng of each herbicide and extracted by SPE according to the protocol described above.

4. Sampling points

In order to have a better assessment of the triazine herbicides use in agriculture over their content in honey, three areas from Romania were taken into account. One area is situated in Transylvania (Cluj County and Bistriţa-Năsăud County), where traditional agriculture is practiced, and another two situated in Moldova (Vaslui County) and Dobrogea (Tulcea County) respectively, where modern agriculture is practiced (Figure 2).

The honey samples were collected in sterilized polyethylene bottles with a volume of 100 mL and kept at room temperature until analysis. Four types of honey were taken into consideration; acacia flower (sample 3C, 8V, 9V and 11V), sun flower (sample 5T, 7V and 10V), colza (sample 4T and 12V) and poly-flora (sample 2C, 13V and 14B).

Figure 2. The map of honey sampling areas

ACKNOWLEDGEMENTS

This study was performed with the support of POSDRU CUANTUMDOC "Doctoral studies for European performance in research and innovation" ID-79407 project funded by the European Social Found and Romanian Government.

REFERENCES

1. Y. Guo, X.Y. Meng, H.-L. Tang, E.Y. Zeng, *Environmental Pollution*, **2008**, *155(1)*, 150.
2. L. Ferencz, A. Balog, *Carpathian Journal of Earth and Environmental Sciences,* **2010***, 5(1)*, 111.
3. A.F. Hernandez, T. Parron, A.T. Tsatsakis, M. Requena R. Alarcon, O. Lopez-Guarnido, *Toxicology,* **2013**, *307*, 136.
4. C. Yanze-Kontchou, N. Gschwind, *Journal of Agricultural and Food Chemistry*, **1995**, *43*, 2291.
5. K.H. Bowmer, *Australian Journal of Soil Research*, **1991**, *29(2)*, 339.
6. A. Drăguş, M.S. Beldean-Galea, R. Mihăiescu, T. Mihăiescu, D. Ristoiu, *Environmental Engineering and Management Journal*, **2012**, *11(2*), 319.
7. D. Vonberg, J. Vanderborght, N. Cremer, T. Putz, M. Herbst, H. Vereecken, *Water Research*, **2014,** *50*, 294.
8. X. Liu, Z. Shen, P. Wang, C. Liu, Z. Zhou, D. Liu, *Journal of Chromatography A*, **2014**, *137*, 58.
9. Q.-X. Zhou, Y.-Y. Gao, *Chinese Chemical Letters*, **2014**, *25(5)*, 745.
10. J.J. Berzas Nevado, C. Guiberteau Cabanillas, M.J. Villaseñor Llerena, V. Rodríguez Robledo, *Microchemical Journal*, **2007**, *87,* 62.
11. P. Li, X. Yang, H. Miao, Y. Zhao, W. Liu, Y. Wu, *Analytica Chimica Acta*, **2013**, *781*, 63.
12. N. Rodríguez-González, M.J. González-Castro, E. Beceiro-González, S. Muniategui-Lorenzo, D. Prada-Rodríguez, *Talanta*, **2014**, *121*, 194.
13. Y. Wang, J. You, R. Ren, Y. Xiao, S. Gao, H. Zhang, A. Yu, *Journal of Chromatography A*, **2010,** *1217*, 4242.
14. X. Yang, R. Yu, S. Zhang, B. Cao, Z. Liu, L. Lei, N. Li, Z. Wang, L. Zhang, H. Zhang, Y. Chen, *Journal of Chromatography B*, **2014,** *972*, 111.
15. K.C. Zacharis I. Rotsias, P.G. Zachariadis, A. Zotos, *Food Chemistry,* **2012**, *134(3*), 1665.
16. M. Suzawa, H.A. Ingraham, *PLoS ONE,* **2008**, *3*, e2117. DOI:10.1371/journal.pone.0002117
17. P. Önnerfjord, D. Barceló, J. Emnéus, L. Gorton, G. Marko-Varga, *Journal of Chromatography A*, **1995**, *737,* 35.
18. M.A. Garcia, M.I. Fernandez, M.J. Melgar, *Bulletin of Environmental Contamination and Toxicology*, **1995**, *54*, 825.
19. S.R. Rissato, M.S. Galhiane, F.R.N. Knoll, B.M. Apon, *Journal of Chromatography A*, **2004**, *1048(2*), 153.
20. K.A. Stoner, B.D. Eitzer, *PLoS ONE*, **2013**, *8(10*), e77550. DOI:10.1371/journal.pone.0077550
21. B. Albero, C. Sanchez-Brunete, J.L. Tadeo, *Journal of Agricultural and Food Chemistry,* **2004**, *52*, 5828.

STUDIA UBB CHEMIA, LX, 2, Tom I, 2015 (p. 125-136)
(RECOMMENDED CITATION)

COMPARATIVE STUDY OF POLYPHENOLS FROM PROPOLIS EXTRACTS OF DIFFERENT ORIGIN

ADRIANA DĂRĂBAN[a], NELI KINGA OLAH[a,b,*], RAMONA FLAVIA CÂMPEAN[b], FLAVIA FURTUNA[b], CODRUTA COBZAC[c,*], GHEORGHE DEHELEAN[a], MARIUS BOJIȚĂ[d], DANIELA HANGANU[d]

ABSTRACT. The propolis, a resinous substance produced by bees, was used from ancient times as one of the best general panaceea. The main active compounds known in propolis are the phenolic acids and flavonoids from the class of polyphenols. This paper presents the flavonoids and phenolic acids evaluation by chromatographic (TLC and HPLC) methods of some propolis samples originating from Arad (4 samples) and Bihor (3 samples) counties, from west of Romania. There were identified the caffeic, ferulic and gallic acids respectively the chrysine and kaempferol. The chrysine content ranges from 0.15 to 1.95 mg/ml and the kaempferol from 0.07 to 8.88 mg/ml. The caffeic acid content ranges from 0.05 to 0.70 mg/ml and the ferulic acid from 0.01 to 1.39 mg/ml.

Keywords: *propolis, polyphenols, flavonoids, phenolic acids, TLC, HPLC.*

INTRODUCTION

Propolis means, in greek language, some that defend the city or the hive. The propolis is a resinous product, made by the honey bees (*Apis mellifera* L.) from the waxes and resinous compounds collected from the trees and other plants. The propolis can have different aspects, generally it is a solid product with gumy aspect, with a color from ocker yellow to red, brown, light brown or greenish [1]. The bees use the propolis to protect the hive against infections, bacterias or fungus.

[a] *"Vasile Goldis" Western University of Arad, Faculty of Medicine, Pharmacy and Dental Medicine, 86 Rebreanu Street, Arad, Romania*
[b] *SC PlantExtrakt SRL, 407059 Rădaia. Cluj, Romania*
[c] *Babes-Bolyai University, Faculty of Chemistry and Chemical Engineering, Cluj-Napoca, Romania*
[d] *Iuliu Haţieganu University of Medicine and Pharmacy, Faculty of Pharmacy, Cluj-Napoca, Romania*
** Correspondent authors: olahdr@aol.com, neliolah@yahoo.com, codruta.cobzac@yahoo.com*

The propolis has been used since ancient times because of its therapeutic effects. It can be used for the treatment of many diseases, because it shows antibacterial, antiseptic and detoxifying effects. It is a basic product used in apitherapy, an alternative medicine very popular in the antic Egypt, Greece and China.

The composition of propolis depends on various factors such as season and vegetation of the area. The chemical analysis of raw propolis show the presence of resins, waxes, essential oil, polyphenols, sugars, aminoacids, vitamins, enzymes, mineral salts, pollen and other solid impurities [2]. The recent studies do not have quantified more than 2-3 % of essential oil represented by aromatic compounds like benzyl-derivatives, vanilin, eugenol in European propolis, sesquiterpenes in Asian propolis and monoterpenes in South American propolis [3]. An other active compound class that is quantitatively important in propolis is the polyphenols represented by flavonoids, mostly aglyka of the glycosidic flavonoids from the plant species from that the bees collect the substances, respectively phenolic acids, mostly hydroxybenzoic derivatives like caffeic acid, ferulic acid or gallic acid [4].

European, Chinese and Argentinian propolis are characterized by the presence of phenolic acids and flavonoids, the most abundant being chrysin (2–4%) [5]. The total phenolic compound content found in ethanolic extract of red propolis (232 mg/g) was higher than that ever found for Brazilian propolis samples [6,7]. These values were similar to those find in temperate climate propolis originating from the species *Populus* sp., a resin-producing plant rich in polyphenols [7,8]. The low flavonoid concentration (43 mg/g) observed in ethanolic extract was similar to that normally found for Brazilian green propolis [8].

Due to its complex chemical composition, a lot of benefic effects of propolis and its extracts were identified. Recent studies highlighted the beneficial effect of hive products on health as they improve circulation, reduce inflammation and stimulates immunity. Propolis is known as one of the most powerful natural antibiotic. The presence of polyphenols and essential oil impart antimicrobial, antifungal, antitumoral, anti-inflammatory, hepatoprotective, antidiabetic, cardioprotective, antiangiogenic and immunomodulatory properties. Moreover, it was proved that propolis contains compounds which regenerate the damaged tissues, improve the liver and pancreas functions and have epithelisant, anti-edematous, radioprotective and antiasthmatic effects [9-11].

Due to its complex composition and special powerful therapeutic effects propolis was used to prepare several medicinal products, administered internally or applied externally and special cosmetic products – shampoo, creams, etc. This wide range of uses is based on its antioxidant effect conferred by the high content of polyphenols belonging mainly to flavonoids and caffeic acid derivatives.

In Romania the apiculture is a wide spread agricultural activity. The bee products were used and studied from long time. Mărghitaș et al. have studied the propolis from Transylvania, Cluj, Hunedoara, Brașov counties from agricultural, chemical and therapeutic point of view. They found that the Transylvanian propolis contains 0.55 – 3.91 mg/g chrysin, 0.56 – 2.66 mg/g galangine and 0.46 – 1.49 mg/g caffeic acid [12,13]. The Moldavian propolis was studied by Croci et al., finding in three different origin samples high quantities of phenolic acid, mainly caffeic acid, ferulic acid, 3,4-dimethoxycinnamic acid and protocatehic acid and also a high content of total flavonoids, around 25 % expressed in quercetine [14,15]. Coneac et al. [16,17] have studied the propolis from Timiș county, Banat, west part of Romania. The aim of their research was to optimize the extraction conditions of polyphenols from propolis and to standardize the hydroalcoholic extract. They have found in the three studied samples important quantities of quercetine (0.386 – 13.2 mg/g), apigenine (0.213 – 13.8 mg/g), kaempferol (0.137 – 3.198 mg/g), rutoside (0.496 – 37.184 mg/g), chrysin (0.638 – 31.9 mg/g) respectively caffeic acid (0.316 – 19.365 mg/g). The qualitative and quantitative analyzes were performed by chromatographic (TLC, HPLC) and spectral methods [12-17], being employed also image analysis combined with appropriate fuzzy clustering method [18].

This study presents the evaluation of the chemical quality of propolis from west part of Romania.

RESULTS AND DISCUSSION

The first step of monitoring of polyphenols from propolis was made by TLC. This analysis show the polyphenol fingerprint of studied samples and can be evaluated the similarities and the differences. In figure 1 and 2 are presented the TLC chromatogram of the studied propolis samples.

The TLC chromatogram show the presence of more polyphenols in the samples originating from Covăsânț, Dorgos and Ștei respectively Livada Beiuș. Caffeic acid and chrysine were identified in all samples; Covăsânț, Dorgos, Ștei and Livada Beiuș samples having the highest concentrations. The less concentrated in polyphenols is the sample from Lipova. It can be observed a lot of similarities and differences between the studied samples, both from qualitative and quantitative point of view. The similarities are due probably by the collection of the pollen and waxes from the same species, the differences are due by the specific species from the bees harvesting areas. In the sample from Dorgos can be seen some special compounds colored in red that are not present in other studied propolis samples.

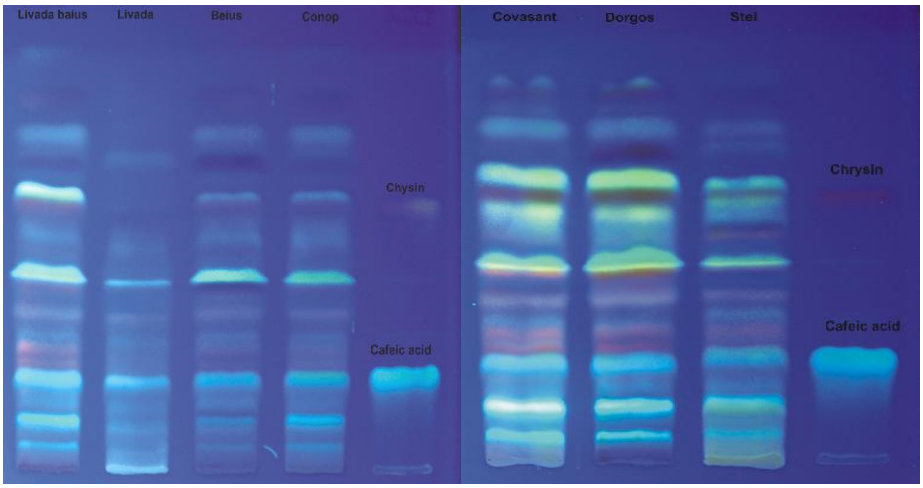

Figure 1. TLC chromatogram in fluorescence at 365 nm, after spraying with Neu-PEG reagent

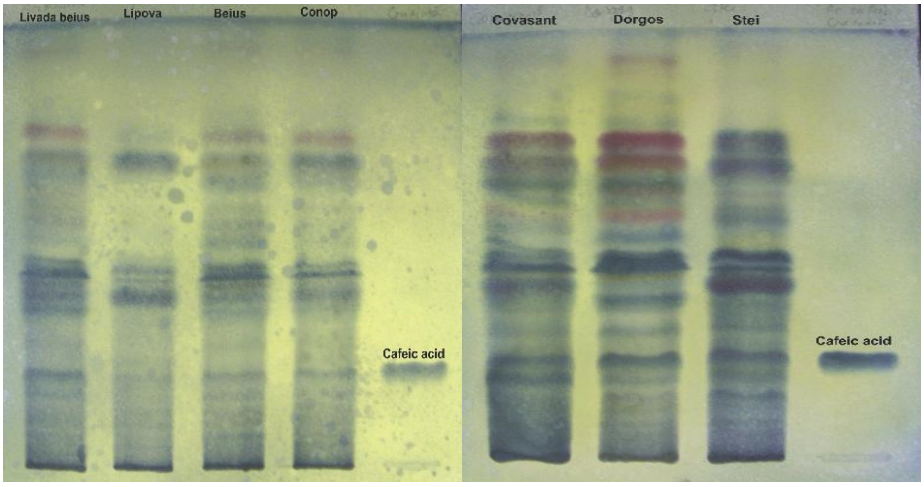

Figure 2. TLC chromatogram in visible light, after spraying with anisaldehyde and phosphomolibdenic reagents

To determine more accurately and to quantify individualy some of polyphenols HPLC analysis was performed. In figures 3-5 are presented the obtained HPLC chromatograms. In table 1 are presented the retention times and the wavelength corresponding to the maximum absorbance from UV-VIS spectra for standards and the separated compounds from the

studied propolis samples. The identification of the individual compounds is based on the comparison of retention times, maximum wavelength values and UV-Vis spectra shapes of the standards and the separated compounds.

It can be observed the presence of caffeic acid in all studied samples, the ferulic acid in the samples originating from Conop, Arad county respectively in all 3 samples from Bihor county. The gallic acid was found just in the sample from Ștei. As flavonoids, kaempferol was found in the samples from Covăsânț, Dorgos, Ștei and Beiuș, respectively chrysine in the samples from Conop, Covăsânț and Ștei.

In figure 6 are presented the calibration curves for the identified compounds (caffeic acid, ferulic acid, gallic acids, chrysine and kaempferol). In table 2 are presented the equations for the calibration curves, correlation factors and the concentrations determined in the propolis extracts.

It can be observed also some peaks that cannot be identified due to lack of standards. So, the compound separated at 1,7 minutes is present in all samples (less Beiuș); 7,6-7,8 minutes in all samples; 10,2-10,9 minutes respectively 22,2-23,4 minutes in all samples (less Ștei); 39,5-41,0 minutes is present just in the samples from Bihor county. These similarities can be explained based on the similar species from the bees harvesting area, while the differences appear probably because of some species specific only for that area.

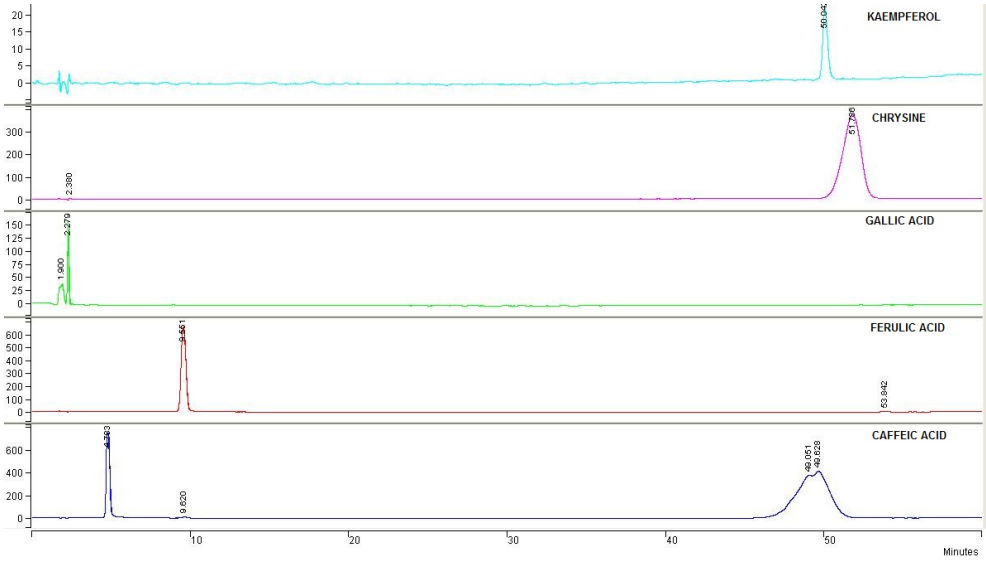

Figure 3. The HPLC chromatogram of standards

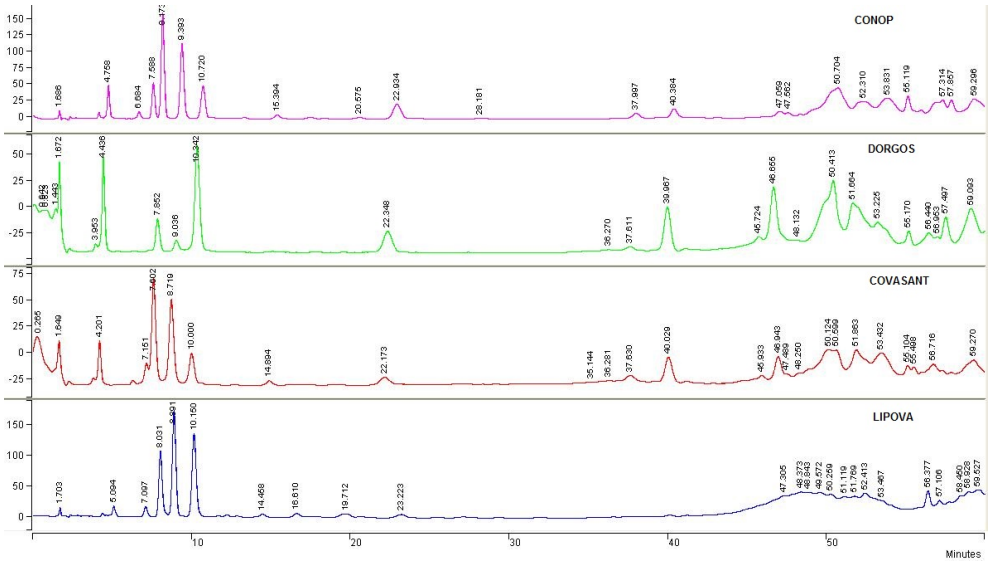

Figure 4. The HPLC chromatogram of the samples from Arad county

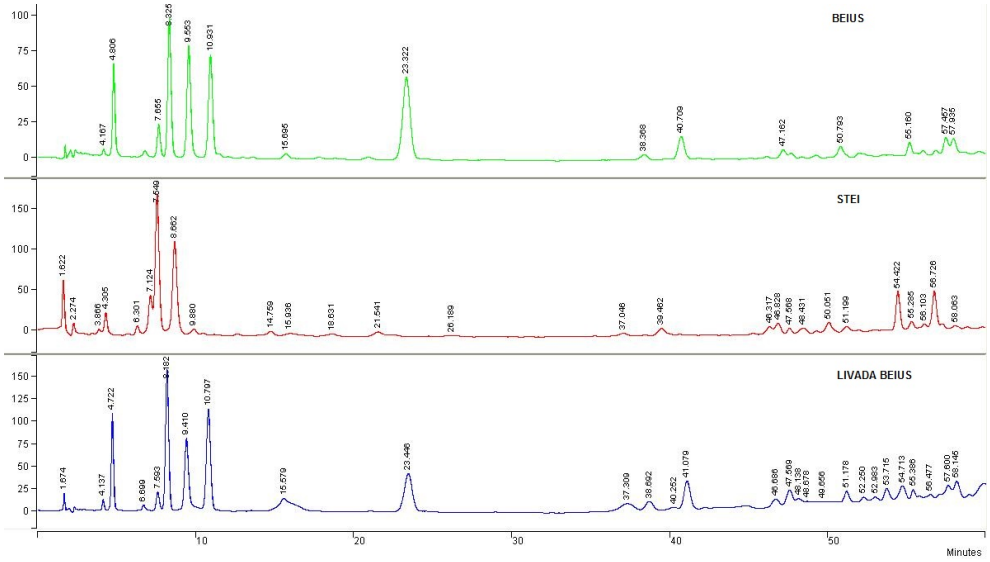

Figure 5. The HPLC chromatogram of the samples from Bihor county

The HPLC results confirm those obtained in the first TLC monitoring step.

HPLC quantitative assessment reveals a high content of flavonoids and phenolic acids in the Dorgos (Arad) sample and less in the Lipova (Arad). These results confirm also the TLC analysis findings.

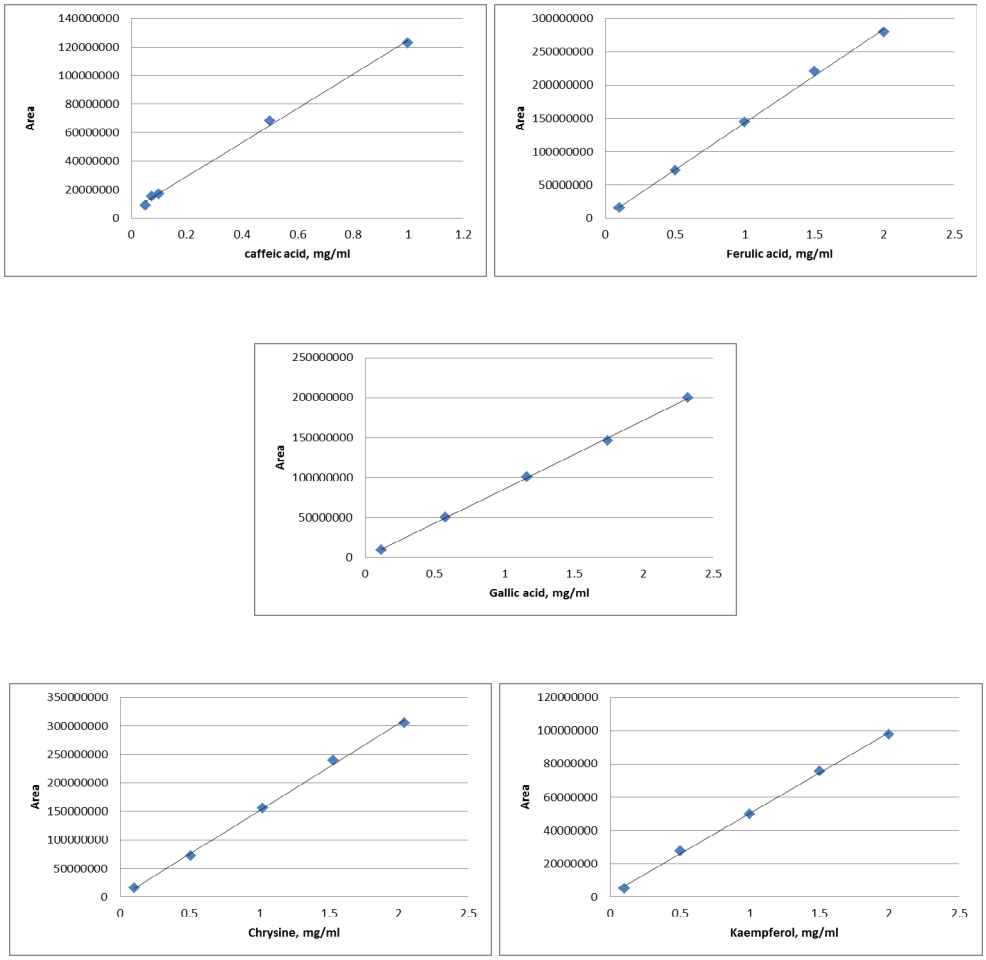

Figure 6. The HPLC standards calibration curves

Table 1. Retention times and maximum wavelength from UV-Vis spectra

Samples		Caffeic acid	Ferulic acid	Gallic acid	Kaempferol	Chrysine
Standards	RT, min	4.9	9.6	2.3	50.0	51.8
	UV-Vis max. abs., nm	238 322	236 321	270	265 365	267 311
Conop	RT, min	4.8	9.4			50.7
	UV-Vis max. abs., nm	240 322	237 320			267 311
Lipova	RT, min	5.1				
	UV-Vis max. abs., nm	238 322				
Covăsânț	RT, min	4.2			50.0	51.9
	UV-Vis max. abs., nm	237 322			267 366	267 312
Dorgos	RT, min	4.4			50.4	
	UV-Vis max. abs., nm	238 322			266 366	
Știei	RT, min	4.3	9.6	2.3	50.0	51.2
	UV-Vis max. abs., nm	239 322	237 321	271	266 366	266 310
Beiuș	RT, min	4.8	9.6		50.8	
	UV-Vis max. abs., nm	239 322	237 321		264 364	
Livada Beiuș	RT, min	4.7	9.4			
	UV-Vis max. abs., nm	238 321	237 321			

If we compare our results with the results obtained for European, Chinese and Argentinian propolis we can observe that the sample from Conop has a comparable chrysine content (1.95 mg/ml in 1:10 extract respectively 1.95 % in raw propolis).

Table 2. HPLC quantitative determinations

Samples	Caffeic acid (mg/ml)	Gallic acid (mg/ml)	Ferulic acid (mg/ml)
Calibration curves equation	$A = 10^8*c + 5*10^6$	$A = 9*10^7*c - 128491$	$A = 10^8*c + 3*10^6$
Correlation factor	0.9979	0.9995	0.9986
Conop	0.05		1.68
Lipova	0.04		
Covăsânț	0.09		
Dorgos	0.70		
Știei	0.20	0.16	0.01
Beiuș	0.40		1.09
Livada Beiuș	0.65		1.39
	Kaempferol, mg/ml	Chrysine, mg/ml	
Calibration curves equation	$A = 5*10^7*c + 2*10^6$	$A = 2*10^8*c - 851324$	
Correlation factor	0.9985	0.9995	
Conop		1.95	
Lipova			
Covăsânț	0.36	0.87	
Dorgos	8.88		
Știei	0.36	0.15	
Beiuș	0.07		
Livada Beiuș			

Comparing the obtained results with the literature data of Romanian propolis we can observe that the chrysin and caffeic acid contents are similar with those from Timiș county and higher that those from Transylvania samples. The kaempferol content of Dorgos sample from Arad county being much higher that was found in the samples from Timiș county.

CONCLUSIONS

Even that Romania was one of the first countries that promoted the propolis study, this paper is one of the first that report the chemical characteristics of the propolis originating from the west part of country, namely from Arad and Bihor counties. This paper present a comparative study of more samples from most important apicultural centers from these counties with the purpose to can have also statistically clear image of the propolis quality of the region.

This study highlight that the propolis from west of Romania have a high polyphenols, flavonoids (chrysine and kampferol) and phenolic acids (caffeic acid, ferulic acid), content that can lead us to presume that it will have also an

important antioxidant capacity. The results shown higher values as those reported for propolis originating from China, Europe or Brasilia and similar or higher than that reported from Timiș county, west of Romania or other regions from Romania. These results propose the propolis collected from this part of Romania to be used in food, cosmetic and pharmaceutical fields, to be raw material for safe and efficient medicinal products, cosmetics or food supplements.

Because the propolis is a natural product obtained by bees from the resins collected from different species, the vegetation from the bees harvesting areas influenced the chemical composition of propolis samples originating from different places. The used chromatographic methods (TLC and HPLC) showed these differences and highlight also the similar compounds.

The used chromatographic methods can be used for the quality evaluation of propolis.

EXPERIMENTAL SECTION

The propolis samples origin and preparation for study

The studied propolis were collected from various beekeepers from west part of Romania, Arad respectively Bihor counties. There were collected 4 samples from Arad county: Conop, Lipova, Covăsânț and Dorgos respectively 3 samples from Bihor county: Beiuș, Livada Beiuș and Ștei (figure 7).

To prepare the propolis for analysis the samples were extracted by grinding the samples and than mixed with 70 % vol. ethanol. The extraction was performed by maceration (cold extraction) using 10 g of propolis and 100 ml solvent. The mixtures were well shaken, and then 48 hours kept in dark, during which were occasionally shaked. At the end, each mixture was filtered. For each sample were prepared three extracts [19].

The TLC analysis

The flavonoides and phenolic acids were determined by thin layer chromatography using a silica chromatographic plate with fluorescence indicator at 254 nm. The mobile phase was toluene (Merck) – diethyl ether – acetic acid 10% (Merck), in proportion of 50:50:10 v/v. The used standards were caffeic acid and chrysin, each having a concentration of 1 mg/mL in methanol. It was applied 15 µL from the samples and 10 µL from each standard. After drying the plate at room temperature, the first chromatogram was observed in the fluorescence at 365 nm, after which the plate was sprayed with Neu-PEG reagent and observed in fluorescence at 365 nm. The second chromatogram was sprayed with a 10% phosphomolybdenic acid solution in methanol, followed by anisaldehyde reagent; the plate was heated at 105-110°C for 5-10 minutes and the chromatograms were observed in visible light [20]. The chromatograms were observed under a Camag reprostar lamp and documentation system equipped with a HP digital camera.

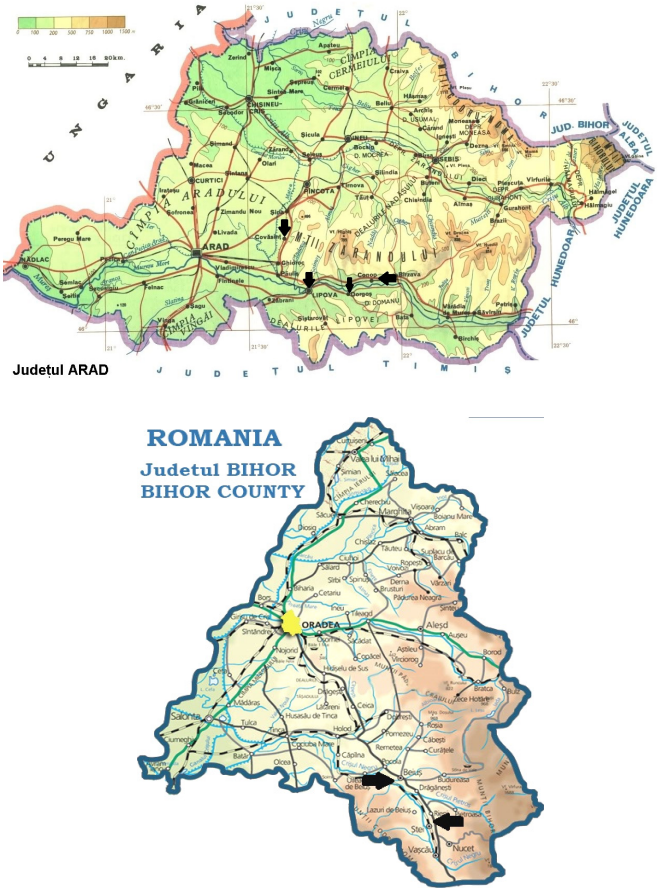

Figure 7. The collection places of studied propolis samples

The HPLC analysis

The determination was carried out on a Varian Star HPLC system. It was used a silica C18 column (Phenomenex, Luna C18, 150 x 4.6 mm, 5 µm). Like mobile phase was used a tertiary gradient prepared from 0.1% (v/v) phosphoric acid (Merck) in water, methanol and acetonitrile (Merck). The elution started with a linear gradient, beginning with isocratic elution followed for the next 30 minutes with 75 % phosphoric acid 0,1%, then for 5 minutes with 69 % phosphoric acid 0,1%, then for 5 minutes with 67 % phosphoric acid 0,1% and at the end for 20 minutes with 54 % phosphoric acid. The flow rate was 1 mL/min [21]. The DAD detector was operated at 280 and 340 nm and the

injection volume was 10 µL for each sample and standard. As standards were used chrysin (1.02 mg/mL), caffeic acid (1 mg/mL), ferulic acid (1 mg/mL), gallic acid (0,116 mg/mL), kaempferol (1 mg/mL), in methanol. For quantitative determination were used different concentrations of standards: caffeic acid (0.05 – 1 mg/ml), ferulic acid (0.1 – 2 mg/ml), gallic acid (0.116 - 2.32 mg/ml), chrysine (0.102 – 2.04 mg/ml) respectively kaempferol (0.1 – 2 mg/ml).

REFERENCES

1. A. Salatino, E. Weinstein Teixeira, G. Negri, *Evid. Based Complement. Alternat. Med.*, **2005**, *2(1)*, 33.
2. E.L. Ghisalberti, P.R. Jefferies, R. Lanteri, J. Matisons, *Experientia*, **1978**, *34*, 157.
3. V. Bankova, M. Popova, B. Trusheva, *Chem. Cent. J.,* **2014**, *8*, 28.
4. M.B. Abubakar, W.Z. Abdullah, S.A. Sulaiman, B.S. Ang, *Evid. Based Complement. Alternat. Med.*, **2014**, *2014*, 371730.
5. C. Gardana, M. Scaglianti, P. Pietta, P. Simonetti, *J. Pharm. Biomed. Anal.*, **2007**, *45(3)*, 390.
6. R.G. Woisky, A. Salatino, *J. Apicult. Res.,* **1998**, *37*, 99.
7. M.R. Ahn, S. Kumazawa,T. Hamasaka, K.S. Bang, T. Nakayama, *J. Agric. Food. Chem.*, **2004**, *52*, 7286.
8. S. Kumazawa, T. Hamasaka, T. Nakayama, *Food Chem.*, **2004**, *84*, 329.
9. P. Premratanachai, C. Chanchao, *Asian Pac. J. Trop. Biomed.*, **2014**, *4(5),* 377.
10. V.C. Wagh, *Adv. Pharmacol. Sci.*, **2013**, *2013*, 308249.
11. J.B. Daleprane, D.S. Abdalla, *Evid. Based Complement. Alternat. Med.*, **2013**, *2013*, 175135.
12. L.A. Mărghitaș, D. Dezmirean, F. Drâglă, O. Bobiș, *Bull.USAMV Anim. Sci. Biotechn.*, **2014**, *71 (2),* 111.
13. L.A. Mărghitaș, D. Dezmirean, O. Bobiș, *Evid. Based Complement. Alternat. Med.*, **2013**, *2013*, 159392.
14. A.N. Croci, B. Cioroiu, D. Lazăr, A. Corciova, B. Ivanescu, M.I. Lazăr, *Farmacia*, **2009**, *57 (1)*, 52.
14. A.N. Croci, B. Cioroiu, D. Lazăr, A. Corciova, B. Ivanescu, M.I. Lazăr, *Farmacia*, **2009**, *57 (1)*, 52.
15. A.N. Croci, D. Lazăr, L. Potorac, A. Corciova, B. Ivanescu, M.I. Lazăr, *Farmacia*, **2009**, *57 (1)*, 104.
16. G.H. Coneac, L. Vlaia, I. Olariu, V. Vlaia, D. Lupuleasa, C. Popoiu, *Farmacia*, **2014**, *62 (2)*, 400.
17. G. Coneac, E. Gafițeanu, D.I. Hădărugă, N.G. Hădărugă, I.A. Pînzaru, G. Bandur, L. Urșica, V. Păunescu, A. Gruia, *Chem. Bull. Politehnica Univ. (Timișoara)*, **2008**, *53 (67) (1-2)*, 56.
18. C. Sârbu, A.C. Moț, *Talanta*, **2011**, *85 (2),* 1112.
19. ***, European Pharmacopoeia, 8th edition, EDQM, **2015**.
20. ***, Homoopathisches Arzneibuch 2013, Deutscher Apotheker Verlag, Stuttgart, **2013**.
21. R. Yan, Y. Cao, B. Yang, *Molecules*, **2014**, *19*, 4409.

STUDIA UBB CHEMIA, LX, 2, Tom I, 2015 (p. 137-146)
(RECOMMENDED CITATION)

ANALYTICAL CAPABILITY AND VALIDATION OF A METHOD FOR TOTAL PETROLEUM HYDROCARBON DETERMINATION IN SOIL USING GC-FID

MARIN ŞENILĂ[a,*], ERIKA LEVEI[a], LĂCRIMIOARA ŞENILĂ[a], OANA CADAR[a], MARIUS ROMAN[a], MIRELA MICLEAN[a]

ABSTRACT. The paper presents the analytical capability and validation of a method for quantitative determination of total petroleum hydrocarbons in soil by gas chromatography with flame ionization detector (GC-FID). In order to validate the method, the main figures of merit such as limit of detection and limit of quantification, working range, precision and recovery were studied and the measurement uncertainty was estimated based on the bottom-up approach according to the international guidelines of ISO/IEC 17025. Limit of detection, estimated from chromatograms measured for spiked blank at low level mass concentration, was 8.3 mg/kg, while limit of quantification was 25 mg/kg. Precision was studied in terms of repeatability and reproducibility for the concentration range of 25 – 1000 mg/kg. Standard deviation of repeatability (sr) was 6.3% (n=10 parallel samples), while standard deviation of reproducibility (s_R) was 9.9 % (n=10 parallel samples). Recovery (%) estimated using a certified reference material (CRM), was 93 ± 7.0 %, while the estimated expanded relative uncertainty was 17.2 %. This paper offers all the steps necessary to validate the determination method for total petroleum hydrocarbons in soil applied according to the standard ISO 16703 and to evaluate the measurement uncertainty for this method. The obtained figures of merit fulfil the requirements of the standardized method and also of the Romanian legislation, and demonstrate that the laboratory can properly apply the method in order to achieve accurate results. The paper represents a model for the method validation in analytical laboratories in order to check the fit for purpose of analytical methods.

Keywords: *GC-FID, total petroleum hydrocarbons, validation, measurement uncertainty, soil, fit for purpose*

[a] *INCDO-INOE2000, Research Institute for Analytical Instrumentation, Donath Str. No. 67, RO-400293, Cluj-Napoca, Romania.*
[*] *Corresponding author: marin.senila@icia.ro.*

INTRODUCTION

All over the world there are numerous sites polluted with petroleum products that may have adverse effects on living organisms' health [1, 2]. Petroleum products results from crude oil by fractional distillation. In a simplified scheme of petroleum refining, crude oil is first distilled into different boiling range fractions. A processed petroleum product contains a complex mixture of many different organic substances counting paraffinic, naphthenic, olefinic, aromatic and polycyclic aromatic hydrocarbons, as well as heteroatoms (N, O, S) containing organic compounds. Also, it may contain traces of metals and organometallic compounds [3, 4].

The persistence and toxicity of different pollutants, between them petroleum hydrocarbons [5-7], created an imperative need for developing reliable methods for their qualitative and quantitative determination in environmental samples. The reliability of a measurement can be expressed by method validation as well as by stating the uncertainty of the measurement result [8-11]. However, the evaluation of measurement uncertainty pose a great challenge for analytical chemists due to the need for a complete understanding of the whole analysis steps and of the method performance parameters.

There are several techniques used for the determination of petroleum hydrocarbon content in soils [12]. Among them, the most known are those based on gravimetry, infrared spectroscopy and gas chromatography with different detection modes (FID, MS), applied subsequent to extractions in different organic solvents [12, 13].

Even if there are numerous instrumental techniques that can be used for petroleum hydrocarbon quantification, the consistent analysis of petroleum products contaminated soil is a complicated task, both due to the complex composition of petroleum products and also due to the complex matrix of soil [3]. Prior to the instrumental determination, the extraction of analyte can be an important uncertainty source. Consequently, the identification and quantification of major sources of uncertainty in the petroleum hydrocarbon determination sequence is necessary. By finding the main sources of uncertainty and critical steps of the determination, the decrease of the uncertainty related to petroleum hydrocarbon determination is possible.

The standardized GC-FID method [14] can be applied for samples with total petroleum hydrocarbon (TPH) (mass fraction) between 100 mg/kg and 10 000 mg/kg soil, expressed as dry matter, but can be adapted to lower concentrations. The method allows the determination of hydrocarbons with a boiling range of 175 °C to 525 °C (n-alkanes from C10 to C40, isoalkanes, cycloalkanes, alkylbenzenes, alkylnaphthalenes and polycyclic aromatic

compounds) [14]. Comparing to the gravimetric or IR methods, gas chromatographic determination offers qualitative information about the components of the sample.

When presenting the measurement results it is necessary to evaluate their confidence intervals [15, 16]. The International Organization for Standardization (ISO) guide [17] recommends the calculation of uncertainty using a model equation, based on evaluation of its uncertainty components, and by using the law of propagation of uncertainty.

There are several options to evaluate the measurement uncertainty existing in the literature [18]. The main ways to assess uncertainty are based on the top-down or bottom-up approaches. In the top-down approach the major sources of uncertainty are considered and estimated, while in the bottom-up approach all the uncertainty sources are thoroughly estimated and only those with significant contributions are used to calculate the measurement uncertainty. The top-down approach is time-consuming and requires a very good understanding of the analytical procedure, but it enables identification of major uncertainty sources and consequently reduction of total measurement uncertainty [16, 19].

The aim of this study was to perform a detailed validation for TPH determination in soil by GC-FID applied according to the standard ISO 16703 and to evaluate the measurement uncertainty for this method. The validation steps taken into account the guidelines of the international standard ISO/IEC 17025 [20]. The measurement uncertainty was calculated using modelling approach following the estimation of combined uncertainty. This paper represents a model for the method validation in analytical laboratories in order to check the fit for purpose of analytical methods.

RESULTS AND DISCUSSION

Method validation

The validation of the analytical procedure for quantitative determination of TPH in soil was performed by evaluating the main figures of merit: limit of detection (LoD), limit of quantification (LoQ), working and linear range, trueness/accuracy and precision (both repeatability and reproducibility) according to the EURACHEM guide requirements [21].

A specific chromatogram for a standard solution used in TPH determination is presented in Figure 1. In the chromatogram, the total peak area is that delimited by the retention times of n-decane and n-tetracontane. Therefore, only semi-volatile (>C10-C16) and non-volatile hydrocarbons (>C16-C40) [22] are included in the TPH parameter measured by this method.

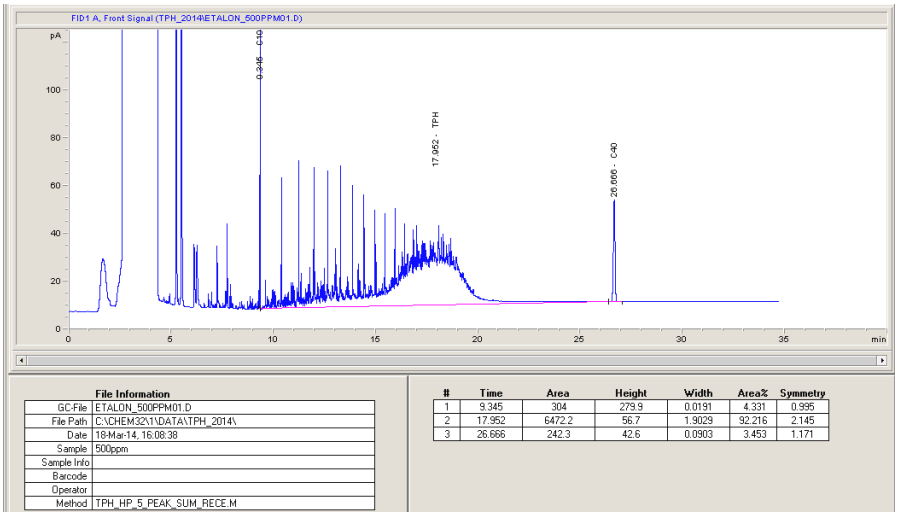

Figure 1. *GC-FID chromatogram of TPH standard (500 mg/kg). The first and the last identified peaks (C10 and C40, respectively) delimitate the retention time window (RTW)*

LoD and LoQ

In order to estimate LoD and LoQ, chromatograms of 10 independent spiked blank solutions at low level mass concentration (10 mg/L) were measured and the standard deviation of signal area was calculated. LoD was estimated for an area equal to the net signal of spiked blank and three times its standard deviation, while LoQ was estimated for a signal equal to the area signal of spiked blank and nine times its standard deviation [20]. The target was to obtain a value for LoQ of at least 25% from alert level for TPH in soil (200 mg/kg) established by Ministerial Order 756 [23] which means a value for LoQ of maximum 50 mg/kg. Data in Table 1 showed that the performance target was achieved by our method.

Table 1. LoD and LoQ for the determination of TPH in soil

Stdev (s) blank signal (signal area)	LoD (3s/b) (mg/kg)	LoQ (9s/b) (mg/kg)
39.5	8.3	25

Ten standard solutions at the calculated LoQ concentration (25 mg/L) were prepared and analysed for its confirmation by evaluation of precision (repeatability) and trueness (recovery). The targeted repeatability expressed as relative standard deviation (RSD) was 20 %, while targeted recovery was 90-115 %.

Working and linear range

At the lower end of the range, the restrictive factor is LoQ, while, at the upper end, limitations are imposed by various effects depending on the instrument response. Linearity was evaluated from the regression function of calibration using 7 standards (25, 50, 100, 250, 500, 750, and 1000 mg/L TPH). The fit for purpose linear range was selected to be between LoQ and 1000 mg/L.

Ten replicates of the 25 mg/L and ten of the 1000 mg/L calibration standards were measured. To check homogeneity of variances, the standard deviations (s_1) and (s_7) of the lowest and the highest concentrations from calibration curves, and the PG ratios (s_1^2/s_7^2 or s_7^2/s_1^2) were calculated and compared with the Fischer value $F_{9;9;0.99} = 5.35$. The values for intercept (a), slope (b), determination coefficient (r^2), and PG ratio are presented in Table 2.

Table 2. Calibration curves for working range LoQ – 1000 mg/L

Parameter	a	b	r^2	PG
TPH	-197.78	14.34	0.9994	4.96

a – intercept; b – slope; r^2 – determination coefficient, PG – test value factor for significant differences of variances at the limits of the linear range

The experimental data showed that variances are homogenous, therefore linear regression curve can be used [24].

Trueness / accuracy

Trueness was studied by evaluating the recovery of a soil CRM (Sandy Loam CRM). Thus, 6 parallel samples of soil CRMs were analysed in order to determine the methods trueness, and the results are presented in Table 3. Average recovery for soil TPH Sandy Loam CRM was 93% with relative expanded uncertainty of 7.0% (n = 6 parallel samples). In addition, trueness was evaluated using the recovery for real soil samples spiked with known content of TPH. To the each 100 g soil sample (6 parallel samples) amounts of 27.8 mg BAM K008 standard were added. Hence, the added THP concentrations were 278 mg/kg. The recovery rate was calculated by taking into account the found concentrations in the enriched samples and the added concentration.

The average recovery for spiked soil samples was 88% with a relative expanded uncertainty of 7.5% (n = 6 parallel samples), which conforms satisfactory performance according to the requirements of ISO 16703 standard (the recovery shall be more than 80% [14]). The possible factors that contribute to the recoveries below 100% may be the loss of parts of analyte during the sample preparation step, due to the volatility of some compounds from TPH class. Thus, when calculate the final result, the average recovery for spiked samples should be considered.

Table 3. Results of analysis of TPH Sandy Loam CRM (mean ± expanded uncertainty, n = 6 parallel samples) and certified value ± expanded uncertainty

Parameter	Measured value (mg/kg)	Certified value (mg/kg)
TPH	3395 ± 238	3650 ± 270

The results showed that the confidence interval of the measured value was within the confidence interval of the certified value.

Precision

Commonly, the precision is estimated in terms of repeatability and reproducibility, and, in our case, were estimated considering within and between days variation, respectively. For the repeatability study the results were obtained by analysing 10 parallel samples by a single operator using the same equipment. The target was to obtain a limit of repeatability (r) below 8.3% (according to the precision data given in ISO 16703). For the reproducibility study, a real soil sample was measured in 10 different days by different operators using the same equipment. The target was to obtain a limit of reproducibility (R) below 28.5% (according to the precision data given in ISO 16703), which mean a standard deviation of reproducibility (s_R) below 10.2 %. According to the obtained results, r was 6.3 %, while s_R was 9.9 % (R = 27 %), which conforms satisfactory performance.

In Table 4 is presented a summary of the results of method validation.

Table 4. Results of method validation for the measurement of TPH in soil by using GC-FID method

Validation parameter	Results
Limit of detection	8.3 mg/L
Limit of quantification	25 mg/L
Linear range	25 – 1000 mg/L
Trueness (recovery)	93% for CRM; 88% for spiked samples
Precision (limit of repeatability, r)	6.3% (n=10 parallel samples)
Precision (limit of reproducibility, R)	27% (n=10 parallel samples)

Measurement uncertainty evaluation

Measurement uncertainty was estimated based on the bottom-up approach [18]. All the contributions were obtained from calibration certificates (volumetric flasks, pipettes, reference materials, etc.) and from statistical analysis of repeated measurements (CRM analysis, precision experiments) through the method validation study performed in the laboratory. In brief, the steps of the method are as shown in Figure 2.

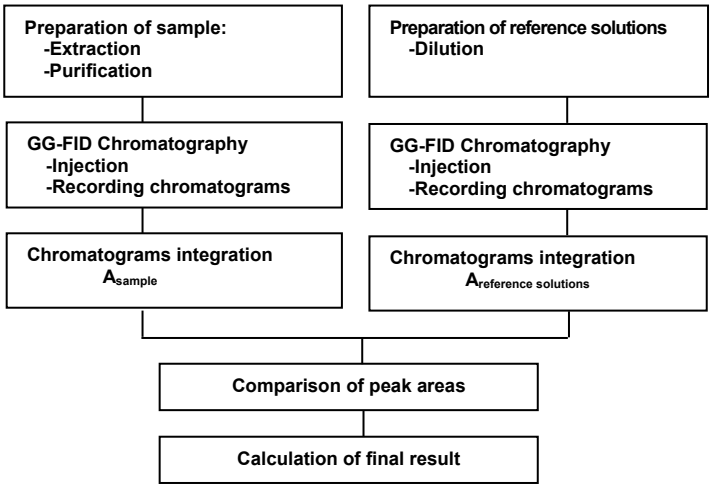

Figure 2. Experimental procedure for the measurement of mass concentration of TPH in soil by GC-FID

The identified main sources of measurement uncertainty were uncertainty of calibration reference materials (Ci), uncertainty of delivered volumes, uncertainty of signal area of the reference solutions, and recovery of the method, as presented in Figure 3 – cause and effects diagram.

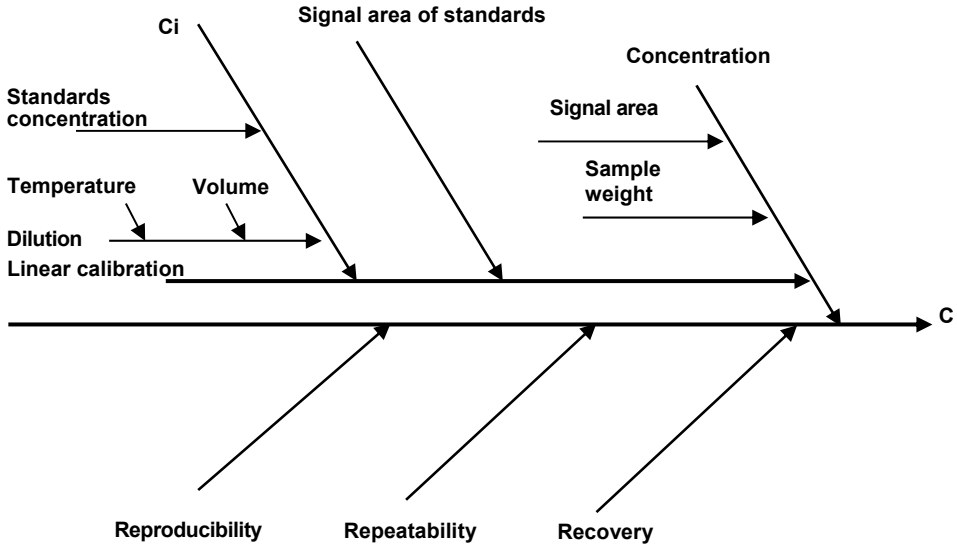

Figure 3. Cause and effects diagram of uncertainties in measurement of mass concentration of TPH by using GC-FID

Uncertainties of GC-FID and analytical balances were calculated from data obtained from calibration certificates (declared uncertainty). After estimation, all sources of uncertainty were combined according to the law of propagation of uncertainties, obtaining the combined standard uncertainty (Uc). The final result was reported as expanded uncertainty (U_E), calculated as $U_E = k \times U_c$, where k is the coverage factor, corresponding to a 95 % confidence level.

Table 5. Uncertainty components of mass concentration of TPH in soil by using GC-FID method

Source	Unit	Value	Standard uncertainty	Interventions	Total standard uncertainty	Relative uncertainty
Concentration of standar(	g/g	0.967	0.009	1	0.009	0.0090
Weight of standard	g	0.10	0.0001	1	0.0001	0.0010
Volumetric flask	mL	10	0.033	7	0.231	0.0230
Pipette	µL	1000	4.60	1	4.60	0.0046
Pipette	µL	750	4.20	1	4.20	0.0056
Pipette	µL	500	3.90	1	3.90	0.0078
Pipette	µL	250	3.70	1	3.70	0.0015
Pipette	µL	100	0.590	1	0.590	0.0059
Pipette	µL	50	0.540	1	0.590	0.0110
Pipette	µL	25	0.520	1	0.540	0.0210
Weight of sample	g	10	0.001	1	0.0001	0.00001
Equipment	g/g	1	0.01	1	0.010	0.0100
Calibration	mg/L	382	14.2	1	14.2	0.0370
Reproducibility	mg/L	404	25.4	1	25.4	0.0630
Dry mass	%	70.0	1.50	1	1.50	0.0210

The combined relative uncertainty was calculated to be 8.6 %. The biggest contribution to combined uncertainty was represented by method reproducibility (28% of the total uncertainty), but also the calibration curve (16% of the total uncertainty) and the use of low volume pipettes (e.g. 9% of the total uncertainty is given by the delivered volume of 25 µL). To calculate the expanded uncertainty of the result of a measurement at the 95 % confidence level, the result for the combined uncertainty was multiplied by a coverage factor of 2. Thus the expanded uncertainty of the TPH determination in soil by FT-IR method is 17.2 %.

Relative uncertainty contributions are used to illustrate the relative impact of different uncertainty components. As presented in Table 5, method reproducibility has the highest contribution to the combined uncertainty, while the weighting of sample has an insignificant contribution to the method uncertainty.

CONCLUSIONS

The paper presents all the steps necessary to evaluate the measurement uncertainty and validate the standardized method for TPH determination in soil according to the ISO 16703 standard in a laboratory in order to demonstrate its

fit for purpose. The studied figures of merit fulfil the requests in terms of LoD and LoQ, accuracy, and precision set out in the ISO 16703 standard. Gas chromatographic determination provides low LoQ, which make it suitable to measure the TPH concentrations at the limits imposed by environmental legislation. Trueness was studied by evaluating the recovery of a soil CRM and also by evaluating the recovery for spiked soil samples. The recovery for spiked samples was in the target imposed by ISO 16703 (higher than 80%). However, since it was well below 100% (only 88%) it should be taken into account when calculate the final result. Also, particular attention should be paid to sample preparation in order to avoid analyte loss during this step. It was demonstrated that that the method can be applied in the testing laboratory for the designed purpose, determination of TPH in soil by GC-FID.

EXPERIMENTAL SECTION

All reagents were of p.a. quality, purchased from Merck (Darmstadt, Germany). Sandy Loam soil (CRM358, Sigma-Aldrich, USA), diesel oil BAM-K008, Federal Institute for Materials Research and Testing, Germany) and 1/1 diesel oil/ lubricating oil mixture (BAM-K010e, Federal Institute for Materials Research and Testing, Germany) certified reference materials (CRMs) were used for the validation procedure. The volumes were measured using calibrated glassware (Hirschmann, Germany).

The method consists in the mixing of 20 g of well homogenized soil with 40 mL of acetone and 20 mL heptane containing n-decane and n-tetracontane to establish the Retention Time Window (RTW), removal of acetone by extraction with water followed by removal of polar substances using Florisil columns and recording of the GC chromatogram.

Standard solutions (25, 50, 100, 250, 500, 750, and 1000 mg/L TPH) prepared from a mixture of 1/1 diesel oil/lubricating oil CRM (BAM-K010e) were used for the external calibration of the instrument. Measurements were carried out using an Agilent Technologies 6890N gas chromatograph (GC) with flame ionization detector (FID). The used capillary column was a 30 m L×0.32 mm ID×0.25 µm, HP-5 95% dimethylpolysiloxane (Agilent J&W). High purity helium (Linde Gas, Romania) was used as carrier gas.

The GC-FID was operated in split mode and the oven temperature was: initial temperature 40°C, held for 6 min, then ramped to 315°C at 20°C/min and held for 15 min. Detector temperature was set at 330°C and the injector temperature was set at 300°C.

ACKNOWLEDGMENTS

This work was supported by Romanian Financing Authority CNCS – UEFISCDI, Partnership Program, BIORESOL (Contract No. 91/2014).

REFERENCES

1. Y. Zhang, M. Liu, H. Chen, G. Hou, *Ecotoxicology and Environmental Safety,* **2014**, *102*, 160.
2. H. Wang, T. Fischer, W. Wieprecht, D. Möller, *Environmental Science and Pollution Research,* **2015**, DOI 10.1007/s11356-014-4049-3.
3. E. Saari, "Towards minimizing measurement uncertainty in total petroleum hydrocarbon determination by GC-FID", dissertation thesis, Faculty of Science of the University of Oulu, *Acta University Oulu A*, 544, **2009**.
4. J.G. Speight, "Handbook of Petroleum Product Analysis", **2002**, John Wiley & Sons, Inc. publication.
5. J. Bramley-Alves, J. Wasley, C.K. King, S. Powell, S.A. Robinson, *Journal of Environmental Management,* **2014**, *142*, 60.
6. C.M. Reddy, T.I. Eglinton, A. Hounshell, H.K. White, L. Xu, R.B. Gaines, G.S. Frysinger, *Environmental Science & Technology*, **2002**, *36*, 4754.
7. S. Chakraborty, D. Weindorf, B. Li, A.A. Ali Aldabaa, R.K. Ghosh, S. Paul, M.N. Ali, *Science of the Total Environment,* **2015**, *514,* 399.
8. T. Frentiu, M. Ponta, R. Hategan, *Chemistry Central Journal*, **2013**, *7*, 43.
9. M. Senila, E. Levei, L. Senila, O. Cadar, G. Oprea, C. Roman, *Studia UBB Chemia*, **2011**, *56*, 27.
10. A. Drolc, A. Pintar, *Accreditation and Quality Assurance*, **2012**, *17*, 323.
11. M. Ponta, T. Frentiu, *Studia Universitatis Babes-Bolyai Chemia*, **2012**, *57*, 7.
12. R.N. Okparanma, *Applied Spectroscopy Reviews*, **2013**, *48*, 458.
13. L. Senila, A. Gog, M. Senila, C. Roman, L. Silaghi-Dumitrescu, *Revista de Chimie*, **2012**, *63*, 557.
14. ISO 16703, 2004, Soil quality – Determination of content of hydrocarbon in the range C10 to C40 by gas chromatography, *International organization for standardization, Geneva, Switzerland*.
15. W. Kessel, *Thermochimica Acta*, **2002**, *382*, 1.
16. A. Drolc, A. Pintar, *Accreditation and Quality Assurance*, **2011**, *16*, 21.
17. JCGM 100:2008, 1995, Guide to the Expression of Uncertainty in Measurement (GUM), *International organization for standardization, Geneva, Switzerland*.
18. S.L.R. Ellison, M. Rosslein, A. Williams, EURACHEM/CITAC, "Quantifying uncertainty in analytical measurement", 3nd edn. LGC, Teddington, **2012**.
19. M. Senila, A. Drolc, A. Pintar, L. Senila, E. Levei, *Journal of Analytical Science and Technology,* **2014**, *5*, 37.
20. ISO/IEC 17025, 2005, General requirements for the competence of testing and calibration laboratories, *International organization for standardization, European Committee for Standardization, Brussels.*
21. EURACHEM, 1998, The fitness for purpose of analytical methods, Eurachem LGC, Teddington European Environment Agency, http://www.eea.europa.eu/data-and-maps/indicators/progress-inmanagement-of-contaminated-sites/progress-in-management-of-contaminated-1.
22. W. Chang, M. Dyen, L. Spagnuolo, P. Simo, L. Whyte, S. Ghoshal, *Chemosphere*, **2010**, *80*, 319.
23. Ministerial Order 756, 1997, Official Gazette of Romania, 303/bis/06.11.1997.
24. ISO 8466-1, 1990, Water Quality – Calibration and evaluation of analytical methods and estimation of performance characteristics - Part 1, *International organization for standardization, Geneva, Switzerland.*

STUDIA UBB CHEMIA, LX, 2, Tom I, 2015 (p. 147-160)
(RECOMMENDED CITATION)

REMOVAL OF Zn(II) IONS FROM AQUEOUS SOLUTION BY ADSORPTION ON MUSTARD HUSKS

DUMITRU BULGARIU[a,b], DORU TOADER JURAVLE[a], LAURA BULGARIU[c,*]

ABSTRACT. Removal of Zn(II) ions by adsorption on a low-cost material, namely mustard husks, was examined in this study. The batch experiments were performed as a function of initial solution pH, adsorbent dose, initial Zn(II) concentration and contact time, at room temperature (25 $\pm$ 0.5°C), in order to establish the optimum conditions of adsorption process. The experimental results have shown that 5.0 g/L of mustard husks is sufficient to remove 73.16% of 54.20 mg/L Zn(II) from 25 mL of aqueous solution, in 60 min of contact time and at initial solution pH of 5.5. The adsorption data fitted well the Langmuir isotherm model, with a maximum adsorption capacity of 12.99 mg/g, while the kinetics of adsorption process is described by pseudo-second order model. The results of this study highlight that the mustard husks can become an efficient and economical alternative for the removal of Zn(II) ions from aqueous effluents.

Keywords: *adsorption, Zn(II) ions, mustard husks, isotherm, kinetics*

INTRODUCTION

Pollution of environment with heavy metals is an important issue in many industrialized regions around the world. Their large utilization and industrial importance have determined the serious pollution of many ecosystems with such pollutants, that unlike organic pollutants are not biodegradable, tend to accumulate in living organisms, and many of them are known to be toxic or carcinogenic.

[a] *"Al.I. Cuza" University of Iaşi, Faculty of Geography and Geology, 20A Carol I str., RO-700506, Iaşi, Romania.*
[b] *Romanian Academy, Branch of Iaşi, Collective of Geography, 18A Carol I str., RO-700506, Iaşi, Romania.*
[c] *Technical University "Gheorghe Asachi" of Iaşi, Faculty of Chemical Engineering and Environmental Protection, 71A D. Mangeron str., RO-700050, Iaşi, Romania*
[*] *Corresponding author: lbulg@tuiasi.ro*

Zinc is an important element for many growing industrial sectors, such as metallurgical industry, electroplating industry, mine drainage, galvanization industry, wood preservative industry, alloy industry, ceramics, batteries manufacturing, etc. [1, 2]. The rapid development of these economical activities have increase the quantities of waste water that contains significant amounts of Zn(II) ions that are directly or indirectly discharged into environment, and that drastically affects its quality. It is well known that zinc is a trace element that is essential for human health, due to its importance in psychological function of living tissues and many biological processes. Nevertheless, too much zinc can cause several serious health problems, such as gastric cramps, skin irritation, vomiting, nausea and anemia [3]. This is the reason why the permissible limit for Zn(II) ions in drinking waters is only 0.5 mg/L [4].

The most common methods involved in the removal of Zn(II) ions and other heavy metals from various types of industrial effluents include chemical precipitation [5, 6], membrane filtration [6, 7], ion exchange [8, 9], electrochemical techniques [10], etc. Unfortunately, most of these methods have several important limitations, such as generation of high quantities of toxic sludge that required further treatments, high cost of operation, high energy consumption, long treatment time and poor selectivity.

Among the conventional methods, the adsorption of heavy metal ions can be considered an inexpensive, eco-friendly and efficient method that have received a special attention during of last years, mainly because is effective in recovery and recycling of retained metal ions, have a low sludge production and is easy to operate. Activated carbon is a well-known conventional adsorbent hat has been widely employed in the wastewater treatment. Unfortunately, its utilization is not feasible due to high price and costs associated with the regeneration as a result of high-degree losses in decontamination processes [11].

Adsorbent materials derived from agricultural wastes have been intensively used as substitutes for such conventional adsorbent. These wastes are usually composed by polymers, especially different types of lignino-celluloses, and are particularly attractive for the removal of environmental contaminants because are cheap, available in large quantities and contains in their structure numerous functional groups that could represent binding sites for metal ions [12]. From these reasons, many studies from literature have reported the utilization of various agricultural wastes, such as: jack fruit peel, mango bark sawdust [13, 14], sawdust [15], rice straw [16], lemon shells [17], etc., for the removal of Zn(II) ions, in various experimental conditions.

The mustard is an annual plant that is intensively cultivated in many regions of the world, mainly due to their widely utilizations in food industry, and recently for the biodiesel production. After harvesting, the mustard seeds are

peeled and selected, and the obtained husks together with low quality seeds are considered a non-value waste that is discharged or incinerated. However, various functional groups, such as carboxyl, hydroxyl, carbonyl, amine, etc. [18] are present in the structure of this low-cost material, suggesting that mustard husks can be a potential adsorbent for the removing of metal ions. In recent studies, we report the ability of such adsorbent material to remove Pb(II) and Cd(II) ions from aqueous solution [18, 19]. The mustard husks were assessed as adsorbent for the removal of some toxic metal ions (such as Cd(II), Pb(II), Cr(VI), Cu(II)) [20-22]), but to the best of our knowledge, this is the first report on the removal of Zn(II) on mustard husks.

In this study, the removal of Zn(II) ions from aqueous solution using mustard husks as low-cost adsorbent was investigated. The influence of the most important experimental parameters that affects the efficiency of adsorption process (initial solution pH, adsorbent dose, initial Zn(II) concentration and contact time) has been examined in batch experiments. Two adsorption isotherm models (Langmuir and Freundlich) and two kinetic models (pseudo-first order and pseudo-second order models) have been used to determine the best fitting model for experimental data. The parameters for each model have been also calculated for the adsorption of Zn(II) onto mustard husks.

RESULTS AND DISCUSSION

In order to characterized the adsorptive performances of mustard husks for Zn(II) removal from aqueous solution, three aspects must be considered, namely: (a) optimization of process parameters; (b) modeling of adsorption isotherms and (c) modeling of adsorption kinetics.

1. Optimization of adsorption process parameters: Many studies from literature have shown that the adsorption of metal ions occurs with maximum efficiency only in well defined experimental conditions [23 24]. Therefore, the first goal of batch adsorption experiments should be to establish the optimum values of most important parameters that affect the adsorption process, such as initial solution pH, adsorbent dose, initial Zn(II) concentration and contact time.

1.1. Effect of initial solution pH: The initial solution pH significantly affects both the dissociation degree of functional groups from adsorbent surface and the speciation and solubility of metal ions in aqueous solution. From this reason, the value of this parameter should be optimized first.

In this study, the influence of initial solution pH on Zn(II) adsorption efficiency onto mustard husks was examined in the pH range between 1.0 and 6.5, and the obtained results are presented in Fig. 1. It can be observed that at initial solution pH higher than 3.5 the removal percent attain the maximum value and remains almost constant (69 – 73%) on entire pH range.

This represents an important advantage in the utilization of mustard husks for removal of Zn(II) ions from aqueous solution, since it does not require a rigorous correction of solution pH in order to attain a high efficiency of adsorption process. In addition, the experimental results illustrated in Fig. 1 indicate that Zn(II) adsorption on mustard husks occurs predominantly by ion exchange interactions. In these interactions are involved the mobile ions from adsorbent structure (Ca^{2+} or Mg^{2+}) and these do not depend by the dissociation degree of functional groups from adsorbent structure. In consequence, the maximum adsorption efficiency is obtained in a wide range of initial solution pH.

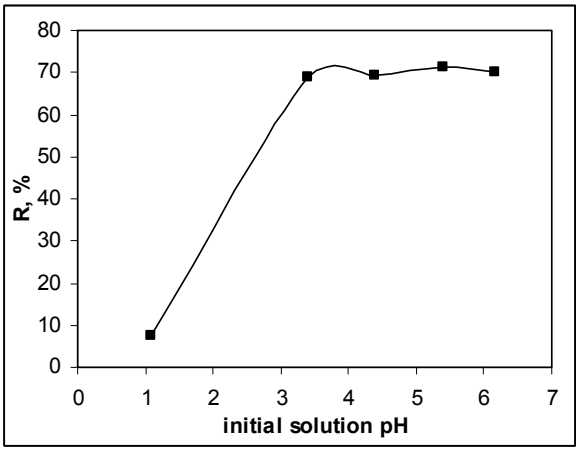

Figure 1. Effect of initial solution pH on Zn(II) adsorption onto mustard husks (c_0 = 54.19 mg/L, adsorbent dose = 5 g/L, contact time = 24 h, t = 25°C).

In strong acid media (pH = 1.5) the adsorption of Zn(II) ions is poor (7.65%), and this is probably due to the fact that the high proton concentration in aqueous solution drastically restricted the interactions between Zn(II) ions and functional groups of adsorbent.

Based on these observations, the optimum initial solution pH for Zn(II) adsorption onto mustard husks was considered to be 5.5 (when 73.16% of Zn(II) ions are removed from aqueous solution), and all further experiments were performed at this pH value.

1.2. Effect of adsorbent dose: The influence of adsorbent dose on the Zn(II) adsorption efficiency was studied using different amounts of mustard husks, in the range of 4.0 – 40.0 g/L, and experimental results (Fig. 2) showed that the adsorption process is highly dependent on this parameter.

Therefore, by increasing the adsorbent dose from 4.0 to 40.0 g/L, the adsorption capacity of mustard husks drastically decrease from 8.23 to 1.09 mg/g. In the same adsorbent dose range, a relatively slow increase in the percent of Zn(II) removal (R,%) from 79.19 to 96.14% was also obtained. Further increase in the adsorbent dose does not change significantly the values of adsorption parameters.

The observed variation is a typical one and can be explained by the increase of the binding sites number as the adsorbent dose rise, until a saturation point is reached, after which no further Zn(II) adsorption occurred [24].

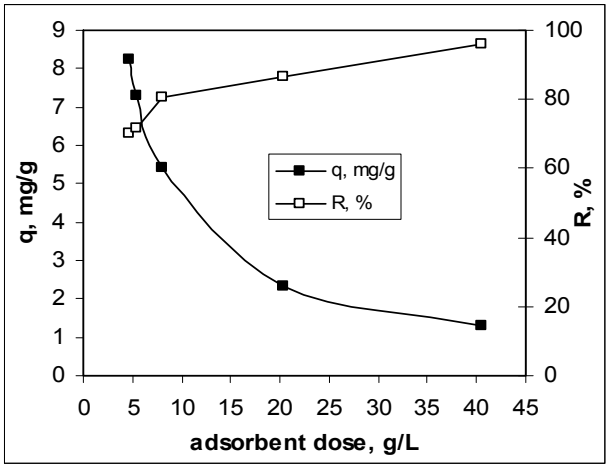

Figure 2. Effect of adsorbent dose on Zn(II) adsorption onto mustard husks (c_0 = 54.19 mg/L, initial solution pH = 5.5, contact time = 24 h, t = 25°C).

Therefore, the optimum adsorbent dose was selected to be as 5.0 g/L, and was used for further experiments.

1.3. Effect of initial Zn(II) concentration: The influence of initial Zn(II) concentration on its adsorption onto mustard husks is presented in Fig. 3. The increase of the initial Zn(II) ions concentration from 13.54 to 189.69 mg/L increased the adsorption capacity of mustard husks from 2.11 to 12.72 mg/g. In the same concentration range, the values of removal percent decrease from 81.26 to 33.68%, with increase of initial Zn(II) concentration.

The opposite variation of the adsorption parameters (q and R) was previously reported [3, 11, 12, 25] and seems determined by the fact that an increase of initial metal ions concentration provide higher driving forces to overcome all mass transfer resistances between solid adsorbent and aqueous solution, and this make that the values of q parameter to increase. However, at higher initial concentration of metal ions, the superficial functional groups of adsorbent are already occupied, and consequently the diffusion of Zn(II) ions appear to be inhibited. In consequence the values of Zn(II) removal percent (R, %) will decrease with increasing of initial metal ions concentration.

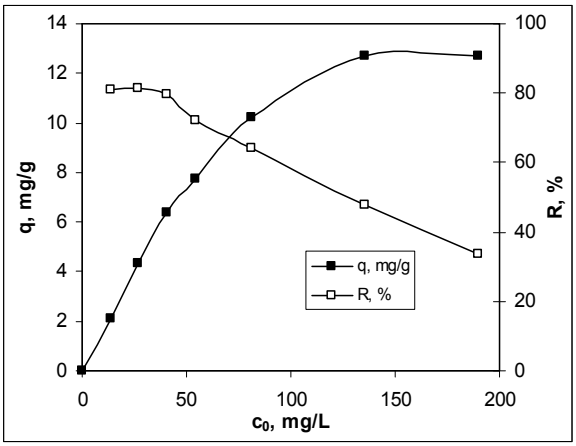

Figure 3. Effect of initial Zn(II) concentration on its adsorption onto mustard husks (initial solution pH = 5.5, adsorbent dose = 5.0 g/L, contact time = 24 h, t = 25°C).

The obtained experimental results have shown that the most efficient removal of Zn(II) ions onto mustard husks occurs when initial Zn(II) concentration is lower than 20 mg/L. In this concentration range (0 – 20 mg/L), the Zn(II) concentration in effluent solution is lower than the value of maximum permissible limit (1.0 mg/L) [26] and mustard husks can be considered an efficient adsorbent in the treatment of wastewater. When initial Zn(II) concentration is higher than 20 mg/L, in order to reduce the metal ions concentration below the permissible limit, are necessary two or more adsorption steps.

1. 4. Effect of contact time: The experimental results (Fig. 4) showed that the adsorption capacity of mustard husk for Zn(II) increase with increasing of contact time. Initially the adsorption process occurs very fast, therefore in the first 30 min more than 63% of Zn(II) ions were retained, after that the rate becomes slower near to equilibrium, which is obtained after 60 min. Once the equilibrium state was reached, the adsorption of Zn(II) ions onto mustard husks did not change significantly.

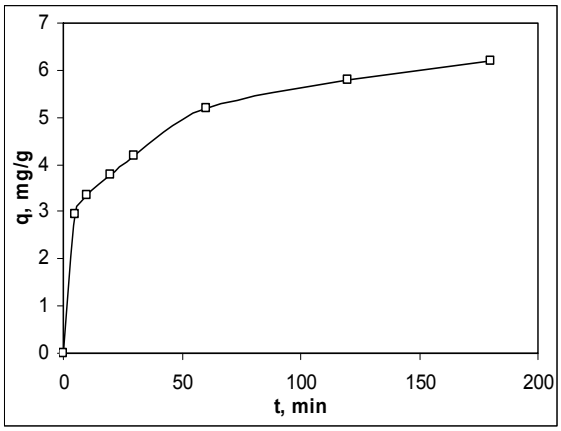

Figure 4. Effect of contact time on Zn(II) adsorption onto mustard husks (c_0 = 54.19 mg/L, initial solution pH = 5.5, adsorbent dose = 5.0 g/L, t = 25°C).

The shape of dependence illustrated in Fig. 4 suggest that the adsorption process of Zn(II) ions from aqueous solution onto mustard husks is the result of two successive stages: (a) first stage where the adsorption rate is very high (first 30 min) which is predominantly determined by the easy of interaction between Zn(II) ions and adsorbent sites that are available in high number, and (b) second stage where the adsorption capacity is almost constant and corresponds to the equilibrium of adsorption process. In the second stage, the number of available sites from adsorbent surface is more reduced, and the diffusion process becomes more important in the binding of Zn(II) ions.

Therefore a contact time of at least 60 min is necessary for the efficient removal of Zn(II) ions from aqueous solution using mustard husks, in mentioned experimental conditions.

2. Adsorption isotherm modeling: Adsorption isotherms are essential for practical design of adsorption system, because their parameters express the surface properties and affinity of adsorbent for a given metal ion. In order to estimate the potential utilization of mustard husks for Zn(II) ions removal from aqueous solution, two isotherm models (Langmuir and Freundlich) were employed to evaluate the adsorption properties of this low-cost adsorbent.

The Langmuir model is the most widely applied model for monolayer adsorption, and is based on the following assumptions: (i) the number of adsorption sites is fixed, (ii) all sites are equivalent, (iii) each site can retain only one metal ion until a complete coverage of adsorbent surface, and (iv)

the retained metal ions do not interact after adsorption [27, 28]. Unlike Langmuir model, the Freundlich isotherm model is used to describe the multi-layers adsorption on heterogeneous surfaces or surfaces supporting sites of different affinities [27, 29]. The linear mathematical equations of these two isotherm models are presented in Table 1.

Table 1. Quantitative characterization of Zn(II) adsorption of mustard husks on the basis of Langmuir and Freundlich isotherm models

Isotherm model	Mathematical equation	Calculated parameters
Langmuir model [27, 28]	$\frac{c}{q} = \frac{1}{q_{\max} \cdot K_L} + \frac{c}{q_{\max}}$	R^2 = 0.9939 q_{max} = 12.9907 K_L = 0.0301
Freundlich model [27, 29]	$\log q = \log K_F + \frac{1}{n} \log c$	R^2 = 0.9141 1/n = 0.5283 K_F = 9.9186

Notation: q_{max} – maximum adsorption capacity (mg/g); K_L – Langmuir constant; K_F and n – constants of Freundlich isotherm model.

The parameters of Langmuir and Freundlich isotherm models have been evaluated from the slopes and intercepts of corresponding linear plots (c/q vs. c for Langmuir model, and log q vs. log c for Freundlich, model respectively – Fig. 5), and the obtained values for Zn(II) ions adsorption onto mustard husks are also summarized in Table 1.

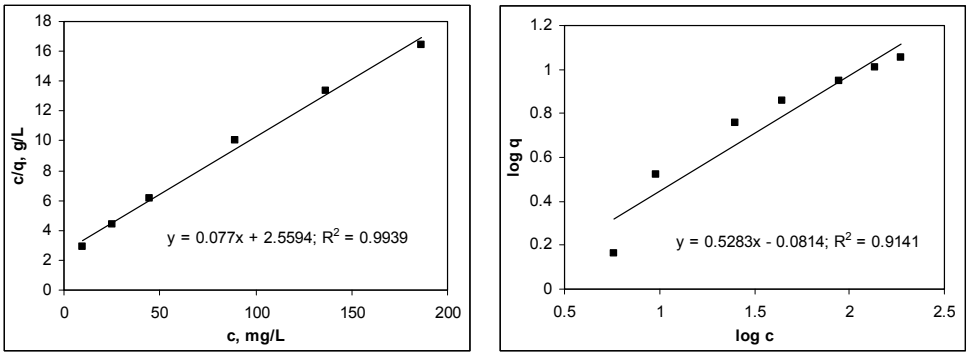

(a) (b)

Figure 5. Graphical representation of Langmuir model (a) and Freunslich model (b) for the adsorption of Zn(II) ions onto mustard husks.

The values of correlation coefficients (R^2) shows that the equilibrium isotherm data obtained in case of Zn(II) ions removal onto mustard husks are very well represented by Langmuir isotherm model. In consequence, the

surface of mustard husks is considered to present made up of homogeneous adsorption and demonstrate the formation of monolayer coverage of Zn(II) ions on the other surface of adsorbent. The maximum adsorption capacity (q_{max}, mg/g) calculated from this model, is comparable with the Langmuir capacities of other agricultural wastes tested as low-cost adsorbents for Zn(II) ions removal from aqueous solution (Table 2).

Table 2. Comparative values of Langmuir adsorption capacities for Zn(II) removal on various types of agricultural wastes

Adsorbent	pH	q_{max}, mg/g	Reference
Palm tree leaves	5.5	14.60	[30]
Maize cobs	7.5	5.77	[31]
Tea factory waste	5.5	8.9	[32]
Mango peel	-	28.21	[33]
Sugarcane bagasse	5.0	31.11	[34]
Lignin	5.5	11.25	[35]
Mustard husks	5.5	12.99	This study

The Freundlich isotherm model is employed to evaluate the adsorption intensity of Zn(II) ions onto mustard husks. The fractional value of 1/n parameter shows that the adsorption of Zn(II) is a favorable process. However, the value of R^2 coefficient obtained for this model is lower than that obtained in case of Langmuir model (Table 1), which indicate that Freundlich isotherm model is not so adequate to describe the adsorption of Zn(II) ions onto mustard husks.

3. Kinetic modeling: In order to analyze the kinetics of adsorption process of Zn(II) ions onto mustard husks, the pseudo-first order and pseudo-second order kinetic model were used. These models are based on the linear equations that are presented in Table 3.

Table 3. Kinetic characterization of Zn(II) adsorption onto mustard husks.

$q_{e, exp}$		6.4192
Kinetic model	Linear equation	Calculated parameters
Pseudo-first order model [36, 37]	$\log(q_e - q_t) = \log q_e - k_1 \cdot t$	R^2 = 0.9734 q_e = 3.4127 k_1 = 0.0079
Pseudo-second order model [36, 37]	$\frac{t}{q_t} = \frac{1}{k_2 \cdot q_e^{\,2}} + \frac{1}{q_e} t$	R^2 = 0.9963 q_e = 6.4935 k_2 = 0.0237

$q_{e, exp}$ – adsorption capacity at equilibrium, obtained experimentally (mg/g),
q_e and q_t - adsorption capacities of Zn(II) at equilibrium and at time t, respectively (mg/g), k_1 - the rate constant of pseudo-first order kinetics equation (min^{-1}), k_2 - the pseudo-second order rate constant (g/mg min).

The kinetics parameters of the pseudo-first order and pseudo-second order kinetics models, calculated from their linear representation ($\log(q_e-q_t)$ vs. t and t/q_t vs. t, respectively) (Fig. 6) are given in Table 3, together with corresponding correlation coefficients (R^2).

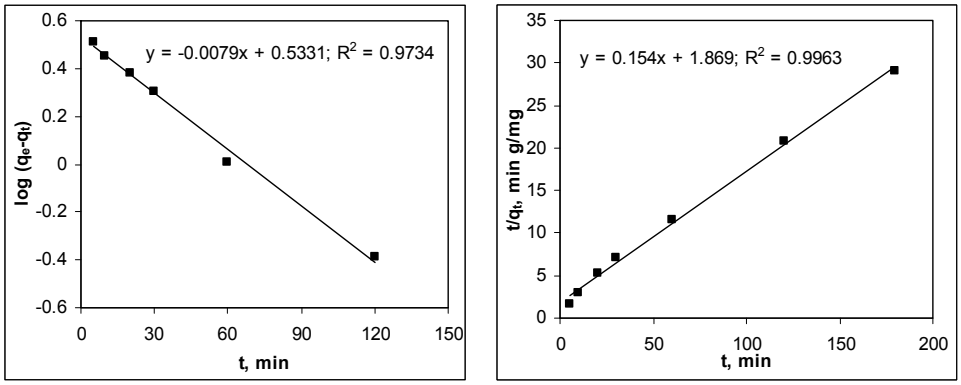

(a) (b)

Figure 6. Linear representation of the pseudo-first order kinetic model (a) and pseudo-second order kinetic model (b) for Zn(II) adsorption onto mustard husks.

It can be observed that the correlation coefficient (R^2 = 0.9963) for the pseudo-second order kinetic model is higher in comparison with the value obtained form the pseudo-first order kinetic model, and the calculated value of adsorption capacity at equilibrium (q_e, mg/g) from the pseudo-second order kinetic model is very close to those obtained experimentally ($q_{e,\,exp}$ = 6.4192 mg/g). These observations clearly indicate that the pseudo-second order kinetic model is more adequate to describe the adsorption kinetic of Zn(II) ions onto mustard husks.

The pseudo-second order kinetic model is based on the assumption that in adsorption process, the rate limiting step is the chemical interaction between metal ions from aqueous solution and functional groups from adsorbent surface [37]. Similar behaviors have been reported for the removal of Zn(II) ions on various types of agro-waste materials [30-34].

CONCLUSIONS

In this study, the removal of Zn(II) ions from aqueous solution by adsorption onto mustard husks was investigated. The experiments were performed in batch systems, as a function of several experimental parameters (such as initial solution pH, adsorbent dose, initial Zn(II) concentration and contact time), in order to establish the optimum experimental conditions.

The experimental results have shown that the highest adsorption capacity of mustard husks was obtained at initial solution pH of 5.5, 5.0 g/L adsorbent dose and a minimum 60 min of contact time, when for an initial Zn(II) concentration lower than 20 mg/L, this material can be considered an efficient adsorbent in the treatment of wastewater.

The Langmuir isotherm model best-fit the equilibrium data for the adsorption of Zn(II) ions onto mustard husks, and the maximum adsorption capacity was 12.99 mg/g. The analysis of kinetic data showed that the adsorption of Zn(II) ions onto mustard husks followed the pseudo-second order kinetic model, and this means that the rate controlling step is chemical interaction (most probable ion exchange type) between superficial functional groups of adsorbent and Zn(II) ions from aqueous solution.

The results presented in this study indicate that mustard husks can be an efficient alternative adsorbent for the removal of Zn(II) ions from aqueous media.

EXPERIMENTAL SECTION

1. Adsorbent material: The mustard husks used as adsorbent in this study was obtained from Faculty of Agriculture (USAMV Iaşi, Romania), from their own production. The agricultural waste was washed several times with double distilled water to remove impurities and dried in air at 65 – 70°C for 24 hours. The obtained material was crushed and sieved to a particle size of 1.0 – 1.5 mm, stored in desiccators and was directly used as adsorbent, without any pre-treatment. The chemical composition of mustard husks was determined using a Bruker EDX spectrometer, and was found to be: 50.41% C, 41.25% O, 1.18% P, 2.23% S, 2.11% N, 1.53% Ca, 0.59% Mg and others 0.71%.

2. Chemical reagents: All chemical reagents were of analytical degree and were used without further purifications. In all experiments, diluted solutions were prepared using fresh double distilled water, obtained from a commercially distillation system.

A stock solution of 680 mg Zn(II)/L was obtained by dissolving zinc nitrate (purchased from Reactivul Bucharest) in double distilled water. All other concentrations, which varied between 13.54 and 189.69 mg/L were prepared by dilution from stock solution. The initial solution pH was obtained by adding small volumes of 0.1 M HNO_3 or NaOH solutions.

3. Adsorption experiments: The adsorption experiments were performed using by batch technique, adding a constant amount of mustard husks (0.125 g) to a volume of 25 mL of solution of known Zn(II) concentration in 150 mL conical flasks, with intermittent stirring for a required period of time.

The effect of initial solution pH was examined at room temperature (25 ± 0.5°C), adjusting the pH values between 1.0 and 6.5. The influence of adsorbent dose on Zn(II) adsorption was also investigated by mixing adsorbent samples between 4.0 and 40.0 g/L with 25 mL of Zn(II) solution (54.20 mg/L) at pH 5.5. The effect of initial Zn(II) concentration on mustard husks adsorption efficiency was studied within 13.54 – 189.69 mg/L concentration range. In case of kinetics experiments, the same amount of adsorbent (0.125 g) was mixed with 25 mL of 54.20 mg/L Zn(II) solution at various time intervals, between 5 and 180 min.

After adsorption procedure was complete, the two phases were separated through filtration, and Zn(II) concentration in filtrate was analyzed spectrophotometrically using xylenol orange (Digital Spectrophotometer S104D, λ = 570 nm, 1 cm glass cell, against blank solution) [38].

The adsorption efficiency of mustard husks for Zn(II) ions from aqueous solution was quantitatively evaluated using the following parameters:

- adsorption capacity (q, mg/g):

$$q = \frac{(c_0 - c) \cdot (V/1000)}{m} \quad (1)$$

- percent of Zn(II) removed (R,%):

$$R = \frac{c_0 - c}{c_0} \cdot 100 \quad (2)$$

where: c_0, c are the initial and equilibrium concentration of Zn(II) ions from aqueous solution (mg/L); V is volume of solution (mL) and m is the mass of adsorbent material (g).

ACKNOWLEDGMENTS

The financial support of this study was ensured by Research contract 109P/31.01.2013 financed by SC. Salubris SA Iaşi and the project PN II 52-141/2008 financed by Romanian Ministry of Education and Research.

REFERENCES

1. O. Abdelwaha, N.K. Amin, E.S.Z. Ashtoukhy, *Chemical Engineering Research and Design*, **2013**, *91*, 165.
2. K.S. Baig, H.D. Doan, J. Wu, *Desalination*, **2009**, *249*, 429.
3. F. Fu, Q. Wang, *Journal of Environmental Management*, **2011**, *92*, 407.
4. Directive 98/83 / EC on the quality of water intended for human consumption: http://europa.eu/legislation_summaries/environment/water_protection_management/l28079_en.htm

5. T.A. Kurniawan, G.Y.S. Chan, W.H. Lo, S. Babel, *Chemical Engineering Journal*, **2006**, *118*, 83.
6. D. Mohan, S. Rajput, V.K. Singh, P.H. Steele, C.U. Pittman, *Journal of Hazardous Materials*, **2011**, *188*, 319.
7. M.J. Rivero, O. Primo, M.I. Ortiz, *Journal of Chemical Technology and Biotechnology*, **2004**, *79*, 822.
8. J. Llanos, P.M. Williams, S. Chemg, D. Rogers, C. Wright, A. Perez, P. Canizares, *Water Research*, **2010**, *44*, 3522.
9. M.A. Barakata, E. Schmidt, *Desalination*, **2010**, *256*, 90.
10. A. Mittal, L. Krishnan, V.K. Gupta, *Separation and Purification Technology*, **2005**, *414*, 125.
11. J. Febrianto, A.N. Kosasih, J. Sunarso, Y.H. Ju, N. Indrawati, S. Ismadji, *Journal of Hazardous Materials*, **2009**, *162*, 616.
12. A. Demirbas, *Journal of Hazardous Materials*, **2008**, *157*, 220.
13. V. Mishra, C. Balomajumder, V.K. Agarwal, *Clean Soil Air Water*, **2010**, *38*, 1062.
14. V. Mishra, C. Balomajumder, V.K. Agarwal, *International Journal of Applied Chemical Science and Research*, **2011**, *2*, 179.
15. L. Agorboude, R. Navia, *Journal of Hazardous Materials*, **2009**, *167*, 536.
16. C.G. Rocha, A.M. Zaia, R.V.S. Alfaya, A.A.S. Alfaya, *Journal of Hazardous Materials*, **2009**, *166*, 383.
17. T.K. Naiya, P. Chowdhury, A.K. Bhattacharya, S.K. Das, *Chemical Engineering Journal*, **2009**, *148*, 68.
18. L. Bulgariu, R.M. Hlihor, D. Bulgariu, M. Gavrilescu, *Environmental Engineering and Management Journal*, **2012**, *11*, 1969.
19. L. Bulgariu, D.I. Tudorache Fertu, M. Gavrilescu, *Annals of the Academy of Romanian Scientists - Series on Chemistry*, **2014**, *1*, 5.
20. A.K. Meena, K. Kadirvelu, G.K. Mishraa, C. Rajagopal, P.N. Nagar, *Journal of Hazardous Materials*, **2008**, *150*, 619.
21. D. Swami, D. Buddhi, *International Journal of Environment and Pollution*, **2006**, *27*, 324.
22. D. Sud, G. Mahajan, M.P. Kaur, *Bioresource Technology*, **2008**, *99*, 6017.
23. A. Dabrowski, Z. Hubicki, P. Podkoscielny, E. Robens, *Chemosphere*, **2004**, *56*, 91.
24. U. Farooq, J.A. Kozinski, M.A. Khan, M. Athar, *Bioresources Technology*, **2010**, *101*, 5043.
25. R.K. Gautam, A. Mudhoo, G. Lofrano, M.C. Chattopadhyaya, *Journal of Environmental Chemical Engineering*, **2014**, *2*, 239.
26. NTPA 001 and 002 / 2005: Available to www.gnm.ro/otherdocs/nsbhrtjqp.pdf.
27. K.H. Chong, B. Volesky, *Biotechnology and Bioengineering*, **1995**, *47*, 451.
28. B.H. Hameed, A.A. Ahmad, N. Aziz, *Chemical Engineering Journal*, **2007**, *133*, 195.
29. L. Bulgariu, C. Cojocaru, B. Robu, M. Macoveanu, *Environmental Engineering and Management Journal*, **2007**, *6*, 425.
30. F.A.A. Al-Rub, *Separation Science and Technology*, **2006**, *41*, 3499.
31. I. Banu, *Revista de Chimie (Bucharest)*, **2008**, *59*, 1375.

32. K.L. Wasewar, M. Atif, B. Prasad, I. M. Mishra, *Desalination*, **2009**, *244*, 66.
33. M. Iqbal, A. Saeed, I. Kalim, *Separation Science and Technology*, **2009**, *44*, 3770.
34. D. Mohan, K.P. Singh, *Water Research*, **2002**, *36*, 2304.
35. X.Y. Guo, A.Z. Zhang, X.Q. Shan, *Journal of Hazardous Material*, **2008**, *151*, 134.
36. Y.S. Ho, G. McKay, *Water Research*, **2000**, *34*, 735.
37. C. Gerente, V.K.C. Lee, P. Lee, G. McKay, *Critical Reviews in Environmental Science and Technology*, **2007**, *34*, 41.
38. J.A. Dean, "*Handbook of Analytical Chemistry*", Mc-Grow Hill Inc., New York, **1995**, chapter 5.

STUDIA UBB CHEMIA, LX, 2, Tom I, 2015 (p. 161-168)
(RECOMMENDED CITATION)

GROUNDWATER CHEMISTRY RENDERING USING DUROV, PIPER AND ION BALANCE DIAGRAMS. STUDY CASE: THE NORTHERN PART OF SIBIU COUNTY

MARIA-ALEXANDRA HOAGHIA[a,b,*], CECILIA ROMAN[a], CLAUDIU TĂNĂSELIA[a], DUMITRU RISTOIU[b]

ABSTRACT. The chemical behaviours of groundwater are dynamic fields of research. Variations and changes of groundwater, as drinking water source composition impress negative effects on human health. In Romania, groundwater represents free and common fresh water. Chemistry and quality of groundwater is changed due to natural and anthropogenic factors. The aim of this study is to determine and evaluate the chemical composition of groundwater from the northern part of Sibiu County using Piper, Durov, and ion balance diagrams. The graphical representations show the type of waters based on the ion content. As results, high concentrations of major anions (SO_4^{2-}, Cl^-, NO_2^-, NO_3^-) and cations (Ca^{2+}, Mg^{2+}, Na^+, K^+) were found and according to Piper and ion balance diagrams, the prominent types of waters are Ca^{2+}-HCO_3^- type.

Keywords: *groundwater, chemical composition, Durov diagram, Piper diagram, ion balanced diagram*

INTRODUCTION

Water is a limited and vital resource for humans and nature. Water quality is significant, especially when it comes to anthropogenic and natural pollution. The importance of groundwater is given not only by its valuable mineral content, as drinking water, but also by its flow of pollutants.

Worldwide, countries face the same problems regarding the deterioration of groundwater quality. Natural pollution affects aquifers (China, India, European countries) composition with high concentrations of arsenic as natural enrichment

[a] *INCDO-INOE 2000, Research Institute for Analytical Instrumentation, 67 Donath, RO-400293, Cluj-Napoca, Romania.*
[b] *Babes-Bolyai University, Faculty of Environmental Science and Engineering, 30 Fantanele, RO-400294, Cluj-Napoca, Romania.*
[*] *Corresponding author: alexandra.hoaghia@icia.ro*

of groundwater [1, 2]. Metal pollution and high concentrations of varied chemical compounds (SO_4^{2-}, Cl^-, NO_2^-, NO_3^-) impress negative influences on groundwater and soil quality [3-6].

In Romania, groundwater resources present significant concentrations of NO_3^-, SO_4^{2-}, Cl^-, Ca^{2+}, Mg^{2+}, Na^+ and K^+ [7]. Dominant types of waters are Mg^{2+}-Ca^{2+}-HCO_3^- and Na^+-HCO_3^- types [8].

The objective of the current study is the determination of the physico-chemical composition of groundwater sources (water wells and streams) using Durov and Schoeller diagrams. The types of water are ascertained depending on the abundance of ions, using Piper and ion balanced diagrams.

RESULTS AND DISCUSSION

Table 1 presents the summary statistics of the physicochemical indicators (pH, EC-electrical conductivity, TDS-total dissolved solids, NO_2^-, NO_3^-, SO_4^{2-}, Cl^-, Na^+, Ca^{2+}, Mg^{2+}, K^+) along with the environmental quality standards according to Romanian legislation [9], World Health Organisation Guidelines for drinking water [10] and U.S. EPA National Primary and Secondary Drinking Water Regulations [11].

Table1. Summary statistics of the physicochemical parameters

Variable		Minimum	Maximum	Water quality standards*	Guidelines values**	MCL***
pH (pH units)		6.99	7.96	6.5-9.5	-	6.5-8.5
EC (µS/cm)		637	1572	2500	-	-
TDS	(mg/l)	319	786	-	-	500
NO_2^-		0.1	7.0	0.5	3.0	1.0
NO_3^-		7.7	252	50	50	10
SO_4^{2-}		30	252	250	-	250
Cl^-		7.9	78	250	-	250
Na^+		6.2	62	200	-	-
Ca^{2+}		51	129	200	-	-
Mg^{2+}		5.9	23	200	-	-
K^+		0.65	13	-	20	-
HCO_3^-		201	592	-	-	-

*According to Romanian Legislation [9], **according to the Guidelines for Drinking Water [10],
***according to U.S. EPA Legislation National Primary and Secondary Drinking Water Regulations [11].

The results show significant values for the indicators with higher values as the standards. Sample water S19 presents the higher value for the TDS (figure 1). Water wells samples S3, S4, S5, S6, S7, S17 and spring samples

S20, S21 present significant values for NO_2^-, while S7 is ten times higher as the MCL (maximum concentration level). Except samples S1, S6, S17, the rest of the water samples exceeds twice and more the NO_3^- MCL. Sample S15 exceeds the SO_4^{2-} MCL, while for the other samples the obtained values are lower as 250 mg/l (MCL).

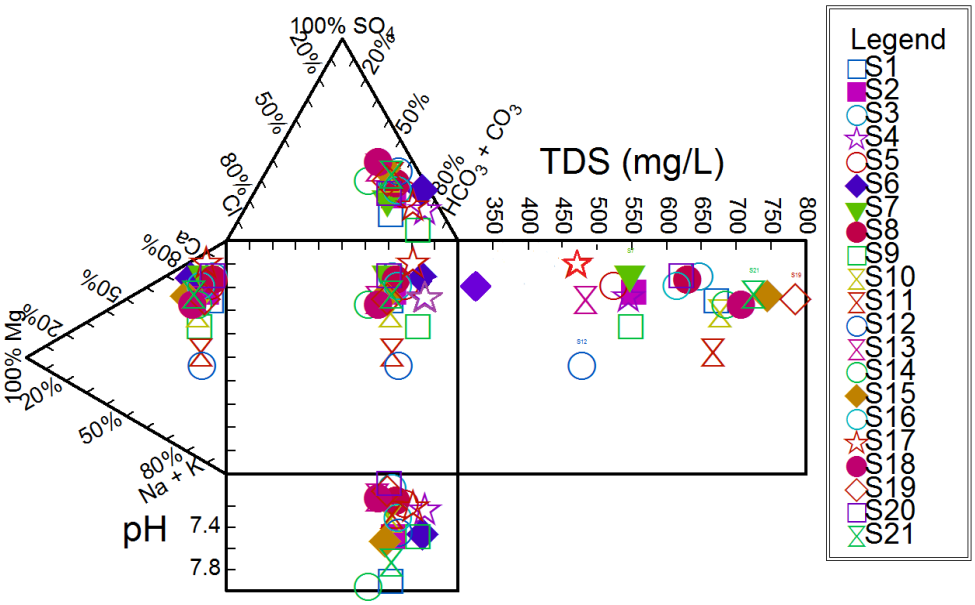

Figure 1. Chemical composition of water samples

The HCO_3^- values are ranging from 201 mg/l (F1) to 592mg/l (F4), with a 444 mg/l mean. The Durov diagram is used to graphically illustrate cations and anions concentrations, related to pH and TDS values (figure 1).

The relative ion concentrations (after the charge balancing) are represented graphically by the ion balanced diagrams.

According to ion balance diagrams, all nineteen well water samples and both public spring samples are Ca^{2+}-HCO_3^- type. Samples S1 and S6 present the lowest amount for the NO_3^- and SO_4^{2-} concentrations (figure 2).

Dispersion of ions is represented using Piper diagram. Largest anion dispersion is represented by HCO_3^- concentration, and the Ca^{2+} concentration has the largest cation dispersion. Pipere diagram shows the dominant water types, which is Ca^{2+}-HCO_3^- type for all water samples, which indicates that the hydrochemistry of the groundwater samples is characterized by alkaline earths which exceed alkali metals [12] (figure 3).

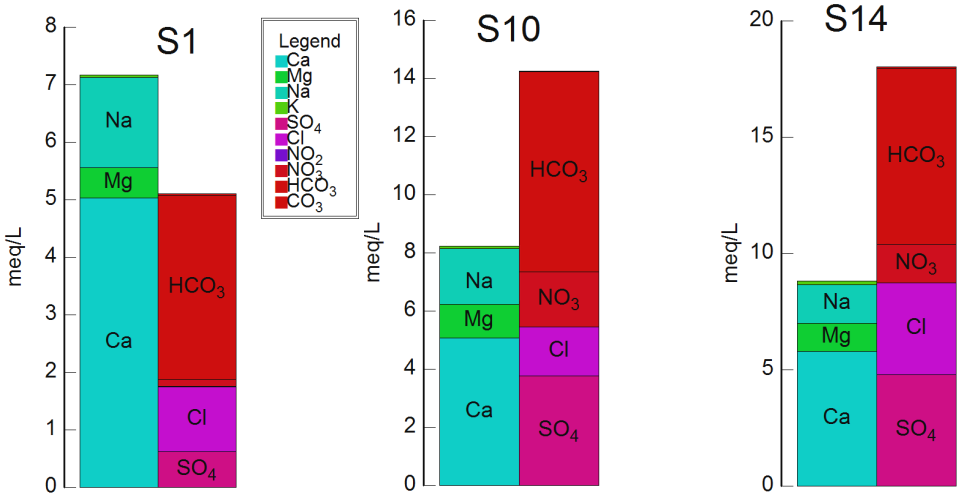

Figure 2. Ion charge balancing representation for samples S1, S10, S14

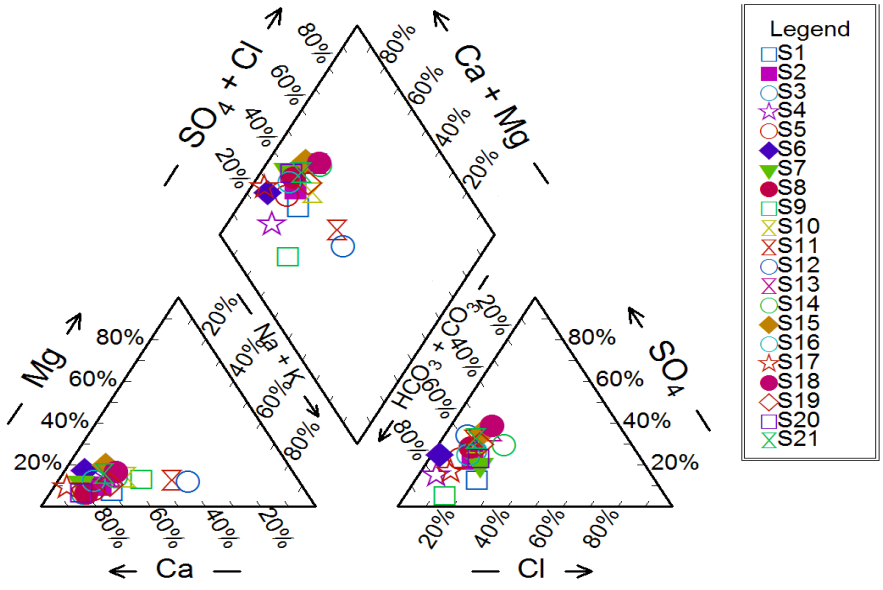

Figure 3. Classification of groundwater types after the ion charge

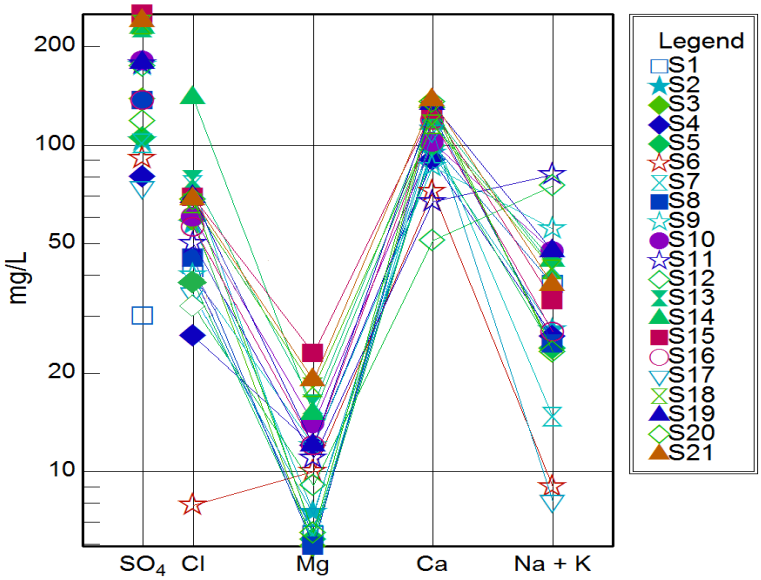

Figure 4. Ion concentrations and the ratio among ions

Variations of the chemical parameters concentrations (SO_4^{2-}, Cl^-, Ca^{2+}, Mg^{2+}, Na^+, K^+) and the ratio among them are represented by Schoeller diagram in figure 4 [13, 14].

Higher concentrations for all water samples are SO_4^{2-} concentrations, while K^+ concentrations are the lower ionic concentrations.

Samples S3, S13, S15, S21 have the highest SO_4^{2-}, Cl^-, Mg^{2+} and Ca^{2+} concentrations, while S4, S6, S7, S17, S19 present the lowest values for same parameters, as Schoeller diagram illustrates.

CONCLUSIONS

The studied groundwater samples, from the northern part of Sibiu County, present significant chemical concentrations for major cations content (Ca^{2+}, Mg^{2+}, K^+, Na^+), main anions (SO_4^{2-}, Cl^-, NO_2^-, NO_3^-, HCO_3^-) and TDS values. Anions concentrations (SO_4^{2-}, NO_2^-, NO_3^-) exceed the MCLs from Romanian standards [8] and WHO Guidelines [9]. The TDS presents high values, while 50% of water samples show high concentrations of SO_4^{2-} (>120mg/l) and all water samples are contaminated with NO_3^- with concentrations among 50 mg/l and 150 mg/l (50 mg/l MCL).

According to Piper diagram and Ion balanced diagrams the water samples (water wells and streams) are classified as Ca^{2+}-HCO_3^- type. Using Piper diagram, the ion dispersion is represented and it indicates that the largest anion dispersion is represented by the HCO_3^- dispersions and the Ca^{2+} concentration has the largest cation dispersion.

EXPERIMENTAL SECTION

Short description of the study area

Well water (S1-S19) and stream (S20, S21) samples were collected from the northern part of Sibiu County, which is situated in the Tarnavelor Plateau. The area is characterized with a temperate continental climate. The annual average air temperature ranges between 7-8 ºC. Annual precipitation ranges from 600 to 700 mm, with monthly and annual variations [15, 16].

Aquifers can be found from 0 to 0.5 m at the minor bed level and from 4 to 5 m in the major bed level and 10 m at the versant level [17]. Groundwater and streams constitute the fresh and free drinking water resources used by the Medias inhabitants.

The quality of groundwater is decay because of the near localized of the water wells from the anthropogenic sources (point sources). Point sources are collecting tanks, dry toilets, stables, waste water and storm drainage system. This situation occurs at national level and in the studied area.

Sampling and sample preparation

Nineteen well water samples (S1-S19) and two spring samples (S20, S21) were collected in the rainy season of 2014 (March). The water samples were stored in 1000 ml pre-cleaned polyethylene-terephthalate (PET) bottles. Samples were kept in a freezer at 4 ºC. For major anions and cations measurements, water samples were filtered using plastic filter unit equipped with 0.45 µm disposable cellulose acetate filter membrane and for the cations samples were acidified using HNO_3^-(67%).

MATERIALS AND METHODS

Instrumentation

The physicochemical parameters (pH, TDS and EC) were measured using a multiparameter Multi 350i WTW (Germany). Using titration with HCl against methyl orange indicator, the HCO_3^- content was analysed

For the anion content (NO_2^-, NO_3^-, SO_4^{2-}, Cl^-), IC 761 Compact Methrom A.G. Switzerland ion chromatograph was used.

Mass spectrometry using a DRC II Perkin-Elmer Inductively Coupled Plasma-Mass Spectrometer (Perkin-Elmer, Canada), was used for the major cations (Mg^{2+}, Ca^{2+}, K^+ and Na^+) determination.

The graphical approaches represented by Piper, Durov, Schoeller and ion balanced diagrams were elaborated using AqQa 1.1 software.

ACKNOWLEDGMENTS

This work was supported by Romanian financial authority CNCS-UEFISCDI, Partnership project VULMIN, Contract No. 52/2012 and Sectorial Operational Program INOVA-OPTIMA, Contract No. 658/2014. This paper is a result of a doctoral research made possible by the financial support of the Sectorial Operational Program for Human Resources Development 2007-2013, co-financed by the European Social Fund, under the project POSDRU/159/ 1.5/S/133391 “Doctoral and postdoctoral excellence programs for training highly qualified human resources for research in the fields of Life Sciences, Environment and Earth”.

REFERENCES

1. Y. Deng, H. Li, Y. Wang, Y. Duan, Y. Gan, *Procedia Earth and Planetary Science,* **2014**, *10*, 100.
2. P. Ravenscroft, W.G. Burgess, K.M. Ahmed, M. Burren, J. Perrin, *Hydrogeology Journal,* **2005**, *13*, 727.
3. G.V. Lavrentyeva, *Journal of Environmental Radioactivity*, **2014**, *135*, 128.
4. J.V. Cruz, M.O. Silva, M.I. Dias, M.I. Prudencio, *Applied Geochemistry,* **2013**, *29*, 162.
5. A.G. Douagui, I.K. Kouame, K. Koffi, A.B.T. Goula, B. Dibi, D.L. Gone, K. Coulibaly, A.M. Seka, A.K. Kouassi, J.M. Mangoua, I. Savane, *Journal of Hydro-environment Research,* **2012**, *6*, 227.
6. M. Miclean, E. Levei, O. Cadar, M. Senila, I.S. Groza, *Carpathian Journal of Earth and Environmental Sciences*, **2013**, *5 (4)*, 93.
7. D.C. Weindorf, L. Paulette, T. Man, *Environmental Pollution,* **2013**, *182*, 92.
8. H.A.L. Rowland, E.O. Omoregie, R. Millot, C. Jimenez, J. Mertens, C. Baciu, S.J. Hug, M. Berg, *Applied Geochemistry,* **2011**, *26*, 1.
9. ***311 Law from 6rd June **2004** that improves and complement 458 Law from 29 July **2002** regarding the quality of drinking water. Official Gazette 2004, Part I, no. 582/30.06.2004 [In Romanian].

10. ***_Guidelines for Drinking-water Quality,_ Fourth Edition, World Health Organization, **2011**. Online source: http://www.who.int/water_sanitation_health/publications/2011/dwq_chapters/en/.
11. ***U.S. Environmental Protection Agency (EPA) National Primary and Secondary Drinking Water Regulations (NPDWRs and NSDWRs or secondary standards): Guidance for Nuisance Chemicals, **2006**. Online sources: http://water.epa.gov/drink/contaminants/#List.
12. P.J.S. Kumar, *Geoscience,* **2013**, *54*, 12208.
13. L. Barbiero, J.P. de Queiroz Neto, G. Ciornei, A.Y. Sakamoto, B. Capellari, E. Fernandes, V. Valles, *Wetlands*, **2002**, *3* (*22)*, 528.
14. R.A. Huizar, G.T. Mendez, R.R. Madrid, *Hydrological Science,* **1998**, *5 (43)*, 669.
15. L. Badea, M. Buza, Gh. Niculescu, M. Sandu, W. Schreiber, M. Serban, A. Kadar, "Relief units from Romania, Apuseni Mountains and Transilvaniei Plateau". ("Unităţi de relief din România. Munţii Apuseni şi Podişul Transilvaniei"), Ars Docendi Press, Bucureşti, **2006**.
16. F. Grecu, "Hârtibaciu hydrographic basin. Elements of morphology" ("Bazinul Hârtibaciu. Elemente de morfologie"), Academiei Press, Bucureşti, **1992**.
17. E.D. Horhoi, "Târnava Mare channel environmental quality: a geoecological study" ("Calitatea mediului înconjurător în Culoarul Tîrnavei Mari: studiu geoecologic"), Logos 1994 Press, Oradea, **2001**.

STUDIA UBB CHEMIA, LX, 2, Tom I, 2015 (p. 169-176)
(RECOMMENDED CITATION)

THERMAL BEHAVIOUR OF POLYURETHANE MATRIX COMPOSITE MATERIALS

ANCUŢA ELENA TIUC[a,*], OVIDIU NEMEŞ[a], IOANA PERHAIŢA[b], HORAŢIU VERMEŞAN[a], TIMEA GABOR[a], VIOREL DAN[a]

ABSTRACT. This paper describes the thermal behaviour of some composite materials, polyurethane foams reinforced with tire rubber waste and fir sawdust. According to experimental results, TG and DTG plots were drawn for finding the thermal stability domains, the partial and total weight loss and the temperature of the maximum weight loss. Composite materials have superior thermal stability of raw materials from which they were made. Increasing the percentage of polyurethane foam results in greater weight loss front of recycled rubber, but lower than fir sawdust and polyurethane foam.

Keywords: *thermal analysis, fir sawdust, polyurethane foam, recycled rubber*

INTRODUCTION

Thermogravimetric analysis (TGA) is a thermal analysis technique which measures the amount and rate of change in the weight of a material as a function of temperature, in static rate or under a temperature program, in a controlled atmosphere.

TGA technique is becoming increasingly used not only in determining the composition of materials but also to predict their thermal stability up to elevated temperatures. In TGA, typical weight loss profiles are analyzed for the amount or percent of weight loss at any given temperature, the amount or percent of non-combusted residue at final temperature, and the temperature of various degradation steps [1, 2].

In the last decade, the incorporation of reinforcements from natural resources such as jute, sisal, hemp, kenaf and wood fibers into polymeric materials to improve their performance has been widely studied [3–8].

[a] *Technical University of Cluj-Napoca, Faculty of Materials and Environmental Engineering, 103-105 Muncii Ave, Cluj-Napoca, Romania.*
[b] *"Raluca Ripan" Institute for Research in Chemistry, Babeş-Bolyai University, Cluj-Napoca, Romania.*
** Corresponding author Ancuta.TIUC@imadd.utcluj.ro*

Polyurethane foams are used in many applications such as automotive, bedding and furniture industry. This is explained by their exceptional characteristics such as sound insulation, energy and shock absorption, consumer comfort and protection from impact. However, polyurethane foam also has some disadvantages, such as low thermal stability and low mechanical strength [9–12].

Thermal degradation of wood is highly dependent on its constituents [13, 14]. The complex structure of wood and the interaction between its components makes it difficult to differentiate the degradation of each component (cellulose, holocellulose, hemicelluloses and lignin) on heat treatment.

The thermal behavior of materials containing wood [15–18], rubber [18, 19] and polyurethane foam [20, 21] is strongly dependent on the composition and interfaces established between components.

The main aspects on the thermal stability of polyurethane foam, fir sawdust, particles of recycled rubber and composite materials obtained from these raw materials, are presented in this study.

RESULTS AND DISCUSSION

For a more complex characterization of the new composite materials based on recycled rubber, fir fibers and polyurethane foam, a thermogravimetric analysis was necessary. Thermal stability of raw materials used to obtain composite materials is an important aspect for their fabrication process; its highest processing temperature being known. Thermal analysis can offer useful information on stability or the temperature range in which the compounds can be used without changing their composition and properties [22], and therefore for possible applications.

Thermal degradation of fir sawdust is dependent on its constituents, the small weight loss before 100°C can be attributed to water evaporation; weight loss rate gradually increased above 200°C and a distinct weight loss appeared between 200–400°C [15]. It is known that the hemicelluloses decompose before lignin and cellulose [16]. Kim et al. confirmed that hemicelluloses degrade between 180–350°C, the lignin degrades between 250–500°C, and the degradation of cellulose takes place between 275–350°C [17].

Thermal decomposition of rubber derived from waste tires is characterized by three distinct decomposition regions: the degradation or volatilization of additives such as oils and stearic acid (200–300°C); the degradation of natural rubber (NR) and styrene–butadiene rubber (SBR), which are the main components of tire rubber (350–480°C) and the decomposition of butadiene rubber (BR) (450–500°C) [18, 19].

The polyurethane foam exhibited three thermal decomposition steps at onset temperatures: the vaporization of any volatiles and unpolymerized medium molecular weight units of the resin component (135°C); the faction of the polyol-

isocyanate bond formed during polymerization where the vaporized isocyanate component and liquid polyol remained (290°C) and char formation from the pyrolysis of the polyol component (450°C) respectively [20, 21].

The temperature domains of the decomposition stages, for new composite materials, starting temperature of weight loss steps, partial and total weight loss and temperature of the maximum weight loss for all samples, are presented in Table 1.

Analyzing the data in Table 1 we can observe that weight loss for the analyzed raw materials is quite different, 66.1% for recycled rubber (R), 83% for fir sawdust (FS) and 94.4% for polyurethane foam (PUF). This behavior is expected and can be explained by the fact that there are different materials. In terms of thermal stability, R has the highest stability (T_{max}=458°C) followed by PUF (T_{max}=381°C) and the last one is FS (T_{max}=359°C). It is expected that the thermal behavior of the raw materials influence the thermal behavior of composite materials of which they are part.

Table 1. Thermal degradation temperatures and weight loss of the investigated samples.

Sample	Temperature domain [°C]	T_{onset*} [°C]	T_{max} [°C]	Partial weight loss [%]	Total weight loss [%]
Polyurethane foam *(PUF)*	25 - 330	253	320	15.3	94.4
	330 - 800	350	381	79.1	
Fir sawdust *(FS)*	25 - 150	45	63	4.0	83.0
	150 - 800	250	359	79.0	
Recycled rubber particles *(R)*	25 – 430	299	372	49.2	66.1
	430 – 800	435	458	16.9	
Recycled rubber and 10% polyurethane foam *(R-PUF10%)*	25 – 320	244	305	9.2	67.2
	320 – 430	331	379	37.7	
	430 - 800	435	460	20.3	
Recycled rubber and 20% polyurethane foam *(R-PUF20%)*	25 – 320	247	308	9.8	69.3
	320 – 430	340	381	40.5	
	430 - 800	439	457	19.0	
Fir sawdust, recycled rubber and 15% polyurethane foam *(R-FS-PUF15%)*	25 – 320	250	310	10.5	69.8
	320 – 430	339	388	33.5	
	430 - 800	429	458	25.8	
Fir sawdust, recycled rubber and 25% polyurethane foam *(R-FS-PUF15%)*	25 – 320	252	320	10.4	73.5
	320 – 430	349	395	37.1	
	430 - 800	437	461	26.0	

T_{onset*} = *starting temperature of weight loss steps.*

Figure 1 shows the TG curves, for composite materials made from particles of recycled rubber and polyurethane foam in different proportion. Total weight loss increases with the increase in the percentage of polyurethane foam used as binder, from 67.2% for sample R-PUF10% to 69.3% for sample R-PUF20%, compared to R 66.1%. Comparing the two composites in terms of thermal stability with raw materials, the sample R-PUF10% has a better thermal stability decomposed at 460°C instead of 458°C, the decomposition temperature for R.

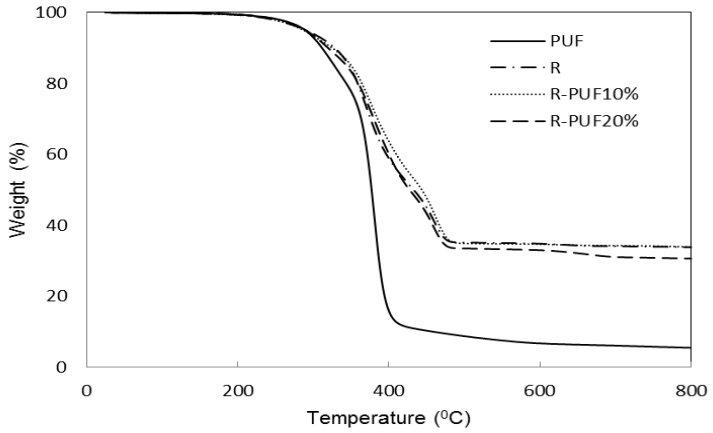

Figure 1. TG curves of the composite materials with rubber (R) and polyurethane foam (PUF)

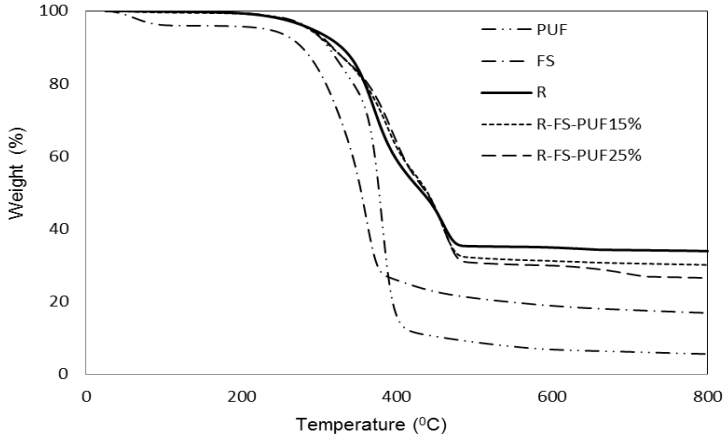

Figure 2. TG curves of the composite materials with rubber (R), fir sawdust (FS) and polyurethane foam (PUF)

For composite materials based on recycled rubber (25%) and fir sawdust (25%) and 15% respectively 25% polyurethane foam as binder, (Figure 2) total weight loss increases with the percentage of binder, from 69.8% to 73.5%, compared to the weight loss of the recycled rubber. The R-FS-PUF25% sample had a higher thermal stability, it decomposed at 461°C, with three degrees higher than major raw material R. In conclusion, the composite material has a better thermal stability than raw materials.

DTG curves, Figure 3, clearly showed that the recycled rubber had two distinct decomposition regions. The first weight loss (49.2%) was between 25–430°C, and was attributed to the degradation or volatilization of additives such as oils and stearic acid and to the degradation of natural rubber (NR) at 372°C. The final weight loss (16.9%) was 430–800°C and it appeared mainly due to the degradation of styrene–butadiene rubber (SBR) at 458°C, and butadiene rubber (BR) at 467°C. The observed degradation trend was in accordance with a former study which attributed the DTG peak temperature of 378°C to NR, 458°C to SBR and 468°C to BR [18].

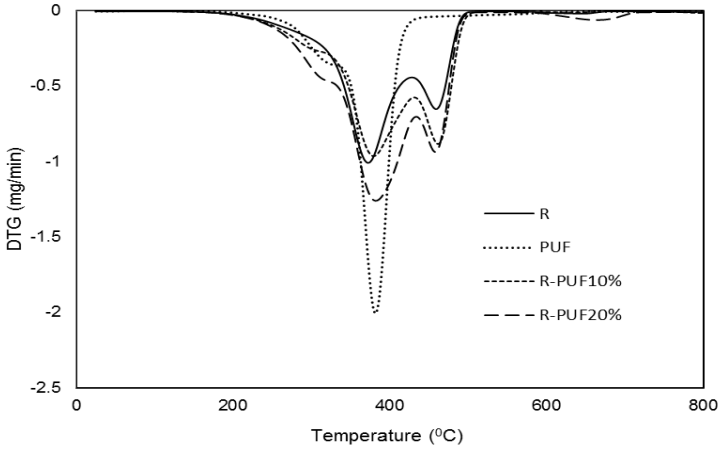

Figure 3. DTG curves of the composite materials with rubber (R) and polyurethane foam (PUF)

In the cases of the composite materials, R-PUF10%, respectively R-PUF20%, if a mass loss occurs at around 247°C due to the scission of the polyol-isocyanate bond formed during polymerization, the weight loss of composite materials increases with the percentage of polyurethane foam used as binder (Figure 3).

On the decomposition curve of fir sawdust (Figure 4), the first peak appeared below 100ºC and can be assigned to the evaporation of water. The second peak at 359°C was broad, which means there was overlapping between the decomposition of hemicelluloses, cellulose, lignin and wood extractives.

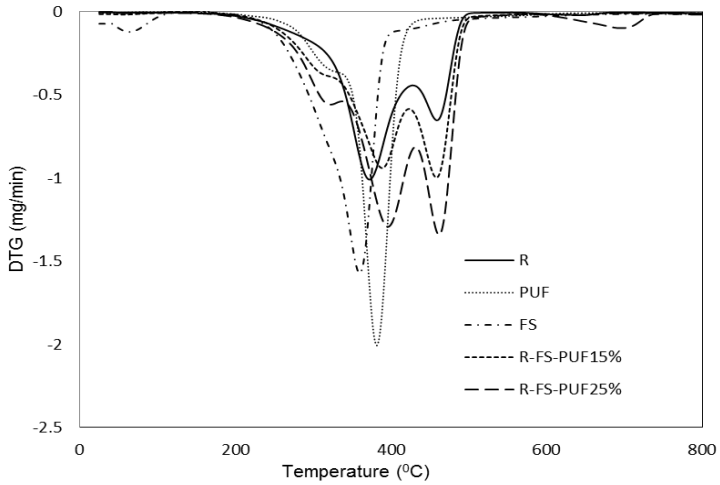

Figure 4. DTG curves of the composite materials with rubber (R), fir sawdust (FS) and polyurethane foam (PUF)

The thermal stability of composite materials with fir sawdust added is better than that of the composite materials with recycled rubber and polyurethane foam only. In Figure 4 is observed that composite materials keep the shape of the recycled rubber decomposition curve, but with a greater weight loss and an increase in decomposition temperature.

CONCLUSIONS

The thermogravimetric plots show that basic research may be possible to describe the mechanisms of thermal decomposition of waste (fir sawdust and rubber from tires) and polyurethane foam, as raw materials.

Weight loss of analyzed raw materials is quite different, 66.1% for R, 83% for FS and 94.4% for PUF, because they are different materials but combined together in well-defined proportions give composite materials with superior properties.

Thermal stability of composite materials investigated are superior to any raw material use in this study and is clearly demonstrated by higher decomposition temperatures of composite materials: 461°C for R-FS-PUF25% and 460°C for R-PUF10% instead of 458°C for R 381°C for PUF and 359°C for FS, the decomposition temperatures of raw materials.

EXPERIMENTAL SECTION

Samples

Samples analyzed in this study are composite materials based on two types of raw materials (fir sawdust and recycled rubber particles from used tires) and polyurethane foam (flexible, with open cell) as binder.

Investigation methods

Thermogravimetric analysis (TGA) we performed on based composite materials with fir sawdust, polyurethane foam and recycled rubber particles, was performed using a Mettler-Toledo TGA/SDTA 851e, 1600°C, Analysis Thermal System.

Measuring conditions. Samples were placed in an alumina crucible and heated at 10°C/min over a temperature range of 25–800°C. The experiments were conducted under a nitrogen atmosphere at a flow of 50 mL/min. Samples weights of TGA were between 15–25 mg in their original state.

ACKNOWLEDGMENTS

This paper was supported by the Post-Doctoral Programme POSDRU/ 159/1.5/S/137516, project co-funded from the European Social Fund through the Human Resources Sectorial Operational Program 2007-2013.

REFERENCES

1. B. Sreedhar, M. Sairam, D.K. Chattopadhyay, P.A.S. Rathnam, D.V. Mohan Rao, *Journal of Applied Polymer Science*, **2005**, *96*, 1313.
2. P. Sukumar, V. Jayashree, M.R. Gopinathan Nair, M.N. Radhakrishnan Nair, *Journal of Applied Polymer Science,* **2009**, *111*, 19.
3. M. Jawaid, H.P.S. Abdul Khalil, *Carbohyd Polym,* **2011**, *86*, 1.
4. C.A. Cateto, M.F. Barreiro, C. Ottati, M. Lopretti, A.E. Rodrigues, M.N. Belgacem, *Journal of Cellular Plastics,* **2013**, *50*, 81.
5. J.M.F. De Paiva, E. Frollini, *Macromolecular Materials and Engineering*, **2006**, *291*, 405.
6. S.-P. Huo, M.-C. Nie, Z.-W. Kong, G.-M. Wu, J. Chen, *Journal of Applied Polymer Science*, **2011**, *125*, 152.
7. C.G. Silva, F. Oliveira, E.C. Ramires, A. Castellan, E. Frollini, *Tappi Journal,* **2012**, *11*, 41.
8. B.-L. Xue, J.-L. Wen, R.-C. Sun, *ACS Sustainable Chemistry & Engineering*, **2014**, *2*, 1474.
9. D. Randall, S. Lee, “The polyurethanes book”, J. Wiley, **2002**, chapter 2.

10. Z. Wirpsza, T.J. Kemp, "Polyurethanes: chemistry, technology, and applications", E. Horwood, **1993**, chapter 3.
11. D.V. Dounis, G.L. Wilkes, *Polymer*, **1997**, *38*, 2819.
12. A.P. Mouritz, Z. Mathys, *Composite Science and Technology*, **2001**, *61*, 475.
13. H.L. Lee, G.C. Chen, R.M. Rowel, *Journal of Applied Polymer Science,* **2004**, *91*, 2465.
14. Q. Liu, C. Lv, Y. Yang, F. He, L. Ling, Journal of Molecular Structure*,* **2005**, *733*, 193.
15. A.N. Shebani, A.J. van Reenen, M. Meincken, *Thermochimica Acta*, **2008**, *471*, 43.
16. M. Gröndahl, A. Teleman, P. Gatenholm, Carbohydrate Polymers, **2003**, *52*, 359.
17. H. Kim, S. Kim, H. Kim, H. Yang, *Thermochimica Acta,* **2006**, *451*, 181.
18. S. Seidelt, M. Müller-Hagedorn, H. Bockhorn, *Journal of Analytical and Applied Pyrolysis*, **2006**, *75*, 11.
19. G.-G. Choi, S.-H. Jung, S.-J. Oh, J.-S. Kim, *Fuel Processing Technology*, **2014**, *123*, 57.
20. C. Beyler, M. M. Hirschler, "Handbook of fire protection engineering*"*, National Fire Protection Association, **2002**, chapter 2.
21. D.U. Shah, F. Vollrath, D. Porter, *Polymer*, **2015**, *56*, 93.
22. A.M. Iurian, I. Perhaiţa, R. Şeptelean, A. Saponar, *Studia UBB Chemia*, **2013**, *LVIII, 1*, 141.

STUDIA UBB CHEMIA, LX, 2, Tom I, 2015 (p. 177-185)
(RECOMMENDED CITATION)

COIR EMPLOYED AS SOILLESS CULTIVATION SUBSTRATE AND ITS INTERFERENCE WITH NUTRIENT SOLUTION DURING TWO TOMATOES CROPPING PERIODES (CASE STUDY)

NIKOLAOS GOUGOULIAS[a],LIVIU GIURGIULESCU[b,*], DIMITRIOS KALFOUNTZOS[a], ALEXANDROS PAPACHATZIS[a], IOANNIS VAGELAS[a], DIMITRIOS FTAKAS[a], DIMITRIOS PATERAS[a], ADAMANTIA CHOULIARA[c]

ABSTRACT. The experiment was conducted in the glasshouse of TEI of Thessalia, for two growing periods, in soilless tomato cultivation, with coir substrate (open system). The electrical conductivity of the inflow solution to crops, fluctuated from 1.80 to 2.55 dS m-1 and pH values ranged from 5.5 to 6.8, while for the efflux solution from the crops, ranged from 2.00 to 3.50 dS m-1 for electrical conductivity, and from 5.5 to 6.9 for pH. On the coir substrate, the electrical conductivity ranged from 0.3 to 1.13 dS m-1 (water extract of 1 part of coir : 5 parts of H2O) and for pH from 5.87 to 6.83 during the first crop period; during the second cultivation, the electrical conductivity it fluctuated from 0.65 to 1.91 dS m-1 and for pH from 5.7 to 6.7. According to this study, 20% of substrate was decomposed, CEC increased, also the salinity status of the coir increased essentially during the second cultivation period, correlated with nitrate and phosphate forms enrichment of the substrate, while a slight negative affection to the crop production was observed; in generally, the coir substrate, is a good choice with excellent results for cultivation return.

Keywords: *soilless cultivation, nutrient solution, coir substrate, tomato.*

INTRODUCTION

In an efficient soilless cultivation (hydroponics), the plants are free from diseases, and grow faster than in the soil; naturally in hydroponics, nutrient solutions used, must be constantly controlled, as far as it concern their chemical composition and concentration as well as the chemical stability of the

[a] *Department of Agronomy Technology, Technological Educational Institute of Thessaly, 41110 Larissa, Greece.*
[b] *Department of Chemistry and Biology, Technical University of Cluj-Napoca, North Universitary Center of Baia Mare, 430122 Baia-Mare, Romania.*
[c] *Informatic's Scientist, data analysis.*
** Corresponding author: giurgiulescu@gmail.com*

substrate employed must be assessed; adverse effects of soilless cultivations result concerning particularly the high cost of controlling systems provision and solution preparation; a significant factor affecting efficiency of nutrient solution in open hydroponic culture systems, is the observed loss of fertilizer and soil pollution, due to non-recycling of the liquids drained [1,2].The development of today's hydroponic's growing systems [3-7], is based on modern distribution systems of nutrient solution [8-12]. In the present study, the efficiency of used method for nutrient solution preparation is assessed, and as it concerns coir as substrate used in the present study, its alteration, during two crop periods, was evaluated [13].

RESULTS AND DISCUSSION

Nutrient solution: It was observed that in the inflow of the solution in two cropping periods, with regard to the electrical conductivity, it was produced a solution with slightly higher values of electrical conductivity (Figure 1). Also the runoff solution for both crops showed values of electrical conductivity, higher than the respective values of the influx solution, affected by the accumulation of salts in the substrate. In (Figure 2) is noted that during the inflow of the solution in both crops, with regard to the pH, it was produced a solution with slightly higher values; the runoff solution showed values of pH, also in generally higher values than the respective values of the influx solution.

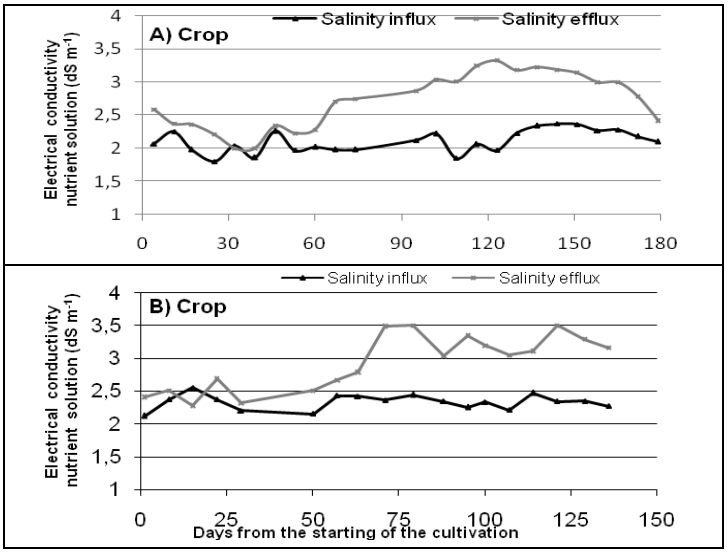

Figure 1. Fluctuations of electrical conductivity of influx and efflux of the nutrient solution of soilless tomato cultivation, during of two crops development

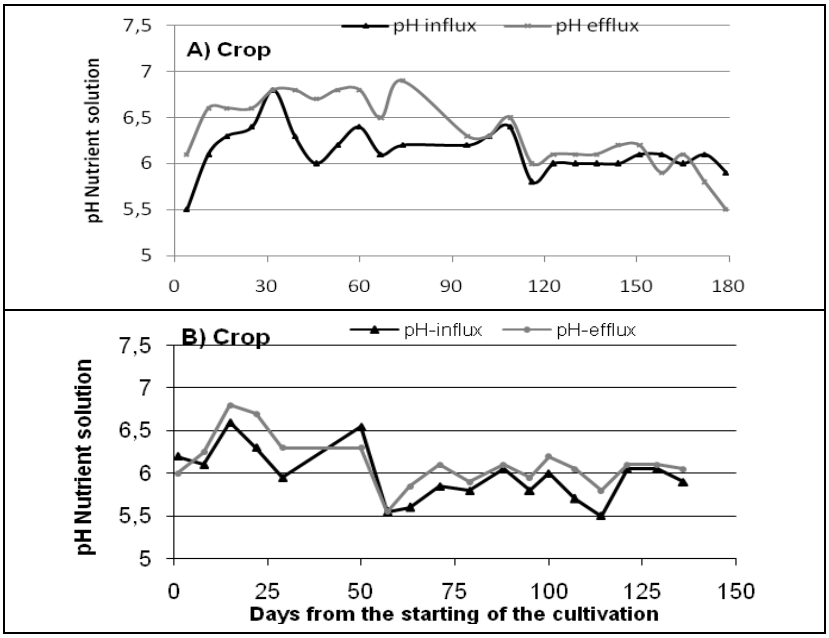

Figure 2. Fluctuations of pH values of the nutrient solution influx and efflux of soilless tomato cultivation, during the two crops development.

Substrate: The values of electrical conductivity were recorded concerning the substrate, during the development of two cultivation periods, as they were affected by the nutrient solution (Figure 3). In the first crop period, it was observed that during early days of cultivation, the electrical conductivity of the substrate was fluctuated, thereafter it was reduced and stabilized at the value of 0.63 dS m^{-1}, 90 days after the starting of the cultivation. At the second crop period, it was observed that for the early days of cultivation the electrical conductivity of the substrate was fluctuated, thereafter it was reduced and stabilized with low fluctuations at the value of 1.40 dS m^{-1}, 79 days after the starting of the cultivation. The values of pH were also recorded concerning the substrate during the two cultivation periods, as they were affected by the nutrient solution, (Figure 4). In the first crop period, the pH of the substrate during the cultivation was fluctuated from 5.87 to 6.83, while during the second crop, it was fluctuated from 5.7 to 6.7. Then, for the second cultivation period (B crop), it was revealed that the electrical conductivity was stabilized at higher values and for pH at lower values, in comparison to A crop; then a significant amount of salts was accumulated in coir during the second cultivation.

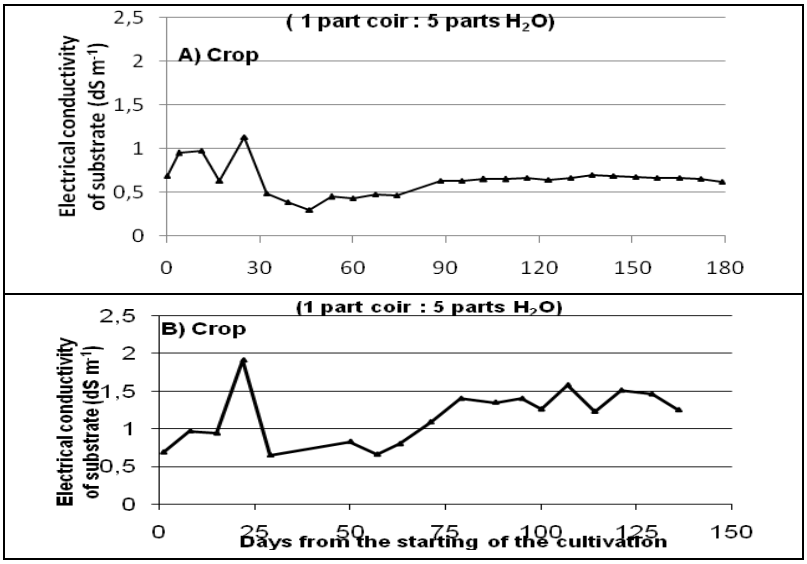

Figure 3. Fluctuations of electrical conductivity the coir substrate of soilless tomato cultivation, during the two crops development.

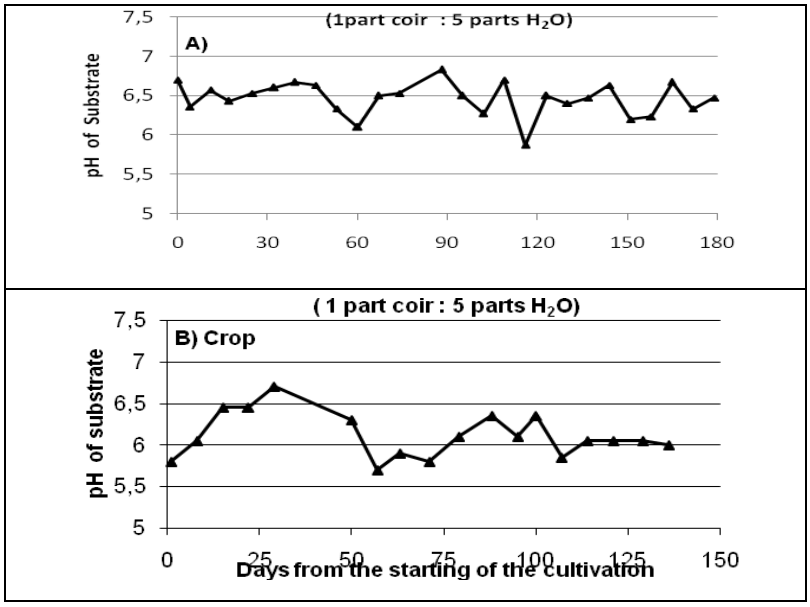

Figure 4. Fluctuations of pH values the coir substrate of soilless tomato cultivation, during of two crops development.

The increased values of electrical conductivity are accompanied by nitrate and P-Olsen forms accumulation in substrate particularly at the end of the B crop, compared with the respective values in the initial material (Table 1). In contrast, the values of pH of substrate resulted at the end of the B crop, decreased compared with the respective values of substrate, resulted at the end of the A crop and the initial substrate. The exchangeable - K forms of substrate resulted, at the end of the A and of the B crop, decreased compared to respective values of the initial substrate. In contrast, available forms Zn, Cu, Mn (extracted with DTPA) of substrate resulted, at the end of the A and of the B crops, increased compared with the respective values of the initial substrate.

Table 1. Chemical properties of the coir substrate used, before and after utilization.

Chemical Property	**Initial Coir (since the starting of the crop)**	**Final Coir at the end of the A crop (or Initial Coir for the starting of the B crop)**	**Final Coir (at the end of the B crop)**
	Commercial material	**wet basis**	
pH (1part substrate: 5parts H_2O)	6.7 ± 0.05	6.1 ± 0.05	5.75± 0.03
$CaCO_3$ (%)	0.13 ± 0.01	0.13 ± 0.01	0
Organic matter (%)	11.71 ± 1.1	8.39 ± 0.8	9.41± 1.0
CEC (cmol kg^{-1} substrate)	49.5 ± 5.7	75.2 ± 6.2	73.25± 6.3
Electrical conductivity, extract (1part substrate: 5 parts H_2O) (dS m^{-1})	0.68 ± 0.01	0.65 ± 0.01	0.94± 0.01
N -total (g kg^{-1})	0.333 ± 0.12	0,19 ± 0.05	0.56 ± 0.18
$N\text{-}NH_4^+$ (mg kg^{-1})	214 ± 14.5	22.6 ± 4.8	5.6 ± 1.7
$N\text{-}NO_3^-$ (mg kg^{-1})	119 ± 11.3	167.6 ± 19.4	172,9± 18.6
Exchangeable-Na (mg kg^{-1})	402.5± 10.2	69.0 ± 3.6	92.0 ± 5.8
P -Olsen (mg kg^{-1})	14.73 ± 2.2	80.36 ± 9.8	145 ± 14.9
Exchangeable-K (mg kg^{-1})	2072.1 ± 101.2	733.2 ± 56.7	898.9 ± 44.8
Zn -Total (mg kg^{-1})	6.03 ± 0.5	24.59 ± 1.1	21.2 ± 1.2
Cu -Total (mg kg^{-1})	-	11.11 ± 0.8	24.1 ± 1.4
Mn -Total (mg kg^{-1})	-	-	31.1 ± 4.7
Zn -DTPA (mg kg^{-1})	1.66 ± 0.07	17.53 ± 2.4	12.66 ± 1.9
Cu -DTPA (mg kg^{-1})	0.56 ± 0.02	4.60 ± 0.8	0.67 ± 0.06
Mn -DTPA (mg kg^{-1})	1.7 ± 0.1	2.85 ± 0.2	2.13 ± 0.2
Moisture (%)	79.65	87.21	82.5

Data represent average means and SE deviation

In briefly, substrate after the second cultivation period utilization, is subjected to some alteration affected by salinity accumulation from nutrient solution, or by relative decomposition of that organic material; the CEC, nitrate forms and P available values of substrate increased but K available forms decreased.

Despite the variations in pH and electrical conductivity of the nutritive solution influxes [14], the plants showed a good development as well as the foliar chemical analysis of plants (Table 2), showed satisfactory nutritional status. The annual production of the first cultivation (A crop) was 100 tn/ha, with mean fruit weight 0.25 kg and of the second cultivation (B crop), 90 tn/ha, with mean fruit weight 0.23 kg.

Table 2. Foliar analysis of plants

	N (%)	**P (%)**	**K (%)**
A crop (120 days after the starting of the cultivation)	3.47	0.65	4
B crop (90 days after the starting of the cultivation)	3.22	0.63	3.90

CONCLUSIONS

The effectiveness of a soilless cultivation system in glasshouse conditions, with coir as substrate, was evaluated, in an experiment of two successive cultivations periods. In according to these results, the produced nutrient solution, showed several fluctuations, in comparison to the values expected, concerning electrical conductivity and pH values.A certain divergence upwardly was observed of the electrical conductivity values for produced nutrient solution; as for pH, it was found also higher values, for both growing periods (A crop & B crop). With regard to the runoff solution (efflux), which seeps of the substrate, also studied during of the two crops periods, the corresponding solution was found with higher values concerning electrical conductivity and pH, in comparison with influx**.** In both crops the coir substrate reached a stabilization status in salinity, after the middle of each cultivation period, but in significantly higher levels for the second cultivation period (B crop).

Particularly, as far as it concerns **coir substrate** evaluation, after two cropping periods utilization, a certain decomposition of the organic material was observed (≈ 20%), and an increase of salinity accumulation correlated with nitrate and phosphate forms enrichment of the substrate; the pH of the substrate was reduced and a significant accumulation of Zn amounts (total and available forms) was recorded.

Despite the marked adverse effects, crops returned satisfactory yields, but a reduction of tomato production about 10%, for B crop was remarked, and that could be attributed to substrate salinity increased values. Nevertheless, coir is estimated as an excellent substrate despite the certain alteration assessed after two periods of employment; the most important is to adopt the necessary recommendations, in order to be respected the necessary settings to the system irrigation-fertilization unity.

EXPERIMENTAL SECTION

In the glasshouse of TEI of Thessalia, situated in Larissa, an open hydroponic's system, with automatic control and production unit of nutrient solutions has been established. Tomato plants in an area of 100 m^2 were cultivated, the first period lasted (A crop) from 14-10-2010 to 11-04-2011 and the second period (B crop) from 17-10-2011 to 29-02-2012. The substrate used was pressurized packages of coir (Table 1); the unit contains three stock solutions, that are in three different barrels (photo:1). The necessary amounts of solution from each barrel come out automatically, by creating the final nutrient solution regulating the EC and pH values by the unit program. According with directives of the supplier, it is recommended for tomato a nutrient solution with pH:6 and electrical conductivity EC: 2 dS m^{-1}.

The content of the three parent nutrient solutions for the first and second crop were:

A´ Barrel: (Ca^{2+} = 507, NO_3^- = 680.6, K^+= 116.8, NH_4^+= 55, Fe^{2+} = 1.8) me/L H_2O.
B´ Barrel: (Mg^{2+}=195, K^+= 644.2, H^+= 286, SO_4^{2-} = 580, NO_3^- = 115.2, PO_4^{3-} = 430) me/L H_2O.
Γ´ Barrel: 6.6 mL concentrated HNO_3 / L H_2O.

Each watering had a duration of 3 min and the inflow of the nutrient solution was 58.9 mL/min. In the first crop, the first 60 days after the starting of the crop, three watering times were applied per day, the next 50 days 4 times and the next 69 days 5 times per day. In the second crop, the first 40 days of the start of the crop, three watering times were applied per day, the next 40 days 4 times, and the next 56 days, 5 times per day.

The purpose of the experiment is to assess the chemical stability of substrate used, to investigate the effectiveness of the system that ensures the desired pH (6) and electrical conductivity values (2dS m^{-1}),and to adopt efficiently the appropriate variations in that adjustment in the unity installed.

METHODS OF ANALYSES

Coir samples were analyzed using the following methods which are referred by [15,16]:

Organic matter was analyzed by chemical oxidation with 1 mol L^{-1} $K_2Cr_2O_7$ and titration of the remaining reagent with 0.5 mol L^{-1} $FeSO_4$.

Both ammonium and nitrate nitrogen were extracted with 0.5 mol L^{-1} $CaCl_2$ and estimated by distillation in the presence of MgO and Devarda's alloy, respectively.

Available P forms (Olsen P) was extracted with 0.5 mol L^{-1} $NaHCO_3$ and measured by spectroscopy.

Exchangeable forms of potassium ware extracted with 1 mol L^{-1} CH_3COONH_4 and measured by flame Photometer (Essex, UK).

Available forms of Mn, Zn, and Cu were extracted with DTPA (diethylene triamine pentaacetic acid 0.005 mol L-1 + CaCl2 0.01 mol L-1 + triethanolamine 0.1 mol L^{-1}) and measured by atomic absorption.

For the determination of total metals Mn, Cu and Zn, 1 g of wet material of coir, were analyzed by digestion at 350 ^{0}C. According to the method described by [17]., (1974) and [18] the sample containing 10 mL HNO_3 + 5 mL $HCLO_4$ were analyzed by Atomic Absorption (Spectroscopy Varian Spectra AA 10 plus, Victoria, Australia). The detection of Mn, Cu and Zn in coir was done with the use of flame of air-acetylene mixture.

Every value of the electrical conductivity or pH, corresponds to the mean of three replicates. Statistical analyses were performed by the use of statistical program MINITAB [19]. Data represent average means and SE deviation.

REFERENCES

1. Gül A., Tüzel I.H., Tuncay Ö., Eltez R.Z. & Zencirkiran E., *International Symposium Greenhouse Management for Better Yield & Quality in Mild Winter Climates*, **1997**, *491,* pp. 389-394.
2. Dasgan H.Y. & Ekici B., *In International Symposium on Soilless Culture and Hydroponics*, **2004**, *697,* pp. 399-408.
3. Manios, V.I., Papadimitriou, M.D. and Kefakis, M.D., *Acta Hort. (ISHS),* **1995**, *408*, 11.
4. Inden, H. and Torres, A., *Acta Hort. (ISHS*), **2004**, *644*, 205.
5. Azad, A.K., Ishikawa, K., Diaz-Perez, J.C., Eaton, T.E.J. & Takeda, N., *Agricultural Sciences*, **2013**, *4*(07), 1.
6. Buwalda, F., van Os, E.A., Giacomelli, G., Samperio Ruiz, G., Vermeulen, T., van Weel, P.A. & Ruijs, M.N.A., *International Symposium on Growing Media and Soilless Cultivation*, **2013**, *1034*, pp. 201-207.

7. Rius-Ruiz, F.X., Andrade, F.J., Riu, J. & Rius, F.X., *Food chemistry*, **2014**, *147*, 92-97.
8. Sonneveld, C., Baas, R., Nijssen, H.M.C. and De Hoog, J., *Journal of Plant Nutrition*, **1999**, *22*(6): 1033.
9. Zekki, H., Gauthier, L. & Gosselin, A. *Journal of the American Society for Horticultural Science*, **1996**, *121*(6), 1082.
10. Bugbee, B., *Acta Horticulture*, **2004**, *648*, 99.
11. Bissonnette, W.M., Wainwright, R.E., Payne, C., Thompson, J., Bromley, R. and Morgan, C., U.S. Patent No. 8,261,486. Washington, DC: U.S. Patent and Trademark Office, **2012**.
12. Domingues, D.S., Takahashi, H.W., Camara, C.A. & Nixdorf, S.L., *Computers and Electronics in Agriculture*, **2012**, *84*, 53.
13. Furlani A.M.C., de Abreu M.F., de Abreu C.A., Furlani P.R. & Bataglia O.C., *International Symposium on Soilless Culture and Hydroponics*, **2004**, *697,* pp. 109-115.
14. Martínez-Cárdenas, L., Reed, D., Kent, M., Ramírez-Vallejo, P., Juárez-López, P., Cruz-Crespo, E., Bugarín-Montoya, R. and García-Paredes, J.D., *International Symposium on Growing Media and Soilless Cultivation,* **2013**, *1034*, pp. 501-504.
15. Hesse, P.R., *A Textbook of Soil Chemical Analysis*. John Murray, London, **1972**.
16. Page, A.L., Miller, R.H. and Keeney, D.R., "Methods of Soil Analysis Part 2: Chemical and Microbiological Properties. Agronomy, ASA and SSSA", Madison, Wisconsin, USA, **1982**.
17. Allen, S.E., Grimshaw, H.M., Parkinson, J.A. and Quarmby, C., "Chemical analysis of Ecological materials", Blackwell Scientific Publications, **1974**.
18. Varian, M., "Flama Atomic Absorption Spectroscopy. Analytical Methods", Varian Australia, **1989**, Publ. N0: 85-100009-00.
19. Ryan, B.F., Joiner, B.L. and Cryer, J.D., "MINITAB Handbook: Updated for release 14", **2005**, 5th edition.

STUDIA UBB CHEMIA, LX, 2, Tom I, 2015 (p. 187-199)
(RECOMMENDED CITATION)

IS STARCH ONLY A VISUAL INDICATOR FOR IODINE IN THE BRIGGS-RAUSCHER OSCILLATING REACTION?

LÉNÁRD-ISTVÁN CSEPEI[a,b,*], CSABA BOLLA[a]

ABSTRACT. In this work we studied the effect of malonic acid concentration on the Briggs-Rauscher oscillating reaction both in absence and in presence of starch, which acts as indicator for the iodine intermediate. For the starch free mixtures, the number of oscillations and the oscillation time increased with the increase of initial malonic acid concentration, while the period time showed the opposite trend. When starch was also present in the Briggs-Rauscher mixture, the number of oscillations, the oscillation time and period length were higher in comparison with the starch free mixtures with the same initial malonic acid concentration. In presence of starch, within one oscillation period, the iodine consumption segment was also longer compared to those measured for the starch free mixtures. This suggests that the starch is not only a simple visual indicator for the iodine intermediate, but it probably acts as a reservoir for iodine due to the starch-triiodide equilibrium during each oscillation cycle. As such, the starch may influence the kinetics of the reaction steps involving the iodine intermediate. Finally, we present a simple method for the treatment of the residual Briggs-Rauscher mixture which enables the removal of the strong acid, the oxidizing agents and the quantitative recovery of the Mn^{2+} catalyst in form of MnO_2. Thereby, this method enables to minimize the environmental effect of the residual mixture before disposing it.

Keywords*: Briggs-Rauscher oscillating reaction, malonic acid, iodine, starch, indicator, starch-triiodide complex, oscillation time, period time, apparent activation energy, nonlinear chemical dynamics, environmental awareness*

INTRODUCTION

The Briggs-Rauscher reaction is a prominent example of the liquid phase oscillating reactions. Although it was discovered more than four decades

[a] *Babeş-Bolyai University, Faculty of Chemistry and Chemical Engineering, Arany János Str., Nr. 11, RO-400084 Cluj-Napoca, Romania.*
[b] *Current adress: Fraunhofer Institute for Interfacial Engineering and Biotechnology IGB, Bio-, Electro- and Chemocatalysis BioCat, Straubing Branch, Schulgasse 11a, 94315 Straubing, Germany.*
** Corresponding author: cslenard@gmail.com*

ago [1], an intensified interest towards this reaction could be observed since the early 2000s.

The net chemical reaction is the iodination of an organic substrate by iodate ion and hydrogen peroxide, catalyzed by Mn^{2+} ion in acidic media [2, 3, 4]. In the first years after its discovery, thirty elementary steps were identified [3, 4] and it was found that a set of thirteen steps - known as skeleton mechanism - describes qualitatively well the nonlinear behavior of the reaction [5, 6]. This mechanism was further refined over the past one and a half decade [7-11].

The intermediates of the reaction (e.g. I_2, I^-, HOI, HIO_2, $IO_2^{\cdot}$, $HOO^{\cdot}$) show more than one extreme point – maximum and minimum – in time. The periodic changes of the iodine concentration can be seen visually: during the reaction colorless-brown-pale yellowish-colorless cycles can be observed. A few reports described that in presence of starch indicator the oscillations of iodine concentration are more visible because of the formation of the starch-triiodide complex: the color of the reacting mixture changes within one period from colorless to deep blue then to brownish and colorless again [1, 12, 13, 14, 15, 16, 17]. In some of these studies spectroscopic methods were applied to learn more details about the involvement of the iodine or starch-triiodide complex in the BR-reaction [15, 16]. Nevertheless, besides the more dramatic color change, no other differences were documented between the oscillations of the starch containing and starch free BR mixtures in the above literature sources.

It is also interesting to mention that the inorganic subset of the Briggs-Rauscher reaction is very similar to the well studied Bray-Liebhafsky oscillating reaction. The Bray-Liebhafsky reaction involves only hydrogen-peroxide, iodate ions and mineral acid. Although the iodine is an intermediate also in this chemical oscillator, up to our best knowledge the effect of starch was not studied yet on the Bray-Liebhafsky reaction.

In our previous studies we also used starch for qualitative observations concerning the iodine formation and consumption upon addition of several substances (ascorbic acid, tartaric acid, pyrogallol and salicylic acid) to the oscillating Briggs-Rauscher mixture [18, 19]. During these experiments, however, we have already noticed some quantitative differences between the oscillations of a starch free and starch containing mixture. As it is known that some organic compounds (such as ascorbic acid and other hydroxyl-group containing organics) interfere strongly with starch-iodine reaction [20], based on our experiments reported in [18, 19] it was not possible to establish what the reason for the observed differences was. These observations triggered a more systematic study on the effect of starch on the reaction [21]. We also varied the malonic acid concentration, because the iodine consumption rate within one oscillation

depends on the malonic acid concentration [13]. Therefore, our goal was also to check the complex interrelation between malonic acid, iodine and starch in this reaction. In the present work we report the phenomenological effect of starch on the oscillation parameters of Briggs-Rauscher reaction studied at different malonic acid concentrations. In the following paper we will report the effect of starch on the kinetics of iodine consumption within one period of oscillation.

RESULTS AND DISCUSSION

In the first series of experiment the initial concentration of malonic acid was varied from 0,031 to 0,199 M while keeping constant the initial concentration of potassium-iodate (0,0675 M), hydrogen peroxide (0,92 M), manganous sulfate (0,0065 M) and sulfuric acid (0,025 M) in absence of starch indicator. During the second series of measurement 0,48 mg/ml starch indicator was added, while keeping the other conditions the same as at the first series of runs. All these experiments were carried out at a temperature of 25ºC. Under every condition, the experiment was repeated typically three times in order to check for the reproducibility of the observed effects. More than that, the quantitative oscillating parameters were statistically analyzed.

The Figure 1 displays the reproducibility test at the lowest malonic acid concentration: three runs of the BR reaction recorded after each other using the same initial composition, in absence of starch. The reproducibility demonstrated on Figure 1 was typical also for measurements under every other condition.

The stock solutions A and B were mixed in the reactor; then the malonic acid and manganese sulfate containing solution C was injected by a rapid delivery piston pipette at the time indicated by the green arrow on Figure 1 (for the composition of the stock solutions A, B and C see the Experimental section).

The oscillation started immediately, without induction period after the injection of the solution C. However, the very first oscillation appearing right after the injection of the solution C was a first, incomplete oscillation, since it did not exhibit a minimum like the subsequent ones. In our previous studies [18, 19, 22, 23] we started to record the potential a few seconds after the mixing of all the three solutions, therefore the first, incomplete oscillation was not observable. After the first, incomplete oscillation there were regular oscillations, i.e. those three in the middle of the Figure 1, possessing well defined minima, maxima and similar shape. The very last oscillation was much broader and had significantly lower amplitude than the regular ones. However, when the malonic acid concentration was higher than 0,075 M, the last oscillation was also regular.

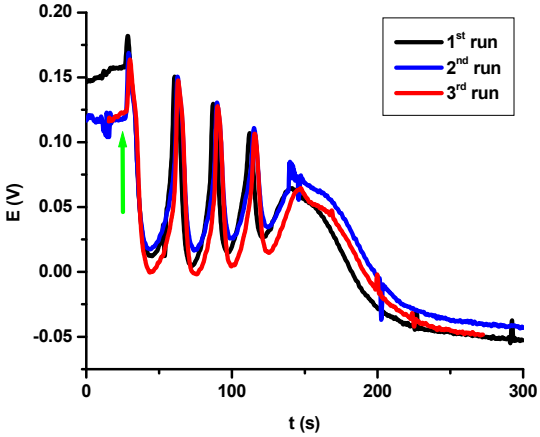

Figure 1. Reproducibility test of the oscillations in a starch free BR-mixture. The malonic acid concentration was 0,031 M.

The following oscillating parameters are considered here:

1) oscillation time (s): the time elapsed from the maximum of the first, incomplete oscillation until the minimum of the last regular oscillation. At malonic acid concentrations higher than 0,075 M the last oscillation was also included in the length of the oscillation time
2) period time (s): the time elapsed between two consecutive oscillatory maxima,
3) amplitude (V): the potential difference between a maximum and minimum,
4) number of oscillations: only the regular oscillations were counted. The last broad oscillation observed at low malonic acid concentrations and the „two-third oscillation" were not taken into account.

As the Figure 1 demonstrates, the peak shapes and parameters are well reproducible. The high frequency potential fluctuations with minor amplitude appeared due to electric noise in the electronic recording system.

Qualitative comparison of the oscillations of starch free and starch containing BR-mixtures

In the followings, the qualitative features of the BR reaction are compared in absence and in presence of starch while keeping constant the initial concentrations of malonic acid, hydrogen peroxide, sulfuric acid and iodate-, manganous ion (Figure 2). It is notable that in presence of starch, the number of oscillations and the oscillation time is much higher than in the starch

free mixture. On the other hand, the period times are visibly longer and the amplitudes throughout the reaction are more uniform when starch is present in the reacting mixture.

As described earlier, one period of oscillation on the E(V) versus time plot consists of four distinct segments [19, 25]: two decreasing segments and two increasing segments with different slopes and lengths. The color changes of the oscillating mixture during one period are described below:

In the starch free mixture, brown coloration appeared during the steep decreasing segment, which indicates iodine formation. During the slightly increasing slope the brown color faded out gradually to pale yellow, indicating relatively slow reaction between iodine and the enolic form of the malonic acid. During the rapidly increasing segment, the mixture became transparent and remained transparent during the relatively slowly decreasing segment. Then the cycle repeated. After the last oscillation, the color of the mixture became deep brown, indicating strong iodine formation and accumulation.

In the starch containing mixture the color turned into deep blue during the fast decreasing segment and it faded out to slightly brownish during the slow increasing slope. During the fast increasing and the relatively slowly decreasing segment the mixture was colorless. At the end of the oscillations the mixture was deep blue because of the formed iodine.

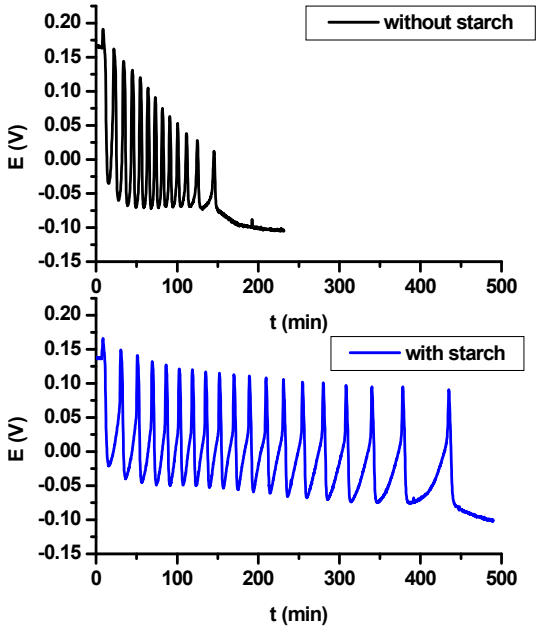

Figure 2. The oscillations recorded in a BR mixture containing 0,131 M malonic acid. The starch concentration: black – 0,00 mg/ml, blue – 0,48 mg/ml.

Quantitative comparison of the oscillations of starch free and starch containing BR-mixtures

The effect of malonic acid concentration on the quantitative parameters listed above is presented here.

First, the number of oscillations was plotted versus the initial malonic acid concentration for both the starch free and starch containing mixtures. A linear increase can be observed in each case (Figure 3, top). In presence of starch, the number of oscillations was approximately two times higher than in the case of starch free mixtures.

The oscillation time increased approximately linearly with the malonic acid concentration for the starch free mixture and apparently exponentially for the starch containing mixture (Figure 3, bottom).

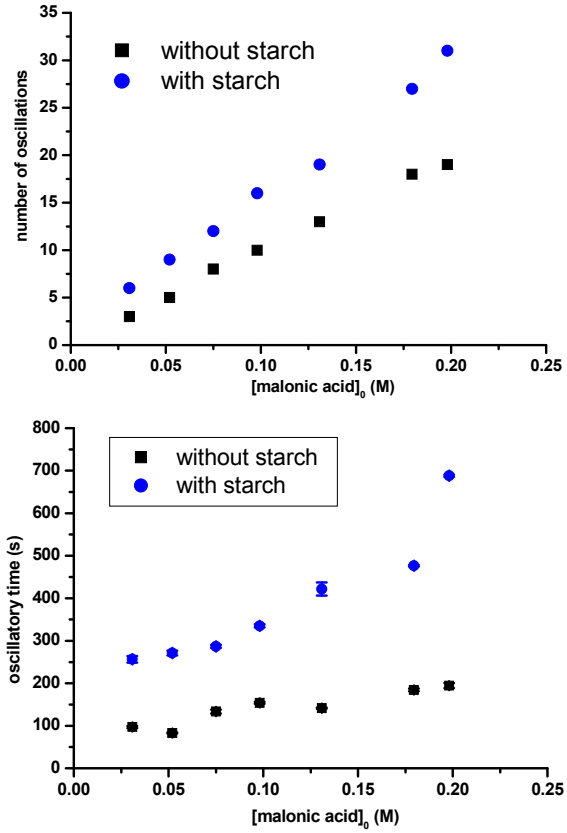

Figure 3. The effect of malonic acid concentration on the number of oscillations and the oscillation time.

In general, the length of the iodine consumption segment (which was evaluated by measuring the lenght of the slowly increasing segment after the potential minimum) was dominant within one cycle of oscillation. This observation is in agreement with the observation of Furrow [13]. In the case of starch free mixture, the iodine consumption segment was 38-45% of the period time. On the other hand, in presence of starch, the iodine consumption constitutes 48-60% of the period time.

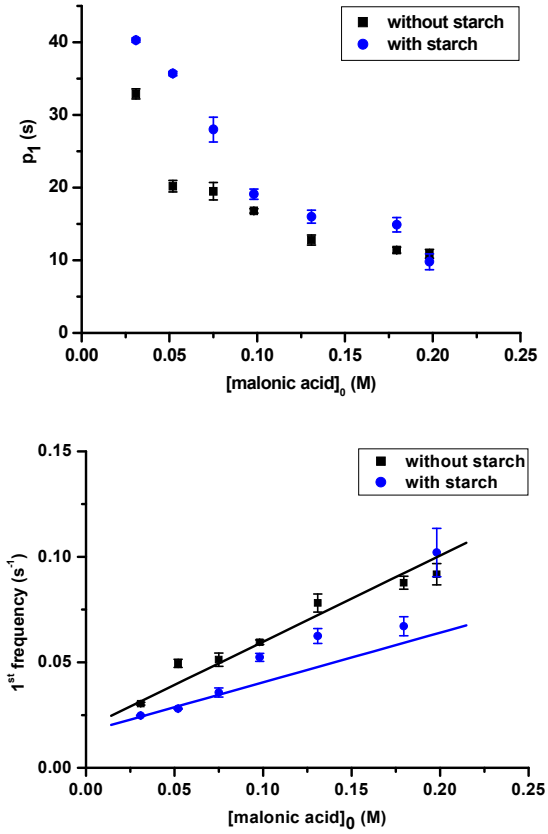

Figure 4. The effect of malonic acid concentration on the first period time and frequency, respectively.

The period time was decreasing with the increase of the malonic acid concentration. This trend was the same for both the starch free and starch containing mixture. However, in the starch containing the period times were higher (Figure 4, top).

Table 1. The dependence of the frequency (f) of the first oscillation on the initial malonic acid concentration.

c_{starch} (mg/mL)	Equation	R^2
0,00	$f = 0{,}02+0{,}41\cdot[\text{malonic acid}]_0$	0,9835
0,48	$f = 0{,}02+0{,}19\cdot[\text{malonic acid}]_0$	0,9090

Similarly to the observation of Furrow, the reciprocal period time (that is equal to the frequency) increases approximately linearly with the substrate concentration [13]. This linear dependence is given on Figure 4 bottom, while the equations of the straight lines are in the Table 1.

Finally, no trend was found between the amplitude of the first three oscillations and the initial concentration of the malonic acid, irrespectively whether starch was present or absent in the mixture.

Determination of the apparent activation energy for the starch containing BR-mixture

In the third series of measurements the reaction temperature was varied between 26 and 52ºC for a BR mixture with 0,199 M malonic acid and 0,48 mg/ml starch. The apparent activation energies were evaluated.

The apparent activation parameters of the BR reaction are usually determined from the temperature dependence of the oscillation time [26, 27] and the period time [12, 25]. In the literature it was noted that both of these quantities decrease exponentially with the temperature. The dimension of the reciprocal oscillation time and period time is the same as the dimension of a first-order rate constant ($second^{-1}$).

The Arrhenius plot of the reciprocal oscillation time and period time, respectively lead to straight lines (Figure 5 and 6). From the slope of these lines the apparent activation energy of the reaction was calculated corresponding to the starch containing mixture. The values are compiled in Table 2, among the apparent activation energies reported in the literature. Due to the fact that the reaction mechanism is very complex – it consists of at least 30 elementary steps in absence of starch – the determined activation energy does not correspond to any of the elementary steps of the BR reaction, but it is „global" or apparent activation energy. In the presence of starch, there is at least one additional equilibrium reaction corresponding to the formation of the starch-triiodide complex. Therefore, due to the above described complexity, it is very difficult to draw conclusions on the effect of starch on the apparent activation energy.

On the other hand, because the reaction mechanism is so complex and the compositions of the BR mixtures reported in the literature are different (Table 2), the apparent activation energies are not comparable directly [27].

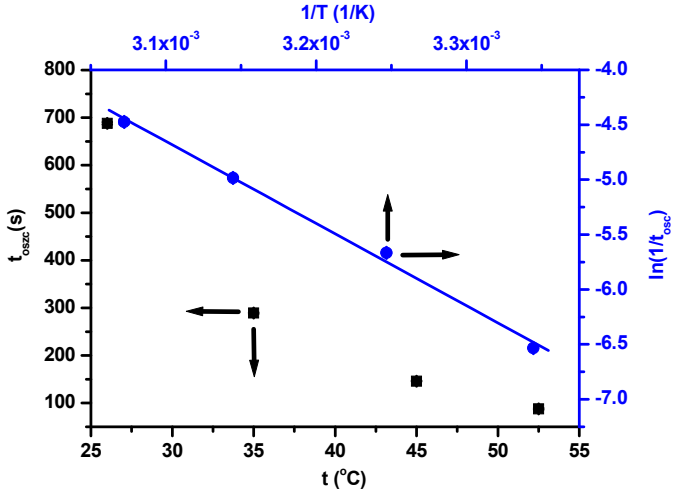

Figure 5. The effect of temperature on the oscillation time (black squares) and the corresponding Arrhenius-plot (blue dots). The malonic acid and starch concentration was 0,199 M and 0,48 mg/ml, respectively.

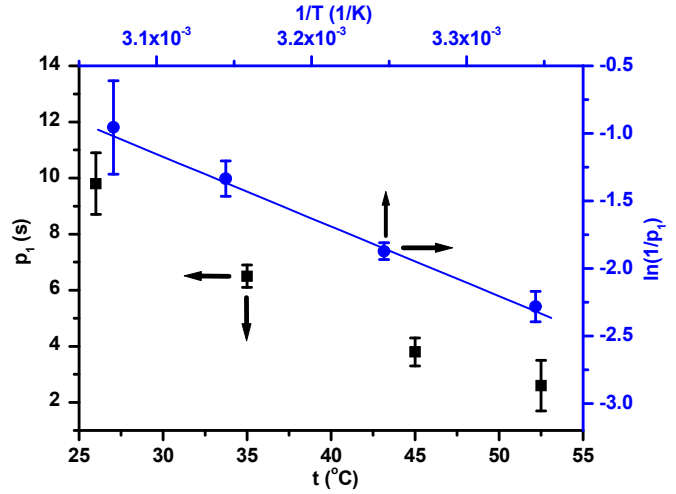

Figure 6. The effect of temperature on the first period time (black squares) and the corresponding Arrhenius-plot (blue dots). The malonic acid and starch concentration was 0,199 M and 0,48 mg/ml, respectively.

Table 2. The apparent activation energy of BR mixtures with different compositions. Ea (I.) – activation energy determined from the temperature dependence of the oscillation time. Ea (II.) – activation energy determined from the temperature dependence of the period time. (a) – this work, n.a. – data not available.

Ref. / Comp.	(a)	23	25	26	27
$[H_2O_2]_0$ (M)	0,92	0,92	0,48	1,20	1,20
$[MA]_0$ (M)	$1,99 \cdot 10^{-1}$	$5,0 \cdot 10^{-2}$	$5,0 \cdot 10^{-2}$	$5,0 \cdot 10^{-2}$	$5,0 \cdot 10^{-2}$
$[KIO_3]_0$ (M)	$6,75 \cdot 10^{-2}$	$6,75 \cdot 10^{-2}$	$6,75 \cdot 10^{-2}$	$6,0 \cdot 10^{-2}$	$3,33 \cdot 10^{-2}$
$[H_2SO_4]_0$ (M)	$2,50 \cdot 10^{-2}$	$2,50 \cdot 10^{-2}$	$2,50 \cdot 10^{-2}$	$4,0 \cdot 10^{-2}$	$2,66 \cdot 10^{-2}$
$[MnSO_4]_0$ (M)	$6,50 \cdot 10^{-3}$	$6,50 \cdot 10^{-3}$	$6,50 \cdot 10^{-3}$	$6,0 \cdot 10^{-3}$	$6,67 \cdot 10^{-3}$
c_{starch} (mg/ml)	0,48	0,00	0,00	0,00	0,00
E_a(I.) (kJ/mol)	62±3	38±2	n.a.	57	68±2
E_a(II.) (kJ/mol)	42±1	51±1	61±7	n.a.	n.a.

CONCLUSIONS

The results of our experiments show that starch does not act only as a simple indicator of iodine intermediate in the oscillatory Briggs-Rauscher reaction. In the presence starch containing mixtures, the number of oscillations and also the period time of oscillations increased compared to the starch free mixture. Additionally, the reaction step involving the iodine and the malonic acid seems to be slowed down significantly in presence of starch in the reacting mixture. This may hint towards the fact the starch acts as a „reservoir" for iodine due to the starch-triiodide reaction, and it may change significantly the kinetics of the reaction steps in which the iodine (and in general, the triiodide anion) is involved. One of these steps is the iodination of the malonic acid, which produces the iodide ion. Another important step is the reaction of iodine with water which produces HOI, another key intermediate of the Briggs-Rauscher reaction. Last but not least, iodine may catalyze the decomposition of the diiodomalonic acid which accumulates gradually over the Briggs-Rauscher reaction [9]. Therefore, in presence of starch, the kinetics of the diiodomalonic acid decomposition step may also be slowed down.

EXPERIMENTAL SECTION

Two stock solutions were prepared according to the procedure described in our previous reports (solution A: 1,84 M hydrogen peroxide, and solution B: 0,27 M potassium iodate and 0,1 M sulfuric acid) [18, 19, 22, 23, 24]. The stock solution C contained 0,026 M manganese sulfate and different malonic acid

concentrations (0,124, 0,208, 0,300, 0,392, 0,542, 0,720, 0,793 M). Starch solution was prepared by dissolution of starch in water at 60ºC and cooled down to room temperature. All chemicals were used without any further purification: H_2O_2 (Merck, p.a), KIO_3 (AnalytiCals, p.a), H_2SO_4 (Riedel de Haen, p.a), $CH_2(COOH)_2$ (Reachim, p.a), $MnSO_4$ (Reactivul, p.a), starch (Reactivul, p.a). Doubly distilled water was used for the preparation of all the solutions.

The stock solutions were mixed in a double walled glass reactor connected to a thermostat. After mixing, the composition of the BR reaction mixture was the following: $[H_2O_2]_0$=0,92 M, $[H_2SO_4]_0$=0,025 M, $[MnSO_4]_0$ = 0,0065 M, $[KIO_3]_0$ = 0,0675 M, whereas the concentration of malonic acid was 0,031; 0,052; 0,075; 0,098; 0,131; 0,180; 0,199 M. A magnetic stirrer and a submersible magnetic bar were used for the thorough stirring of the BR mixture. The reaction was monitored employing an iodide ion selective electrode (Radelkis, Budapest) and a double junction saturated calomel electrode as reference electrode. The variation of the potential in time has been registered using a computer eqipped with a National Instruments® data acquisition card. Then the E(V) vs time plots along with the further data analysis were made in Origin program.

The first series of measurements was carried out without addition of starch, while the second in presence of 0,48 mg/ml starch. Both measurement series were done at 25 ºC. The third series of measurement consisted of temperature variation in four steps between 26 and 52 ºC, using the following BR composition: $[H_2O_2]_0$ = 0,92 M, $[H_2SO_4]_0$ = 0,025 M, $[MnSO_4]_0$ = 0,0065 M, $[KIO_3]_0$ = 0,0675 M, [malonic acid]$_0$ = 0,199 M, and starch concentration of 0,48 mg/ml. Three measurements were carried out under every condition. The parameters (oscillation time, period time, number of oscillations, amplitude) were averaged over the three measurements, and the standard deviation was calculated. The standard deviation was used as weighting factor for linear regression.

We present here also the treatment method that we developed for decreasing significantly the environmental impact of the residual reaction mixture. The residual BR mixture contains always unreacted hydrogen peroxide, sulphuric acid, manganese- and iodate ions and sometimes significant amounts of iodine from the decomposition of iodo-malonic acid. Since all of these compounds are of environmental concern, all the residual BR-mixture was collected in a larger beaker and treated in the following way: first sodium-tiosulphate was added which transformed the iodine into iodide ion. The iodide ion reacted with the residual iodate ion and produced iodine. Therefore, the sodium-tiosulphate was added until the iodine formation completely ceased – this signaled that all the residual iodate ions were completely consumed from the mixture. Then sodium carbonate was added in order to reduce the acidity of the mixture. At slightly basic pH the Mn^{2+} ion was oxidized to MnO_2 by the dissolved O_2 (the oxygen being a product of the BR-reaction as well) [29].

$$2\ Mn^{2+} + 4HO^- + O_2 \rightarrow 2MnO_2 + 2H_2O \qquad (R1)$$

The formed MnO_2 decomposed catalytically the residual amounts of H_2O_2 to O_2 and H_2O. After sedimentation, the MnO_2 was separated by filtration. Therefore, by treating of the residual BR-mixture with two inexpensive chemicals such as sodium-tiosulphate and carbonate it was possible to remove all the strong oxidizing agents, the mineral acid and to recover quantitatively the heavy metal ion in form of MnO_2. At the end, the solution contained only sodium-, potassium-, iodide, sulphate- and residual tiosulphate ions which are environmentally much less harmful.

ACKNOWLEDGEMENT

L. I. Csepei acknowledges the scholarship awarded by the PROFIL Group for the Cluj-Szeged Student Exchange Program to the University of Szeged, Hungary, Faculty of Natural Sciences. L.I. Csepei thanks Dr. G. Szabó for sharing part of her lab-equipments and for the valuable discussions; Prof. Dr. I.C. Popescu for the iodide ion selective electrode.

REFERENCES

1. T.S. Briggs, W.C. Rauscher, *J. Chem. Educ.*, **1973**, *50*, 496.
2. D.O. Cooke, *Int. J. Chem. Kinet.*, **1980**, *12*, 683.
3. S.D. Furrow, R.M. Noyes, *J. Am. Chem. Soc.*, **1982**, *104*, 38.
4. S.D. Furrow, R.M. Noyes, *J. Am. Chem. Soc.*, **1982**, *104,* 42.
5. S.D. Furrow, R.M. Noyes, *J. Am. Chem. Soc.*, **1982**, *104*, 45.
6. P. De Kepper, I.R. Epstein, *J. Am. Chem. Soc.*, **1982**, *104*, 49.
7. S.D. Furrow, R. Cervellati, G. Amadori, *J. Phys. Chem. A*, **2002**, *106*, 5841.
8. G. Szabo, A. Csavdari, L. Onel, G. Bourceanu, Z. Noszticzius, M. Wittmann, *J. Phys. Chem. A*, **2007**, *111*, 610.
9. R. Cervellati, E. Greco, S.D. Furrow, *J. Phys. Chem. A*, **2010**, *114*, 12888.
10. R. Cervellati, S.D. Furrow, *Russ. J. Phys. Chem. A*, **2013**, *87*, 13, 2121.
11. G. Holló, K. Kály-Kullai, T.B. Lawson, Z. Noszticzius, M. Wittmann, N. Muntean, S.D. Furrow, G. Schmitz, *J. Phys. Chem. A,* 2014, 118, 26, 4670.
12. A.K. Dutt, R.S. Banerjee, *Z. Phys. Chem. Leipzig*, **1982**, *263*, 2, 298-304.
13. S.D. Furrow, *J. Phys. Chem.*, **1995**, *99*, 11131.
14. R. Cervellati, S.D. Furrow, S. De Pompeis, *Int. J. Chem. Kinet.*, **2002**, *34* (6), 357.
15. M.J. Mahon, A.L. Smith, *J. Phys. Chem.*, **1985**, *89*, 1215.

16. B.Z. Chowdry, A.P. Mendham, J. Tetteh, R. Withnal, *ChemPhysChem*, **2002**, *5*, 443.
17. S.D. Furrow, *J. Chem. Ed.*, **2012**, *89*, 1421.
18. L.I. Csepei, A Briggs-Rauscher reakció oszcillációinak leállítása (The Cessation of the Oscillations of Briggs-Rauscher Reaction), Bachelor Diploma Thesis, Babes-Bolyai University, Faculty of Chemistry and Chemical Engineering, **2005**.
19. L.I. Csepei, Cs. Bolla, *Studia UBB Chemia*, **2009**, *54*, 4, II, 249.
20. S.S. Sharma, S. Sharma, V.K. Rai, *Annals of Botany*, **1990**, *65*, 281.
21. L.I. Csepei, Cs. Bolla, I. Pontos, The Effect of Malonic Acid Concentration on the Briggs-Rauscher Reaction in Presence and Absence of Starch, 13th International Conference of Chemistry, Hungarian Technical Scientific Society of Transylvania, Cluj-Napoca, 8-11 November **2007**.
22. L.I. Csepei, Inhibiţia reacţiei oscilante Briggs-Rauscher cu acid salicilic (Inhibition of Briggs-Rauscher Reaction with Salicylic Acid), Master Diploma Thesis, Thesis, Babes-Bolyai University, Faculty of Chemistry and Chemical Engineering, **2006**.
23. L.I. Csepei, A hőmérséklet hatása a Briggs-Rauscher reakcióra (The effect of Temperature upon the Briggs-Rauscher Oscillating Reaction), 8th Scientific Conference on Technical Sciences, 7-9 April **2006**.
24. L.I. Csepei, Cs. Bolla, *Studia UBB Chemia*, **2011**, *55*, I, 285.
25. I. Pontos, Bachelor Thesis, Babes-Bolyai University, Faculty of Chemistry and Chemical Engineering, **1999**.
26. R. Ramaswami, N. Ganapathisubramanian, *J. Chem. Educ.*, **1979**, *56*, 321-325.
27. R. Cervellati, K. Höner, S.D. Furrow, F. Mazzanati, S. Costa, *Helv.Chim. Acta*, **2004**, *87*, 133-155.
28. J.A. Thoma, D. French, The Starch-Iodine-Iodide Interaction. Part I. Spectrophotometric Investigations, *J. Am. Chem. Soc.*, **1960**, *82 (16)*, 4144-4147.
29. D. Harvey, Modern Analytical Chemistry, McGraw Hill, **2000**, 345-346.

STUDIA UBB CHEMIA, LX, 2, Tom I, 2015 (p. 201-206)
(RECOMMENDED CITATION)

QUANTITATIVE ANALYSIS OF THE NONCOMPLIANT LANDFILL CONSTITUENTS

MICHAELA BIANCA SOPORAN[a,*], OVIDIU NEMEŞ[a]

ABSTRACT. In order to establish the nature and composition of the municipal wastes located in the municipal landfill Pata Rât, Cluj-Napoca, ten samples were collected in depth, every meter. Aiming the landfill characterization, the nature and the percentage composition of the materials was determinate.

Keywords: *waste, landfill, material, composition.*

INTRODUCTION

The aim of this work is to determine the landfill waste structure to further define the strategies concerning the waste selection and the obtained gas quantities. Studies were made on material degradation from noncompliant landfills, nearby Cluj-Napoca. We considered the analysis is influenced by waste composition distribution randomly deposited over time. The waste collection from an area of approximately 400.000 inhabitants was not done selective and the storage was mixed and uncontrolled. During the filling process, there was no plan for covering the storage and now, it is almost impossible to specify the time when the waste was disposed. The prolonged time of approximately 35 years of filling and the constituent layers resulted from the evolution of all materials and products that were stored indicate no periodicity in the composition of layers, by height. [1], [2]

This paper highlights the composition of waste stored in Pata Rât landfill. We mention that this study is the first which was achieved on this site.

RESULTS AND DISCUSSION

Knowing the waste nature and distribution is a very important way in determining the method of landfill operation [3-8]. In order to show the more precisely as possible the waste distribution in the Pata Rât landfill we

[a] *Technical University of Cluj-Napoca, Faculty of Materials and Environmental Engineering, Department Environmental Engineering and Sustainable Development Entrepreneurship, 103-105 Muncii Ave, Cluj-Napoca, Romania.*
[*] *Corresponding author: bianca.soporan@yahoo.com*

have analysed 10 samples collected as described. The composition variation of municipal waste is depicted in figure 1, from a to j.

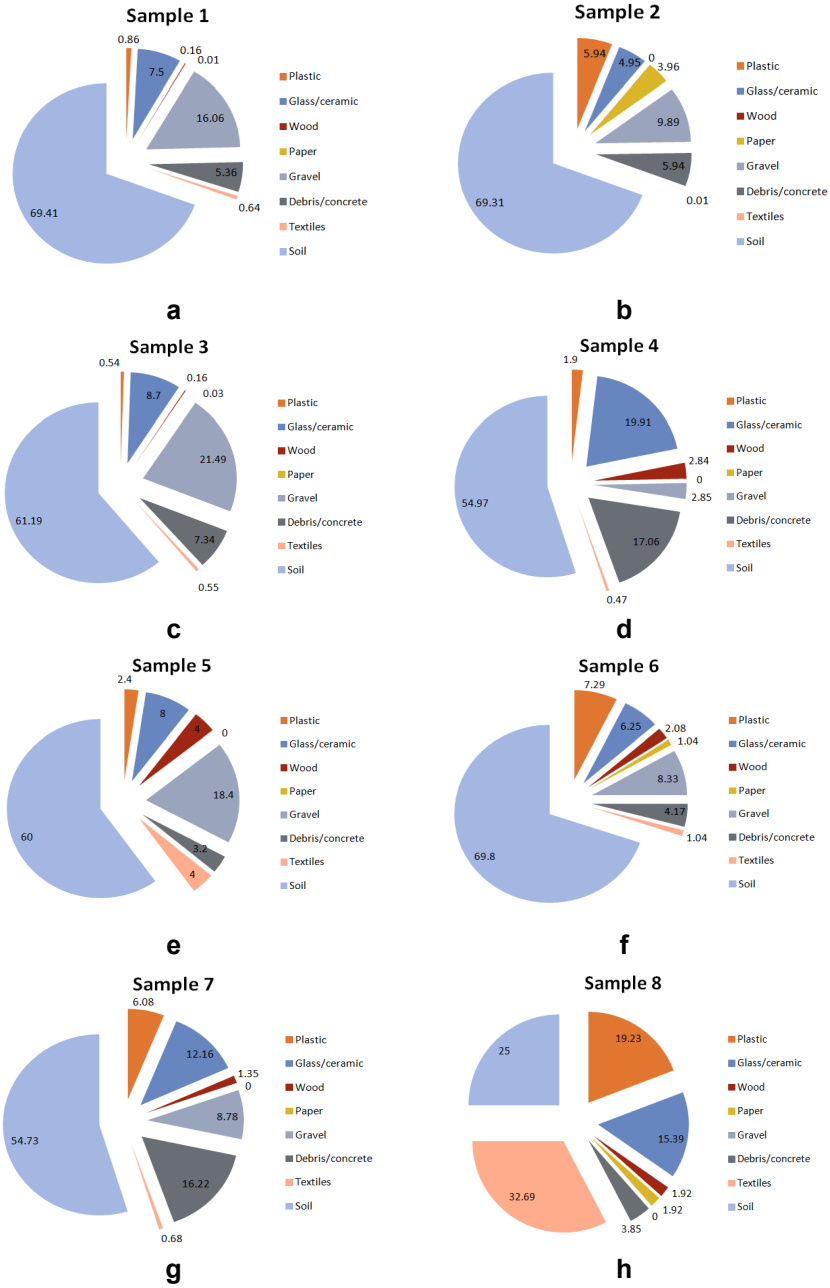

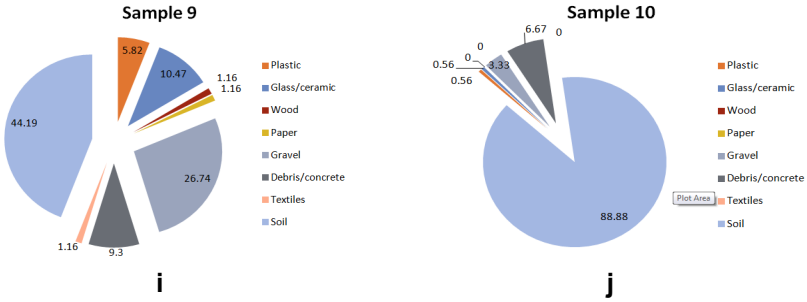

Figure 1. Material percentage variation in municipal waste samples

Analysis of samples has led to the establishment of their composition which varies as follows:

- plastic 0.56 ÷ 23% range;
- glass in 0.56 ÷ 19.91% range;
- wood in 0 ÷ 4% range;
- paper in 0 ÷ 3.96% range;
- textiles in 0 ÷ 32.69% range ;
- construction debris and concrete in 3.2 ÷ 17.06% range;
- soil in 25 ÷ 88% range.

In order to find the average composition of the waste layer, the following procedure was adopted: the minimum and the maximum values was removed from each category, then irrelevant results were excluded for establishing the results taken into account to determine the average composition and finally, averages values were calculated for each category of material. The irrelevant results had been considered as the highest maximum and the lowest minimum. [1]

After the plastic percentage from landfill was calculated, using data from Figure 1 and the above procedure, the following situation appeared: the maximum and minimum elimination (sample 3 and sample 8), the considered outcome (sample 1, sample 2, sample 4, sample 5, sample 6, sample 7, sample 9 and sample 10). The average balanced concentration is:

$$C_{A\ plastic}\,[\%] = 3.85625\% \cong 3.86\%.$$

Similarly, the average compositions of other components was calculated. Considering the results above, the following average composition of the analysed landfill area was calculated without minimum and maximum elimination).

The results of applying this methodology are shown in Table 1:

Table 1. The municipal waste average composition in Pata Rât landfill, Cluj-Napoca

Concentration	UM	Balanced average	Average
Plastic	%	3.86	5.06
Glass/ceramics	%	9.18	9.39
Wood	%	1.21	1.37
Paper	%	0.52	0.81
Gravel	%	11.14	11.59
Debris/concrete	%	7.36	7.91
Textiles	%	1.07	4.12
Soil	%	60.45	59.75

The analysis made showed that the macroscopic recoverable materials (plastic, glass, wood, paper, textiles) has an approximate share of 20%. The inert material, (gravel and debris) has a share of approximately 20%, while the resulting waste degradation along with the soil have a share of 60%.

In this analysis, we have taken into account that the researches on municipal waste which contains also high quantities of construction and demolition waste and soil layers from the excavations and coatings. Therefore, we consider sampling in each layer cannot disregard this fact, so we propose a method to assess the potential recovery status of a non-compliant landfill.

Landfill materials can be grouped in three major parts: the recoverable component (macro); the inert component; the resulted component from biodegradable waste degradation.

In order to determine the components percentage, the following procedure was proposed: zoning the deposit according to historical known deposit activity; preliminary assessment of the areas according to their potential; establishment of potential components for analysis and evaluation at the macroscopic level; mapping of potential analysed areas; source and operating decisions analysis.

Excluding technological exploitation issues, we proposed a method for assessing the potential by determining the waste components. Considering that landfill was made randomly, the method for determining components should be based on vertical and horizontal sampling.

Vertical sampling step should be of 1-2 m and horizontal sampling step should be 10-15 m. The propose method is based on the experiment made to determine the landfill material degradation. The assumption made in the sense that there was a filling order and the corresponding specified time, was not checked by the measurements.

CONCLUSIONS

Analysing the results of municipal waste composition from noncompliant landfill nearby Cluj-Napoca, we found that we cannot draw a clear conclusion on the relationship between the values measured and the layer from which the sample had been taken. We believe that waste was not deposited successively, in an order from the bottom to the top. At the same time, the waste deposit randomly determined sequence of different compositions that cannot be characterized or assigned to a certain period of time.

We proposed a useful landfill characterization, knowing that the filling and the technological treatments were random and difficult to quantify. We made this analysis as a characterization of noncompliant landfill components.

EXPERIMENTAL SECTION

In order to determine the material composition of municipal waste from noncompliant Pata Rât landfill, Cluj-Napoca, a 10 m deep driller pit was realised and sampled every meter.

Drilling was made with a mobile drilling facility operated by SC Minesa - Research and Design Institute of Mining SA - Cluj-Napoca. [2]

Analyses were performed in the *Laboratory Testing of National Research and Development Institute for Industrial Ecology*, ECOIND, from Bucharest.

The tests made on samples for determining the composition of deposited materials were done in two stages: determination of macro characterization and the micro state of degraded waste.

ACKNOWLEDGMENTS

Project: *Parteneriat interuniversitar pentru excelență în inginerie* - PARTING, agreement: POSDRU/159/1.5/S/137516.

REFERENCES

1. M.B. Soporan, *Studies on municipal waste degradation and physical-chemical activity assessment in noncompliant landfill* - PhD Thesis, Technical University of Cluj-Napoca, Faculty of Materials and Environmental Engineering, Department of Environmental Engineering and Sustainable Development Entrepreneurship, Cluj-Napoca, Romania, **2012**, chapter 3.

2. ***, Protocol contract research type Partnerships, *VALENDEM* acronym, 2nd stage, 3rd phase, *Preliminary Experiments for Landfill Gas Characterization,* Technical University of Cluj-Napoca*,* **2011**, chapter 3.
3. M.B. Soporan, V.F. Soporan, G. Bătrînescu, E.A. Cociș, O. Nemeș, *Studia UBB Chemia*, **2012**, *3*, 5.
4. M.B. Soporan, V.F. Soporan, O. Nemeș, E.A. Cociș, *Reviews on opportunities of landfill gas recovery*, SIDOC Project – Doctoral students' session, SICOM, Technical University of Cluj-Napoca, Romania, 21 iunie **2012**.
5. M.T. Barral Silva, A.M. Menduina, Y.C. Seijo, F. Diaz-Fierros Viqueira, *Waste Management & Research*, **2007**, *25*, 99.
6. Y. Zhao, L. Song, R. Huang, L. Song, X. Li, *Waste Management & Research,* **2007**, *25*, 130.
7. ***, European Energy and Transport - Trends to 2030 - update 2007, http://ec.europa.eu/dgs/energy_transport/figures/trends_2030_update_2007/energy_transport_trends_2030_update_2007_en.pdf;
8. ***, European Environment Agency, The road from landfilling to recycling: common destination, different routes, ISBN: 978-92-9167-930-0, http://www.eea.europa.eu/publications/brochure_2007_4;
9. ***, United States Environmental Protection Agency, Washington, D.C. 20460, Conducting Remedial Investigations/Feasibility Studies for Municipal Landfill Sites, http://www.epa.gov/superfund/policy/remedy/pdfs/540p-91001-s.pdf

STUDIA UBB CHEMIA, LX, 2, Tom I, 2015 (p. 207-218)
(RECOMMENDED CITATION)

ENVIRONMENTAL IMPLICATIONS CONCERNING THE CHEMICAL COMPOSITION AND PARTICLE DISTRIBUTION OF ANTI – SKID MATERIAL

DANA FLORINA MUNTEAN[a,*], ILARIE IVAN[b], LIANA MURESAN[a]

ABSTRACT. Anti skid material (AM) used to improve the traffic conditions could affect the particulate matter emissions during winter. The investigated AM sample contains silica particles to improve the friction coefficient between tires and road surface and crystalline sodium chloride as anti glaze agent. We found also some interesting rusty particles containing iron hydroxide (lepidocrocite and goethite) mixed with fine quartz sliver. Compression test shows that those particles have a low strength being able to be disintegrated in harsh traffic conditions. The powder resulted after crushing of rusty particles feature fine fractions with diameter in the range of 1 – 10 μm. Such fractions were found in the collected sedimenting particles (SP) proving their ability to be suspended in atmosphere. The monitoring performed with Automatic Monitoring Air Quality Stations shows the average values for $PM_{2.5}$; PM_{10} and SP are below the maximum accepted limit. However the registered values were high in days with intensive car traffic and lower in other days. The situation could be improved by a proper sorting of rusty particles from re-circulated anti skid material.

Keywords: *anti - skid material, particulate matters, lepidocrocite, PM_{10}, $PM_{2.5}$*

INTRODUCTION

Particulate matter (PM) monitoring is one of the main environmental issues in the European Union. Several regulations were adopted in order to develop a suitable management of such emissions [1, 2]. PM_{10} and $PM_{2.5}$ are the reference for particulate emissions from various urban activities [3, 4]. The health risk is increased for the monitored particulate matter emissions (e.g. $PM_{2.5}$ and PM_{10}) due to their ability to be inhaled. The risk depends on the aerosol size and the breathing air velocity [5], related to the possibly

[a] *Protection Agency Cluj, Calea Dorobanţilor Str., No. 99, RO-400609, Cluj-Napoca, Romania.*
[b] *Technical University of Cluj-Napoca, Muncii Ave. No. 103 -105, RO-400641, Cluj-Napoca, Romania.*
* *Correspondent author: muntean_nina@yahoo.com*

harmful components. Previous studies show a heterogeneous composition for PM_{10} and $PM_{2.5}$ which contains mainly minerals but also organic phases depending on the source. Anthropogenic activities, as well as acid rain and particulate emission, present erosive action on the environment being a major source of particulate matter [6, 7]. Another major anthropogenic source is the automotive traffic by combustion emission as well as floating mineral particles suspension due to the air currents.

For instance, automotive traffic PM emission measured in 2011 in Istanbul shows 28.5 % in winter and only 3.9 % in summer [8]. Why more PM emission in winter? It is an interesting subject to follow. The automotive traffic particulate emission have two major sources: combustion particles such as soot and organic aerosols (which depends on the each car combustion system and filters) [9, 10] and mineral fine fractions resulted from the tires interaction with the roads surface (which feature a strong dependence on the weather and precipitation level) [11, 12]. It was observed that soot and organic aerosols have small diameters in the range of PM2.5 meanwhile mineral particles are rather situated in PM_{10} range.

The road dust induces air floating particles due to the interaction with the moving cars [13, 14]. An important source of minerals in the dust is the asphalt and the road shoulder erosion at the contact with the car tires [12]. The breaking procedure enhances the abrasion, which increases with the friction coefficient. Anti – skid material is often used to adjust the road friction coefficient during the winter. This granular material acts as a rough dust between the tire and the road surface. It is subjected to an average grinding in such condition affecting its structure, certainly being able to release fine mineral fractions. These are incorporated into the road dust and further suspended in the air [12].

Similar study evidence the re-suspension tendency for the sedimenting particles on the adjacent snow layers due to their small size which are very sensitive to a significant modification of air velocity [14, 15]. The re-suspension process act mainly due to the lower cohesive forces observed for the fine particles which are lifted up by ascension force. Such mechanism could increase the PM_{10} and $PM_{2.5}$ air level during winter when is expected to be lower than in summer.

The anti skid material prove to be a major pollution source during winter. All mention aspects reveals that the mechanical behavior of the anti – skid material under traffic condition is the cause of pollution increasing. Such properties are directly influenced by the chemical composition and particle dispersion. The aim of present paper is to analyze the composition of anti-skid material used in Cluj-Napoca and to identify it's components in the PM_{10} and $PM_{2.5}$ emissions.

RESULTS AND DISCUSSION

AM contains two kinds of components: silica particles (mended to increase the friction coefficient between cars tires and road surface) and an anti – frost agent to prevent the glaze formation (usually sodium chloride is used).

The collected AM samples have a composition based on silica particles ranging from 1 to 10 mm. The total mineral amount represents 80 % and the rest of 20 % is the sodium chloride as anti – frost agent. A closer observation of the collected samples evidence silica particles having rounded shape and some intriguing brown particles (rusty like) having an unknown nature. They seem to be mineral conglomerates with a complex microstructure.

Sodium chloride particles are crystallized in cubic system featuring large crystals having cubic and octahedral particles as typical forms related to the BCC structure.

The mineral composition of AM sample was determined by XRD spectroscopy. The AM particles were grinded in a ball mill to obtain a powder suitable to be subjected at XRD investigation. The obtained diffractogram is presented in Figure 1a.

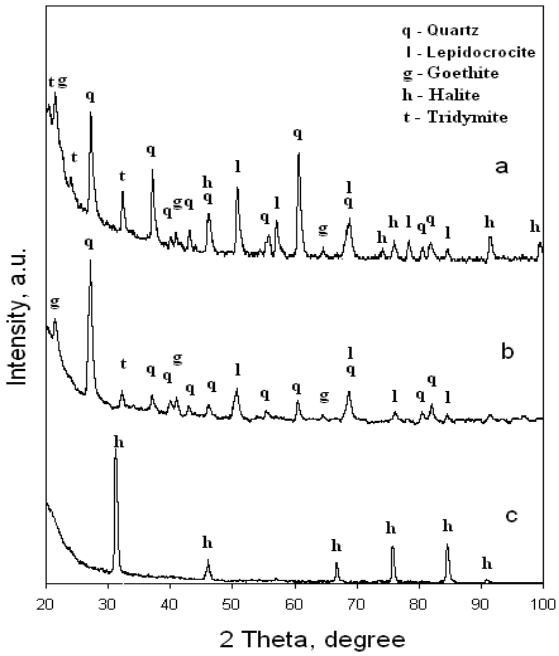

Figure 1. The X - ray diffraction spectrum for the investigated anti-skid material: a) grinded non skid material, b) grinded iron hydroxide particles and c) halite particles.

It features well developed peaks related to the crystalline state of the sample. The dominant mineral found in the composition is quartz, having the most intense peaks. Sodium chloride was identified as crystalline halite. Each component amount was appreciated based on the XRD peaks relative intensities related to its structure factor. All identified components of AM sample are listed in Table 1 as well as their amount in the sample and their optical features in cross polarized light.

The significant presence of Tridymite (an allotrope of quartz) is sustained by it's presence in common river sand in Romania due to the sedimentation condition [16, 17]. Moderate quantities of tridymite found in silica granular material is a collateral evidence that the gravel used in the investigated anti skid material is dug up into a local gravel - plant (e.g. Harghita county – due to the proximity to the Sf. Ana volcano). Quartz has a hexagonal compact crystal lattice meanwhile trydimite is orthorhombic (it derives from quartz by intensive heat treatments as found in volcanic eruptions. Both quartz and tridymite particles feature a light green gray aspect in cross polarized light, Figure 2a. Their morphology is derived from broken silica spherical particles. It features several rounded particles mixed up with broken ones having sharp edges crossed at small angles.

Table 1. Components properties of AM sample

Component	Quartz	Lepidocrocite	Goethite	Halite	Tridymite	Total
Wt.%	60	10	8	10	12	100
Particle size range, μm	30 - 250	10 - 250	10 - 250	30 - 500	30 - 250	-
Color in cross polarized light	Green-gray	Reddish-brown	Reddish-brown	Pale white	Green-gray	-

The most interesting findings in AM are the iron hydroxides in crystalline form of: lepidocrocite and goethite. In figure 2a appears as brown particles having 30 – 50 μm. Their presence in AM sample proves to be related to the intriguing brown particles observed at macroscopic analysis. Therefore, we separated from the AM sample a significant number of rusty particles as well as a significant number of halite. Each category was crushed separately and resulted powders were investigated by XRD. The obtained spectra are presented in figure 1b and 1c.

Even more intriguing is the results of rusty particles composition. The major component over 65 % is the mixture of lepidocrocite (γ – iron hydroxide) accompanied by its allotrope goethite (α – iron hydroxide). The surprise is the evidence of quartz (35 %). It is really an interesting quest: how could be explained such composition revealed for the rusty particles. Some evidences to

reveal the mystery was found in the mineralogical microscopy performed with cross polarized light on the rusty particles powder, Figure 2b. It appear to be a refined mixture of quartz slivers having 20 – 30 μm (some of them presents rounded shape due to their log proliferation in open environment and some are fresh broken featuring sharp edges). The iron hydroxides act as a binder of quartz slivers. It is possibly in condition of road traffic.

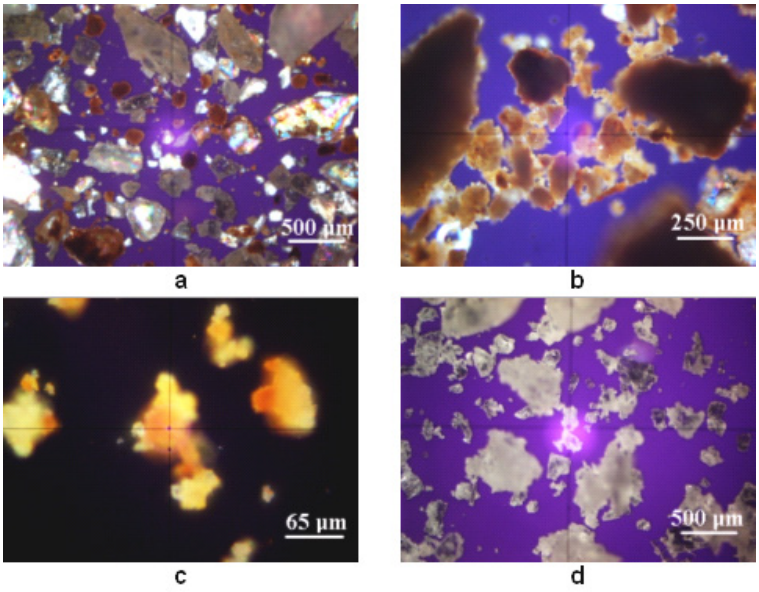

Figure 2. The cross polarized light microphotographs:
a) broken anti-skid material particles, b) broken iron hydroxide particles,
c) fine fractions of iron hydroxide particles, and d) halite particles.

A more detailed view catch some individualized iron hydroxide particles, figure 2c, having diameters between 10 – 50 μm. Their appearance is agglomerated, sustained the ability as mineral binder in relative humid environment.

The quartz particles from the street dust physical interacts with the car cassis rust in presence of anti skid material and relative humidity typical for winter and forms micro aggregates like those observed in Figure 2b. Considering several cycles of coalescence between micro aggregates finally results macroscopic particles such those observed in AM sample. This is a major fact which proves that AM sample contains re-circulated anti skid material re collected from the road sides. The implication for environment could be important even is able to become an environmental hazard.

Sodium chloride extracted from AM sample was also subjected to XRD. It reveals peaks only for halite, proving its high purity. The micro-structural aspect is presented in figure 2d, a fine mixture of cubs and octahedral crystal forming domains with polyhedron shape. Hence, sodium chloride is very solvable in aqueous or humid environment it is not a problem to interfere with air particulate matter suspensions.

The compression test results shows broking strength of 2054 MPa for silica particles and 840 MPa for iron hydroxide conglomerate. Silica particles compression strength strongly depends on the flawless structure. The values are in good agreement with the data in literature [18]. It proves that quartz particles have a good quality and are more resistant at mechanical solicitation than the other particles found in AM. Particularly, the iron hydroxide conglomerate feature small quartz slivers in composition, fact observed in Figure 2b. They act as cracking promoters reducing the compression strength as well as the particle cohesion.

Considering the interaction between car tires and road surface it exhibits local solicitation higher than 1000 MPa, fact which leads to the inevitable disintegration of rusty particles. Furthermore, the silica granules from anti – skid material acts as milling bodies refining the size of iron hydroxides as well as quartz slivers. Figure 2 b and 2c gives us some dimensional clues that fine particle could result after disintegration process. It needs to be considered diameters such 1, 2.5, 10, 20, up to 50 μm. All sizes range could be easy generated by automotive traffic.

The decaying of rusty particles in winter condition under pressure leads to the formation of fine particles below 10 μm diameter. The evidence of disintegration at microscopic level was traced out by dispersing the milled powder in deionized water under intensive agitation. Thin layer of particles were transferred on glass slide by immersion in the agitated dispersion for 30 seconds, followed by natural drying. The glass slide was microscopically inspected under cross polars and the resulted images are presented in Figure 3a. The iron hydroxide particles are very abundant, many of them features diameters around 20 μm but there are several finest particles in the range of 1 – 10 μm. All these fine micro - particles are able to be floated by air currents along the roads formed by automotive traffic [13, 14].

The thin layer was also subjected to XRD. Resulted a pattern is very similar with the one in Figure 1b. It proves that lepidocrocite, goethite and quartz slivers are able to form individualized PM_{10}; $PM_{2.5}$ and floating – sedimentable particles into the atmosphere. The data in literature state that any material particles spreaded or abandoned on the street are enclosed in the common street dust, and after is subjected to the air re-suspension [12, 15]. If so, we expect to found in winter atmosphere some other minerals belonging to the street adjacent environment decaying (e.g. clay mineral and perhaps calcite, very often found in the ground in Cluj-Napoca).

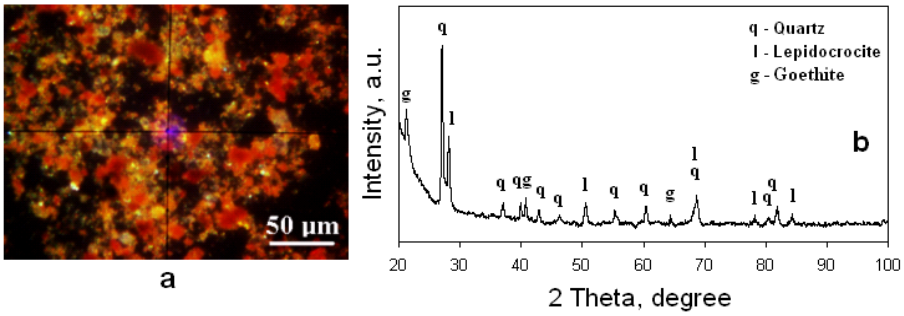

Figure 3. Thin layer of rusty particles powder transferred on glass slide via aqueous dispersion: a) cross polarized light microphotograph and b) XRD pattern.

Therefore, we collected particulate matter samples from atmosphere for the most representative winter months (December 2011, January 2012, and February 2012). The sedimenting particles (SP) collected were subjected to the XRD analysis. Resulted spectra are presented in Figure 4. Each of them present very well developed peaks proving the high crystalline state of the samples. The composition is the same for all three samples. The average characteristics are centralized in Table 2.

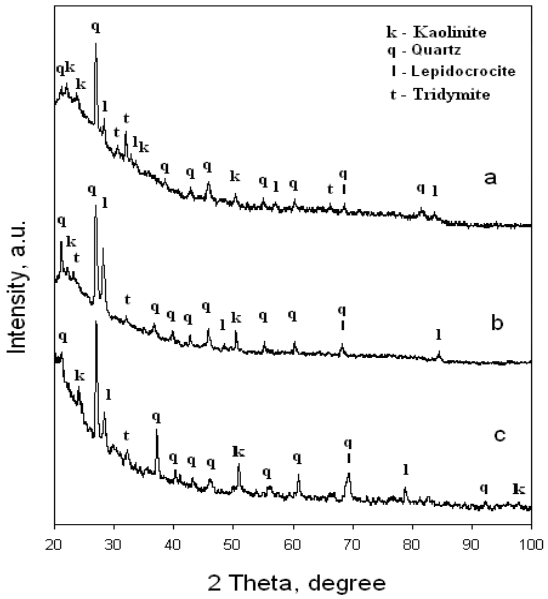

Figure 4. The X - ray diffraction spectrum for the sedimentable particles collected from air: a) December 2011, b) January 2012, and c) February 2012.

Table 2. Components properties of SP sample

Component	Quartz	Lepidocrocite	Kaolinite	Tridymite	Total
Wt.%	70	15	10	5	100
Particle size range, μm	1-30	1-30	1-10	1-30	-
Color in cross polarized light	Green-gray	Reddish-brown	Blue-white	Green-gray	-

Note: some isolated micro – particles could exceed 50 μm diameter

Microstructure of the sedimenting particles collected in December 2011 contains well dispersed fine microscopic particles. The cross polarized light inspection, Figure 5a, reveals a mixture of fine quartz particles together with lepidocrocite, kaolinite and tridymite. The detail at high magnification presented in Figure 5b, reveals better the shape and size of the minerals involved. The dimension ranges as well as mineral color in polarized light are centralized in Table 2. Similar observations were found for the SP samples collected in January 2012 and February 2012, the mineralogical microscopy results being displayed in Figure 5 c - f at average and high magnification.

Caolinite presence in the SP composition is interesting during winter because it is a clay mineral which belongs to the street adjacent areas. Its presence in the street dust is more signaled in summer [13]. The winter condition with snow and frost areas inhibits the decaying of street adjacent areas (the top ground is frost no particle is able to move under air currents). Still, a kaolinite amount of 10 % could be usual in winter considering the remains incorporated in street dust in autumn.

Quartz found in SP samples has two sources during winter: the soil decaying remains and the quartz slivers resulted from disintegration of rusty particles found in AM sample. It is the dominant mineral representing 70 % of SP average composition. But, the major prove of air disperse particulate maters generated by the anti – skid material is the presence of lepidocrocite at 15 % amount. Its particle size varies in a range of 1 – 30 μm as can be observed in Figure 5 b, d, and f. The evidenced range contains the most hazardous air particulate matters such $PM_{2.5}$ and PM_{10}.

The tridymite presence in SP samples as traces (over 5 %) also proves of particulate emissions caused by anti –skid material. In the real condition the multiple interactions between car tires and road surfaces intermediated by AS sample leads also to degradation of silica particles, some of them being crystallized as tridymite. The bilateral shock compression during car braking could promote cracks along silica crystal imperfection favoring the particle disintegration.

An amount of 15 % lepidocrocite was found in SP sample. It was induced in atmosphere by the same way as quartz slivers. Mineralogical microscopy evidence a lot of lepidocrocite particles in the range of 1-10 μm, sizes able to be incorporated in the $PM_{2.5}$ and PM_{10} emissions. It is interesting that goethite do not appear in SP sample. It is possible that goethite fine particles exposed for a long term to the winter environmental condition to transform themselves into lepidocrocite via natural decaying [19 – 20].

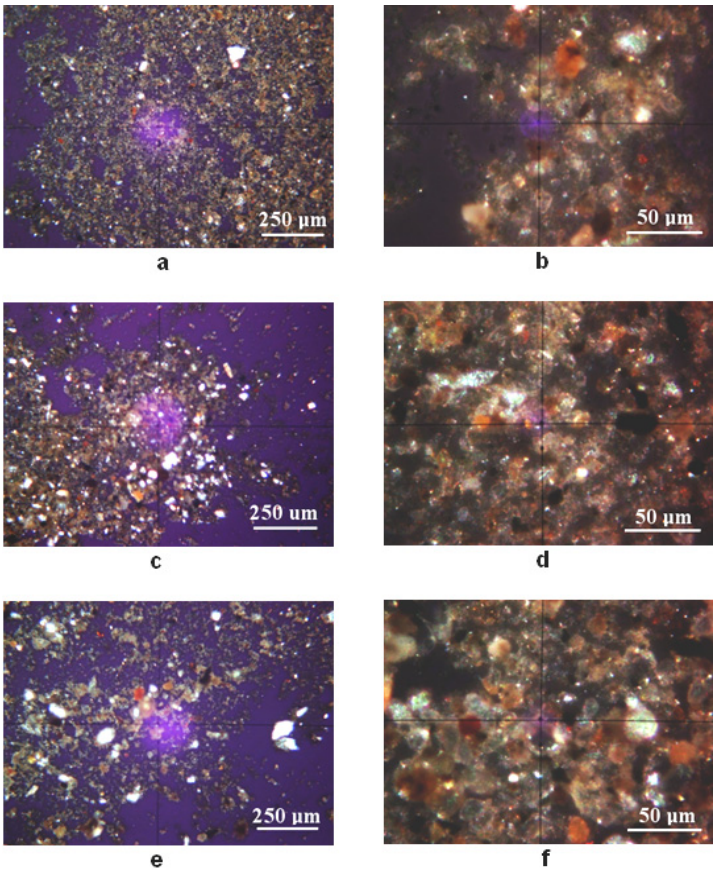

Figure 5. The cross polarized light microphotographs – different magnifications: a,b) December 2011, c,d) January 2012, and e,f) February 2012.

The particulate matter emissions were also quantitative measured using the Automatic Monitoring Air Quality Stations in the custody of Environmental Protection Agency of Cluj. Achieved data were centralized in Table 3.

Table 3. Particulate matter emissions data

Emission type		December 2011	January 2012	February 2012
$PM_{2.5}$, $\mu g/m^3$	min.	2.17	2.90	6.53
	max.	47.50	64.73	53.85
	average	28.19	23.50	35.23
PM_{10}, $\mu g/m^3$	min.	2.72	5.25	9.25
	max.	49.32	52.76	52.58
	average	27.37	19.95	31.33
SP, g/m^2/month	average	5.73	5.97	6.02

$PM_{2.5}$ emissions average value ranges from 23.50 to 35.23 $\mu g/m^3$ for all monitoring period. The risk level is low, because the average value is far away from the maximum limit. However, in days with high automotive traffic were signaled slightly exceeds of the limit: in 31 January 2012 was registered a peak of 64.73 $\mu g/m^3$ (an excess with 14.73 $\mu g/m^3$); and in 23 February 2012 was registered a peak of 53.85 $\mu g/m^3$ (an excess with 3.85 $\mu g/m^3$). The slightly exceeding mentioned is caused by the conjugated effect of intensive car traffic with presence of anti – skid material on the road surface.

The same variation could be observed for PM_{10}, Table 3, the average values are really lower than the accepted limit. The fact sustains that the environmental risk is low. However the PM_{10} maximum registered exceeds the limit with: 2.76 $\mu g/m^3$ in January 2012, and with 2.58 $\mu g/m^3$ in February 2012 at the same days reported for $PM_{2.5}$. The SP emissions are in a good range, below the maximum limit of 17 g/m^2/month, no exceed were registered. Overall, the environmental risk is very low, because the average value is far away from the maximum limit.

A proper street management could reduce the effect of AS material related particulate matter emissions by an adequate sorting of re-circulated anti –skid material.

CONCLUSIONS

Anti – skid material investigated in present study contains silica particles (e.g. quartz and trydimite) to increase the friction coefficient between cars tires and road surface and halite (sodium chloride) as anti glaze agent. Some interesting rusty particles were found in the anti skid material used in Cluj-Napoca in the 2011 – 2012 winter. The XRD and mineralogical microscopy analysis found that their composition is a micro-structured mixture of iron hydroxides (e.g. lepidocrocite and goethite) with fine quartz slivers. Compression test shows a good strength of silica particles of AM and a low strength for rusty particles. These ones are mechanically disintegrated by the force action between

car tires and street surface. Silica particles having a higher strength act as milling bodies of the rusty particles. We milled some of rusty particles and the resulted powder was dispersed in deionized water. Aqueous dispersion evidences the formations fine fraction in the range of 1 – 10 μm. The particulate matter samples collected from air from December 2011 to February 2012 proves the incorporation of lepidocrocite and quartz slivers from anti skid material. Lepidocrocite amount reached in SP sample is situated at 15 %. The results of monitoring performed with Automatic Monitoring Air Quality Stations prove that the emissions are directly increased with the car traffic on the Aurel Vlaicu Street. The average values for PM2.5, PM10 and SP are below the maximum accepted limit, so the risk level is low. Finally, we can conclude that a better management of anti skid material could be improved to reduce the particulate matter emission during winter by a proper sorting of re-circulated anti skid material.

EXPERIMENTAL SECTION

Anti skid material samples were collected in the 2011 – 2012 winter from the distribution points around Aurel Vlaicu Street in Cluj-Napoca, Romania. Equal quantities of anti skid material were mixed together to obtain an average representative sample (AM). AM sample was further grinded in a ball mill to obtain a mixture of broken particles which are suitable for physic and chemical analysis.

The particulate emissions into the atmosphere were monitored with Aurel Vlaicu Air Station. There were collected from air monthly samples of sedimentable particles (SP) via wet deposition for December 2011, January 2012, and February 2012. The SP dispersion was dried by evaporation, resulted powder was considered for analysis in present paper. PM_{10} and $PM_{2.5}$ were also monitored for the area of interest using the Automatic Air Quality Monitoring stations driven by Environmental Protection Agency of Cluj.

Mineralogical composition was elucidated by XRD spectroscopy using a DRON 3 diffractometer equipped with data acquisition module and Matmec IV.0 soft. The XRD spectra were obtained using a Cu k_α radiation. Mineral were identified from XRD patterns using Match 1.0 identification soft powered by Crystal Impact Company and PDF2 (Powder Diffraction File database second edition).

Particles size and morphology were investigated using the mineralogical microscopy with cross polarized light, using a Laboval 2 microscope produced by Carl Zeiss Jena. Digital capture was performed with a Samsung Camera having 10 Mpx. The special microscopic interpretation and particles measuring were developed using Image J 1.40g soft as a free resource provided by National Institute of Health of USA.

Compression tests were performed on a standard compression machine registering the broken pressure at compression for some of the particles within the anti skid material.

REFERENCES

1. L. Gidhagen, H. Johansson, G. Omstedt, *Atmospheric Environment*, **2009**, *43*, 1029.
2. M. Gerboles, D. Buzica, R.J.C. Brown, R.E. Yardley, A. Hanus-Illnar, M. Salfinger, B. Vallant, E. Adriaenssens, N. Claeys, E. Roekens, K. Sega, J. Jurasovic, S. Rychlik, E. Rabinak, G. Tanet, R. Passarella, V. Pedroni, V. Karlsson, L. Alleman, U. Pfeffer, D. Gladtke, A. Olschewski, B. O'Leary, M. O'Dwyer, D. Pockeviciute, J. Biel-Cwikowska, J. Tursic*, Atmospheric Environment*, **2011**, *45*, 3488.
3. S. Vardoulakis, P. Kassomenos, *Atmospheric Environment*, **2008**, *42*, 3949.
4. T. Maté, R. Guaita, M. Pichiule, C. Linares, J. Díaz, *Science of the Total Environment*, **2010**, *408*, 5750.
5. C.C. Botar, *Studia UBB Chemia*, LVIII, **2013**, *4*, 23.
6. A.G. Hosu-Prack, I. Petean, G. Arghir, L.D. Bobos, I. Iurcut, M. Tomoaia-Cotisel, *Carpathian Journal of Earth and Environmental Sciences*, **2013**, *8, 4,* 75.
7. Y.F. Fan, Z.Q. Hu, Y.Z. Zhang, J.L. Liu, *Construction and Building Materials*, **2010**, *24*, 1975.
8. M. Koçak, C. Theodosi, P. Zarmpas, U.I., A. Bougiatioti, O. Yenigun, N. Mihalopoulos, *Atmospheric Environment*, **2011**, *45*, 6891.
9. Q. Yao, S.Q. Li, H.W. Xu, J.K. Zhuo, Q. Song, *Energy*, **2009**, *34*, 1296-1309.
10. F. Yan, E. Winijkul, S. Jung, T.C. Bond, D.G. Streets, *Atmospheric Environment*, **2011**, *45*, 4830.
11. H. Tervahattu, K.J. Kupiainen, M. Raisanen, T. Makela, R. Hillamo, *Journal of Hazardous Materials*, **2006**, *132*, 39.
12. J. Berger, B. Denby, *Atmospheric Environment*, **2011**, *45*, 3692.
13. A.G. Hosu-Prack, I. Petean, G. Arghir, L.D. Bobos, M. Tomoaia-Cotisel, *Studia UBB Chemia*, **2010**, *55*, 93.
14. M. Kauhaniemi, J. Kukkonen, J. Härkönen, J. Nikmo, L. Kangas, G. Omstedt, M. Ketzel, A. Kousa, M. Haakana, A. Karppinen, *Atmospheric Environment*, **2011**, *45*, 3646.
15. D. Martuzevicius, L. Kliucininkas, T. Prasauskas, E. Krugly, V. Kauneliene, B. Strandberg, *Atmospheric Environment*, **2011**, *45*, 310.
16. I. Seghedi, A. Szakacs, M. Kovacs, R. Rosu, Z. Pecskay, *Institute of Geology and Geophysics*, **1995**, *76, (7),* 49.
17. M. Radoane, N. Radoane, D. Dumitriu, C. Miclaus, *Carpathian Journal of Earth and Environmental Sciences*, **2006**, *1, (2),* 13.
18. J. Kimberley, K.T. Ramesh, O.S. Barnouin, *Journal of Geophysical Research*, **2010**, *115*, 1.
19. Y. Cudennec, A. Lecerf, *Solid State Sciences*, **2005**, *7 (5)*, 520.
20. R.V. Morris, H.V. Lauer, *Journal of Geophysics Research*, **1981**, *86, (B11),* 10893.

STUDIA UNIVERSITATIS
BABEŞ-BOLYAI

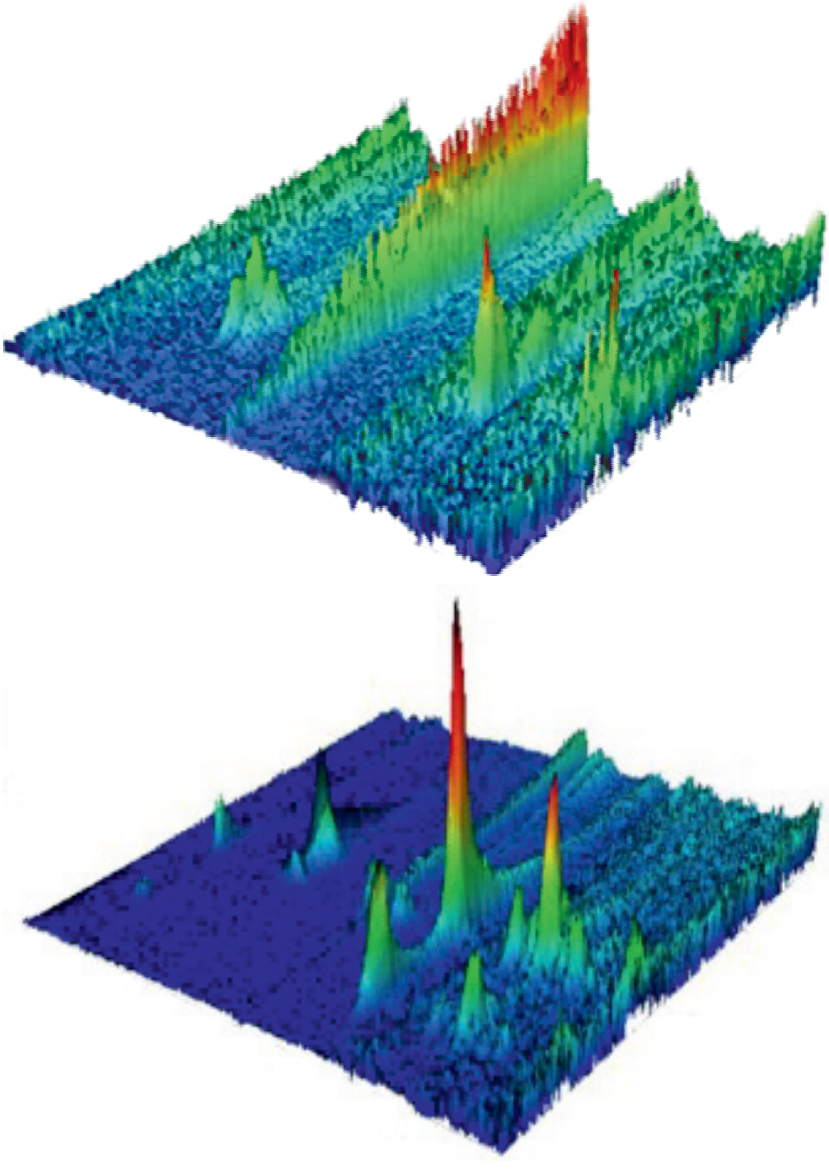

CHEMIA

2/2015
Tom II

STUDIA
UNIVERSITATIS BABEŞ-BOLYAI

CHEMIA

2/2015
Tom II

EDITORIAL BOARD OF
STUDIA UNIVERSITATIS BABEŞ-BOLYAI CHEMIA

http://chem.ubbcluj.ro/~studiachemia/; studiachemia@chem.ubbcluj.ro
http://www.studia.ubbcluj.ro/serii/chemia/index_en.html

YEAR **Volume 60 (LX) 2015**
MONTH **JUNE**
ISSUE **2, Tom II**

S T U D I A
UNIVERSITATIS BABEŞ–BOLYAI
CHEMIA

2
Tom II

STUDIA UBB EDITORIAL OFFICE: B.P. Hasdeu no. 51, 400371 Cluj-Napoca, Romania, Phone + 40 264 405352

CUPRINS – CONTENT – SOMMAIRE – INHALT

Studia Universitatis Babes-Bolyai Chemia has been selected for coverage in Thomson Reuters products and custom information services. Beginning with V. 53 (1) 2008, this publication is indexed and abstracted in the following:

- Science Citation Index Expanded (also known as SciSearch®)
- Chemistry Citation Index®
- Journal Citation Reports/Science Edition

STUDIA UBB CHEMIA, LX, 2, Tom II, 2015 (p. 219-228)
(RECOMMENDED CITATION)

RESIN TYPE INFLUENCE ON MOULDED PARTS FINAL DIMENSIONS

SEVER-ADRIAN RADU[a], VASILE DANUȚ LEORDEAN[a], NICOLAE BÂLC[a], OVIDIU NEMEȘ[b,*]

ABSTRACT. Silicone rubber moulding is a perfect solution to fill the gap between rapid prototyping and prototyping injection moulding. Silicone moulds reproduce the tiniest of details, so the quality of the pattern is critical; they are also a fast and affordable solution for functional prototypes and low volume production. A experimental method using vacuum casting of resin parts in flexible moulds is presented in this paper. During the experimental investigations technological features of casted material, volume of air traps, optimal working parameters and dimensional accuracy of the manufactured parts were studied. Based on these results, the corrective coefficients applicable to CAD dimensions in order to fabricate the master models by SLS were determined.

Keywords: *Rapid Prototyping, Resin injection, Viscosity, Silicone rubber moulds*

INTRODUCTION

The Rapid Tooling (RT) technology has evolved a lot in the last decades. Today it is possible to fabricate a complex pattern and other tooling for casting in a few hours while a casting may take up to several days. In the last decades, many companies have made great investments to improve manufacturing technologies in order to develop new products [1]. These technologies include CAD (Computer Aided Design) software and they are used to design complex geometries and also for solving some problems with high degrees of difficulty, including the medical field [2, 3]. In the last decade, many researches about RP (Rapid Prototyping) and RT (Rapid Tooling) technologies have been released, while the casting of the wax parts in a silicone rubber moulds was less studied [4÷6]. The resin patterns can be obtained at room temperature or in special conditions with good accuracy using vulcanizing silicone rubber moulds. Others author like Yang and Hannula, [7] studied the influence of injection parameters

[a] *Technical University of Cluj-Napoca, Faculty of Machine Building, 103-105 Muncii Blvd., RO-400641, Cluj-Napoca, Romania.*
[b] *Technical University of Cluj-Napoca, Faculty of Materials and Environmental Engineering, 103-105 Muncii Blvd., RO-400641, Cluj-Napoca, Romania.*
[*] *Corresponding author: ovidiu.nemes@sim.utcluj.ro*

on the dimensional stability of resin patterns produced by injection moulding process. In our case, we found the relation between various process parameters and their dependency on other parameters [8]. From all the parameters studied, it was found that the injection temperature is relevant for the dimensional accuracy of the parts. Nowadays, RT technology is the perfect options to solve the problems on resin moulded request by the market. It is estimated that total profits on new products are often reduced by as much as 60% because of the company's inability to get the product market quickly enough [9].

In the last few years, RT technology has evolved toward building moulds that provide up to 40% faster cycles than are possible with conventional technology [10]. That emphasis on productivity accompanies a shift in applications from prototype to full production tooling.

The advantages of flexible moulds are: efficiency, by reducing waste and energy consumption; agility for enable customization and flexibility for the modification and implementation of design concepts [11÷14].

In this paper, a new concept for obtaining flexible moulds together with the CAD model used for optimal dimensioning of rubber moulds is presented.

RESULTS AND DISCUSSION

In order to determine the influence of the resin type used in the manufacture of flexible moulds, measurements of resins moulded parts were achieved using Zeiss Navigator Prismo equipment, according to the sketch shown in Figure 1.

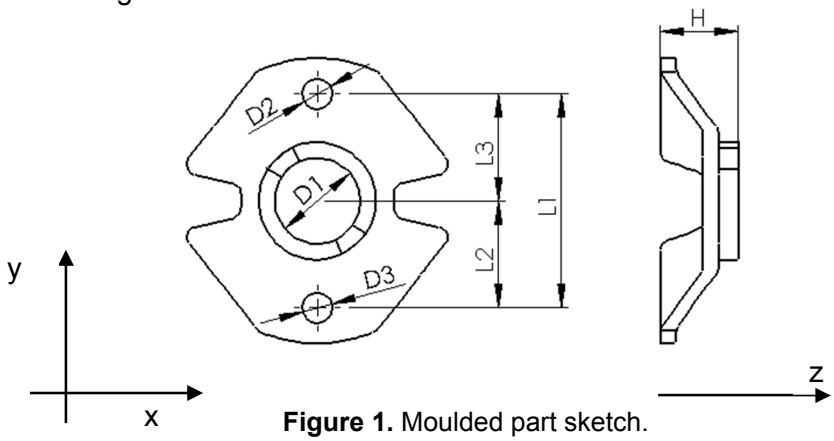

Figure 1. Moulded part sketch.

Additionally, the circularity deviations of diameters D1 = ∅24, D2, D3 = ∅8.4 has been analysed (denoted in the following by D1 = Dim. 1.1, D2 = Dim. 2.1, and D3 = Dim. 3.1) as well as the flatness deviation relative to dimension 7 in measurement sketch (denoted in the following by Dim. 7.1). Dimensions

measured were compared with CAD model and master model dimensions. Dimensions 1, 2, 3 are measured on the Y axis, 4, 5, 6 are the dimensions measured in the X axis and 7 is the only dimension measured on Z. It can be seen that on the axis X the average deviation is below the 1.5%, on the Y axis it has a value less than 0.65%, while the Z axis deviations occur up to 4%.

Then the percentage contractions of each dimension have been measured by comparing the required dimensions of resins parts and the CAD model, but also in relation to the dimensions of SLS master model. Deviations recorded (mean of 5 values measured) are shown in figure 2 and figure 3.

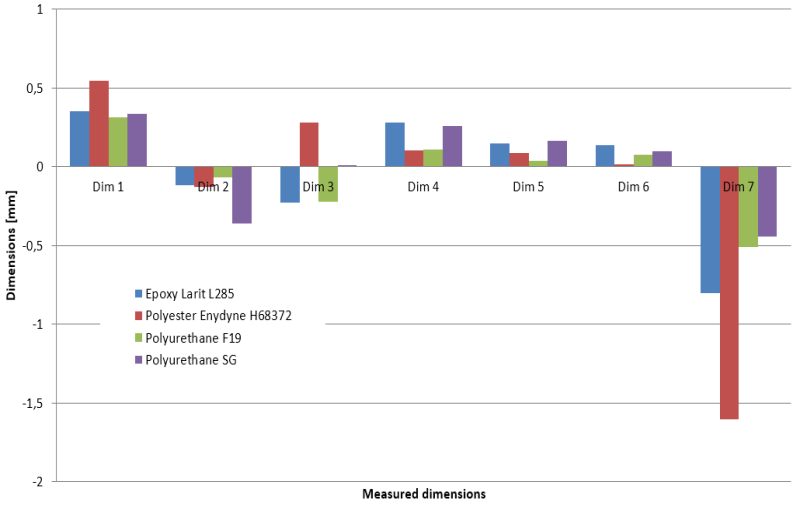

Figure 2. Deviations of resins parts dimensions related to CAD model and SLS master model

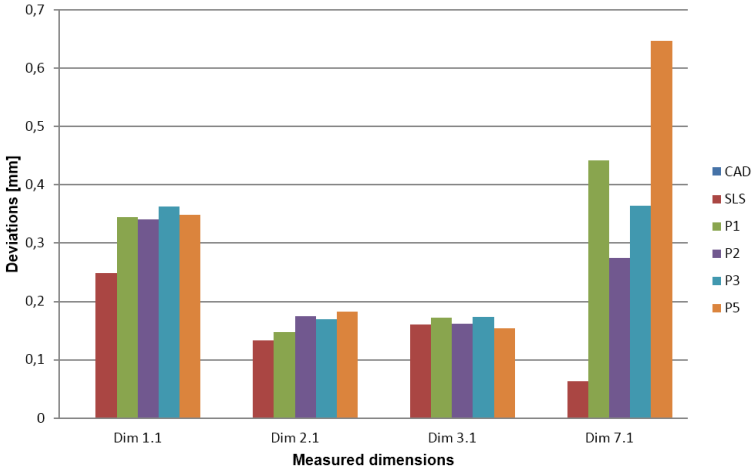

Figure 3. Flatness and circularity deviations

One of the main experimental parameters, important in achieving the flexible moulds, is the viscosity of the resin.

Figure 4 shows the variation in viscosity of the polyurethane resin based on mixing time of the two components of the resin while keeping constant the temperature at which the mould is heated. We observe that, if the times mixing increase, the resin viscosity increase also, due to the polymerization reaction.

Figure 5 presents the variation of viscosity according to the temperature of the mixture, keeping this time constant during the mixing of the components. It is noted that the viscosity increases also with the temperature if the mould is heated.

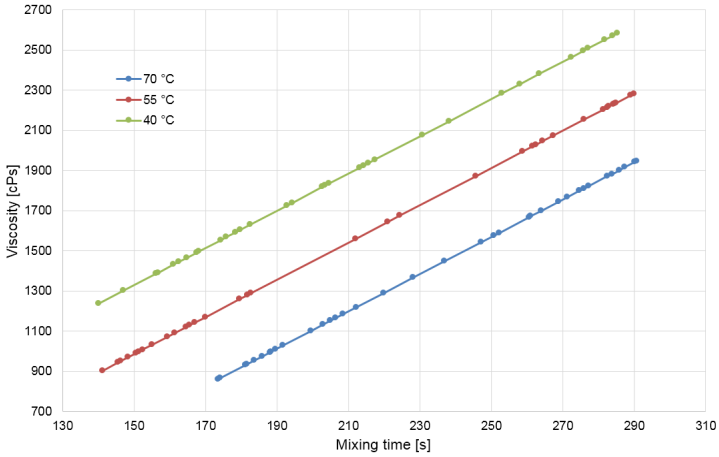

Figure 4. The variation of the viscosity depending on the time of mixing.

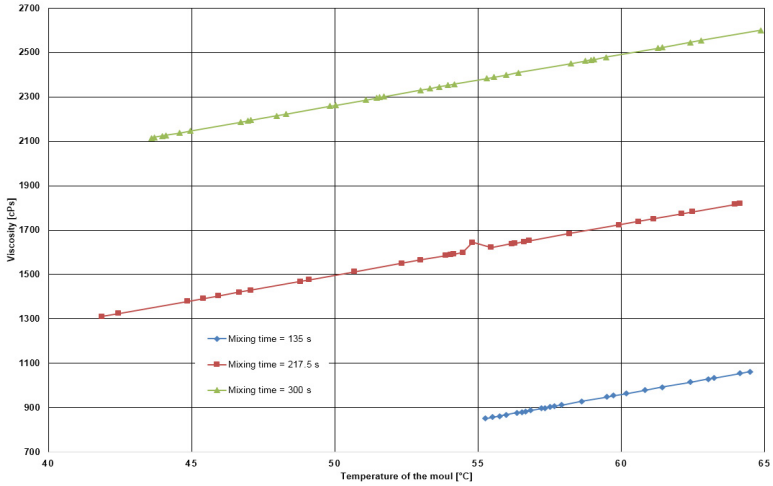

Figure 5. The variation of the viscosity depending on the temperature of the mould.

Experimental determination of resin density after polymerization is also very important in making the final product with the desired characteristics.

Because the resins used in casts are made up of two components (the density is known to each one) it is very difficult to determine the density of the mixture by theoretical methods. For this reason they have been made geometric forms with defined volume, for which the density is easily calculated [16].

After the curing of the resins and weighing each rectangular piece (figure 6) the calculating the volume density was easily determined.

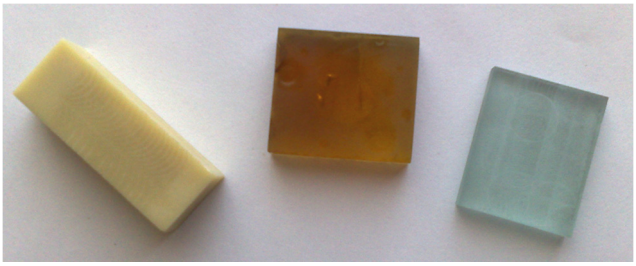

Figure 6. Rectangular pieces well defined volume

In order to determine resin density (ρ) after polymerization, the volume for each parallelepiped was calculated according to the relationship:

$$V = L \cdot l \cdot h \tag{1}$$

where: V – part volume [cm^3]; L – length of the part [cm]; l – width of the part [cm]; h – height of the part [cm].

The experimental values of density after polymerization, $\rho = m/L\ l\ h$, were showed in table 1 together with the main geometrical parameters of the rectangular obtained pieces.

Table 1. Determination of resins density after polymerization

	Polyurethane F19 resin	Epoxy resin	Polyester resin
Parts dimensions [cm]	L = 3.8360 l = 1.3840 H = 1.2550	L = 2.7980 l = 2.2400 H = 0.4850	L = 2.8200 l = 2.4500 H = 0.7500
The volume [cm^3]	6.6628	3.0397	5.1818
Weight rectangular pieces [g]	7.0995	3.5056	6.0512
Density [g/cm^3]	1.0655	1.1533	1.1678

Experimental determination of density resin after polymerization led to the determination of the weightings of the CAD model [17]. The resin parts dimensions, based on the relationship 3, are presented in table 2.

Table 2. Resin parts dimensions

Sample	D1 [mm]	D2 [mm]	D3 [mm]	L1 [mm]	L2 [mm]	L3 [mm]	H [mm]
CAD model	24.0000	8.4000	8.4000	60.0000	30.0000	30.0000	17.2500
SLS part	23.7158	8.1326	7.5519	59.6925	29.9099	29.7820	17.2502
P. 1.1	24.3669	8.5692	7.8162	60.3033	30.1146	30.1885	16.7955
P. 1.2	24.3929	8.5398	7.8669	60.6776	30.3894	30.2871	16.3860
P. 1.3	24.0076	7.7905	8.2621	59.7460	29.7431	30.0022	16.8426
P. 1.4	24.5381	7.9463	8.8660	60.7144	30.3630	30.3505	15.7217
P. 1.5	24.4680	8.5664	8.0395	59.9678	30.1239	29.8433	16.4893
P. 2.1	24.4064	8.5830	8.2510	59.7979	30.2808	29.5160	15.4736
P. 2.2	24.5332	8.1908	8.7364	60.1256	29.9437	30.1803	15.8147
P. 2.3	24.6897	8.2416	8.8475	60.2111	30.1658	30.0431	15.4242
P. 2.4	24.6918	8.2649	8.8297	60.4084	30.1153	30.2913	15.8715
P. 2.5	24.4099	8.0754	8.7258	59.9858	29.9291	30.0553	15.6499
P. 3.1	24.1477	7.8780	8.3704	59.8086	29.7456	30.0606	17.0035
P. 3.2	24.3205	8.4434	8.0568	60.2403	30.3325	29.9072	16.1595
P. 3.3	24.3405	8.5333	7.9884	60.1635	30.1717	29.9907	16.5231
P. 3.4	24.4162	8.7627	7.9184	60.2740	30.0003	30.2723	17.1941
P. 3.5	24.3462	8.0380	8.5589	60.0662	29.9231	30.1398	16.8124
P. 5.1	24.4812	8.0184	8.5206	60.6067	30.1122	30.4931	16.4912
P. 5.2	24.3312	7.8027	8.4163	60.4418	30.0365	30.4053	16.8814
P. 5.3	24.4570	8.4673	8.1602	60.4080	30.4476	29.9589	16.0380
P. 5.4	24.1264	7.9940	8.4313	59.7262	30.2254	29.5007	17.5102
P. 5.5	24.2779	7.9265	8.5231	60.1156	29.9969	30.1183	17.1020

$$M = \frac{1}{n} \cdot \sum_{i=1}^{n} x_i \tag{3}$$

where: n – the number of items summed; x_i – measured dimensions which will be summed;

In order to calculate the contraction, the relation 4 was applied.

$$C = \frac{d_{CAD} - d_{masurat}}{d_{CAD}} \cdot 100 \tag{4}$$

where: d_{CAD} – projected dimensions [mm]; $d_{masurat}$ – measured dimensions [mm];

From Table 3 it is noted that the dimensional deviations relative to the CAD model for ∅24 mm rate does not exceed the value of 0.55 mm in absolute value (for polyester resin), which is the relative error of less than 2.27%.The Z axis is the biggest errors found in polyester resin which reached 9.29% relative error. On the Y axis we share dimensional deviations from 60 mm up to 0.28 mm for epoxy resin which means maximum relative errors of 0.46%. It was determined experimentally by mixing polyurethane resin viscosity 40 g component A and 60 g component B using rotational viscometer using a disc Rheotest S6 ∅18 mm diameter at a speed of 50 rev/min.

The initial temperature of the two components was increased to 22°C and 30°C temperature in just 45 seconds. Following research it was noted that the *Z* axis all types of vacuum casting resin used to have high levels of dimensional variation, to around 3 ÷ 9.3% with a maximum deviation of about 8% for the polyester resin. These high values and deviations occurred because of problems closing the moulds, because, if the both halves of the mould are not tightening, the risk that the mould is not filled with resin appears.

Table 3. The relative dimensional error of the resin parts compared to the CAD model

Dimensions	Value [mm]	Resin	Measured average dimensions [mm]	Error	
				[mm]	[%]
D1	24	Epoxy resin	24.3547	+0.3547	1.47
		Polyester resin	24.5462	+0.5462	2.27
		Polyurethane F19	24.3142	+0.3142	1.3
		Polyurethane SG95	24.3347	+0.3347	1.39
D2	8.4	Epoxy resin	8.2824	-0.1176	1.39
		Polyester resin	8.2711	-0.1289	1.53
		Polyurethane F19	8.3310	-0.0690	0.82
		Polyurethane SG95	8.0417	-0.3583	4.26
D3	8.4	Epoxy resin	8.1701	-0.2299	2.73
		Polyester resin	8.6780	+0.2780	3.31
		Polyurethane F19	8.1785	-0.2215	2.63
		Polyurethane SG95	8.4103	+0.0103	0.12
L1	60	Epoxy resin	60.2818	+0.2818	0.46
		Polyester resin	60.1057	+0.1057	0.17
		Polyurethane F19	60.1105	+0.1105	0.18
		Polyurethane SG95	60.2596	+0.2596	0.43
L2	30	Epoxy resin	30.1468	+0.1468	0.48
		Polyester resin	30.0869	+0.0869	0.28
		Polyurethane F19	30.0346	+0.0346	0.11
		Polyurethane SG95	30.1637	+0.1637	0.54
L3	30	Epoxy resin	30.1343	+0.1343	0.44
		Polyester resin	30.0172	+0.0172	0.05
		Polyurethane F19	30.0741	+0.0741	0.24
		Polyurethane SG95	30.0952	+0.0952	0.31
H	17.25	Epoxy resin	16.4470	-0.8030	4.65
		Polyester resin	15.6467	-1.6033	9.29
		Polyurethane F19	16.7385	-0.5115	2.96
		Polyurethane SG95	16.8045	-0.4455	2.58

To avoid this inconvenient it is recommended that future the CAD model to be compensated with some correction factors.

CONCLUSIONS

Thermosetting resins generally are practical in nature at temperatures between 40°C and 70°C responsive to 2 and 5 minutes.

Viscosity of polyurethane resin should be up to a maximum of 1400 cPs, after this value there is a risk that the rapid polymerization of the silicone rubber moulds not to be filled. The amount of 1400 cPs viscosity is reached by mixing the two components of the resin for up to 3 minutes, to a mould temperature of 40°C.

The resin parts are casted in vacuum moulding the silicone rubber on the Y axis deviation does not exceed 1%.

Vacuum castings polyester resin has high dimensional deviations on the 3 axis, Z axis is the most affected with the relative error of 9.29%.

X -axis scaling coefficient is 1, the scaling factor Y-axis has the value 0.99, while the Z-axis scaling coefficient has the value of 1.04 for the epoxy resin Larit L285, 1.1 to H68372 polyester resin, 1.03 for F19 polyurethane resin and polyurethane resin 1.02 for SG95.

EXPERIMENTAL SECTION

For experimental determination of the density, function of body weight, the piece it weighed in air and in a liquid. The relationship used for calculating the density of moulded parts [15], of the resin is:

$$\rho_p = \frac{m_{p\_air}}{m_{p\_air} - m_{p\_water}} \cdot \rho_{water} \tag{2}$$

where:

ρ_p – density of analysed part [g/cm^3]; m_{p_air} – piece mass, weighed in air [g]; m_{p_water} – piece mass, weighed in water [g]; ρ_{water} – water density [g/cm^3].

The viscosity of the used resins was determined using rotational viscometer Rheotest S6. The unit contains 19 sets of wheels and gears (from 0.3 - 100 rpm), thus allowing optimal choice of scales for measuring structural viscosity and it is used not only for determining the dynamic viscosity of Newtonian liquids but also to conduct thorough examinations on rheological non-Newtonian fluids.

The volumes of bubbles in casting in silicone rubber moulds were made using Shimadzu electronic balance, model AX 120.

Water density was measured using thermo-digital dens meter. The value of measured density is 0.9976 g/cm^3 at 22 °C.

The density of the water was measured using a thermo-digital dens meter, Anton Paar DMA 33N and the balance used to weighing the parts resin is VWR SE 1202 model.

In terms of measuring the vacuum castings a machine Zeiss Navigator Prismo was used.

ACKNOWLEDGMENTS

This paper was supported by the European Social Fund through POSDRU Program, DMI 1.5, ID 137516 PARTING.

REFERENCES

1. M. Horacek, S. Lubos, *9th World Conference on Investment Casting*, San Francisco, pp.1-20, **1996**.
2. P. Bere, M.V. Dudescu, N. Balc, P. Bere, A.M. Iurian, O. Nemes, *Materiale Plastice*, **2014**, *51*, 2, 145-149.
3. A. Popescu, L. Hancu, P. Bere, *Applied Mechanics and Materials*, **2013**, *371*, 394-398.
4. H. Iancau, P. Bere, M. Borzan, L. Hancu, A. Crai, *Materiale Plastice*, **2008**, *45*, 3, 251-256.
5. P. Yarlagadda, T.S. Hock, *Journal of Materials Technology*, **2003**, *138*, 75-81.
6. I.P. Ilyas, C.M. Taylor and K.W. Dalgarno, *Proceedings of the 6th National Conference of Rapid Design, Prototyping and Manufacturing, High Wycombe*, June, 10, **2005**, 109-116.
7. Y. Yang, S.P. Hannula, *Materials Science and Engineering*, **2008**, *1-2* (*477*), 63-68.
8. R. Sever-Adrian "Cercetari teoretice si experimentale privind turnarea sub vid a pieselor complexe nemetalice" – teza de doctorat, Cluj-Napoca, **2011**.
9. B. O'Donnchadha, A. Tansey, *Journal of Materials Processing Technology*, **2004**, *1* (*153-154*), 28-34.
10. S.A. Radu, D. Fratila, *Proceedings of the Romanian Academy – series A*, ISSN 1454-9069, **2012**, *4*(*13*), 343-350.
11. I. Gibson, L.K. Cheung, S.P. Chow, W. L. Sheung, S.L. Beh, W. Savalani, S.H. Lee, *Rapid Prototyping Journal*, **2006**, *1*(*12*), 53-58.
12. I.P. Ilyas, C.M. Taylor and K.W. Dalgarno, *Proceedings of the 6th National Conference of Rapid Design, Prototyping and Manufacturing, High Wycombe*, June, 10, **2005**, 109-116.
13. J.E. Folkestad, R.L. Johnston, *Journal of Industrial Technology*, **2001**, *4*(*17*), 1-7.

14. D.R. Bareta, A.S. Pouzada, C.A. Costa, *PMI International Conference on Polymer and Moulds Innovations*, Gent/Belgium, **2007**.
15. Shimadzu Corporation Kyoto, *Instruction Manual for Simple Specific Gravity Measurement* Kit AW/AX/AY Series, Japan, **2010**.
16. R. Sever-Adrian “Cercetari teoretice si experimentale privind turnarea sub vid a pieselor complexe nemetalice” – teza de doctorat, Cluj-Napoca, **2011**.
17. P. Berce, N. Bâlc, N. Caizar, R. Pacurar, S.A. Bratian, I. Fodorean, *Tehnologii de fabricație prin adăugare de material și aplicațiile lor*, ISBN 978-973-27-2396-8, Editura Academiei Romane, Bucuresti, **2014**.

STUDIA UBB CHEMIA, LX, 2, Tom II, 2015 (p. 229-240)
(RECOMMENDED CITATION)

COMPUTING THE ANTI-KEKULÉ NUMBER OF CERTAIN NANOTUBES AND NANOCONES

MEHAR ALI MALIK[a,*], MUHAMMAD IMRAN[a]

ABSTRACT. Let *G(V,E)* be a connected graph. A set *M* subset of *E* is called a *matching* if no two edges in *M* have a common end-vertex. A matching *M* in *G* is *perfect* if every vertex of *G* is incident with an edge in *M*. The perfect matchings correspond to Kekulé structures which play an important role in the analysis of resonance energy and stability of hydrocarbons. The anti-Kekulé number of a graph *G*, denoted as *ak(G)*, is the smallest number of edges which must be removed from a connected graph *G* with a perfect matching, such that the remaining graph stay connected and contains no perfect matching.

In this paper, we calculate the anti-Kekulé number of $TUC_4C_8(S)[p,q]$ nanotube, $TUC_4C_8(S)[p,q]$ nanotori for all positive integers *p, q* and $CNC_{2k-1}[n]$ nanocones for all positive integers *k* and *n*.

Keywords: *Perfect matching, Anti-Kekulé number, Nanotubes, Nanocones*

INTRODUCTION

Mathematical chemistry is a branch of theoretical chemistry in which we discuss and predict the chemical structure by using mathematical tools and does not necessarily refer to the quantum mechanics. *Chemical graph theory* is a branch of mathematical chemistry in which we apply tools of graph theory to model the chemical phenomenon mathematically. This theory plays a prominent role in the fields of chemical sciences. A *moleculer / chemical graph* is a simple finite graph in which vertices denote the atoms and edges denote the chemical bonds between these atoms in the underlying chemical structure. It is important to mention that the hydrogen atoms are often omitted in a molecular graph.

A *nanostructure* is an object of intermediate size between microscopic and molecular structures. It is a product derived through engineering at molecular scale. This is something that has a physical dimension smaller than 100 nanometers, ranging from clusters of atoms to dimensional layers. *Carbon nanotubes* (CNTs)

[a] *Department of Mathematics, School of Natural Sciences, National University of Sciences and Technology, Sector H-12, Islamabad, Pakistan*
** Corresponding author: alies.camp@gmail.com*

are types of nanostructure which are allotropes of carbon and have a cylindrical shape. Carbon nanotubes, a type of fullerene, have potential in fields such as nanotechnology, electronics, optics, materials science, and architecture. Carbon nanotubes provide a certain potential for metal-free catalysis of inorganic and organic reactions. Nanotube-based field emitters have applications as nanoprobes in metrology and biological and chemical investigations and as templates for the creation of other nanostructures. *Carbon nanocones* are conical structures which are allotropes of carbon having at least one dimension of the order one micrometer or smaller.

An edge set M of a graph G is called a matching if no two edges in M have a common end vertex. A matching M of G is perfect if every vertex of G is incident with an edge in M. In organic moleculer graphs, perfect matchings correspond to Kekulé structures, playing an important role in analysis of the resonance energy and stability of hydrocarbon compounds [1]. For example, it is well known that carbon compounds without Kekule structures are unstable. The study of Kekule structures of chemical compounds is very important, because they have many "hidden treasures" that may explain their physical and chemical properties [2]. The notations used in this paper are mostly taken from [3].

The *anti-Kekulé number* of a connected graph G is the smallest number of edges that must be removed from the graph G such that the remaining graph is still connected but has no Kekulé structures. For benzenoids, Vukičević and Trinajstić proved in [4] that the anti-Kekulé number of parallelograms with at least three rows and at least three columns is equal to 2, they also showed in [5] that cata-condensed benzenoids have anti-Kekulé number either 2 or 3 and both classes are characterized. Later on, Veljan and Vukičević showed that the anti-Kekulé numbers of the infinite triangular, rectangular and hexagonal grids are 9, 6 and 4, respectively [6]. For fullerene graphs, Vukičević showed that the anti-Kekulé number of the icosahedron C_{60} (buckminister fullerene) is 4. In general, Kutnar et al. proved in [7] that the anti-Kekulé number of all leapfrog fullerene graphs is either 3 or 4 and afterwards Yang et al proved that the anti-Kekulé number of all fullerene graphs is 4 [8]. For further study on anti-Kekulé number of different graphs please consult [9, 10, 11].

Let $G(V,E)$ be a connected graph with vertex set V and edge set E and let G has at least one perfect matching (i.e., Kekulé structure). For $S \subseteq E(G)$, let $G-S$ denote the graph obtained from G by deleting all the edges in S. We call S an anti-Kekulé set if $G-S$ is connected but has no perfect matching. The anti-Kekulé set of minimum cardinality in G is called the anti-Kekulé number, and denoted by $ak(G)$.

MAIN RESULTS

In this paper, we calculate the anti-Kekulé number of $TUC_4C_8(S)[p,q]$ nanotube and $TUC_4C_8(S)[p,q]$ nanotori. The anti-Kekulé number of $CNC_{2k}[n]$ nanocones $\forall\, k \in \mathbb{N}$, was discussed by the present authors in [12]. Now we discuss the anti-Kekulé number of $CNC_{2k-1}[n]$ nanocones $\forall\, k \in \mathbb{N}$.

RESULTS FOR NANOTUBES

In this section, we compute the anti-Kekulé number for $TUC_4C_8(S)[p,q]$ nanotube. This nanotube is a net of C_4 and C_8, and it can be constructed by alternating C_4 and C_8 following a trivalent decoration as shown in Fig. 2. This type of tiling can cover a cylinder and a torus nanotube. In a 2 -dimensional lattice of the $TUC_4C_8(S)[p,q]$ nanotube, p is the number of octagons in one row and q is the number of periods in the whole lattice. A period consist of two rows of edges as shown in Fig. 1. Further detail on the construction of $TUC_4C_8(S)[p,q]$ nanotubes can be found in [13].

Carbon nanotubes are molecular-scale tubes of graphitic carbon with outstanding properties. They are among the stiffest and strongest fibres known, and have remarkable electronic properties and many other unique characteristics. For these reasons they have attracted huge academic and industrial interest, with thousands of papers on nanotubes being published every year. Commercial applications have been rather slow to develop, however, primarily because of the high production costs of the best quality nanotubes.

For our purpose, we call the vertices of degree 2 as the *boundary* vertices of a nanotube. One can observe that the boundary vertices lie on the first and the last layer of the nanotube.

Theorem 2.1 *Let* $G = TUC_4C_8(S)[p,q]$ *nanotube, then* $ak(G) = 3$.

Proof. Consider the set $S = \{e_1, e_2, e_3\} \subseteq E(G)$, then the graph $G - S$ contains a vertex v such that v is adjacent to two vertices of degree 1, say u and w (see Fig. 1). Since the vertices u and w cannot be matched simultaneously, the graph $G - S$ is connected but contains no perfect matching. This implies that $ak(G) \leq 3$.

Conversely, let $U = \{e, e'\} \subseteq E(G)$. We will show that the graph $G - U$ is connected and it contains a perfect matching. Clearly, the graph $G - U$ will be connected if and only if e and e' are not adjacent to the same boundary vertex.

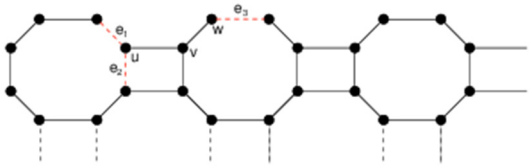

Figure 1. One period of the graph of $TUC_4C_8(S)[p,q]$ with Anti-Kekulé set $S = \{e_1, e_2, e_3\}$ shown by the red edges.

The graph G is tiled with the cycles of lengths 4 and 8, such that each period contain p octagons and there are q such periods. Then the order of G is $|V(G)| = 8pq$ and the number of cycles of length 4 (and length 8 as well) in G is $p(2q-1)$. Let us label all the cycles of length 4 and 8 in G by $C^4_{k,l}$ and $C^8_{k,l}$ (respectively), where $1 \le k \le q$ and $1 \le l \le p$ (see Fig. 2). Let $E(C^4_{k,l})$ (and $E(C^8_{k,l})$) denote the edge set of the cycle $C^4_{k,l}$ (resp. $C^8_{k,l}$) and let $E(C^4_{k,l}) = E^1(C^4_{k,l}) \cup E^2(C^4_{k,l})$, where $E^1(C^4_{k,l})$ and $E^2(C^4_{k,l})$ be the sets containing alternatively the edges of the cycle $C^4_{k,l}$, for each k and l.

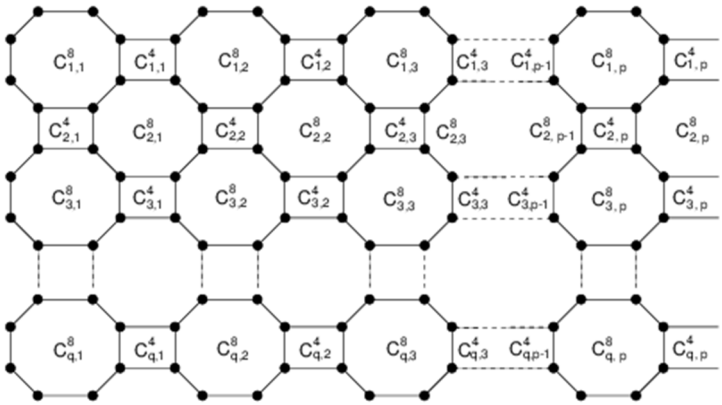

Figure 2. The cycles of length 4 and 8 in $TUC_4C_8(S)[p, \frac{q+1}{2}]$ nanotube

Similarly, let $E(C^8_{k,l}) = E^1(C^8_{k,l}) \cup E^2(C^8_{k,l})$, where $E^1(C^8_{k,l})$ and $E^2(C^8_{k,l})$ be the sets containing alternatively the edges of the cycle $C^8_{k,l}$, for each k and l.

It can be observed that $|E^1(C^4_{k,l})| = |E^2(C^4_{k,l})| = 2$. Clearly, either $E^1(C^8_{k,l})$ or $E^2(C^8_{k,l})$ contains some edges of the cycles of length 4. Without loss of generality, we assume that

$$\begin{cases} E^2(C^8_{k,l}) \cap \{E(C^4_{k+i,l}) \cup E(C^4_{k,l-j})\} = \varnothing, & for \quad k = odd; \\ E^2(C^8_{k,l}) \cap \{E(C^4_{k+i,l}) \cup E(C^4_{k,l+j})\} = \varnothing, & for \quad k = even, \end{cases} \tag{1}$$

where $i \in \{-1,1\}, j \in \{0,1\}$. We can define two disjoint perfect matchings in G as follows.

$$M_1 = \bigcup_{k,l} E^1(C^8_{k,l}) \quad and \quad M_2 = \bigcup_{k,l} E^2(C^8_{k,l}). \tag{2}$$

Clearly, $M_1 = \bigcup_{k,l} E(C^4_{k,l})$ and $M_2 = E(G) - M_1$. We consider the following three cases.

Case 1. Let e and e' do not lie on a cycle of length 8. Then we have a perfect matching M_1 (or M_2) in the connected graph $G - U$.

Case 2. Let one of e and e' lie on a cycle of length 8. Suppose on contrary that e lies on $C^8_{k,l}$, then without loss of generality we can assume that $e \in E^1(C^8_{k,l})$. Then we have a perfect matching M_2 in the connected graph $G - U$.

Case 3. Suppose that both e and e' lie on the cycles $C^8_{k,l}$ and $C^8_{s,t}$ (respectively), for $1 \le k, s \le q$ and $1 \le l, t \le p$.

When $(k,l) \neq (s,t)$ then if $e \in E^1(C^8_{k,l})$ and $e' \in E^1(C^8_{s,t})$, then M_2 is a perfect matching in the connected graph $G - U$. Similarly, when $e \in E^1(C^8_{k,l})$ and $e' \in E^2(C^8_{s,t})$, then $M' = M_1 - E^1(C^8_{k,l}) + E^2(C^8_{k,l})$ is the required perfect matching in the connected graph $G - U$.

When $(k,l) = (s,t)$, both edges e and e' lie on the same cycle of length 8, say $C^8_{k,l}$. Then we have the following two subcases.

(1) Let e and e' lie in the same class, say $E^1(C^8_{k,l})$. Then M_2 will be a perfect matching in the connected graph $G - U$.

(2) Let e and e' lie in different classes, say $e \in E^1(C^8_{k,l})$ and $e' \in E^2(C^8_{k,l})$. When e and e' are adjacent, it is clear that the edges e and e' cannot be adjacent to the same boundary vertex, as the graph will be disconnected. Then consider a matching N' in $G-U$ defined in four cases corresponding to the possibilities of the edges e and e', as follows.

$$N' = M_1 - \bigcup_{i,j} E^1(C^8_{k+i,l+j}) \cap \{e\},\ where\ (i,j) = \begin{cases} (0,0)\ and\ (0,1); \\ (0,0)\ and\ (2,0); \\ (0,0)\ and\ (0,-1); \\ (0,0)\ and\ (-2,0). \end{cases} \tag{3}$$

It can be seen that each pair of octagons in the matching defined in Equ. 3 are joined by the cycle $C^4_{k+i,l+j}$, where

$$(i,j) = \begin{cases} (0,0)\ \ for\ \ k = odd\ \ \ and\ \ \ (0,1)\ \ for\ \ k = even; \\ (1,0); \\ (0,-1)\ for\ k = odd\ and\ (0,0)\ for\ k = even; \\ (-1,0). \end{cases} \tag{4}$$

Since $e \in E^1(C^8_{k,l})$ therefore $e \in M_1$ and thus lies on a cycle of length 4, whereas e' does not. Let $E(C^4_{k+i,l+j}) = \{c_1, c_2, c_3, c_4\}$, for (i,j) as mentioned in Equ. 4. Clearly, $e \in \{c_1, c_2, c_3, c_4\}$. Then label these edges with $e = c_1$ in the clockwise direction starting from e.

Now, using the matching defined in Equ. 3, we can construct a matching N in the graph $G-U$ as follows.

$$N = N' - \{c_3\} + \{c_2, c_4\}. \tag{5}$$

Then N is a perfect matching in the connected graph $G-U$, which implies that $ak(G) \geq 3$, and completes the proof.

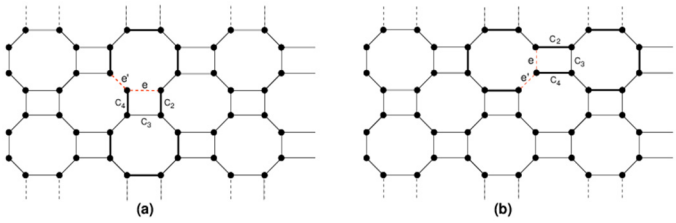

Figure 3. The matching for the pair of octagons corresponding to the first two cases in Equ. (3). The rest of the periods are matched by the matching M_1.

RESULTS FOR $TUC_4C_8(S)[p,q]$ NANOTORI

The $TUC_4C_8(S)[p,q]$ nanotorus (or nanotori) is obtained from the $TUC_4C_8(S)[p,q]$ nanotube by joining the ends of the tube, so giving it the shape of a torus. The spoke type edges in the last layer will be joined to the corresponding vertices in the first layer (see Fig. 4).

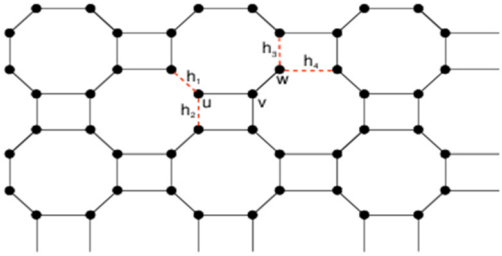

Figure 4. The embedded graph of the $TUC_4C_8(S)[3,2]$ nanotori

Theorem 2.2 *Let* $G = TUC_4C_8(S)[p,q]$ *nanotori, then* $ak(G) = 4$.

Proof. Consider a period of the 3-regular graph of $TUC_4C_8(S)[p,q]$ nanotori, as shown in Fig. 5. Let E_1, E_2 and E_3 be the edge partitions of $E(G)$ containing all the edges labelled e_1, e_2 and e_3, respectively. It is easy to see that E_1, E_2 and E_3 form three (disjoint) perfect matchings in G.

Let $S = \{h_1, h_2, h_3, h_4\} \subseteq E(G)$, as shown in Fig. 4. Then the graph $G - S$ contains a vertex v such that v has two pendent vertices adjacent to it, which cannot be matched simultaneously. Since no more than two vertices from S are adjacent to a single vertex, the graph G remains connected. Thus, $ak(G) \leq 4$.

Conversely, let $U = \{b_1, b_2, b_3\} \subseteq E(G)$, where all edges of U are not adjacent to a single vertex in G. We have the following three cases to be discussed.

Case 1. When all elements of U belong to same edge class, say E_1. Then we have M_2 (or M_3) as a perfect matching in the graph $G - U$.

Case 2. When two elements of U belong to the same edge class, say E_1. Then the third element of U can be in one of the remaining two edge classes, say E_2. Thus E_3 will be a perfect matching in the connected graph $G - U$.

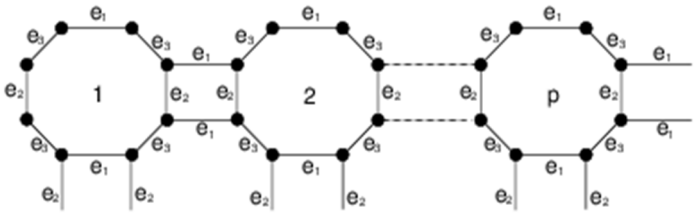

Figure 5. A period of $TUC_4C_8(S)[p,q]$ nanotori

Case 3. When all elements of U belong to different edge classes, say $b_1 \in E_1$, $b_2 \in E_2$ and $b_3 \in E_3$. Consider the labeling of all the cycles of length 4 and 8 in G, as done in Theorem 2.1, respectively by $C^4_{k,l}$ and $C^8_{k,l}$. With one extra row of edges joining the vertices in the last row to corresponding vertices in the first row, and thus $1 \le k \le q+1$ and $1 \le l \le p$. Since $b_1 \in E_1$, which is the class of all horizontal edges, we can assume that $b_1 \in E(C^4_{k,l})$, for some k and l. Label the edges of $C^4_{k,l}$ with $\{c_1, c_2, c_3, c_4\}$ and let $b_1 = c_1$. Consider a matching M in $G-U$ defined as follows.

$$M = E_1 - \{c_1, c_3\} + \{c_2, c_4\}. \tag{6}$$

Clearly, M is a perfect matching in the connected graph $G-U$. Thus $ak(G) \ge 4$, which completes the proof.

RESULTS FOR $CNC_k[n]$ NANOCONES

Now we determine the anti-Kekulé number of $CNC_k[n]$ nanocones, where $k = 2q-1, q \ge 2, n \ge 1$. This family of nanocones is parameterized in such a manner that k denotes the length of the cycle placed at the core of the nanocone and n is the number of hexagonal layers placed at the conical surface of the nanocone. Now we calculate the anti-Kekulé number of this class of nanocones.

Theorem 2.3 *Let G be the graph of $CNC_k[n]$ nanocone, where $k = 2q-1, q \ge 2, n \ge 1$, then $ak(G) = 2$.*

Proof. First we show that $ak(G) \le 2$. For this purpose, consider a set $S = \{s_1, s_2\} \subseteq E(G)$ and a $\{uvw\}-$path in G as shown in Fig. 6. Then,

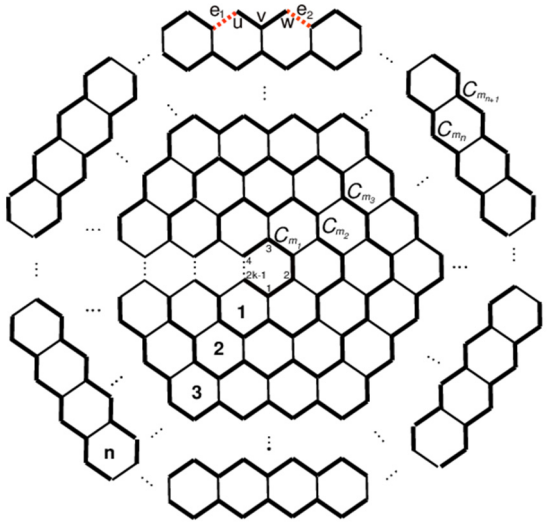

Figure 6. A representation of $CNC_k[n]$ nanocone, with k being an odd integer, with C_{n+1} cycles and a $uvw-$path.

there does not exist any perfect matching in the graph $G-S$. Thus $ak(G)\leq 2$.

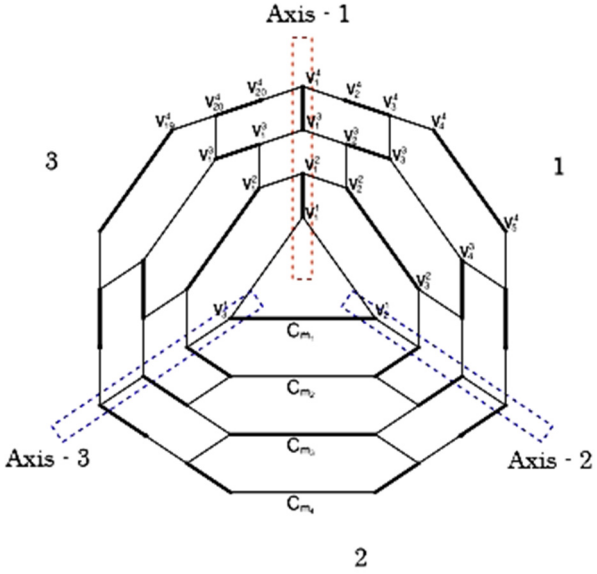

Figure 7. The perfect matching M_1 in $CNC_3[3]$ nanocone obtained by matching the edges on Axis-1. M_2 and M_3 can be obtained by matching other Axis.

Conversely, let $C_{m_i} = \{v_1^i, v_2^i, \ldots, v_{m_i}^i\}$, for $1 \le i \le n+1$, be the cycles as shown in Fig. 7. Then the length of the cycle C_{m_i} is $m_i = k(2i-1)$. Clearly, m_i (for $1 \le i \le n+1$) is always odd.

There are k different perfect matchings of the graph G (as constructed in Fig. 7, for $k = 3$), which can be obtained by relabeling the vertices of the graph or just by rotating the graph G. Let $M_1, M_2, \ldots, M_k$ be the perfect matchings in the graph G obtained by selecting the edges of the graph G lying on different axis. The k axis of the $CNC_k[n]$ nanocone (k odd) are shown in Fig. 8.

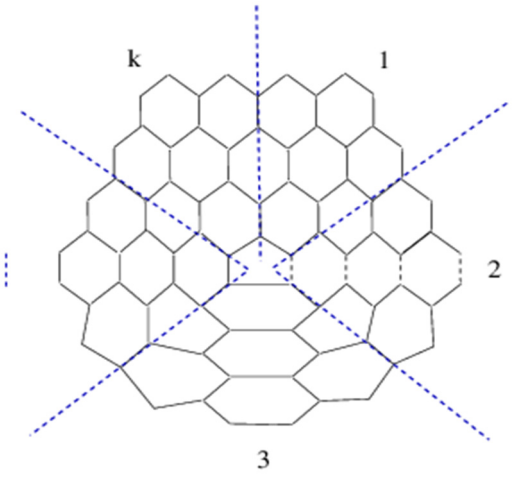

Figure 8. The k axis for the $CNC_k[n]$ nanocone for odd k

The k perfect matchings M_l, for $1 \le l \le k$, are defined as follows.

$$M_l = \{v^i_{l+2(l-1)(i-1)} v^{i+1}_{l+2(l-1)i},\ v^i_{l+2(l-1)(i-1)+s} v^i_{l+2(l-1)(i-1)+s+1},\ v^{i+1}_{l+2(l-1)i+s} v^{i+1}_{l+2(l-1)i+s+1} \mid$$
$$1 \le i \le n+1,\quad s+z \equiv z(\mathrm{mod}\, m_i),\quad where\ i, s\ are\ odd\}.$$

It can be seen that the $(l)-$phase of the matchings M_l and M_{l+1}, for $1 \le l \le k-1$, are same (see Fig. 7, for instance), and the rest of the phases are all different. The edges lying on the axis lines are not included in any phase.

Let $e \in E(G)$, then we have the following two cases.

Case 1. When e lies on an axis line. Since each matching M_l, $1 \le l \le k$, contains a single axis line. There will be $k-1$ perfect matchings in the graph $G-\{e\}$.

Case 2. When e does not lie on an axis line. Then e lies in one of the k phases of the nanocone, say phase$-(l)$. Then if e belongs to the edges of the graph G matched under M_l then we have $k-2$ perfect matchings M_t, $1 \le t \le k$ where $t \ne l$ and $t \ne l+1$, in the connected graph $G-\{e\}$. Thus $ak(G) \ge 2$, which completes the proof.

CONCLUDING REMARKS

The perfect matchings in a graph correspond to Kekulé structures which play an important role in the analysis of resonance energy and stability of hydrocarbons. Nanotubes and nanocones are allotropes of carbon having enormous applications in the field of nanotechnology, electronics, optics, materials science, and architecture. In this study, we proved that the anti-Kekulé number of the finite families of $TUC_4C_8(S)[p,q]$ nanotubes, $TUC_4C_8(S)[p,q]$ nanotubes $\forall p,q \in \mathbb{N}$ and for $CNC_{2k}[n]$ nanocones $\forall k,n \in \mathbb{N}$, is respectively 3, 4 and 2. Calculations showed that the anti-Kekulé number of almost all nanotubes is 2 or 3 in finite case and 4 or 5 if we consider their infinite 2 D lattices. Furthermore, our result of the anti-Kekulé number of a nanotorus agree with the anti-Kekulé number of fulerenes [8].

ACKNOWLEDGMENT

This research is supported by National University of Sciences and Technology, Islamabad, Pakistan and by the Higher Education Commission of Pakistan via grant no. 20-3067/NRPU/R&D/HEC/12/831.

REFERENCES

1. I. Gutman, O. Polansky, Mathematical Concepts in Organic Chemistry, *Springer-Verlag, Berlin*, **1986**.
2. M. Randic, *Chem. Rev*, **2003**, *103*, 34.
3. N. Trinajstic, Chemical Graph Theory, CRC Press, Boca Raton, FL, **1992**.
4. D. Vukičević, N. Trinajstić, *J. Math. Chem.*, **2007**, *42*, 575.
5. D. Vukičević, N. Trinajstić, *J. Math. Chem.*, **2008**, *43*, 719.
6. D. Veljan, D. Vukičević, *J. Math. Chem.*, **2008**, *43*, 243.
7. K. Kutnar, J. Sedlar, D. Vukičević, *J. Math. Chem.*, **2009**, *45*, 431.
8. Q. Yang, D. Ye, H. Zhang, *MATCH Commun. Math. Comput. Chem.*, **2012**, *67*, 281.
9. S. Tang, H. Deng, *Dig. J. Nanomater. Bios.,* **2011**, *6*, 439.
10. A. Xavier, A. S. Shanthi, M. J. Raja, *Intel. J. Pure App. Math.*, **2013**, *86*, 1019.
11. D. Ye, *Discr. Appl. Math.*, **2013**, *161*, 2196.
12. M.A. Malik, S. Hayat, M. Imran, *J. Comput. Theor. Nanos.*, accepted, in press.
13. M. Stefu, M. V. Diudea, *MATCH Commun. Math. Comput. Chem.*, **2004**, *50*, 133.

STUDIA UBB CHEMIA, LX, 2, Tom II, 2015 (p. 241-250)
(RECOMMENDED CITATION)

ON SOME TOPOLOGICAL INDICES OF THE GENERALIZED HIERARCHICAL PRODUCT OF GRAPHS

FREYDOON RAHBARNIA[a,*], MOSTAFA TAVAKOLI[a]
ALI REZA ASHRAFI[b]

ABSTRACT. The generalized hierarchical product of graphs was introduced very recently by L. Barriére et al. In this paper, revised Szeged and new version of Zagreb indices of generalized hierarchical product of two connected graphs are obtained. Using the results obtained here, some known results are deduced as corollaries. Finally, we obtain the Sz^*, M^*_1 and M^*_2 indices of the zig-zag polyhex nanotube $TUHC_6[2n, 2]$, linear phenylene F_n, hexagonal chain L_n and truncated cube as a consequence of our results.

Keywords: *Generalized hierarchical product, Cartesian product, Revised Szeged index, Zagreb indices.*

INTRODUCTION

Throughout this paper all graphs considered are finite, simple and connected. The **distance** *d(u,v)* between the vertices *u* and *v* of a graph *G* is equal to the length of a shortest path that connects *u* and *v*. Suppose *G* is a graph with vertex and edge sets *V = V(G)* and *E = E(G),* respectively. Suppose *e = uv∈ E(G)*. The set of vertices of *G* whose distance to the vertex *u* is smaller than the distance to the vertex *v* is denoted by $N_u^G(e)$. In addition, let $N_0^G(e)$ denote the set of vertices with equal distances to *u* and *v*. The **Szeged** and **revised Szeged indices** of the graph *G* are defined as:

$$Sz(G) = \sum_{e=uv\in E(G)} |N_u^G(e)||N_v^G(e)| \text{ [1, 2, 3]},$$

$$Sz^*(G) = \sum_{e=uv\in E(G)} \left(|N_u^G(e)| + \frac{|N_0^G(e)|}{2}\right)\left(|N_v^G(e)| + \frac{|N_0^G(e)|}{2}\right) \text{ [4, 5, 6]}.$$

[a] *Department of Mathematics, Ferdowsi University of Mashhad, P. O. Box 1159, Mashhad 91775, Iran.*
[b] *Department of Pure Mathematics, Faculty of Mathematical Sciences, University of Kashan, Kashan 87317-51167, I.R. Iran.*
* *Corresponding author: Rahbarnia@ferdowsi.um.ac.ir*

The **Zagreb indices** have been introduced by Gutman and Trinajstic as $M_1(G) = \sum_{u \in V(G)} (deg_G(u))^2$ and $M_2(G) = \sum_{uv \in E(G)} deg_G(u) deg_G(v)$, where $deg_G(u)$ denotes the degree of vertex u [7, 8]. In [9], a new version of Zagreb indices were defined as $M_1^*(G) = \sum_{uv \in E(G)} [\varepsilon_G(u) + \varepsilon_G(v)]$, $M_1^{**}(G) = \sum_{u \in V(G)} (\varepsilon_G(u))^2$ and $M_2^*(G) = \sum_{uv \in E(G)} \varepsilon_G(u) \varepsilon_G(v)$, where $\varepsilon_G(u)$ is the largest distance between u and any other vertex v of G. The total connectivity index $\zeta(G)$ of a graph G is defined as $\zeta(G) = \sum_{u \in V(G)} \varepsilon_G(u)$, see [10].

A graph G with a specified vertex subset $U \subseteq V(G)$ is denoted by $G(U)$. Suppose G and H are graphs and $U \subseteq V(G)$. The **generalized hierarchical product**, denoted by $G(U) \Pi H$, is the graph with vertex set $V(G) \times V(H)$ and two vertices (g, h) and (g', h') are adjacent if and only if $g = g' \in U$ and $hh' \in E(H)$ or, $gg' \in E(G)$ and $h = h'$, see Figure 1. This graph operation introduced recently by Barriere et al. [11, 12] and found some applications in computer science. The **Cartesian product**, $G \times H$, of graphs G and H has the vertex set $V(G \times H) = V(G) \times V(H)$ and $(u, x)(v, y)$ is an edge of $G \times H$ if $u = v$ and $xy \in E(H)$ or, $uv \in E(G)$ and $x = y$ [13, 14].

We denote by P_n and C_n the path and cycle with n vertices, respectively. A bipartite graph is a graph whose vertices can be partitioned into two disjoint subsets U_1 and U_2 such that every edge connects a vertex in U_1 to one in U_2; that is, U_1 and U_2 are independent sets. Our other notations are standard and taken mainly from the standard books of graph theory.

RESULTS AND DISCUSSION

We first introduce some notations. Let $G = (V, E)$ be a graph and $U \subseteq V$. In $G(U)$, an u–v path through U is an u–v path in G containing some vertex $w \in U$ (vertex w could be the vertex u or v). Let $d_{G(U)}(u,v)$ denote the length of a shortest u –v path through U in G. Notice that, if one of the vertices u and v belong to U, then $d_{G(U)}(u,v) = d_G(u,v)$. Furthermore, let $\varepsilon_{G(U)}(u) = max\{ d_{G(U)}(v, u) \mid v \in V(G(U))\}$, then $\zeta(G(U))$, $M_1^*(G(U))$, $M_2^*(G(U))$ and $M_1^{**}(G(U))$ can be defined as follows:

$$\zeta(G(U)) = \sum_{u \in V(G(U))} \varepsilon_{G(U)}(u),\ M_1^*(G(U)) = \sum_{uv \in E(G(U))} [\varepsilon_{G(U)}(u) + \varepsilon_{G(U)}(v)],$$

$$M_1^{**}(G(U)) = \sum_{u \in V(G(U))} (\varepsilon_{G(U)}(u))^2 \text{ and}$$

$$M_2^*(G(U)) = \sum_{uv \in E(G(U))} \varepsilon_{G(U)}(u)\varepsilon_{G(U)}(v).$$

For an edge $e = ab$ of $G(U)$, $N_a^{G(U)}(e)$ denotes the set of vertices closer to a than b through U in G and $N_0^{G(U)}(e)$ denotes the set of equidistant vertices of e through U in $G(U)$, i.e.

$$N_a^{G(U)}(e) = \{u \in V(G(U)) \mid d_{G(U)}(u,a) < d_{G(U)}(u,b)\},$$
$$N_0^{G(U)}(e) = \{u \in V(G(U)) \mid d_{G(U)}(u,a) = d_{G(U)}(u,b)\}.$$

Then $Sz^*(G(U))$, $Sz^{**}(G(U))$ and $Sz^{***}(G(U))$ can be defined as follows:

$$Sz^*(G(U)) = \sum_{e=uv \in E(G)} \left(|N_u^{G(U)}(e)| + \frac{|N_0^{G(U)}(e)|}{2}\right)\left(|N_v^{G(U)}(e)| + \frac{|N_0^{G(U)}(e)|}{2}\right),$$
$$Sz^{**}(G(U)) = \frac{1}{2}\sum_{e=uv \in E(G(U))} \left(|N_u^{G(U)}(e)|\,|N_v^{G}(e)| + |N_v^{G(U)}(e)|\,|N_u^{G}(e)|\right),$$
$$Sz^{**}(G(U)) = \frac{1}{2}\sum_{e=uv \in E(G(U))} \left(|N_u^{G(U)}(e)|\,|N_u^{G}(e)| + |N_v^{G(U)}(e)|\,|N_v^{G}(e)|\right).$$

Therefore, it is clear that if $U = V(G)$, then $Sz^{**}(G) = Sz(G)$.

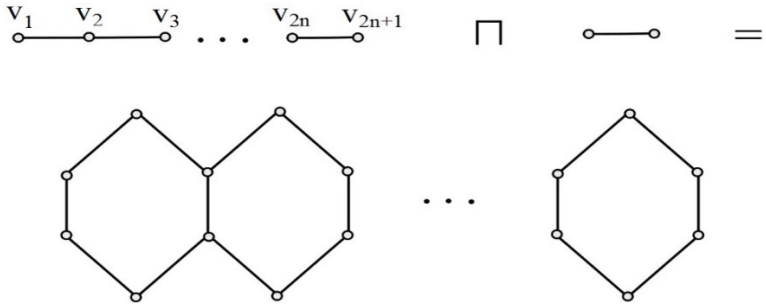

Figure 1. Hexagonal chain $L_n = P_{2n+1}(U) \sqcap P_2$, where $U = \{v_1, v_3, v_5, \ldots, v_{2n+1}\}$.

Lemma 1. (See [12]). Let G and H be graphs with $U \subseteq V(G)$. Then we have

(a) If $U = V(G)$, then the generalized hierarchical product $G(U) \sqcap H$ is the Cartesian product of G and H ,
(b) $|V(G(U) \sqcap H)| = |V(G)||V(H)|$, $|E(G(U) \sqcap H)| = |E(G)||V(H)| + |E(H)||U|$,
(c) $G(U) \sqcap H$ is connected if and only if G and H are connected,

(d) $d_{G(U)\Pi H}((g,h),(g',h')) = \begin{cases} d_{G(U)}(g,g') + d_H(h,h') & \text{if } h \neq h', \\ d_G(g,g') & \text{if } h = h'. \end{cases}$

Theorem 2. Let G and H be two connected graphs and let U be a nonempty subset of $V(G)$. Then

$$Sz^*(G(U)\Pi H) = |V(H)|(|V(H)|-1)^2 Sz^*(G(U)) + |V(H)|Sz^*(G) + |V(H)|(|V(H)|-1)\left(Sz^{**}(G(U)) - Sz^{***}(G(U))\right) + \frac{1}{2}|E(G)||V(G)|^2|V(H)|(|V(H)|-1) + |U||V(G)|^2 Sz^*(H).$$

Proof. Let G and H be two connected graphs and let U be a nonempty subset of $V(G)$. For our convenience, we partition the edge set of $G(U)\ \Pi H$ into two sets,

$$E_1 = \{(g,h)(g',h') \mid gg' \in E(G) \text{ and } h = h' \in V(H)\},$$
$$E_2 = \{(g,h)(g',h') \mid hh' \in E(H) \text{ and } g = g' \in U\}.$$

Let $e = (g,h)(g',h) \in E_1$. Suppose $(x,y) \in V(G(U)\ \Pi H)$, thus by Lemma 1, $(x,y) \in N^{G(U)\Pi H}_{(g,h)}(e)$, if $y = h$ and $x \in N^G_g(gg')$ or, $y \neq h$ and $x \in N^{G(U)}_g(gg')$. Therefore, we have

$$|N^{G(U)\Pi H}_{(g,h)}(e)| = (|V(H)|-1)\,|N^{G(U)}_g(gg')| + |N^G_g(gg')|,$$
$$|N^{G(U)\Pi H}_{(g',h)}(e)| = (|V(H)|-1)\,|N^{G(U)}_{g'}(gg')| + |N^G_{g'}(gg')|,$$
$$|N^{G(U)\Pi H}_0(e)| = (|V(H)|-1)\,|N^{G(U)}_0(gg')| + |N^G_0(gg')|.$$

Thus, the summation of $[|N^{G(U)\Pi H}_{(g,h)}(e)| + \frac{1}{2}|N^{G(U)\Pi H}_0(e)|] \times [|N^{G(U)\Pi H}_{(g',h')}(e)| + \frac{1}{2}|N^{G(U)\Pi H}_0(e)|]$ over all edges of E_1, is equal to:

$$Sz_1 = |V(H)|(|V(H)|-1)^2 Sz^*(G(U)) + |V(H)|Sz^*(G) + |V(H)|(|V(H)|-1)\left(Sz^{**}(G(U)) - Sz^{***}(G(U))\right) + \frac{1}{2}|E(G)||V(G)|^2|V(H)|(|V(H)|-1).$$

On the other hand, assume that $e = (g,h)(g,h') \in E_2$ and let $(x,y) \in V(G(U)\ \Pi H)$, thus by Lemma 1, $(x,y) \in N^{G(U)\Pi H}_{(g,h)}(e)$ if $y \in N^H_h(hh')$. Then

$$|N^{G(U)\Pi H}_{(g,h)}(e)| = |V(G)||N^H_h(hh')|, \quad |N^{G(U)\Pi H}_{(g,h')}(e)| = |V(G)||N^H_{h'}(hh')|,$$

$$|N_0^{H(U)\Pi H}(e)| = |V(G)||N_0^H(hh')|.$$

Therefore, the summation of

$$[|N_{(g,h)}^{G(U)\Pi H}(e)| + \tfrac{1}{2}|N_0^{G(U)\Pi H}(e)|][|N_{(g',h')}^{G(U)\Pi H}(e)| + \tfrac{1}{2}|N_0^{G(U)\Pi H}(e)|]$$

over all edges of E_2, is equal to:

$$Sz_2 = |U||V(G)|^2 Sz^*(H).$$

By summation of Sz_1 and Sz_2, the result can be proved. □

By definition of Sz^*, Sz^{**} and Sz^{***}, we have

$$2Sz^*(G) - Sz^{**}(G) + Sz^{***}(G) = \frac{1}{2}|E(G)||V(G)|^2.$$

In the above theorem, if we set $U = V(G)$, then by the above equality, we obtain the following corollary.

Corollary 3. Let G and H be two connected graphs. Then

$$Sz^*(G\times H) = |V(H)|^3 Sz^*(G) + |V(G)|^3 Sz^*(H).$$ □

Theorem 4. Let G and H be two connected graphs and let U be a nonempty subset of $V(G)$. Then

$$M_1^*(G(U)\,\Pi H) = |V(H)|M_1^*(G(U)) + |U|M_1^*(H) + 2|E(G)|\zeta(H) + 2|E(H)|\sum_{u\in U}\varepsilon_{G(U)}(u).$$

Proof. Let G and H be two connected graphs and let U be a nonempty subset of $V(G)$. For our convenience, we partition the edge set of $G(U)\,\Pi H$ into two sets,

$$E_1 = \{(g,h)(g',h') \mid gg' \in E(G) \text{ and } h = h' \in V(H)\},$$

$$E_2 = \{(g,h)(g',h') \mid hh' \in E(H) \text{ and } g = g' \in U\}.$$

Suppose $(x,y) \in V(G(U)\,\Pi H)$, then by Lemma 1,

$$\varepsilon_{G(U)\Pi H}((x,y)) = \varepsilon_{G(U)}(x) + \varepsilon_H(y).$$

Therefore,

$$M_1^*(G(U)\,\Pi H) = \sum_{(g,h)(g',h')\in E(G(U)\Pi H)}[\varepsilon_{G(U)\Pi H}((g,h)) + \varepsilon_{G(U)\Pi H}((g',h'))]$$

$$= \sum_{(g,h)(g',h)\in E_1} [\varepsilon_{G(U)\Pi H}((g,h)) + \varepsilon_{G(U)\Pi H}((g',h))]$$
$$+ \sum_{(g,h)(g,h')\in E_2} [\varepsilon_{G(U)\Pi H}((g,h)) + \varepsilon_{G(U)\Pi H}((g,h'))]$$
$$= \sum_{h\in V(H)} \sum_{gg'\in E(G)} \left(\varepsilon_{G(U)}(g) + 2\varepsilon_H(h) + \varepsilon_{G(U)}(g')\right)$$
$$+ \sum_{g\in U} \sum_{hh'\in E(H)} \left(2\varepsilon_{G(U)}(g) + \varepsilon_H(h) + \varepsilon_H(h')\right) = |V(H)|M_1^*(G(U))$$
$$+ |U|M_1^*(H) + 2|E(G)|\zeta(H) + 2|E(H)| \sum_{u\in U} \varepsilon_{G(U)}(u). \qquad \square$$

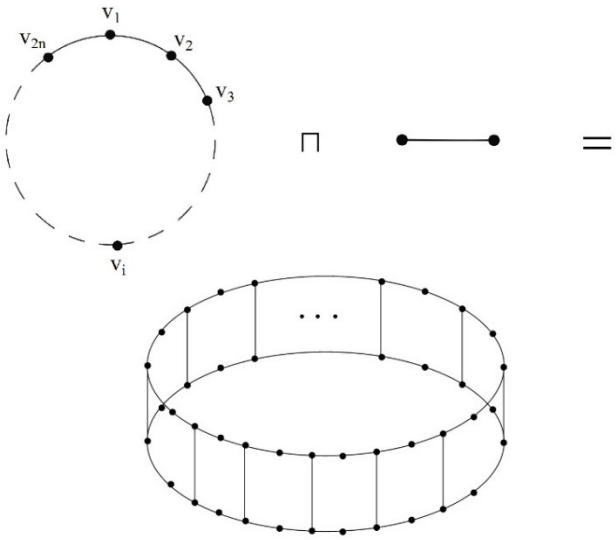

Figure 2. The zig-zag polyhex nanotube $TUHC_6[2n,2] = C_{2n}(U)\ \Pi P_2$, where $U = \{v_2, v_4, \ldots, v_{2n}\}$.

By a similar argument as in the proof of the previous theorem, we have:

Theorem 5. Let G and H be two connected graphs and let U be a nonempty subset of $V(G)$. Then

i). $M_2^*(G(U)\ \Pi H) = |V(H)|M_2^*(G(U)) + |U|M_2^*(H) + \zeta(H)M_1^*(G(U)) + |E(G)|M_1^{**}(H) + |E(H)| \sum_{u\in U} (\varepsilon_{G(U)}(u))^2 + M_1^*(H) \sum_{u\in U} \varepsilon_{G(U)}(u)$.

ii). $M_1^{**}(G(U)\ \Pi H) = |V(H)|M_1^{**}(G(U)) + |V(G)|M_1^{**}(H) + 2\zeta(G(U))\zeta(H)$. $\square$

The exact formulas for M_2^* of the Cartesian product of graphs were obtained in [9]. We claim that this result is incorrect. The aim of the next corollary is to improve this result. In the part (*i*) of the above theorem, if we set $U = V(G)$, we obtain the following corollary.

Corollary 6. Let G and H be two connected graphs. Then

$$M_2^*(G \times H) = |V(H)|M_2^*(G) + |E(G)|M_1^{**}(H) + \zeta(H)M_1^*(G) + |V(G)|M_2^*(H) + |E(H)|M_1^{**}(G) + \zeta(G)M_1^*(H).$$ □

For the graphs in Figs.1 and 2, namely, zig-zag polyhex nanotube $TUHC_6[2n,2]$ and hexagonal chain L_n , some graph invariants were studied in [15, 16, 17, 18]. Here we obtain Sz^*, M_1^*, M_2^* and M_1^{**} of zig-zag polyhex nanotube and the hexagonal chain L_n.

Example 7. Consider the zig-zag polyhex nanotube $TUHC_6[2n,2]$ (see Fig. 2). Diudea, who was the first chemist which considered the problem of computing topological indices of nanostructures, introduced the notation $TUHC_6$. The zig-zag polyhex nanotube is the graph $C_{2n}(U)\ \Pi P_2$, where $U = \{v_2, v_4, \ldots, v_{2n}\}$, see Fig. 2. On the other hand, one can easily see that $Sz^{**}(C_{2n}(U)) = Sz^{***}(C_{2n}(U)) = Sz^*(C_{2n}) = 2n^3$ and $Sz^*(C_{2n}(U)) = 2n(n^2 - 1)$ and so, by Theorem 2, we have

$$Sz^*(TUHC_6[2n,2]) = 20n^3 - 4n.$$

Example 8. Consider the hexagonal chain L_n (see Fig. 1). The hexagonal chain L_n is the graph $P_{2n+1}(U)\ \Pi P_2$, where $U = \{v_1, v_3, \ldots, v_{2n+1}\}$, see Fig. 1. On the other hand, it is not difficult to check that $Sz^*(P_{2n+1}) = Sz^*(P_{2n+1}(U)) = \frac{4}{3}n^3 + 2n^2 + \frac{2}{3}n$, $Sz^{**}(P_{2n+1}(U)) = \frac{4}{3}n^3 + 2n^2 + \frac{5}{3}n$ and $Sz^{***}(P_{2n+1}(U)) = \frac{8}{3}n^3 + 2n^2 - \frac{2}{3}n$ and so, by Theorem 2, we obtain

$$Sz^*(L_n) = \frac{44}{3}n^3 + 24n^2 + \frac{43}{3}n + 1.$$

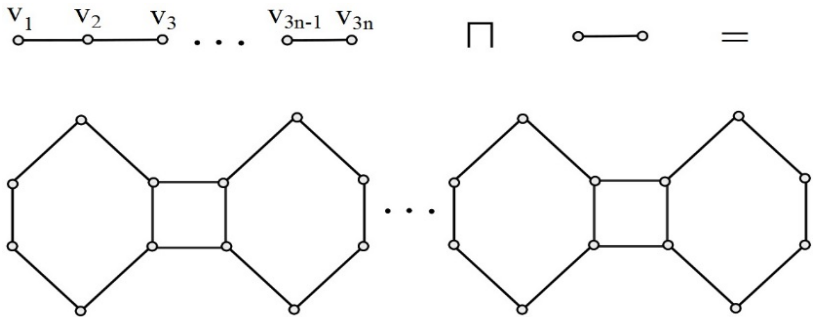

Figure 3. The linear phenylene $F_n = P_{3n}(U)\ \Pi P_2$, where $U = \{v_{3k+1} \mid 0 \le k \le n-1\} \cup \{v_{3k} \mid 1 \le k \le n\}$.

Example 9. Consider the linear phenylene F_n including n benzene ring (see Fig. 3). The linear phenylene F_n is the graph $P_{3n}(U)\ \Pi P_2$, where $U = \{v_{3k+1} \mid 0 \le k \le n-1\} \cup \{v_{3k} \mid 1 \le k \le n\}$, see Fig. 3. On the other hand, it is not difficult to check that $Sz^*(P_{3n}) = Sz^*(P_{3n}(U)) = \frac{9}{2}n^3 - \frac{1}{2}n$, $Sz^{**}(P_{3n}(U)) = \frac{9}{2}n^3 + \frac{1}{2}n$ and $Sz^{***}(P_{3n}(U)) = 9n^3 - \frac{9}{2}n^2 - \frac{1}{2}n$ and so, by Theorem 2, we obtain $Sz^*(F_n) = Sz^*(P_{3n}(U)\ \Pi P_2) = 54n^3$.

In [19, Example 3.2], the authors claim that $Sz(F_n) = 54n^3 - 4n$. We claim that this result is incorrect. By [19, Example 3.2], $Sz(F_1) = 50$ and $Sz(F_2) = 424$ that, are incorrect. The correct values are $Sz(F_1) = 54$ and $Sz(F_2) = 432$. Note that F_n is bipartite and so $Sz^*(F_n) = Sz(F_n)$. On the other hand, by the above example, $Sz^*(F_n) = 54n^3$ and so, $Sz(F_n) = 54n^3$.

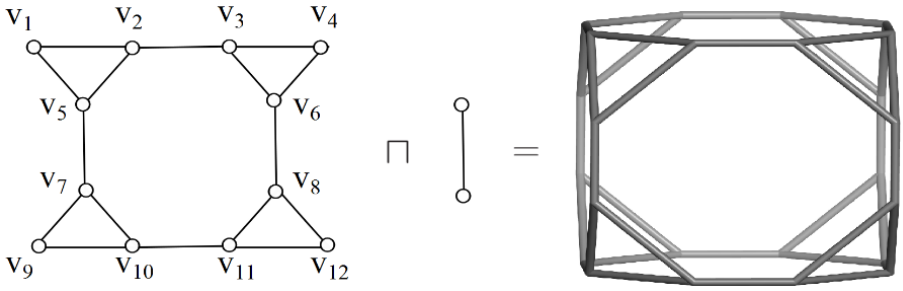

Figure 4. The molecular graph of truncated cube $H = G(U)\ \Pi P_2$, where $U = \{v_1, v_4, v_9, v_{12}\}$.

Example 10. Let H be the graph of truncated cube. Then $H = G(U) \Pi P_2$, where $U = \{v_1, v_4, v_9, v_{12}\}$, as shown in Figure 4. It is not difficult to check that $Sz^*(G) = Sz^*(G(U)) = 526$, $Sz^{**}(G(U)) = 380$, $Sz^{***}(G(U)) = 280$ and so, by Theorem 2, we have $Sz^*(H) = Sz^*(G(U) \Pi P_2) = 3264$.

Example 11. Consider the hexagonal chain L_n and the zig-zag polyhex nanotube $TUHC_6[2n,2]$ and truncated cube H depicted in Figs. 1, 2 and 4, respectively, such that n > 1. One can easily see that $M_1^*(P_{2n+1}(U)) = 6n^2$, $M_2^*(P_{2n+1}(U)) = \frac{14}{3}n^3 - \frac{2}{3}n$, $M_1^*(C_{2n}(U)) = 4n^2$, $M_2^*(C_{2n}(U)) = M_1^{**}(C_{2n}(U)) = M_1^{**}(C_{2n}) = 2n^3$, $M_1^*(G(U)) = 160$, $M_2^*(G(U)) = 400$, $\sum_{g\in U} \varepsilon_{C_{2n}(U)}(g) = n^2$, $\sum_{g\in U} (\varepsilon_{C_{2n}(U)}(g))^2 = n^3$, $\sum_{g\in U} \varepsilon_{P_{2n+1}(U)}(g) = \begin{cases} \frac{3}{2}n^2 + 2n + \frac{1}{2} & 2 \mid n \\ \frac{3}{2}n^2 + 2n & 2 \nmid n \end{cases}$,

$\sum_{g\in U} (\varepsilon_{P_{2n+1}(U)}(g))^2 = \begin{cases} \frac{7}{3}n^3 + 4n^2 + \frac{5}{3}n & 2 \mid n \\ \frac{7}{3}n^3 + 4n^2 + \frac{2}{3}n & 2 \nmid n \end{cases}$, $\sum_{g\in U} \varepsilon_{G(U)}(g) = 20$, $\sum_{g\in U} (\varepsilon_{G(U)}(g))^2 = 10$ and so, by Theorems 4 and 5, for n > 1, we have:

1. $M_1^*(L_n) = M_1^*(P_{2n+1}(U) \Pi P_2) = \begin{cases} 15n^2 + 14n + 3 & 2 \mid n \\ 15n^2 + 14n + 2 & 2 \nmid n \end{cases}$.
2. $M_1^*(TUHC_6[2n,2]) = M_1^*(C_{2n}(U) \Pi P_2) = 10n(n+1)$.
3. $M_2^*(L_n) = M_2^*(P_{2n+1}(U) \Pi P_2) = \begin{cases} \frac{35}{3}n^3 + 19n^2 + \frac{28}{3}n + 2 & 2 \mid n \\ \frac{35}{3}n^3 + 19n^2 + \frac{25}{3}n + 1 & 2 \nmid n \end{cases}$.
4. $M_2^*(TUHC_6[2n,2]) = M_2^*(C_{2n}(U) \Pi P_2) = 5n^3 + 10n^2 + 5n$.
5. $M_1^*(H) = M_1^*(G(U) \Pi P2) = 432$.
6. $M_2^*(H) = M_2^*(G(U) \Pi P_2) = 1296$.

ACKNOWLEDGMENTS

We are indebted to the referee for correcting our calculations in The research of the first and second authors was supported by a grant from Ferdowsi University of Mashhad; (No. MA92296RAH). The research of the third author is partially supported by the University of Kashan under grant no 159020/111.

REFERENCES

1. S. Klavžar, A. Rajapakse, I. Gutman, The Szeged and the Wiener index of graphs, *Appl. Math. Lett.,* **1996**, *9*, 45.
2. M. Tavakoli, F. Rahbarnia, A.R. Ashrafi, Further results on hierarchical product of graphs, *Discrete Appl. Math*., **2013**, *161*, 1162.
3. M.H. Khalifeh, H. Yousefi-Azari, A.R. Ashrafi and S.G. Wagner, Some new results on distance-based graph invariants, *European J. Combin*., **2009**, *30*, 1149.
4. T. Pisanski, M. Randić, Use of the Szeged index and the revised Szeged index for measuring network bipartivity, *Discrete Appl. Math.,* **2010**, *158*, 1936.
5. M. Randić, On generalization of Wiener index for cyclic structures, *Acta Chim. Slovenica,* **2002**, *49*, 483.
6. R. Xing, B. Zhou, On the revised Szeged index, *Discrete Appl. Math*., **2011**, *159*, 69.
7. I. Gutman, N. Trinajstic, Graph theory and molecular orbitals. Total *π*-electron energy of alternant hydrocarbons, *Chem. Phys. Lett.,* **1972**, *17*, 535.
8. I. Gutman, B. Ruscic, N. Trinajstic, C.F. Wilcox, Graph theory and molecular orbitals. XII. Acyclic polyenes, *J. Chem. Phys.,* **1975**, *62*, 3399.
9. M. Ghorbani and M.A. Hosseinzadeh, A New Version of Zagreb Indices, *Filomat*, **2012**, *1*, 93.
10. A.R. Ashrafi, M. Saheli, M. Ghorbani, The eccentric connectivity index of nanotubes and anotori, *J. Comput. Appl. Math.,* **2011**, *235*, 4561.
11. L. Barriére, F. Comellas, C. Dafló, M.A. Fiol, The hierarchical product of graphs, *Discrete Appl. Math.,* **2009**, *157*, 36.
12. L. Barriére, F. Comellas, C. Dafló, M.A. Fiol and M. Mitjana The generalized hierarchical product of graphs, *Discrete Math.,* **2009**, *309*, 3871.
13. R. Hammack, W. Imrich and S. Klavžar, Handbook of Product Graphs, Second edition, Taylor Francis Group, **2011**, chapter 5.
14. M. Tavakoli, H. Yousefi-Azari, A.R. Ashrafi, Note on edge distance-balanced graphs, *Trans. Combin.,* **2012**, *1*, 1.
15. M. Eliasi, A. Iranmanesh, The hyper-Wiener index of the generalized hierarchical product of graphs, *Discrete Appl. Math.,* **2011**, *159*, 866.
16. M.V. Diudea, Polyhex tori originating in square tori. In: M.V. Diudea, Ed., Nanostructures-Novel Architecture, NOVA, New York, **2005**, 111.
17. M.V. Diudea, M. Stefu, B. Parv, and P.E. John, Wiener index of armchair polyhex nanotubes. *Croat*. *Chem. Acta*, **2004**, *77*, 111.
18. P.E. John and M.V. Diudea, Wiener index of zig-zag polyhex nanotubes, *Croat*. *Chem. Acta*, **2004**, *77*, 127.
19. M. Arezoomand, B. Taeri, Applications of generalized hierarchical product of graphs in computing the Szeged index of chemical graphs, *MATCH Commun. Math. Comput. Chem.,* **2010**, *64*, 591.

STUDIA UBB CHEMIA, LX, 2, Tom II, 2015 (p. 251-258)
(RECOMMENDED CITATION)

SOME CONNECTIVITY INDICES OF CAPRA-DESIGNED PLANAR BENZENOID SERIES $Ca_n(C_6)$

MOHAMMAD REZA FARAHANI[a], **MIRANDA PETRONELLA VLAD**[b]

ABSTRACT. A molecular graph can be transformed using map operations, one of these, named Capra, being defined by *Diudea*. In this paper, we focus on the structure of *Capra-designed planar benzenoid series* $Ca_n(C_6)$ ($k\geq 0$) and compute some connectivity indices of this family. A connectivity index is a real number related to a molecular graph and is invariant under graph automorphism.

Keywords: *Benzenoid, Capra map operation, Connectivity index.*

INTRODUCTION

Let $G=(V,E)$ be a molecular graph with the vertex set $V(G)$ and the edge set $E(G)$. $|V(G)|=n$, $|E(G)|=e$ are the number of vertices and edges. In chemical graph theory, the vertices and edges correspond to the atoms and bonds, respectively; the number of incident edges in the vertex v is its degree, denoted by d_v. The vertices u and v are adjacent if there exist an edge $e=uv$ between them. A molecular graph is a connected graph, i.e. there exist a path between any pair of vertices.

A variety of topological indices have been defined; a topological index is a real number related to the structure of graph, which is invariant under graph automorphism.

In 1975 Randić proposed a structural descriptor called the branching index [1-4] that later named the Randić molecular connectivity index (or simply Randić index). It is defined as:

$$\chi(G) = \sum_{e=uv\in E(G)} \frac{1}{\sqrt{d_u d_v}}$$

[a] *Department of Mathematics of Iran University of Science and Technology, (IUST) Narmak, Tehran 16844, Iran, Mr_Farahani@Mathdep.iust.ac.ir*
[b] *Dimitrie Cantemir University, Bucharest, Faculty of Economic Sciences, No 56 Teodor Mihali Street, 400591, Cluj Napoca, Romania, mirandapv@yahoo.com*

Recently, a version, called the Sum-connectivity index, was introduced by *Zhou* and *Trinajstić* [5,6]:

$$X(G) = \sum_{v_u v_v} \frac{1}{\sqrt{d_u + d_v}}$$

where d_u and d_v are the degrees of the vertices u and v, respectively.

More recently, *Vukicevic* and *Furtula* [7] proposed two topological indices, named *geometric-arithmetic index* and *atom-bond connectivity index* (denoted by *GA(G)* and *ABC(G),* respectively), see [7-9]. They are defined as follows:

$$GA(G) = \sum_{e=uv \in E(G)} \frac{2 \times \sqrt{d(u)d(v)}}{d(u) + d(v)}$$

$$ABC(G) = \sum_{e=uv \in E(G)} \sqrt{\frac{d(u) + d(v) - 2}{d(u)d(v)}}$$

Definition 1. Let G be a molecular graph and d_v being the degree of vertex $v \in V(G)$. We divide the vertex set *V(G)* and edge set *E(G)* of *G* into several partitions, as follow:

$$\forall i, \delta < i < \Delta, V_i = \{v \in V(G) \mid d_v = i\},$$
$$\forall j, 2\delta \le j \le 2\Delta, E_j = \{e = uv \in E(G) \mid d_v + d_u = j\}$$
$$\forall k, \delta^2 \le k \le \Delta^2, E_k^* = \{e = uv \in E(G) \mid d_v \times d_u = k\}.$$

Note that $\delta = Min\{d_v \mid v \in V(G)\}$ and $\Delta = Max\{d_v \mid v \in V(G)\}$.

MAIN RESULTS AND DISCUSSION

In this section, we compute Randić connectivity index, sum- connectivity index, geometric-arithmetic index and atom-bond connectivity index of Capra-designed planar benzenoid series $Ca_k(C_6)$.

A mapping is a new drawing of an arbitrary planar graph *G* on the plane. Capra map operation was introduced by *Diudea* [10,11]. This method enables one to build a new structure, according to Figure 1 and Definition 2:

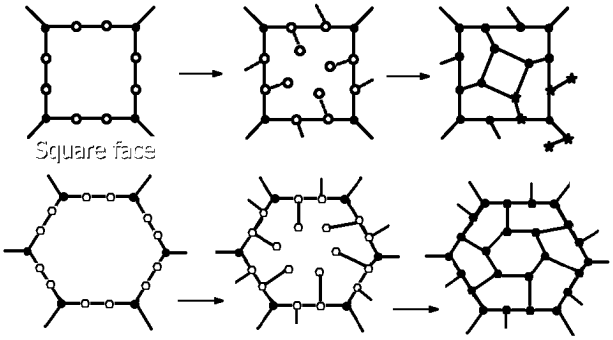

Figure 1. Capra map operation on the square and hexagonal face, respectively

Definition 2. Let *G* be a cyclic planar graph. Capra map operation is achieved as follows:

(i) insert two vertices on every edge of G;
(ii) add pendant vertices to the above inserted ones and
(iii) **c**onnect the pendant vertices in order (-1,+3) around the boundary of a face of G. By running these steps for every face/cycle of *G,* one obtains the Capra-transform of *G Ca(G)*, see Figure 1.

By iterating the Capra-operation on the hexagon (i.e. benzene graph C_6) and its Ca-transforms, a benzenoid series, as shown in Figures 2 and 3, can be designed. We will use the Capra-designed benzene series to calculate some connectivity indices (see below).

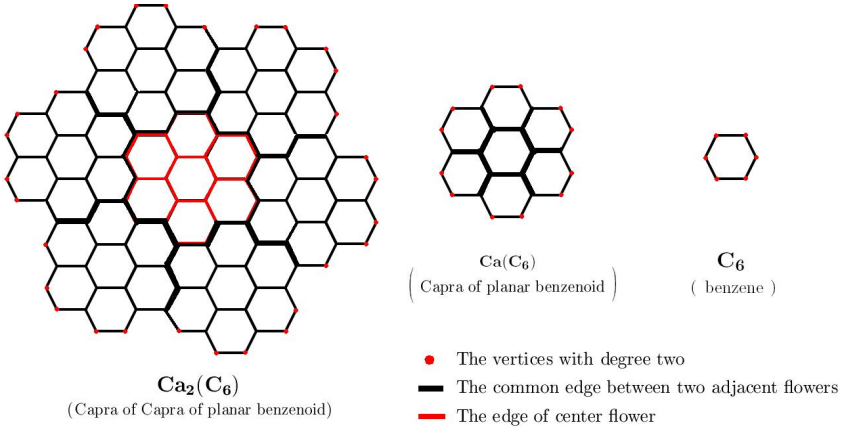

Figure 2. The first two graphs: *Ca(C6)* and *Ca2(C6)* of the benzenoid family *Cak(C6)*. Coloring is according to Definition 1.

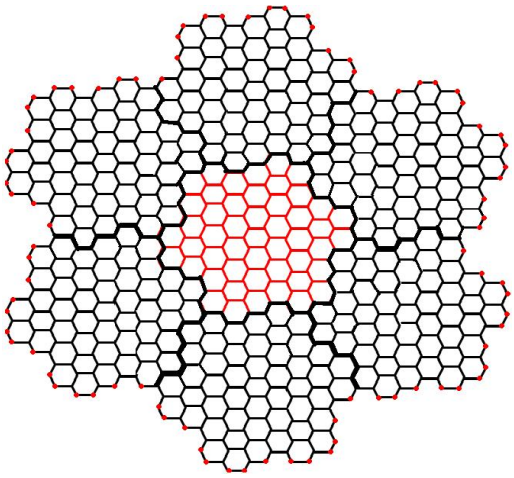

Figure 3. Graph $Ca_3(C_6)$ is the third member of Capra-designed planar benzenoid series.

Theorem 1. Let $G=Ca_k(C_6)$ $k\in N$ be the Capra-designed planar benzenoid series. Randić connectivity index is as follows:

$$\chi(Ca_k(C_6)) = \frac{2(7^k)+(4\sqrt{6}-1)3^{k-1}+1}{2}$$

Proof. Let $G=Ca_k(C_6)$ $(k\geq 0)$ be the Capra-designed planar benzenoid series. The structure $Ca_k(C_6)$ collects seven times of structure $Ca_{k-1}(C_6)$ (we call "flower" the substructure $Ca_{k-1}(C_6)$ in the graph $Ca_k(C_6)$). Therefore, by a simple induction on k, the vertex set of $Ca_k(C_6)$ will have $7\times|V(Ca_k(C_6))|-6(2\times 3^{k-1}+1)$ members. Because, there are $3^{k-1}+1$ and 3^{k-1} common vertices between seven flowers $Ca_{k-1}(C_6)$ in $Ca_k(C_6)$, marked by full black color in the above figures. Also, by a similar inference, the edge set $E(Ca_k(C_6))$ has $7\times|E(Ca_k(C_6))|-6(2\times 3^{k-1}+1)$ members. Thus, there are 3^{k-1} and 3^{k-1} common edges, see Figures 2 and 3. Now by solving the recursive sequences, $n_k=|V(Ca_k(C_6))|$ and $e_k=|E(Ca_k(C_6))|$. Thus the size of vertex set and edge set of Capra-designed planar benzenoid series $Ca_k(C_6)$ $(k\geq 0)$ are equal to:

$$|V(Ca_k(C_6))|=2\times 7^k+3^{k+1}+1,\ |E(Ca_k(C_6))|=3(7^k+3^k).$$

Now, we can divide $V(Ca_k(C_6))$ and $E(Ca_k(C_6))$ to two and three partitions, respectively (See Definition 1). According to Figures 2 and 3, we see that the number of vertices with degree two of graph $Ca_k(C_6)$ (denoted

by $v_2^{(k)}$) is equal to $6(3\left(\frac{v_2^{(k-1)}}{6}\right)-6$. Therefore, we have $v_2^{(k)} = 3v_2^{(k-1)} - 6$ $= 3(3v_2^{(k-2)} - 6) - 6 = \ldots = 3^k v_2^{(0)} - 6\sum_{i=0}^{k-1} 3^i = \mathbf{3^{k+1}} + \mathbf{3}$ and $e_4^{(k)} = |E_4| = |E_4^*|$ $= v_2^{(k-1)} = \mathbf{3^k} + \mathbf{3}$.

Alternatively, the number of vertices of degree three is $|V_3| = |\{v \in V(Ca_k(C_6)) \mid d_v = 3\}| = 2(7^k - 1)$, (denoted by $v_3^{(k)}$).

On the other hand, according to the structure of Capra-designed planar benzenoid series, *G=Ca_k(C₆)*, $e_5^{(k)} = |E_5| = |E_6^*| = 2v_2^{(k)} - 2e_4^{(k)}$. Thus, $e_5^{(k)} = 2v_2^{(k)} - 2v_2^{(k-1)} = \mathbf{4(3^k)}$. The size of edge set E_5 and E_6^* is: $e_5^{(k)} = 2(3^{k+1} + 3 - 3^k - 3) = \mathbf{4(3^k)}$. Thus, it is obvious that:

$$\begin{aligned} e_6^{(k)} &= |E_6| = |E_9^*| = 3\left(7^k + 3^k\right) - e_5^{(k)} - e_4^{(k)} \\ &= 3\times 7^k + 3^{k+1} - 4\times 3^k - 3^k - 3 \\ &= 3\times 7^k - 2\times 3^k - 3 \\ &= \mathbf{3(7^k - 2(3^{k-1}) - 1)}. \end{aligned}$$

Then, by using of size $V_2, V_3, E_4, E_4^*, E_5, E_6^*, E_6$ and E_9^*, we can compute Randić connectivity index of Capra-designed planar benzenoid series *G=Ca_k(C₆)* as follows:

$$\begin{aligned} \chi(Ca_k(C_6)) &= \sum_{uv \in E(Ca_k(C_6))} \frac{1}{\sqrt{d(u)d(v)}} \\ &= \sum_{uv \in E_9^*} \frac{1}{\sqrt{d(u)d(v)}} + \sum_{uv \in E_6^*} \frac{1}{\sqrt{d(u)d(v)}} + \sum_{uv \in E_4^*} \frac{1}{\sqrt{d(u)d(v)}} \\ &= \frac{|E_9^*|}{\sqrt{9}} + \frac{|E_6^*|}{\sqrt{6}} + \frac{|E_4^*|}{\sqrt{4}} \\ &= \frac{3(7^k - 2(3^{k-1}) - 1)}{\sqrt{9}} + \frac{4(3^k)}{\sqrt{6}} + \frac{3^k + 3}{\sqrt{4}}. \end{aligned}$$

Finally, the Randić index of *Ca_k(C₆)* is

$$\chi(Ca_k(C_6)) = \frac{\mathbf{2(7^k) + (4\sqrt{6} - 1)3^{k-1} + 1}}{\mathbf{2}}.$$

thus completing the proof of Theorem 1.

Theorem 2. Sum-connectivity index of Capra-designed planar benzenoid series $Ca_k(C_6)$ for integer k is equal to:

$$X(\mathbf{Ca_k(C_6)}) = \frac{3(\mathbf{3^{k-1}+1})+\sqrt{6}(\mathbf{7^k-1})}{\mathbf{2}} + \mathbf{3^{k-1}}\left(\frac{12\sqrt{5}-5\sqrt{6}}{5}\right).$$

Proof: By using the results from the above proof, it is immediate that

$$\begin{aligned} X(Ca_k(C_6)) &= \sum_{e=uv\in E(G)} \frac{1}{\sqrt{d_u+d_v}} \\ &= \sum_{e=uv\in E_4} \frac{1}{\sqrt{d_u+d_v}} + \sum_{e=uv\in E_5} \frac{1}{\sqrt{d_u+d_v}} + \sum_{e=uv\in E_6} \frac{1}{\sqrt{d_u+d_v}} \\ &= \frac{|E_4|}{\sqrt{4}} + \frac{|E_5|}{\sqrt{5}} + \frac{|E_6|}{\sqrt{6}} \\ &= \frac{3^k+3}{\sqrt{4}} + \frac{4(3^k)}{\sqrt{5}} + \frac{3(7^k-2(3^{k-1})-1)}{\sqrt{6}}. \end{aligned}$$

Thus $X(\mathbf{Ca_k(C_6)}) = \frac{3(\mathbf{3^{k-1}+1})+\sqrt{6}(\mathbf{7^k-1})}{\mathbf{2}} + \mathbf{3^{k-1}}\left(\frac{12\sqrt{5}-5\sqrt{6}}{5}\right).$

Theorem 3. Geometric-Arithmetic index and Atom-Bond connectivity index of Capra-designed planar benzenoid series are equal to (for all $k \in N$)

$$GA(Ca_k(C_6)) = 3(7^k) + \left(\frac{8\sqrt{6}}{5}-1\right)3^k$$

$$ABC(Ca_k(C_6)) = 2(7^k) + (\frac{15\sqrt{2}-8}{2})3^{k-1} + (\frac{3\sqrt{2}-4}{2})$$

Proof. Let $G=Ca_k(C_6)$ $(k\geq 1)$ be Capra-designed planar benzenoid series. According to the proof of Theorem 1, we have $|E_6| = |E_9^*| = 3(7^k - 2(3^{k-1}) - 1)$, $|E_5| = |E_6^*| = 4(3^k)$ and $|E_4| = |E_4^*| = 3^k + 3$. Thus, we can compute two connectivity topological indices geometric-arithmetic index and atom-bond connectivity index of $G=Ca_k(C_6)$ for any $k\geq 1$ as follows:

$$GA(Ca_k(C_6)) = \sum_{uv \in E(Ca_k(C_6))} \frac{2\sqrt{d(u)d(v)}}{d(u)+d(v)}$$

$$= \sum_{e=uv \in E_4} \frac{2\sqrt{4}}{4} + \sum_{e=uv \in E_5} \frac{2\sqrt{6}}{5} + \sum_{e=uv \in E_6} \frac{2\sqrt{9}}{6}$$

$$= e_6^{(k)} \frac{6}{6} + e_5^{(k)} \frac{2\sqrt{6}}{5} + e_4^{(k)} \frac{4}{4}$$

$$= 3(7^k) + \left(\frac{8\sqrt{6}}{5} - 1\right) 3^k$$

The geometric-arithmetic index of $Ca_k(C_6)$ is

$$GA(Ca_k(C_6)) = 3(7^k) + \left(\frac{8\sqrt{6}}{5} - 1\right) 3^k.$$

Finally,

$$ABC(Ca_k(C_6)) = \sum_{uv \in E(Ca_k(C_6))} \sqrt{\frac{d(u)+d(v)-2}{d(u)d(v)}}$$

$$= \sum_{uv \in E_9^*} \frac{1}{\sqrt{d(u)d(v)}} + \sum_{uv \in E_6^*} \frac{1}{\sqrt{d(u)d(v)}} + \sum_{uv \in E_4^*} \frac{1}{\sqrt{d(u)d(v)}}$$

$$= e_6^{(k)} \sqrt{\frac{6-2}{9}} + e_5^{(k)} \sqrt{\frac{5-2}{6}} + e_4^{(k)} \sqrt{\frac{4-2}{4}}$$

$$= 3(7^k - 2(3^{k-1}) - 1)\frac{2}{3} + 4(3^k)\frac{\sqrt{2}}{2} + (3^k + 3)\frac{\sqrt{2}}{2}.$$

Therefore, atom-bond connectivity index of $Ca_k(C_6)$ will be

$$ABC(Ca_k(C_6)) = 2(7^k) + \left(\frac{15\sqrt{2}-8}{2}\right)3^{k-1} + \left(\frac{3\sqrt{2}-4}{2}\right).$$

Here, the proof of Theorem 3 is completed.

ACKNOWLEDGMENTS

The authors are thankful to Professor Mircea V. Diudea, Faculty of Chemistry and Chemical Engineering, Babes-Bolyai University for his precious support and suggestions.

REFERENCES

1. M. Randić, On characterization of molecular branching, *J. Amer. Chem. Soc*., **1975**, *97,* 6609.
2. M. Ghorbani and M. Ghazi, *Digest. J. Nanomater. Bios*., **2010**, *5(4),* 1107.
3. M. Ghorbani and M. Ghazi, *Digest. J. Nanomater. Bios*., **2010**, *5(4),* 837.
4. J. Rada, O. Araujo, and I. Gutman, *Croat. Chem. Acta*, **2001**, *74,* 225.
5. B. Zhou and N. Trinajstić, On a novel connectivity index, *J. Math. Chem.,* **2009**, *46*, 1252.
6. B. Zhou and N. Trinajstić, On general sum-connectivity index, *J. Math. Chem.,* **2010**, *47*, 210.
7. D. Vukicevic and B. Furtula, *J. Math. Chem*., **2009**, *46,* 1369.
8. L. Xiao, S. Chen, Z. Guo and Q. Chen, *Int. J. Contemp. Math. Sci.,* **2010**, *5(45),* 2225.
9. Y. Yuan, B. Zhou and N. *Trinajstić, J. Math. Chem.,* **2010**, *47,* 833.
10. M.V. Diudea, Capra-a leapfrog related operation on maps, *Studia UBB Chemia*, **2003**, *48* (2), 3.
11. M.V. Diudea, Nanoporous carbon allotropes by septupling map operations. *J. Chem. Inf. Model*, **2005**, *45,* 1002.

STUDIA UBB CHEMIA, LX, 2, 2015 (p. 259-269)
(RECOMMENDED CITATION)

FAT CONTENT IN YOGHURTS VERSUS NON-FAT FORTIFYING–A RHEOLOGICAL AND SENSORIAL APPROACH

INA VASILEAN[a], IULIANA APRODU[a], LIVIA PATRASCU[a*]

ABSTRACT. This study investigated the effect of fat content (3.5; 1.5 and 0.1 % w/w), together with total solids content on selected rheological and sensorial characteristics of yoghurt samples fermented with exopolysaccharides producing lactic acid bacteria (*Streptococcus termophilus* and *Lactobacillus delbrueckii* ssp. *Bulgaricus*). Rheological flow and oscillatory tests showed that all tested yoghurt samples behave like thixotropic fluids. Pronounced hysteresis areas were obtained for skimmed yoghurts with added solids (skim milk powder and lactose, 2 and 3% w/v). Higher levels of fat favored the flow properties of the yogurt samples, enabling the formation of more stable viscoelastic gel networks. Sensorial characteristics were highly appreciated for samples with higher fat content.

Keywords**:** *yoghurt, exopolysaccharides, fat content, fortification, flow, viscoelastic gel*

INTRODUCTION

Fermented milk products are very popular all over the world[1], mainly because of their sensorial characteristics but also due to their potential in maintaining and even improving consumers` health [2]. The most widely used lactic acid bacteria for yogurt fermentation are *Streptococcus thermophilus* and *Lactobacillus delbrueckii* ssp. *Bulgaricus*, which are responsible for the development of specific taste and consistency.

The structure, microstructure and rheological characteristics of the yogurts highly influence the perception of the product during consumption [3]. It is well known that many technological parameters and starter culture can modulate textural properties of the yoghurts [4]. The knowledge of the yoghurt rheological properties can offer essential information about products texture

[a] *Universitatea Dunarea de Jos, Facultatea de Stiinta si Ingineria Alimentelor, Str. Domneasca, Nr. 111, RO-800201 Galati, Romania.*
[*] *Corresponding author: livia.mantoc@ugal.ro*

and gel stability. Skriver et al. [5] investigated both rheological and sensorial characteristics of stirred yogurts showing that gel firmness can be correlated with viscoelastic properties (G′, G″) while palatability was closely related to the shear stress. It is well known that textural and rheological characteristics of fermented lactic products with low fat and high protein content differ from those with no added solids, milk supplementation strongly influencing the texture of fermented products [6]. In order to improve rheological properties of skimmed dairy products different methods for increasing total solids content are approached. These compositional modifications are required in order to overcome problems associated with weak texture gels and whey separation [7].

Yoghurt bacteria can form a polysaccharide covering lair named glycocalyx. These macromolecular compounds can be partially released during fermentation process being generically named exopolysaccharides (EPS). The EPS producing starter bacteria ensure a stable yoghurt structure, a more consistent texture and higher viscosity by preventing gel rupture and whey releasing [8, 9, 10, 11,12]. The presence of EPS in lactic fermented milk products was found to improve rheological properties due to their thickening capacity, texture and products taste [13]. The EPS also have excellent water binding properties [14]. It was shown that yoghurt viscosity depends on EPS concentration and their specific volume [11]. However, Amatayakul et al. [15] concluded that using EPS-producing lactic acid bacteria could not compensate the reduction of total solids of yoghurt and these starter cultures are not efficient in improving the firmness of the low solid content products.

The aim of the present study was first to obtain yoghurt samples with different fat contents through fermentation with a pure culture of EPS producing lactic acid bacteria, and to characterize the obtained products in terms of rheological and sensory properties. Moreover, the influence of skim milk powder and lactose addition on the properties of skimmed yogurt was tested.

RESULTS AND DISCUSSION

Quality of the set yogurt obtained by fermenting milk with different fat contents (3.5, 1.5 and 0.1%) with EPS producing lactic acid bacteria was estimated by testing rheological behavior and sensory properties of the samples.

Rheological analyses. Two different types of tests were performed for rheological characterization of the samples: controlled shear-rate measurements by progressively increasing and decreasing the shear rate to check the viscosity dependence by the shear rate and small deformation oscillatory rheological test to gain insight into the structural particularities of the samples.

The flow parameters and hysteresis loop area obtained when performing shear thinning tests on the yoghurts with different fat contents are presented in Table 1.

Table 1. Rheological flow parameters for yoghurt samples with different fat and total solids content

Sample	Yield stress, Pa	Hysteresis area, Pa/s	Rate index		Viscosity, Pa*s	
			up curve	down curve	up curve	down curve
FY	1.907±0.01	18.1±0.35	0.350±0.01	0.409±0.01	1.017±0.03	0.778±0.02
NY	0.348±0.01	4.5±0.01	0.644±0.01	0.679±0.00	0.107±0.01	0.091±0.01
SY	1.632±0.01	30.4±0.21	0.324±0.02	0.445±0.01	0.907±0.01	0.516±0.01
SY_1	3.210±0.3	70.0±0.74	0.263±0.01	0.384±0.1	2.007±0.2	1.107±0.1
SY_2	3.344±0.3	71.2±0.77	0.260±0.00	0.374±0.01	2.098±0.12	1.198±0.03

Values represent means of three replicates ± SD. FY - Yoghurt with high fat content (3.5% fat w/w); NY – Partially skimmed yoghurt (1.5% fat w/w); SY – Skimmed yoghurt (0.1% fat w/w); SY_1 – Skimmed yoghurt enriched with 2% skim milk powder and 2% lactose (w/v); SY_2 - Skimmed yoghurt enriched with 3% skim milk powder and 3% lactose (w/v).

The flow behavior of the yogurt samples is represented in Figures 1 and 2. In order to improve appearance and quality of low fat yoghurts we proceeded to the fortification with skim milk powder (2 and 3% w/v) and lactose (2 and 3% w/v). Rheological characteristics of skimmed yoghurt were compared with those of the fortified products (Figure 2). Flow test revealed the thixotropic behavior for tested yoghurt samples as indicated by rate index values (Table 1). The shear thinning characteristic can be also seen in viscosity curves (decreasing viscosity when increasing shear rate) (Figures 1 and 2).

Regarding hysteresis phenomenon one can see that yoghurt with normalized fat content to 1.5% (w/w) recorded the lowest value, indicating that when speaking of yoghurts, high fat content does not necessary ensure flow stability. Moreover, samples with high fat contents (3.5% w/w) requested a rather high yield stress value (calculated with Bingham equation) in order to flow, compared to the samples with 1.5% and 0.1% fat contents and no added foreign solids. Adding solids to the skimmed yoghurt samples resulted in higher values for the yield stress, with no significant differences ($p>0.05$) between SY_1 and SY_2 sample (Table 1). The yoghurt samples supplemented with 2% of lactose and skim milk powder (SY_1) presented higher values of the hysteresis area compared to the un-fortified skimmed yogurt. Further increase of the solid content (SY_2 sample) did not led to significant differences ($p>0.05$) in terms of hysteresis area.

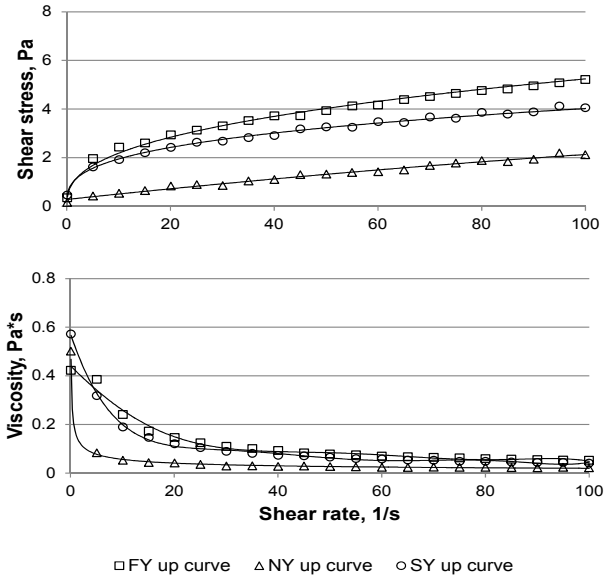

Figure 1. Flow behaviour of yoghurt samples with different fat contents. FY - Yoghurt with high fat content (3.5% fat w/w); NY – Partially skimmed yoghurt (1.5% fat w/w); SY – Skimmed yoghurt sample (0.1% fat w/w);

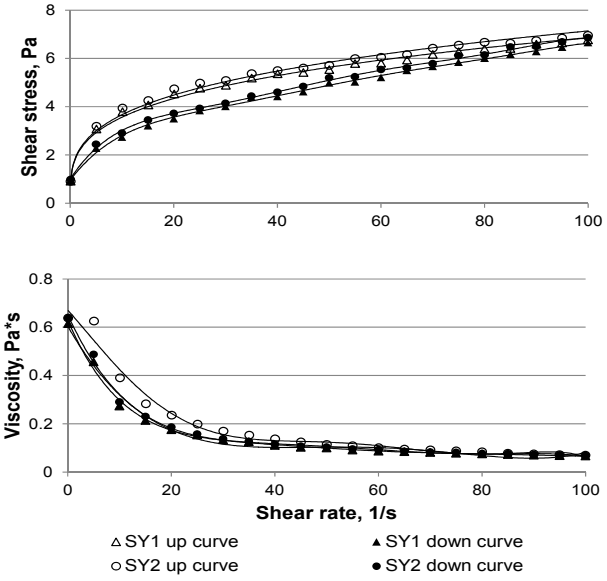

Figure 2. Flow behaviour of the skimmed and fortified yoghurt samples. SY_1 – Skimmed yoghurt sample enriched with 2% skim milk powder and 2% lactose (w/v); SY_2 - Skimmed yoghurt sample enriched with 3% skim milk powder and 3% lactose (w/v)

Protein addition to the skimmed milk samples (SY_1 and SY_2) resulted in higher viscosity and shear stress values compared to the skimmed yoghurt with no added solids (SY) (Figure 1 and 2). Therefore, protein addition might be considered appropriate for improving yogurt structure by favoring a thicker gel network formation. These findings are in agreement with Bhullar et al. [16], who stated that supplementation of the yogurt samples with 2% (w/v) of whey protein concentrate led to increased viscosity and reduced syneresis. The lack of fat in yoghurt structure could affect EPS interaction with product components, resulting in higher hysteresis areas during flow (Figure 2). This phenomenon can be explained by the presence of higher number of protein-protein links, which result in a denser gel network and fewer protein-water links [17, 18, 15].

EPS presence into the samples highly influences the viscosity and other rheological properties of the yogurts. Patel *et al*. [19] stated that EPS exhibit remarkable thickening and shear-thinning properties, and display high intrinsic viscosities. Broadbent et al. [20] found that the amount of EPS produced in lactic fermented milk products is influenced by the environment composition (C:N ratio) and growing conditions. In our case the amount of synthesized EPS, reported by Vasilean et al. [21] when using the same yogurt preparation procedure, was relatively close in case of the samples obtained from whole fat and partially skimmed milk (71.46 and 71.07 mg/l respectively), and lower in case of the yogurt obtained from skimmed milk (63.65 mg/l). The addition of protein and lactose to the skimmed milk before fermentation did not favor the EPS amount from yoghurt samples (63.51 mg/l for SY_1 sample and 68.89 mg/l for SY_2). Thus the viscosity increment in fortified samples could not be necessarily attributed to EPS presence.

Analyzing oscillatory rheology results presented in Figure 3, the soft solid structure can be observed for all yoghurt samples. For the entire range of tested frequency, G' values overcame the G``, indicating that yoghurt samples behaved like elastoviscous fluids. The yoghurt sample with high fat content (FY) presented the highest value of elastic modulus. In agreement with the flow test observations, the SY sample presented a more elastic (solid like behaviour) structure with respect to NY sample. We appreciate that this phenomenon could be explained by different molecule distribution within the gel network and by the different bond type participating to network formation and stabilization. As indicated by Van Vliet et al. [22] the rheological properties of yoghurts are influenced by the strength of protein-protein interactions, the number of bonds per cross-section of the strand, relaxation times for the network bonds, and the orientation of the strands within the matrix. Thus presence of higher amount of protein-fat-protein links alowed higher fluidity in comparison to the samples where the protein-protein interactions are predominant.

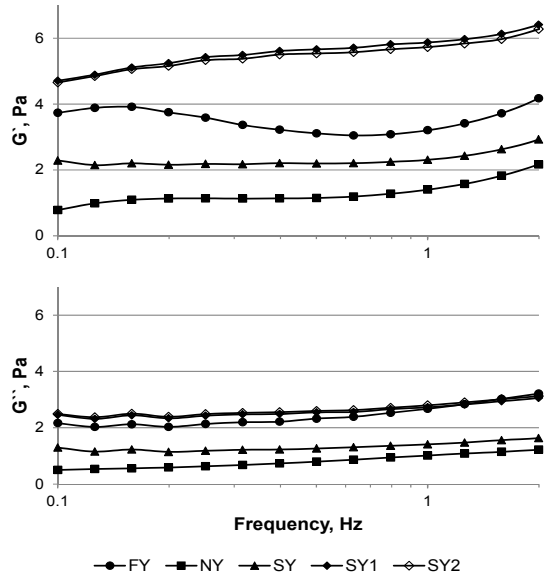

Figure 3. The influence of total fat content and milk fortification on viscoelastic moduli of set yoghurt samples. FY - Yoghurt with high fat content (3.5% fat w/w); NY – Partially skimmed yoghurt (1.5% fat w/w); SY – Skimmed yoghurt (0.1% fat w/w); SY_1 – Skimmed yoghurt enriched with 2% skim milk powder and 2% lactose (w/v); SY_2 - Skimmed yoghurt enriched with 3% skim milk powder and 3% lactose (w/v).

Addition of 2% skim milk powder together with 2% lactose to the skimmed yoghurt samples determined an increase of the gel network density. The fortification most probably led to the reduction of pores dimensions thus causing the increase of viscoelastic moduli values. There observations are in agreement with the literature [23, 24, 5, 4, 25]. Lee and Lucey [26] stated that the physical and sensory properties of yogurt gels are greatly influenced by the total solids content of the yogurt milk, especially the protein content, the G′ values of yogurt increasing with the increase of the total solids content. However, further increase of the total solids quantity in case of SY2 sample did not led to significant variation of G` and G`` values.

Sensorial analysis. The results of sensorial analysis of the yoghurt samples are represented in figure 4. As one can see fat content together with product fortification significantly influenced products sensorial characteristics ($p<0.01$).

The color of the samples with higher fat contents (3.5% and 1.5%) was better appreciated by the assessors probably because of their higher luminosity, and no significant differences between these two samples ($p>0.05$) was obtained. Concerning the samples with low fat content, regardless of the enrichment with skim milk powder and lactose, the color

was medium appreciated (Figure 4). The non-fat solid addition to the skimmed milk before fermentation with EPS producing lactic acid bacteria had no significant influence on the color attribute ($p>0.05$).

Panelists found no odor for the yoghurt samples with 3.5 and 1.5% fat (FY and NY), with no significant differences between the two samples ($p>0.05$). On the other hand, some unspecific smell was identified in case of the skimmed yogurt samples, regardless of non-fat solids supplementation ($p>0.05$).

The same trend was observed in case of the syneresis attribute. No syneresis phenomenon was observed for FY and NY samples ($p>0.05$). The highest amount of separated whey was obtained in case of skimmed yoghurt sample (SY), and the addition of skim milk powder and lactose resulted in the decrease of released whey, with significant differences between SY2 and SY or SY1 samples.

Regarding firmness, the most appreciated sample was FY, while the lowest score was obtained for SY sample. The firmness values ($p<0.01$) varied significantly with the yogurt sample, except for NY and SY2 samples when no differences were registered ($p>0.05$). The addition of higher amounts (3% w/v) of skim milk powder and lactose to the skimmed yoghurts determined the perception of firmness attribute similar to yoghurts with medium fat content. The same trend was observed in case of consistency.

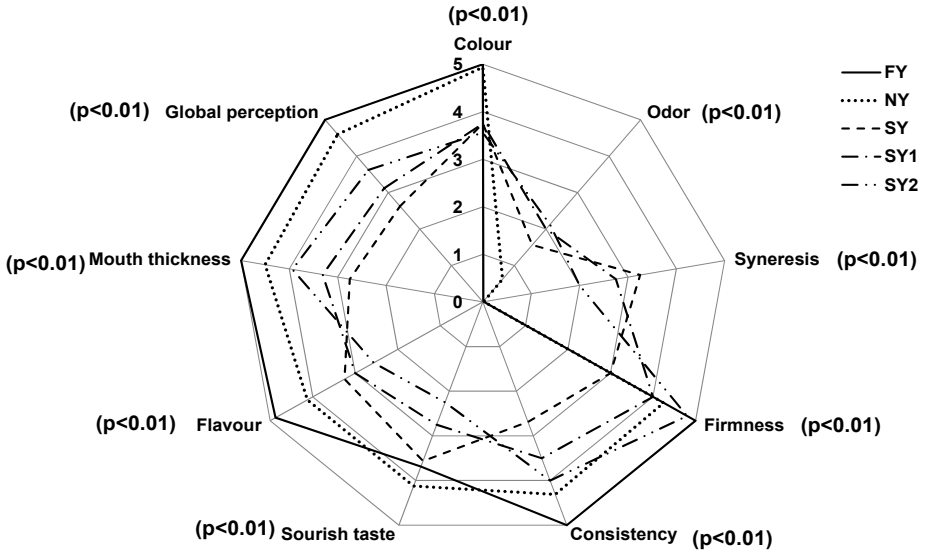

Figure 4. Sensorial characteristics of set yoghurt types fermented with EPSs releasing starter culture, as a function of fat and total solids content. FY - Yoghurt with high fat content (3.5% fat w/w); NY – Partially skimmed yoghurt (1.5% fat w/w); SY – Skimmed yoghurt (0.1% fat w/w); SY_1 – Skimmed yoghurt enriched with 2% skim milk powder and 2% lactose (w/v); SY_2 - Skimmed yoghurt enriched with 3% skim milk powder and 3% lactose (w/v).

The sourish taste of the yogurt was masked by the fat content and lactose addition, being perceived with similar intensity for FY, NY and SY samples ($p>0.05$). The SY_1 with SY_2 samples registered the lowest scores with no significant differences between values ($p>0.05$), but with significant differences with respect to FY, NY and SY samples ($p<0.01$).

The flavour of the fat containing yogurt samples (FY and NY) was better appreciated, whereas the addition of lactose and skim milk powder had no contribution to flavour attribute.

Regarding mouth thickness, the skimmed yoghurt got the lowest appreciation scores. The addition of non-fat solids to the skimmed milk before lactic fermentation led, to some extent, to the improvement of the yogurt thickness.

When considering the global perception, the yogurt samples with fat in composition (FY and NY) the most appreciated by the panelists, while with the skimmed yoghurt sample got the lowest scores (Figure 4). The same conclusion was drawn based on the real score values estimated by taking into account the importance coefficient of every attribute as seen in Figure 5.

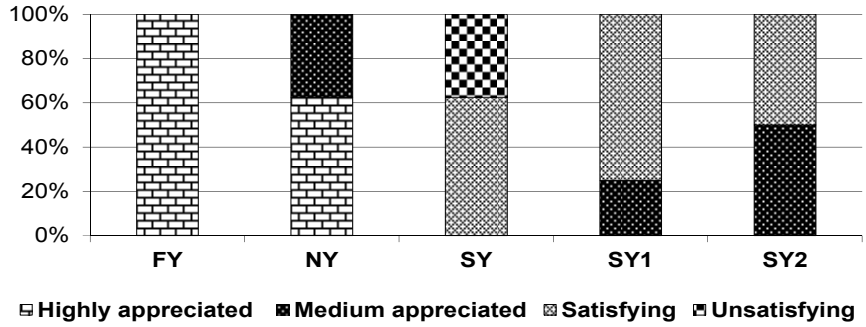

Figure 5. Global perception of yoghurt samples as indicated by importance coefficient of every assessed sensory attribute.

CONCLUSIONS

Yogurt samples with different fat contents were obtained through fermentation with EPS producing lactic acid bacteria. Rheological tests showed that all yoghurt samples behave like viscoelastic gels. We appreciate that the interactions between EPS released by lactic acid bacteria and other macromolecular components, such as proteins, allowed formation of viscoelastic network with proper flow characteristics. Better

rheological properties were obtained in case of the yogurts with high fat levels. When considering the skimmed yoghurt, increasing the total solids level proved to be an appropriate method of improving the rheological characteristics of the gel. This observation is in good agreement with sensorial appreciation showing that increasing the non-fat solid content of yogurts support denser and firmer gel structure formation. However, sensorial characteristics were better appreciated in case of the samples with 3.5% and 1.5% fat with respect to the skimmed yogurts.

EXPERIMENTAL SECTION

Yoghurt preparation. Commercial UHT treated milk with different fat contents was used for yogurt preparation: whole milk with 3.5% (w/w) fat and 11.82% (w/w) total solids; partially skim milk with 1.5% (w/w) fat and 10.67 % (w/w) total solids and skim milk with 0.1% (w/w) fat and 9.02% (w/w) total solids.

In order to increase the total solids content, the skim milk was fortified with skim milk powder (2 and 3% w/w) and lactose (2 and 3% w/w). The addition of lactose to the milk is favorable for lactic acid bacteria growth [21]. Set yoghurt was produced using mixed culture of thermophilic lactic acid bacteria containing *Streptococcus termophilus* and *Lactobacillus delbrueckii* ssp. *Bulgaricus* (commercial name YF-L 812, Chr. Hansen). This lactic acid bacteria mixture was shown previously to produce EPS in yoghurt samples [21].

The milk was first tempered at 45°C and afterwards was inoculated with the starter culture according to producer specifications. The inoculated milk was immediately poured in plastic containers and was incubated at 43°C until pH 4.6 was reached. Yoghurt samples were subsequently cooled and were stored in refrigeration at 4°C before analysis. All samples were obtained in triplicate.

Rheological analyses. The rheological behaviour of the yogurt samples was determined after 24h of storage 4°C with an AR2000ex rheometer (TA Instruments, Ltd). Analyses were performed using a cone - plate geometry with 40 mm in diameter and 2^o cone angle, and a gap of 1000 μm. Prior to analyses yoghurt samples were stirred in order to homogenize composition with released whey if any.

In order to observe flow behaviour of tested samples, a stepped flow step was applied and shear rate was increased from 0.1 to 100 s^{-1}, and then decreased back to 0.1 s^{-1}. Temperature was set to 20 ^oC. Tests were performed in triplicate and mean values were represented in graphs.

The viscoelastic domain was determined by performing strain sweep test and a critical strain of 5% was estimated. The frequency sweep

tests were further performed at a controlled strain of 0.5% and the elastic modulus (*G'*) and viscous modulus (*G"*) were monitored while increasing the oscillation frequency from 0.1 to 2 Hz.

The rheology data were analyzed using TA Rheology Advantage Data Analysis Software V 4.8.3 and the mathematical models of Power Low and Bingham were used to fit the experimental results.

Sensory evaluation. The sensory analysis of the yoghurt was performed after 24 hours of storage at 4^{o}C by a panel consisting on twenty trained assessors, equally distributed by gender, aged between 20 to 30 years in proportion of 70 % the other 30 % were aged between 30 to 40 years old. The samples (~100 mL of yoghurt) were purred in plastic cups and tempered at 10÷12 ^{o}C before testing.

The ten attributes assessed are listed and defined in Table 2. Products quality was appreciated by a 5 points system. The Importance Coefficients (Table 2) for each attribute was decided based on the relevance to the global quality of the yogurt. The real/final sensory score was estimated by multiplying the score of each attribute by its importance coefficient [27]. The importance coefficient is established individually, depending on the research aim so that the most significant characteristics for the study could be followed.

Table 2. Attributes used by the sensory panel for describing the sensory properties of yoghurt samples

Attribute	*Definition*	*Importance coefficient*
Odor	Identification of characteristic smell or any flavour defects as unspecific, foreign or masked odor	0.05
Flavour	General evaluation of flavour and identification of any defects	0.05
Colour	Colour evaluation (white, whitish, yellow or yellowish)	0.1
Syneresis	Visual observation of separated whey on the surface of the set yoghurt	0.15
Gel firmness	Estimation of gel fragility, hardness, gelatinous or gumminess structure	0.15
Consistency	Evaluation of gel viscosity by stirring the yoghurt sample with a spoon	0.15
Sourish taste	Evaluation of the sour taste intensity	0.05
Sweetness	Evaluation of the sweet taste intensity	0.05
Mouth thickness	Perceived as the degree of thickness when swallowing the yogurt at normal-high eating rate	0.1
Global perception	Global appreciation of the product considering the above mentioned attributes	0.15

REFERENCES

1. G. Campbell-Platt, *Food Research International*, **1994**, *27(3)*, 253.
2. S. Otles, O. Cagindi, *Pakistan Journal of Nutrition*, **2003**, *2(2)*, 54.
3. J. M. Aguilera, *Food Technology*, **2000**, *11*, 56.
4. I. Sodini, F. Remeuf, S. Haddad, G. Corrieu, *Critical reviews in food science and nutrition*, **2004**, *44(2)*, 113.
5. A. Skriver, J. Holstborg, K. B. Qvist, *Journal of Dairy Research*, **1999**, *66*, 609.
6. M. N. Oliveira, I. Sodini, F. Remeuf, G. Corrieu, *International Dairy Journal*, **2001**, *11(11)*, 935.
7. L. Ramchandran, N. P. Shah, *LWT-Food Science and Technology*, **2010**, *43(5)*, 819.
8. G. M. Costin, T. Florea, *BIIL*, **2004**, *19 (1)*,1.
9. L. De Vuyst, F. De Vin, F. Vaningelgem, B. Degeest, *International Dairy Journal*, **2001**, *11*, 687.
10. P. Raus-Mediedo, J. Hugenholtz, P. Zoon, *International Dairy Journal*, **2002**, *12*, 163.
11. A. Laws, Y. Gu, V. Marshall, *Biotechnology Advances*, **2001**, *19*, 597.
12. P. A. Laws, M. V. Marshall, *International Dairy Journal*, **2001**, *11*, 709.
13. A. D. Welman, I. S. Maddox, *Trends in biotechnology*, **2003**, *21(6)*, 269.
14. L. De Vuyst, B. Degeest, *FEMS Microbiology Reviews*, **1999**, *23*, 153.
15. T. Amatayakul, A. L. Halmos, F. Sherkat, N. P. Shah, *International Dairy Journal*, **2006**, *16*, 40.
16. Y. S. Bhullar, M. A. Uddin, N. P. Shah, *Milchwissenschaft*, **2002**, *57(6)*, 329.
17. A. N. Hassan, J. F. Frank, K. A. Schmidt, S. I. Shalabi, *Journal of Dairy Science*, **1996**, *79(12)*, 2098.
18. V. M. Marshall, H. L. Rawson, *International Journal of Food Science and Technology*, **1999**, *34*,137.
19. A. K. Patel, P.Michaud, R. R. Singhania, C. R. Soccol, A. Pandey, *Food Technology and Biotechnology*, **2010**, *48(4)*, 451.
20. J. R. Broadbent, D. J. McMathon, D. L. Welker, C. J. Oberg, S. Moineau, *Journal of Dairy Science*, **2003**, *86*, 407.
21. I. Vasilean, R. Segal, A. Vasile, *Annals of the University Dunarea de Jos of Galati-Fascicle VI: Food Technology*, **2011**, *35(1)*, 92.
22. T. Van Vliet, H. J. M. Van Dijk, P. Zoon, P. Walstra, *Colloid and Polymer Science*, **1991**, *269(6)*, 620.
23. C. G. Biliaderis, M. M. Khan, G. Blank, *International Dairy Journal*, **1992**, *2(5)*, 311.
24. C. Wacher-Rodarte, M. V. Galvan, A. Farres, F. Gallardo, V. M. Marshall, M. Garcia-Garibay, *Journal of Dairy Research*, **1993**, *60(02)*, 247.
25. Y. Peng, M. Serra, D. S. Horne, J. A. Lucey, *Journal of Food Science*, **2009**, *74*, 666.
26. W. J. Lee, J. A. Lucey, *Asian-Aust. Journal of Animal Science*, **2010**, *23(9)*, 1127.
27. M. Bulancea, G. Iordachescu, "*Textura produselor alimentare"*, Ed. Aius, Craiova, **2006**.

STUDIA UBB CHEMIA, LX, 2, Tom II, 2015 (p. 271-279)
(RECOMMENDED CITATION)

ASSESSMENTS OF ELECTRONIC PROPERTIES IN PHENOTHIAZINE CARBALDEHYDE REGIOISOMERS SERIES

BALASZ BREM[1], EMESE GAL[1], TÁMAS LOVÁSZ[1], CASTELIA CRISTEA[1,*], LUIZA GĂINĂ[1] AND LUMINIŢA SILAGHI-DUMITRESCU[1]

ABSTRACT. Regioselective C-formylation of phenothiazine using N,N-dimethylformamide is revisited and optimized synthesis of 10-methyl-10*H*phenothiazine-carbaldehyde regioisomers are presented. Recorded NMR and UV-Vis spectroscopic data are compared in the regioisomers series. Fluorescence emissions in the visible range are described. Density Functional Theory (DFT) computational results regarding structural characteristics in the regioisomers series are supporting the recorded spectral properties.

Keywords: *Phenothiazine carbaldehyde, UV-Vis absorption, Fluorescence, DFT.*

INTRODUCTION

Phenothiazine is a redox-active compound well known as a potent pharmacophoric group for medicinal applications [1], but also a suitable building block for new materials mainly based on UV-Vis absorption and fluorescence emission properties modulated by carrefully selected substitution patterns [2]. In this context, phenothiazine carbaldehide derivatives appear as versatile substrates for extending the functionalization of the parent heterocyclic unit. Literature survey indicate the phenothiazine-3-carbaldehyde as the most widely employed precursor mainly because it can be readily prepared by rather simple Vilsmeyer [3], or Duff [4] formylation procedures. Even though the preparation of phenothiazine-1-, 2-, and 4-carbaldehyde regioisomers was also previously reported, these regioisomers were less employed as precursors for further functionalization of phenothiazine unit.

[1] *"Babes-Bolyai" University, Faculty of Chemistry and Chemical Engineering, RO-400028, Cluj-Napoca, Romania*
[*] *Corresponding author: castelia@chem.ubbcluj.ro*

The Vilsmeier-Haack formylation of a phenothiazine substrate is based on aromatic electrophilic substitution reaction directed by the electron donor effect of the heterocyclic N atom mainly increasing the electron density in the *para* position of the adjacent aromatic ring. This procedure was first applied to 10-methyl-phenothiazine substrate and generated 3-formyl-10-methyl-phenothiazine in up to 50% yields [5]. Convenient formylation conditions were described for the preparation of 3-formyl-10-methyl-phenothiazine and 3,7-diformyl-10-methyl-phenothiazine using N,N-dimethylformamide (DMF) and phosphorous(V)oxychloride for generating the electrophile [6]. A modified procedure gave 97% yield 10-ethyl-3-formyl-phenothiazine when using chloroform solvent [7]

The microwaves assisted Duff formylation procedure using urotropine in acetic acid showed regioselectivity for position 3 and gave satisfactory results in the formylation of both phenothiazine and 10-methyl-phenothiazine substrates with less environmental burden [8].

Lithiation and subsequent formylation using DMF as electrophile is another method designated to the preparation of heteroaromatic aldehydes bearing a formyl group adjacent to the heteroatom. When subjected to this procedure, phenothiazine may generate both C^1 (*ortho* to the N directing atom) and C^4 (*ortho* to the S directing atom) substitution products [9]. However a preference for substitution in the position *ortho* to the heterocyclic nitrogen atom was observed in the case of 10*H*-phenothiazine. A double lithiation experiment indicate the C^1 substited product in the presence of DMF, but other electrophiles such as acetyl chloride gave the N substited product [10]. An ingenious two step procedure was developed based on the formation of an unstable carbamate intermediate which favorize C^1-lithiation and generate the electrophilic substitution product exclusively at the carbon center [11] When sterically hindred N-methylformanilide was employed, 4-formyl-phenothiazine was preferentially formed [12]. 10-alkyl-phenothiazines appeared to undergo lithiation at position C^4 when using butyl lithium in the presence of TMEDA [13]. This strategy can be applied for the introduction of a formyl group at position C^3 of the phenothiazine core only based on a halogen-litium exchange reaction applied to a halogenated phenothiazine substrate followed by subsequent treatment with DMF electrophyle [14].

In this work, the regioselective C-formylation of phenothiazine substrate in the presence of DMF was achieved by modulating the chemical reactivity of the heterocycle towards electrophilic substitution and optimal experimental conditions are described. The electronic properties of the prepared C-formyl-N-methyl-phenothiazine regioisomers were discussed based on NMR and UV-Vis absorption/emission spectroscopic data recorded in solution. Theoretical computational data were employed in supporting the fine tunable electronic properties in the regioisomers series.

RESULTS AND DISCUSSIONS

Synthesis of 10-Methyl-phenothiazine carbaldehyde regioisomers

10-Methyl-10*H*phenothiazine-1-, 2- and 4-carbaldehyde regioisomers **1, 2, 4** were successfully obtained by a two-steps procedure involving a phenothiazine-lithium intermediate further trapped by the treatment with dimethylformamide (DMF) electrophile. A careful selection of the reaction conditions (substrate, lithium reagent, reaction temperature) was required in order to obtain satisfactory yields of each target regioisomer (scheme 1). Thus, when starting with N-methyl-phenothiazine substrate and *n*-BuLi reagent a hydrogen lithium exchange occurred at 0 °C preferentially under the *orto* directing effect of the heterocyclic sulfur atom (affording phenothiazine-4-carbaldehyde **4** in 43% yields). At 0 °C the nitrogen *orto* directing effect was prevalent in the 10H-phenothiazine substrate and the sterically hindered 10-methyl-phenothiazine-1-carbaldehyde **1** was obtained in 25% yield after a subsequent alkylation of the 1-formyl-10Hphenothiazine intermediate. The preparation of phenothiazine 2-carbaldehyde **2** was best achieved by subjecting 2-chloro-10-methyl-phenothiazine substrate to halogen-lithium exchange using metallic lithium under sonochemical conditions in the presence of DMF. 10-Methyl-10*H*phenothiazine-3-carbaldehyde was obtained in 80% yields by an adapted Vilsmeyer procedure using 1,2-dichloroethane solvent.

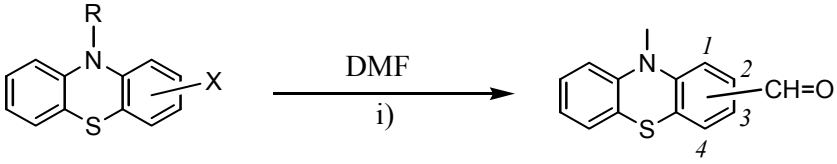

R=H, X=H,	i) *n*BuLi/Et_2O 0°C, ii) NaH/THF, H_3C-I	**1** *1*-CHO 22%
R=Me, X= Cl	i) Li/Et_2O,))), 30 °C, 6h	**2** *2*-CHO 43%
R=Me, X=H	i) $POCl_3$/DCE, 90 °C, 6h	**3** *3*-CHO 80%
R=Me, X=H	i) TMEDA/*n*Bu-Li,r.t.,20 min	**4** *4*-CHO 61%

Scheme 1. *Regioselective C-formylation of 10Hphenothiazine derivatives.*

The recorded ^{1}H-NMR spectra are collectively presented in figure 1 for regioisomers **1-4**, thus giving the possibility of inspecting the key signals and comparing the deshielding effects induced by electronic conjugation, steric hindrance and magnetic anisotropy of the aldehyde group.

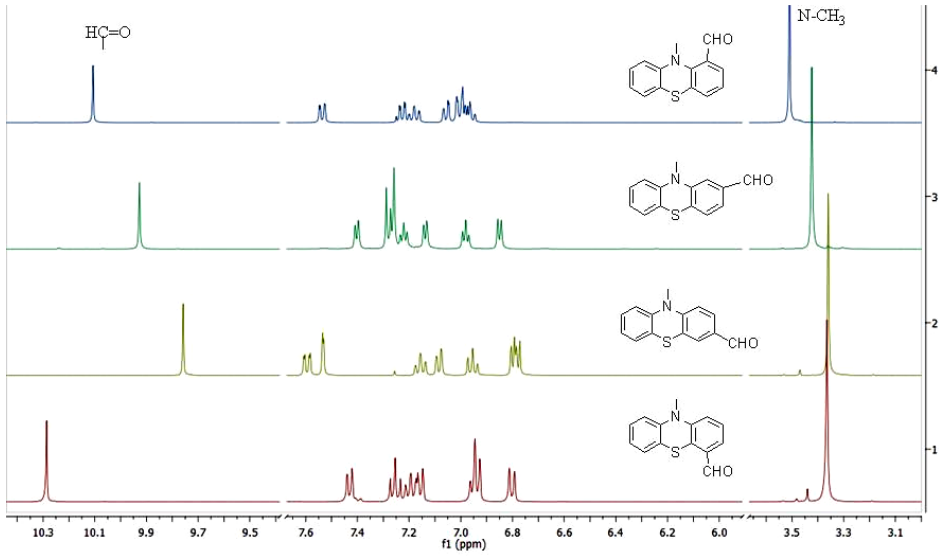

Figure 1. 400 MHz ^{1}H-NMR spectra of 10-methyl-10-*H*phenothiazine-carbaldehyde regioisomers in $CDCl_3$ (from top to bottom: **1, 2, 3, 4**) in $CDCl_3$

Electronic properties

The molecular structures of the regioisomesr **1-4** have been studied by using density functional theory. The energies corresponding to the optimized geometries (E) in ground states and frontier molecular orbitals (E_{HOMO}, E_{LUMO}) were computed at the using Spartan programme [15] and the results are presented in Table 1.

Taking into consideration the calculated E values (Table 1) the stability of regioisomers **1-4** may be correlated to the substitution pattern of the phenothiazine unit and falls in the order: phenothiazin-1-< 4-< 2-< 3-yl in concordance with a steric hindrance in positions 1 of the heterocycle and favourable extended n-π conjugation in position 2, or 3 respectively.

The frontier molecular orbital plots presented in figure 2 show a participation to the HOMO of all the atoms joint in the heterocyclic system, while LUMO appears localized on the formyl substituent and its adjacent benzene ring with a selective participation of the heteroatoms according to the substitution pattern (N atomic orbitals participates to LUMO in the case of **1** and **3**, while S atomic orbitals participates to LUMO in the case of **2** and **4** regioisomers).

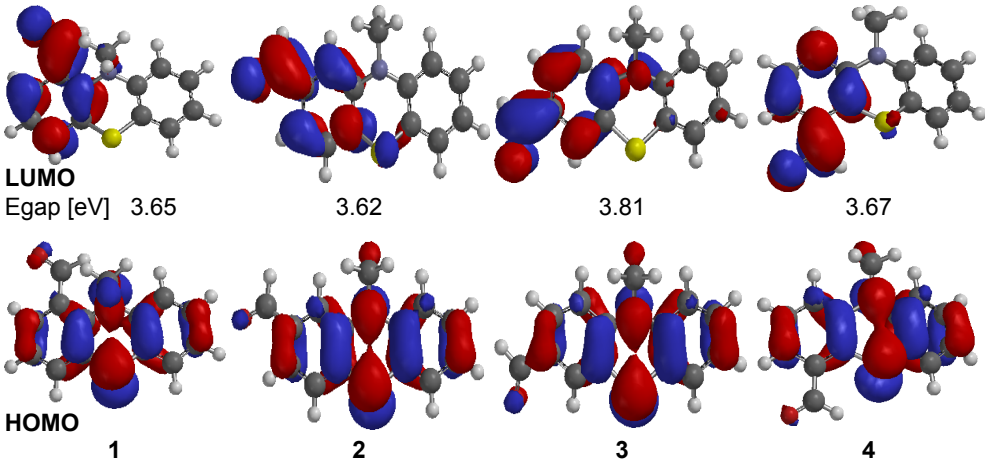

Figure 2. Frontier molecular orbital plots of
10-methyl-phenothiazine-carbaldehyde regioisomers

Each phenothiazine carbaldehyde **1-4** show two absorption bands, situated in the UV region (Table 1) with larger extinction coefficients for the higher frequency band which can be assigned to allowed π→π* transitions involving the excitation of the electrons from the aromatic rings; the forbidden n→π* transitions may be responsible for the low intensity band situated at longer wavelengths. These absorption bands appear slightly affected by the position of the auxochrome formyl group, except for the case of **3** which reveals a hypsochromic shift of aprox. 30 nm for the band situated at longer wavelength (Table 1); in agreement with this experimental evidence **3** is also characterized by the largest computed HOMO-LUMO energy gap of the series (figure 2).

Upon excitation with either of the two UV absorption maxima, each regioisomer **1-4** exhibited emission bands in solution with maxima situated in the visible region (figure 3). A correlation between the position of the emission band and the substitution pattern of the heterocycle indicate a red shift of the emission maxima according to the auxochrome position in the following order: phenothiazine-1yl-<2-yl<-3-yl<-4-yl-carbaldehyde. Larger Stokes shift values are noticeable in the case of **1** and **3** which can be correlated to geometrical changes upon excitation, from a non-planar ground-state of the phenothiazine moiety to a largely planarized excited state [16] and corroborated with computational results regarding LUMO electron distribution (figure 2).

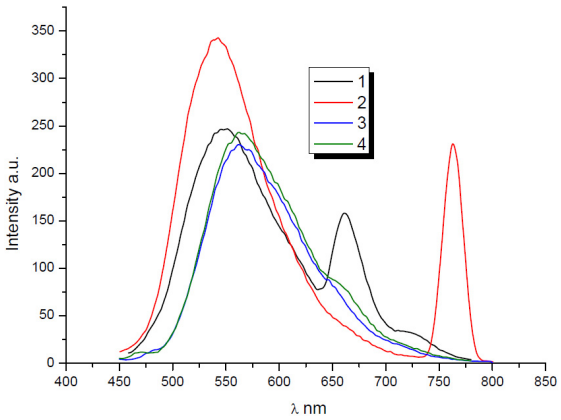

Figure 3. Fluorescence emission spectra of 10-methyl-10*H*phenothiazine carbaldehyde regioisomers **1-4** in 0.02mM in DCM.

Table 1. Electronic properties of phenothiazine carbaldehyde **1-4** determined by UV-Vis absorption/emission spectroscopy 10^{-4} M in DCM and molecular modelling

Cpd	$\lambda_{max, abs}$ (ε) [nm]	$\lambda_{max, em}$ [nm]	Stokes shift [cm^{-1}]	E_{HOMO} [eV]	E_{LUMO} [eV]	E [hartree]
1	277 (54400) 411 (3180)	543 670	9400	-5.25	-1.60	-1068.264
2	282 (109200) 418 (4730)	551, 730	5700	-5.35	-1.73	-1068.274
3	282 (60950) 381 (5900)	567	8600	-5.37	-1.56	-1068.275
4	277 (58600) 419 (6170)	571	6300	-5.37	-1.70	-1068.269

CONCLUSIONS

Adequate experimental conditions for regioselective C-formylation of 10-methyl-10*H*-phenothiazine substrate were described.

Evidences of photophysical properties of phenothiazine carbaldehyde regioisomers were brought by means of UV-Vis absorption/emission spectroscopy which indicated fine tunable absorptions in the UV region and fluorescence emission in visible region according to the position of the formyl auxochrome.

EXPERIMENTAL SECTION

*10-methyl-10Hphenothiazin-1-carbaldehyde (**1**).*

a) To a solution of phenothiazine (4 g, 20 mmol) in 150 ml of dry ethyl ether *n*-BuLi (31 ml 25 mmol, 1.6 M in hexane) was added under argon atmosphere at 0°C. The reaction mixture was stirred 10 hours at room temperature and then DMF (1.5 g, 20 mmol, 0.944 g/cm^3) was added drop wise at 0°C. After it was stirred one hour at room temperature, the reaction mixture was hydrolyzed with ice cold aqueous HCl 0.5 N. The mixture was shaken vigorously and the organic layer was then separated. The aqueous phase was extracted three times with ethyl ether (50 ml). The organic phases were collected, washed with water and dryed ower magnesium sulfate. After the evaporation of the solvent under vacuum, the red viscous residue was purified by column chromatography (silica gel, hexane/ethyl acetate= 10/1) to give 10Hphenothiazin-1-carbaldehyde 1.14g (25%) m.p.= 81-82°C, (lit. 81-83°C [12])

b) To a suspension of NaH (0.174 g, 4.4 mmol) in dry THF (20 ml) was added under continuous stirring, a solution of 10H-phenothiazine-1-carbaldehyde (1g 4.4 mmol) in 10 ml dry THF (under inert atmosphere). The mixture was stirred for 4h, at 0-5°C. To the obtained solution, was added methyl iodide (0.62g, 4.4 mmol 2.28 g/cm^3) and the mixture was stirred at room temperature for 10 hours. The reaction mixture was treated with 100 ml water and extracted three times with ethyl ether (30ml). The organic phase was collected and dryed over magnesium sulfate. After evaporation of the organic solvent the crude product was purified by column chromatography (silica gel, hexane/ethyl acetate= 10/1) to give (0.95 g 90%) yellow powder m.p.= 75-77°C, (lit. 70-71°C [17])

δ_H (300 MHz, $CDCl_3$) 3.62 (3H, s, CH_3), 6.85 (1H, d, *J* 7.8 Hz, H_9), 7.00 (1H, td, *J* 7.5, 1.9 Hz, H_7), 7.07-7.13 (2H, m, H_6, H_8), 7.14 (1H, dd, *J* 2.0, 7.8 Hz, H_4,), 7.28 (1H, t, *J* 7.8 Hz, H_3,), 7.43 (1H, dd, *J* 2.0, 7.6 Hz, H_2), 9.56 (1H, s, CHO); δ_C (75 MHz, $CDCl_3$) 43.9, 118.4, 122.6, 124.1, 125.6, 126.5, 126.6, 127.6, 130.6, 131.1, 131.3, 146.4, 146.8, 189.7; MS m/z (EI, 70eV) 241 (M^+).

*10-methyl-10Hphenothiazin-2-carbaldehyde (**2**).*

10-methyl-2-chloro-10*H*phenothiazine (247 mg, 1 mmol) was solved in dry diethyl ether (25ml) under inert atmosphere, metallic lithium (7 mg, mmol) and dry dimethylformamide (146 mL, 2 mmol) were added. The reaction mixture was sonicated in an ultrasonic bath at 30°C for 6h. The mixture was poured into ice (50 g), and then extracted with dichloromethane and the two layers were separated; after evaporation of the organic solvent the crude product was purified by column chromatography with toluene as eluent. Yellow-brown powder (103.6 mg, 43%), mp 69-71°C, (lit bp 220°C/3 torr [18]);

δ_H (600 MHz, $CDCl_3$) 3.39 (3H, s, CH_3), 6.82 (1H, d, *J* 8.1Hz, H_9), 6.95 (1H, t, *J* 7.4Hz, H_7), 7.11 (1H, d, *J* 7.5Hz, H_6), 7.19 (1H, t, *J* 7.4 Hz, H_8), 7.23-7.24 (2H, m, H_1, H_4), 7.37 (1H, d, *J* 7.6 Hz, H_3), 9.89 (s, 1H, CHO); δ_C (150 MHz) 35.5, 112.2, 114.6, 121.9, 123.0, 125.8, 127.2, 128.1(2C), 132.6, 135.9, 144.9, 146.4, 191.6; MS m/z (EI, 70eV), 241 ($M^{+\cdot}$).

*10-methyl-10Hphenothiazin-3-carbaldehyde (**3**)*

DMF (24 mmol) was cooled to 0°C, then $POCl_3$ (24 mmol) was added drop wise and the mixture was stirred at room temperature for one hour. A solution of 10-methyl-10*H*-phenothiazine (20 mmol) dissolved in 1,2-dichloroethane (30 ml) was added slowly and the reaction mixture was stirred at 90°C for 6 hours. After cooling, an ice cold saturated solution of sodium acetate (30 ml) was added drop wise to the reaction mixture. The product was extracted with ethyl acetate, and the extract was dried over magnesium sulfate and then concentrated to dryness.

Yellow precipitate recrystallized from toluene (3.85g, 80%), mp 88°C lit 81-82 [19]; δ_H (600 MHz, $CDCl_3$) 3.36 (s, 3H), 6.78 (1H, d, *J* 8.0 Hz, H_9), 6.80 (1H, d, *J* 8.4 Hz, H_1), 6.95 (1H, t, *J* 8.4 Hz, H_7), 7.08 (1H, dd, *J* 1.4, 7.6 Hz, H_6), 7.15 (1H, td, *J* 1.4, 8.4 Hz, H_8),7.53 (1H, d, *J* 2 Hz, H_4), 7.60 (1H, dd, *J* 2.0, 8.4 Hz, H_2), 9.76 (1H, s, CHO); δ_C (150 MHz, $CDCl_3$) 35.8, 113.7, 114.8, 122.4, 123.6 123.8, 127.2, 127.8, 130.5, 131.1, 144.0, 150.9, 190.0; m/z (EI, 70eV) 241 ($M^{+\cdot}$).

*10-methyl-10Hphenothiazin-4-carbaldehyde (**4**)*

10-methylphenothiazine (2 g, 8.8 mmol) was dissolved in dry ethyl ether (50 cm^3). After 10 min under argon atmosphere, TMEDA (3.32 cm^3, 22 mmol) was added followed by *n*-butyllithium (13.8 cm^3 of a 1.6 M solution in hexane, 22 mmol). The mixture was kept at room temperature for 0.5 h, then cooled at 0°C before dry DMF (1.6 g, 0.948 g/cm^3, 22 mmol) was added. The mixture was stirred for 20 min at room temperature. The reaction mixture was poured into cooled aqueous HCl (4.5% w/v; 180 cm^3) and further stired for 30 min. The organic phase was separated and the aqueous phase was extracted with chloroform (3x100 cm^3). The combined organic phases were dried and evaporated to give an orange oil. The crude product was subjected to column chromatography (silica gel, hexane/ethyl acetate=8/1), yellow crystals (1.38 g, 61%) mp 110-112°C (lit. 110-111°C [20])

Yellow crystals, (0.97g, 43%), mp 110-112°C (lit[13], 110-111°C); δ_H (600 MHz, $CDCl_3$) δ 3.46 (s, 3H, CH_3), 6.89 (1H, d, *J* 8.1 Hz, H_9), 6.95 (1H, t, *J* 7.8 Hz, H_7), 7.03 (1H, d, *J* 7.8 Hz, H_1), 7.17-7.21 (2H, m, H_6, H_8), 7.28 (1H, t, *J* 7.8 Hz, H_2), 10.31 (1H, s, CHO); δ_C (150 MHz, $CDCl_3$) 36.5, 115.3, 119.8, 122.8, 123.6, 124.5, 126.7, 127.7, 127.9, 130.4, 133.0, 145.2, 145.9, 190.4. m/z (EI, 70eV) 241 ($M^{+\cdot}$), 226.

AKNOWLEDGMENTS

This work was possible due to the financial support of the Sectorial Operational Program for Human Resources Development 2007-2013, co-financed by the European Social Fund, under the project number POSDRU/ 159/1.5/S/132400 with the title "Young successful researchers – professional development in an international and interdisciplinary environment" (B. Brem).

REFERENCES

1. K. Pluta, B. Morak-Młodawska, M Jeleń, *Eur. J. Med. Chem*., **2011**, *46*, 3179.
2. a) C. Garcia, R. Oyola, L.E. Pinero, R. Arce, J. Silva, V. Sanchez, *J. Phys. Chem. A.* **2005**, *109*, 3360; b) Meyer T., Ogermann D., Pankrath A., Kleinermanns K., Müller T.J.J., *J. Org. Chem*. **2012**, *77*, 3704; c) Zhang X., Qiu X., Lu R., Zhou H., Xue P., Liu X., *Talanta*, **2010**, *82*,1943.
3. A. Vilsmeier, A. Haak, *Ber. Dtsch. Chem. Ges.*, **1927**, *60(1)*, 119.
4. J.C. Duff, *J. Chem. Soc*., **1941**, 547.
5. Ng.Ph. Buu-Hoï, N.G. Hoán, *J. Chem. Soc.*, **1951**, 1834.
6. V. Fărcăşan, I. Oprean, C. Bodea, *Rev. Roum. Chim*., **1968**, *13*, 647; (b) V. Fărcăşan, I. Oprean, C. Bodea, *Rev. Roum. Chim*., **1970**, *15*, 1433.
7. Y. Tian, M. Zhang, X. Yu, G. Xu, Y. Ren, J. Yang, J. Wu, X. Zhang, X. Tao, S. Zhang, M. Jiang, *Chem. Phys. Lett.,* **2004**, *388*, 325.
8. L. Gaina, D. Porumb, I. Silaghi-Dumitrescu, C. Cristea, L. Silaghi-Dumitrescu, *Can. J. Chem*., **2010**, *88*(1), 42.
9. a) G. Gauquil, A. Cassadavall, E. Cassadavall, *Bull. Soc. Chim. Fr.*, **1960**, 1049; b) H.W. Gschwend, H.R. Rodriguez, *Org. React.*, **1979**, *26*, 47; c) A. Halberg, A.R. Martin, *J. Heterocycl. Chem.*, **1982**, *19*, 433; d) A. Halberg, A.R. Martin, *Synth. Commun.*, **1983**, *13*, 467; e) A. Halberg, I. Al-Showaier, A.R. Martin, *J. Heterocycl. Chem.*, **1983**, *20*, 1435.
10. J. Mortier, T.H. Nguyen, D. Tilly, A.S. Castanet, *ARKIVOC*, **2007**, *vi*, 47.
11. A.R. Katritzky, L.M. Vazquez de Miguel, G.W. Rewcastle, *Synthesis*, **1988**, *3*, 215.
12. A. Hallberg, A. Martin, *J. Heterocyclic Chem.*, **1982**, *19*, 433.
13. a) H. Gilman, P.R. Van Ess, D.A. Shirley, *J. Am. Chem. Soc.*, **1944**, *66*, 1214; b) R.D. Nelson, *Iowa State Coll. J. Sci.*, **1953**, *27*, 229.
14. S. Ebdrup, *J. Chem. Soc., Perkin Trans.,* **1998**, *1,* 1147.
15. SPARTAN 06 Wavefunction, Inc. Irvine, CA.
16. L. Yang, J.K. Feng, A.M. Ren, *J. Org. Chem.,* **2005**, *70*, 5987.
17. G. Cerbai, L.Turbanti, *Bollettino chimico farmaceutico*, **1969**, *108* (7), 433.
18. G. Cauquil, A. Casadevall, *Bull. Soc. Chim.Fr.*, **1955**, 768.
19. H. Spreitzer, M. Scholz, G. Gescheidt, J. Daub, *Liebigs Annales*, **1996**, *12*, 2069.
20. J. Bergman, L. Renstrom, B. Sjoberg, *Tetrahedron,* **1980**, *36* (17), 2505.

STUDIA UBB CHEMIA, LX, 2, 2015 (p. 281-293)
(RECOMMENDED CITATION)

DIRECT AND SIMULTANEOUS QUANTIFICATION OF ATORVASTATIN AND AMLODIPINE IN TABLETS BY NIR SPECTROSCOPY

ANDREEA LOREDANA VONICA-GLIGOR[a,b,c], TIBOR CASIAN[a], ANDRA REZNEK[a], IOAN TOMUȚĂ[a*], FELICIA GLIGOR[b]

ABSTRACT. Near infrared spectroscopy (NIRS) is a technique widely used for direct and non-destructive analysis of solid samples. A NIRS method for the simultaneous quantification of atorvastatin and amlodipine in fixed-dose combination tablets was developed and fully validated. The PLS calibration model was developed based on the 26 samples prepared according to a D-optimal experimental design with 2 factors and 5 levels. The best predictive model for atorvastatin was developed using standard normal variate pre-processing method, 7 PLS factors; the best predictive model for amlodipine was developed using first derivate followed by standard normal variate pre-processing method and 7 PLS factors. The method was validated in terms of linearity, trueness, precision and accuracy. The validation results show that the method is reproducible, precise and has good accuracy and linearity profiles. Furthermore, comparative data obtained on independent samples shows no statistical difference ($p>0.05$) between the results predicted by the NIRS method and the values obtained using HPLC reference method. So, NIRS based on PLS multivariate calibration could be a suitable tool for the non-destructive, direct and simultaneous prediction of the chemical composition of a fixed-dose combination that includes two APIs in a single tablet and is helpful in achieving the goals of Process Analytical Technology (PAT).

Keywords: *near infrared spectroscopy, simultaneous quantification, amlodipine, atorvastatin, chemometry*

[a] *University of Medicine and Pharmacy Iuliu Haţieganu, 41 V. Babeş str., RO-400023, Cluj-Napoca, Romania*
[b] *Lucian Blaga University, 2A L. Blaga str., RO-550169, Sibiu, Romania*
[c] *S.C. Polipharma INDUSTRIES, 156 Alba Iulia str., RO-550052, Sibiu, Romania*
** Corresponding author: tomutaioan@umfcluj.ro*

INTRODUCTION

A single-pill combination drug is a fixed-dose combination (FDC) that includes two or more active pharmaceutical ingredients (APIs) combined in a single dosage form. FDC can benefit patients through the potential increase in efficacy and/or a reduced incidence of adverse effects, the convenience in terms of administration and compliance and potentially lower costs of manufacturing compared to the costs of producing separate products administered concurrently [1]. The amlodipine/atorvastatin single pill has been shown to improve patients‘ achievement of national-guideline-recommended blood pressure and lipid target levels and exhibits a safety profile consistent with its parent compounds. This combination pill is now available in Europe in formulations containing either 5 or 10 mg amlodipine and 10 mg atorvastatin [2,3].The combination is indicated for patients suffering from both high blood pressure and high levels of cholesterol and has had worldwide sales of more than $600 million in 2013.

The manufacturing process typically involves several unit operations, such as blending, granulation, tableting, and coating, all of which can have critical influences on the final quality of the product. Process monitoring is a methodology that guarantees a high-predefined quality standard and offers the possibility to react during the process if any parameters drift from the normal operating range, but it requires quick methods. Process monitoring is the goal of Process Analytical Technology (PAT). PAT is defined by the Food and Drug Administration (FDA) and European Medicines Agency (EMA) as a concept which implies the design and control of pharmaceutical processes through real time measurements of critical process parameters that could affect quality assurance [4,5]. Direct analysis of intact solid dosage forms as whole tablets is considered to be a very important goal for NIRS analysis in the pharmaceutical industry, with increasing needs of on-line or in-line testing for process monitoring according to PAT [6,7].

In the field of APIs quantification in tablets, including fixed-dose combinations, the high performance liquid chromatography (HPLC) technique is widely used due to good selectivity, specificity and linear range [8]. Until now, only HPLC methods were developed and validated for the simultaneous quantification of both APIs (atorvastatin and amlodipine) in fixed-dose combinations [9,10]. However, this requires sample preparation, chromatographic separation of the analytes and takes hours, so therefore it is currently only done off-line [6,7,11]. Near InfraRed Spectroscopy (NIRS) is a non-destructive technique that allows the direct quantification of chemical properties such as the active pharmaceutical ingredients content [6,7,12] or physical characteristics as pharmaceutical properties [13,14] of tablets and powder blends for tableting

[11,15,16]. NIRS can be used to perform quantitative analysis of one, two or more compounds in different matrices, like pharmaceutical powder blends for tableting or tablets. The advantages of the NIRS method are numerous: non-invasive and non-destructive techniques, no sample preparation, high frequency of spectrum acquisition, as well as a large number of molecules which could be quantified [6]. Many papers are reporting the determination of API content in tablets by NIRS methods [12,17], but only a few are focusing on the prediction of two or more APIs and/or excipients in the composition of powder blends or tablets [6,7,18].

The aim of this work was to develop and validate a NIRS method for direct and simultaneous quantification of amlodipine and atorvastatin in tablets, using a direct, fast, non-invasive and non-destructive technique that requires no sample preparation.

RESULTS AND DISCUSSION

The NIR spectra of tablets contain both chemical information related with APIs and excipients contents and physical information related with tablet compaction. Therefore, pre-processing methods and wavelength selection ranges should be carefully chosen to extract the chemical information that is mainly correlated with the APIs concentration, in order to develop robust calibration models.

Spectra investigation

The calibration model was built after recording twenty spectra of each tablet formulation. Overall 520 tablets spectra were recorded and analyzed for the calibration model development (Figure 1). The NIR spectra of pure APIs is also presented (a1 – atorvastatincalcium; b1 – amlodipinebesilate) in the same figure.

Development of calibration models

The development of calibration models for APIs assay is an iterative technique and consisted in checking the predictive ability of several spectral pre-processing methods in association with different spectral regions with high NIR absorbance of the APIs of interest. By applying different spectra pre-processing methods in combination with different spectral regions a large number of models was generated. Among these, the most potentially interesting 6 models for each API were selected and presented in Table 1.

Table 1. Statistical parameters and number of principal components for atorvastatincalcium and amlodipinebesilate, without data pre-processing as well as after different spectra pre-processing

Atorvastatincalcium						
Pre-processing method*	none a	SLS b	SNV C	FD d	SLS-4 e	SNV-4 f
Spectral range (cm^{-1})**	R1	R1	R1	R1	R4	**R4**
Number of PLS factors	8	7	7	7	7	**7**
R^2	0.9408	0.9411	0.9423	0.9349	0.9586	**0.9588**
RMSECV (% w/w)	0.353	0.352	0.348	0.374	0.295	**0.292**
Bias	-0.00015	-0.00026	0.000301	-0.00010	-0.000477	**-0.00025**
Amlodipinebesilate						
Pre-processing method*	none g	MSC h	SLS i	SNV j	FD+SLS k	FD+SNV l
Spectral range (cm^{-1})**	R1	R1	R1	R1	R1	**R1**
Number of PLS factors	9	8	8	8	7	**7**
R^2	0.9675	0.9737	0.9733	0.9738	0.9757	**0.9768**
RMSECV (% w/w)	0.353	0.318	0.320	0.318	0.306	**0.299**
Bias	-0.000073	-0.00074	-0.00054	-0.00034	-0.000592	**-0.000551**

*none-no pre-processing, SLS-straight light substraction, SNV-standard normal variate, FD-first derivate, MSC-multiplicative scattering correction, FD+MSC – first derivative followed by multiplicative scattering correction, FD+SNV – first derivative followed by standard normal variate

**R1-Spectra range 1 region: 10000-4200cm^{-1}; R4-Spectra range 4 region: 10000-8270; 7700-7120; 6800-5616; 5400-4243 cm^{-1}.

In the case of the atorvastatincalciumcalibration, based on the analysis of different calibration models, the models generated using 4 spectra range had the best results. As the R^2 values of the models are very close, this parameter does not allow any clear differentiation between the models. Regarding RMSECV, the (f) model seems to be slightly better than the (b), (c) and (e) models: its RMSECV is the smallest. Thus, (f) was the selected model which was the most fitted for this purpose, and the model candidate for method validation according to current pharmaceutical requirements. The shape of the spectra after pre-processing according to this model is presented in Figure 1, a_2. In the case of the amlodipine besilatecalibration, the results look very similar, R^2 values of the models are very close, so the models were selected based on RMSECV values. Regarding RMSECV, the (l) model seems to be slightly better than the (h), (i), (j) or (k) models: its RMSECV is the smallest. The shape of the spectra after pre-processing according to this model is presented in Figure 1, b_2. The predictive ability of the chosen models was checked on independent samples in the validation step.

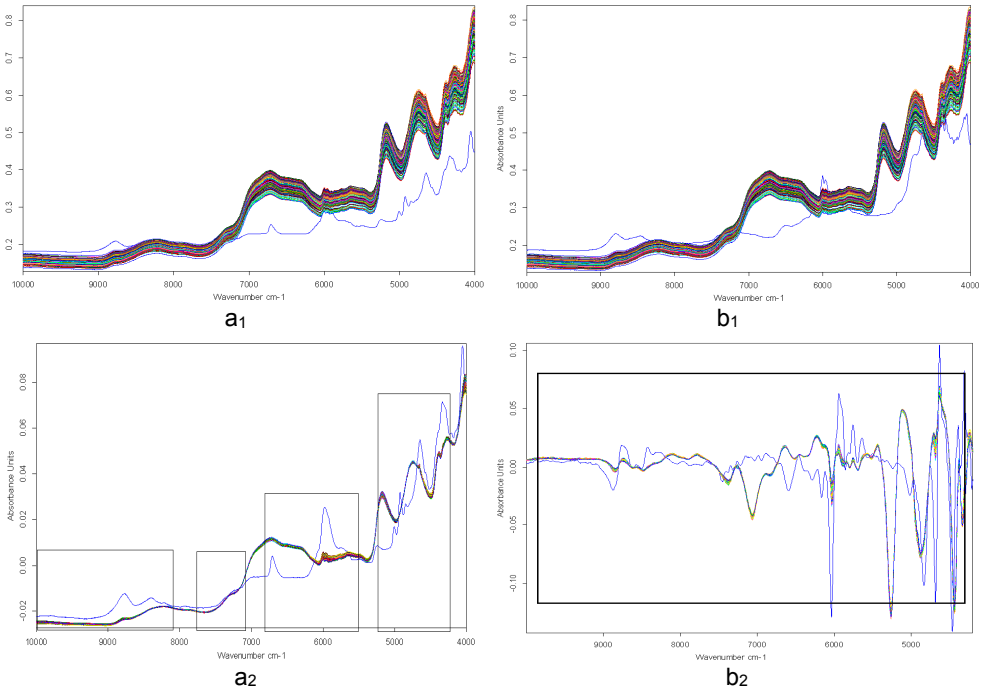

Figure 1. NIR spectra of tablets without preprocessing (a_1, b_1) and pre-processed using SNV-4 method (a_2) for atorvastatin calcium and FD+SNV method for amlodipine besilate (b_2); blue line in a_1, a_2– atorvastatincalcium; blue line in b_1,b_2 - amlodipine besilatespectrum

Validation of the method

Validation was based on ICH Q2 guidance and included linearity, range of application, accuracy, precision (repeatability and intermediate precision), and was done on validation samples. Independent validation samples similar to the calibration samples were prepared at 3 different active content levels (corresponding to 80, 100 and 120% concentrations) of each API (formulation N7, N13, N19, Table 4). The predictive performance of the chosen models was evaluated based on accurate profiles computed on the external validation samples. Accuracy represents the total error concept which is the sum of the trueness (systematic error) and precision (random error) and was evaluated by determining the accuracy profile following the methodology proposed by Hubert *et all* [23, 24]. Table 2 shows the validation results obtained with the developed NIR model (f, SNV-4) for atorvastatincalcium (standard normal variate pre-processing, 7 PLS factors and 4 spectral regions: 10000-8270; 7700-

7120; 6800-5616; 5400-4243cm^{-1}) and model (I, FD+SNV) for amlodipine besilate (first derivative followed by standard normal variate pre-processing, 7 PLS factors and 1 spectral regions: 10000-4200cm^{-1}).

Table 2. Validation results of the NIRS method

for the quantification of **atorvastatin calcium (f, SNV – 4)**						
Conc. level (mg/tablet)	Trueness		Precision		Accuracy	
	Relative bias (%)	Recovery (%)	Repeatability (RSD %)	Intermediate precision (RSD %)	Relative tolerance limits (%)	Tolerance limits (mg/tablet)
9.31	-0.568	99.43	1.54	1.65	[-4.50, 3.37]	[8.89, 9.62]
10.34	1.475	101.48	0.99	1.09	[-1.13, 4.08]	[10.22, 10.77]
11.37	-0.091	99.91	0.50	0.80	[-2.57, 2.38]	[11.08, 11.64]
for the quantification of **amlodipine besilate (I, FD+SNV)**						
Conc. level (mg/tablet)	Trueness		Precision		Accuracy	
	Relative bias (%)	Recovery (%)	Repeatability (RSD %)	Intermediate precision (RSD %)	Relative tolerance limits (%)	Tolerance limits (mg/tablet)
12.48	-0.823	99.18	1.33	1.49	[-4.48, 2.84]	[11.92, 12.83]
13.87	0.498	100.50	1.03	1.17	[-1.84, 2.83]	[13.61, 14.26]
15.26	-0.257	99.74	1.83	2.11	[-4.40, 3.88]	[14.59, 15.85]

The trueness of the method was evaluated by calculating the relative bias and the recovery. The recovery had very good values (close to 100%) for both APIs at all three concentration levels. The minimum value was 99.18 at a low concentration level of amlodipine besilate and maximum 101.48 at a medium concentration level of atorvastatincalcium. The precision evaluated as repeatability (intra-day precision) and intermediate precision (repeatability over different days) shows also good values for both APIs and at all concentration levels. The best repeatability and intermediate precision values were obtained at medium concentration levels for both APIs.

Figure 2 shows the linearity profile and the accuracy profiles of the NIRS method. The linearity profile of the method was evaluated by plotting the determinate concentration of APIs in validation samples by NIRS method as a function of introduced concentration. The linearity profile of the NIRS method for both APIs is shown in Figure 2 (left).The dashed limits on the graph correspond to the accuracy profile and the dotted curves represent the acceptance limits at ±5% expressed in the concentration unit per tablet. As seen in the Figure 2, the R^2 and the slope values are close to 1 for both APIs, confirming the linearity of the method for the direct and simultaneous quantification of atorvastatin and amlodipine in tablets.

For the accuracy profile the acceptance limits were set at ±5%, as required for the determination of API in pharmaceutical products [13].The β-expectation tolerance limits should be included in the acceptance limits. As seen in Figure 2, the β-expectation tolerance limits are fully included within the ±5% acceptance limits for both APIs, so it can be concluded that the NIRS method provides results with adequate accuracy for simultaneous atorvastatin and amlodipine assay, in tablets without any sample preparation over the range of 9.31-11.37 mg/tablet for atorvastatincalcium and 12.48-15.26 for amlodipinebesilate. The largest relative tolerance limits for atorvastatin calcium (-4.50%, 3.37%) were at the lowest concentration level and the largest relative tolerance limits for amlodipine besilate (-4.40%, 3.88%) were at the highest concentration level. The best accuracy was obtained at the medium concentration level for both APIs.

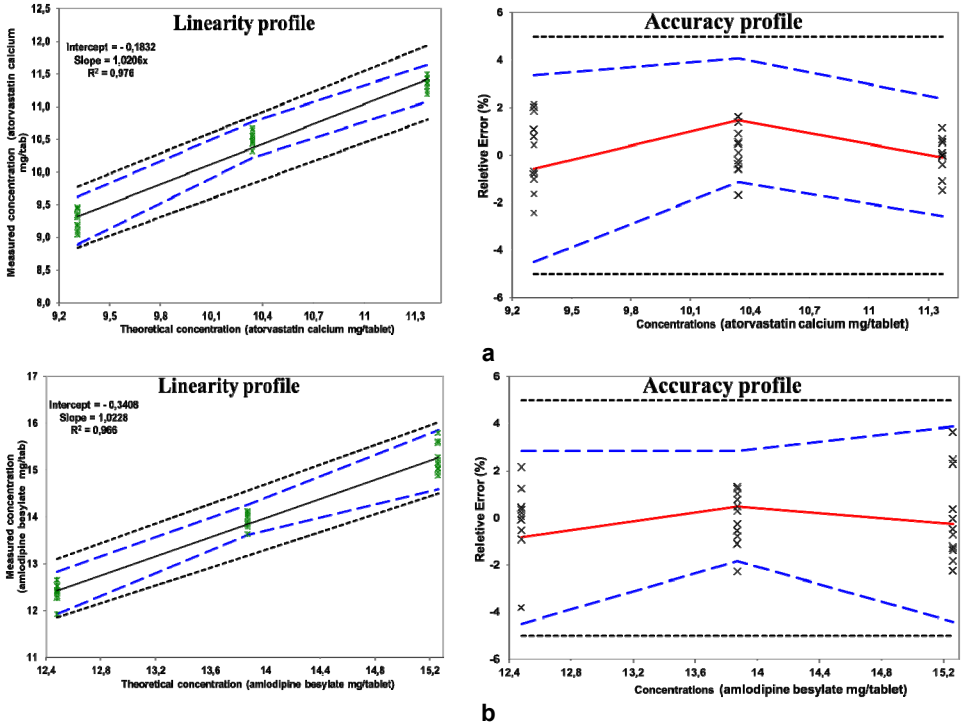

Figure 2. The linearity profiles (left) and accuracy profiles (right) the obtained for the NIRS method of simultaneous quantification of atorvastatincalcium (a) and amlodipine besilate (b).

According to the data presented above in Table 2 and Figure 2, the NIRS method using model (f, SNV-4) for atorvastatincalcium (standard normal variate pre-processing, 7 PLS factors and 4 spectral regions: 10000-8270; 7700-7120; 6800-5616; 5400-4243cm^{-1}) and model (l, FD+SNV) for amlodipine besilate (first derivative followed by standard normal variate pre-processing, 7 PLS factors and 1 spectral region: 10000-4200cm−1) is reproducible, accurate and linear (has an accuracy profile and a linearity profile within the acceptance limits set at ±5%,). So, it can be concluded that the NIRS method is linear, sufficiently precise and accurate for the direct (without any sample preparation) and simultaneous quantification of both APIs (atorvastatin and amlodipine) in tablets.

Application of the method

The results presented in the validation section indicated that the method could be used for the direct and simultaneous determination of atorvastatin and amlodipine content in tablets with active content 10 mg APIs/table (over the range of 9.31-11.37 mg/tablet for atorvastatin as atorvastatin calcium and over the range of 12.48-15.26 for amlodipine as amlodipine besylate). The NIRS method has been applied for the simultaneous quantification of both APIs in 4 control samples of tablet batches containing 10 mg APIs/tablet, strength which is the expected in the tablets available on the market. A reference HPLC method has also been used for APIs assay in the same control samples. The results obtained with the NIRS method and reference HPLC methods are shown in Table 3.

Table 3. Results obtained on control samples by NIRS method and HPLC reference method

	Atorvastatin			Amlodipine		
Control samples	HPLC*	NIRS	Recovery** (%)	HPLC*	NIRS	Recovery** (%)
P1	10.22	10.64	104.15	13.91	13.63	97.95
P2	10.29	10.45	101.56	13.81	14.01	101.43
P3	10.34	10.51	101.65	13.54	13.90	102.71
P4	10.60	10.43	98.39	13.80	14.11	102.24
Mean	10.36	10.51	101.44	13.77	13.91	101.08
SD		0.09			0.21	
t_{exp}		1.519			1.133	
P (type 1 error)		0,179			0.301	

*HPLC reference method
** Calculated as 100 ×NIR/HPLC

The NIRS predicted values for APIs content in control samples were compared with values obtained by the reference HPLC method, in terms of active content recovery, and the Student t test has been used for comparison of the methods. As presented in Table 3, similar results were obtained by both methods (NIRS and reference HPLC method). The average recovery was 101.44 for atorvastatin and 101.08 for amlodipine. The results did not show any statistical difference ($p>0.05$) between the results obtained using NIRS method and results obtained using the reference HPLC method.

CONCLUSIONS

In this work a NIRS method was explored for the direct, fast, non-destructive and non-invasive quantitative analysis of two APIs in a fixed-dose combination tablet. The two components were determined simultaneously using pre-processed spectra (standard normal variate, first derivative followed by standard normal variate) together with PLS multivariate calibration. The method was validated in terms of trueness, precision and accuracy, for active contents of 90-100-110%. The validation shows good statistical results and furthermore, application of the method and on real samples similar with the tablets on the marked proved that results obtained with NIRS are similar with those obtained by HPLC, used as reference method.

According to the data presented in this paper, NIRS based on PLS multivariate calibration could to be a suitable tool for non-destructive, direct and simultaneous prediction of the chemical composition of a fixed-dose combination that includes two active pharmaceutical ingredients (atorvastatin and amlodipine) combined in a single dosage form and is helpful in achieving the goals of Process Analytical Technology (PAT).

EXPERIMENTAL SECTION

Materials

Atorvastatin calcium (Hetero, India), amlodipine besylate (Hetero, India), microcrystalline cellulose (JRS Pharma, Germany), calcium carbonate (SPI Pharma, France), sodium croscarmellose (JRS Pharma, Germany), corn starch (Colorcon, UK) silicon dioxide (RohmPharma Polymers, Germany), magnesium stearate (Union Derivan, Germany).

Sample preparation for NIR analysis

A protocol was followed for calibration and validation, in order to develop and validate a robust NIRS method for the simultaneous quantification of two APIs. The protocol included batches and days as sources of variability. A training calibration set consisting in 26 different formulations of tablets containing different amounts of atorvastatincalcium and amlodipine besilate was prepared according to a D-optimal experimental design with 2 variables and 5 levels generate by Modde 10 software (Umetrics, Sweden) (Table 4).

Table 4. Composition of calibration/validation set according to an D-optimal experimental design

Exp Name	X_1 mg/tablet	X_2 mg/tablet	Exp Name	X_1 mg/tablet	X_2 mg/tablet
N1	8,27	11,09	N14	11,37	13,87
N2	9,31	11,09	N15	12,41	13,87
N3	10,34	11,09	N16	8,27	15,26
N4	11,37	11,09	N17	9,31	15,26
N5	12,41	11,09	N18	10,34	15,26
N6	8,27	12,48	**N19***	11,37	15,26
N7*	**9,31**	**12,48**	N20	12,41	15,26
N8	10,34	12,48	N21	8,27	16,64
N9	11,37	12,48	N22	9,31	16,64
N10	12,41	12,48	N23	10,34	16,64
N11	8,27	13,87	N24	11,37	16,64
N12	9,31	13,87	N25	12,41	16,64
N13*	10,34	13,87	N26	12,41	16,64

X_1– atorvastatincalcium, X_2 - amlodipinebesilate * - validation samples

Table 5. Qualitative and quantitative composition of calibration and validation samples

Concentration level	1 [a] 80%	2 [a,b] 90%	3 [a,b] 100%	4 [a,b] 110%	5 [a] 120%
Tablets composition (mg/tablet)					
Atorvastatin calcium	**8.27**	**9.31**	**10.34**	**11.37**	**12.41**
Amlodipine besylate	**11.09**	**12.48**	**13.87**	**15.26**	**16.64**
Microcrystalline Cellulose	78.26	75.84	73.42	71.00	68.58
Calcium carbonate	30.00	30.00	30.00	30.00	30.00
Croscarmellose sodium	6.00	6.00	6.00	6.00	6.00
Corn starch	15.00	15.00	15.00	15.00	15.00
Silicon dioxide	0.38	0.38	0.38	0.38	0.38
Magnesium stearate	1.00	1.00	1.00	1.00	1.00
	150.0	**150.0**	**150.0**	**150.0**	**150.0**

[a] calibration samples for API assay; [b] validation samples for API assay;

In the tablets the amount of APIs was between 8.27 – 12.41 mg/tablet for atorvastatin calcium and between 11.09–16.64 mg/tablet for amlodipine, respectively. This amount results from the preparation of atorvastatincalcium and amlodipine tablets with 10mg of each API/tablet and 150 mg tablet weight. The amount of API/tablet was 8.27, 9.31, 10.34, 11.37, 12.41 mg atorvastatin calcium and 11.09, 12.48, 13.87, 15.26, 16.64 mg amlodipine besilate respectively, corresponding to 80, 90, 100, 110 and 120% API content in the formulations (Table 5).

Tablets were prepared by direct compression. In detail, atorvastatincalcium, amlodipinebesilate, microcrystalline cellulose, calcium carbonate, sodium croscarmellose, corn starch and silicon dioxide were mixed using a planetary mixer (PRS type, Erweka, Germany) for 5 min. The powder blend for tableting was passed through the 0.8 mm sieve and remixed for 3 minutes in the same mixer. Subsequently, magnesium stearate was added to the mixture and mixed for 1 minute. A total of 150 mg of powder for tableting was filled in a die (Ø 7mm) and compressed using an eccentric tablet press (Riva, UK).

NIR analysis

NIR spectra were recorded using a Fourier-transform NIRS analyser (Antaris, TermoElectron, SUA) in Reflectance Sampling configuration. Each reflectance spectrum was acquired via OMNIC software (Termo Scientific, USA) by integrating 32 scans taken over a wave number between 4000cm^{-1} to 10000cm^{-1} with 8cm^{-1} resolution. Twenty different NIR measurements on twenty different tablets of the same batch tablets sample were recorded.

Model calibration

For the development of calibration models the PLS (Partial Least Squares) regression method from the OPUS Quant 6.5 (Bruker Optics, Germany) was used. Different pre-processing methods were applied in combination with the whole spectra or different spectral regions in order to find models with high predictive ability [19]. The predictive ability of a model was evaluated according to the following classical criteria: RMSECV (root mean square error of cross-validation), high correlation coefficient (R^2), low number of PLS factors and low bias [20,21]. The optimal numbers of factors for PLS were determined by a cross-validation procedure with groups of two spectra (each side of the sample being represented by a spectrum) [22].

Method validation

For validation, external independent sets of samples are needed. In order to validate the NIRS methods, the formulations from calibration sets corresponding to 90, 100 and 110% APIs content, (formulations N7, N13 and N19) were prepared using the same methodology presented previously. Four replicates for each concentration level were prepared in three different days as validation samples. There are several validation parameters that must be determined in order to be consistent with the recommendations of International Conference of Harmonization (ICH) and other regulatory (EMA, FDA) guidelines: accuracy, precision (repeatability and intermediate precision), linearity and range of application. The validation was performed according to the strategy proposed by Hubert *et al* [23] with slight modification according with a recent review on NIRS methods validation [24]. Calculation of the validation parameters (trueness, precision, accuracy) was performed in Microsoft Office Excel 2010 (Microsoft Corporation, USA)

Reference methods

Atorvastatin and amlodipine assay in tablets were performed using a reference HPLC-UV validated method. The chromatographic parameters were: column Phenomenex Luna C18 (2) 150 x 4,6mm x5µm; mobile phase acetate buffer (0.025M, pH 4.5): acetonitrile in gradient (0-2min, 55:45v/v; 2-5min 75:25vv); flow rate of 1.5 ml/min. The detection was performed at 236nm for atorvastatin and 246nm for amlodipine. Under the given chromatographic conditions the retention time was 2.01 minutes for atorvastatin and 4.01 minutes for amlodipine.

ACKNOWLEDGMENTS

This paper was published under the frame of European Social Found, Human Resources Development Operational Program 2007-2013, project no. POSDRU/159/1.5/S/136893

REFERENCES

[1]. C.S. Gautam, L. Saha, *British Journal of Clinical Pharmacology*. **2008**, *65*, 795.
[2]. R. Blank, F.D. Hobbs, J. Zamorano, X. Girerd, *Drugs Today* (Barc). **2007**, *43*, 157.
[3]. S.G. Chrysant, *Clin Drug Investig.* **2008**, *28*, 713.

[4]. ***EMA Reflection Paper: Chemical, pharmaceutical and biological information to be included in dossiers when Process Analytical Technology (PAT) is employed. http://www.ema.europa.eu/docs/en_GB/document_library/Other/2009/10/WC500004890.pdf (accessed 02/03/2015).
[5]. ***FDA Guidance for Industry: PAT – A Framework for Innovative Pharmaceutical Development, Manufacturing, and Quality Assurance. http://www.fda.gov/downloads/Drugs/GuidanceComplianceRegulatoryInformation/Guidances/ ucm070305.pdf (accessed 02/03/ 2015).
[6]. M. Jamrógiewicz, *J Pharm Biomed Anal.* **2012**, *66*, 1.
[7]. T. De Beer, A. Burggraeve, M. Fonteyne, L. Saerens, J.P. Remon, C. Vervaet, *Int J Pharm.* **2011**, *417*, 32.
[8]. I.A. Tuhuţiu, D. Casoni, C. Sârbu, *Studia UBB Chemia,* **2012**, *LVII (2)*, 83.
[9]. A. Jena, M. Madhu, S. Latha, *IJPSR*, **2010**, *1*, 100.
[10]. D.A. Shah, K.K. Bhatt, M.B. Shankar, R.S. Mehta, T.R. Gandhi, S.L. Baldania *Indian J Pharm Sci.* **2006**, *68(6)*, 796.
[11]. C. Sîrbu, I. Tomuță, L. Vonica, M. Achim, L.L. Rus, E. Dinte, *Farmacia,* **2014**, *62*, 48.
[12]. I. Tomuta, R.Iovanov, A.L. Vonica, S.E. Leucuta, *Sci Pharm*. **2011**, *79*, 885.
[13].I. Tomuta, R. Iovanov, E. Bodoki, L. Vonica, *Drug Dev Ind Pharm.* **2014**, *40*, 549.
[14]. M. Donoso, E.S. Ghaly, *Pharm Dev Technol.* **2005**, *10,* 211.
[15]. L.B. Marić, B.D. Jović, S.D. Petrović, A.M. Nikolić, I.J. Homšek, *J. Serb. Chem. Soc.* **2014**, *79*, 331.
[16]. P.F. Chavez, P. Lebrun, P.Y. Sacré, C. Bleye, L. Netchacovitch, S. Cuypers, J. Mantanus, H. Motte, M. Schubert, B. Evrard, P. Hubert, E. Ziemons, *Int J Pharm.* **2015**, *486*, 13.
[17]. C.V. Liew, A.D. Karande, P.W. Heng, *Int J Pharm*. **2010**, *386*, 138.
[18]. K. Järvinen, W. Hoehe, M. Järvinen, S. Poutiainen, M. Juuti, S. Borchert, *Eur J Pharm Sci.* **2013**, *48*, 680.
[19]. A. Porfire, L. Rus, A.L. Vonica, I. Tomuță, *J Pharm Biomed Anal.* **2012**, *70*, 301.
[20]. J. Mantanus, E. Ziémons, P. Lebrun, E. Rozet, R. Klinkenberg, B. Streel, B. Evrard, P. Hubert,*Talanta* **2010**, *80*, 1750.
[21]. I.A. Sima, R.D. Naşcu-Briciu, C. Sârbu, *Rev. Roum. Chim*., ***2013***, *58*(7-8), 705.
[22]. T. Naes, T. Isaksson, T. Fearn, T. Davies, A User-Friendly Guide to Multivariate Calibration and Classification. NIR Publications. Chichester, 2002, chapter 1.
[23]. P. Hubert, J.J. Nguyen-Huu, B. Boulanger, E. Chapuzet, P. Chiap, N. Cohen, P.A. Compagnon, W. Dewé, M. Feinberg, M. Lallier, M. Laurentie, N. Mercier, G. Muzard, C. Nivet, L. Valat, E. Rozet, *J Pharm Biomed Anal.* **2007**, *45*, 82.
[24]. C. De Bleye, P.F. Chavez, J. Mantanus, R. Marini, P. Hubert, E. Rozet, E. Ziemons, *J Pharm Biomed Anal.* **2012**, *69*, 125.

STUDIA UBB CHEMIA, LX, 2, 2015 (p. 295-308)
(RECOMMENDED CITATION)

MINOXIDIL AND NEOPTIDE TOPICAL APPLICATION REINFORCED BY LOW-LEVEL LASER THERAPY ON AN ANIMAL MODEL OF ALOPECIA

MEDA SANDRA ORĂSAN[a], ANDREI CONEAC[b*], CARMEN MIHAELA MIHU[b], CODRUŢA MARE[c], ADRIANA MURESAN[d]

ABSTRACT. This study investigated on a rat model the hair regrowth effects of Low-Level Laser Therapy as monotherapy or concomitant therapy with topical application of two chemical treatments that are used in human patients with hair loss: Minoxidil 2% - Hairgrow (Dar Al Dawa Pharma/Amman, Jordan) and Neoptide (Ducray/ Boulogne, France).

Results of hair regrowth evaluated by macroscopical images (photographs), trichoscopy (with a dermatoscope) and grown hair weight (from a surface area of 1cm²) revealed that Minoxidil 2% therapy was more efficient than Neoptide. Topical treatments were less efficient than LLLT exposure alone. Both combined therapies: LLLT plus Minoxidil 2% and LLLT with Neoptide induced better hair regrowth than topical applications. Our study proves that not all the products recommended for human use have the same hair regrowth efficiency on an animal model and that a combined therapy (laser plus topical substance) may bring supplementary benefits.

Keywords: *hair regrowth, low-level laser therapy, combined treatment, Minoxidil 2%, Neoptide, trichoscopy*

INTRODUCTION

More than half of the population worldwide suffers from a hair loss disorder [1]. Androgenetic alopecia (AGA) is the most common cause of hair loss, affecting more than half of the males over 40 years old and females over

[a] *"Iuliu Hatieganu" University, Faculty of General Medicine, Physiopathology Department, 8 Victor Babes str., RO-400012, Cluj-Napoca, Romania*
[b] *"Iuliu Hatieganu" University, Faculty of General Medicine, Histology Department, 8 Victor Babes str., RO-400012, Cluj-Napoca, Romania*
[c] *"Babes-Bolyai" University, Faculty of Economics and Business Administration, Department of Statistics – Forecasts - Mathematics, 58-60 Teodor Mihali str., RO-400591, Cluj-Napoca, Romania*
[d] *"Iuliu Hatieganu" University, Faculty of General Medicine, Physiology Department, 8 Victor Babes str., RO-400012, Cluj-Napoca, Romania*
** Corresponding author: andrei.coneac@gmail.com*

65 [1]. AGA is a chronic dermatological disorder defined as thin diffuse hair loss over the vertex and frontal area of the scalp in females and it is accompanied by hairline recession at the temples in males. The disease is caused by androgen excess (testosterone and its derivate dihydrotestosterone) and it is due to the susceptibility of hair follicles to androgen miniaturization. Heredity also plays a part [1].

Minoxidil 2% topical therapy in female patients, as well as Minoxidil 5% and Finasteride treatment in males represent the only FDA approved drugs for AGA. As currently used therapies proved not to be effective in all patients, scientists focused on finding new quality therapies for hair loss and treatment. Laser has thus become an interesting and encouraging field of research as it has already been demonstrated that red or near-infrared light determines tissue repair. Low Level Laser Therapy (LLLT) may provide a promising treatment option for patients who do not respond to classical treatment. LLLT represents a type of laser which produces low power, coherent monochromatic red light, promotes regeneration and stimulates cellular activity [2]. The device was previously tested and recorded positive results on wound healing, nerve regeneration, joint pain relief, stroke recovery and mucositis treatment [3,4,5,6,7,8,9]. LLLT delivers fluences of 1-10J/cm² with a power density of 3-90mW/cm² and has demonstrated beneficial effects in various skin conditions as well [10].

In the late 1960's the usual wavelengths ranged from 500-1100 nm, therefore Endre Mester used a low-power ruby laser (694nm) on a mice animal model. During his study on cargiogenic potential of lasers, he discovered that the therapy applied determined an unexpectedly significant hair regrowth on the test areas [11,12]. LLLT was since considered a potential treatment for hair loss [13]. The photobiomodulation produced by LLLT stimulates epidermal stem cells in the follicle bulge and determines the shifting of the follicles from telogen (resting phase) to the anagen (active) phase of the hair growth cycle [1]. Laser phototherapy is thought to prolong the duration of anagen and prevent premature catagen development (hair falling phase) [14,15]. LLLT alters cell metabolism through photodissociation of inhibitory nitric oxide (NO), leading to increase adenosine triphosphate (ATP) production and modulation of reactive oxygen species (ROS) [16]. It also determines induction of transcription factors that cause protein synthesis, triggering cell proliferation, alteration of cytokine levels, growth factors, inflammatory mediators and significant tissue oxygenation [17]. LLLT has been proved to produce vasodilation and increased blood flow with important therapeutic effect in alopecia [17-19].

Recently, a large number of commercial devices using LLLT have been promoted with increased media attention and significant marketing budgets.

Professional and home-based LLLT devices may have a hand-held design or consist of a therapy helmet for hands-free use. Most of the studies claim that LLLT of the scalp at 655nm significantly improves the hair counts in males with AGA, with an increase in the number of terminal hairs and in shaft diameter, together with a decrease of vellus hairs [20, 21]. Few clinical trials have been conducted on these LLLT devices and results are controversial. The therapeutic effect remains unclear due to the lack of independent long-term placebo-controlled clinical studies and due to analyzing issues [21, 22]. Further research is required to establish the efficacy on hair regrowth in comparison to classic topical solutions [22, 23].

The objective of our study was to determine whether treatment with a low-level laser device, the US FDA-cleared HairMax Lasercomb, is efficient in inducing hair growth in vivo, on an animal model in single usage (standard parameters, 3 minutes therapeutic exposure) and in combination with topical therapy: Minoxidil 2% (Hairgrow, Dar Al Dawa Pharma/Amman, Jordan) and Neoptide (Laboratoires Dermatologiques Ducray/ Boulogne, France).

RESULTS AND DISCUSSION

A) Macroscopic and Microscopic Evaluation

Macroscopic examination of the skin surface on day 30 of treatment enabled us to assess the *in vivo* hair regrowth effect induced by topical daily application of Minoxidil 2% in Group I. We comparatively evaluated the test area and the control area of each rat from this group and the majority of rats showed positive hair regrowth under this therapy. Regarding the macroscopic score, 4 rats had Type 4 hair regrowth on the test area (marked increased hair regrowth, full, thick fur), 2 rats had Type 3 (moderately increased hair growth with no visible skin area), one rat showed Type 2 (low hair density, with the visualization of the skin) and another one Type 1 (uneven hair growth on the test area, skin easily seen). Trichoscopic examination of the same study group revealed an equal distribution (3:3 ratio) between Type 4 and Type 3 hair regrowth pattern.

Group II (treated with Neoptide 0.3 ml topical daily application) had a moderate hair growth effect, as the test area presented Type 3 hair regrowth in 4 rats, Type 2 hair regrowth in 3 rats and only 1 rat recorded a maximum hair regrowth result (Type 4 hair regrowth pattern). Tricoscopy evaluation however showed that Type 4 pattern was misinterpreted and, in fact, it was a case of moderately increased hair growth.

LLLT laser therapy in Group III (applied for 3 minutes, three times per week) enhanced hair regrowth. Both microscopic and macroscopic assessment revealed that half of the rats in the study group had Type 4, marked increased hair regrowth on the test area. Type 3 pattern was diagnosed in 2 rats and an equal number had Type 2 pattern.

When evaluated by macroscopic aspect, the majority of animals in Group IV (LLLT plus Minoxidil 2%) revealed marked increased hair regrowth (Type 4 in 5 rats), suggesting a powerful therapeutic effect. Moderately increased hair regrowth (Type 3) was encountered in 2 rats on the test area, and only one had low hair density (Type 2). Tricoscopy evaluation enabled us to correctly assess the hair regrowth result and to notice that one Type 3 pattern was misinterpreted as marked increased hair growth. 75% of the animals in this group recorded an efficient hair growth effect induced by this combined therapy.

Group V, treated with LLLT plus Neoptide, recorded similar results to LLLT laser Group III: 4 rats with Type 4 hair regrowth, 2 rats with Type 3 and 2 with Type 2. The results were arrived at by macroscopic and trichoscopic assessments.

The comparative evaluation of the experimental groups show that the lowest hair regrowth effect was noticed in Group II (Neoptide) ($p>0.05$). As far as topical treatment is concerned, we found out that topical Minoxidil 2% application (in Group I) was significantly better in inducing hair regrowth, even thought the p-value was over 0.05 (Table 1, Table 2).

Table 1. The macroscopic score from the treated area and the control area, expressed in the 0-5 scale described in literature. Results are expressed with Exact Wilcoxon-Signed-Rank Test * = $p<0.05$.

Treatment	**Macroscopic score Median Percentile (25^{th}-75^{th})**	***Mean ± SD***	***P value***
Group 1	3.00 (2.25-3.75)	*2.88±0.991*	
Minoxidil 2%			*0.102*
Control	2.50 (1.25-3.00)	*2.38±1.061*	
Group 2	3.00 (2.00-3.00)	*2.75±0.707*	
Neoptide			*0.257*
Control	2.00 (1.25-3.75)	*2.38±1.188*	
Group 3	3.00 (2.25-3.75)	*3.00±0.756*	
HairMax			*0.034**
Control	2.00 (1.25-3.00)	*2.25±1.035*	
Group 4	4.00 (3.00-4.00)	*3.50±0.756*	
HairMax + Minoxidil 2%			*0.038**
Control	2.50 (2.00-3.00)	*2.50±0.926*	
Group 5	3.50 (2.25-4.00)	*3.25±0.886*	
HairMax + Neoptide			*0.023**
Control	2.00 (1.25-3.00)	*2.25±1.035*	

By comparing the outcomes of LLLT performed with HairMax Laser Comb, we noticed that in Group III (treated only with the laser device) it had a significant hair growth effect ($p<0.05$). Still, LLLT monotherapy was less efficient on hair regrowth than the combined treatment regimen with daily topical application of the Minoxidil or Neoptide compounds.

LLLT plus Minoxidil 2% (in group IV) and LLLT with Neoptide (in Group V) seem to be equally successful therapies in inducing hair regrowth, facts revealed both by macroscopic and trichoscopic assessment ($p<0.05$). Out of the five study groups, the best hair regrowth effect was noticed by macroscopic and trichoscopic assessment in Group IV (Laser + Minoxidil 2%) ($p<0.05$) (Table 1, Table 2).

Table 2. Trichoscopy score from the treated area and the control area, expressed in the 0-5 scale defined by using a dermatoscope. Results are expressed with Exact Wilcoxon-Signed-Rank Test. * = $p<0.05$.

Treatment	Trichoscopic score Median Percentile (25^{th}-75^{th})	*Mean ± SD*	*P value*
Group 1	3.00 (2.25-4.00)	*3.00±1.069*	
Minoxidil 2%			*0.102*
Control	2.5 (1.25-3.00)	*2.38±1.061*	
Group 2	3.00 (2.25-3.00)	*2.75±0.463*	
Neoptide			*0.157*
Control	2 (1.25-3.00)	*2.25±1.035*	
Group 3	3.00 (2.25-3.75)	*3.00±0.756*	
HairMax			*0.034**
Control	2 (1.25-3.00)	*2.25±1.035*	
Group 4	4.00 (3.25-4.00)	*3.63±0.744*	
HairMax + Minoxidil 2%			*0.024**
Control	2.5 (2.00-3.00)	*2.50±0.926*	
Group 5	3.50 (2.25-4.00)	*3.25±0.886*	
HairMax +Neoptide			*0.023**
Control	2 (1.25-3.00)	*2.25±1.035*	

B) HAIR WEIGHT DETERMINATION

Regarding the hair growth differences recorded between the test area and control area of the same animal, hair weight evaluation showed that the sum of differences in the Minoxidil study group was of 40.6 mg/cm². The weight of newly grown hair was the lowest in the Neoptide treatment protocol (Group II), the difference in hair weight being of 38,3 mg/cm². Both Minoxidil and Neoptide topical compounds induced a statistically significant hair regrowth on the test areas ($p<0.05$) (Table 3).

Compared to the control area from the same rat, the hair weight increased significantly in the LLLT treated groups (Group III, IV and V). Group III had a hair weight difference of 45.4mg/cm² between the test and control area of the rats. The highest hair weight was recorded for LLLT plus Minoxidil treated animals (Group IV), with a sum of hair weight differences of 57.1mg/cm². Group V (LLLT and Neoptide) has a lower, but still significant hair growth result, with a total of hair increase, (evaluated by hair weight difference) of 51.8 mg/cm². Statistic analysis enabled us to say that LLLT therapy (in monotherapeutic regimen or in combination with Minoxidil or Neoptide) has induced a better regrowth effect than topical therapy alone ($p<0.05$) (Table 3).

Table 3. The hair weight removed from one cm^2 in the treated area and the control area, expressed in mg/cm^2. Results are expressed with Exact Wilcoxon-Signed-Rank Test. * = $p<0.05$.

Treatment	Hair weight (mg/cm^2) Median Percentile (25^{th}-75^{th})	*Mean ± SD*	*P value*
Group1	42.40 (38.37-48.15)	*42.53±6.03*	
Minoxidil 2%			*0.012**
Control	38.25 (31.25-42.47)	*37.46±6.09*	
Group 2	44.10 (42.02-47.15)	*44.51±2.83*	
Neoptide			*0.012**
Control	39.25 (36.00-42.95)	*39.72±3.99*	
Group 3	44.25 (42.30-51.62)	*45.48±5.68*	
HairMax			*0.012**
Control	38.85 (35.5-43.47)	*39.81±5.47*	
Group4	48.50 (44.87-52.3)	*48.70±4.77*	
HairMax + Minoxidil 2%			*0.012**
Control	40.35 (36.87-45.82)	*41.56±5.29*	
Group5	45.15 (41.82-49.27)	*44.80±5.01*	
HairMax +Neoptide			*0.012**
Control	39.00(34.37-42.22)	*38.32±5.74*	

In the attempt to discover an effective treatment for hair loss, new therapies for alopecia have been studied on rats, hamsters and even stump-tailed macaque [24, 25].

LLLT has been tested on animal models and significant hair regrowth has been reported, but the optimum wavelength and dosimetric parameters still need to be determined [26]. According to literature LLLT stimulates hair regrowth in mice under chemotherapy-induced alopecia. LLLT applied on a rat animal model determined a significant hair regrowth in the HairMax treated groups, 5 days earlier than in the control and sham-control animals, as reported by a Satino study [27].

HairMax Laser Comb Professional 12 was screened for safety and received the US-FDA approval for medical use since 2007 [28]. In clinical use it is recommended for the scalp, 8 minutes, three times per week and its good compliance is due to the fact that it does not leave residue on the scalp, as topically applied substances do [10].

The incidence of adverse effects of LLLT is rather low: dry skin (5.1%), pruritus (2.5%), skin tenderness (1.3%), irritation (1.3%) and warm sensation at the site of application (1.3%) [1,10]. In our study no side effects were recorded in the LLLT treated groups (III, IV and V).

Minoxidil 2%, that we used in two of our study groups (I and IV) was not specially devised for hair loss problems and its hair growing effect has accidentally been discovered as a side effect.

The mechanism underlying the hair growth effect is therefore not completely clear yet. The drug action is directed to the mesenchymal cells from the follicular dermal papilla of the hair follicle (DP) which controls the growth and differentiation of hair matrix cells [26]. DP associated stem cells are the site of expression of genes related to hair growth, being under the negative effect of androgen mediated events, and under the positive stimulation of Wnt proteins and wound growth factors [29].

Possible indirect drug action is represented by the vasodilation produced by Minoxidil that generates an increased blood flow to the DP [26]. Minoxidil contains an N-oxide group able to release NO, an important cellular signaling molecule, also functioning as a vasodilator [30]. Minoxidil is also a potassium channel blocker, which also leads to vasodilation of the scalp blood vessels. This direct mechanism of action involving the ATP sensitive K+ channels was highly investigated [31]. New hair growth induced by Minoxidil can also be due to local irritation related to it or some components of the vehicle [26]. Researchers also suspect that Minoxidil may act in inducing hair regrowth through the immune system, as it stimulates prostaglandin synthethase-1 and the subsequent production of PGE(2) [32,33].

Literature did not mention any dysplastic or atypical changes in follicular germinal epithelium during or after application of topical minoxidil, and did not reveal the development of new follicles (follicular neogenesis) [26]. Studies performed on animal models with Minoxidil topical therapy described the shortening of telogen (resting phase), a premature entry in anagen phase (active) of the resting follicles, an action meant to prolong the anagen and leading to hair regrowth [34,35]. Larger hair follicles were reported in the morphometric evaluation of human scalp biopsies after treatment with topical minoxidil in a vehicle made up of propylene glycol, water and ethanol [26]. The alcohol and propylene glycol present in topical preparations can dry the scalp, causing dandruff and contact dermatitis. Nanosome formulation reduces the rate of contact dermatitis from the vehicle [36,37].

A systemic review of the side-effects of Minoxidil as hair loss treatment for AGA patients, done by Cochrane, underlined significant differences between 2% and 5% formulation, the latter determining an increased rate of general side-effects, such as: pruritus, skin irritation, dermatitis with a slightly elevated rate of hair growing in places other than the scalp, burning or irritation of the eye, redness, unwanted hair growth elsewhere on the body and even temporary hair loss or exacerbation of hair loss [38,39,40]. Serious side effects such as: severe allergic reactions, chest pain, dizziness, fainting, tachycardia, unexplained weight gain, or swelling of the hands and feet, were rarely reported [41]. Our study findings are in agreement with literature reports as no side effects were recorded in the Minoxidil 2% treated animal groups (I and IV).

The three types of evaluation methods applied in our study support the idea that Minoxidil 2% has a good hair growth inducing effect in the topical application regimen on animal model. Our results correlate with other literature data on Minoxidil efficacy. An Uno and Kurata study, performed on fuzzy rats in 1993, reported that topical application of Minoxidil, Diazoxide and Copper peptide produced a conversion from short vellus to long terminal hairs, an enlargement of the follicular size and a prolongation of anagen phase [31,42]. In human studies, hair loss reduction and growth of new hair is noticed after 4 months of 1 ml application/day Minoxidil topical treatment and after 6 months there was an increased in hair count with 13.2% [43,44,45]. Unfortunately, even though Minoxidil is the most commonly used topical hair growth compound, the monotherapy has a positive response rate in just 20-56% of the cases and AGA continues to progress [31,45].

Neoptide, on the other hand, is a promising topical treatment for hair regrowth as some human studies revealed. With a proper blend of vitamin B3, amino acids and botanicals, it significantly reduces the hair loss in female patients, simultaneously boosting the hair mass. The association of Neoruscine, Nicotinamide and GP4G facilitates optimal nutritional exchange in the hair bulb and provides an energy-activating role.

In agreement with this, our own study data revealed that just the topical therapy does not offer a proper therapeutic response. We also noticed that LLLT is a powerful hair growth promoter by itself. Our results showed *that* hair density was increased when topical treatment and LLLT therapy were associated. The combination of the two induced a statistically significant hair regrowth which suggests that LLLT reinforces the chemical compound. Another possible hypothesis is that through the vasodilation created by LLLT the substance applied topically on the scalp has a better absorption rate which eases the active compounds delivery to the hair bulb. It will be our purpose, in a next research, to determine through high affinity chromatography, the absorption rate of the topical treatment.

The originality of our study research relies on the fact that LLLT was applied in conjunction with the gold standard treatment of AGA (Minoxidil 2%) and also with a new compound (Neoptide) which is thought to be an effective hair growth inducer in clinical practice. Another innovative aspect is Neoptide application on an animal model of alopecia, which was not done before.

CONCLUSIONS

An overall improvement of the test area with higher hair density was reported in all our study groups, though the results did not reach statistical significance for groups I and II when evaluation by macroscopical images (photographs) or trichoscopy (with a dermatoscope) was performed.

Results of the hair weight assessment (from a surface area of 1cm²) revealed that treatment with Minoxidil 2% induced significant hair regrowth. The lowest hair growth effect was noticed after treatment with Neoptide. Thus our study proves that not all the products recommended for human use are having the same hair regrowth efficiency on an animal model.

We also found a statistically significant difference in the increase of hair density between LLLT treated areas and control areas. Our results suggest that low-level laser treatment is more efficient than single use of topical therapy while the combined therapy (laser plus topical application) brings even supplementary benefits. The applied therapy was well tolerated as no adverse effects were reported on the animal model used.

Research on prevention and reversal hair loss continues to be a challenging subject. Further studies are required not only to compare efficiency of different therapies but also to identify the optimal length of laser treatment, the duration of the response and more importantly the long term safety of the newly implemented LLLT.

EXPERIMENTAL SECTION

Study design

40 adult Wistar-Bratislava rats were preselected for their telogen (resting) phase of the hair cycle according to age (around 120 days) from the Animal Facility of UMF “Iuliu Hatieganu” Cluj-Napoca. The Wistar albino rats of either sex, weighing about 200 g, were acclimatized to the experimental room in the Physiology Department of UMF Cluj, at a temperature of 23 Celsius degrees, in controlled humidity conditions with a 12:12 h light and dark cycle for 14 days prior to the experiment. We housed maximum 2 animals

per cage, offering them free access to standard pellets as basal diet and water ad libitum. Following the experiment they were euthanized according to the current regulations.

The study has obtained ethical committee clearance from the Institutional Animal Ethics Committee (IAEC) of Iuliu Hatieganu University of Medicine and Pharmacy Cluj-Napoca.

In order to create the alopecia animal model we induced general anesthesia and used electric hair clippers for the dorsal animal fur, followed by shaving which allowed us to create two rectangular areas, each of 2 cm width and 4 cm length. The denuded areas were symmetrically situated on both sides of the mid dorsal line, the right area provided for testing and the left as control.

We randomly assigned the animals to 5 experimental groups, each consisting of 8 rats. The treatment was performed for 1 month (Table 4).

Table 4. Experimental groups and treatments

GROUP	PRODUCT	MANUFACTURER/ CITY, COUNTRY	DETAILS	EXPOSURE DOSE	TREATMENT FREQUENCY
I	Minoxidil 2%, HairGrow	Dar Al Dawa Pharma / Amman, Jordan	topical application	0.3 ml	daily
II	Neoptide, Traitement antichute	Laboratoires Dermatologiques Ducray/Boulogne, France	topical application	0.3 ml	daily
III	HairMax Laser Comb 12	Lexington International LLC/ USA	laser exposure 655nm, <5mW	3 minutes	three times/ week
IV	Minoxidil 2% + HairMaxLaser	Dar Al Dawa Pharma, Lexington International LLC	topical laser exposure	0.3 ml 3 minutes	daily three times/ week
V	Neoptide + HairMaxLaser	Laboratoires Dermatologiques, Lexington International LLC	topical laser exposure	0.3 ml 3 minutes	daily three times/ week

The Lasercomb device

LLLT was applied by exposing the test area of each rat in Group III to HairMax Laser, at standard parameters (<5mW, continuous emission) for 3 minutes, with a frequency of three times/week. Group IV received daily

application of 0.3 ml Minoxidil 2% plus LLLT exposure three times per week, while Group V had 0.3 ml Neoptide daily topical application associated with 3 minutes LLLT, three times per week (Monday, Wednesday, Friday).

The HairMax Laser Comb Professional 12 is a hand-held Class 3R lower level laser therapy device. It contains a single laser module that emulates 12 beams: 6 of them at a wavelength of 635nm (±5%) and 6 beams at 655nm (±5%) [10].The device uses a technique of parting the subject's hair by special combs that are attached to it. By aligning the teeth with the laser beams, the hair can be parted, excluding possible obstruction and improving the delivery of distributed laser light energy to the skin surface.

The topical therapy

Topical therapy consisting of 0.3 ml solution was applied on the denuded test area of the rats daily in all test groups, except Group III, restricted to LLLT exposure. Group I received Minoxidil 2% daily application, while Group II was topically treated with Neoptide. Group IV had Minoxidil 2% topical application associated with LLLT for 3 minutes, three times per week (Monday, Wednesday, Friday). Group V also received combined therapy with Neoptide daily application together with laser therapy exposure, in the same specified regimen.

The systematic (IUPAC) name of Minoxidil is 6-Piperidin-1-ylpyrimidine-2,4-diamine 3-oxide. The chemical formula is a Chemical data formula $C_9H_{15}N_5O$, with a molecular mass of 209.251 g/mol. The Pharmacokinetic data include: its biotransformation (metabolism) primarily hepatic (90%), a half-life of 4.2 h and renal excretion [24].

Neoptide (Laboratoires Dermatologiques Ducray/Boulogne, France) is a hair growth promoter containing a peptide complex: Tetrapeptide, Neoruscine, Niconamid and guanosine (5') tetraphospho (5') guanosine abbreviated as GP4G.

Efficacy evaluation

On day 0, during the hair removal procedure with electric clippers, we defined a surface of 1 cm² and gathered the cut hairs in an aluminum foil. The hairs were then weighed with an analytical balance in the Chemistry Experimental Laboratory of the Physiology Department. Once the alopecia animal model was prepared, we photographed the macroscopic aspect and stored the images for each experimental group in electronic folders. We also used a hand held Dermatoscope (Dermlite DL3) to visualize the denuded area of the rats, followed by the capturing of the trichoscopy images and storage in electronic folders.

At the completion of 1 month treatment, the assessment of hair regrowth was evaluated in all study groups. We used both qualitative and quantitative methods, to ensure a correct evaluation process. For qualitative assessments of macroscopic and trichoscopic stored images, an observer, blind to the experiment, was used.

Macroscopic aspect and Trichoscopy are two qualitative assessments with results expressed on a scale of clinical aspect, subjectively perceived. The scale may be either defined in percentage according to the examples provided by literature, or devised by the researcher. We applied an evaluation scoring system based on the comparison of the treated area with the control of the same animal, as it has been successfully used before. The 4 stages of our scoring system were defined as: Type 1 (uneven hair growth on the tested area, skin can be easily seen), Type 2 (low hair density, with the visualization of the skin), Type 3 (moderately increased hair growth with no visible skin area), Type 4 (marked increased hair regrowth, full, thick fur). Both methods are approximations of hair growth that do not provide the possibility of precise measurement of the new grown hairs, as counting the number of hairs per unit and the determination of their diameter are not possible. Macroscopic aspect and Trichoscopy cannot quantify minor increases in hair density, which are considered a reliable sign of hair regrowth.

On the other hand, hair weight evaluation is able to determine slight increases in hair density. Hair weight is a quantitative and objective evaluation technique, based on precise measurement of hair from a predetermined area.

Statistic analysis

Descriptive statistics of the variables were expressed through mean and standard deviations. As variables are either ordinal or scale, but not normally distributed, the median value and the first and third quartile are also presented. Comparison between the treated area and the control one was based on the Wilcoxon Rank Test, a non-parametric test applied for two related samples. Significant effect of the treatment applied was considered when a p-value < 0.05 was obtained.

ACKNOWLEDGMENTS

This paper was published under the frame of the European Social Found, Human Resources Development Operational Programme 2007-2013, project no. POSDRU/159/1.5/S/138776.

REFERENCES

[1]. P. Avci, G.K. Gupta, J. Clark , N. Wilkonkal, M.R. Hamblin, *Lasers Surg Med*, **2014**, *46*(2), 144.
[2]. A Schindl, M. Schindl, H. Pernerstorfer-Schon, L. Schindl, *J Investig Med*, **2000**, *48*(5), 312.
[3]. J.M. Bjordal, C. Couppe, R.T. Chow, J. Tuner, E.A. Ljunggren, *Aust J Physiother*, **2003**, *49*(2), 107.
[4]. L. Brosseau, V. Welch, G. Wells, et al, *Cochrane Database Syst Rev*, **2000**, *2*, CD002049
[5]. R. G. Cauwels, L.C. Martens. *Eur Arch Paediatr Dent*, **2011**, *12*(2), 118.
[6]. A. Christie, G. Jamtvedt, K.T. Dahm, R.H. Moe, E.A. Haavardsholm, K.B. Hagen, *Phys Ther*, **2007**, *87*(12), 1697.
[7]. G. Jamtvedt, K.T. Dahm, I. Holm, S. Flottorp, *BMC Health Serv Res*, 2008, *8*, 145.
[8]. M.M Schubert, F.P. Eduardo, K.A. Guthrie, et al, *Support Care Cancer*, **2007**, *15*(10), 1145.
[9]. G.B. Silva, E.F. Mendonca, C. Bariani, H.S. Antunes, M.A. Silva, *Photomed Laser Surg,* **2011**, *29*(1), 27.
[10]. J.J. Jumenez, T.C. Wikramanayake, W. Bergfeld, et al, *Am J Clin Dermatol*, **2014**, *15*(2), 115.
[11]. E. Mester, G. Ludany, M. Sellyei, B. Szende, G. Gyenes, G.J. Tota, *Langenbecks Arch Chir*, **1968**, *322*, 1022.
[12]. D. Barolet, *Semin Cutan Med Surg*, **2008**, *27*(4), 227.
[13]. A.I. Metelitsa, J.B. Green, *Semin Cutan Med Surg*, **2011**, *30*(3), 144.
[14]. T.C. Wikramanayake, R. Rodriguez, S. Choudhary, et al, *Lasers Med Sci*, **2012**, *27*(2), 431.
[15]. M. Leavitt, G. Charles, E. Heyman, D. Michaels, *Clin Drug Investig*, **2009**, *29*(5), 283.
[16]. J.T. Eells, M.T. Wong-Riley, J. Verhoeve, et al, *Mitochondrion*, **2004**, *4*(5–6), 559.
[17]. H. Chung, T. Dai, S.K. Sharma, Y.Y. Huang, J.D. Carroll, M.R. Hamblin, *Ann Biomed Eng*, **2012**, *40*(2), 516.
[18]. N.L. Lohr, A. Keszler, P. Pratt, M. Bienengraber, D.C. Warltier, N. Hogg, *J Mol Cell Cardiol*, **2009**, *47*(2), 256.
[19]. E. Makihara, S. Masumi, *Nihon Hotetsu Shika Gakkai Zasshi*, **2008**, *52*(2), 167.
[20]. R.J. Lanzafame, T.T. Blanche, A.B. Bodian, R.P. Chiacchierini, A. Fernandez-Obregon, E.R. Kazmirek, *Lasers Surg Med*, **2013**, *45*(8), 487.
[21]. M.R. Avram, N.E. Rogers, *J Cosmet Laser Ther*, **2009**, *11*(2), 110.
[22]. A.K. Gupta, D. Daigle, *J Dermatol Treat*, **2014**, *25*(2), 162.
[23]. A.K. Gupta, D.C. Lyons, W. Abramovits, *Skinmed*, **2014**, *12*(3), 145.
[24]. P. Balakrishnan, S. Shanmugam, W.S. Lee, et al, *Int J Pharm*, **2009**, *377*(1), 1.
[25]. R.C. Wester, et al, *J Invest Dermatol*, **1984**, *82*(4), 353
[26]. J.T. Headington, *Dermatologica*, **1987**, *175* (2), 19.
[27]. J.L. Satino, M. Markou, *Int J Cos Surg Aest Dermatol*, **2003**, *5*, 113.

[28]. M. Leavitt, G. Charles, E. Heyman, D. Michaels, *Clin Drug Investig*, **2009**, *29*(5), 283.
[29]. M.P. Zimber, C. Ziering, F. Zeigler, et al, *J Drugs Dermatol*, **2011**, 10, 1308.
[30]. P.H. Proctor, *Arch Dermatol*, **1989**, *125*(8), 1146.
[31]. K. Shorter, N.P. Farjo, S.M. Picksley, V.A. Randall, *FASEB J*, **2008**, *22*(6), 1725.
[32]. J.F. Michelet, S. Commo, N, Billoni, Y.F. Mahe, B.A. Bernard. *J Invest Dermatol*, **1997**, *108*(2), 205.
[33]. R. Wolf, H. Matz, M. Zalish, A. Polack, E. Orion. *Dermatol Online J*, **2003**, *9*(3), 7.
[34]. A.G. Messenger, J. Rundegren, *Br J Dermatol,* **2004**, *150*, 186.
[35]. R. Dhurat, M.S. Sukesh, G. Avhad, A. Dandale, A. Pal, P. Pund, *Int J Trichology*, **2013**, *5*(1), 6.
[36]. Dandruff and Seborrheic Dermatitis". Medscape.com. Retrieved 2009-10-09.
[37]. P. Balakrishnan, S. Shanmugam, W.S. Lee, *Int J Pharmaceutics*, **2009**, *377*(1-2), 1.
[38] E.J. van Zuuren, Z. Fedorowicz, B.Carter, R.B. Andriolo, J. Schoones, *Cochrane Database Syst Rev*, **2012**, *16*, 5.
[39] E.J. van Zuuren, Z. Fedorowicz, B. Carter, *Br J Dermatol*, **2012**, *167*(5), 995.
[40]. M. Hordinsky, A. Donati, *Am J Clin Dermatol*, **2014**, *15*(3), 231.
[41]. Minoxidil Official FDA information, side effects and uses". Drugs.com. Retrieved 2015-04-01.
[42]. M. Li, A. Marubayashi A, Y. Nakaya, K. Fukui, S. Arase, *J Invest Dermatol*, **2001**, *117*(6), 1594.
[43]. A. Tosti, B. Duque-Estrada, *Expert Opin Pharmacother*, **2009**, *10*, 1017.
[44]. J.M. Mella, M.C. Perret, M. Manzotti, H.N. Catalano, G. Guyatt, *Arch Dermatol*, **2010**, *146*, 114.
[45]. U. Blume-Peytavi, K. Hillmann, E Dietz, D. Canfield, N. Garcia Bartels, *J Am Acad Dermatol*, **2011**, *65*(5), 1126.

STUDIA UBB CHEMIA, LX, 2, 2015 (p. 309-320)
(RECOMMENDED CITATION)

RAPID SIMULTANEOUS LC/MS^2 DETERMINATION OF RIFAMPICIN AND 25-DESACETYL RIFAMPICIN IN HUMAN PLASMA FOR THERAPEUTIC DRUG MONITORING

CRISTINA MIHAELA GHICIUC[a], NICOLETA RADUCANU[b], FARCZÁDI LÉNÁRD[c], LAURIAN VLASE[d,*], CĂTĂLINA ELENA LUPUȘORU[a], CONSTANTIN MIRCIOIU[e], BRINDUSA TILEA[f]

ABSTRACT. A rapid and sensitive liquid chromatography coupled with tandem mass spectrometry (LC/MS^2) method for the simultaneous quantification of rifampicin and its main active metabolite 25-desacetyl rifampicin in human plasma was developed and validated. The separation was performed on a Gemini NX C18 column under isocratic conditions using a mobile phase of 40:60 (V/V) methanol and 2mM ammonium formate in water, at 40 ºC, with a flow rate of 0.6 mL/min. The detection of rifampicin and its metabolite was performed in multiple reaction monitoring mode using an ion trap mass spectrometer with positive electrospray ionization. The human plasma samples (0.1 mL) were deproteinized with methanol and aliquots of 0.3 µL from supernatants obtained after centrifugation were directly injected into the chromatographic system. The method shows a good linearity ($r > 0.993$), precision (CV < 8.2%) and accuracy (bias < 6.3%) over the range of 411 - 19737 ng/mL for rifampicin and good linearity ($r > 0.992$), precision (CV < 10.1%) and accuracy (bias < 8.2%) over the range of 70 - 3379 ng/mL for 25-desacetyl rifampicin. The lower limit of quantification (LLOQ) was 411 ng/mL and recovery was between 90.3-108.2% for rifampicin, whereas for 25-desacetyl rifampicin the LLOQ was 70 ng/mL and recovery between 93.1-107.5%, respectively. The developed and validated method is simple, rapid

[a] *Department of Pharmacology, School of Medicine, "Gr.T. Popa" University of Medicine and Pharmacy Iasi, 16 Universitatii Str., Iasi, RO-700115, Romania*
[b] *PhD Student, "Carol Davila" University of Medicine and Pharmacy Bucharest, 7 Traian Vuia Str., Bucharest, sector 1, RO-020955, Romania*
[c] *Vim Spectrum SRL, Sighisoarei 409, RO-547367, Corunca, Targu-Mures, Romania*
[d] *Department of Pharmaceutical Technology and Biopharmacy, Faculty of Pharmacy, University of Medicine and Pharmacy "Iuliu Haţieganu", Cluj-Napoca, 8 Victor Babeş Str., RO-400012 Cluj-Napoca, Romania*
[e] *Department of Pharmaceutical Technology and Biopharmacy, Faculty of Pharmacy, "Carol Davila" University of Medicine and Pharmacy Bucharest, 7 Traian Vuia Str., Bucharest, sector 1, RO-020955, Romania*
[f] *Infectious Diseases Department M4, Clinical Scineces, Faculty of Medicine, University of Medicine and Pharmacy, 38 Gh. Marinescu Str., RO-540139, Târgu Mures, Romania*
** Corresponding author: Laurian.vlase@umfcluj.ro*

and specific for the high throughput simultaneous determination of rifampicin and 25-desacetyl rifampicin in human plasma and was successfully applied in therapeutic drug monitoring of rifampicin in patients with tuberculosis.

Keywords: *rifampicin, 25-desacetyl rifampicin, LC/MS^2, human plasma*

INTRODUCTION

Rifampicin, a semisynthetic antibiotic produced from *Streptomyces mediterranei* (Fig. 1) is used as first-line therapy for the treatment of tuberculosis in combination with at least one other anti-tuberculosis drug. As the incidence of infections is increasing, rifampicin is also preferred in combination therapy in the treatment of infections associated with prosthetic devices (e.g., implantable cardiac electronic devices) or in antimicrobial-resistant infections, especially methicillin-resistant Staphylococcus aureus (MRSA) [1,2].

Rifampicin is characterized by wide inter- and intra-individual variability in healthy volunteers, but also in tuberculosis patients [3]. Although the majority of patients respond to a standardized therapy, low drug concentrations are commonly associated with treatment failure or bacteria resistance, resulting in poor clinical outcomes [4,5]. 25-desacetyl-rifampicin is the main active metabolite of rifampicin, thus it is also responsible on the clinical efficiency of the treatment [3]. Rifampicin stimulates the metabolism of isoniazid and of other concomitant administered drugs and also induces its own metabolism over the first few weeks of treatment. In most patients with reduced renal or hepatic function, the doses should be reduced to prevent toxicity, but for rifampicin doses might need to be increased to avoid under-dosing due to enzyme induction. The determination of rifampicin and its metabolite in biological samples is useful for the evaluation of rifampin pharmacokinetics in combination therapy, facilitating early screening of therapeutic failure and preventing adverse effects [6,7]. Pharmacokinetic/ pharmacodynamic studies are needed to evaluate the interrelation between the free plasma drug concentration and microbiological and clinical outcomes of the treatment with rifampicin [5].

Several chromatographic analytical methods have been reported for the determination of rifampicin and 25-desacetyl rifampicin involving various techniques such as high performance thin layer chromatography (HTPLC) [7], high performance liquid chromatography (HPLC) [11], liquid chromatography coupled with mass spectrometry (LC-MS/MS) [10,12,13].

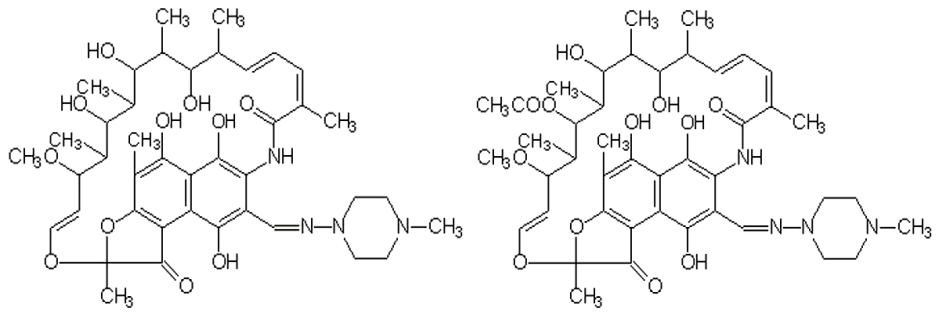

Figure 1. Chemical structures of rifampicin (left) and 25-desacetyl rifampicin (right)

Rifampicin can be determined using HPTLC [7], which is a quick and cheap method, however LC/MS methods are much more sensitive and more selective. HPLC methods have also been used for the determination of rifampicin [11], but we decided to develop a new LC/MS method due to its better selectivity in comparison to HPTLC and HPLC methods.

For analysis of biological samples using chromatographic methods, the samples must first undergo an extraction / purification process. A purification process often used is solid phase extraction (SPE) [9]. Although it is a very effective purification method, it is time consuming and raises the cost of analysis significantly. A fast, simple and inexpensive method for biological sample purification is protein precipitation (PP) method, widely used especially when LC/MS analysis is employed [10,12,13].

RESULTS AND DISCUSSION

Sample preparation

Although the MS detection type and parameters greatly influence the sensitivity of LC/MS assay methods, the sample preparation method can also have an influence on the chromatographic background noise level and can create suppression effects. Generally the analyte is extracted from the matrix prior to analysis using SPE or LLE for reasons such as sample purification and sample pre-concentration. The extraction processes (both SPE and LLE) are tedious, time and resource consuming, and will usually require the use of internal standards in order to reduce extraction variability. For these reasons PP as a sample processing technique is recommended whenever high-throughput and low extraction variability are required. The

disadvantage of PP is the fact that the samples are not highly purified as in the case of SPE or LLE, samples get diluted in the process, thus reducing sensitivity. The sample preparation technique must be chosen in a way to assure the best performance needed for a given analysis, whether reduced time and costs are needed, or a high sensitivity is needed.

The range of the calibration curves was adapted to the expected concentration levels of biological samples to be analyzed, 411.2 - 19737.6 ng/mL for rifampicin and 70.4 - 3379.2 ng/mL for 25-desacetyl rifampicin, respectively. As the developed analytical method shows good sensitivity for both analytes, the PP extraction method (which implies sample dilution) was considered a good alternative to SPE or LLE providing shorter processing times and high reproducibility.

The method developed by us requires samples of only 0.1 mL plasma, processed by PP with methanol (0.3 mL), the supernatant being injected into the HPLC system directly after centrifugation. The sensitivity obtained meets the requirements in order for the method to be usable for the given drug monitoring application and absolute recoveries were close to 100%.

LC-MS assay

The detection parameters were optimized in order to achieve best sensitivity and specificity for both rifampicin and 25-desacetyl rifampicin. Both compounds were ionized in ESI source by proton addition, giving pseudomolecular ions with m/z 824 for rifampicin and m/z 750 for 25-desacetyl rifampicin. By fragmentation, these ions are broken down to ions with m/z 792 for rifampicin and m/z 732 for 25-desacetyl rifampicin respectively (Fig. 2 and Fig 3). The extracted ion chromatograms (EIC) of m/z 792 from m/z 824 for rifampicin and m/z 732 from m/z 750 for 25-desacetyl rifampicin were analyzed for quanfication purposes. In the chromatographic conditions of the method the retention times were 1.1 minutes for rifampicin and 0.6 minutes for 25-desacetyl rifampicin, with a run-time per sample of 1.4 minutes. Typical chromatograms of human plasma samples spiked with rifampicin and 25-desacetyl rifampicin at LLOQ are shown in Fig. 3. No interfering peaks attributed to plasma components were observed at the retention times of rifampicin and 25-desacetyl rifampicin (Fig.3).

Assay validation

Validation of the method was carried out in accordance with international regulations [14]. Calibration curves prepared in human blank plasma were linear for both rifampicin and 25-desacetyl rifampicin over their concentration ranges of 411.2 - 19737.6 ng/mL, and 70.4 - 3379.2 ng/mL respectively.

Correlation coefficients were greater than 0.993 for rifampicin and greater than 0.992 for 25-desacetyl rifampicin. The lower limit of quantification (LLOQ) was established at 411.2 ng/mL for rifampicin and 70.4 ng/mL for 25-desacetyl rifampicin. Results for within-day and between-day precision and accuracy determined during the validation are shown in Tables 1 and 2 for rifampicin, and Tables 3 and 4 for 25-desacetyl rifampicin, respectively. All values for accuracy and precision were within acceptance criteria (< ±15%) [14]. Recovery values were between 90.3-108.2% for rifampicin and 93.1-107.5% for 25-desacetyl rifampicin.

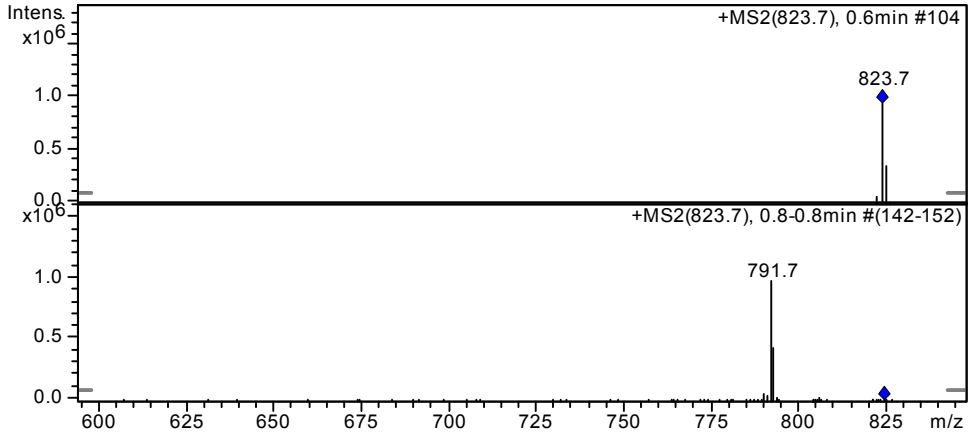

Figure 2. MS spectra of rifampicin – MS spectra (upper image), MS/MS spectra (lower image)

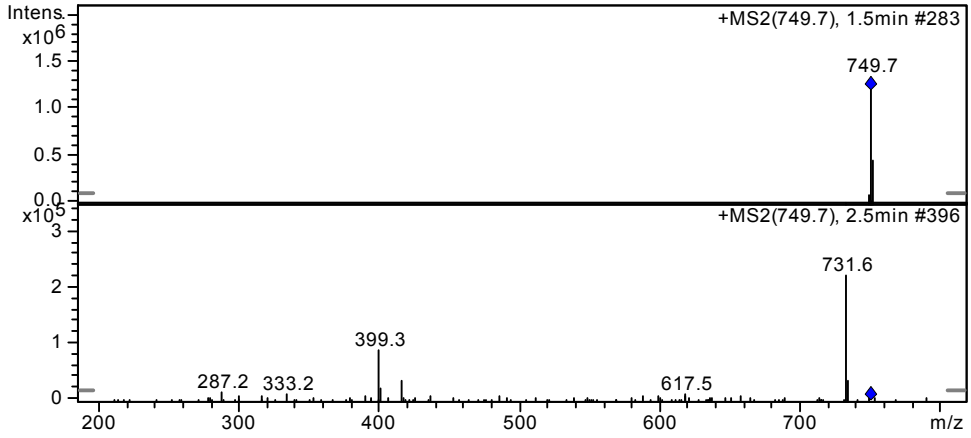

Figure 3. MS spectra of 25-desacetyl rifampicin – MS spectra (upper image), MS/MS spectra (lower image)

Method application

The validated method for simultaneous determination of rifampicin and 25-desacetyl rifampicin in human plasma was successfully applied in therapeutic drug monitoring and pharmacokinetic assessment of rifampicin and 25-desacetyl rifampicin in tuberculosis patients. Typical chromatograms of rifampicin and 25-desacetyl rifampicin in a tuberculosis patient plasma sample is shown in Fig. 3 and the overlapped plasma profiles obtained in the whole study (spaghetti plot chart) are presented in Fig. 4.

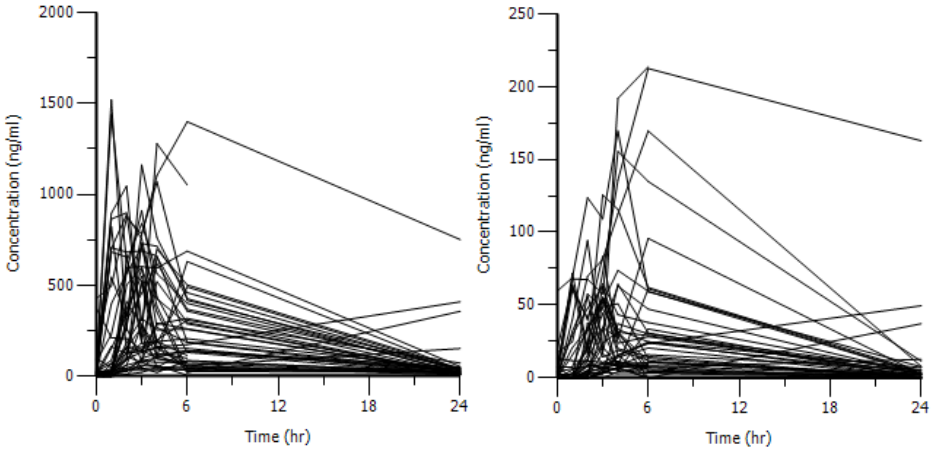

Figure 4. Overlapped plasma profiles of rifampicin (left) and 25-desacetyl rifampicin (right) administrated to patients with tuberculosis (600 mg rifampicin/day)

CONCLUSION

Antimicrobial therapeutic drug monitoring could be an important tool in clinical practice if the administered drug shows large inter-subject variability in pharmacokinetics or when the patient's compliance is poor. Therefore, quantification of drug in plasma is an important issue in clinical practice to enhance efficacy and to reduce toxicity.

The LC/MS^2 method developed by us for the quantification of rifampicin and 25-desacetyl rifampicin is specific, accurate, fast and inexpensive, as long as the analytical technology used (LC/MS) is available. It is one of the fastest analytical methods for simultaneous determination of rifampicin and 25-desacetyl rifampicin in biological matrices published, also having the advantage of using a simple, high throughput sample preparation technique. The method has a runtime of 1.4 minutes. Compared to other methods described in literature with runtimes of 2.1 minutes [10], 3.5 minutes [12] and 6 minutes [13]. This allows for shorter analysis times and higher throughput,

especially when large batches of samples need to be analysed. The faster runtimes were achieved without loss of accuracy or precision of the method. For rifampicin the within-day precision ranged from 1.0% to 7.7%, with an accuracy (bias, %) of -6.3% to 5.3%, while between-day precision ranged from 3.0% to 8.2%, with an accuracy (bias, %) of -3.2% to 4.7%. For 25-desacetyl rifampicin the within-day precision ranged from 1.8% to 4.2%, with an accuracy (bias, %) of 0.1% to 8.2%, while between-day precision ranged from 5.3% to 10.1%, with an accuracy (bias, %) of -2.5% to 1.0%. These values are similar to those of other methods described in literature [10,12,13]. The sample preparation using protein precipitation is simple and fast, ideal for high throughput LC-MS methods, and is also used in other methods described in literature [10, 12, 13]. The lower limit of quantification was 411 ng/mL for rifampicin and 70.4 ng/mL for 25-desacetyl rifampicin, higher than other methods described for the quantification of rifampicin [10, 12, 13] and 25-desacetyl rifampicin [10]. However, the purpose of our analytical method was its suitability for therapeutic drug monitoring, when steady-state plasma concentrations are much higher than after single-dose administration and a shorter analysis time is more desirable than a higher sensitivity.

The method was successfully applied in therapeutic drug monitoring of rifampicin and 25-desacetyl rifampicin in patients with tuberculosis.

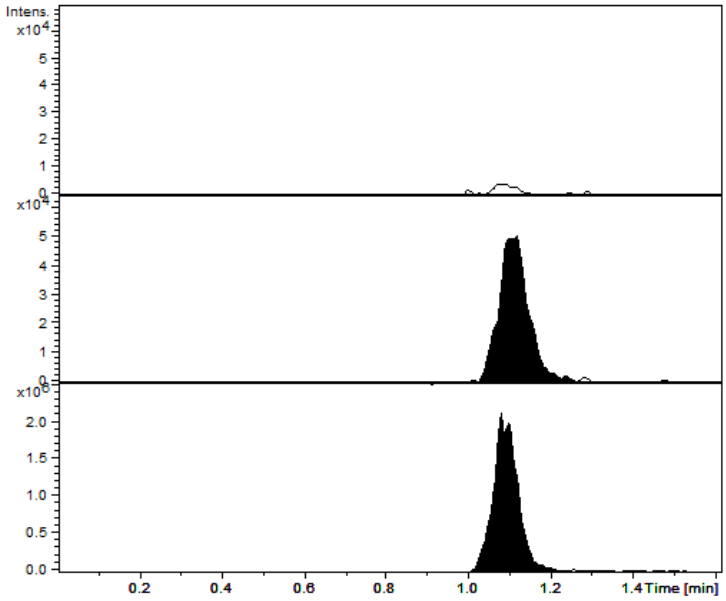

Figure 5. Representative chromatograms of blank sample (upper image); plasma spiked with rifampicin at lower limit of quantification (411 ng/mL, middle image); and a plasma sample from a patient under treatment with 600 mg rifampicin/day, sample taken after 2h from administration, concentration found 13672 ng/mL (lower image).

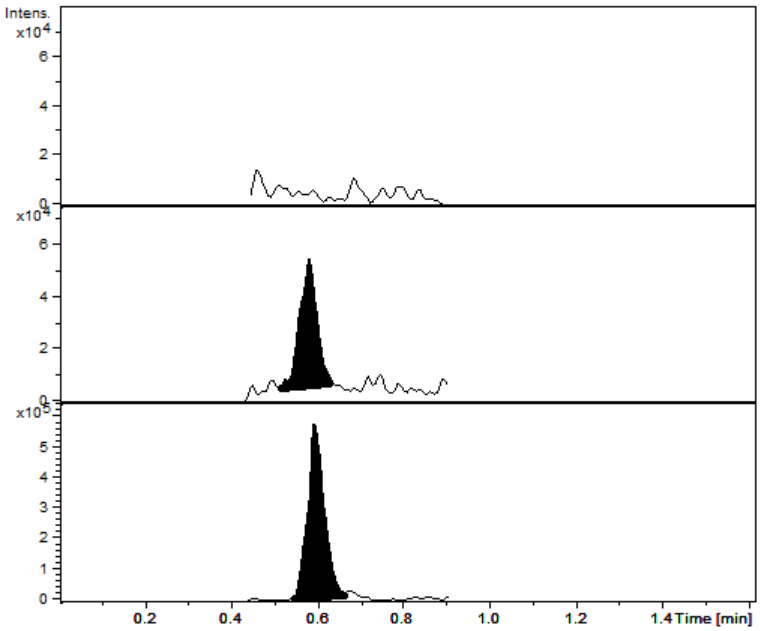

Figure 6. Representative chromatograms of blank sample (upper image); plasma spiked with 25-desacetyl rifampicin at lower limit of quantification (70 ng/mL, middle image); and a plasma sample from a patient under treatment with 600 mg rifampicin/day, sample taken after 2h from administration, concentration found 645 ng/mL (lower image).

Table 1. Within-day precision, accuracy and recovery (n = 5) for rifampicin

$c_{nominal}$ ng/mL	Mean c_{found} ng/mL (± S.D.)	CV %	Bias %	Recovery % (± S.D.)
411.2	436.5±33.6	7.7	6.2	94.8±8.6
822.4	770.4±13.5	1.8	-6.3	100.8±10.2
3289.6	3241.0±67.8	2.1	-1.5	108.2±11.6
9868.8	10390.5±101.6	1.0	5.3	96.6±9.6

Table 2. Between-day precision, accuracy and recovery (n = 5) for rifampicin

$c_{nominal}$ ng/mL	Mean c_{found} ng/mL (± S.D.)	CV %	Bias %	Recovery % (± S.D.)
411.2	430.3±35.4	8.2	4.7	96.2±12.8
822.4	804.6±44.2	5.5	-2.2	100.1±12.9
3289.6	3182.8±203.3	6.4	-3.2	90.3±4.7
9868.8	10191.6±304.1	3.0	3.3	102.2±12.7

Table 3. Within-day precision, accuracy and recovery (n = 5) for 25-desacetyl rifampicin

$c_{nominal}$ ng/mL	Mean c_{found} ng/mL (± S.D.)	CV %	Bias %	Recovery % (± S.D.)
70.4	74.0±2.7	3.7	5.1	99.4±6.6
140.8	152.3±2.7	1.8	8.2	102.1±4.9
563.2	577.8±24.5	4.2	2.6	97.3±6.3
1689.6	1691.8±61.3	3.6	0.1	99.4±7.0

Table 4. Between-day precision, accuracy and recovery (n = 5) for 25-desacetyl rifampicin

$c_{nominal}$ ng/mL	Mean c_{found} ng/mL (± S.D.)	CV %	Bias %	Recovery % (± S.D.)
70.4	71.13±4.9	7.0	1.0	99.6±9.2
140.8	140.33±14.1	10.1	-0.3	96.4±2.3
563.2	549.35±29.0	5.3	-2.5	93.1±0.9
1689.6	1659.9±126.2	7.6	-1.8	107.5±3.2

EXPERIMENTAL SECTION

Reagents

Rifampicin and 25-desacetyl rifampicin reference standards were from USP (Rockville, MD, USA). Gradient grade methanol for liquid chromatography and ammonium formate of analytical-reagent grade were supplied by Merck KGaA (Darmstadt, Germany). Bidistilled deionised water for injections was supplied by the Infusion Solution Laboratory of the University of Medicine and Pharmacy Cluj-Napoca (Cluj-Napoca, Romania). Human blank plasma was obtained from healthy volunteers, both male and female.

Apparatus

The apparatus and equipment used were: Sigma (Osterode am Harz, Germany) 204 series Centrifuge; Mettler-Toledo (Greifensee, Switzerland) Analytical Plus Balance and Mettler-Toledo (Greifensee, Switzerland) Precision Standard Balance; Scientific Industries (New York, USA) Vortex Genie 2 mixer; Elma (Singen, Germany) Transsonic 700/H Ultrasonic bath. An Agilent Technologies (Darmstadt, Germany) 1100 series LC/MS system was used consisting of: G1312A binary pump, G1379A in-line degasser, G1329A autosampler, G1316A column thermostat and an 1100 SL Ion Trap Detector.

Chromatographic and spectrometric conditions

A Phenomenex (Torrance, California, USA) Gemini NX C18 (50 x 2.0 mm i.d., 3.0 μm) chromatographic column was used for separation, using a mobile phase of a 40:60 (V/V) mixture of methanol and 2mM ammonium formate in water under isocratic conditions, kept at 40 ºC with a flow rate of 0.6 mL/min. Detection of rifampicin and 25-desacetyl rifampicin was carried out using multiple reaction monitoring (MRM) mode of the ion trap mass spectrometer with electrospray ionization (ESI) source, positive ionization (capillary exit 175 V, nebulizer 60 psi (nitrogen), dry gas (nitrogen) at 11 L/min, dry gas temperature 350ºC). The column effluent was diverted to waste for the first 0.4 minutes in order to keep the ESI source clean of contamination. The extracted ion chromatograms (EIC) of m/z 792 from m/z 824 for rifampicin and m/z 732 from m/z 750 for 25-desacetyl rifampicin were analyzed (MS^2 mode).

Standard solutions

Stock solutions of 1.028 mg/mL rifampicin and 0.440 mg/mL 25-desacetyl rifampicin were prepared by dissolving the appropriate quantity of substance in methanol. Working solutions of rifampicin (41.12 μg/mL) and 25-desacetyl rifampicin (7.04 μg/mL) were prepared by appropriate dilution of stock solutions in human blank plasma. The working solutions were then used to prepare seven plasma calibration standards and three quality control standards for both rifampicin and 25-desacetyl rifampicin. Concentrations of calibration standards for rifampicin were between 411.2 ng/mL and 19737.6 ng/mL, and quality control standards had concentrations of 822.4 ng/mL (low), 3289.6 ng/mL (medium) and 9868.8 ng/mL (high). For 25-desacetyl rifampicin the calibration standards were between 70.4 ng/mL and 3379.2 ng/mL, and quality control standards had concentrations of 140.8 ng/mL (low), 563.2 ng/mL (medium) and 1689.6 ng/mL (high). All calibration standards and quality control standards were prepared by diluting the appropriate volumes of the working solutions with blank plasma.

Sample preparation

0.1 mL of standard and plasma sample respectively were added to a 1.5 mL plastic tube and precipitated with 0.3 mL methanol. The samples were then vortex-mixed (10 seconds) and centrifuged (3 minutes at 12000 rpm), and 0.15 mL of the supernatants were transferred to autosampler vials and 0.3 μL were injected into the HPLC system.

Method validation

Rifampicin and 25-desacetyl rifampicin concentrations were determined automatically by the instrument's QuantAnalysis data system using the peak areas, using the external standard method. The calibration curve model was determined to be $y = b + ax$, weighted ($1/y^2$) linear regression, where y is the peak area and x is the concentration of the analyte (μg/mL).

Within-day precision and accuracy were determined analyzing five different samples (n = 5) of each of the QC standards (low, medium, high) in the same run. The between-day precision and accuracy were determined analyzing five different samples (n = 5) of each of the QC standards (lower, medium, higher), each on one of five different days. Precision was expressed as the coefficient of variation (CV %) of five samples, while accuracy was expressed as relative difference between mean of measured and the calculated concentrations (bias %). The lowest calibration standard with an accuracy and precision within the 20% acceptance was established as the lower limit of quantification (LLOQ). Relative recovery values (at LLOQ and low, medium, high QC levels) were determined by comparing chromatographic peak areas of spiked plasma samples with peak areas of samples in pure solvent, both having the same concentration of rifampicin and 25-desacetyl rifampicin respectively [15-16].

ACKNOWLEDGMENTS

This work was supported by CNMP Romania – PNII– D4 – Parteneriate in domenii prioritare, project number 42148/1.10.2008.

REFERENCES

1. G.N. Forrest, K. Tamura. *Clin Microbiol Rev,* **2010**, *23*, 14-34.
2. A.L. Stavrakis, J.A. Niska, J.H. Shahbazian, A.H. Loftin, R.I. Ramos, F. Billi, K.P. Francis, M. Otto, N.M. Bernthal, D.Z. Uslan, L.S. Miller*, Antimicrob Agents Chemother*. **2014**, *58*, 2377-2386.
3. D. Marchidanu, N. Raducanu, D.S. Miron, F.S. Radulescu, V. Anuța, I. Mircioiu, I. Prasacu. *Farmacia,* **2013**, *61,* 398-410.
4. F. Fahimi, P. Tabarsi, F. Kobarfard, B.D. Bozorg, A. Goodarzi, F. Dastan, N. Shahsavari, S. Emami, M. Habibi, J. Salamzadeh. Int J Tuberc Lung Dis, **2013**, *17,* 1602-1606.
5. M. Regazzi, A.C. Carvalho, P. Villani, A. Matteelli*. Clin Pharmacokinet*, **2014**, *53,* 489-507.
6. B.C. Moldoveanu, C.M. Ghiciuc, C.E. Lupuşoru. *Arch. Balk. Med. Union*. **2011**, *46,* 299-302.

7. D.H. Shewiyoa, E. Kaale, P.G. Risha, B. Dejaegher, J. Smeyers-Verbeke, Y. Vander Heyden, *Journal of Chromatography A*, **2012**, *1260*, 232– 238.
8. D.H. Vu, R.A. Koster, M.S. Bolhuis, B. Greijdanus, R.V. Altena, D.H. Nguyen, J.R.B.J. Brouwers, D.R.A. Uges, J.W. Calffenaar. *Talanta,* **2014**, *121*, 9–17.
9. K.H. Hee, J.J. Seo, L.S. Lee. *Journal of Pharmaceutical and Biomedical Analysis*, **2015**, *102*, 253–260
10. L.C. Winchester, A.T. Podany, J.S. Baldwin, B.L. Robbins, C.V. Fletcher. *Journal of Pharmaceutical and Biomedical Analysis,* **2015**, *104,* 55–61.
11. C. Magis-Escurra, J. van den Boogaard, D. Ijdema, M. Boeree, R. Aarnoutse. *Pulmonary Pharmacology & Therapeutics,* **2012**, *25*, 83-86.
12. J. Xu, H. Jin, H. Zhu, M. Zheng, B. Wang, C. Liu, M. Chen, L. Zhou, W. Zhao, L. Fu, Y. Lu, *Clinical Therapeutics,* **2013,** *35(2),* 161-168.
13. A. Srivastava, D. Waterhouse, A. Ardrey, S.A. Ward. *Journal of Pharmaceutical and Biomedical Analysis,* **2012**, *70*, 523–528.
14. Guidance on the Investigation of Bioavailability and Bioequivalence. The European Agency for the Evaluation of Medicinal Products, Committee for Proprietary Medicinal Products, **2001**, CPMP/EWP/QWP/1401/98.
15. D. Mihu, L. Vlase, S. Imre, C.M. Mihu, M. Achim, D.L. Muntean, *Studia UBB Chemia*, **2009**, *54(3)*, 151.
16. M. Achim, D. Muntean, L. Vlase, I. Bâldea, D. Mihu, S. E. Leucuţa, *Studia UBB Chemia*, **2009**, *54(3)*, 7.

STUDIA UBB CHEMIA, LX, 2, Tom II, 2015 (p. 321-329)
(RECOMMENDED CITATION)

SYNTHESIS AND STRUCTURAL CHARACTERIZATION OF STRONTIUM CONTAINING BIOACTIVE GLASSES

MARIA STEINER[a], ROZALIA VERES[a,*], VIORICA SIMON[a]

ABSTRACT. Bioactive glasses of SiO_2-CaO-SrO-P_2O_5 system, wherein SrO progressively replaced up to 4 mol% CaO, were produced using the sol–gel route. Their structural properties and bioactivity were tested using differential thermal analysis (DTA), X-ray diffraction (XRD) and Fourier transform infrared spectroscopy (FT-IR). Based on the DTA results, the 110 ºC dried gels were subjected to heat treatment at 600 ºC. X-ray diffractograms show a predominant amorphous character for all samples. FT-IR results indicate few changes in the local structure by progressive addition of strontium. The soaking of samples for 14 days in biological fluid resulted in the formation of hydroxyapatite layer that delivered characteristic infrared absorption band sensitive to strontium content.

Keywords: *bioactive glasses; sol-gel; strontium; in vitro bioactivity.*

INTRODUCTION

Osteoporosis is a skeletal disorder characterized by compromised bone strength predisposing to an increased risk of fracture [1]. In osteoporotic bone, osteoclasts resorb too much bone, while osteoblastic bone formation is not sufficient to counterbalance this, resulting in reduced bone mineral density, weak and brittle bones [2].

Therefore, in last decades there has been large amount of work on developing synthetic materials for bone regeneration and replacing. Bioactive glasses are a group of synthetic materials with bone bonding properties first discovered by Hench [3, 4]. They have the ability of direct bonding to bone via formation of a surface carbonated hydroxyapatite layer when exposed to simulated body fluid (SBF) [5, 6]. Many bioactive glass compositions including copper [7], silver [8] magnesium [9], zinc [10, 11] and strontium as dopants have been studied and have shown considerable efficacy in bone regeneration [12-15].

[a] *Babeș-Bolyai University, Faculty of Physics & Institute of Interdisciplinary Research in Bio-Nano-Sciences, Cluj-Napoca RO-400084, Romania*
** Corresponding author: rozalia.veres@ubbcluj.ro*

It was reported that the introduction of strontium ions into silicate matrix leads to bone formation and inhibites bone resorption by osteoclasts, promoting the increase of bone density and resistance [16, 17]. The advantages of strontium-doped bioactive glasses are based on the controlled release of the Sr ions that stimulate the activity of osteoblast cells. Strontium can substitute for calcium in bioactive glasses, and this replacement may induce few structural changes [14] that influence the gradual degradation of the bioactive material, with effects on new bone formation on the implant surface [18, 19].

The objective of the present study was to produce new sol–gel derived bioactive glasses of SiO_2-CaO-SrO-P_2O_5 system and to characterize their structural properties and bioactivity.

RESULTS AND DISCUSSION

In the investigated $65SiO_2 \cdot 5P_2O_5 \cdot (30-x)CaO \cdot xSrO$ glass system ($0 \leq x \leq 4$ mol%) we explored five compositions, i.e. x = 0, 0.5, 1, 2 and 4 mol%. The corresponding samples were noted Sr0, Sr0.5, Sr1, Sr2 and Sr4, respectively.

The TGA curves for all samples present several regions of weight loss (Figure 1). The first weight loss is associated with an endothermic peak in DTA curve that occurs around 80 ºC and can be ascribed to the loss of free water molecules. A second weight loss can be observed until 400 ºC. This loss can be associated with the elimination of water caged in pores and the decomposition of residual nitrates. The peaks observed around 550 ºC arise from dehydroxylation [20]. Based on these results, a thermal treatment at 600 ºC was considered.

The X-ray diffraction patterns for all samples treated at 600 ºC for 2 hours (Figure 2) indicate a predominant amorphous structure, without significant crystalline phases. The large diffraction peaks at about 32º might show a tendency to calcium strontium phosphate crystals (JCPDS 34-0484), excepting the sample without strontium oxide.

The structural properties of the glasses treated at 600ºC were also analyzed through Fourier Transform Infrared Spectroscopy (FTIR). The absorption band recorded at 3512 cm^{-1} (Figure 3) can be assigned to silanol groups linked to molecular water through hydrogen bonds and the band appeared at 1648 cm^{-1} to the bending mode of adsorbed molecular water [21]. The bands occurring in the spectral region 1560-1370 cm^{-1} correspond to carbonate species arising from the slight reaction between the glass samples and carbon dioxide from the atmosphere and might be also due to the formation of small quantities of calcium/strontium carbonates [22]. The broad band located in 1300-800 cm^{-1} range is present in all the samples and is specific for silica-based bioactive glasses [23-24]. The shoulder at 1234 cm^{-1} is attributed to

bending mode of Si–O–Si group. The peak observed at 1062 cm^{-1} can be assigned to the Si-O-Si asymmetric stretching mode of bridging oxygen (BO), whereas the shoulder situated at 939 cm^{-1} can be attributed to the Si-O asymmetric stretching mode of the non-bridging oxygen bonds (NBO) [25, 26]. A decrease of this signal intensity is noticed with the increase of SrO content. Withal, a shift of the absorption band assigned to Si–O–Si vibrations to lower wavenumbers is observed, suggesting the shortening of Si–O–Si bonds in the vicinity of large Sr cations [27, 28]. In all the investigated glasses is observed around 551 cm^{-1} a band which corresponds to bending vibration of amorphous P-O bond [29]. Furthermore, the band situated in the range 510-460 cm^{-1} can be ascribed to the Si–O–Si bending mode.

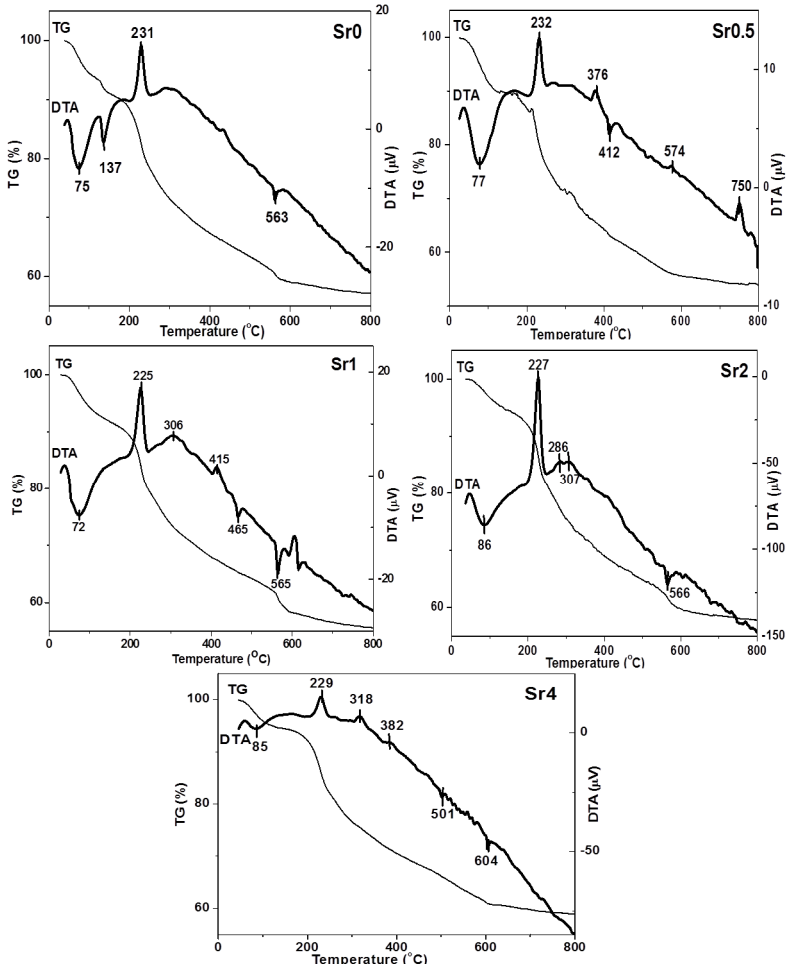

Figure 1. The DTA and TGA curves for xerogel samples dried at 110 ºC.

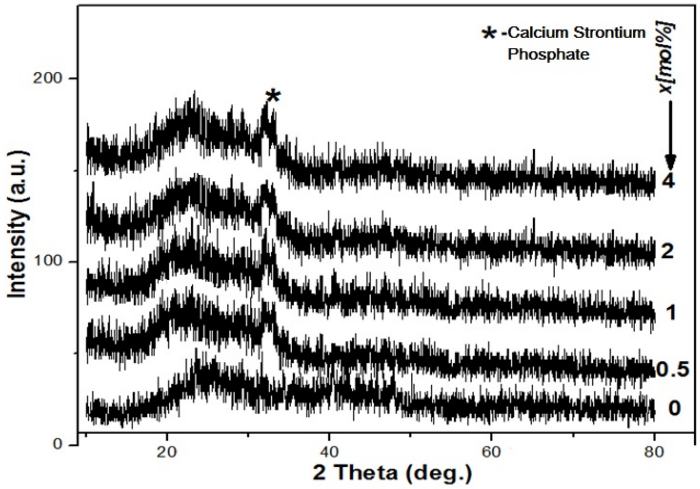

Figure 2. XRD patterns of $65SiO_2 \cdot 5P_2O_5 \cdot (30\text{-}x)CaO \cdot xSrO$ glass samples.

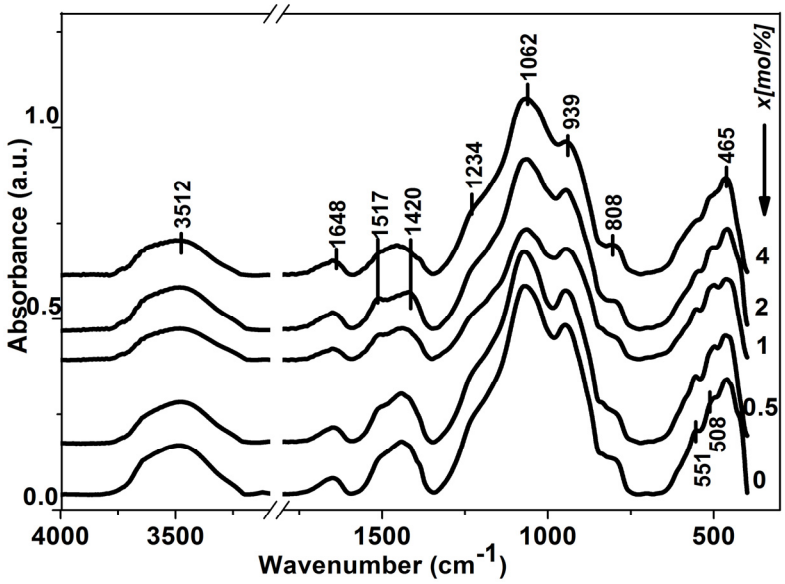

Figure 3. FT-IR spectra of $65SiO_2 \cdot 5P_2O_5 \cdot (30\text{-}x)CaO \cdot xSrO$ glasses treated at 600 ºC.

The bioactivity of the glasses was evaluated by soaking the samples during 14 days in SBF solution and characterizing them by XRD and FTIR techniques.

The XRD patterns for the immersed samples indicate the formation of a crystalline layer on the surface of the glasses (Figure 4), being observed one peak well developed at value 2θ=32.2º which corresponds to the formation of hydroxyapatite (HA) crystals. This characteristic peak of apatite is observed in all specimens having lower peak intensity with the increase of strontium amount. It can be observed that for all the Sr concentrations, the glasses still indicate a good bioactivity.

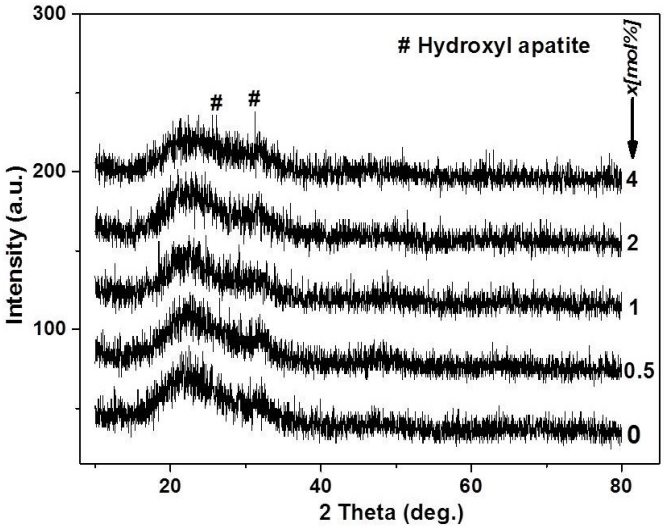

Figure 4. XRD patterns of $65SiO_2 \cdot 5P_2O_5 \cdot (30\text{-}x)CaO \cdot xSrO$ samples after immersion in SBF for 14 days.

FTIR spectra of all glasses show few changes after immersion in SBF (Figure 5) in comparison with the spectra before immersion.

All the spectra clearly show as the non-bridging oxygen Si-O band situated at 920 cm^{-1} decreased in intensity after immersion. The band from 790 cm^{-1} appeared in the spectra after immersion being assigned to Si-O-Si between the two adjacent silicates tetrahedra [30-32] which is an indicator for the formation of a silica gel layer. Furthermore, the band situated at 878 cm^{-1} appeared in all the glasses and might correspond to the formation of complex carbonate species connected with the presenceof Ca^{2+} ions on the surface [33]. Very clear changes can be seen in the region 520–620 cm^{-1}, being the characteristic area for apatite. The doublet observed at 567 and 614 cm^{-1} in all the investigated glasses corresponds to P–O bending vibrations in a PO_4^{3-} tetrahedron in hydroxyapatite [33] and denotes the glasses bioactivity.

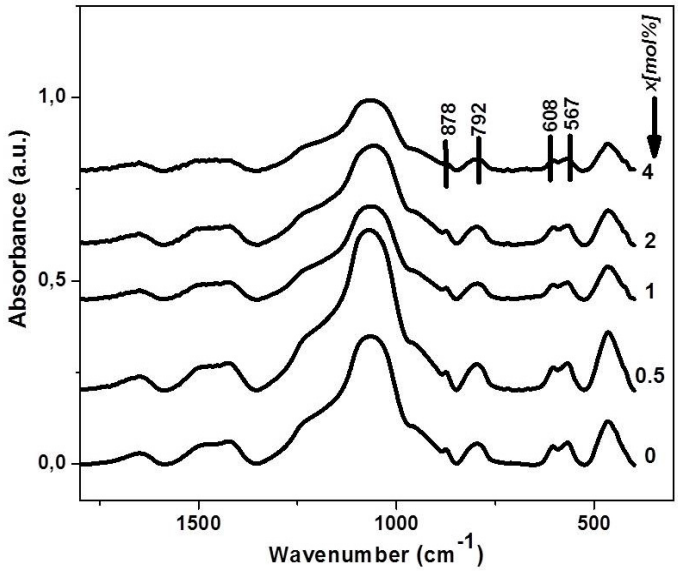

Figure 5. FTIR spectra of $65SiO_2 \cdot 5P_2O_5 \cdot (30\text{-}x)CaO \cdot xSrO$ glasses after immersion in SBF for 14 days.

CONCLUSIONS

Bioactive glasses based on SiO_2-CaO-SrO-P_2O_5 system were obtained by sol–gel method. The structure of the samples thermally stabilized at 600 ºC has a predominant amorphous character. The substitution of CaO with SrO up to 4 mol % does not inhibit the samples bioactivity, but the progressive increase of SrO content leads to the decrease of the absorption band assigned to the bioactive self-assembling hydroxyapatite layer. The samples can be considered for further investigation with respect to their bioactivity required for biomaterials used as scaffolds in bone tissue regeneration.

EXPERIMENTAL SECTION

Samples of $65SiO_2$-$5P_2O_5$-(30-x)CaO-xSrO bioactive glass system (x= 0, 0.5, 1, and 4 mol%) were prepared following the sol-gel route. The precursors of SiO_2, P_2O_5, CaO and SrO used for the synthesis of the glasses were tetraethylorthosilicate (TEOS), triethylphosphate (TEP), calcium nitrate tetrahydrate and strontium nitrate, respectively. All reagents were of analytical grade purity. In the first stage TEOS was mixed with HNO_3 aqueous solution

having molar ratios TEOS:H_2O:HNO_3=1:9:0.1 and stirred for 1h, then was added TEP and the stirring was continued for more 1h. In the second stage both strontium and calcium nitrates were dissolved in water. Finally the solutions were mixed together under continuous stirring for 1 h for the completion of hydrolysis reaction. The obtained sols were left 7 days at 37 ºC for gelation and maturation, then the samples were dried for 24 h at 110 ºC, and thermally treated at 600 ºC for 2 h.

Differential thermal analysis and thermogravimetric analysis

DTA/TG analysis were performed on Shimadzu type derivatograph DTG-6OH SHIMADZU equipment, with a heating rates of 10 ºC/min using alumina open crucibles, in order to investigate the thermal behavior of the dried sample.

X-ray diffraction

The 600 ºC treated samples were analyzed using an X-ray Shimadzu XRD-6000 diffractometer with a monochromator of graphite for CuKα radiation (λ=1.5418Å) with Ni-filter. The diffractograms were recorded in 2θ range from 10º to 80º with a speed of 2°/min. The operation voltage and current were 40kV and 30mA, respectively.

FT-IR spectroscopy

The FT-IR spectra were recorded at room temperature in the 400-4000 cm^{-1} spectral range in absorbance mode with a JASCO FT/IR-6200 spectrometer, with an instrumental resolution of 4 cm^{-1}. An amount of 2 mg of powder sample was thoroughly mixed with 200 mg of KBr and compressed to form pellets.

Assessment of the bioactivity

Hydroxyapatite forming ability of the bioactive glasses was studied by immersing the samples in simulated body fluid (SBF) that has the ion concentrations and pH nearly equal to that of human blood plasma [34]. The samples immersed in SBF were kept in an oven at 37 ºC for 14 days. The weight of glass per volume of SBF was 10 mg/ml for each sample. After 14 days the powders were filtrated, rinsed several times with distillate water and dried at room temperature.

ACKNOWLEDGMENTS

The author R. Veres wishes to thank for the financial support of the Sectorial Operational Program for Human Resources Development 2007-2013, co-financed by the European Social Fund, under the project number POSDRU/159/1.5/S/132400 with the title „Young successful researchers – professional development in an international and interdisciplinary environment”.

REFERENCES

1. Osteoporosis Prevention, Diagnosis, and Therapy, *National Institutes of Health Consens Statement,* **2000**, March 27-29; *17*, 1.
2. Y.C. Fredholm, N. Karpukhina, D.S. Brauer, J.R. Jones, R.V. Law, R.G. Hill, *Journal of the Royal Society*, **2012**, *7*, 880.
3. L.L. Hench, R.J. Splinter, W. C. Allen, T. K.Greenlee, *Journal Biomedical Materials Research Symposium*, **1971**, *2*, 117.
4. L.L. Hench, H.A. Paschall, *Journal of Biomedical Materials Research*, **1973**, *7*, 25.
5. P.J. Marie, P. Ammann, G. Boivin, C. Rey, *Calcified Tissue International*, **2001**, *69*, 121.
6. P. J. Marie, *Current opinion in pharmacology*, **2005**, *5*, 633.
7. V. Timar, R. Ciceo-Lucacel, O. Hulpus, I. Ardelean, *Modern Physics Letters B* **2009**, *23*, 747.
8. K. Magyari, R. Stefan, D.C. Vodnar, A. Vulpoi, L. Baia, *Journal of Non-Crystalline Solids*, **2014**, *402*, 182.
9. P.I. Riti, A. Vulpoi, O. Ponta, V. Simon, *Ceramics International*, **2014**, *40*, Part B, 14741.
10. R. Ciceo Lucacel, O. Ponta, V. Simon, *Journal of Non-Crystalline Solids*, **2012**, *358*, 2803.
11. R. Veres, E. Vanea, C. Gruian, L. Baia, V. Simon, *Composites: Part B*, **2014**, *66*, 83.
12. M.D. O'Donnell, R. G. Hill*, Acta Biomaterialia*, **2010**, *6*, 2382.
13. G. Boivin, P. Deloffre, B. Prrat, G. Panezer, M. Boudeull, Y. Mauras, P. Allain, Y. Tsouderos, P.J. Meunier, *Journal of Bone and Mineral Research*, **1996**, *11*, 1302.
14. J.R. Jones, E. Gentleman, J. Polak, *Elements*, **2007**, *3*, 393.
15. S. Hesaraki, M. Gholami, S. Vazehrad, S. Shahrabi*, Materials Science and Engineering*, **2009**, *30*, 383.
16. E. Gentleman, Y.C. Fredholm, G. Jell, N. Lotfibakhshaiesh, M.D. O'Donnell, R.G. Hill, M.M. Stevens, *Biomaterials*, **2010**, *31*, 3949.
17. Y. Fredholm, N. Karpukhina, R.V. Law, R.G. Hill, *Journal of Non-Crystalline Solids*, **2010**, *356*, 2546.
18. A. Merolli, P.T. Leali, P.L. Guidi, C. Gabbi, *Journal of Materials Science: Materials in Medicine*, **2000**, *11*, 219.
19. Y. Fredholm, M.M. Stevens, R. Hill, *Proceedings of the 8th World Biomaterials Congress 28 May-1 June* **2008**, Amsterdam RAI.
20. L. Lefebvre, J. Chevalier, L. Gremillard, R. Zenati, G. Thollet, D. Bernache Assolant, A. Govin, *Acta Materialia*, **2007**, *55*, 3305.
21. S. Jehabi, H. Oudadesse, J. Elleuch, S. Tounsi, H. Keskes, P. Pellen, T. Rehai, A. El Feki, H. El Feki, *Journal of the Korean Society for Applied Biological Chemistry*, **2013**, *56*, 533.

22. M.D. O'Donnell, P.L. Candarlioglu, C.A. Miller, E. Gentleman, M.M. Stevens, *Journal of Materials Chemistry*, **2010**, *20*, 8934.
23. M. Sitarz, M. Handke, W. Mozgawa, *Spectrochimica Acta Part A*, **2000**, *56*, 1819.
24. V. Aina, G. Malavasi, A. Fiorio Pla, L. Munaron, C. Morterra, *Acta Biomaterialia*, **2009**, 5, 1211.
25. K. Omori, *Am Mineral*, **1971**, *56*, 1607.
26. A. Aronne, *Journal of Non-Crystalline Solids,* **2005**, *351*, 3610.
27. C. Chen, D. Huang, W. Zhu, X. Yao, *Applied Surfaces Science*, **2006**, *252*, 7585.
28. R. Veres, C. Ciuce, V. Simon, *Studia UBB Chemia,* **2011**, *3,* 193.
29. Z. Hong, R.L. Reis and J.F. Mano, *Journal of Biomedical Materials Research Part A*, **2009**, *88*, 304.
30. D.S. Brauer, N. Karpukhina, M.D. O'Donnell, R.V. Law, R.G. Hill, *Acta Biomaterialia*. **2010**, *6*, 3275.
31. C.Y. Kim, A.E. Clark, L.L. Hench, *Journal of Non-Crystalline Solids*, **1989**, *113*, 195.
32. X. Chen, X. Chen, D.S. Brauer, R.M. Wilson, R.G. Hill, N. Karpukhina, *Materials*, **2014**, *7*, 5470.
33. A. Goel, R.R. Rajagopal, J.M.F. Ferreira, *Acta Biomaterialia*, **2011**, *7*, 4071.
34. T. Kokubo, H. Kushitani, S. Sakka, T. Kitsugi, T. Yamamuro, *Journal of Biomedical Materials Research*, **1990**, *24*, 721.

STUDIA UBB CHEMIA, LX, 2, Tom II, 2015 (p. 331-341)
(RECOMMENDED CITATION)

DEVELOPMENT OF MULTIWALLED CARBON NANOTUBES BASED SOLID PHASE EXTRACTION FOR THE DETERMINATION OF TRACE LEVEL OF Mn(II) AND Sn(IV) IN RIVER WATER SAMPLES

SHAHRAM NEKOUEI[a,*], FARZIN NEKOUEI[a]

ABSTRACT. This paper reports a multiwalled carbon nanotubes (MWCNTs) modified with 3-amino-7-dimethylamino-2-methylphenazine (Neutral Red, NR) as a new solid phase extractor for determination of ultra trace amounts of Mn(II) and Sn(IV). The metal ions were retained on -column filled with the solid phase at a flow rate of 3.0 mL/min. The retained metal ions were eluted with 3 mol L^{-1} solution of HCl and measured by flame atomic absorption spectroscopy (FAAS). The effect of different variables such as, sample pH, concentration of 3-amino-7-dimethylamino-2-methylphenazine (Neutral Red, NR), sample flow rate, eluting solution and the effect of interfering ions have been investigated systematically. The calibration graph was linear in the range of 0.4-100 μg L^{-1} and 0.6-150 for Mn(II) and Sn(IV), respectively. Under optimized conditions, the limit of detections (LOD) were 0.12 and 0.16 μg L^{-1} for Mn(II) and Sn(IV), respectively. The method was used for determination of target metal ions in some water samples from rivers located in industrial and nonindustrial areas.

Keywords: *Solid phase extraction; 3-amino-7-dimethylamino-2-methylphenazine (Neutral Red, NR); Multiwalled carbon nanotubes; river water samples; Flame atomic absorption spectrometry, Mn(II) AND Sn(IV)*

INTRODUCTION

Natural processes as well as antropogenic activities are both sources of metals and their compounds into the environment. Since exposure to heavy metals is potentially harmful their monitoring in environmental, biological and clinical samples even at trace levels is nowadays required by law and other regulations in many cases [1]. Mining operations and heavy industry in the developing world is leading to the accumulation of high concentrations of

[a] *Young Researchers and Elite Club, Science and Research Branch, Islamic Azad University, Tehran, Iran*
** Corresponding author: sh.nekouei@hotmail.com*

toxic heavy metals in natural waters. Today, it is understood that exposure to heavy metals may seriously affect human health. [2]

Manganese is an essential element for human life, however, excessive levels of manganese are detrimental to the organism. Humans exposed to very high levels of manganese over a long time can develop mental and emotional disturbances and slow, clumsy body movements. Therefore, the determination of trace amounts of manganese in samples from various matrices is very important for certain areas of study. [3]

Tin is widely used in industry due to features such as low melting point, affinity to form alloys, and corrosion resistance. Exposure to Sn and its compounds can produce several effects such as neurological, hematological and immunological. Inhalation of inorganic compounds of Sn can induce to pneumoconiosis and ingestion may lead to gastrointestinal effects. Exposure to organic compounds of Sn inhibits the synthesis of hemeoxygenase and may be genotoxic, while its skin contact may cause severe irritation and burning. Other effects include kidney and liver damage [4].

Solid-phase extraction (SPE) is one of the most employed preconcentration methods that can be applied in off-line or online systems, with the advantage of possible automatization. SPE consists of the retention of metal species (or its derivatives) on the appropriate solid sorbent packed in a column or microcolumn and the later desorption with the adequate solvent. Thus, the concentration and separation of the analyte from the rest of sample matrix is achieved. [5] Solid-phase extraction (SPE), owing to its flexibility, absence of emulsion, simplicity, sampling in the field, safety, and ease of automation, is a preferred method for separation and enrichment of the target. SPE requires that the adsorbent possess a stronger selective adsorption ability. [6]

Carbon nanotubes (CNTs) are one of the most commonly used building blocks of nanotechnology. With one hundred times the tensile strength of steel, thermal conductivity better than all but the purest diamond, and electrical conductivity similar to copper, but with the ability to carry much higher currents, they seem to be a very interesting material. Carbon nanotubes (CNTs) have been proposed as a novel solid phase extractor for various inorganic and organic materials at trace levels. [7]

Carbon nanotubes (CNTs) have become attractive materials, since its discovery in 1991, because of their novel structure characteristics. [8-18] Recently, Carbon nanotubes as an adsorbent for the preconcentration of traces heavy metals have become very popular. [19-29]

In this article, we have modified MWCNTs using NR and applied this functionalized material to SPE coupled with FAAS for simultaneously determination of Mn(II) and Sn(IV) in the water samples from rivers located in industrial and nonindustrial areas. Also for the validity of the method the Mn(II) and Sn(IV) levels in the final solutions were determined by ICP-AES using the general procedures.

RESULTS AND DISCUSSION

To obtain a sufficiently high efficiency of a SPE procedure, the study was focused on optimization of the extraction parameters containing, pH, amounts of NR and adsorbent, sample volume, elution conditions such as volume and concentration of eluent, flow rate of solution and matrix ions.

Effect of pH

The pH value plays an important role with respect to the adsorption of different ions on CNTs.[25] To evaluate the effect of pH on the extraction efficiency of Mn(II) and Sn(IV) as NR chelates adsorb on multiwalled carbon nanotubes, the pH of the sample solutions, were adjusted to fit in the range of 2–10. It is observable in Fig. 1, quantitative recoveries (>95%) were obtained for all studied ions at the pH range of 6–8. So, the pH 7 was selected for all subsequent studies.

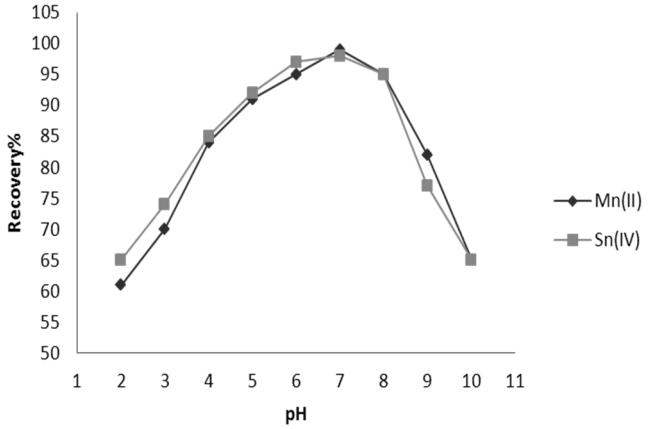

Figure 1. The effect of pH on the recoveries of the metal ions (N= 3.0.)

Effect of eluent type

The elution of the absorbed analytes could be achieved by using an appropriate eluent solution capable of effectively striping them from the MWCNTs and bring them into the solution [26]. Thus, the effects of various eluents (nitric acid, hydrochloric acid and acetic acid) on the recoveries of Mn(II) and Sn(IV) ions from multiwalled carbon nanotubes modified with NR were also investigated. The results are shown in Table 1. The results indicated that 3 mol L^{-1} HCl was sufficient for quantitative elution (>95%). Furthermore, the influence of eluent volume (1–5 mL) on the recoveries was studied by using 3 mol L^{-1} HCl. By adding 2 mL of 3 mol L^{-1} HCl, quantitative recoveries

were obtained for all analyte ions. The recoveries were not quantitative for the other eluents listed in Table 1. Therefore, 2 mL of 3 mol L^{-1} HCl was used as eluent for further work.

Table 1. The effect of various eluents on the analyte ion recoveries.

Eluent Recovery %		
	Mn(II)	**Sn(IV)**
1 mol L^{-1} HCl	92±0.4	91±1.3
2 mol L^{-1} HCl	95±3.0	95±2.4
3 mol L^{-1} HCl	99±2.2	98±1.6
1 mol L^{-1} HNO_3	85±2.8	88±1.2
2 mol L^{-1} HNO_3	89±1.1	91±1.1
3 mol L^{-1} HNO_3	91±3.0	90±2.0
1 mol L^{-1} CH_3COOH	67±2.6	73±3.1
2 mol L^{-1} CH_3COOH	73±1.2	78±2.5
3 mol L^{-1} CH_3COOH	77±1.3	68±2.5

Effect of amount of chelating agent

To evaluate the effect of ligand on the recovery of metal ions, different amounts of NR solution (3×10^{-4} mol L^{-1}) in the range of 0-5 mL was investigated. As presented in Fig. 2, the recoveries of analyte ions increased with increasing amounts of NR added and reached a constant value over 95% with at least 3 mL. The recovery values of analytes were quantitative at the amounts of ligand range of 3-5 mL. Hence, 3 mL of ligand was selected for subsequent studies. At lower concentrations, the amount of ligand is insufficient to extract all the analyte in the solution. But at higher concentrations, all the analyte species were used, thus, process of complex formation was stop and the percentage of recoveries remained nearly constant, in other words, the limiting factor is analyte concentration.

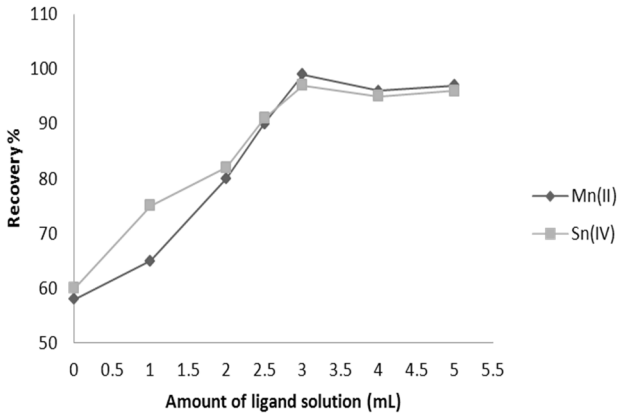

Figure 2. Effect of amount of ligand solution on the recoveries of analytes.

Effect of amounts of adsorbent (MWCNTs)

The amount of solid phase extraction material is another important factor on the column studies to obtain quantitative recoveries. On the other hand, an excess amount of the adsorbent can also prevent the quantitative elution of the retained metals by a small volume of the eluent. To estimate the impact of adsorbent mass on the recovery of metal ions, different amounts of adsorbent (50-400 mg), packed into an SPE column, were investigated, following the preconcentration procedure. The recoveries of metal ions increased with increasing amounts of adsorbent. For less than 200 mg of adsorbent, the recoveries amounts are not quantitative and it is due to by-passing of the liquid in the SPE column [19]. Thus absorbent weight of 200 mg was found to be suitable for this purpose.

Effect of the sample volume

The preconcentration and separation of the analytes are usually performed at a lower concentration. In order to improve the relative sensitivity of the procedure when determining very low concentration of analytes, a relative large sample volume is usually suggested. Therefore, the maximum volume of sample solution was investigated by increasing the volume of metal ion solution by passing 100–600 mL of sample solutions. The effects of sample volumes on the recoveries of the two analytes are shown in Figure 3. The results showed that the maximum sample volume could be up to 500 mL with the recovery >95%. Therefore, 500 mL of sample solution was adopted for the preconcentration of analytes from sample solutions. The preconcentration factor (PF) is calculated by the ratio of the highest sample volume (500 mL) and the lowest eluent volume (2 mL). The preconcentration factor was calculated as 250.

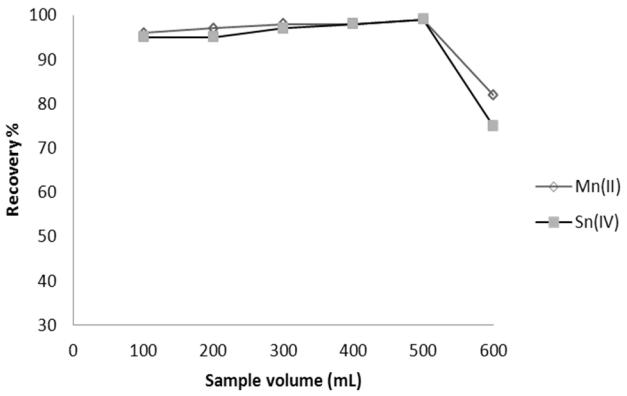

Figure 3. Effect of sample volume on the recoveries of analytes (N= 3.0)

Flow rates of sample and eluent solutions

The influences of the flow rates of sample and eluent solutions on the retentions of Mn(II) and Sn(IV) were also investigated keeping other conditions constant. Low flow rates can be time consuming. The flow rates were investigated in the range of 1–5 mL min−1 and under the optimum conditions (pH and eluent type). It was found when the flow rates of the sample and eluent solutions were at the range of 1.0-3.0 and 1.0-4.0 mL min^{-1}, The recoveries of analytes were quantitative. At higher flow rates, there was a decrease in the recovery in that there was not sufficient contact time between MWCNTs and sample solution. Therefore, all the studies were carried out for flow rates of sample and eluent solutions at a flow rate of 3.0 mL/min.

Effect of foreign ions

The influences of possible matrix ions in the environmental samples and some transition metals on the recoveries of analytes on multiwalled carbon nanotubes were also examined.

The obtained results were presented in Table 2. The tolerance limit is defined as ions had no significant interferences in the preconcentration and determination of the analyses. This is due to the low adsorbing capacity or rates for interfering ions. These results demonstrate that the method has a good tolerance to interference and is suitable for Mn(II) and Sn(IV) detection.

Table 2. Effect of interfering ions on the recoveries of the analytes (N= 3).

Ion	Concentration (mg L^{-1})	Recovery (%)[a]	
		Mn(II)	Sn(IV)
Ag^+, K^+, Na^+, Cl^-, Li^+, I^-	10000	98±1	95±1
SO_4^{-2}, Ca^{2+}, CO_3^{-2}, Br^-, $C_2O_4^{-2}$	8000	98±1	97±2
Mg^{2+}, F^-	6000	96±2	98±1
HCO_3^{-2}, NO_3,	3000	99±1	97±2
PO_4^{-3}, CH_3COO^-	1500	95±2	96±3
Ni^{2+}, Pb^{2+}	500	96±3	95±1
Cd^{2+} , Mo^{5+}	250	98±2	98±2
Pd^{2+}	100	95±1	98±3
Hg^{2+}, Al^{3+}, Cr^{3+}	10	97±2	99±2

[a] Mean ± standard deviations.

Adsorption capacity

For investigation of the adsorption capacity of multiwalled carbon nanotubes, 0.1 g MWCNTs was added to 50 ml of solution containing 1.0 mg of metal ion at pH 7.0. After shaking for 30 min, the mixture was filtered. Ten milliliters of the supernatant solution was diluted to 100 ml and determined by flame atomic absorption spectrometry. This procedure was repeated for each analyte ions separately. The capacity of modified MWCNTs for Mn(II) and Sn(IV) was found to be 86.6 and 77.8 mg g^{-1}, respectively.

Analytical performance

Using the optimized experimental conditions, calibration curves of enrichment process were linear in the range of 0.4-100 μg L^{-1} and 0.6-150 μg L^{-1} for Mn(II) and Sn(IV), respectively. The detection limits, based on three times the standard deviation of 10 runs of blank solution, were found to be 0.12 and 0.16 μg L^{-1} for Mn(II) and Sn(IV), respectively. The relative standard deviation (RSD), nine determinations of 1.0 μg L^{-1} of Mn(II) and Sn(IV) were 4.0 and 2.6%, respectively (N=9). The correlation coefficients for Mn(II) and Sn(IV) were 0.9997, 0.9995, respectively. The preconcentration factor for the proposed method was 250.

Analytical applications

A solid phase extraction method was applied to determination of trace Mn(II) and Sn(IV) in water samples from river located in industrial and nonindustrial areas. Various amounts of analytes were also spiked to these water samples. The results are given in Table 3 and Table 4. A good agreement was obtained between the added and measured Mn(II) and Sn(IV) amounts. The accuracy of the method was verified by the analysis of samples spiked with known amounts of the analytes. These results indicated the suitability of NR-MWCNT for selective SPE and determination of trace Mn(II) and Sn(IV) in environmental samples. The river water samples were also analysed by (ICP-AES). As Table 3 and Table 4. shows there is a good agreement between the results obtained by the proposed method with those obtained by the ICP-AES. This reveals the capability of the method for determination of Mn(II) and Sn(IV) in all real samples without considerable error. In Table 5, the relative comparison of analytical performance with those reported in the literature [26-29].

Table 3. The results for determination of Pd(II) and Cd(II) in various river water samples by FAAS

Sample	Added (μg L^{-1})		Found [a] (μg L^{-1})		Recovery (%)		RSD(%)	
	Mn(II)	Sn(IV)	Mn(II)	Sn(IV)	Mn(II)	Sn(IV)	Mn(II)	Sn(IV)
River Water[b]	-	-	71.48±0.06	84.28±0.02	-	-	1.1	2.3
	100	100	173.93±0.02	182.52±0.03	101.43	99.04	1.1	1.4
	200	200	275.12±0.04	285.65±0.05	101.34	100.48	1.3	1.3
River Water[c]	-	-	65.25±0.05	50.65±0.04	-	-	3.0	2.1
	100	100	164.79±0.07	153.56 ±0.09	99.72	101.93	2.9	2.7
	200	200	265.61±0.05	241.41±0.09	100.51	96.31	3.1	2.5
River Water[d]	-	-	61.14±0.01	67.19±0.02	-	-	1.9	2.6
	100	100	162.22±0.02	164.74±0.01	100.67	98.53	1.5	2.2
	200	200	263.16±0.04	260.11±0.03	100.77	97.35	2.8	1.5
River water[e]	-	-	5.31±0.05	12.61±0.05	-	-	1.8	2.1
	100	100	103.31±0.03	109.64 ±0.07	98.10	97.36	2.6	1.5
	200	200	205.16±0.09	211.51±0.09	99.92	99.48	1.5	2.3

[a] $\bar{x}$ ± ts $\sqrt{n}$ at 95% confidence (N = 5)
[b] From karoon river, located in a industrial area
[c] From zayande rood river, located in a industrial area
[d] From khour musa, located in a industrial area
[e] From pole zohre located in a nonindustrial area

Table 4. The results for determination of Pd(II) and Cd(II) in various river water samples by ICP-AES.

Sample	Added (μg L^{-1})		Found [a] (μg L^{-1})		Recovery (%)		RSD(%)	
	Mn(II)	Sn(IV)	Mn(II)	Sn(IV)	Mn(II)	Sn(IV)	Mn(II)	Sn(IV)
River Water[b]	-	-	71.35 ±0.01	84.15±0.01	-	-	2.1	2.1
	100	100	173.62±0.05	181.85±0.03	101..32	98.75	1.1	1.9
	200	200	275.12±0.04	285.65±0.05	101.51	100.79	1.2	2.1
River Water[c]	-	-	65.25±0.05	50.65±0.04	-	-	1.2	2.1
	100	100	164.79±0.07	153.56 ±0.09	99.56	100.89	2.4	2.7
	200	200	265.61±0.05	241.41±0.09	100.04	99.18	1.2	1.7
River Water[d]	-	-	61.14±0.01	67.19±0.02	-	-	1.8	2.1
	100	100	162.22±0.02	164.74±0.01	102.47	99.14	1.5	2.2
	200	200	263.16±0.04	260.11±0.03	101.99	97.17	1.2	2.9
River water[e]	-	-	5.31±0.05	12.61±0.05	-	-	1.0	2.0
	100	100	103.31±0.03	109.64 ±0.07	97.66	101.03	2.2	2.9
	200	200	205.16±0.09	211.51±0.09	99.89	100.27	1.6	3.1

[a] $\bar{x}$ ± ts $\sqrt{n}$ at 95% confidence (N = 5)
[b] From karoon river, located in a industrial area
[c] From zayande rood river, located in a industrial area
[d] From khour musa, located in a industrial area
[e] From pole zohre located in a nonindustrial area

Table 5. Comparison of the proposed method with recent studies reported in literature using solid phase extraction

Analytes	Medium	Eluent (mol L^{-1})	PF[a]	LOD[b] (µg L^{-1})	Reference
Cu^{2+} , Cd^{2+} , Mn^{2+}	pH=9	1 (HNO_3)	28.9	0.13–0.58	26
Mn^{2+}	pH=10	0.5 (HCl)	17	0.7	27
Sn^{2+}, Sn^{4+}	pH=2	1.0 (HNO_3)	100	0.7-1.1	28
Mn^{2+}, Pb^{2+}	pH=9	2.0 (HNO_3)	-	0.6-1	29
Mn^{2+}, Sn^{4+}	pH=7	3 (HCl)	250	0.12-0.16	This work

[a] PF: Preconcentration factor
[b] LOD: Limit of detection

EXPERIMENTAL

Apparatus

A Metrohm pH-meter (model 691, Switzerland) was used in order to adjust the pH at desirable values. A Chemtech Analytical Instrument model CTA-3000 atomic absorption spectrometer (Bedford, England) equipped with a flame burner was used for analysis of the understudy metals, including lamp currents and wavelength were those recommended by the manufacturer. All metals were measured under optimized operating conditions by FAAS with an air–acetylene flame. Inductively coupled plasma (ICP) model Varian Liberty 150AX Turbo was used for the validity of concentration determination of the analyte.

Standard solutions and reagents

Analytical reagent-grade chemicals were used in this work. All the plastic and glassware were cleaned by soaking in 10% HNO_3 solution and then rinsed with distilled water prior to use. Standard solutions (1000 mg L^{-1}) of Mn(II) and Sn(IV) ions were prepared from high purity compounds, supplied by E. Merck (Darmstadt, Germany). The working standard solutions were prepared by diluting stock standard solution. A 3×10^{-4} mol L^{-1} solution of (NR) reagent was prepared by dissolving 0.008 gr of it it in 100 mL water. McIlvaine's buffer solution in the pH range of 2-10 was used to adjust pH values by adding 16.47 mL of Na_2HPO_4 and 3.53 mL of acid citric. Multiwalled carbon nanotube was purchased from Aldrich, (Milwaukee, WI, USA). The BET (Brunauer–Emmett-Teller) surface area and density of nanotubes were 300 m^2 g^{-1} and 2.1 g mL^{-1}, respectively.

Preparation of the column

Two-hundred milligrams of multiwalled carbon nanotubes was loaded into an SPE column (10 mm × 150 mm). A polypropylene frit was placed at each end of the column to prevent loss of the adsorbent. Before use, 3 mol L^{-1} HCl were passed through the column to clean it.

Recommended procedure

A standard solution containing 0.4-100 μg L^{-1} of Mn (II) and 0.6-150 μg L^{-1} of Sn(IV) and the pH value was adjusted to 7 with McIlvaine's buffer solution. then NR was added to form the [metal-(NR)] chelates. After that, the solutions passed through the column gravitationally. Subsequently, metal ions retained on the MWCNT, were eluted with the desired volume and concentration of eluent. The eluent was analyzed for the determination of metal concentrations by flame atomic absorption spectrometry and inductively coupled plasma atomic emission spectrometry (ICP-AES).

Sample preparations

The river water samples were collected from the rivers located in industrial and non industrial areas. The water samples were filtered through a 0.45 μm PTFE Millipore filter. After adjusting to the desired pH values, the solutions were passed through the column gravitationally.

CONCLUSION

The proposed method offers a simple, inexpensive, selective and sensitive method for the enrichment of Mn(II) and Sn(IV) using MWCNTs modified by NR as a solid-phase extractant for SPE coupled with FAAS. The proposed method was proved to be simple, rapid and reliable and could be used for studied metal ions determination in environmental samples. The high accuracy of the proposed method was confirmed by recovery test with standard addition method. The possible interference of some important ions was investigated and no important interference was encountered. The MWCNTs has great potential as an adsorbent for the preconcentration and determination of trace metal ions in complex samples. The accuracy and validity of the method is provable by the comparison among the resultant results of the proposed method and those obtained by ICP-AES method (Table 3 and Table 4). High sensitivity and selectivity, and also the good detection limits and high preconcentration factor (PF=250.0) which is comparable or higher than the other solid-phase extraction methods in literature (mentioned at section 2.10)

REFERENCES

1. L. Prusa, J. Dedina, J. Kratzer, *Anal. Chim. Acta*, **2013**, *804,* 50.
2. I. Hagarová, M. Bujdoš, P. Matúš, J. Kubová, *Spectrochim. Acta. A*, **2013**, *88*, 75.
3. A. Khajeh, E. Sanchooli, *J. Food. Compos. Anal*, **2010**, *23*, 677.
4. S.V. De Azevedo, F.R. Moreira, R.C. Campos, *Anal. Chim. Acta*. **2013**, *46*, 245.
5. C.H. Latorre, J.A. Méndez, J.B. García, S.G. Martín, R.M.P. Crecente, *Anal. Chim. Acta*. **2012**, *749*, 16.
6. L. Xi, Zh. Zhao-Hui, Zh. Hua-Bin, H. Yu-Fang, Y. Xiao, N. Li-Hua, *Chin. J. Anal. Chem*, **2011**, *39*, 839.
7. M. Tuzen, K.O. Saygi, C. Usta, M. Soylak, *Biores. Technol*, **2008**, *99*, 1563.
8. S. Iijama, *Nature*, **1991**, *354*, 56.
9. S. Iijama, T. Ichihashi, *Nature*, **1993**, *363*, 603.
10. C. Pan, S. Xu, H. Zou, Zh. Guo, Y. Zhang, B. Guo, *J. Am. Soc. Mass. Spectrom*. **2005**, *16*, 263.
11. N. Pourreza, K. Sheikhnajdi, *Talanta*, **2012**, *99*, 507.
12.M. Soylak, Y.M, Unsal, *Food. Chem. Toxicol,* **2010**, *48*, 1511.
13. Y. Liu, Y. Li, Zh. Q. Wu, X.P. Yan, *Talanta*, **2009**, *79*, 1464.
14. N. Rastkari, R. Ahmadkhaniha, *J. Chromatogr. A*, **2013**, *1286*, 22.
15. A. Duran, M. Tuzen, M. Soylak, *J. Hazard. Mater.* **2009**, *169,* 466.
16. J. Li, Q. Su, K.Y. Li , Ch. F. Sun, W.B. Zhang, *Food. Chem*, **2013**, *141*, 3714.
17. E. Zakharchenko, O. Mokhodoeva, D. Malikov, N. Molochnikova, Y. Kulyako. G. Myasoedova, *Proc. Chem,* **2012**, *7*, 268.
18. L. Guo, H.K. Lee, *J. Chromatogr. A*, **2011**, *1218*, 9321.
19. M. Moazzen, R. Ahmadkhaniha, M. Es'haghi Gorji. M. Yunesian, N. Rastkari. *Talanta*, **2013***, 115*, 957.
20. Sh. K. Wadhwa, M. Tuzen, K. Gul Kazi, M. Soylak, *Talanta*. **2013**, *116*, 205.
21. P. Kueseng, J. Pawliszyn, *J. Chromatogr*. A, **2013**, *1317*, 199.
22. B. Dai, M. Cao, G. Fang, B. Liu, X. Dong, M. Pan, Sh. Wang, *J. Hazard. Mater,* **2012**, *219–220*, 103.
23. X. Liu, X. Wang, F. Tan, H. Zhao, X. Quan, J. Chen, L. Li, *Anal. Chim. Acta*, **2012**, *727*, 26.
24. X. Chen, Zh. Zhang, X. Yang, J. Li, Y. Liu, H. Chen, W. Rao, Sh. Yao, *Talanta*, **2012**, *99*, 959.
25. Zh. Zang, Zh. Hu, Zh. Li, Q. He, X. Chang, *J. Hazard. Mater*, **2009**, *172*, 958.
26. C. Karadas, T. Turhan, D. Kara, *Food. Chem*, **2013**, *141,* 655.
27. V.A. Lemos, C.G. Novaes, M.A. Bezerra, *J. Food Compos. Anal*, **2009**, *22*, 337.
28. R. Caldorin, A.A. Menegario, *Microchim. Acta*, **2007**, *157*, 201.
29. Gh. Daneshvar Tarigh, F. Shemirani, *Talanta*. **2013**, *115*, 744.

STUDIA UBB CHEMIA, LX, 2, Tom II, 2015 (p. 343-353)
(RECOMMENDED CITATION)

CLOUD POINT EXTRACTION AND SPECTRO-PHOTOMETRIC DETERMINATION OF As(III) USING BRILLIANT BLACK BN AS AN EXTRACTION AGENT IN WATER SAMPLES

SHAHRAM NEKOUEI[a,*], FARZIN NEKOUEI[a]

ABSTRACT. Cloud point methodology was successfully used for the extraction of trace amounts of arsenic (III) s a prior step to their determination by spectro-photometry. For the proposed method, Brilliant Black BN (BBB), trioctylamine (TOA), Triton X-114, and NaCl were applied as chelating, sensitizing agent, extraction and co-extraction agents, respectively. A linear calibration curve in the range of 8-1000 μg L^{-1} of Brilliant Black BN (BBB) was acquired. Under the optimized conditions, the limit of detection (LOD) was 2.4 μg L^{-1} and the relative standard deviation (RSD) for 2.4,100 and 400 μg L^{-1} were 1.26, 2.05 and 1.18, respectively (n = 11). The application of the work is determination of arsenic (III) quantities in the various samples by spectrophotometric method. In addition, in this work TOA plays the same role of cationic surfactant and as a novel ion pairing reagent that was innovatively used instead of common cationic surfactants such as cetyltrimethylammonium bromide (CTAB).

Keywords: *Cloud point extraction; Brilliant Black BN (BBB); trioctylamine (TOA); water samples; Spectrophotometry,* As(III)

INTRODUCTION

Arsenic (As) is widely distributed in the environment, water, soils, sediments and rocks in its different forms (As(III), As(V) and organic species) [1]. Occupational exposure and arsenic poisoning may occur in persons working in industries involving the use of inorganic arsenic and its compounds, such as wood preservation, glass production, nonferrous metal alloys, and electronic semiconductor manufacturing. Inorganic arsenic is also found in coke oven emissions associated with the smelter industry [2]. It was ranked as the No. 1 of

[a] *Young Researchers and Elite Club, Science and Research Branch, Islamic Azad University, Tehran, Iran*
** Corresponding author: sh.nekouei@hotmail.com*

hazardous element and has serious effects on plants, animals and human health [3]. Millions of people worldwide are exposed to arsenic in their drinking water and ingested arsenic is an established cause of bladder, lung, and skin cancer. In addition to cancer, arsenic in water has also been associated with cardiovascular disease, skin lesions, diabetes, reproductive disorders, cognitive deficits in children and other health effects [4]. The linkage between arsenic contamination in water, arsenic concentration and accumulation in various biological samples, and oxidative DNA damage, has been proved [5]. Exposing to arsenic induces increases in DNA double strand breaks in both cell lines [6]. Because of the importance of this issue, a lot of researchers have done studies regarding measuring of Arsenic by various methods [7]. Also there are some works previously reported regarding determination of arsenic by spectrophotometric methods in the literature [13-16].

Cloud point extraction (CPE) is an outstanding alternative to conventional solvent extraction method because it produces high extraction efficiencies and pre-concentration factors, by using inexpensive and non-toxic reagents [3].

In the last decade, the increase of attention and interest upon the use of aqueous micellar solution has been found in field of separation science [17]. The cloud point extraction (CPE) technique has also been applied as a procedure for determination and removal of dyes and pigments as well as analyzing metals. [18,19]. In the present work, we applied CPE for the determination of arsenic (III) quantities in the various samples by BBB as the ligand which has made the work as a novel method.

RESULTS AND DISCUSSION

In this study, As (III) ion interacted with Brilliant Black BN, an anionic dye, which led to the formation of (As-Brilliant Black BN) complex. This complex was extracted by mixed-micelle mediated extraction through the ion pairing reagent (TOA) and non-ionic (Triton-X114) surfactants. The absorption spectra of As-BBB-TOA complexation showed a maximum absorption band at 616 nm. To obtain the maximum absorbance and sensitivity, we need to optimize various conditions which can affect the extraction. Hence, the effects of various operating conditions have been investigated and the optimum concentrations have been established for CPE.

In the present work, in order to study As (III) ion, a procedure is adopted which As (III) was used in the presence of BBB ion as a chelating agent. The interaction between arsenic and BBB that has four anionic sites to interaction with target metals led to the formation of $[As\text{-}BBB]^{1-}$ anionic complex. With regard to the fact that, hydrophobic ion-associated complexes could be more

efficiently extracted into surfactant-rich phase than ionic ion-associated complexes, small amount of ion pairing reagent (TOA) also as the sensitizing agent and a cationic auxiliary ligand was added. The addition of ion pairing reagent (sensitizing agent) improves the selectivity and sensitivity of the metal determinations. So, TOA+ as sensitivity enhancement agent was added, producing a neutral and stable ion-pair complex (ternary ion-association system), [As-BBB-TOA]. Most importantly, a colored ligand such as BBB takes the solution to visible area and as a matter of fact, in spectrophotometric method, the study of visible absorption area would be the most convenient and accurate type of detection because numerous solvents and reagents used in CPE and liquid-liquid extraction (LLE) have adsorption spectra in UV area which interfere in the determination of the goal analytes. After that, we used TOA as the ion pairing reagent, cationic surfactant, sensitizing agent and a cationic auxiliary ligand. ion pairing reagent can interact with dye and/or the metal–dye complex as an individual molecule or aggregates. With regard to the fact that, hydrophobic ion-associated complexes could be more efficiently extracted into surfactant-rich phase than ionic ion-associated complexes, small amount of ion pairing reagent (TOA) was added. The addition of sensitizing agent improves the selectivity and sensitivity of the metal determinations. In the last step, NaCl was used as the electrolyte to increases the efficient extraction.

Effect of pH

pH is an important analytical parameter that significantly influence the formation of metal–ligand complex. Therefore, in order to acquire the favorable preconcentration efficiencies, the pH values were studied in the ranges of 1.0–8.0. For this range we studied the various values of Na_2HPO_4 with acid citric to make the buffer to reach the desired pH.

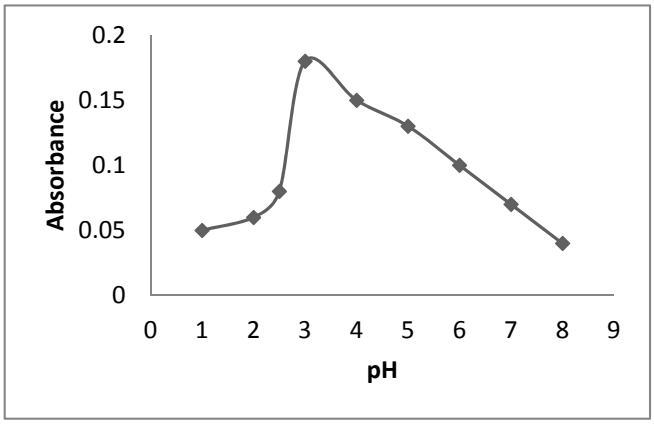

Figure 1. The concentration effect of pH on CPE

Thus the highest absorbance was obtained at pH 3. It is shown in Fig. 1. Probably, at lower pH values the rate of complex formation is low and at higher pH values the complex decomposes. Hereby, pH 3 was selected for the further experiments by 1.5 mL of *McIlvaine's buffer* solution.

Effect of Brilliant Black BN dye concentration

For studying the effect of Brilliant Black BN on extraction of Arsenic (50 μg L^{-1}), a solution containing Arsenic and various amounts of Brilliant Black BN was provided. The extraction efficiency was the highest when 1.33×10^{-5} mol L^{-1} (2ml) of Brilliant Black BN was applied. Thus, it was chosen for subsequent experiment. As it is observable in Fig. 2, at higher concentrations the absorbance declined, because the excessive Brilliant Black BN could be co-extracted into the surfactant rich phase, thus decreased the extraction efficiency of target complex.

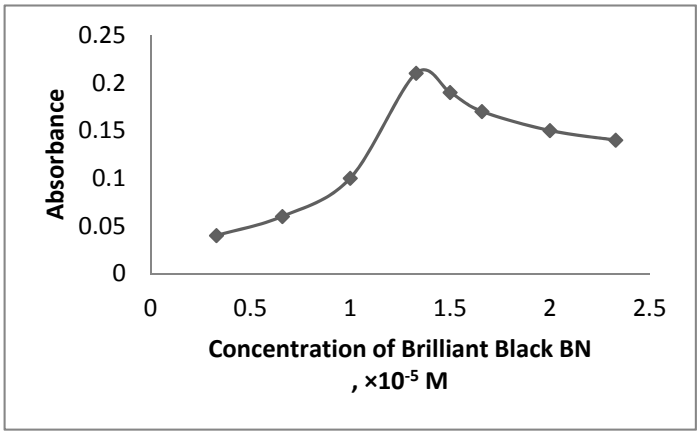

Figure 2. The concentration effect of Brilliant Black BN on CPE

Effect of ion pairing reagent concentration

With regard to the fact that, hydrophobic ion-associated complexes could be more efficiently extracted into surfactant-rich phase than ionic ion-associated complexes, small amount of TOA^+ was added in the presence of 50 μg L^{-1} of arsenic.

Amines lead to aminium salts in the presence of acids like HCl, HBr and HI due to protonation.

$$TOA + HCl \longrightarrow TOA^+ Cl^- \quad (1)$$

The result was the formation of [As-(BBB)-TOA] hydrophobic complex. Also, in order to improve the sensitivity and selectivity as well as increasing the efficiency of CPE, initially, three amines such trioctylamine (TOA), triethyamin (TEA) and tripropylamine (TPA) were considered and investigated in the range of 0.05-0.4% v/v. The best extraction yield was obtained in presence of TOA. Therefore, to the use of TOA was decided for further studies. The effect of TOA concentration, used as sensitive improving auxiliary ligand, on the extraction yield of As(III) was studied in range of 0.05-0.4% v/v. The effect of concentration of TOA as well as TEA and TPA on extraction yield is shown in Fig. 3. The extraction yield gradually increased by increasing TOA concentration up to 0.2% v/v, and quickly declined at higher concentrations. This is probably because of an increase in the blank absorbance and decrease the absorbance of ternary ion association also, excessive presence of TOA^+ in the solution can act as a competitor for As(III) in complexation with BBB. As a result, the 0.2% v/v TOA solution was selected as the optimal ion pairing reagent concentration.

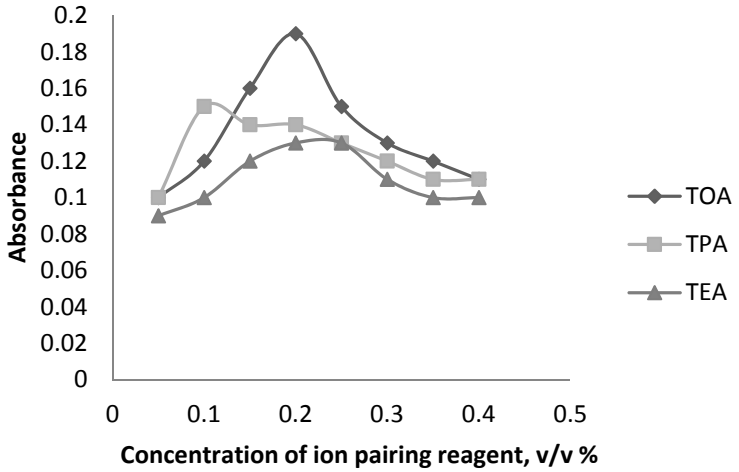

Figure 3. The concentration effect of ion pairing reagent on CPE

Effect of non-ionic surfactants

Optimization of this parameter was carried out in order to accomplish a minimum desirable surfactant concentration with maximum extraction efficiency. some non-ionic surfactants including Triton X-114, Triton X-100 and Triton X- 45 (0.1-0.45% (v/v)) were applied to CPE. Among them Triton X-114 was selected due to its higher extraction efficiency. Triton X-114 was chosen as

a surfactant due to its low cloud point temperature and high density of surfactant-rich phase, this facilities phase separation by centrifugation. So, for further studies it was chosen. With increasing the surfactant concentration up to 0.3% (v/v) the signal increased. Thus, it was used as optimum concentration. At lower concentrations, the extraction efficiency of the complexes is low, probably because of an inadequacy in the assemblies to entrap the hydrophobic complex quantitatively. The preconcentration was decreased at higher concentrations due to increase in the volume of the surfactant-rich phase. Therefore, the measured absorbance as a result of sensitivity is decreased. The results are shown in Fig. 4.

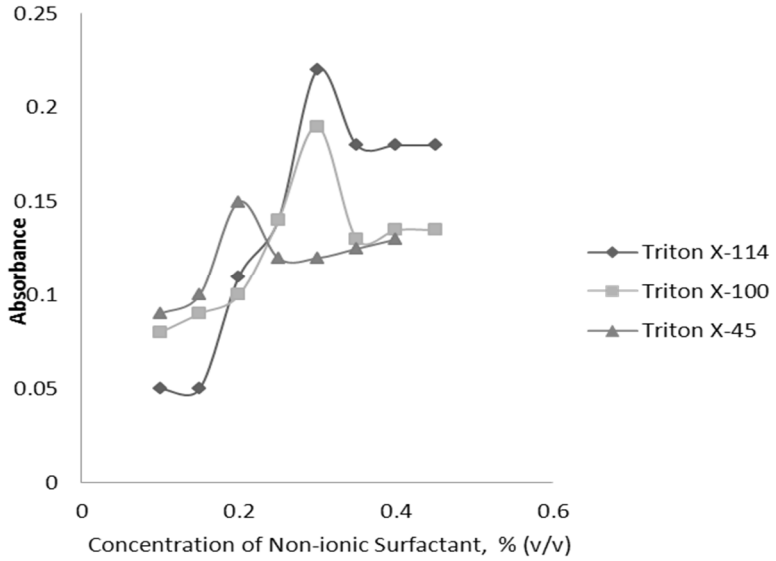

Figure 4. The concentration effect of Non-ionic Surfactant on CPE

Effect of ionic salt concentration

To investigate the influence of electrolyte concentration on the extraction efficiency, 0.1 mol L^{-1} NaCl and KCl were surveyed to solution in various amounts as the co-extraction agents. NaCl showed a more increase on the absorbance of solution. Thus, it was chosen for the further studies. It increased the extraction efficiency of arsenic up to 1.0×10^{-2} mol L^{-1} and was chosen to next studies. The salting-out ability of the cations follows the Hofmeister series (Na^{+}> K^{+}) and can be related to the ions from Gibbs' free energy of hydration. (Fig. 5)

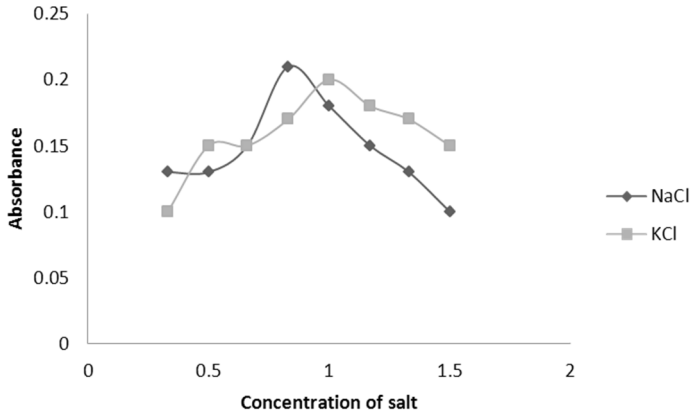

Figure 5. The concentration effect of salt on CPE

Effect of incubation time and centrifuge time and rate

For investigation of effective preconcentration and easy phase separation, the centrifugation time, equilibration temperature and incubation time were optimized. The results demonstrated that centrifuging for 5 min at 3500 rpm leading to the highest extraction of As(III). Additionally, the influence of time on the extraction of As(III) was surveyed in the time range of 5-20 min which the maximum absorbance was acquired 10 min. The influence of equilibration temperature in the range of 20-60 °C was investigated. It was established that 45 °C is sufficient for the quantitative analysis.

Analytical performance

Analytical characteristic data of the proposed CPE for As(III) was studied. In the range of 8 to 1000 μg L^{-1} the calibration curve for arsenic was linear. The limit of detection (LOD) was 2.4 μg L^{-1} and was calculated according to 3 S_{blank} /s, where S blank was obtained from the standard deviation for 10 replicate measurements of a blank solution, and s is the slope of the calibration graph. The regression equation was acquired by the least square method is $A = 2.19 \times 10^{-3} C_{As} + 1.75 \times 10^{-2}$ for 8-1000 μg L^{-1} of As(III) with a correlation coefficient of 0.998 (n = 10), where A is the absorbance and C_{As} shows the concentration of As(III) in μg L^{-1}. The relative standard deviation (RSD) at 2.4 and 100 and 400 μg L^{-1} were 1.26, 2.05 and 1.18, respectively (n = 11). The preconcentration factor was 21.4.

Interference studies

The validity of the method was assessed by investigating the effect of various foreign ions which are likely to interfere in the determination.

Usually coexisting ions may influence on objective determination of As(III) by CPE. To verify this assumption, solutions containing 100 μg L^{-1} of As(III) were taken with different amounts of foreign ions and recommended procedure was followed. The results were summarized in Table 1.

Table 1. The effect of other species on the determination of 100 μg L^{-1} of As(III)

Foreign ions	Tolerance limit (μg mL^{-1})
Cl^-, Na^+, K^+, NH_4^+, NO_3^-	1000
Cu^{2+}, Pb^{2+},Li^+, Ca^{2+}	800
Ag^+, HCO_3^-, Cd^{2+}	500
Br^-, HPO_4^{2-}	250
Ni^{2+}, Sn^{2+}, Co^{2+}	100
Al^{3+} , Fe^{3+}, Cr^{6+}, Sb^{3+}	50

APPLICATION

The proposed method was employed for the determination of As(III) in various water samples. Five replicates determinations were carried out and the obtained results (Table 2) were satisfactory. The high percentage recovery was confirmed the accuracy, precision and the independence of the procedure from the matrix interference.

Table 2. Determination of Arsenic in different Water samples and recovery tests

Sample	As (III) added (μg L^{-1})	As (III) Found [a] (μg L^{-1})	Recovery (%)	RSD (%)
River water [b]	-	61.17 ± 0.12	-	2.1
	50	110.58 ± 0.16	99.47	1.6
	100	159.15 ± .080	98.75	2.9
River water [c]	-	14.96 ± 0.51	-	1.1
	50	62.76 ± 0.17	96.61	3.0
	100	112.50 ± 0.11	97.86	2.5
Tap water	-	8.21 ± 0.16	-	2.1
	50	58.14 ± 0.10	99.88	2.1
	100	110.51 ± 0.19	102.12	2.3
Well water	-	20.15 ± 0.03	-	2.1
	50	71.81 ± 0.17	102.37	1.7
	100	118.60 ± 0.04	98.81	1.8
Spring water	-	22.17 ± 0.09	-	2.0
	50	70.84± 0.18	98.16	2.5
	100	121.15 ± 0.04	99.16	3.0

[a] $\bar{x} \pm ts\sqrt{n}$ at 95% confidence (n = 5)
[b] zayande rood river, Esfahan (located in an industrial area)
[c] beshar river-tang-e-sorkh village branch(located in a nonindustrial area)

EXPERIMENTAL

Apparatus

Absorption spectra and absorbance measurements were made by a Shimadzu UV-1800, UV–Vis spectrophotometer using 1 cm quartz cells (1.0 mL). A Metrohm digital pH meter (model 691) with a combined glass electrode was applied to measure pH values. A Hettich universal 320 centrifuge was used to hasten the phase separation.

Standard solutions and reagents

The non-ionic surfactant Triton X-114 (3%, v/v) (Sigma-Aldrich, Steinheim, Germany) was used without further purification. Stock standard solution of Arsenic was prepared from the 1000 mg L^{-1} As(III) standard by dissolving appropriate amount of As_2O_3 (Merck, Darmstadt, Germany) in 3 M NaOH and pH 7.0 with 5 M HCl solution. The 1.0×10^{-4} mol L^{-1} of Brilliant Black BN(Merck, Germany), solution was obtained by dissolving 0.0086 g of it in 100 ml water. A 3% v/v stock solution of trioctylamine (TOA) (Sigma-Aldrich) was attained by diluting 3.0 mL of the reagent to 100 mL water containing 1 mL of HCl (0.1 mol L^{-1}) in a volumetric flask. The McIlvaine's buffer solution was provided by 4.11 ml of 0.2 M Na_2HPO_4 in 15.89 ml of 0.1 M citric acid. Stock solution of NaCl (1.0×10^{-1}) was prepared by dissolving 0.584 gr of it in distilled water and diluting to 100 mL in a flask.

Procedure

An aliquot of the solution containing As(III) (in the range of 8-1000 µg L^{-1}), 2 mL of Brilliant Black BN (1.0×10^{-4} mol L^{-1}), 1.5 mL of 3% (v/v) of Triton X-114, 1 mL of 3% TOA, 1.75 mL of 0.1 mol L^{-1} of NaCl and 1.5 mL of *McIlvaine's buffer* (pH =3) was transferred into a 15 mL tube, and equilibrated at 45 ^{o}C in a thermostat bath for 10 min. The separation into two phases was accelerated by centrifuging at 3500 rpm for 5 min. The contents of tubes were cooled in an ice-bath for 6 minutes, the surfactant-rich phase became viscous, and the upper aqueous phase was decanted. The surfactant-rich phase of this procedure was dissolved and diluted to 0.7 mL with the methanol and transferred into a quartz cell. The absorbance spectrum of the solution was measured at the 616 nm. A blank solution that was prepared in the same way except that distilled water was used instead of As(III) was also submitted to the same course of action and its spectrum was measured.

Sample preparation

Different water samples were preconcentrated. All the collected samples were spiked with a suitable amount of standard solution of As(III). All the aforementioned samples were filtered through a 0.44μm membrane to remove the suspended and floated particles. Standard addition method was applied so as to calculate recovery values and check accuracy of results.

CONCLUSION

The proposed work was found to be very simple, direct, very selective and sensitive. The limit of detection of the proposed method seems to be satisfactory. The possible interference of some important ions was investigated and no important interference was encountered. The Simplicity in operation, good precision, being economical, low extraction time and the lack of the toxic solvents presence in the method are from other benefits of the work. The proposed method formed hydrophobic ion-associated complex, and the hydrophobic complexes are more extractable by Triton X-114 than the non hydrophobic complexes. Spectrophotometry of such colored ternary complexes probably provides the most sensitive, relatively simple and fast approach to trace metal analysis. This reason is extendable to contrast among the ligandless extractions and those have one or more ligands. In addition, the percentage recoveries were higher than 96% confirming the accuracy. Considering the achieved results, the arsenic quantities, in water samples of the river located in industrial area is considerably higher than the nonindustrial one. And well water and spring water (as unpurified samples) have more quantities of arsenic as compared to tap water (as purified sample). This method gives reasonably good detection limit, wide linearity and also good standard deviations.

ACKNOWLEDGEMENT

The authors state their gratitude to Young Researchers and Elite Club, Science and Research Branch, Islamic Azad University, Tehran, Iran, for financial support of this work (Grant 1392).

REFERENCES

1. J.A. Baig, T.G. Kazi, A.Q. Shah, M.B. Arain, H.I. Afridi, G.A. Kandhro, Sumaira Khan, *Anal. Chim. Acta*, **2009**, *651*, 57.
2. E. Priha, I. Ahonen, P. Oksa, *Am. J. Ind. Med,* **2010***, 39*, 402.

3. Baig J.A., Kazi T.G., Shah A.Q., Arain M., Afridi H.I., Kandhro G.A., Sumaira Khan, Naeemullah, A.S. Soomro, **2010**, *Food. Chem. Toxicol*, *48*, 3051.
4. D. Melak, C. Steinmaus, C. Ferreccio, K. Kalman, R. Parra, J. Acevedo, L. Pérez, S. Cortés, A.H.Y. Smith, Yuan, J. Liaw, *Toxical. Appl. Pharm*, **2014**, *274*, 225.
5. P. Hinhumpatch, M. Ruchirawat, P. Navasumrit, K. Chaisatra, J. Promvijit, C. Mahidol, *Toxical. Appl. Pharm*, **2013**, *273*, 569.
6. H. Xie, S. Huang, S. Martin, Sr J.P. Wise, *Mutat. Res-Gen. Tox. En*, **2014**, *760*, 33.
7. G. Yang, W. Xiao-Ru, C. Xuan, Y. Jing-Jing, F. Sen-Chun Lee, *Chinese J Anal Chem*, **2009**, *37*, 1738.
8. Y. Zhang, S. Qiang, J. Sun, T. Hang, M. Song, *J. Chromatogr. B*., **2013**, *917-918*: 93.
9. P. Thambidurai, A.K. Chandrashekhar, D. Chandrasekharam; *Procedia Earth Planet. Sci*, **2013**, *7*, 834.
10. A.H. Pétursdóttir, J. Feldmann, G. Gunnlaugsdóttir, E.M. Krupp, *Food. Chem*, **2014**, *150*, 353.
11. W.R. Cullen, K.J. Reimer, M.M. Moriarty, W.M. Lai, I. Koch, L. Cui, C. Combs, E.M. Krupp, J. Feldmann; *Sci. Total. Environ*, **2014**, *466-467*, 90.
12. C.M.M. Santos, M.A.G. Nunes, I.S. Barbosa, G.L. Santos, M.C. Peso-Aguiar, M.G.A. Korn, E.M. Flores, V.L. Dressler, *Spectrochim. Acta. B*, **2013**, *86*, 108.
13. B. Narayana, T. Cherian, M. Mathew, C. Pasha, *Ind. J. Chem. Tech.* **2006**, *13*, 36.
14. S.F.P. Pereira, S.L.C. Ferreira, G.R. Oliveira, D.C. Palheta, B.C. Barros. *Eclet. Quim.* **2008**, *33*, 23.
15. A. Pillai, G. Sunita, V.K. Gupta, *Anal. Chim. Acta*. **2000**, *408*, 111.
16. T. Cherian, B. Narayana, *Anal. Lett*. **2005**, *38*, 2207.
17. J.H. Harwell, J.F. Scamehorn, "Surfactant Based Separation Processes", Marcel Dekker Inc, New York, 1989: Chapter 1.
18. Sh. Abedi, F. Nekouei, *E. J. Chem*, **2011**, *8*, 1588.
19. R. Mousavi, F. Nekouei, *E. J. Chem*, **2011**, *8*, 1606.

STUDIA UBB CHEMIA, LX, 2, Tom II, 2015 (p. 355-370)
(RECOMMENDED CITATION)

ANTIOXIDANT CONTENT IN ROMANIAN TRADITIONAL DISTILLED ALCOHOLIC BEVERAGES

BIANCA MUREȘAN[a], CLAUDIA CIMPOIU[a], ANAMARIA HOSU[a], CRISTINA BISCHIN[a], EMESE GAL[a], GRIGORE DAMIAN[b], EVA FISCHER-FODOR[c], RADU SILAGHI-DUMITRESCU[a,*]

ABSTRACT. Reported here is a first detailed analysis of the antioxidant activity in traditional fruit-derived distilled alcoholic beverages from Romania ("țuica"). A distinctly highest activity, paralleled by Folin-Ciocalteu data and UV-vis absorbances, was seen in the most common type of such brandy, made of plums; other samples included brandies made of apples, pears, fruit mixtures, wine, and cereals. In fact, the values seen for the plum brandy were, even before maturation with wood, similar to those of commercially-available wood-maturated whisky. Increases of up to one order of magnitude in antioxidant activity were seen in all brandies upon maturation with various types of wood – with mulberry tree by far the most efficient, followed by oak and cherry – and with lowest values seen for acacia. Attempts to identify anticancer activity in concentrated extracts prepared from plum brandy, failed. Copper electron paramagnetic (EPR) signals are shown for the first time in such brandy samples.

Keywords: *brandy; antioxidant; polyphenol; hemoglobin; EPR*

INTRODUCTION

The beneficial effects on human health and disease prevention (cardiovascular, neurodegenerative, colon cancer) of moderately consumed wine and brandy are correlated with their antioxidant capacity, especially due to the higher ability of the polyphenolic compounds to quench free radical species [1-14].

[a] *Faculty of Chemistry and Chemical Engineering, Babeş-Bolyai University, 11 Arany Janos str., RO-400028, Cluj-Napoca, Romania*
[b] *Faculty of Physics, Babeş-Bolyai University Cluj-Napoca, Romania*
[c] *Tumor Biology Laboratory, The I. Chiricuta Oncology Institute, Cluj-Napoca, Romania*
** Corresponding author: rsilaghi@chem.ubbcluj.ro*

Polyphenols and antioxidant capacity are almost absent in the case of vodka, gin and rum. However, whisky and brandy have an intermediate antioxidant capacity between red and white wine. In this case, polyphenols come from the wood of the storage container during the maturation process [15,16]. Numerous studies show that storage of wine or other alcoholic beverage, especially in oak barrels, may lead to significant changes in the polyphenolic composition, due to the transformation of native compounds as well as to the hydrolysis of tannins or lignin from the woods [7,17-25]. Recently, new technologies have been developed in order to simplify the aging process and to decrease the cost of preservation of brandy in wood barrels. Thus, one potential alternative technology consists in adding of wood pieces to the beverage kept in stainless steel tanks [26,27].

Although there are numerous studies regarding the antioxidant capacities of some distilled alcoholic beverages (cognac, liquor, whisky) [9,28,29], limited data have been obtained in the case of traditionally-produced brandies in Romania (tuica or palinca). As opposed to the use of cereals in other European countries (Scotland, Ireland, Northern Europe), traditional Romanian distilled beverages are based on processing of various autochthonic of fruits such as plums, apples, pears, cherries, apricots, berries. The distillation of the fermented fruit pulp is typically performed in cooper stills, with open fire, followed by a maturation phase in oak barrels [30].

According to the alcoholic concentration (37 vol % cf. current legislation), Romanian fruit brandies are classified as superior distilled drinks palinca (the name is a translation of the similar Hungarian product, palinka), obtained by a mixture of fruits, or slibovita, obtained by distillation and redistillation of plum marc, and inferior assortments known as spirits. The tuica, other traditional beverage obtained typically exclusively from plums, is produced at various alcohol concentrations, depending on region [31,32].

The purpose of this study was to investigate the relationship between polyphenolic content of various types of traditional distilled Romanian beverages and the antioxidant capacities under the influence of different types of wood used during the maturation process. Herein, besides traditional methods used to investigate antioxidant capacities of food and drinks (ABTS, DPPH) [16,33,34], a new physiologically relevant method based on hemoglobin ascorbate peroxidase activities is applied.

RESULTS AND DISCUSSION

General features

There are only a few data regarding the quality of Romanian distilled fruit beverages, mainly focused on technical analyses such as relative density, alcohol concentration, total and volatile acidity, pH, total dry extract, total polyphenol index and volatile compounds [31,32,35]. However, a detailed analysis of the antioxidant character has not been reported. By contrast, it is known that several kinds of polyphenolic compounds such as ellagic acid, gallic acid and lyoniresinol could be detected in whisky; nevertheless, a majority of them come from oak barrels, due to the higher concentration of alcohol, in the maturation process [36]. Here, some traditional and new methods for the characterization of antioxidant capacities were applied for the analysis of 5 types of Romanian brandy; additionally, the effect of maturation in the presence of different species of wood was also examined.

All studied brandy samples have an alcoholic concentration between 47 and 52 % very close to the commercial distilled beverage, whisky. Copper is the only detected metal in all samples, having a concentration between 0.1627-0.377 ppm; this is an acceptable level according to the current legislation (5 ppm legal limit (Monitorul oficial al Romaniei, part I, Nr. 268.11 VI 1999)). The metals found in alcoholic beverage may have different sources including raw materials, brewing, process type and equipment, bottling, aging/storage and adulteration [37]. The presence of Cu in the studied alcoholic distilled beverage was detected here for the first time, in our knowledge, using not only elemental analysis but also EPR spectroscopy (Supplementary Information, Figure S1).

UV-vis spectra

All analyzed brandy samples display UV-vis absorbance between 200 and 320 nm (Figure 1 A) - a region specific for the absorption of aromatic and unsaturated compounds. The difference in the absorption intensity of spectra suggests the diversity of the compounds found in these brandies. The highest intensity was obtained for plum brandy and the lowest for wine and corn ones. Considering that antioxidants present here are organic compounds, presumably polyphenolic compounds, one would expect a good correlation between the intensity of the spectra and the antioxidant activity of the samples. Compared to other distilled beverages (Fig. 1 B), the spectrum of the Romanian tuica has a visible difference in the intensity of absorbance at 250 nm. At 275 nm, the tuica appears to be more similar to whisky and tequila; in fact, below 300 nm, its absorbance (and, hence, its organic content – implying antioxidant activity) are the highest among all samples tested.

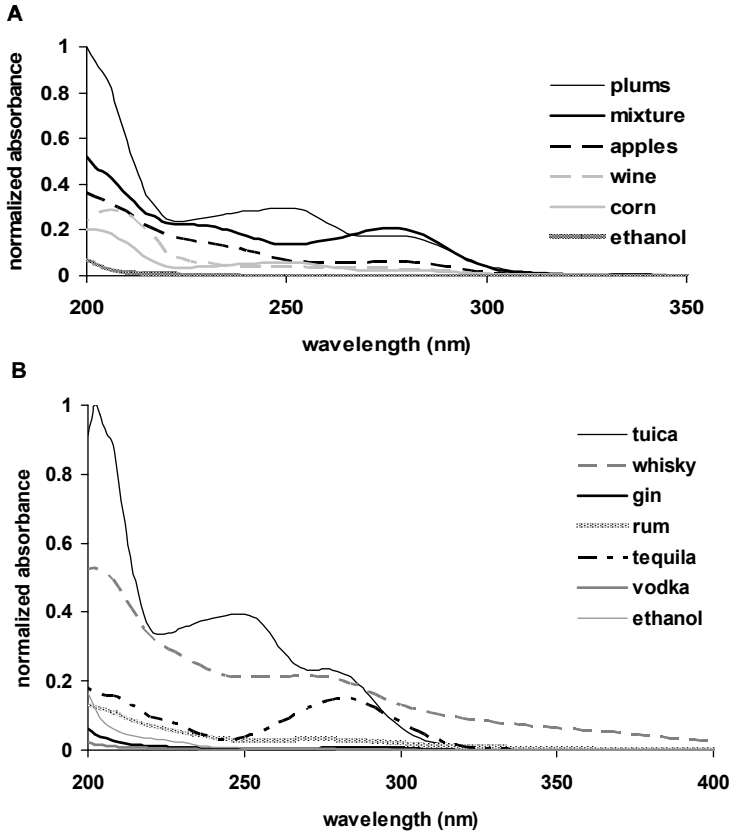

Figure 1. UV-vis spectra of Romanian brandy samples (A) and other commercial distilled beverage (B).

Chromatographic analyses

The attempts to detect antioxidant compounds from tested Romanian brandies by TLC were, unfortunately, unsuccessful even in the case of concentrated samples. This may suggest that part of the responsible compounds for antioxidant activity were also volatile (as seen in the following sections, chemical analysis does reveal a certain polyphenolic content). On the other hand, the chromatogram obtained for the maturated brandies (Fig. 2) indicates specific and obvious differences in the type and content of compounds: the highest amounts were in mulberry tree (1), cherry (3) and oak (2) samples. It must be specified that in the case of maturated brandies the sample pre-concentration is not necessary.

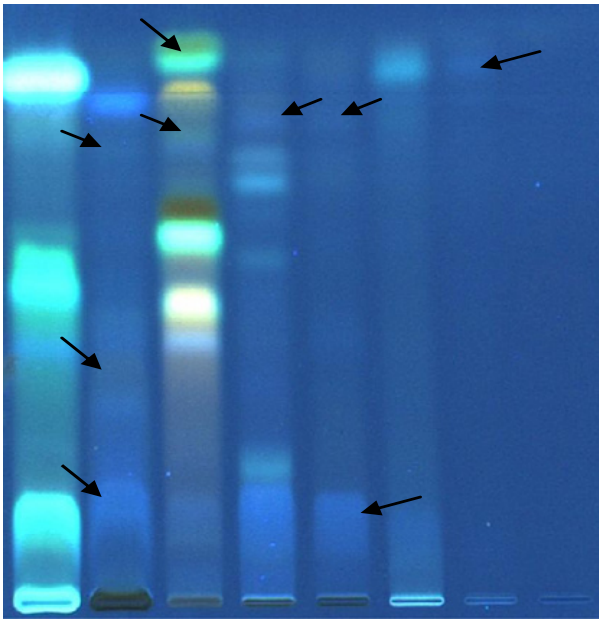

Figure 2. TLC separation of maturated brandies on silica gel 60 F_{254} with ethyl acetate: methanol: water (7.7: 1.3: 1, v/v/v) as mobile phase. Derivatization with NP/PEG, UV 366nm. Control sample is represented by plums brandy before maturation, obtained by concentration of initial extracts 20 times by evaporation, lyophilization and suspension of the residue in ethanol.

The separation shows that the largest number of separated compounds are found in the brandy maturated in mulberry, followed by brandies maturated in oak and cherry. Furthermore, a distinction regarding the number of separated compounds and their concentration can be done. The specific compounds presented only in the particular brandy are marked with arrow on the chromatogram. All these characteristics of TLC separation allow the differentiation of analyzed samples according to the wood and can be used as fingerprinting of maturated brandies.

DPPH and Folin-Ciocalteu reagent based assays

Figure 3 reveals a close correlation between the DPPH assay, which is widely used for biologically relevant antioxidant capacity evaluation, due to its simplicity and low cost, and total polyphenolic content, determined by Folin-Ciocalteu assay. Both methods are based on electron transfer mechanisms and are suitable for aqueous systems.

The simple end-time measurement of DPPH percentage bleached used for the analyses of the 5 Romanian types of brandy indicates that the highest polyphenolic contents appears to be in the case of the plum brandy. No significant differences were obtained between the apple brandy and the mixed sample (apple + plum mixture); the lowest concentration of polyphenols was found in the corn brandy. Also, kinetic measurements were employed to compare a plum brandy sample (not maturated with wood) and commercial whisky. Similar results were obtained measuring the area under the curve (described in Methods section) between plum brandy (553±5) and whisky (551±1) and a slight difference was shown in the case of end point experiments (0.048±0.006 for the plum brandy and 0.075±0.001 for whisky). Taking into account that plum brandy samples had not been maturated yet with wood, the antioxidants in this brandy originate mainly from consumable plant materials, not from wood hydrolysis – which may in principle be considered an advantage over other European distilled beverages such as whisky or vodka.

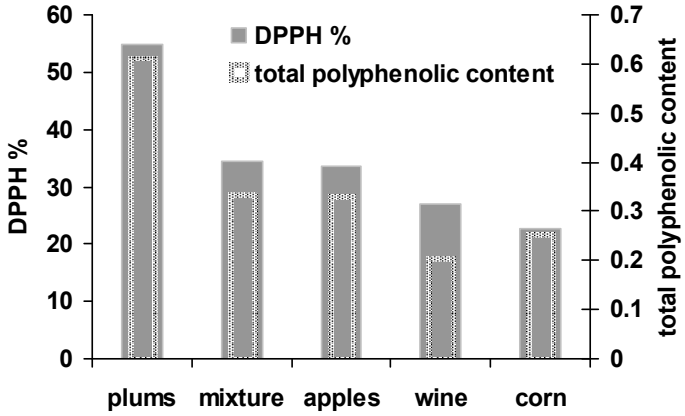

Figure 3. DPPH based assay and Folin-Ciocalteu data for the 5 types of Romanian brandy.

TEAC assay

In Fig. 3 the antioxidant capacity of the aqueous and ethanolic extracts of the brandies is analyzed, using the simplest and cheaper test TEAC, which is based on the ability of antioxidants to react directly with ABTS$^{\bullet}$ radical. The extracts, obtained after lyophilization and resuspension in 20-time smaller volumes of solvent (either water or alcohol) would be expected to contain a higher concentration of antioxidants (10-20 times) than the original brandy samples.

Kinetic measurements were performed measuring both the difference of the absorbance, which is directly correlated with the antioxidant capacities of the samples and area under the curve, which is inversely correlated with the antioxidant capacities. Thus, for the first case, (Fig. 4 A) the ethanolic extract displayed measurable amounts (in line with DPPH and Folin-Ciocalteu assays on the intact brandy), much larger than the water extracts.

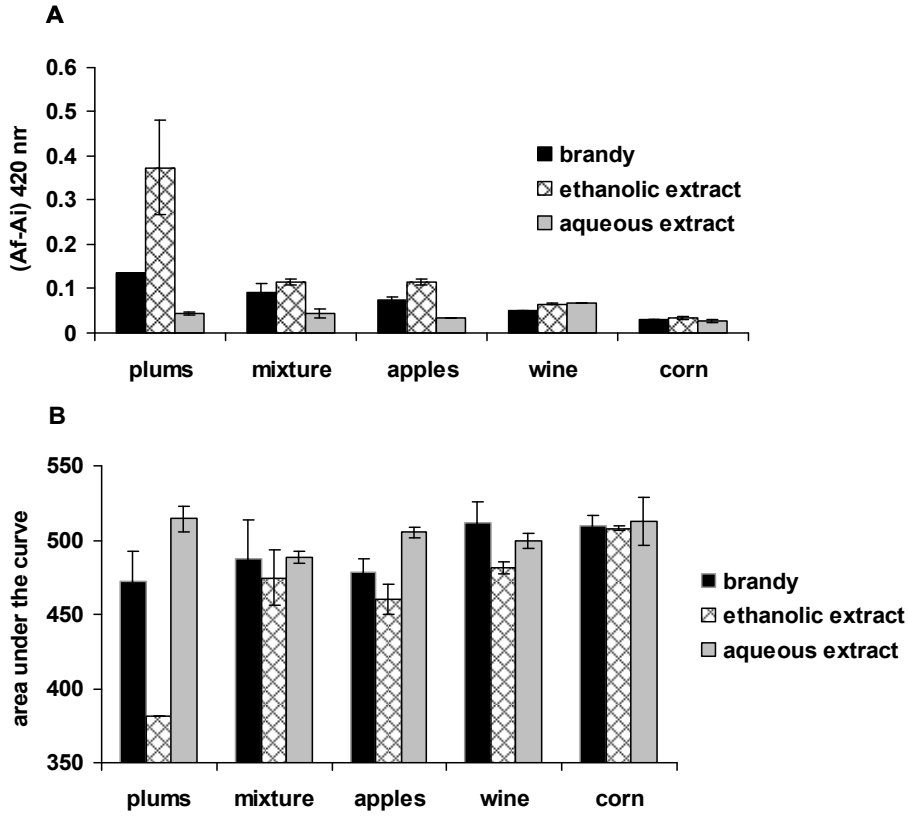

Figure 4. ABTS assay reflected in total change in absorbance (A) and area under the curve (B), obtained for aqueous and ethanolic extract of 5 types of Romanian brandy.

A good correlation could be observed between the difference of absorbance and the second parameter used for the characterization of antioxidant capacities - area under the curve shown in Figure 4 B. Although one may have expected a higher antioxidant capacity of the ethanolic extract, due to the increased concentration of original solution (20 times), this could not be observed - most probably due to loss of antioxidant content during the

lyophilization process. Indeed, one must consider that since these brandies are obtained via distillation, the majority of the compounds would also be volatile (of the type illustrated in Table S3 in Supporting Information) – or at least predisposed to being carried by vapors of the volatile compounds. Reference [35] does in fact list a few compounds that, while volatile, may also be targets for free radicals and hence act as antioxidants.

The characteristic parameters of the kinetic curve, fitted using a bi-exponential function, are described in Tab. S1 (Supporting Information). Thus, two concomitant processes of different rates occur during this reaction, most probably due to the structure of the antioxidants, reflected in a different rate consuming of $ABTS^{\bullet}$ radicals.

Kinetics data of the consumption of ABTS radical by polyphenols, obtained by EPR measurements fitted using a mono-exponential function (due to the different time scales between this experiment and UV-vis experiment), show a good correlation with UV-vis experiments for plums and corns brandy (Figure 5).

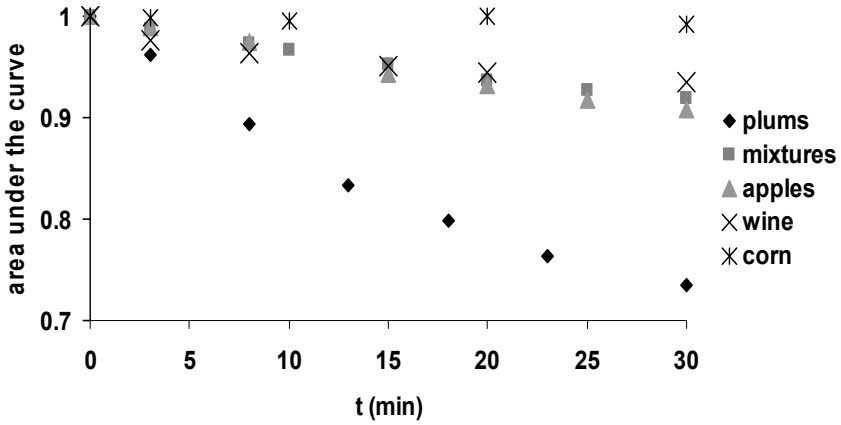

Figure 5. Kinetic of the consumption of $ABTS^{\cdot+}$ radical during an EPR experiment for 5 type of Romanian brandy. Area under the curve was normalized and corresponded to the integration of each EPR spectrum.

Effects of maturation

UV-vis spectra of maturated brandies with wood show an increase in the intensity of absorbance, especially in the case of mulberry tree, compared with original sample (Figure 6). A good similarity can be observed for oak and cherry spectra. One would expect a correlation between the UV-vis characteristics and the antioxidant capacity.

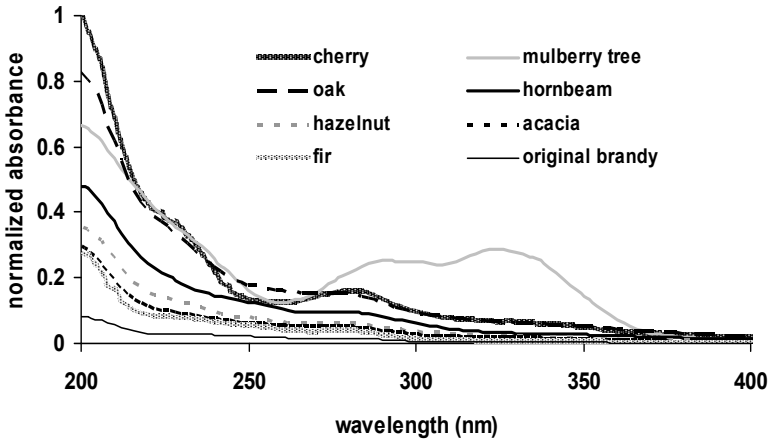

Figure 6. UV-vis spectra of the maturated brandies.

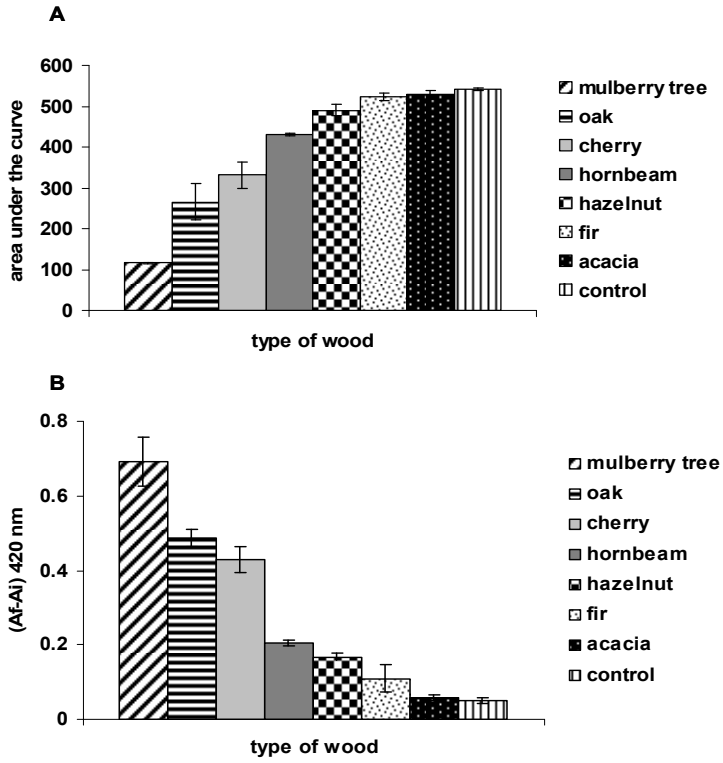

Figure 7. The effect of different wood used in the maturation process of plums brandy, reflected in the ABTS parameters: total change in absorbance (A) and area under the curve (B).

Indeed, a significant improvement of the antioxidant capacity (compared to original samples) was achieved after the maturation of brandies using different pieces of wood species. The results presented in Fig. 7 (kinetic parameters fitted using a bi-exponential function are presented in Supplementary Information, Table S2) show that the best improvement, in agreement with the chromatogram shown in Figure 2 and UV-vis spectra shown in Figure 6, was obtained for mulberry tree followed by oak. Acacia and fir woods proved to have the lowest influence on this process.

HAPX assay

A new physiologically relevant method proposed for the evaluation of antioxidant capacities is based on the ascorbate peroxidase activity of hemoglobin, as described in detail in [38-44]. Under some natural (physical effort) or pathological conditions such as haemolytic anaemias, subarachnoid

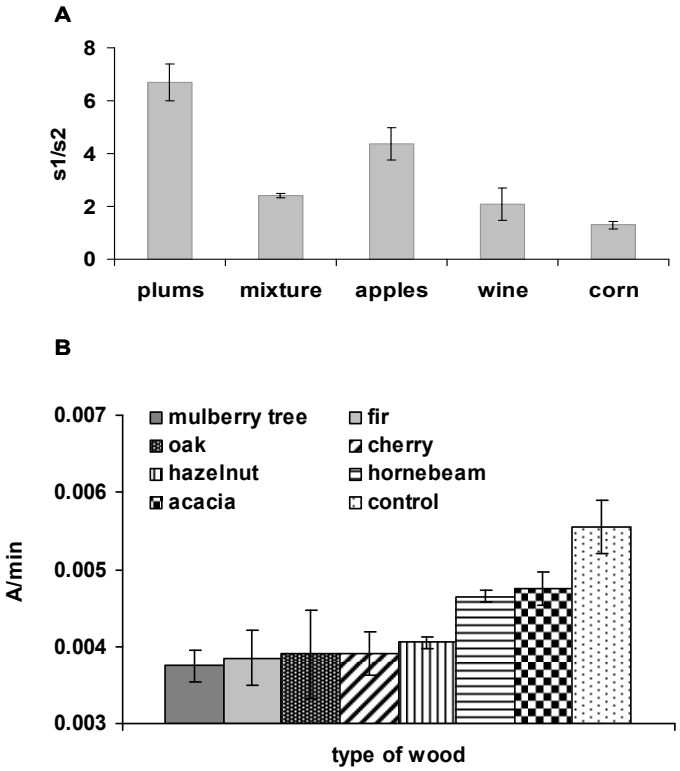

Figure 8. A. HAPX results reflected in the change of slope at 290 nm, for the Romanian analyzed brandies. S1/s1 represents the ratio between slope 1 and slope 2. B. HAPX assay results reflected in the change of slope at 290 nm, for the plums brandy maturated with different types of wood.

haemorrage and rhabdomyolysis, globins can initiate free radical chemistry, in particular by interaction of the ferric form of hemoglobin (met) with peroxide yielding two strong oxidants: ferryl iron and a protein-bound free radical. Ascobate has the ability to reduce plasma methhemglobin, ferryl hemoglobin and globin radicals. Other antioxidants compounds present in the sample can also interact with these highly oxidant species during the catalytic cycles of these reaction; these easily could be observed in the inhibition of ascorbate hemoglobin dependent oxidation [45].

HAPX applied for Romanian brandy shows a good correlation with traditional methods used for evaluation of antioxidant capacity (ABTS, DPPH) (Figure 8 A). Plums sample was proved to have the best antioxidant capacity, and corn brandy the lowest. The results obtained using this method for the maturated samples are shown in Figure 8 B. With some few exceptions, a good correlation can be observed between the results obtained here and in the ABTS test. Thus, the higher antioxidant capacity was achieved for the brandy maturated in the presence of a piece of mulberry tree species, followed, unlike on the ABTS results, by the fir wood, oak and cherry. The lowest antioxidant capacity was observed, as in the ABTS experiments, for the acacia wood.

Cell culture tests

The antioxidant contents of various foodstuffs is often cited as indicative of health-promoting effects; alcoholic beverages make no exception, as reviewed in the Introduction. Biological tests were in this context performed on 20-fold concentrated extracts of the plum brandy, following methodologies described elsewhere [46]. Unfortunately, no anticancer effect was detected – nor was any other protective or toxic effect noticed.

CONCLUSIONS

Reported here is a first detailed analysis of the antioxidant activity in traditional fruit-derived distilled alcoholic beverages from Romania (“țuica”). By far, the highest activity is seen in the most common type of such brandy, made of plums. In fact, these values are, even before maturation with wood, similar to those of commercially-available wood-maturated whisky. Increases of up to one order of magnitude in antioxidant activity were seen in all brandies upon maturation with various types of wood – with mulberry tree by far the most efficient, followed by oak. Attempts to identify anticancer activity in concentrated extracts prepared from plum brandy were not successful. Copper electron paramagnetic (EPR) signals are shown for the first time in such brandy samples.

EXPERIMENTAL SECTION

5 types of brandy (from plums, mixture of plums and apples, apples, wine and corn) produced simultaneously with a similar alcoholic concentration were collected directly from a producer originating from the Bistrita-Nasaud county in Romania. From the same region, 7 pieces of different species of wood were collected from mulberry tree, oak, hazelnut, acacia, fir, cherry and hornbeam. Whisky (commercial brand, 40 vol % alcohol) was obtained from a local store.

ABTS (2,2'-azino-bis(3-ethylbenzothiazoline-6-sulphonic acid), DPPH, and ascorbic acid were purchased from Sigma-Aldrich (Germany). The Folin-Ciocalteu reagent (standard solution 2 N, 1: 10 dilution) was obtained from Merck KGaA (Germany). Bovine hemoglobin, purified according to the Antonini and Brunori procedure [47], was oxidized to met hemoglobin (metHb) by ferricyanide treatment.

Silica gel $60F_{254}$ thin layer chromatographic (TLC) plates (10x10cm) were purchased from Merck, Darmstadt (Germany). NP (Natural Product) was prepared by dissolution of 1 g of diphenylboronic acid aminoethyl esther in 200 mL ethyl acetate; PEG solution was prepared by dissolution of 10 g polyethylene glycol 400 (Macrogol) in 200 mL dichloromethane.

Brandy aging (maturation) occurred in the presence of a piece of wood (3 cm^3), in plastic containers, at 4ºC, during 24 hours. Then, the samples were decanted and analyzed. Selected samples of brandies were concentrated on a water bath at 40^{o}C under mild vacuum (water suction), until the final volume of sample was decreased 20-fold. The obtained extracts were lyophilized and then, the residues were suspended in ethanol and water, respectively.

Thin layer chromatography

20 μL of each concentrated brandy samples and those obtained by maturation with different types of wood were applied as 8mm bands with a rate of 30nL/s to the TLC plate using a semi-automatic applicator device (Linomat V, Camag). The plates were developed in normal chromatographic twin trough chamber (Camag) pre-saturated for 30 minutes with mobile phase - ethyl acetate: methanol: water (7.7: 1.3: 1, v/v/v). The dried developed plate was heated at 1000C for 3 min, dipped while still hot in the NP solution, dried in cold air and then immersed in the PEG solution. The plates dipping were performed using an immersion device (Camag). The detection was performed under UV light (254 nm and 366 nm) and under visible light, before and after the dipping of the plates in the NP/PEG solutions and the documentation of the plates was performed using a TLC vizualizer device (Digistore 2 - Camag).

The total polyphenolic content was determined using the Folin-Ciocalteu assay, described in [45]. For each sample, 1.5 mL Folin-Ciocalteu reagent were added to 1 mL brandy, and samples were incubates in the dark for 5 minutes. Then, 1.2 mL sodium carbonate (0.7 M) were added and samples were incubated in the dark for 2 h, at which point the solution turned deep blue to various degrees, depending the sample. The absorbance of the blue samples was recorded at 760 nm, on a Cary 50 UV-vis spectrometer (Varian).

DPPH assay

A stock solution of 0.09 mg/mL was prepared. 1 mL of DPPH solution was added to the 2 mL brandy and the samples were incubated for 15 minutes at room temperature, followed by measurement of the absorbance at 517 nm. Besides the end-point experiment, kinetics measurements were also performed for 30 minutes, at 517 nm. Typical decay curves were obtained for every sample, allowing one to calculate the total change in absorbance (ΔA), which is directly correlated with antioxidant capacities of the samples, as well as the calculation of the area under the curve, which is inverse correlated with the antioxidant capacities.

Trolox equivalent antioxidant capacities (TEAC) assay

The ABTS radical was enzymatically obtained by 2 hours of incubation of 2 mM reduced ABTS solution in 5 mM sodium acetate pH 5.5, with 50 nM horseradish peroxidase and 1.3 mM hydrogen peroxide. The radical was separated from the enzyme using a 10 kDa cut-off amicon filter. For this assay, kinetic measurements were performed. In a quartz cuvette, 50 µl ABTS radical was added to the 900 µl PBS buffer and 10 µl brandy. The decrease of the ABTS radical absorbance was monitored at 420 nm. As in the DPPH methods, the evaluation of the antioxidant capacities of the sample can be obtained using the total change in absorbance as well as via the calculation of the area under the curve.

The inhibition of hemoglobin ascorbate peroxidase activity (HAPX) assay was conducted as in [45]. For this experiment, kinetic measurements were performed. Thus, in a quartz cuvette, 14 µl metHb of 1mM, 13 µl peroxide of 60 mM and 10 µl were added to 952 sodium acetate buffer, pH 5.5 - after which the absorbance changes were monitored at 290 nm. After absorbance stabilization, the reaction was triggered by the addition of 50 µl ascorbate of 50 mM. The kinetic profile for ascorbic acid degradation after the addition of met-Hb, was linear for least 100 s. For the evaluation of the hemoglobin ascorbate peroxidase activity, the slope of the linear decrease was calculated (corresponding to the oxidation of ascorbate).

EPR measurements were performed as described in [46].

ACKNOWLEDGMENTS

We are thankful to Mr. Ioan Bodea (BBU) for technical assistance, Prof. Carmen Socaciu (USAMV) for helpful discussions, prof. Tiberiu Frentiu (UBB) for elemental analyses, and The Romanian Ministry for Education and Research (grants PCCE 140/2008, PCE 488/2012) for funding. This study was partially funded by the Sectoral Operational Programme for Human Resources Development 2007-2013, co-financed by the European Social Fund, under the project POSDRU/159/1.5/S/132400 - "Young successful researchers – professional development in an international and interdisciplinary environment".

REFERENCES

1. F. Cimino,V. Sulfaro, D. Trombetta, A. Saija, A. Tomaino, *Food Chem.,* **2007**, *103*, 75-81
2. D. Di Majo, M. La Guardia, S. Giammanco, L. La Neve, M. Giamanco, *Food Chem.*, **2008**, *111*, 45-49
3. N. Paixao, R. Perestrelo, J.C. Marques, J.S. Camara, *Food Chem.*, **2007**, *105*, 204-214
4. I.G. Roussis, I. Lambropoulous, P. Tzimas, A. Gkoulioti, V. Marinos, T. Tsoupeis, I. Boutaris, *J. Food Compost Anal.*, **2008**, *21*, 614-621
5. F. Que, L. Mao, X. Pan, *Food Res. Int.*, **2006**, *39*, 581-587
6. M. Scwartz, M.C. Rodriguez, C. Martinez, V. Bosquet, D. Guillen, C.G. Barroso, *Food Chem.*, **2009**, *116*, 29-33
7. S. Canas, V. Casanova, A.P. Belchior, *J. Food Compost Anal.*, **2008**, *21*, 626-633
8. A. Stasko, V. Brezova, M. Mazur, M. Certik, M. Kalinak, M. Gesheid, *Food Sci. Techol.*, **2008**, *41*, 2126-2135
9. G.G. Duthie, M.W. Pedersen, P.T. Gardner, P.T. Morrice, A.M. Jenkinson, D.B. McPhail, G.M. Steele, *Eur. J. Clin. Nutr.*, **1998**, *52*, 733-736
10. M. Gronbaek, U. Becker, D. Johansen, A. Gottschau, P. Schohr, H.O. Hein, G.S. Jensen, T.I. Sorensen, *Ann. Intern. Med.*, **2000**, *133*, 411-419
11. E.N. Frankel, A.L. Waterhouse, P.L. Teissedre, *J. Agric. Food Chem.*, **1995**, *43*, 890-894
12. S. Yoshioka, T. Terashita, H. Yoshizumi, N. Shirasaka, *Biosci. Biotechnol. Biochem.*, **2011**, *75*, 2278-2282
13. L.B. Mann, J.D. Folts, *Pathophysiology*, **2004**, *10*, 105-112
14. D.M. Goldberg, B. Hoffman, J. Yang, G.J. Soleas, *J. Agr. Food Chem.*, **1999**, *47*, 3978-3985
15. D.M. Goldberg, B. Hoffman, J. Yang, G.J. Soleas, *J. Agric. Food Chem.*, **1999**, *47*, 3978-3985
16. H. Aoshima, H. Tsunoue, H. Koda, Y. Kiso, *Food Chem.*, **2004**, *52*, 5240-5244

17. A.B. Cerezo, W. Tesfaye, M.E. Soria-Diaz, M.J. Torija, E. Mateo, M.C. Garcia-Parrilla, A.M. Troncoso, *J. Food Comp. Anal.*, **2010**, *23*, 175-184
18. D. Matejicek, O. Mikes, B. Klejdus, D. Sterbova, V. Kuban, *Food Chem.*, **2005**, *90*, 791-800
19. S. Kallinthraka, M.I. Salacha, I. Tzourou, *Food Chem.*, **2009**, *113*, 500-505
20. V.T. Karathanos, C. Syrimbei, A. Chiou, A. Karathanos, D.P. Makris, *J. Food Compost. Anal.*, **2008**, *21*, 667-671
21. J.A. Avila-Reyes, N. Almaraz-Abarca, E.A. Delgado-Alvarado, L.S. Gonzalez-Valdez, G.V. Del Toro, E.D. Paramo, *Food Res. Int.*, **2010**, *43*, 296-300
22. M.R.G.B.S. Valles, Y.D. Garcia, P. Del Valle Arguelles, P.L. Lobo, *Food Sci. Biotechnol.*, **2010**, *19*, 1129-1134
23. S. Pecic, M. Veljovic, S. Despotovic, I. Leskosek-Cukalovic, M. Jadranin, V. Tesevic, M. Nikdic, Nikicevic, *Eur. Food Res. Technol.*, **2012**, *235*, 479-487
24. R.R. Madrera, D.B. Gomis, J.J.M. Alonso, *J. Agric. Food Chem*, **2003**, *51*, 7969-7973
25. J.R. Mosedale, *Forestry*, **1995**, *68*, 204-230
26. S. Canas, I. Caldeira, A.P. Belchior, *Food Chem.*, **2013**, *138*, 2460-2467
27. I. Caldeira, O. Anjos, V. Portal, A.P. Belchior, S. Canas, *Anal. Chim. Acta*, **2010**, *660*, 43-52
28. A.M. Alonso, R. Castro, M.C. Rodriguez, D.A. Guillen, C.G. Barroso, *Food Res. Int.*, **2004**, *37*, 715-721
29. W. Li, T. Beta, *Food Chem.*, **2011**, *127*, 968-975
30. N.I. Pohomaci, *Tuica and natural brandies (in Romania)*; Ed, Ceres: Bucharest, 2002.
31. D. Beceanu, M. Niculaua, *Cercetari Agronomice in Moldova*, **2009**, *XLII*, 49-61
32. D. Beceanu, M. Niculaua, I. Moraru, R.M. Anghel, *Cercetari Agronomice in Moldova*, **2010**, *XLIII*, 61-77
33. J. Tabart, C. Kevers, J. Pincemail, J.O. Defraigne, J. Dommes, *Food Chem.*, **2009**, *113*, 1226-1233
34. M.D. Rivero-Perez, M.L. Gonzalez-Sanjose, M. Ortega-Heras, P. Muniz, *Food Chem.*, **2008**, *111*, 957-964
35. T.E. Rusu Coldea, C. Socaciu, M. Parv, D. Vodnar, *Not. Bot. Horti. Agrobo.*, **2011**, *39*, 109-116
36. K. Koga, A. Taguchi, S. Koshimizu, Y. Sua, Y. Yamada, N. Shirasaka, H. Yoshizumi, *J. Food. Sci.*, **2007**, *72*, S212-S217
37. J.G. Ibanez, A. Carreon-Alvarez, M. Barcena-Soto, N. Casillas, *J. Food Compost. Anal.*, **2008**, *21*, 672-683
38. J. Dunne, D.A. Svistunenko, A.I. Alayash, M.T. Wilson, C.E. Cooper, *Adv. Exp. Med. Biol.*, **1999**, *471*, 9-15
39. C.E. Cooper, R. Silaghi-Dumitrescu, M. Rukengwa, A.I. Alayash, P.W. Buehler, *Biochim Biophys Acta*, **2008**, *1784*, 1415-20
40. B.J. Reeder, D.A. Svistunenko, C.E. Cooper, M.T. Wilson, *Antioxidant & Redox Signaling*, **2004**, *6*, 954-966
41. B.J. Reeder, M. Grey, R.L. Silaghi-Dumitrescu, D.A. Svistunenko, L. Bulow, C.E. Cooper, M.T. Wilson, *J. Biol. Chem.*, **2008**, *283*, 30780-7

42. R. Silaghi-Dumitrescu, B.J. Reeder, P. Nicholls, C.E. Cooper, M.T. Wilson, *Biochem. J.*, **2007**, *403*, 391-5
43. N.B. Vollaard, B.J. Reeder, J.P. Shearman, P. Menu, M.T. Wilson, C.E. Cooper, *Free Radic Biol. Med*. **2005**, *39*, 1216-28
44. N.B. Vollaard, B.J. Reeder, J.P. Shearman et al., *Spors Med.*, **2005**, *35*, 1045-1062
45. A.C. Mot, G. Damian, C. Sarbu, R. Silaghi-Dumitrescu, *Redox Rep.*, **2009**, *14*, 267-74
46. J.D. Tamokou, J.R. Chouna, E. Fischer-Fodor, G. Cherches, O. Barbos, G. Damian, D. Benedect, M. Duma, A.P. Efouet, H.K. Wabo, J.R. Kuiate, A. Mot, R. Silaghi-Dumitrescu, *PLoS One*, **2013**, *8*
47. E. Antonini, M. Brunori, *Hemoglobin and Myoglobin in their Reaction with Ligands*; North-Holland: Amsterdam, 1971

STUDIA UBB CHEMIA, LX, 2, Tom II, 2015 (p. 371-378)
(RECOMMENDED CITATION)

SYNTHESIS OF NEW BENZOTHIAZOLYL-PHENOTHIAZINE DERIVATIVES

BALASZ BREM[a], EMESE GAL[a], CASTELIA CRISTEA[a], LUIZA GĂINĂ[a], ADRIANA GROZAV[b,*], VALENTIN ZAHARIA[b] AND LUMINIŢA SILAGHI-DUMITRESCU[a]

ABSTRACT. A series containing 1-, 2-, 3- and 4-(benzothiazol-2yl)-10*H*phenothiazine derivatives was advantageously prepared by the condensation of each corresponding phenothiazine-carbaldehyde regioisomer with 2-amino-benzenethiol. The reaction conditions were optimized and the structures of the new compounds were unambiguously assigned based on high resolution nuclear magnetic resonance spectroscopy and mass spectrometry.

***Key words**: phenothiazine, benzothiazole, NMR*

INTRODUCTION

Benzothiazole derivatives consisting of a cumulative structural motif formed by the 5-membered heteroaromatic ring, the fused benzene unit and diverse substituents attached in various positions (especially mercapto groups) already found important industrial applications in anti-oxidant formulations, components in metal finishing liquors [1], vulcanization accelerators in the rubber industry [2] and fungicides [3]. Various 2-substituted benzothiazoles (2-aryl benzothiazole) received much attention due to potential uses as imagining agents [4] and anticancer agents [5].

Several procedures were developed for the synthesis of benzothiazoles (scheme 1). One method involves the condensation of 2-aminothiophenols with carboxylic acids [6] or aldehydes [7, 8] respectively, under oxidative conditions (reported oxidants: bromine, iodine, quinine, metal salts). Another method involves the transition-metal-catalyzed intramolecular cyclization of thioanilides [9]. Most

[a] *"Babes-Bolyai" University, Faculty of Chemistry and Chemical Engineering, RO-400028, Cluj-Napoca, Romania*
[b] *"Iuliu Haţieganu" University of Medicine and Pharmacy, Faculty of Pharmacy, RO-400012, Victor Babes 41, Cluj-Napoca, Romania*
** Corresponding author: adriana.ignat@umfcluj.ro*

efforts were focused on noble metal catalysts, such as Ru, Rh, Pd, but the iron-catalysed [10] synthesis may benefit from the low toxicity and large availability of iron derivatives. Metal-free methods starting from alkyl amines [11] or aryl ketones [12] at high temperature under oxidative conditions were also reported. The third method involves the condensation of 2-aminothiophenols with β-ketonitriles [13], β-ketoesters [14] or β-diketones [15] under microwave activation at high temperature or in the presence of catalytic ammounts of Bronsted acids.

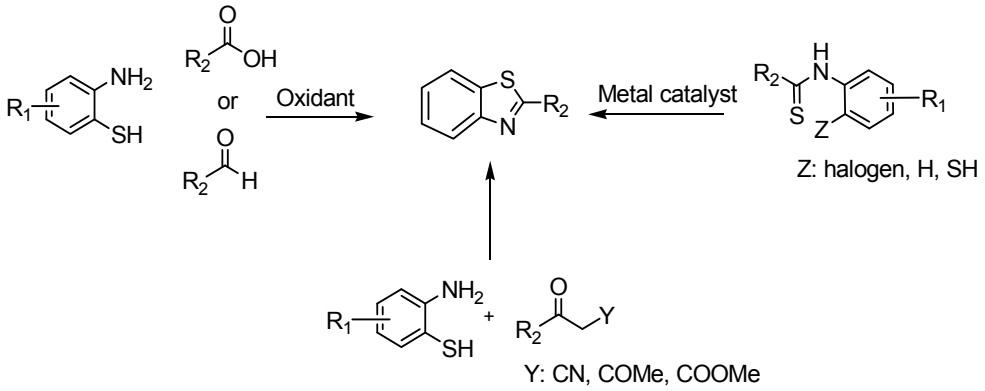

Scheme 1

Continuing our investigations dedicated to the synthesis of new polyheteroaromatic structures containing phenothiazine and thiazole units assembled in the same molecular structure [16], in this work we described an advantageous procedure for the synthesis of new derivatives with joint phenothiazine and thiazole units.

RESULTS AND DISCUSSIONS

The synthetic strategy applied in this work is based on the condensation of aldehydes with o-aminobenzenethiols under thermal activation conditions. A series of benzothiazolyl-phenothiazine derivatives was prepared starting with a phenothiazine-carbaldehyde derivative (10*H*-phenothiazin-1-carbaldehyde, 10-methyl-10*H*-phenothiazin-1-, 2-, 3-, and 4-carbaldehyde regioisomers, 10-methyl-7-bromo-10*H*-phenothiazin-3-carbaldehyde and 10-methyl-10*H*-phenothiazin-3,7-dicarbaldehyde respectively) and *ortho*-aminobenzenethiol which were severely heated in DMSO solvent (Scheme 2). No other oxidant was required when working-up in the presence of atmospheric oxygen.

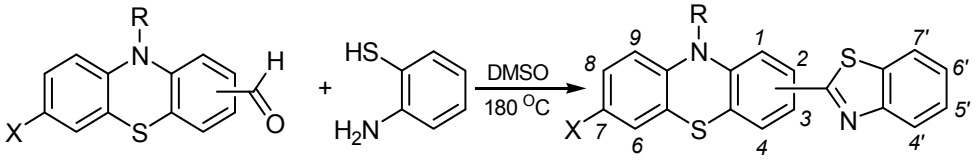

R = -H, -CH_3
X = -H, -CHO, -Br

1 *1*-thiazolyl, R=H, x= H
2 *1*-thiazolyl, R=CH_3, x= H
3 *2*-thiazolyl, R=CH_3, x= H
4 *3*-thiazolyl, R=CH_3, x= H
5 *4*-thiazolyl, R=CH_3, x= H
6 *3*-thiazolyl, R=CH_3, x= Br
7 *3*-thiazolyl, R=CH_3, x=thiazolyl

Scheme 2

This convenient procedure gave satisfactory yields even in the case of sterically hindered substrates such as 10-methyl-10*H*-phenothiazin-1-carbaldehyde or 10*H*-phenothiazin-1-carbaldehyde Best yields were obtained in the preparation of 2-benzotiazolyl-phenothiazine. The products are stable crystalline compounds with a yellow colour.

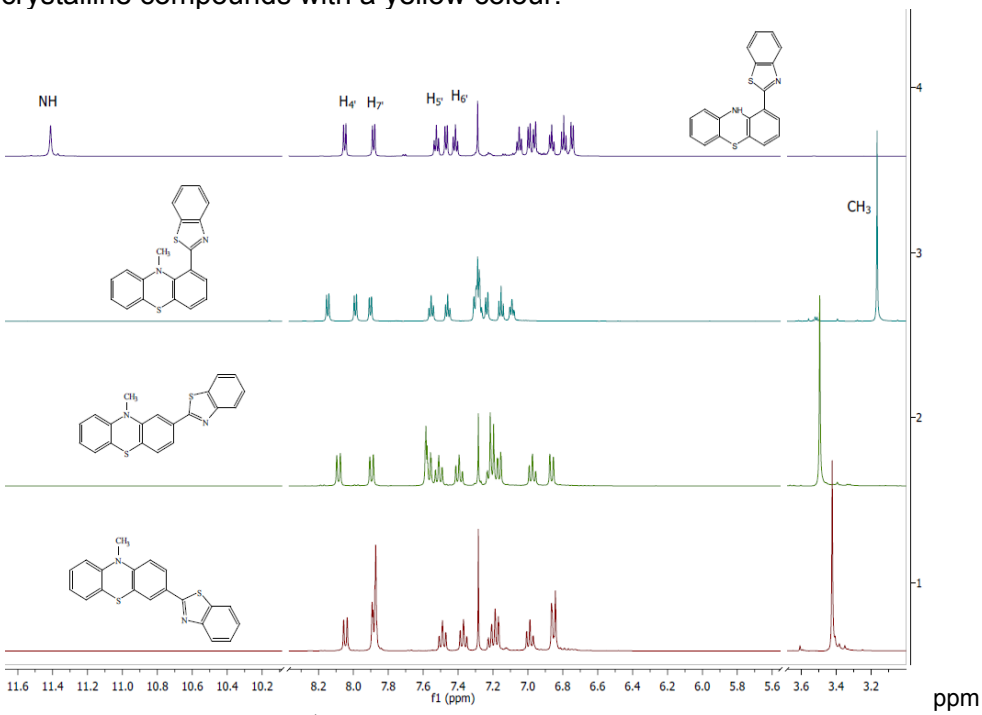

Figure 1. 600 MHz ^{1}H-NMR spectra of benzothiazol-2yl-phenothiazine regioisomers in $CDCl_3$

The structures of the new compounds were unambiguously assigned based on HRMS and NMR spectroscopic data. 2D-NMR 1H-1H homocorrelation and ^{1}H-^{13}C-heterocorrelation experiments were performed in order to completely assign the signals of the nuclei present in the two heterocyclic units. As it may be seen from figure 1 which collectively presents the ^{1}H-NMR spectra of the series of regioisomers **1-5**, the benzothiazolyl moiety is responsible for generating the most deshielded signals, accompanied by the protons of the phenothiazine unit situated in the closest neighboring position. An inspection of the chemical shifts recorded in the case of sterically hindered structures **1** and **2** suggest a preferred bisectional orientation of the benzothiazolyl substituent in respect to the aromatic ring of the phenothiazine unit. The ring current of the benzothiazolyl unit induces a magnetic anisotropy observable in the chemical shifts of the substituents situated in the *peri* position (a deshielding of the NH signals in **1** and a shielding of $-CH_3$ signals in **2** respectively).

CONCLUSIONS

A convenient procedure for the preparation of new heteroaromatic compounds with joint phenothiazine and thiazole units was developed based on thermal activated condensation of *ortho*-aminobenzenethiol with phenothiazine carbaldehydes.

EXPERIMENTAL SECTION

HRMS spectra were recorded using Thermo LTQ *Orbitrap XL* mass spectrometer.

NMR spectra were recorded at room temperature on 400 or 600 MHz Bruker Avance instruments. Chemical shifts are expressed in δ (ppm) relative to standard tetramethylsilane (TMS).

O-amino-benzenethiol was purchased from Sigma_Aldrich.

Phenothiazine carbaldehydes were prepared according to previously reported procedures.

General procedure for the synthesis of benzothiazol-2yl-phenothiazine derivatives

Ortho-Aminobenzenethiol (4mmol, 0.5g) and the corresponding phenothiazinyl aldehyde (4mmol) dissolved in 50 ml DMSO were heated at 180 ^{o}C on oil bath for 6 h. After cooling down to room temperature, the mixture was poured in water and extracted with ethyl acetate. The

organic phase was dried over Mg_2SO_4 and the solvent was removed under vacuum. The residue was purified by recrystallisation from ethanol or by column chromatography (eluent toluene).

1-(benzo[d]thiazol-2-yl)-10H-phenothiazine (1)
Purification by flash chromatography, gave 0.9 g, 68 % as orange solid.

HRMS (ESI+): $[M+H^+]$ found 333.0454, $C_{13}H_{13}N_2S$ requires 333.0515.

^{1}H-NMR (600MHz, $CDCl_3$): δ (ppm) = 6.72 (d, 1H, H_9, ^3J =7.62Hz), 6.76 (t, 1H, H_7, ^3J = 7.8 Hz), 6.83 (t, 1H, H_8, ^3J = 7.2 Hz), 6.93 (d, 1H, H_4, ^3J = 7.62Hz), 6.96 (d, 1H, H_6, ^3J =7.44 Hz), 7.02 (td, 1H, H_3, ^3J = 7.8 Hz, ^4J = 0.9 Hz), 7.39 (t, 1H, $H_{6'}$, ^3J = 7.44 Hz), 7.44 (dd, 1H, H_2, ^3J =7.86Hz, ^4J = 0.66Hz), 7.49 (t, 1H, $H_{5'}$, ^3J = 7.32 Hz), 7.85 (d, 1H, $H_{7'}$, ^3J =8.1 Hz), 8.01 (d, 1H, $H_{4'}$, ^3J =8.1 Hz), 11.38 (s, 1H, NH)

^{13}C-NMR (125 MHz, $CDCl_3$): δ (ppm) = 115.5 (C_q, C_1), 115.8 (C_H, C_7), 117.7 (C_q, C_{4a}), 120 (C_q, C_{5a}), 121.1 (C_H, $C_{4'}$), 121.3 (C_H, C_7), 122.6 (C_H, $C_{7'}$), 123 (C_H, C_8), 125.5 (C_H, C_6), 126.4 (C_H, $C_{6'}$), 127.5 (C_H, C_2), 128.2 (C_H, C_6), 128.5 (C_q, C_3), 133.2 (C_q, $C_{7a'}$), 140.8 (C_q, C_{9a}), 141.7 (C_q, C_{10a}), 153 (C_q, $C_{4a'}$), 168.3 (C_q, $C_{2'}$);

1-(benzo[d]thiazol-2-yl)-10-methyl-10H-phenothiazine (2)
Purification by recrystallisation, gave (0.8g, 58 %) as orange solid.

HRMS (ESI+): $[M+H^+]$ found 347.0611, $C_{13}H_{13}N_2S$ requires 347.0671.

^{1}H-NMR (600MHz, $CDCl_3$): δ (ppm) = 3.16 (s, 3H, N-CH_3), 7.09 (td, 1H, H_4,^3J = 8 Hz, ^4J = 1.74 Hz), 7.15 (t, 1H, H_3, ^3J = 7.7 Hz), 7.23 (d, 1H, H_9, ^3J =7.56Hz), 7.26-7.31 (m, 3H, H_8, H_7, H_6), 7.45 (t, 1H, $H_{6'}$, ^3J = 7.5 Hz), 7.55 (t, 1H, $H_{5'}$, ^3J = 7.5 Hz), 7.90 (dd, 1H, H_2, ^3J = 7.68 Hz, ^4J = 1 Hz), 7.99 (d, 1H, $H_{7'}$, ^3J = 8 Hz), 8.15 (d, 1H, $H_{4'}$, ^3J = 8.1 Hz);

^{13}C-NMR (125 MHz, $CDCl_3$): δ (ppm) = 43.3 (CH_3, **C_a**), 121 (C_H, **C_7**), 121.6 (C_H, **$C_{7'}$**), 123.3 (C_H, **$C_{4'}$**), 124.3 (C_H, **C_3**), 124.6 (C_H, **C_4**), 125.4 (C_H, **$C_{6'}$**), 126.2 (C_H, **$C_{5'}$**), 126.9 (C_H, **C_9**), 127 (C_q, **C_{4a}**), 127.7 (C_H, **C_8**), 128.7 (C_H, **C_6**), 128.8 (C_q, **C_{5a}**), 129.8 (C_H, **C_2**), 132.8 (C_q, **C_1**); 136.4 (C_q, **$C_{7a'}$**), 144 (C_q, **C_{9a}**), 147 (C_q, **C_{10a}**), 152.8 (C_q, **$C_{4a'}$**), 165.5 (C_q, **$C_{2'}$**);

2-(benzo[d]thiazol-2-yl)-10-methyl-10*H*-phenothiazine (3)
Purification by recrystallisation, gave 1.1 g, 81 % as yellow solid.

HRMS (ESI+): $[M+H^+]$ found 347.0616, $C_{13}H_{13}N_2S$ requires 347.0671.

^{1}H-NMR (400MHz, $CDCl_3$): δ (ppm) = 3.47 (s, 3H, N-CH_3), 6.84 (d, 1H, H_9, ^3J = 7.8 Hz), 6.95 (td, 1H, H_3, ^3J = 7.48 Hz, ^4J = 0.8 Hz), 7.14 (dd, 1H, H_6, ^3J = 7.6 Hz, ^4J = 1.3 Hz), 7.17-7.21 (m, 2H, H_4, H_8), 7.37 (td, 1H, $H_{6'}$, ^3J = 8 Hz, ^4J = 0.9 Hz), 7.48 (td, 1H, $H_{5'}$, ^3J = 8.2 Hz, ^4J = 1 Hz), 7.53-7.56 (m, 2H, H_1, H_7), 7.87 (d, 1H, $H_{7'}$, ^3J = 8 Hz), 8.06 (d, 1H, $H_{4'}$, ^3J = 8.2 Hz);

^{13}C-NMR (100 MHz, $CDCl_3$): δ (ppm) = 35.6 (CH_3, C_a), 112.2 (C_H, C_1), 114.4 (C_H, C_9), 121.6 (C_H, $C_{7'}$), 122 (C_H, C_7), 122.6 (C_H, C_{4a}), 122.8 (C_H, C_3), 123.1 (C_H, $C_{4'}$), 125.3 (C_H, $C_{5'}$), 126.4 (C_H, $C_{6'}$), 127.2 (C_H, C_1), 127.3 (C_H, C_6), 127.5 (C_q, C_{5a}), 127.8 (C_H, C_8), 132.9 (C_q, C_2), 135 (C_q, $C_{7a'}$), 145.3 (C_q, C_{9a}), 146.4 (C_q, C_{10a}), 154.1 (C_q, $C_{4a'}$), 167.8 (C_q, $C_{2'}$);

3-(benzo[d]thiazol-2-yl)-10-methyl-10H-phenothiazine (4)

Purification by recrystallisation, gave 0.9 g, 65 % as yellow solid (m.p. = 160-161^{o}C).

HRMS (ESI+): [M+H$^+$] found 347.0610, $C_{13}H_{13}N_2S$ requires 347.0671.

^{1}H-NMR (400MHz, $CDCl_3$): δ (ppm) = 3.39 (s, 3H, N-CH_3), 6.82 (d, 2H, H_9, H_1,^3J = 8.2 Hz), 6.95 (td, 1H, H_7, ^3J = 7.4 Hz, ^4J = 0.8 Hz), 7.14-7.20 (m, 2H, H_8, H_6), 7.34 (td, 1H, $H_{6'}$, ^3J = 8 Hz, ^4J = 0.84 Hz), 7.46 td, 1H, $H_{5'}$, ^3J = 8.2 Hz, ^4J = 1 Hz), 7.84-7.86 (m, 3H, $H_{7'}$, H_2, H_4), 8.02 (d, 1H, $H_{4'}$, ^3J = 8 Hz);

^{13}C-NMR (100 MHz, $CDCl_3$): δ (ppm) = 35.6 (CH_3, C_a), 114.1 (C_H, C_1), 114.5 (C_H, C_9), 121.6 (C_H, $C_{7'}$), 122,7 (C_q, C_{4a}), 122.9 (C_H, C_7), 123.1 (C_H, $C_{4'}$), 124.2 (C_q, C_{5a}), 124.9 (C_H, C_2), 125.96 (C_H, $C_{5'}$), 126.4 (C_H, $C_{6'}$), 127.1 (C_H, C_1), 127.36 (C_H, C_6); 127.7 (C_H, C_8), 128 (C_q, C_3), 134.9 (C_q, $C_{7a'}$), 144.8 (C_q, C_{9a}), 148.2 (C_q, C_{10a}), 154.2 (C_q, $C_{4a'}$), 167.1 (C_q, $C_{2'}$);

4-(benzo[d]thiazol-2-yl)-10-methyl-10*H*-phenothiazine (5)

Purification by recrystallisation, gave 0.8 g, 60 % as yellow solid.

HRMS (ESI+): [M+H$^+$] found 347.0615, $C_{13}H_{13}N_2S$ requires 347.0671.

^{1}H-NMR (400MHz, $CDCl_3$, ppm): δ (ppm) = 3.15 (s, 3H, N-CH_3), 6.57 (d, 1H, H_9, ^3J = 8 Hz), 6.63 (t, 1H, H_7, ^3J = 7.5 Hz), 6.68 (d, 1H, H_1, ^3J = 8.04 Hz), 6.8 (d, 1H, H_6, ^3J = 7.3 Hz), 6.92 (m, 1H, H_8), 7.01 (t, 1H, H_2, ^3J = 8 Hz), 7.18 (m, 2H, $H_{6'}$, H_3), 7.29 (m, 1H, $H_{5'}$), 7.7 (d, 1H, $H_{7'}$, ^3J = 7.92 Hz), 7.89 (d, 1H, $H_{4'}$, ^3J = 8.08 Hz);

^{13}C-NMR (100 MHz, $CDCl_3$): δ (ppm) = 35.3 (CH_3, C_a), 113.5 (C_H, C_9), 115.5 (C_H, C_1), 121 (C_H, $C_{7'}$), 122 (C_H, C_7), 122.9 (C_H, $C_{4'}$), 123.2 (C_q, C_{4a}), 123.7 (C_H, $C_{6'}$), 124.9 (C_q, C_{5a}), 125.7 (C_H, C_3), 126.5 (C_H, $C_{5'}$), 127.2 (C_H, C_6), 127.6 (C_H, C_2); 128.4 (C_H, C_8), 131 (C_q, $C_{7a'}$), 135 (C_q, C_4), 145.9 (C_q, C_{9a}), 145.95 (C_q, C_{10a}), 152.8 (C_q, $C_{3a'}$), 164.8 (C_q, $C_{2'}$);

3-(benzo[d]thiazol-2-yl)-7-bromo-10-methyl-10H-phenothiazine (6)

Purification by recrystallisation, gave 1.1 g, 68 % as greenish-yellow solid.

HRMS (APCI$^+$): [M+H$^+$] found 426.9755, $C_{20}H_{14}N_2S_2Br$ requires 424.9776.

^{1}H NMR (400MHz, $CDCl_3$): δ (ppm) = 3.38 (s, 3H, N-CH_3), 6.71 (d, 1H, H_9, ^3J = 9.24 Hz), 6.89 (d, 1H, H_1, ^3J = 8.5 Hz), 7.23-7.26 (m, 2H, H_6, H_8), 7.36 (t, 1H, $H_{6'}$, ^3J = 6.24 Hz), 7.47 (t, 1H, $H_{5'}$, ^3J = 7.3 Hz), 7.81-7.85 (m, 2H, H_2, H_4), 7.87 (d, 1H, $H_{7'}$,^3J = 8.2 Hz), 8.02 (d, 1H, $H_{4'}$,^3J = 8.2 Hz);

^{13}C NMR (100 MHz, $CDCl_3$): δ (ppm) = 35.7 (CH_3), 114.3 (C_H, C_1), 115.4 (C_q, C_7), 115.6 (C_H, C_9), 121.6 (C_H, $C_{7'}$), 123 (C_H, $C_{4'}$), 125 (C_q, C_{4a}), 125.1 (C_H, $C_{6'}$), 126 (C_H, C_4), 126.4 (C_H, $C_{5'}$), 127.3 (C_H, C_2), 128.4 (C_q, C_{5a}), 129.5 (C_H, C_6); 130.4 (C_H, C_8), 134.9 (C_q, C_3), 144.1 (C_q, $C_{7a'}$), 147.7 (C_q, C_{9a}), 154.2 (C_q, $C_{3a'}$), 166.9 (C_q, $C_{2'}$);

3,7-bis(benzo[d]thiazol-2-yl)-10-methyl-10*H*phenothiazine (7)
Purification by recrystallisation, gave 0.6 g, 63 % as yellow solid.

HRMS (APCI$^+$): [M+H$^+$] found 480.0653, $C_{27}H_{18}N_3S3$ requires 480.0653.

^{1}H-NMR (400MHz, $CDCl_3$): δ (ppm) = 3.42 (s, 3H, N-CH_3), 6.93 (d, 2H, H_1, H_9, ^3J = 8.32 Hz), 7.36 (t, 2H, $H_{6'}$, ^3J = 7.6 Hz), 7.48 (t, 2H, $H_{5'}$, ^3J = 7.6 Hz), 7.81-7.86 (m, 4H, H_2, H_4), 7.88 (d, 2H, $H_{7'}$, ^3J = 8.2 Hz), 8.03 (d, 2H, $H_{4'}$, ^3J = 8.2 Hz);

^{13}C-NMR (100 MHz, $CDCl_3$): δ (ppm) = 35.5 (CH_3, C_a), 114.9 (C_H, C_9), 121.5 (C_H, C_a), 122.8 (C_H, $C_{7'}$), 123.9 (C_H, C_7), 124.9 (C_q, C_{4a}), 126 (C_H, $C_{4'}$), 126.3 (C_H, $C_{5'}$), 126.9 (C_H, $C_{6'}$), 128.3 (C_q, C_3), 134.7 (C_q, $C_{7a'}$), 145.9 (C_q, C_{9a}), 154 (C_q, $C_{3a'}$), 166.7 (C_q, $C_{2'}$).

ACKNOWLEDGMENTS

This paper was published under the frame of European Social Found, Human Resources Development Operational Programme 2007-2013, project no. POSDRU/159/1.5/S/136893" (A. Grozav) and also contains results of a doctoral research made possible by the financial support of the Sectoral Operational Programme for Human Resources Development 2007-2013, co-financed by the European Social Fund, under the project POSDRU/159/1.5/S/ 132400 -"Young successful researchers – professional development in an international and interdisciplinary environment" (B. Brem).

REFERENCES

1. J.K. Reichert, J. Lochtman, R. Miiller, I. Kanen, *Jahrestagung der FG Wasserchemie in der GdCh, Badenweiler*, **1993**.
2. R.B. Spies, B.D. Andresen and D.W. Rice Jr., *Nature*, **1987**, *327*, 697.

3. I. Liska, E.R. Brouwer, A.G.L. Ostheimer, H. Lingeman, U.A.T. Brinkman, R.B. Geerdink and W.H. Mulder, *Int. J. Environ. Anal. Chem.*, **1992**, *47*, 267.
4. P. Reddy, Y. Lin, H. Chang, *Arcivoc.,* **2007**, *XVI*, 113.
5. Y. Heo, Y. Song, B. Kim, J. Heo, *Tetrahedron Lett.,* **2006**, *47,* 3091.
6. (a) H. Sharghi, O. Asemani, *Synth. Commun*., **2009**, *39*, 860. (b) X. Wen, J. El Bakali, R. Deprez-Poulain, B. Deprez, *Tetrahedron Lett.,* **2012**, *53*, 2440. (c) V.K. Tandon, M. Kumar, *Tetrahedron Lett.* **2004**, *45*, 4185. (d) K. Yamamoto, H. Watanabe, *Chem. Lett.* **1982**, 1225.
7 (a) A.J. Blacker, M.M. Farah, M.I. Hall, S.P. Marsden, O. Saidi, J.M. Williams, *J. Org. Lett.,* **2009**, *11*, 2039. (b) C. Mukhopadhyay, P.K. Tapaswi, *Tetrahedron Lett.,* **2008**, *49*, 6237. (c) M.A. Chari, D. Shobha, T. Sasaki, *Tetrahedron Lett.,* **2011**, *52*, 5575. (d) S.S. Patil, V.D. Bobade, *Synth. Commun*., **2010**, *40*, 206. (e) S.M. Inamdar, V.K. More, S.K. Mandal, *Tetrahedron Lett.,* **2013**, *54*, 579.
8. S.P.G. Costa, A.M.F. Oliveira-Campos, J.A. Ferreira, G. Kirsch, *J. Chem. Res. (S)*, **1997**, 314, *J. Chem. Res.* (M), **1997**, *9,* 2001.
9. (a) P. Saha, T. Ramana, N. Purkait, A.M. Ashif, R. Paul, T.J. Punniyamurthy, *Org. Chem.,* **2009**, *74*, 8719. (b) G. Evindar, R.A. Batey, *J. Org. Chem*., **2006**, *71*, 1802. (c) D. Yang, H. Fu, L. Hu, Y. Jiang, Y. Zhao, *J. Org. Chem.,* **2008**, *73*, 7841. (d) J. Peng, M. Ye, C. Zong, F. Hu, L. Feng, X. Wang, Y. Wang, C. Chen, *J. Org. Chem.,* **2011**, *76*, 716. (e) E.A. Jaseer, D.J.C. Prasad, A. Dandapat, G. Sekar, *Tetrahedron Lett.,* **2010**, *51*, 5009. (f) T. Itoh, T. Mase, *Org. Lett.,* **2007**, *9*, 3687. (g) D. Ma, S. Xie, P. Xue, X. Zhang, J. Dong, Y. Jiang, *Angew. Chem., Int. Ed.,* **2009**, *48*, 4222.
10. H. Wang, L. Wang, J. Shang, X. Li, H. Wang, J. Guia, A. Leiab, *Chem. Commun.,* **2012**, *48,* 76.
11. T.B. Nguyen, L. Ermolenko, W.A. Dean, A. Al-Mourabit, *J. Org. Lett*., **2012**, *14*, 5948.
12. Y. Liao, H. Qi, S. Chen, P. Jiang, W. Zhou, G. Deng, *J. Org.Lett.,* **2012**, *14*, 6004.
13. K. Sukanta, B. Koh, E.R. Biehl, *J. Heterocycl.Chem.,* **2006**, *43*, 1609.
14. (a) K. Sukanta, H. Zhang, E.R. Biehl, *Heterocycles,* **2005**, *65*, 2119.(b) L. Cai, X. Ji, Z. Yao, F. Xu, Q. Shen, *Chin. J. Chem.*, **2011**, *29*, 1880.
15. (a) Z.-X. Wang, H.-L. Qin, *J. Heterocycl. Chem.,* **2005**, *42*, 1001. (b) M.S. Mayo, X. Yu, X. Zhou, X. Feng, Y. Yamamoto, M. Bao, *Org. Lett*., **2014**, *16*, 764.
16. A. Ignat, T. Lovasz, M. Vasilescu, E. Fischer-Fodor, C.B. Tatomir, C. Cristea, L. Silaghi-Dumitrescu, V. Zaharia, *Arch. Pharm. Chem. Life Sci.,* **2012**, *345*, 574.

STUDIA UBB CHEMIA, LX, 2, 2015 (p. 379-388)
(RECOMMENDED CITATION)

CELL@CELL HIGHER DIMENSIONAL STRUCTURES

ATENA PARVAN-MOLDOVAN[a] AND MIRCEA V. DIUDEA[a*]

ABSTRACT. Local domains of *n*-spaces surrounded by the common Euclidean 3D-space may exist in complex chemical (mineral or synthetic) structures. In this paper, two classes of the simplest clusters embedded in n-dimensional spaces higher than three are designed by operations on maps and their properties discussed.

Keywords: *graph, n-dimensional space, n-cube, torus, cluster*

INTRODUCTION

The gravitational theory (general relativity) describes our universe having the geometry of three-dimensional space with the fourth-dimension being the time. The so-called 3 + 1 space gives an accurate description of the universe we observe. A stellar black hole is believed to be formed by the gravitational collapse of a massive star (from five to several tens of the solar mass). Understanding the universe led us to the need of learning about spaces of dimensions higher than three. The aim of finding domains of *n*-spaces surrounded by the common Euclidean 3D-space, in complex chemical (mineral or synthetic) structures promoted our efforts towards a systematic design of n-dimensional hyper-structures. Let, for the beginning, introduce to some basic mathematical notions.

A ***convex hull*** (envelope) [1-3] of a set *X* of points in the Euclidean space is the smallest convex set that contains *X*. A set of points is called convex if it contains all the line segments connecting each pair of its points. The convex hull of a finite set *S* of points is the set of all its convex combinations; in a convex combination, each point x_i is weighted by a coefficient α_i such that the coefficients are all non-negative and their sum is one. For each choice of coefficients, the resulting convex combination is a point in the convex hull, and the whole convex hull can be generated by choosing coefficients in all possible ways. One can write the convex hull as the set:

[a] *Department of Chemistry, Faculty of Chemistry and Chemical Engineering, Babes-Bolyai University, 400028 Cluj, Romania*
** Corresponding author: diudea@chem.ubbcluj.ro*

$$\left\{ \sum_{i=1}^{|S|} \alpha_i x_i \mid (\forall_i : \alpha_i \geq 0) \wedge \sum_{i=1}^{|S|} \alpha_i = 1 \right\} \quad (1)$$

The convex hull of a finite point set $S \in \mathbf{R}^n$ forms a convex polygon, for n = 2, or, in general, a convex polytope in $\mathbf{R}^n$. Every convex polytope in $\mathbf{R}^n$ is the convex hull of its vertices.

There are six regular 4D-polytopes, also called polychora: 5-Cell {3,3,3}; 8-Cell {4,3,3}; 16-Cell {3,3,4}; 24-Cell {3,4,3}; 120-Cell {5,3,3} and 600-Cell {3,3,5}. Five of them can be associated to the Platonic solids but the sixth, the 24-cell has no close 3D equivalent; it consists of 24 octahedral cells, 6 cells meeting at each vertex. Among them, 5-Cell and 24-Cell are self-cage-dual while the others are pairs: (8-Cell & 16-Cell); (120-Cell & 600-Cell). In the above, {p, q, r,…} are the Schläfli symbols: the symbol {p} denotes a regular polygon for integer p, or a star polygon for rational p; the symbol {p, q} denotes a 3D-object tessellated by p-gons while q is the vertex-figure (i.e. the number of p-gons surrounding each vertex); the symbol {p, q, r} describes a 4D-structure, in which r 3D-objects join at any edge (r being the edge-figure) of the polytope, and so on. The Schläfli symbol has the nice property that its reversal gives the symbol of the dual polyhedron. The 4D polytopes have been first described by Schläfli [4].

In dimensions 5 and higher, there are only three kinds of convex regular polytopes no non-convex regular polytopes exists. Let us give some details, in the following.

The ***n-simplex***[1], with Schläfli symbol {3^{n-1}}, and the number of its k-faces $\binom{n+1}{k+1}$, is a generalization of the triangle or tetrahedron to arbitrary dimensions. A simplex is an n-dimensional polytope, which h is the convex hull of its n+1vertices. For example, a 0-simplex is a point, a 1-simplex is a line segment, a 2-simplex is a triangle, a 3-simplex is a tetrahedron, and a 4-simplex is a 5-cell. A simplex may be defined as the smallest convex set containing the given vertices. A regular n-simplex may be constructed from a regular (n − 1)-simplex by connecting a new vertex to all original vertices by the common edge length.

The convex hull of any nonempty subset of k+1 points that define an n-simplex is called a *face* of the simplex; faces are simplexes themselves. In particular, the convex hull of a subset of size k+1 (of the n+1 defining points) is a k-simplex and is called a k-face of the n-simplex. The 0-faces (i.e., the points themselves) are called the *vertices*, the 1-faces are called the *edges*, the (n − 1)-faces are called the *k-faces* (or *facets)*, and the sole n-face is the whole n-simplex itself.

The ***hypercube*** [1] is a generalization of the 3-cube to *n*-dimensions; it is also called an *n*-cube and commonly denoted Q_n. It is a regular polytope with mutually perpendicular sides, thus being an orthotope. It has the Schläfli symbol $\{4,3^{n-2}\}$ and k-faces given by $2^{n-k}\binom{n}{k}$. Figure 1 illustrates the 4-cube, i.e., 8-Cell or Tesseract, as painted by the Italian painter Juseppe Zaccuri, Milano.

Figure 1. HyperCube by Juseppe Zaccuri, Milano

The ***n-orthoplex* or cross-polytope** [1] has the Schläfli symbol $\{3^{n-2},4\}$ and k-faces $2^{k+1}\binom{n}{k+1}$; it exists in any number of dimensions and is the dual of *n*-cube. The cross-polytope is the convex hall of its vertices; its facets are simplexes of the previous dimensions, while its vertex figures are other cross-polytopes of lower dimensions.

To investigate an *n*-dimensional polytopes, a formula, also due to Schläfli [4], is used

$$\sum_{i=0}^{n-1}(-1)^i f_i = 1-(-1)^n \tag{2}$$

For n=4, eq (2) reduces to the well-known Euler [5] relation

$$v-e+f=2(1-g) \tag{3}$$

with *v*, *e*, *f* and *g* being the vertices, edges, 2-faces and the genus, respectively; *g*=0 for the sphere and *g*=1 for the torus.

RESULTS AND DISCUSSION

The n-dimensional spaces may be locally present in minerals or artificial chemicals [6]. Some 4-dimensional 13-atom clusters: MaMb12 or M13, M=Fe, Pd, Ru, Rh was found to show giant magnetic moments [7]. Other simple molecules as B4Cl4, $Co(CO)_4^-$, etc. may be described in dimensions higher than three. In this respect, two simplest classes of clusters showing dimensionality higher than three will be introduced as follows.

P-Centered Clusters

Body centered clusters derived from the Platonic solids are easily drawn, as shown in Figure 2; their figure count is given in Table 1. These small clusters, excepting DoP.21, were next transformed by operations on maps [8-10] in their 2-dual, medial (i.e. rectified) and truncated derivatives (Figures 3 to 6). P-centered clusters represent cell-duals of polyhedra with the same number of cells around a central one; they are objects of Euclidean 4D-space, as shown by the figure count (Tables 2 to 5) cf. eq (2). This idea can be extended to objects other than Platonics.

The name of clusters can be made in at least three ways, as shown in the bottom of figures and tables; the “endohedral” @ symbol was used, starting from the core and going radially, to the exterior, the suffix number counting the points/atoms in the whole structure.

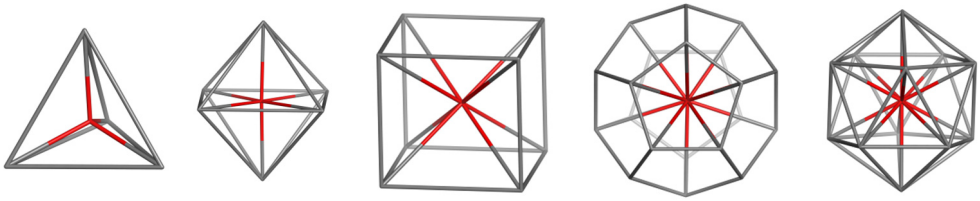

TP.5	OctP.7	CP.9	DoP.21	IcoP.13
P@T.5	P@Oct.7	P@C.9	P@Do.21	P@Ico.13
P@T4@T.5	P@T8@Oct.7	P@(Py4)6@C.9	P@(Py5)12@Do.21	P@T20@Ico.13

Figure 2. Body centered clusters derived from the Platonic solids

Table 1. Figure count for clusters in Figure 2

Cluster	v	e	f_3	f_5	f_6	f	p1	p2	p3	M	c	Sum(f)	Sym	p_k; (M)
TP	5	10	10	0	0	10	4	0	0	1	5	0	3	T; 0; 0 (T)
OctP	7	18	20	0	0	20	8	0	0	1	9	0	4	T;0;0 (Oct)
CP	9	20	12	6	0	18	0	6	0	1	7	0	4	0;Py4; 0 (C)
DoP	21	50	30	0	12	42	0	12	0	1	13	0	5	0;Py5;0 (Do)
Icop	13	42	50	0	0	50	20	0	0	1	21	0	5	T; 0; 0 (Ico)

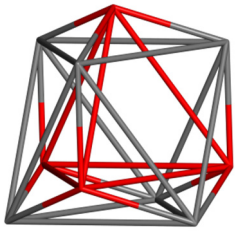

Du(TP).10
T@Oct.10

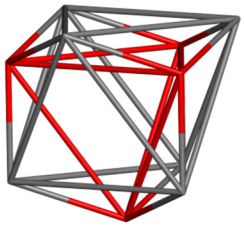

Med(TP).10
T@Oct.10

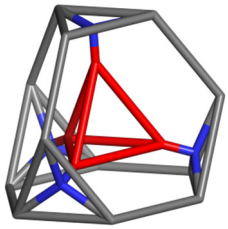

Tr(TP).20
T@(TT4;T4)@TT.20

Figure 3. TP-derived structures

Table 2. Figure count for clusters derived from TP cluster

T-structure	v	e	f_3	f_5	f_6	f	p1	p2	p3	M	c	Sum(f)	Sym	p_K; (M)
TP.5	5	10	10	0	0	10	4	0	0	1	5	0	3	T; 0; 0 (P; T)
Du(TP).10	10	30	30	0	0	30	4	4	0	2	10	0	3	T; Oct= AP_3; 0 (T;Oct)
Med(TP).10	10	30	30	0	0	30	4	4	0	2	10	0	3	T; Oct= AP_3; 0 (T;Oct)
Tr(TP).20	20	40	20	0	10	30	4	4	0	2	10	0	3	T;TT; 0 (T; TT)

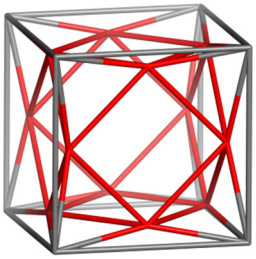

Du(OctP).20
CO@((AP4)6;T8)@C.20

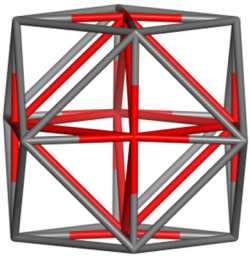

Med(OctP).18
Oct@(Oct8;(Py4)6)@CO.18

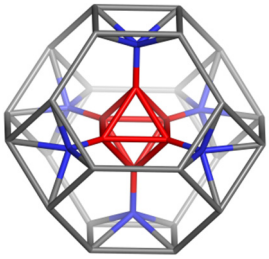

Tr(OctP).36
Oct@(TT8;(Py4)6)@TO.36

Figure 4. OctP-derived structures

Table 3. Figure count for clusters derived from OctP cluster

Oct-structure	v	e	f_3	f_5	f_6	f	p_1	p_2	p_3	M	c	Sum(f)	Sym	p_K; (M)
OctP.7	7	18	20	0	0	20	8	0	0	1	9	0	4	T;0;0 (P;Oct)
Du(OctP).20	20	60	44	12	0	56	8	6	0	2	16	0	4	T;Ap4;0 (CO;C)
Med(OctP).18	18	60	52	6	0	58	8	6	0	2	16	0	4	Oct; Py4 (Oct; CO)
Tr(OctP).36	36	78	32	6	20	58	8	6	0	2	16	0	4	TT;Py4;0 (Oct;TO)

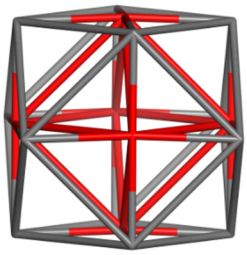

Du(CP).18
Oct@(Oct8;(Py4)6)@CO.18

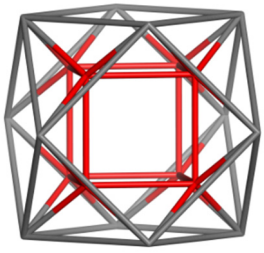

Med(CP).20
C@((AP4)6;T8)@CO.20

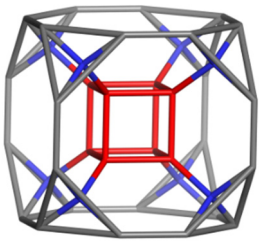

Tr(CP).40
C@((HTO)6;T8)@TC.40

Figure 5. CP-derived structures

Table 4. Figure count for clusters derived from CP cluster

C-structure	v	e	f_3	f_5	f_6	f	p_1	p_2	p_3	M	c	Sum(f)	Sym	p_k; (M)
CP.9	9	20	12	6	0	18	0	6	0	1	7	0	4	0;Py4; 0 (P;C)
Du(CP).18	18	60	52	6	0	58	8	6	0	2	16	0	4	Oct; Py4 (Oct; CO)
Med(CP).20	20	60	44	12	0	56	8	6	0	2	16	0	4	T;Ap4;0 (C; CO)
Tr(CP).40	40	80	32	6+6	12	56	8	6	0	2	16	0	4	T;HTO;0 (C; TC)

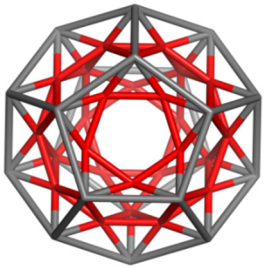

Du(IcoP).50
ID@((AP5)12;T20)@Do.50
Med(DoP).50=Do@((AP5)12;T20)@ID.50

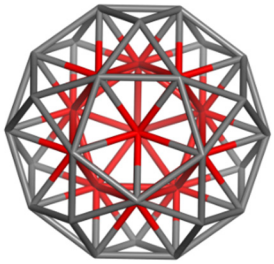

Med(Icop).42
Ico@(Oct20;(Py5)12)@ID.42

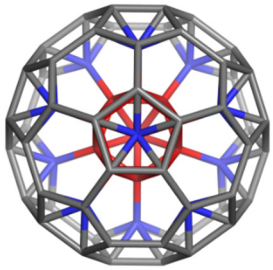

Tr(Icop).84
Ico@(TT20;(Py5)12)@C60.84

Figure 6. IcoP-derived structures

Table 5. Figure count for clusters derived from IcoP cluster

Ico-structure	v	e	f_3	f_5	f_6	f	p_1	p_2	p_3	M	c	Sum(f)	Sym	p_k; (M)
IcoP.13	13	42	50	0	0	50	20	0	0	1	21	0	5	T; 0; 0 (P; Ico)
Du(IcoP).50	50	150	110	24	0	134	20	12	0	2	34	0	5	T;AP5;0 (ID30;Do20)
Med(Icop).42	42	150	130	60	12	142	20	12	0	2	34	0	5	Oct; Py5;0 (Ico;ID30)
Tr(Icop).84	84	192	80	0	62	142	20	12	0	2	34	0	5	TT; Py5; 0 (Ico;C60)

Note that Tr(Icop).84 is related to the Samson cluster, that consists of twenty truncated tetrahedra TT (Friauf polyhedra), icosahedrally arranged, with a central atom inside each TT, all together counting 104 points/atoms [11-13]; the central shell forms an icosahedron. It is related to intermetallic phases. Intermetallics [14] represent compounds involving two or more metals, e.g.Laves phases (AB_2), e.g., $MgCu_2$, $MgZn_2$ and $MgNi_2$, size packing phases, such as Frank-Kasper, phases, etc. They can display desirable magnetic, superconducting and chemical properties, due to their strong internal order and mixed (metallic and covalent/ionic bonding, respectively). Intermetallics have promoted novel materials development.

Cell-in-Cell Clusters

Let now introduce the selective truncation operation (for general map operations, the reader is invited to consult refs [8-10, 15]: it leaves unchanged the non-marked points/atoms. In this simple way, cell-in-cell clusters can be designed (Figure 7); the figure count for these structures is listed in Table 6.

Further examples are shown in Figures 8 and 9 while their figure count is given in Table 7. Observe the double-shell torus T(4,12)Q4T5.96 (Figure 9, left), with a square tube section; every sector can be counted as an n-cube (see Figure 9, right). It was proposed by Diudea [16] as a model for the galactic black holes.

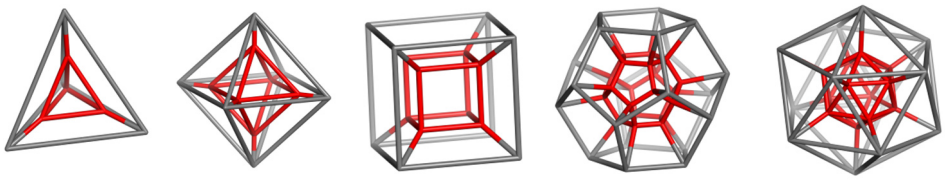

T@T.8 T@(P3)4@T.8 | Oct@Oct.12 Oct@(P3)8@Oct.12 | C@C.16 C@C6@C.16 | Do@Do.40 Do@((P5)12@Do.40 | Ico@Ico.24 Ico@((P3)20@Ico.24

Figure 7. Selectively truncated body centered clusters of the Platonic solids

Table 6. Figure count for selectively truncated body centered clusters Trs(P@M); M= Platonic solids

	Trs(P@M)	v	e	f_3	f_4	f_5	f	p_k	M	Cell	Sum(f)	Sym	p_k; M
1	.T@T.8	8	16	8	6	0	14	4	2	6	0	3	P3 (T;T)
2	Oct@Oct_12	12	30	16	12	0	28	8	2	10	0	4	P3 (Oct;Oct)
3	C@C.16	16	32	0	24	0	24	6	2	8	0	4	P4 (C;C)
4	Do@Do.40	40	80	0	30	24	54	12	2	14	0	5	P5 (Do;Do)
5	Ico@Ico.24	24	72	40	30	0	70	20	2	22	0	5	P3 (Ico;Ico)

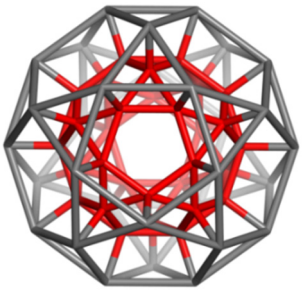

ID@ID.60
ID@((P5)12;(P3)20)@ID.60

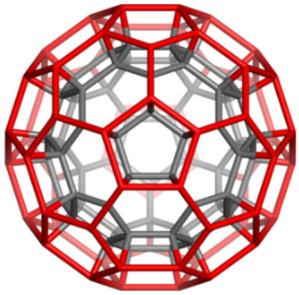

C_{60}@C_{60}.120
C_{60}@((P5)12;(P6)20)@C_{60}.120

Figure 8. Other "cell-in-cell" structures

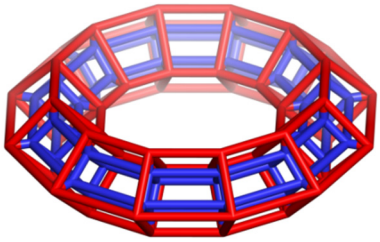

T(4,12)Q4T5.96

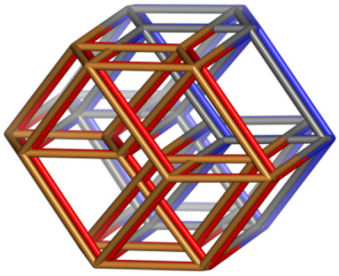

Q6(TU(4,8)Q6T7.64

Figure 9. A double-wall torus with the square section and 12 units Q4 (left); a detailed Q6 unit (right)

Table 7. Figure count for the objects in Figures 4 and 5

Structure	0	1	f3	f4	f5	f6	2	p3	p5	p6	m	3	4	5	Sum(f)
ID@ID.60	60	150	40	60	24	0	124	20	12	0	2	34	0	0	0
C_{60}@C_{60}.120	120	240	0	90	24	40	154	0	12	20	2	34	0	0	0
T(4,12)Q_4T_5.96	96	240	0	216	0	0	216	0	0	0	0	84	12	0	0*
Q6.64	64	192	0	240	0	0	240	0	0	0	0	160	60	12	0

* in case of Torus, the right member of (2) gives all time zero, because the torus is a surface of genus g=1.

It is the time to show a lower bound for the clusters existing in dimensions higher than three:

Theorem. A cluster of points/atoms with at least two (concentric) shells belongs to n-spaces higher than tridimensional.

Proof. A polytope is convex if any of its *k*-facets is shared by at least two *k*+1-facets. In particular, for *n*=4, *k* =2 while *k*+1 is a 3-facet, i.e. a cell. In other words, any 2-facet must share at least two 3-facets: the actual cell and the whole envelope. Next, the cluster is bound by 3-facets, thus the polytope is of dimension 3+1=4. This condition is already reached in P-centered clusters (Figure 2; Table 1), as much as in the "cell-in-cell" double-shell clusters (Figure 7). This is a lower bound condition and the theorem is demonstrated.

At the end, two pairs of clusters are presented: Med(CP).20 & Du(OctP).20 (Figure 10, left) and Med(DoP).50 & Du(IcoP).50 (Figure 10, right); they illustrate the sphere inversion event and is equivalent to tesseract moving on the fourth dimension (i.e. the time), a proof in addition that double-shell clusters belong to higher-dimensional spaces.

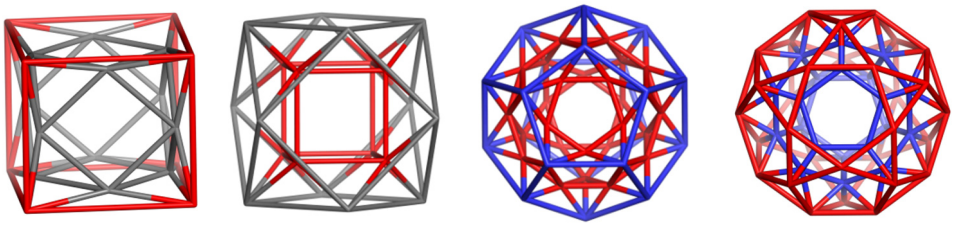

CO@C.20
CO@((AP4)6;T8)@C
Med(CP).20

C@CO.20
C@((AP4)6;T8)@CO
Du(OctP).20

ID@Do.50
ID@((AP5)12;T20)@Do
Med(DoP).50

Do@ID.50
Do@((AP5)12;T20)@ID
Du(IcoP).50

Figure 10. Sphere inversion by 4D-clusters: moving on the fourth dimension

COMPUTATIONAL DETAILS

The design and properties of the studied structures was performed by our original CVNET [17] and Nano Studio [18] software programs.

CONCLUSIONS

Some 4D-and higher-dimensional structures have been designed by using operations on maps, and their topological properties discussed. Multi-shell clusters appear frequently in minerals/chemicals and such analysis as we performed here could help in structure elucidation efforts.

There is a trend in Chemistry, Physics and even Astronomy to consider the *n*-dimensional spaces locally mixed/interlaced with the actually perceptible 3-dimensional Euclidean space. It seems that 3D-space and nD-spaces

simultaneously exist, as a manner of highly organizing the matter. The difficulty of visualization of the higher dimensions arises from the fact that only projections of the whole nD-structure can be seen in 3D- or even 2D-spaces.

ACKNOWLEDGEMENTS

Thanks are addressed to Dr. Csaba L. Nagy, Faculty of Chemistry and Chemical Engineering, "Babes-Bolyai" University, Cluj, Romania, for computational help.

REFERENCES

1. *http://en.wikipedia.org/wiki/Convex_hull; http://en.wikipedia.org/wiki/Simplex*; *http://en.wikipedia.org/wiki/Cross-polytope; http://en.wikipedia.org/wiki/Hypercube.*
2. H.S.M. Coxeter, *Regular Polytopes, 3rd ed.* New York: Dover, **1973**.
3. B. Grünbaum, *Convex Polytopes*, Graduate Texts in Mathematics (2nd ed.), Springer, **2003**.
4. L. Schläfli, *Theorie der vielfachen Kontinuität Zürcher und Furrer*, Zürich, 1901 (Reprinted in: Ludwig Schläfli, 1814-1895, Gesammelte Mathematische Abhandlungen, Band 1, 167–387, Verlag Birkhäuser, Basel, **1950**).
5. L. Euler, *Novi Comm. Acad. Scient. Imp. Petrop*. **1758**, *4*, 109-160.
6. V. Ya. Shevchenko, G.V. Zhizhin, A.L. MacKay, in: M.V. Diudea, C.L. Nagy (Eds.), *Diamond and Related Nanostructures*, Springer, Dordrecht, **2013**, Chap.17, p. 311.
7. B.V. Reddy, S.N. Khanna and B.I. Dunlap, *Phys. Rev. Lett.***1993**, *70*(21), 3323.
8. M.V. Diudea, M. Stefu, P.E. John and A. Graovac, *Croat. Chem. Acta,* **2006**, *79*, 355.
9. M.V. Diudea, *J.Chem.Inf.Model.*, **2005***, 45*,1002.
10. M.V. Diudea, *Studia UBB Chemia*, **2003**, *48* (2), 3.
11. S. Samson, *Acta Cryst.* **1965**, *19*, 401.
12. S. Samson, *Acta Cryst.* B, **1972**, *28*, 936.
13. M. de Boisieu, J. M. Dubois, M. Audier and B. Dubost, *J. Phys., Cond. Matter*, **1991**, *3*, 1.
14. *http://en.wikipedia.org/wiki/Intermetallic*
15. M.V. Diudea, in: M.V. Diudea, C.L. Nagy, Eds., Diamond and Related Nanostructures, Springer, Dordrecht, Heidelberg, New York, London, **2013**, Chap. 19, p. 333.
16. M.V. Diudea, *Int. J. Chem. Model*., **2015**, *7*, 000.
17. M. Stefu and M.V. Diudea, CageVersatile_CVNET, *Babes-Bolyai Univ.* Cluj, **2005**.
18. Cs. L. Nagy, M.V. Diudea, NANO-Studio, *Babes-Bolyai Univ.* Cluj, **2009**.

STUDIA UBB CHEMIA, LX, 2, 2015 (p. 389-397)
(RECOMMENDED CITATION)

ANTIOXIDANT AND HEPATOPROTECTIVE EFFECT OF CHITOSAN VERSUS VITAMIN E IN EXPERIMENTAL CARBON TETRACHLORIDE-INDUCED LIVER INJURIES

CRISTIAN CEZAR LOGIN[a,*], ANDRAS-LASZLO NAGY[b], ADRIANA MUREŞAN[a], REMUS MOLDOVAN[a], NICOLETA DECEA[a], DOINA DAICOVICIU[a], SIMONA CLICHICI[a]

ABSTRACT. The aim of our study was to assess the hepatoprotective and antioxidant effects of chitosan as compared with vitamin E in experimental toxic liver injury induced by carbon tetrachloride. Blood and liver samples were collected in order to assess hepatocytolisis (AST, ALT), oxidative stress (MDA, carbonyl proteins, GSH, SH groups, SOD and CAT), and histopathology examination was performed in order to asses inflammation and fibrosis. Liver enzymes level showed a significant, progressive increase after repeated exposure to CCl_4, first in liver tissue, then in the blood. Malondialdehyde and carbonyl proteins significantly increased, and GSH progressively decreased. Chitosan increased the GSH in the liver tissue to a value superior to that of the control group and decreased the AST and MDA level both in the liver and in the blood to values comparable to that of control group. Chitosan decreased carbonyl proteins level in the liver but slightly increased them in the blood. Vitamin E had similar effects concerning liver function and lipid peroxidation, but paradoxically, it induced protein peroxidation both in blood and in liver tissue. Histological modifications support the observed biochemical changes.

Keywords: *chitosan, vitamin E, fibrosis, antioxidants*

INTRODUCTION

The liver plays an essential role in the metabolism of a numerous toxic substances that enter the organism through the gastro-intestinal tract [1, 2]. Chronic exposure to small doses of carbon tetrachloride (CCl_4) leads

[a] *Iuliu Haţieganu University of Medicine and Pharmacy, Department of Physiology, 1 Clinicilor Street, Cluj-Napoca, Romania*
[b] *University of Agricultural Sciences and Veterinary Medicine, Department of Veterinary Toxicology, 3-5 Mănăştur Street, Cluj-Napoca, Romania*
[*] *Corresponding author: cezar.login@umfcluj.ro*

to formation of trichloromethyl and trichloromethyl peroxy radicals which, in turn, are able to oxidase the polyunsaturated fatty acids (PUFA) of the cell membrane and to induce oxidative injuries [3, 4]. Membrane injuries will lead to hepatocytes necrosis [5] and release of the liver enzymes. The oxidative stress will induce an increase in the activity of antioxidant enzymes (SOD, CAT, GPx) [5] and of the endogenous antioxidants level (GSH, SH), followed by a decrease, when the endogenous reserves will be depleted [6]. The use of synthetic and natural antioxidant substances have positive effects against oxidative stress induced liver injuries [3, 4, 7-9]. Vitamin E is capable to protect the PUFA against the reactive oxygen species (ROS) and can be used as an efficient antioxidant substance for the membranes [8, 9]. In toxic hepatitis induced by repeated experimental exposure to small amounts of carbon tetrachloride, vitamin E is able to scavenge free radicals, thus reducing the lipid peroxidation and protecting the endogenous antioxidants [10, 11]. Chitosan (CS) is a polymer obtained through the deacetylation of the chitin found in the exoskeleton of the marine shellfish. It has hemostatic [12], anti-inflammatory and antibacterial properties [13-15]. Recent studies also underlined its antioxidant and hepatoprotective properties and its ability to reduce the oxidative stress [16]. The aim of our study was to assess the antioxidant and hepatoprotective effects of chitosan as compared with vitamin E in experimental toxic liver injury induced by carbon tetrachloride.

RESULTS AND DISCUSSIONS

The mean values of the lipid and protein peroxidation products are presented in tables 1 and 2, of the non-enzymatic antioxidants in tables 3 and 4, and of the enzymatic antioxidants in table 5. Statistical significant differences ($p<0.05$) between groups are marked as follows: [a] (Ctrl-CCl_4), [b] (Ctrl-VitE), [c] (Ctrl-CS), [d] (CCl_4-VitE), [e] (CCl_4-CS), [f] (VitE-CS).

Table 1. Mean values of the malondialdehyde in plasma and liver tissue

Group	*Day 15*		*Day 30*	
	Plasma (nmol/ml)	Tissue (nmol/mg prot.)	Plasma (nmol/ml)	Tissue (nmol/mg prot.)
Ctrl	2.37±0.36[a]	0.061±0.017[a]	1.26±0.17	0.078±0.009[a]
CCl_4	2.82±0.31	0.092±0.015	1.30±0.60	0.101±0.023
CCl_4+VitE	2.81±0.55	0.072±0.022	1.40±0.20	0.086±0.015
CCl_4+CS	2.42±0.38	0.075±0.020	1.32±0.20	0.085±0.016

Table 2. Mean values of the carbonyl proteins in plasma and liver tissue

Group	*Day 15*		*Day 30*	
	Plasma (nmol/mg prot.)	Tissue (nmol/mg prot.)	Plasma (nmol/mg prot.)	Tissue (nmol/mg prot.)
Ctrl	1.13±0.32[b, c]	2.72±0.74[c]	1.21±0.14[b,c]	2.77±0.75
CCl_4	1.72±0.59	3.21±0.49[e]	1.44±0.45[d]	2.38±0.76
CCl_4+VitE	1.71±0.48	3.22±0.66	2.05±0.47	2.76±0.35
CCl_4+CS	2.10±0.50	1.75±0.61	1.73±0.34	2.82±0.84

Table 3. Mean values of the reduced glutathione (GSH)

Group	*Day 15*		*Day 30*	
	Plasma (nmol/ml)	Tissue (nmol/mg prot.)	Plasma (nmol/ml)	Tissue (nmol/mg prot.)
Ctrl	17.62±3.43[a,b]	0.63±0.28[a,b,c]	6.13±1.53[b,c]	1.42±0.36[b,c]
CCl_4	14.12±2.60[d]	2.20±0.70[e]	5.66±0.79[d,e]	0.93±0.51[d,e]
CCl_4+VitE	5.90±0.81[f]	2.41±1.09	10.16±1.64	2.16±0.34
CCl_4+CS	14.85±5.44	3.98±1.45	10.48±1.18	1.97±0.42

Table 4. Mean values of Sulfhydryl Groups (SH)

Group	*Day 15*		*Day 30*	
	Plasma (µmol/ml)	Tissue (µmol/mg prot.)	Plasma (µmol/ml)	Tissue (µmol/mg prot.)
Ctrl	0.081±0.015[c]	0.056±0.007	0.132±0.029[a,c]	0.078±0.013[a,c]
CCl_4	0.088±0.040[e]	0.052±0.007	0.084±0.022[d]	0.054±0.012[e]
CCl_4+VitE	0.069±0.028[f]	0.066±0.029	0.158±0.036[d]	0.062±0.013
CCl_4+CS	0.015±0.003	0.060±0.019	0.064±0.026	0.043±0.007

Table 5. Mean values of the enzymatic antioxidants plasma

Group	SOD (U/ml)		CAT (U/ml)	
	Day 15	*Day 30*	*Day 15*	*Day 30*
Ctrl	6848.57±984.86[a,b]	11344±1721.08[a,c]	5.26±0.49[a]	8.98±0.96
CCl_4	10418.16±1463.55	13606±1520.50[d,e]	6.53±0.40	8.52±0.43
CCl_4+VitE	9259.53±1046.89	10310±684.79[f]	7.62±1.46	8.23±1.10
CCl_4+CS	8897.06±2608.63	9306±576.22	6.56±1.75	8.57±0.46

After CCl_4 administration, our study identified a significant increase in MDA level both in plasma (day 30) and in liver tissue (day 15 and 30), which suggests the onset of the oxidative stress first in the liver and then in the blood. CCl_4 administration first stimulated the antioxidant enzymes levels (SOD, CAT) and induced a decreased of endogenous antioxidants (GSH,

SH). Good correlations between MDA and GSH have been identified (ρ=0.57). After vitamin E administration, our studied identified a significant increase of GSH level in the liver tissue to a level superior to that of the control group. After chitosan administration, a significant GSH increase was observed (day 15) in the liver tissue as compared with the CCl_4 exposed rats, and the level remained increased until the end of the experiment (day 30). Our results identified biochemical changes similar to those described in the literature [5, 17-21]. Both chitosan and vitamin E are able to decrease the oxidative stress level.

Carbon tetrachloride also induced an increase in carbonyl proteins level in the plasma, but not in the liver tissue. Neither vitamin E, nor chitosan protected the proteins against oxidative stress. Paradoxically, both substances demonstrated a slightly pro-oxidant effect on the proteins. Vitamin E administration induced protein peroxidation in the plasma, while the liver tissue values were not significantly modified as compared with the control group, changes that can be explained by the dual effect of vitamin E [11, 22, 23]. This effect was less visible concerning chitosan; its administration decreased protein oxidation in the liver tissue, while the plasma levels remained slightly increased. Anraku *et al.*, using a low molecular weight chitosan, also observed a decrease in plasma albumin peroxidation [24]. It is possible that the antioxidant effect on the proteins might be related to the molecular weight of the chitosan.

Table 6. Mean values of the liver enzymes

Group	AST (U/ml)		ALT (U/ml)	
	Day 15	*Day 30*	*Day 15*	*Day 30*
Ctrl	$42.93\pm8.37^{a,b,c}$	$58.46\pm16.15^{a,b,c}$	$35.88\pm3.92^{a,b,c}$	$45.48\pm13.10^{a,b,c}$
CCl_4	153.69 ± 18.55^{e}	$229.82\pm41.09^{d,e}$	172.10 ± 20.28^{e}	$220.61\pm54.68^{d,e}$
CCl_4+VitE	155.33 ± 27.58^{f}	186.37±18.95	147.00±34.39	152.24±19.45
CCl_4+CS	124.19±16.46	181.99±26.69	129.87±17.54	173.57±35.26

After the oxidative injuries, transaminases (AST, ALT) are released in the serum. AST is much more specific for liver injuries [25]. Our research identified a significant increase in liver enzymes levels after CCl_4 administration during the entire experiment, proportional with the duration of the exposure to CCl_4. AST serum level correlates with MDA level both in plasma (ρ=0.792) and in liver tissue (ρ=0.493). After vitamin E administration, some studies identified a decrease in the AST and ALT levels. We also identified a gradual decrease in AST level after vitamin E treatment, without arriving to values similar to those of the control group. The use of natural antioxidants in toxic liver injuries has hepatoprotective and antioxidant effects. Previous studies identified the antioxidant capacity of the chitosan in toxic liver pathology [16, 26]. Our study identified a decrease in AST levels after chitosan administration. Our results are

consistent with those found in the literature. Vitamin E and chitosan, administered simultaneously with CCl_4, have different effect of the oxidative stress and liver injuries. Both substances have the ability to decrease the transaminase levels, but none of them, in the used doses, completely protects against the action of CCl_4. In the context of our experiment, chitosan has superior antioxidant effects as compared with the vitamin.

Microscopic examination of the liver sections from animals of the control group revealed normal liver architecture. In the experimental groups at both sampling intervals, the most obvious lesions were represented by vacuolar dystrophy and hepatocellular necrosis, mainly in the central areas. Degenerated hepatocytes from the central areas presented clear cytoplasmic vacuoles of different size. Some of the hepatocytes presented numerous small vacuoles, the cytoplasm having a foamy aspect, other hepatocytes suffer hydropic change, characterized by hypertrophy and ballooning of the hepatocytes with a centrally located nucleus. Some hepatocytes presented granular degeneration. In some areas diffuse dilatation of the sinusoids was also evident (figures 1 and 2).

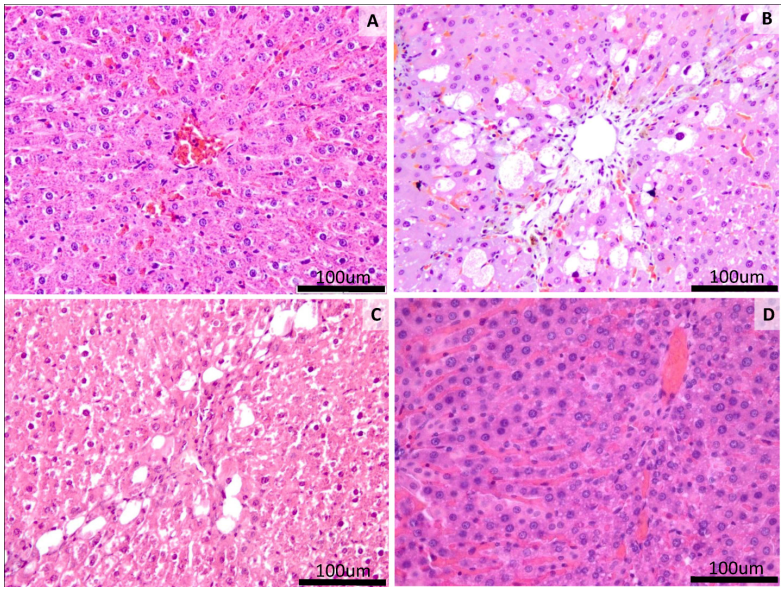

Figure 1. Histological changes in different experimental groups on the 15th day. Control group (A): central area, normal hepatic architecture; CCl_4 group (B): vacuolization of the hepatocytes from central areas; CCl_4+VitE group (C): hepatocellular vacuolization and necrosis; CCl_4+Chitosan group (D): discrete microvesicular steatosis, hepatocytes with a foamy aspect near the central areas, HE stain, original magnifications of 200×, Scale bar=100 μm.

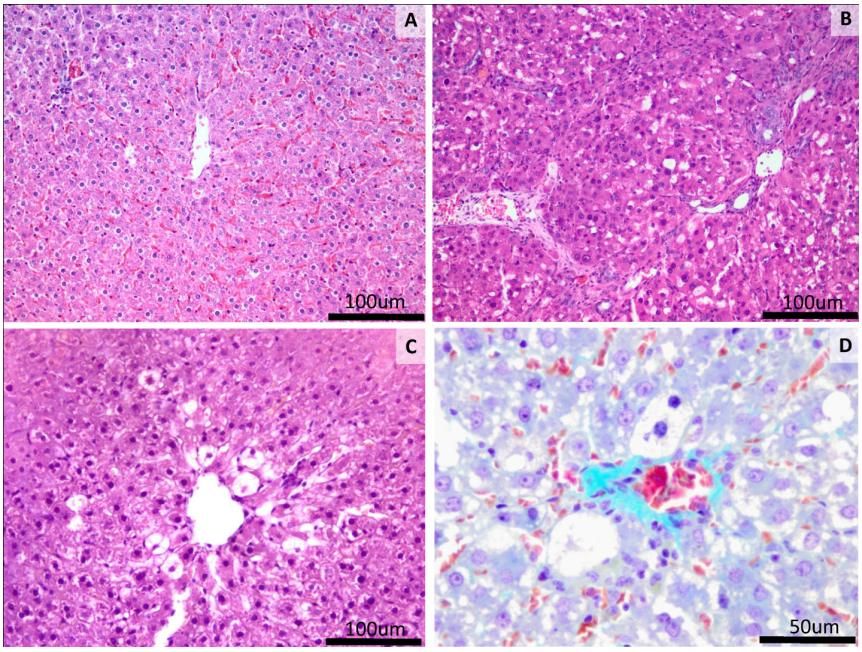

Figure 2. Histological changes in different experimental groups on the 30th day. Control group (A): central area, normal morphology, slight congestion; CCl_4 group (B): vacuolization of the hepatocytes from the central areas, centro-central bridges of degenerated and necrotic hepatocytes, oval cell hyperplasia; CCl_4+VitE group (C): hepatocellular vacuolization and necrosis in the central areas; CCl_4+Chitosan group (D): microvesicular steatosis and ballooning degeneration of the hepatocytes from central areas; HE stain (A,B,C), Masson's trichrome stain (D) original magnifications of 200× (A,B,C), 400x (D); Scale bar=100μm (A,B,C), Scale bar=50μm (D).

CONCLUSIONS

Our study confirmed the antioxidant effects of chitosan. Chitosan is able to decrease lipid peroxidation and to protect the endogenous antioxidant systems against the toxic effects of CCl_4. Only discrete histological liver injuries have been observed after chitosan administration. Vitamin E also demonstrates antioxidant properties, but the severity of the histological liver injuries was higher as compared to chitosan. In the used dose, the chitosan has a superior antioxidant and hepatoprotective effect as compared to vitamin E.

EXPERIMENTAL SECTION

Sixty four female Wistar rats, randomly distributed into four equal groups, have been used. The animals have been maintained at 23±2°C in the biobase of the Department of Physiology, Iuliu Haţieganu University of Medicine and Pharmacy Cluj-Napoca, Romania. The animals received standard food and water *ad libitum.* The experiment took place with the approval of the Ethical Committee of Iuliu Haţieganu University of Medicine and Pharmacy, Cluj-Napoca, and respected the Directive 86/609/EEC. Group I (Ctrl) received, by gavage, 0.9 ml/kg b.wt. sunflower oil, twice a week, for 30 days. Group II (CCl_4) received, by gavage, 1.2 ml/kg b.wt. CCl_4 25%, diluted in sunflower oil, twice a week, for 30 days. Group III (CCl_4+vit E) received, in addition to the CCl_4, 5 mg/kg b.wt. vitamin E (Sicomed®, 30 mg/ml vials) daily, intramuscular injections. Group IV (CCl_4+CS) received, in addition to the CCl_4, daily intraperitoneal injection with 3 mg/kg b.wt. chitosan (Sigma-Aldrich®, molecular weight 190-310 kDa, deacetylation degree 75-85%). After 15 and 30 days, eight animals from each group were anesthetized with ketamine. Blood samples were taken from the retroorbitary sinus. Animals were euthanized by cervical dislocation. Liver samples were taken for biochemical assessment and a portion of the liver was fixed in formaldehyde for histological examination.

Malondialdehyde levels in the plasma and in the liver were assessed using the method of Conti [27]. Protein peroxidation was estimated through the measurement of the protein carbonyl groups using the method of Reznick [28]. The total amount of proteins was assed using Bradford method [29]. SOD activity was assessed using the method described by Flohe [30], and CAT activity using the method described by Pippenger *et al.* [31]. Sulfhydryl groups (SH) and reduced glutathione (GSH) were assessed using the method of Hu [32, 33]. Liver function was evaluated using the activity of ALT and AST enzymes in the blood with commercial assay kits (Diagnosticum Zrt. Budapest) [34].

Liver tissue samples were fixed in 10% buffered neutral formalin, embedded in paraffin; the sections were made at 4 micrometers with a microtome Leica RM 2125 RT and stained by Haematoxiline-Eosine and Masson's trichrome methods. The slides were examined under a microscope Olympus BX 51. The images were taken with Olympus DP 25 digital camera and processed by a special image acquisition and processing program: Olympus Cell B. Sections were scored by an independent observer blinded to the experimental protocol. The following lesions were scored according to Knodell Histological Activity Index (HAI): portal inflammation, periportal/bridging necrosis, intralobular degeneration/focal necrosis and fibrosis (Knodell) [35].

Statistical analysis was performed using non-parametric tests (Mann-Whitney, Kruskal-Wallis, Wilcoxon, Spearman non-parametric correlation). The analysis was done for every moment of the experiment and also concerning the dynamic of the parameters, using MedCalc 14.0 sofware. The results were expressed as mean±SD. *P* values were considered significant if <0.05.

ACKNOWLEDGEMENTS

This paper was published under the frame of European Social Found, Human Resources Development Operational Program 2007-2013, project no. POSDRU/159/1.5/S/138776, and was partially supported by PNCDI2 Research Project no. 12.131/2008.

REFERENCES

1. P.L. Wolf, *Indian journal of clinical biochemistry*. **1999**, *14*, 59.
2. J.A. Knight, *Journal of infusion nursing: the official publication of the Infusion Nurses Society*. **2005**, *28*, 108-117.
3. R. Joshi, J.P. Kamat, T. Mukherjee, *Chemico-biological interactions*. **2007**, *167*, 125.
4. N. Vargas-Mendoza, E. Madrigal-Santillan, A. Morales-Gonzalez, J. Esquivel-Soto, C. Esquivel-Chirino, Y.G.-R.M. Garcia-Luna, J.A. Gayosso-de-Lucio, J.A. Morales-Gonzalez, *World journal of hepatology*. **2014**, *6*, 144.
5. R. Simeonova, M. Kondeva-Burdina, V. Vitcheva, M. Mitcheva, *BioMed research international*. **2014**, 706302.
6. D.J. Reed, M.W. Fariss *Pharmacological reviews*. **1984**, *36*, 25s-33s.
7. Z.F. Zhang, Y. Liu, L.Y. Lu, P. Luo *Chinese journal of natural medicines*. **2014**, *12*, 488.
8. G.B. Kavishankar, S.S. Moree, N. Lakshmidevi, *Phytomedicine : international journal of phytotherapy and phytopharmacology*. **2014**, *21*, 1026.
9. Y.J. Li, L.Y. Li, J.L. Li, L. Zhang, F. Gao, G.H. Zhou, *Asian-Australasian journal of animal sciences*. **2015**, *28*, 374.
10. R. de Cabo, J.R. Burgess, P. Navas, *Journal of bioenergetics and biomembranes*. **2006**, *38*, 309.
11. H. Ochi, S. Takeda, *Gerontology*. **2015**, *61*, 319.
12. H. Hattori, M. Ishihara, *Biomedical materials*. **2015**, *10*, 015014.
13. Y. Wen, F. Yao, F. Sun, Z. Tan, L. Tian, L. Xie, Q. Song, *Materials science & engineering. C, Materials for biological applications*. **2015**, *48*, 220.
14. Y. Tang, L. Xie, M. Sai, N. Xu, D. Ding, *Materials science & engineering. C, Materials for biological applications*. **2015**, *48*, 1.
15. S. Ebrahimiasl, A. Zakaria, A. Kassim, S.N. Basri, *International journal of nanomedicine*. **2015**, *10*, 217.

16. P. Ramasamy, N. Subhapradha, V. Shanmugam, A. Shanmugam, *International journal of biological macromolecules*. **2014**, *65*, 559.
17. E. Al-Sayed, M.M. Abdel-Daim, *Planta medica*. **2014**, *80*, 1665.
18. M.M. Hafez, O.A. Al-Shabanah, N.O. Al-Harbi, M.M. Al-Harbi, S.S. Al-Rejaie, S. M. Alsurayea, M.M. Sayed-Ahmed, *Oxidative medicine and cellular longevity*. **2014**, 893212.
19. Y. Liu, Q. Liu, G. Ye, A. Khan, J. Liu, F. Gan, X. Zhang, S. Kumbhar, K. Huang, *Journal of agricultural and food chemistry*. **2015**, *63*, 242.
20. Y.H. Wang, X.J. Xu, H.L. Li, *International immunopharmacology*. **2014**, *22*, 126.
21. X. Pu, W. Fan, S. Yu, Y. Li, X. Ma, L. Liu, J. Ren, W. Zhang, *Canadian journal of physiology and pharmacology*. **2015**, *93*, 39.
22. S.M. Tabei, S. Fakher, M. Djalali, M.H. Javanbakht, M. Zarei, H. Derakhshanian, M.R. Sadeghi, E. Mostafavi, F. Kargar, *Bratislavske lekarske listy*. **2015**, *116*, 115.
23. M.F. Vrolijk, A. Opperhuizen, E.H. Jansen, R.W. Godschalk, F.J. Van Schooten, A. Bast, G.R. Haenen, *Redox biology*. **2015**, *4c*, 272.
24. M. Anraku, M. Kabashima, H. Namura, T. Maruyama, M. Otagiri, J.M. Gebicki, N. Furutani, H. Tomida, *International journal of biological macromolecules*. **2008**, *43*, 159.
25. S. Lores Arnaiz, S. Llesuy, J.C. Cutrin, A. Boveris, *Free radical biology & medicine*. **1995**, *19*, 303.
26. T.I. Jeon, S.G. Hwang, N.G. Park, Y.R. Jung, S.I. Shin, S.D. Choi, D.K. Park, *Toxicology*. **2003**, *187*, 67.
27. M. Conti, P.C. Morand, P. Levillain, A. Lemonnier, *Clinical chemistry*. **1991**, *37*, 1273.
28. A.Z. Reznick, L. Packer, *Methods in enzymology*. **1994**, *233*, 357.
29. M.M. Bradford, *Analytical Biochemistry*. **1976**, *72*, 248.
30. L. Flohe, F. Otting, *Methods in enzymology*. **1984**, *105*, 93.
31. C.E. Pippenger, R.W. Browne, D. Armstrong, *Methods in molecular biology*. **1998**, *108*, 299.
32. M.L. Hu, *Methods in enzymology*. **1994**, *233*, 380.
33. S. Mureşan, A. Filip, V. Simon, A.F. Gal, V. Miclăuş, N. Decea, R. Moldovan, A. Mureşan, *Studia UBB Chemia*. **2003**, *LVIII*, *7*.
34. H.U. Bergmeyer, P. Scheibe, A. W. Wahlefeld, *Clinical chemistry*. **1978**, *24*, 58.
35. R.G. Knodell, K.G. Ishak, W.C. Black, T.S. Chen, R. Craig, N. Kaplowitz, T.W. Kiernan, J. Wollman, *Hepatology*. **1981**, *1*, 431.

STUDIA UBB CHEMIA, LX, 2, 2015 (p. 399-408)
(RECOMMENDED CITATION)

MODELLING AND SIMULATION OF BOD AND COD FOR EFFLUENT LEVELS OF AN AERATION TANK FROM GHERLA WASTE WATER TREATMENT PLANT

MARIUS-DANIEL ROMAN[a*], RALUCA-ANDREEA FELSEGHI[a], MIRCEA-VLAD MUREŞAN[b]

ABSTRACT. The modelling results of BOD and COD for an aeration tank from Gherla's WWTP by Matlab/Simulink software program has no significant difference, because the results are close enough to the real ones that allow the user to make a good prediction regarding this parameters. A true validation of these results, including experimental validation of simulations of the entire collecting data was realistic. Validated process models can be used for dynamic simulations, for example, with different kinds of input data. In simulations the mathematical equations of process model are solved and the results given. Models and software for simulation have the possibility to control and evaluate the parameters. The presented control strategies use mainly ideal conditions, given the circumstances, for controllers and plant operations.

Keywords: *simulation, modelling, Matlab, flow; BOD, COD.*

INTRODUCTION

Simulation of activated sludge, is based on phenomena such as carbon oxidation, nitrification and denitrification, must necessarily account for a large number of reactions between of components. Mathematically is needed while to providing realistic predictions, the reactions must be representative of the most important fundamental processes occurring within the system. In this case the term process is used to mean a distinct event acting upon one or more system components. Furthermore, the model should quantify both the rate, concentration dependence and the relationship that one component has to another in a reaction, of each process [7].

[a] *Technical University of Cluj-Napoca, Building Services Engineering Department, 128-130 Boulevard December 21 Str., RO-400604, Cluj-Napoca, Romania*
[b] *Technical University of Cluj-Napoca, Engineering Materials and the Environment Department, 28 Memorandumului, 400114 Cluj-Napoca, Romania*
** Corresponding author: Marius.ROMAN@insta.utcluj.ro*

In this case for a model is important to have something representative in the design and operation of wastewater treatment systems, it must be possible to evaluate parameter values which are wastewater specific and to estimate concentrations of important components in the influent [7]. The first step is to identify the components of relevance in the model. In this case these are BOD, COD, TN and others. The second step is to identify the biological processes occurring in the system, for example the transformations or the conversions that happen and write mathematical relations that describe the process. The third step is to use a simulation program. In this study were used Matlab/Simulink software. Although a number of environmental factors can influence the parameter values, these are specific factors in the wastewater, pH and temperature.

The two most common parameters used to recognize the composition of wastewater are the biochemical oxygen demand (BOD) and the chemical oxygen demand (COD). BOD_5 is a measure of how much dissolved oxygen is consumed by aerobic bacteria in 5 days at 20 ^oC. It is the broad measure of the strength of the organic matter in a waste stream. The typical range of BOD_5 in domestic wastewater ranges from 100 to 300 mg/L. COD is chemical oxygen demand and is measured chemically by digestion with acid. There exists a definite correlation between the COD and BOD under certain conditions and by determining the COD, the information about the BOD of the wastewater can be derived, but it is highly waste dependent [1], [2].

When a wastewater treatment system can be modelled, a certain number of simplifications and assumptions must be added in order to take the model tractable. Often this simplifications and assumptions are implicit, which may cause the user to overlook them. The system operates at constant temperature, because many of the coefficients are functions of temperature, their functionality would have to be explicitly expressed in the rate expressions, in order for time-variant temperature fluctuations to be considered.

It is known that the pH influences many of the coefficients. The inclusion of the alkalinity in the model allows the user to detect potential problems with pH control. The effects of limitations of nitrogen, phosphorus and other inorganic nutrients on the removal of organic substrate and on cell growth have not been considered. The coefficients for nitrification are assumed to be constant and to incorporate any inhibitory effects that other waste constituents are likely to have on them [3].

The purpose of this model is to find a mathematical model able to determine certain effluent levels, for BOD and COD concentrations depending on influent and effluent.

Khaled & Gina 2014 obtained in the case studies, for parameters COD and BOD in different plants of variable types and treatment capacities, that the correlation between BOD_5 and COD is generally linear, except in some rare cases where the relation was polynomial and sometimes doesn't have a definite pattern. However, this rare indefinite pattern might be due to inaccuracy in determination of the BOD_5 and COD parameters in such cases. Since the BOD and COD are correlated, the estimation of BOD_5 values using the quick COD test, and plant specific biodegradability index (which is the slope of the plotted correlation) became possible and relatively reliable. Thus, it can be used as a check parameter to evaluate performance for quick action. For existing wastewater treatment plants the BOD/COD correlation should be developed, to compromise the use of these parameters. In order to establish the BOD/COD correlation for a particular existing wastewater, one should have both COD and BOD5 values for several representative wastewater samples. From graphics the BOD_5 values versus the COD values then use the regression analysis to develop the correlation. The plotted BOD_5 and COD figures indicated that there is a clear linear positive correlation for most case studies, which differs from plant to another [2].

RESULTS AND DISSCUSIONS

Were performed 22 simulations for BOD to increasing values of inflow starting from 155.79 m^3/h up to 400.54 m^3/h. Influent flow values and the influent concentrations were taken from experimentally determined data from treatment plant using the analysis method according to STAS 6560-82 [5].

Table 1. Experimental values for BOD

Probes	Influent flow	Influent BOD	Effluent BOD	Probes	Influent flow	Influent BOD	Effluent BOD
	m^3/h	mg/l	mg/l		m^3/h	mg/l	mg/l
1	155.79	179.00	9.00	12	220.46	261.50	12.35
2	156.92	264.00	12.00	13	221.04	275.60	12.82
3	165.67	219.00	11.00	14	236.51	82.00	3.00
4	179.67	114.00	4.80	15	255.92	132.00	9.00
5	184.71	155.00	8.10	16	258.10	88.00	3.50
6	190.58	121.20	5.26	17	276.45	127.00	5.33
7	193.33	195.50	9.84	18	282.21	123.00	5.10
8	195.08	203.00	10.78	19	297.42	93.00	3.78
9	199.42	308.00	6.00	20	302.60	118.00	4.90
10	201.08	269.50	12.55	21	394.80	106.00	4.00
11	215.07	83.00	3.10	22	400.54	158.00	8.20

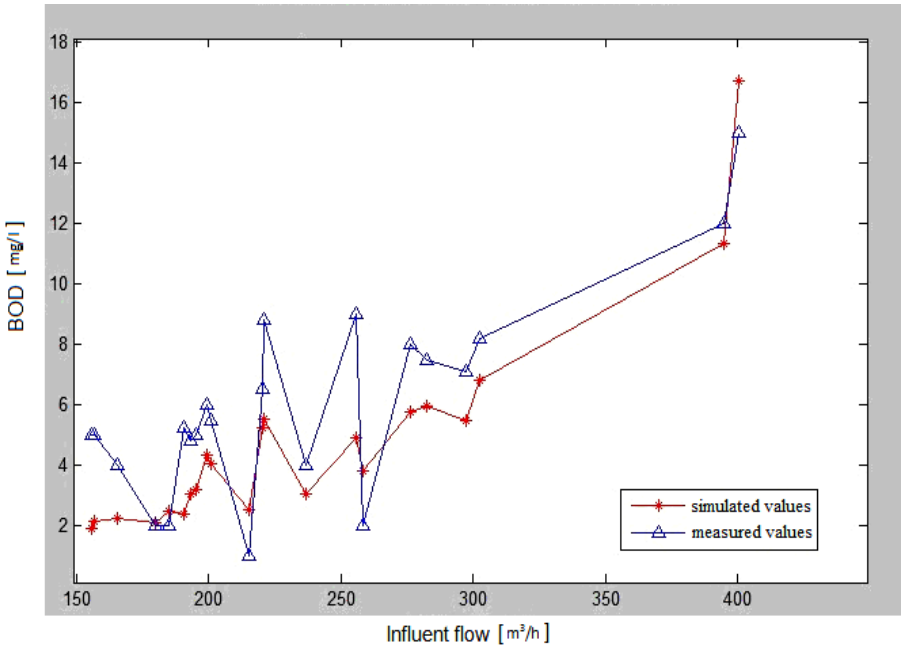

Figure 1. Simulated and measured values of BOD from Gherla's WWTP

Simulation results from data obtained were compared with those determined experimentally. In the case of biochemical oxygen demand after 5 days was obtained the graph from figure 1. It may be noted that the data obtained from simulation and the data obtained experimentally keeps tendency, which otherwise have no trend. The data measured at the plant can vary widely from day to day even for the same rate, this being also very difficult to simulate. But with this mathematical model results are close enough to the real ones that allow the user to make a good prediction of biochemical oxygen demand after 5 days, knowing the inflow of water and oxygen concentration standard.

As was shown in the graphic all data were simulated in according to standard NTPA-001/2005, below 25 mgO_2/l, although influent concentrations values were between 82 and 308 mgO_2/l. The dissolved oxygen concentration can be measured by an electrochemical sensor for continuous determination of oxygen [6]. For COD, were performed 19 simulations for the increasing values of flow starting from 110.00 m^3/h up to 257.00 m^3/h. Concentration values from the influent and effluent have been determined experimentally by potassium dichromate method according to SR ISO 6060/1996 [5].

Table 2. Experimental values for COD

Probes	Influent flow	Influent COD	Effluent COD	Probes	Influent flow	Influent COD	Effluent COD
	m^3/h	mg/l	mg/l		m^3/h	mg/l	mg/l
1	110.00	346.56	63.84	11	142.63	470.08	54.24
2	114.38	470.08	54.24	12	171.25	264.00	46.80
3	121.71	519.20	61.60	13	171.38	331.00	55.90
4	122.33	546.56	68.32	14	201.42	293.00	92.20
5	125.04	342.72	28.56	15	202.25	252.72	94.88
6	125.25	428.40	66.64	16	212.08	288.00	76.80
7	129.58	508.80	57.60	17	212.63	205.20	84.14
8	132.25	431.20	70.40	18	255.96	212.00	54.40
9	130.00	380.64	58.56	19	257.00	280.80	93.60
10	141.79	518.40	57.60				

The results obtained of the simulation are compared to the experimental ones as was shown in figure 2. If in the case of biochemical oxygen demand after 5 days the results can vary widely from one day to another day, from a flow or even at the same flow, in case of oxygen concentration determined by the COD also from the influent and effluent varies more than in the previous simulation.

This absence of linearity is present as well in simulation of this parameter, but the trend keeps disorganized pattern of actual data. However data from simulation is close to the real values and the mathematical model can be used to predict the effluent of the oxygen concentration normally determined experimentally with COD method.

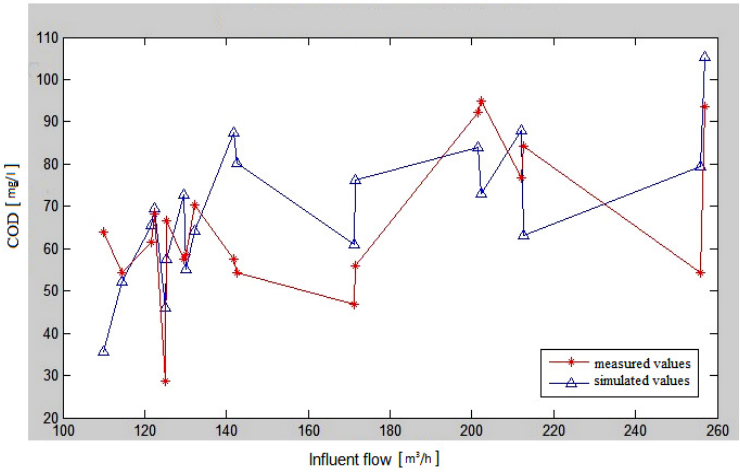

Figure 2. Simulated and measured values of COD from Gherla's WWTP

All simulation data are below to the maximum allowed by the standard NTPA-001/2005, below 125 mg / l. Block diagram of the model in Simulink can be seen in figure 3. In the left diagram can be seen the two input quantities of inflow in m^3/h and biochemical oxygen demand after 5 days from the entry into the tank. The two enter in a multiplier which forwards them to the position S.

After completing the steps in the S output as is represented in figure 3, but also are sent to the workspace in the form of a matrix. Simulation time is set to 120 minutes.

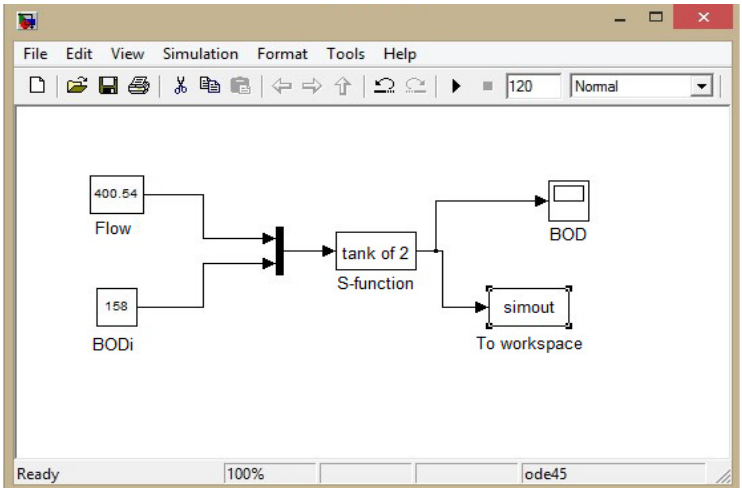

Figure 3. Block diagram of the model in Simulink

Data collected from the wastewater treatment plant keeps approximately a uniform trend, this was underlined by the results of simulations. In simulation we can't see a very good overlap of simulated results over determined experimentally, because the tank is circular and in case of rectangular tanks which is enough close to ideal form.

In some instances the tank geometry is very important for modelling, because in circular tanks the flow rate is smaller than in case of rectangular tanks, but it is not a rule.

CONCLUSIONS

In this paper, a procedure for getting a set of solutions for development of a mathematical model must incorporate the major events occurring within a system in a manner which is consistent with established knowledge about that system.

In the model should be included only those processes which are essential to a realistic solution and must select rate expressions for them that allow the use of simplified solution techniques without detracting from the applicability of the results.

The formal modelling of systems has been done with a mathematical model, which attempts to find analytical solutions enabling the prediction of the behavior of the system from a set of parameters and initial conditions. Modelling techniques include statistical methods, computer simulation, system identification, and sensitivity analysis; however, one of these is as important as the ability to understand the underlying dynamics of a complex system. Models applied for prediction aim at providing an accurate and fast image of a real systems behavior under different conditions [7].

Models may be linear with respect to variables or parameters; furthermore, a model can be nonlinear to parameters and linear to variable [8]. Linear models are used frequently, because the analytical solution can be found. For nonlinear models numerical solutions are predominant. Term mechanistic, physiological and white-box are used to describe that models structure is based on physical, chemical and biological laws.

Simulation is a reasonable way to extrapolate performance and scaling up process; additionally, it helps in understanding behavior and mechanisms of processes. Also the effects of system parameters and disturbances can be investigated using process simulation [9].

EXPERIMENTAL SECTION

We considered a tank which has: width 8.15 m and height of 5.7 m, with the volume of 4050 m^3. It was considered as a static system with a piston-type flow with changing parameters as the water moves into the tank.

Were taken into account the following simplifying assumptions:

- All parameters are constant in radial section of the reactor (flow piston type).
- The flow rate is considered constant.
- Flow regime is considered ideal (flow regime shift (type D).
- Density and water temperature are considered constant and have not been taken into account.
- The influence of pH was not taken into account, which is assumed constant.
- Ammonification was considered constant.

- Biomass concentration in the tank was considered constant (specific death rates, the increase is much smaller than reaction rates).
- The vapour pressure of the water surface was not been considered.

To achieve simulation method was used Matlab/Simulink software. The mathematical model of the aeration tank consists of a system by a differential equation for each parameter to be determined. For numerical solutions of differential equations using the method of integration ODE45 (Dormánd-Prince) with variable step and relative tolerance of 10^{-3}. For calculation was used Matlab program version 7.14.0.739.

Knowing the size of the tank could calculate the cross section area as follows:

Wetted area is calculated first using the formula:

$$A_u = H \cdot l \tag{1}$$

where: A_u - wetted area [m^2]
H - height of the tank [m]
l - width of the tank [m]

Wetted perimeter is then calculated:

$$P_u = 2 \cdot (H + l) \tag{2}$$

Pu - wetted perimeter [m].

This is necessary to determine equivalent diameter, which has the following formula:

$$D_{ech} = 4 \cdot \frac{A_u}{P_u} \tag{3}$$

Dech - equivalent diameter [m]

Having calculated the equivalent diameter of the cross-sectional area can be calculated:

$$A = \frac{\pi \cdot (D_{ech})^2}{4} \tag{4}$$

A - cross-sectional area of the tank considered [m^2]

Input flow is known from experimental data and calculated using the above area can cause water flow rate:

$$w = \frac{F}{A} \tag{5}$$

W - water flow rate [m / h]; F - experimentally measured water flow [m^3/h]

All these equations are part of the mathematical model, namely the algebraic equations of the model.

Differential equations of the model are:

For BOD_5:

$$\frac{dBOD_5}{dt} = -Y_1 \cdot \frac{\left(BOD_5 - C_i\right)}{w} \tag{6}$$

For COD:

$$\frac{dCOD}{dt} = -Y_2 \cdot \frac{\left(COD - C_i\right)}{w} \tag{7}$$

where:

$\frac{dBOD_5}{dt}$ - represents the changes in biochemical oxygen demand after 5 days

Y_1 - theoretical stoichiometric ration

Y_2 - theoretical stoichiometric ration

C_i - standard oxygen concentration (1.5 mg / ml)

In the last decade, stringent quality standards are being applied to effluent plants, whether by regulatory authorities or environmentally concerned plant management. More often than not now, limits on nitrates, ammonia, phosphates, suspended solids, etc. are applied to outfalls [4].

To realise an optimum biological process, it is necessary to assure the best environment for the bacteria. A few important parameters are oxygen, pH and temperature, as well as suspended solids which indicate the bacteria concentration in the tank. Advanced monitoring of the bacteriological processes based on oxygen, ammonia and nitrate makes it possible to satisfy strict legal regulations and to optimize energy consumption at the same time.

Acknowledgments

This paper is supported by the Sectoral Operational Programme Human Resources Development POSDRU/159/1.5/S/137516 financed from the European Social Fund and by the Romanian Government.

REFERENCES

1. J. Hur, B.-M. Lee, T.-H. Lee, D.-H. Park, *Sensors*, **2010**, *10(4)*: 2460-2471.
2. K.Z. Abdalla, G. Hammam, *International Journal of Sciences: Basic and Applied Research*, **2014**, *13*, *1*, 42.
3. M. Henze, W. Gujer, T. Mino, M. van Loosdrecht, *Scientific and Technical Report*, **2000**, 6–8-16-26.
4. M.D. Roman, M.V. Muresan*, International Journal of Latest Research in Science and Technology*, **2014**, *3, 2*, 30.
5. NTPA-001/2005, *Normative act regarding the determination of limits of loading with pollutants of industrial and town wastewaters at evacuation in natural receptors*, **2005**.
6. E.M. Pică, *Development and study of an electrochemical sensor for continous determination of oxygen*, PhD Thesis, University Babes-Bolyai, Cluj-Napoca, **1990**.
7. H. Haimi, M. Mulas, K. Sahlstedt R. Vahala, *Helsinki University of Technology Water and Wastewater*, **2009**, *9*, 7.
8. S.A. Dellana, D. West, *Environmental Modelling & Software*, **2008**, *24*, *1*, 96.
9. S. Marsili-Libelli, *Advances in Biochemical Engineering/Biotechnology,* **1989**, *38*, 90-148.
10. http://www.water.me.vccs.edu/courses
11. http://www.eea.europa.eu
12. http://www.environmental-expert.com
13. http://www.iasj.net
14. https://fortress.wa.gov

STUDIA UBB CHEMIA, LX, 2, 2015 (p. 409-419)
(RECOMMENDED CITATION)

KINETICS OF THE CORROSION PROCESS OF HOT DIP GALVANIZED STEEL REINFOCEMENT IN FRESH CONCRETE

VASILE RUS[a,c,*], ANDREEA HEGYI[b], HORAȚIU VERMEȘAN[c], ANCUȚA ELENA TIUC[c]

ABSTRACT. The quality of concrete structures is largely reflected by its durability. According to literature, the rebar corrosion initiation is delayed and the life duration of concrete structures reinforced with hot dip galvanized rebar is extended with up to 70 years compared to life duration of concrete structures reinforced with non-galvanized steel rebar. It is well known that the galvanized rebar surface activates in contact with the alkaline environment of fresh concrete, forming a crystalline compound namely calcium hydroxizincate. This crystalline compound is important for the kinetic and corrosion mechanism of rebar embedded in concrete. This work aims to evidence the galvanized rebar corrosion kinetics in fresh concrete, during the concrete hardening. Electrochemical methods were used during experiments. The test results show an activation of the zinc layer of galvanized rebar in contact with the alkaline environment of concrete, during the first days after rebar embedding in concrete. Zinc corrosion products formation lead to better corrosion resistance of galvanized steel rebar, compared to the resistance of non-galvanized steel rebar.

Keywords: *hot dip galvanized steel reinforcement, concrete, corrosion, calcium hydroxizincate*

INTRODUCTION

The quality of reinforced concrete structure is given by its durability, which is the period of time the structure maintains all the characteristics required for the proper use as established in the design. The technical performances of reinforced concrete structures decrease exponentially with time, due to the exponential increase of the degradation rate of both concrete and reinforcement. [1, 2, 8, 9, 15]

[a] *S.C. Betak S.A., 4 Industriei str., RO-420063, Bistrita, Romania*
[b] *INCD URBAN-INCERC, 117 Calea Floresti, RO-400524, Cluj-Napoca, Romania*
[c] *Technical University of Cluj-Napoca, Faculty of Materials and Environmental Engineering, 103-105 Muncii Blvd., RO-400641, Cluj-Napoca, Romania*
** Corresponding author: rusvasile@betak.ro*

According to literature, the main factors that cause the reinforced concrete degradation are (starting from the most important to the least important): reinforcement corrosion, acid solutions aggression, sulfate attack, alternating wet and dry conditions, repeated freeze-thaw cycles, levigation, internal stress, external forces, salt crystallization, the aggregates reaction with concrete, and abrasion. [10, 11] Note that the reinforcement corrosion is the main cause for concrete degradation and for the reinforced concrete structures and components durability decrease.

Corrosion of reinforced concrete structures should be studied regarding concrete/steel rebar system interaction with the surrounding environment, and regarding the rebar interaction with concrete [12].

Many rebar corrosion protection methods are proposed worldwide, all having both advantages and disadvantages. Among these, hot dip galvanizing of steel reinforcement has been studied for the past 50-60 years and based on theoretical and electrochemical arguments, laboratory and in situ testing, is proved to be one of the most effective corrosion protection methods up to this day. [1-7, 13-16] Hot dip galvanizing is used for 2% of the total amount of steel reinforcement in the US and for 1% in Europe, but these values are increasing every year, especially for the structures designed to be used in extremely corrosive, marine or tropical climate environments. [1, 2, 7, 13-16]

Literature [3-6, 13-16] indicates that corrosion occurs 2-3 days after the hot dip galvanized steel rebar contact with fresh concrete. Corrosion products forms following the corrosion initiation, some of which some play a passivation role, such as calcium hydroxizincate, while other corrosion products, such as zinc oxides and hydroxides - that are insoluble in water, do not have a passivation role. In order to obtain calcium hydroxizincate, about 10 μm thick zinc coating is used. Because the corrosion products layer is adherent and compact at the surface of the galvanized steel reinforcement, it is more resistant to corrosion. On the other hand, zinc is less noble than steel, thus ensuring steel cathodic protection. As such, the steel is protected for as long as the zinc layer is not fully consumed.

Previous results obtained by the authors [17-21] support the fact that by using hot dip galvanized reinforcements the durability of concrete structures is increased and the work in this paper searches to clear the kinetics of the corrosion process of hot dip galvanized steel reinforcement in fresh concrete.

The aim of the experiments was to analyze the kinetics of hot dip galvanized steel rebar in fresh concrete, until concrete hardening. This study is important because most reactions in concrete take place in this phase; such as the cement hydration – hydrolysis, the concrete pH stabilization, and the activation of the hot dip galvanized steel rebar surface, followed by the calcium hydroxizincate formation [13-16].

RESULTS AND DISCUSSION

The experimental chronoamperometry curves were plotted, showing the current density variation for 24 hours, at constant potential. Experimental tests of samples with non-protected or with hot dip galvanized reinforcement embedded in various concrete age were made. Concrete age is given by the time passed since concrete pouring (samples preparations) till the tests. This time, the samples were all kept in identical conditions in laboratory. The results are shown in Figure 1 and Figure 2.

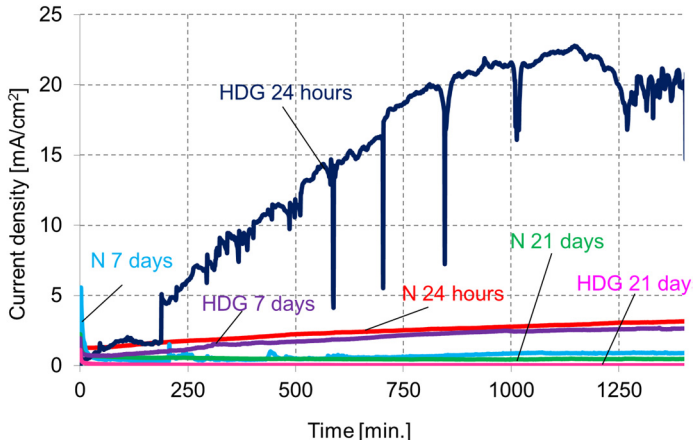

Figure 1. Current density evolution for the galvanized and non-galvanized steel rebar, during concrete hardening

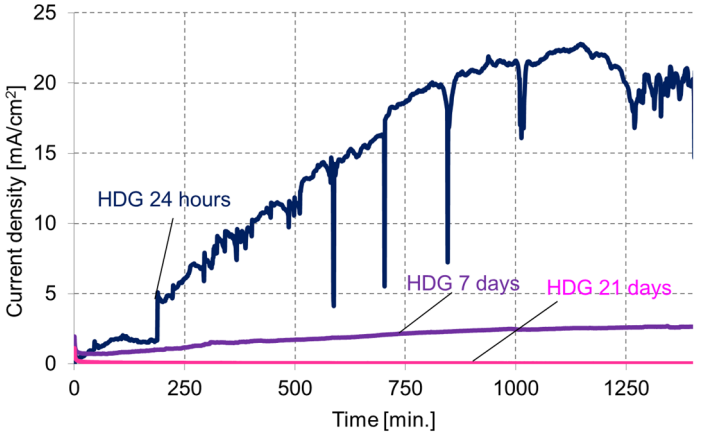

Figure 2. Current density evolution for the galvanized steel rebar in concrete, during concrete hardening

Twenty-four hours after concrete casting, the current density is high in the case of the hot dip galvanized rebar. This was considered an activation indicator due to the fact that the zinc-coating surface of galvanized rebar activates when introduced in alkaline concrete environment. Thus, a fraction of zinc is consumed, resulting specific corrosion products. The peaks of the "HDG 24 hours" plot indicate that the passive layer regenerates. This layer is subsequently attacked by alkaline concrete and destroyed.

According to the chronoamperometry tests of galvanized steel rebar, the corrosion current density strongly decreases after 7, respectively 21 days from the concrete casting (Figure 2). This is a qualitative sign for the zinc corrosion rate dropping due to the formation of a thicker or more compact corrosion products layer. Moreover, as it can be seen, the diagram of concrete/ HDG rebars samples after 21 days since rebars embedment, does not show current densities peaks. This was interpreted as a passive layer formation on HDG rebars surface, enough resistant to prevent metal surface activation and corrosion.

By comparing the data obtained, it can be seen that 24 hours after concrete casting, the zinc coating on steel rebar exhibit a much stronger activation than the non-galvanized steel. The tests conducted 7 days after concrete casting, show that the difference between the current densities of galvanized and non-galvanized reinforcement is much lower compared to the values found 24 hours after rebar embedding in concrete. However, the values obtained for the galvanized steel samples are higher, showing a higher corrosion rate compared to that of the non-galvanized steel rebar.

Twenty-one days after rebar embedment in concrete, the current density drops significantly, both for the galvanized and non-galvanized rebar. This was considered a stabilization point for the two metals surfaces due to the formation of specific corrosion products layer. This time however, the current density of galvanized steel was very low; it almost linearly increased with time and was lower than the current density of non-galvanized steel.

Twenty-one hours after rebar embedment in concrete, the galvanized steel showed a lower corrosion rate compared to the non-galvanized steel, due to the protective corrosion products layer formation on zinc surface. Although this corrosion products passive layer also formed on the non-galvanized steel surface, the passivizing capacity of the corrosion products layer on zinc surface was stronger, as shown by the current density decrease with time.

The linear polarization plots recorded, in Tafel interpretation, are shown in Figure 3. The corrosion potential, corrosion current and corrosion rate are shown in Table 1.

From Figure 3 and Table 1 it can be seen that the galvanized rebar/ fresh concrete system, noted with „initial HDG", show the more negative corrosion potential (-1424 mV). This indicates a powerful activation of the zinc surface immediately after rebar embedment in the alkaline environment of fresh

concrete. Also, the corrosion current of this system is the highest (115.62 μA/cm^2), indicating a high corrosion rate. On contrary, the non-galvanized steel rebar/ fresh concrete system, noted with „initial N", shows a potential shifts toward positive values, with 794 mV, but still remaining in the negative domain of metal surface activation. The corrosion current recorded for the non-galvanized rebar system is lower compared to the galvanized rebar system. Thus, the corrosion rate of the non-galvanized steel rebar system is lower immediately after rebar embedment in fresh concrete, when compared to the galvanized rebar system.

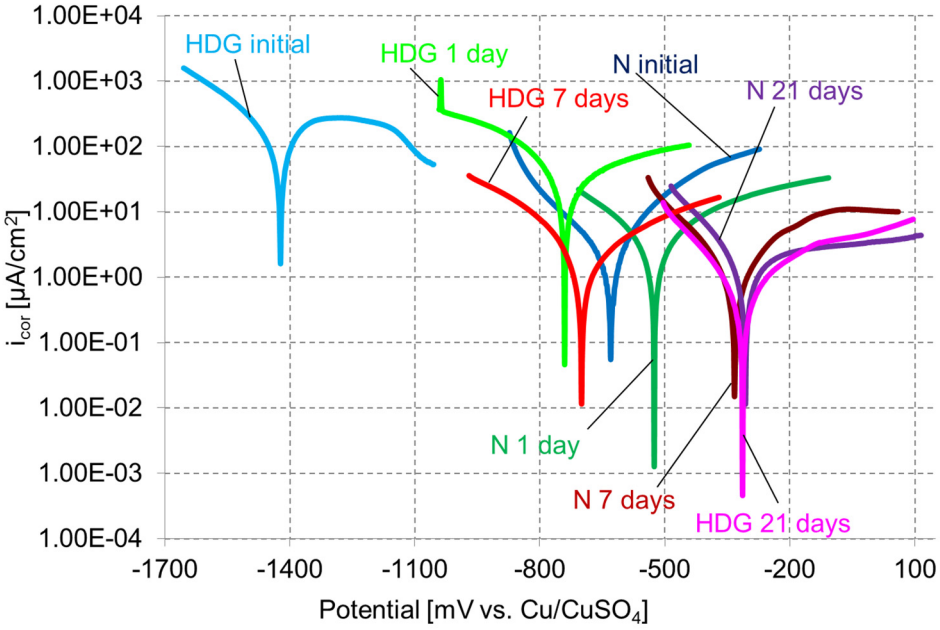

Figure 3. Tafel plots recorded for the samples with galvanized or non-galvanized steel rebar in concrete

Tests conducted 24 hours after rebar embedment in concrete show a corrosion potential fast shifting toward positive values and a corrosion current decrease, for all samples. Even so, the corrosion potential of galvanized steel remains more negative, with 215 mV, and the corrosion current values remains much higher compared to the non-galvanized steel. These results are also supported by literature. According to literature [3-6], zinc reacts with the alkaline environment when introduced in fresh concrete, forming a passive layer that is essential for subsequent corrosion protection.

The electrochemical systems kept in laboratory for 7 days were tested. The results showed passivation of both rebar types, as the corrosion potential shifted towards positive values. Also, the corrosion current decreased.

Between day 7 and day 21, the both rebar system starts to stabilize. The corrosion potential becomes more positive and the corrosion current values decrease. During this period of time, the differences between the two rebar systems corrosion potentials and corrosion currents are smaller compared to previous time intervals.

Table 1. Kinetic corrosion parameters determined from the polarization curves for the galvanized and non-galvanized steel samples, at various concrete ages

Electrochemical system	E [mV]	$i_{cor.}$ [μA/cm^2]	$v_{cor.}$ [μm/an]
N Initial	-630	19.59	227.19
N 1 day	-525.5	12.11	140.48
N 7 days	-333	1.18	13.69
N 21 days	-313.5	0.94	10.94
HDG initial	-1424	115.62	1734.37
HDG 1 day	-740.5	60.80	911.97
HDG 7 days	-701.5	1.62	24.36
HDG 21 days	-315	0.65	9.69

Tests conducted on the electrochemical systems 21 days after concrete casting indicate rebar passivation. The corrosion potential for the galvanized steel sample is -315 mV, and for the non-galvanized steel sample is -313.5 mV. Also, the corrosion current strongly decreases in both rebar types.

As seen in Figure 3, the corrosion current of galvanized rebar is lower 24 hours after concrete casting. During the first 7 days after rebar embedding in concrete, the potential shift toward positive values is stronger (with 722.5 mV). In the same time, the corrosion current decreases. According to this data, most of the passive layer forms during this period of time. Experimental results show that the passive layer does not form during the first 24 hours from the rebar embedding in concrete. During the time interval between day 7 and day 21, the corrosion current decrease was lower (0.98 μA/cm^2), even though the corrosion potential shifted significantly toward positive values (386.5 mV).

The changes that occur in the corrosion kinetics of the non-galvanized steel, as shown in Figure 3, are not as significant when compared to the galvanized steel system. The corrosion potential shifts toward positive values, indicating the steel passivation in hardened concrete. The corrosion current also decreases. Although the non-galvanized steel system corrosion current is initially lower compared to the galvanized steel, 21 days later after rebar embedment in concrete, it becomes higher. This shows a higher rate of non-galvanized steel corrosion, 21 days after concrete casting.

Regarding the effectiveness of corrosion protection, the galvanized rebar showed a higher corrosion rate in the first 7 days when compared to the non-galvanized rebar. During the time interval between day 7 and day 21 from rebar embedment in concrete, the corrosion rates of both rebar types reverses. The effectiveness of corrosion protection EP (Scheme 1) becomes positive: 11.45%. This is an indicator of a passive layer formation on the galvanized rebar surface.

If we consider the corrosion rate constant during the first 7 days after rebar embedment in concrete and equal with the initial corrosion rate, the zinc layer thickness would decrease with approximately 34 μm. If we consider the corrosion rate constant during the first 7 days after rebar embedment in concrete and equal to the corrosion rate in the 7th day after rebar embedment in concrete, a 0.5 μm zinc layer thickness would have been consumed. As the corrosion rate is not constant during this time interval, the simple arithmetic mean of these two values was calculated. Thus, the consumed zinc layer calculated thickness, of approximately 17 μm, is close to the values found in the literature (10-15 μm) when an efficient passive layer forms on the galvanized rebar surface.

According to data shown in Table 1, neither of the rebar systems reaches the passive state condition 21 days after concrete casting. According to Table 1, the corrosion potential of the HDG electrochemical system, 21 days after concrete casting (HDG 21), indicates a lower rebar corrosion, close to passivation state, while the corrosion potential of the N 21 system, indicates a higher rebar corrosion (50%).

CONCLUSIONS

The conclusions from experimental data are:

1. Zinc surface activates after galvanized steel rebar embedment in fresh concrete. This is evidenced by the corrosion current density recorded using chronoamperometric method and by the kinetic parameters recorded using the linear polarization method. All the experimental values found decreased with time (hours, days) after galvanized rebar embedding in fresh concrete.

2. The studied parameters decrease with time was due to a passive layer formation on the galvanized rebar surface, which inhibits corrosion process. Additional testing of passive layer was not conducted, considering it was as described/ in accordance with literature.

3. The galvanized steel rebar surface showed an initial higher activation compared to the non-galvanized steel rebar. However, it displayed a faster and stronger passivity. Thus, the corrosion potential shift toward positive values was more significant (1109 mV) for the galvanized sample, compared to the non-galvanized sample corrosion potential (316.5 mV). Also, the galvanized steel rebar corrosion rate decreased in time from higher values (911.9 μm/year) compared to the non-galvanized steel rebar corrosion rate (of 227.2 μm/year) to lower values (9.7 μm/year) compared to the non-galvanized rebar (10.9 μm/year).

Initially, the HDG steel surface strongly activates due to contact with alkaline concrete. Corrosion products form on the galvanized surface, with passivation role, as shown by the corrosion potential shifting toward positive values and by the corrosion current and corrosion rate values decrease. Twenty-one days after both reinforcement types embedment, the kinetic parameters show a much more reduced corrosion of HDG rebars corrosion compared to non-galvanized rebars.

EXPERIMENTAL SECTION

The electrochemical cell used, as shown in Figure 4, has the following components: the working electrode (the rebar), the reference electrode - $Cu/CuSO_4$, and the graphite counter electrode, all embedded in the fresh concrete matrix. All the experiments were conducted on the same concrete type; using PC 52 ø8 mm reinforcement, and using hot dip galvanized (HDG) or non-galvanized (N) rebar samples.

The reinforcement rods were galvanized by immersion in a hot galvanizing bath at a temperature of 450°C, thus obtaining a 140 μm thick zinc layer. The coating thickness obtained through hot dip galvanizing was determined by electromagnetic method, using a PHYNIX – Surfix device, and by testing the coating dissolution, according to SR ISO 1460 and SR EN ISO 2178.

The samples were built by introducing the three electrodes (working electrode, reference electrode and counter electrode) in fresh concrete (right after concrete preparation). The samples were kept in laboratory conditions until testing.

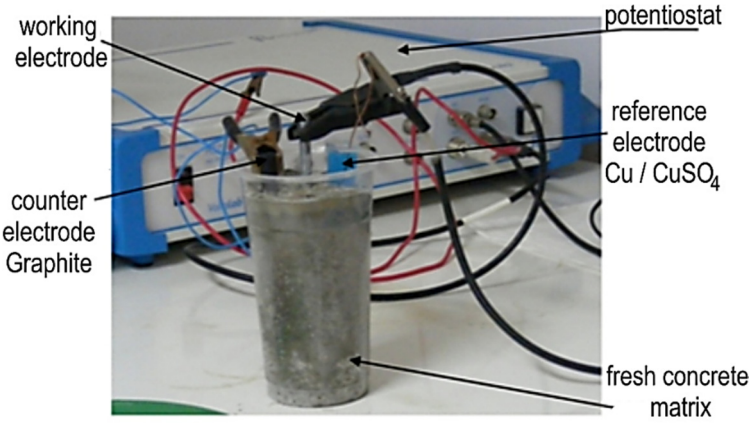

Figure 4. The electrochemical cell

The C 20/25 class concrete was prepared according to the mix design shown in Table 2, according to NE 012-2007 normative. The CEM I 42.5N cement used had the oxide composition as shown in Table 3.

The built electrochemical systems were coded as following:

(HDG x) – Hot dip galvanized steel rebar in concrete; tested x days after rebar embedment in concrete;

(N x) – Non-galvanized steel rebar in concrete, tested x days after rebar embedment in concrete.

Table 2. The concrete used for samples building, submitted to electrochemical testing

The basic components for 1 m^3 concrete		[Kg/ m^3 concrete]
Water		123
CEM I 42.5N cement		308,3
Total of aggregates		1869
Size of aggregates used [mm]	0-4 mm	1121,4
	4-8 mm	747,6

Table 3. The oxide composition of the cement used for the concrete preparation

No.	Cement type	Oxide composition [%]										
		P.C.	SiO_2	Al_2O_3	Fe_2O_3	CaO	MgO	K_2O	Na_2O	TiO_2	SO_3	Cl^-
1	CEM I 42.5 N	2.05	15.06	6.23	3.5	61.9	7.0	1.0	0.25	0.31	2.58	0.015

Information regarding the process kinetics is obtained by analyzing the chronoamperometry curves at the constant potential of 500 mV (vs. Cu/CuSO4). The current density was recorded every 60 seconds for 24 hours at various concrete maturation stages (1 day, 7 days, 21 days after rebar embedment in concrete).

Quantitative information was obtained using linear polarization. The potential scanned with a rate of 2 mV/sec, for ±300 mV compared to the open circuit potential, at room temperature. Based on the Tafel experimental plots, the main kinetic indicators were recorded (corrosion potential, corrosion current and corrosion rate). The experiments were conducted after various numbers of days since rebar embedment in concrete (immediately after, and 1, 7 and 21 days after rebar embedment in concrete).

The effectiveness of corrosion protection offered by hot dip galvanization method for each time period after the concrete preparation was calculated using equation (1)

$$\mathrm{EP} = \frac{v_{cor.}^{N} - v_{cor.}^{ZT}}{v_{cor.}^{N}} * 100[\%] \quad (1)$$

where:
$v_{cor.}^{N}$ = non-galvanized steel corrosion rate, [mm/year];
$v_{cor.}^{ZT}$ = galvanized steel corrosion rate, [mm/year].

ACKNOWLEDGMENTS

This paper was supported by the project “Improvement of the doctoral studies quality in engineering science for development of the knowledge based society-QDOC” contract no. POSDRU/107/1.5/S/78534, project co-funded by the European Social Fund through the Sectorial Operational Program Human Resources 2007-2013.

REFERENCES

1. M.C. Alonso, I. Martinez, J. Fullea, V. Ibarra, In-situ monitoring of galvanised reinforced concrete structures. The Spanish experience, INTERGALVA, Madrid **2009**.
2. C. Andrade, C. Alonso, *Constr Build Mater*, **1996**, *10*(5), 315.
3. C. Andrade, C. Alonzo, Electrochemical Aspects of Galvanized Steel, in Galvanized Steel Reinforcement in Concrete, Elsevier, Editor S.R. Yeomans, **2004**, 111.
4. T. Belleze, M. Malavolta, A. Quaranta, N. Ruffini, G Roventi, Corrosion behavior in concrete of three differently galvanized steel bars, Cement & Concrete Composites, **2006**, 28.
5. M. Carbucicchio, R. Ciprian, F. Ospitali, G. Palombarini, *Corrosion Science,* **2008**, *50* (9), 2605.

6. I. Cornet, B. Bresler, Galvanized reinforcement for concrete – II, International Lead Zinc Research Organization, New York, **1981**, 1.
7. J.A.A. Gonzàlez, *British Corrosion Journal,* **1982**, *17*(1), 21.
8. I. Lingvay, Coroziunea provocata de curenții de dispersie vagabonzi, Ed. Electra, București, **2005**, *25*, 113.
9. C. Mircea, Durabilitatea elementelor și structurilor de beton precomprimat-http://www.incerc cluj.ro, iunie **2005**, 7.
10. V. Nicolau, Betonul armat, Ed. Tehnică, București, **1962**, 7, 25, 93, 108, 163.
11. I. Nicula, T. Oneț, Beton armat, Ed. Didactica și Pedagogică, București, **1982**, *5*, 40.
12. T. Visan, Electrochimie si coroziune pentru doctoranzii ELCOR, Ed. PRINTECH, Bucuresti, **2002.**
13. S.R. Yeomans, Galvanized Steel in Reinforced Concrete, Elsevier B.V., Amsterdam, **2004**, 297.
14. S.R. Yeomans, Considerations of the characteristics and use of coated steel reinforced in concrete, NISTIR 5211, Univ. New South Wales, Canbera, **2004**.
15. C. Budan, D.N. Stoica, A.M. Cotescu, *Revista Romana de Materiale*, **2010**, *40*(2), 132-140.
16. S.R. Yeomans, *Corrosion*, **1994**, *50*, 72.
17. Andreea Hegyi, H. Vermeșan, G. Vermeșan, V. Rus, Internaționale Conference on Advanced Composites Engineering COMAT Brasov **2010**, 116.
18. Andreea Hegyi, H. Vermeșan, G. Vermeșan, V. Rus, E. Grunwald, Research on the corrosion protection of galvanized rebar in concrete, Jahrbuch Oberflachen technic, band 66, Eugen G. Leuze Verlag, Germania, **2010**, 229.
19. Andreea Hegyi, H. Vermeșan, V. Rus, *International Review of Applied Science & Engineering,* **2010**, *1*(1-2), 45.
20. Andreea Hegyi, V. Rus, C. Bumbuc, H. Vermeșan, *Metalurgia International,* **2011**, *16*, 6, 10.
21. Andreea Hegyi, H. Vermeșan, C. Bumbuc, *Metalurgia International,* **2010**, *15*, 11, 74.